Spectra and Light Curves of Type Ia Supernovae for Probing Dark Energy

Final Report — Sep 2009 – Dec 2012

Applicant/Institution: University of Oklahoma

Street Address: HLD Dept. of Physics and Astronomy, 440 W. Brooks, Rm 100, Norman, OK 73019-2061

Principal Investigator: Edward Baron

Address: HLD Dept. of Physics and Astronomy, University of Oklahoma, 440 W. Brooks, Rm 100, Norman, OK 73019-2061

Telephone Number: 405-325-3961 x36323

Email: baron@ou.edu

Grant Number: DE-FG02-07ER41517

Funding Opportunity Announcement Number: DE-PS02-08ER08-01

DOE/Office of Science Program Office: High Energy Physics

DOE/Office of Science Program Office Technical Contact: Dr. Kathleen Turner

I. SUMMARY

The progress over the course of the grant period was excellent. We went from 3-D test codes to full 3-D production codes. We studied several SNe Ia. Most of the support has gone for the 3 years of support of OU graduate student Brian Friesen, who is now mature in his fourth year of research. It is unfortunate that there will be no further DOE support to see him through to the completion of his PhD.

II. PUBLICATIONS

- D. Branch, L. C. Dang, & E. Baron, *Comparative Direct Analysis of Type Ia Supernova Spectra. V. Insights from a Larger Sample and Quantitative Subclassification*, PASP, (2009), **121**, 238–247.
- P. H. Hauschildt, & E. Baron, *A 3D Radiative Transfer Framework: IV. Spherical & Cylindrical Coordinate Systems*, A&A, (2009) **498**, 981–985.
- E. Baron, P. H. Hauschildt, & B. Chen, *A 3D Radiative Transfer Framework: V. Homologous Flows*, A&A, (2009) **498**, 987–992.
- S. Knop, P. Hauschildt, & E. Baron, *Co-moving frame radiative transfer in spherical media with arbitrary velocity fields II. Large Scale Applications*, A&A, (2009), **501**, 813–820.
- D. Jack, P. H. Hauschildt, & E. Baron, *Time-dependent Radiative Transfer with PHOENIX* A&A, (2009), **502**, 1043–1049.
- Soma De, E. Baron, & P. H. Hauschildt, *On the Hydrogen Recombination Time in Type II Supernova Atmospheres*, MNRAS, (2010), **401**, 2081–2092.
- P. Höflich, K. Krisciunas, A. M. Khokhlov, E. Baron, G. Folatelli, M. Hamuy, M. M. Phillips, N. Suntzeff, L. Wang, *Secondary Parameters of Type Ia Supernova Light Curves*, ApJ (2010), **710**, 444–455.

- P. H. Hauschildt, & E. Baron, *A 3D Radiative Transfer Framework: VI. PHOENIX/3D example applications*, A&A, (2010) **509**, A260000.

- Soma De, E. Baron, & P. H. Hauschildt, *The effects of multi-level atoms, composition, and non-resonant processes on hydrogen recombination: A full radiative transfer calculation*, MNRAS, (2010), in press.

- P. H. Hauschildt, & E. Baron, *A 3D Radiative Transfer Framework: VI. PHOENIX/3D example applications*, A&A, (2010) **509**, A260000.

- Soma De, E. Baron, & P. H. Hauschildt, *Hydrogen Recombination with Multilevel atoms*, MNRAS, (2010), **403**, 936–946.

- S. James & E. Baron, *Searching for Hydrogen in Type Ib Supernovae*, ApJ, (2010), **718**, 957–962.

- A. Seelmann, P. H. Hauschildt, & E. Baron, *A 3D Radiative Transfer Framework: VII. Arbitrary Velocity Fields in the Eulerian Frame*, A&A, (2010) **522**, A102, 4pp.

- D. Jack, P. H. Hauschildt, & E. Baron, *Theoretical light curves of type Ia supernovae*, A&A, (2011), **528**, A141, 11pp.

- P. H. Hauschildt, & E. Baron, *A 3D radiative transfer framework: VIII. OpenCL implementation*, A&A, (2011), **533**, A127, 6pp.

- D. Jack, P. H. Hauschildt, & E. Baron, *Near-infrared light curves of type Ia supernovae*, A&A, (2012), **538**, A132, 5pp.

- D. Jack, P. H. Hauschildt, & E. Baron, *A 3D radiative transfer framework: IX. Time Dependence*, A&A, (2012) **546**, A39.

- E. Baron, P. Höflich, K. Krisciunas, I. Dominguez, A. Khokhlov, M. Phillips, N. Suntzeff, & L. Wang, *A Physical Model for SN 2001ay, a normal, bright, extremely slow declining Type Ia supernova*, ApJ, (2012) **753**, 105, (10pp).

- Brian Friesen, E. Baron, David Branch, Bin Chen, Jerod T. Parrent, R. C. Thomas, *Supernova Resonance–scattering Line Profiles in the Absence of a Photosphere*, ApJS, (2012) **203**, 12.

- Bin Chen, Xinyu Dai, & E. Baron, *Inclination-Dependent AGN Flux Profiles From Strong Lensing of the Kerr Space-Time*, ApJ, (2012), in press.

- E. Baron, P. H. Hauschildt, B. Chen, & S. Knop, *A 3D radiative transfer framework: X. Arbitary Velocity Fields in the Co-Moving Frame*, A&A, 2012, textbf548, A67, 9pp.

- A. Berkner, P. H. Hauschildt, & E. Baron, *3D Radiative Transfer Effects in Parametrized Starspots*, A&A, **in press**

III. TALKS

- E. Baron, "Measuring the Universe with Supernovae", International Year of Astronomy Public Talk, Sam Noble Museum of Natural History, Norman, OK, Sep 3, 2009.

- E. Baron, "Measuring the Universe with Supernovae", Astronomy Club of Tulsa, Tulsa Community College, Tulsa, OK, Feb. 26, 2010.

- E. Baron, "Understanding Hydogen in Type Ib Spectra", Fourth Meeting of the 3rd Coast Astronomical Society, Tallahassee, FL, May 20, 2010.

- Soma De, "Time dependent radiative transfer using `PHOENIX` and its application dton core collapse SNe and cosmic recombination", 215th AAS meeting, Washington, DC January 4–7, 2010.

- Soma De, "Time dependent radiative transfer using `PHOENIX` and its application dton core collapse SNe and cosmic recombination", Aspen Winter meeting on the high redshift universe, Aspen, CO, February 7–13, 2010.

- Soma De, "Time dependent radiative transfer using `PHOENIX` and its application dton core collapse SNe and cosmic recombination", Seminar at University of Maryland,

College Park, MD, April 5, 2010.

- Soma De, "Time dependent radiative transfer using `PHOENIX` and its application dton core collapse SNe and cosmic recombination", Seminar at Space Telescope Science Institute, Baltimore MD, April 8, 2010.

- Soma De, "Time dependent radiative transfer using `PHOENIX` and its application dton core collapse SNe and cosmic recombination", Seminar at Caltech, Pasadena, CA, April 19, 2010.

- Soma De, "Time dependent radiative transfer using `PHOENIX` and its application dton core collapse SNe and cosmic recombination", Seminar at CfA-Harvard, Cambridge, MA, April 22, 2010.

- "Hydrogen in Type Ib Supernovae", Contributed talk Progenitors and environments of stellar explosions, Paris, France, June 28, 2010.

- "Generalized 3-D Radiative Transfer for Astrophysical Atmospheres", Invited talk, Cool Stars 16, Aug 30, 2010.

- "On Using Type Ia Supernovae as Cosmological Probes", Colloquium at Trieste Astronomical Observatory (INAF/OATS) and the Astronomy Unit of the Physics Dept. of the Trieste University (UNI/TS), April 27, 2011.

- GrK Lectures on Radiative Transfer, Hamburger Sternwarte, Hamburg, 2011

- "On Using Type Ia Supernovae as Cosmological Probes", SFB Colloquium at DESY, Hamburg, Germany June 29, 2011.

- "Introduction to Radiative Transfer", Summer School of Antartic Astronomy, Chinese Academy of Sciences, Beijing, China, August, 2011.

- "Using Quantitative Spectroscopy to Understand Core Collapse Progenitor Systems", Seminar at University of Basel, Basel, Switzerland, September, 2011.

- "The Melding", Seminar Discussion, SNe Ia Infrared Workshop, Pitt PACC, University of Pittsburgh, March 30, 2012.
- "An Overview of Quantitative Supernova Spectroscopy", Northern Astrophysics Colloquium, Hamburg, Germany July 8, 2011.
- "SNe Ia Theory: The Explosion Zoo", Invited Talk, SNe Ia Infrared Workshop, Pitt PACC, University of Pittsburgh, March 29, 2012.
- "The Melding", Invited Talk/Discussion, SNe Ia Infrared Workshop, Pitt PACC, University of Pittsburgh, March 30, 2012.
- "A Physical Model for SN 2001ay", Invited Talk, Cook's Branch Meeting on Astronomy: Supernova Cosmology and Looking into the Future Montgomery, TX, April 13, 2012.

IV. PUBLISHED PAPERS

Publications of the Astronomical Society of the Pacific, **123**:765–776, 2011 July

Comparative Analysis of Peculiar Type Ia 1991bg-like Supernovae Spectra

Brandon A. Doull and E. Baron

Homer L. Dodge Department of Physics and Astronomy, The University of Oklahoma, Norman, Oklahoma; doull@nhn.ou.edu

Received 2011 April 7; accepted 2011 May 16; published 2011 June 14

ABSTRACT. Spectroscopic analyses of Type Ia supernovae have shown that there exist four spectroscopic groups—cool, broad line, shallow silicon, and core normal—defined by the widths of the Si II features λ5972 and λ6355. The 1991bg-like SNe Ia are classified as "cool." Cool SNe Ia are dim, undergo a rapid decline in luminosity, and produce significantly less ^{56}Ni than normal Type Ia supernovae. They also have an unusually deep and wide trough in their spectra at around 4200 Å and a relatively strong Si II absorption attributed to λ5972. We examine the spectra of supernova (SN) 1991bg and the cool SN 1997cn, SN 1999by, and SN 2005bl using the highly parameterized synthetic spectrum code SYNOW, and we find general agreement with similar spectroscopic studies. Our analysis reveals that this group of supernovae is fairly homogeneous, with many of the blue spectral features well fit by Fe II. The nature of the spectroscopic commonalities and the variations in the class are discussed. Finally, we examine intermediates such as SN 2004eo and discuss the spectroscopic subgroup distribution of Type Ia supernovae.

Online material: color figures

1. INTRODUCTION

Type Ia supernovae (hereafter SNe Ia) are important objects in the study of nucleosynthesis, stellar evolution, and modern cosmology. It is believed that SNe Ia are thermonuclear explosions of carbon-oxygen white dwarfs that have approached to within about 1% of the Chandrasekhar mass (1.39 $M_{\odot}$) (Hillebrandt & Niemeyer 2000; Höflich et al. 2010). In cosmology, SNe Ia were suggested early on (Baade 1938) to be useful as standard candles for making accurate distance measurements in the determination of cosmological parameters, because of both their significant homogeneity in absolute bolometric magnitude and large apparent brightness. With modern supernova surveys such as the Supernova Cosmology Project, ESSENCE Supernova Survey, Nearby Supernova Factory, Palomar Transient Factory, Supernova Legacy Survey, and the Large Synoptic Survey Telescope, accurate measurements of these parameters based on SNe Ia at varying redshifts have been and continue to be made (Perlmutter et al. 1999; Wood-Vasey et al. 2007; Miknaitis et al. 2007; Copin et al. 2006; Law et al. 2009; Conley et al. 2011; Abell et al. 2009). It has even been possible to measure the rate of expansion of the universe and put limits on cosmological models (Riess et al. 1998; Goobar et al. 2000; Wood-Vasey et al. 2007; Riess et al. 2009; Hicken et al. 2009; Chuang & Wang 2011; Parkinson et al. 2010). It is because of this important role SNe Ia play that a deep understanding of their properties, variations, and evolution is vital.

In our study we have narrowed our focus to the "cool" spectroscopic subgroup, epitomized by SN 1991bg that occurred in NGC 4374, and so-called "intermediates" that could potentially bridge the gap between the four spectroscopic subgroups. We used the highly parameterized synthetic spectrum code SYNOW to model the spectra of several cool SNe Ia. To better understand the SYNOW code and its use, see Branch et al. (2007, 2003, 2002), and for more in-depth technical details, see Fisher (2000). The spectra range from a few days before B maximum to as late as one month after B maximum in the optical spectra with wavelengths from the Ca II H and K features in the blue to the Ca II infrared triplet. The spectra have been corrected for redshift of their host galaxies and normalized to remove the slope of the continuum, as we are primarily interested in spectral features for making line identifications. This normalization, described in Jeffery et al. (2007), also serves to facilitate the comparisons between different supernovae. Extremely noisy spectra have been smoothed using boxcar smoothing.

In § 2 the method of spectroscopic subclassification is discussed. In § 3 the properties, progenitors, and possible explosion mechanisms of 1991bg-like SNe Ia are reviewed, and in § 4 our line identifications are given and compared with similar studies. In § 5 we discuss the potential of intermediates to fill in the gaps between the seemingly discrete subgroups.

2. SPECTROSCOPIC SUBGROUPS

For decades, SNe Ia had been accepted for use as standard candles based on their apparent homogeneity, but in 1991 two very peculiar supernovae, SN 1991bg (Filippenko et al. 1992a; Leibundgut et al. 1993) and SN 1991T (Waagen et al. 1991; Filippenko et al. 1992b) challenged the validity of such use.

According to work completed by Li et al. (2001) and recently updated (Li et al. 2010) the peculiarity rate for SNe Ia could be as high as 30%, with rates of 1991bg-like SNe Ia up to 15%. These observed peculiarities instigated the search for parameters that could be used to find a photometric and spectroscopic standard relation, in order to make SNe Ia standardizable candles.

The first relation was found by Phillips (1993), who used a small sample of well-observed SNe Ia to identify a very strong correlation between peak luminosity and initial decline rates, parameterized by Δm_{15}. The Δm_{15} parameter measures the decline in brightness of the B band from maximum until 15 days after maximum. The Phillips relation indicates that brighter objects will have slower decline rates than dim objects, which decline rapidly. An analogous spectroscopic relation was suggested by Nugent et al. (1995). Nugent's spectral relation measures the ratio of the strength of the Si II features λ5972 and λ6355, denoted by $\mathcal{R}$ (Si II). The standard relations, both photometric and spectroscopic, are due in large part to temperature differences caused by the amount of radioactive ^{56}Ni synthesized during the explosion.

Single-parameter modeling of SNe Ia is indeed useful, but in cases of extremely peculiar SNe, such as SN 1991bg and SN 1991T, other means of accurate and efficient subclassification are necessary. Several such classification schemes exist. One scheme proposed by Benetti et al. (2005) is based on the evolution of Si II λ6355 line velocity, while another, proposed by Branch et al. (2006), uses the pseudo–equivalent widths of the Si II lines λ5972 and λ6355.

By measuring the velocity of Si II λ6355 10 days past B maximum as well as the evolution of the velocity of this feature, Benetti et al. (2005) found not only a spread in velocities between different SNe Ia, but also a distribution in velocity gradients. Plotting these gradients reveals three groups of SNe Ia that Benetti et al. (2005) labels as faint, high temporal velocity gradient (HVG), and low temporal velocity gradient (LVG) (Benetti 2005; Benetti et al. 2005). The faint subgroup corresponds to subluminous 1991bg-like events with low expansion velocities and a large velocity gradient. The HVG group contains normal SNe Ia with high expansion velocities and a high velocity gradient. Finally, the LVG group contains both normal SNe Ia and the brightest SNe Ia. This group has, on average, lower expansion velocities than the HVG group and a low velocity gradient.

In the scheme of Branch et al. (2006), the pseudo–equivalent widths of Si II lines λ5972 and λ6355 are measured and plotted (since emission lines are present in the spectra, these are not true equivalent widths, but rather widths whose limits of integration have been chosen by eye). We followed the example of Branch et al. (2006) and plotted the width of the λ5972 feature versus the width of the λ6355 feature for a sample of SNe Ia. This plot can be seen in Figure 1 and shows a cluster of core-normal (CN) SNe Ia with three discrete branches representing the peculiar

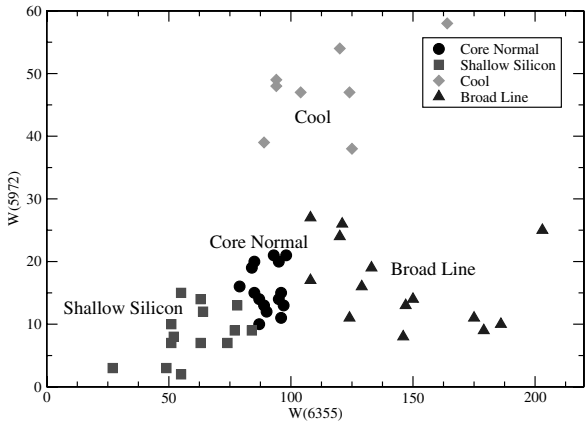

FIG. 1.—Pseudo–equivalent widths of λ5972 vs. λ6355. Data come from Branch et al. (2009) and Branch (2011, private communication). See the electronic edition of the *PASP* for a color version of this figure.

spectroscopic subgroups of cool (CL), broad line (BL), and shallow silicon (SS). The cool SNe correspond to Benetti's faint, BL tend to fall into the HVG group, and the LVG contains both CN and SS.

In this method, each of the spectroscopic subgroups have their own differing properties and are named accordingly. Core-normal SNe are the most common and well-studied SNe Ia and are found in the region of highest density in the pseudo–equivalent width (W-W) plot of Figure 1. SN 1994D is an example of a CN Type Ia. BL SNe Ia have Si II lines whose absorptions are broader and deeper than core-normal SNe and thus form the lower right branch of the W-W plot in Figure 1. The SNe Ia in the BL subgroup generally have the same ions that are present in CN, but with higher velocities. One such BL Type Ia is SN 2002bo (Branch et al. 2006). The SS SNe fall to the lower left of the plot in Figure 1 because of their smaller values for Si II widths, but otherwise they have normal SNe Ia spectra. (The cool SNe will be discussed in depth in § 3.) Although the plot indicates that there are separate spectroscopic subgroups, the borders are not defined by a clear demarcation; instead, some overlap exists. We call the SNe Ia that lie between different subgroups "intermediates."

3. COOL TYPE Ia SUPERNOVAE

Spectroscopically peculiar SNe Ia that fall into the cool subgroup share several distinct characteristics. Most notably, cool SNe are subluminous. SN 1991bg had V and B maxima that were 1.6 and 2.5 mag, respectively, lower than ordinary SNe Ia (Filippenko et al. 1992a). The cool SNe also have much faster declines from peak luminosity than do core-normal SNe. Typically, cool SNe have $\Delta m_{15}(B) \approx 1.9$, while core-normal SNe have $\Delta m_{15}(B) \approx 1.1$ (Taubenberger et al. 2008). Light curves

of SN 1991bg and SN 1994D can be found in Figure 2 showing appropriate $\Delta m_{15}(B)$ values. It has been established that ^{56}Ni production is fundamental to determining SNe Ia peak luminosities (Arnett et al. 1985; Branch & Tammann 1992). Analyses of SN 1991bg and other cool SNe have indicated ^{56}Ni production of only about one-sixth of the amount synthesized during a normal event (Mazzali et al. 1997). Spectroscopically, we see primarily that cool SNe have an unusually deep and wide absorption trough at around 4200 Å and a very strong Si II λ5972 absorption, as shown in Figure 3. The 4200 Å trough is well fit by Ti II, which can be explained by its low excitation temperature and the cool nature of these SNe Ia (Filippenko et al. 1992a; Mazzali et al. 1997). Finally, cool SNe also have a strong and narrow absorption at about 5675 Å, usually attributed to Na D λ5893 (Filippenko et al. 1992a; Garnavich et al. 2004).).

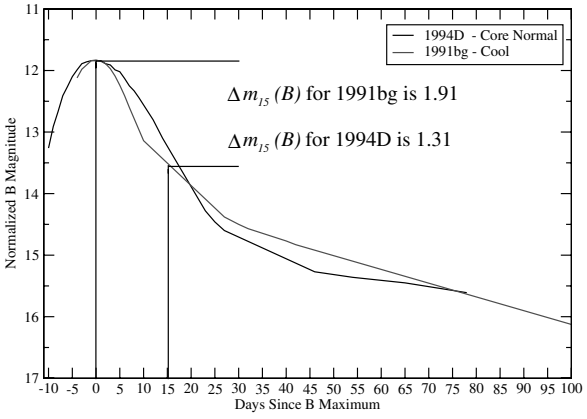

FIG. 2.—CN vs. CL cecline rate comparisons. The Δm_{15} values originate from Pastorello et al. (2007), light-curve data for 1991bg come from Turatto et al. (1996), and light-curve data for 1994D come from Patat et al. (1996). See the electronic edition of the *PASP* for a color version of this figure.

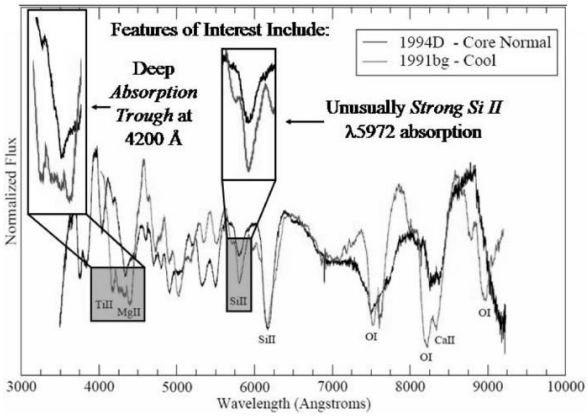

FIG. 3.—CN vs. CL spectra comparisons. See the electronic edition of the *PASP* for a color version of this figure.

3.1. Progenitors

To date, many theories and models have been proposed in attempts to describe the progenitors that lead to SNe Ia, as well as to account for their diversity. Two common scenarios leading to SNe Ia are generally accepted. One scenario is a single degenerate (SD) case proposed by Whelan & Iben (1973) in which a white dwarf (WD) accretes mass until the Chandrasekhar mass ($M_{\rm Ch}$) is approached, igniting carbon in the core, undergoing thermonuclear instability, and ending with the complete disruption of the WD. A competing scenario proposed by Iben & Tutukov (1984), as well as Webbink (1984), involves two orbiting WDs, where loss of angular momentum due to the emission of gravitational waves leads to an inspiral and eventual merger. The merger of two WDs is referred to as double degenerate (DD). Extensive work has been done to investigate how either a SD scenario or a DD scenario can possibly explain both the homogeneity of SNe Ia while at the same time account for the observed diversity.

SNe Ia appear to be homogeneous because the structure of the WD progenitor and the explosion is determined by nuclear physics (Höflich et al. 2010). That is, the WD is supported by degenerate electron pressure, thermonuclear energy gives the energy production during explosion, and light curves are driven by the decay of synthesized radioactive ^{56}Ni. According to Höflich (2006), the aspects most important to understanding the diversity are the conditions just prior to explosion and the type of burning mechanism. The basic types of burning can be distinguished as detonation and deflagration. Deflagration occurs with a burning front propagating due to heat transport across the front at a speed of 0.5–0.8% of the speed of sound (Timmes & Woosley 1992). On the other hand, in detonations compressional heat ignites carbon and oxygen in front of a shock that propagates supersonically (Höflich 2006).

SD models using delayed detonation—a process where deflagration occurs followed by a transition to detonation—show promise in reproducing observations (Khokhlov 1991). Varying the amount of preexpansion and burning during the deflagration phase, as well as a few other secondary parameters, can explain the diversity among SNe Ia in a SD scenario (Hoeflich et al. 1993; Höflich et al. 2010). Namely, Höflich et al. (2010) decreases the density where transition from deflagration to detonation occurs and in so doing reduces the amount of ^{56}Ni synthesized, thus producing subluminous SNe Ia. It should be noted that the trigger for transition from deflagration to detonation is still not fully understood. When considering the DD scenario, recent work using the smoothed particle hydrodynamics code GADGET3 shows promise in reproducing subluminous SNe Ia, akin to 1991bg-like SNe Ia (Pakmor et al. 2011, 2010). They find that this type of merger reproduces

the observed results and may be a path to the production of 1991bg-like SNe Ia.

Another method used to investigate SNe Ia progenitors is population synthesis. Through this method, the observed delay time distribution (DTD) of SNe Ia can be used to place limits upon progenitor models and formation scenarios. Taking an observational approach, Maoz & Badenes (2010) derive the SN rates and DTD using supernova remnants in the Magellanic Clouds. Maoz & Badenes (2010) find that DTD is proportional to t^{-1}, in agreement with the DD DTD found from population synthesis of DD. Maoz et al. (2011) also confirm this DTD result using star formation history. The general findings of population synthesis are that neither channel, SD or DD, can produce the observed number of SNe Ia (Ruiter et al. 2009; Mennekens et al. 2010). Mennekens et al. (2010), using the Brussels population synthesis code, find that the morphological shape of the observed DTD cannot be fit by the SD scenario alone. Instead, a combination of both SD and DD scenarios will fit the morphological shape but produces approximately three times fewer SNe Ia than are observed. A similar study by Ruiter et al. (2009), using the population synthesis code `StarTrack`, also finds that the combination of SD and DD scenarios fits the observed shape of DTD, but accounts for 10 times fewer SNe Ia than are observed. Population synthesis would then seem to indicate that neither scenario alone can produce the morphological shape of the DTD and that even the combination of both cannot produce the absolute number of observed SNe Ia.

4. LINE IDENTIFICATIONS IN COOL GROUP

We begin our analysis of CL SNe Ia by making line identifications. Identifying lines in SNe can be a difficult process and is further complicated in cool SNe due to the large number of ions with lower excitation temperatures and many metals that potentially are present as blends in the 4200 Å trough. Our sample contains spectra from SN 1991bg, SN 1997cn, SN 1999by, and SN 2005bl. We find the nine ions—O I, Na I, Mg II, Si II, S II, Ca II, Ti II, Cr II, and Fe II—of varying strengths and levels of stratification fit most of the observed spectral features well for all epochs considered with a 10th ion, Ca I, present in the early spectra.

All with respect to B maximum, we will make comparisons of five subsets of spectra from different epochs. In § 4.1 we compare SN 1999by and SN 2005bl at day -3. The observed and synthetic spectra for this comparison are shown in Figure 4 and the fitting parameters are listed in Tables 1 and 2. In § 4.2 we analyze the spectra of SN 1991bg, SN 1997cn, SN 1999by, and SN 2005bl just past B maximum. These spectra can be found in Figures 5 and 6, with fitting parameters listed in Tables 3–6. Synthetic spectra and line identifications for SN 1991bg at day 18 and SN 2005bl at day 19 are summarized in § 4.3 and displayed in Figure 7, with fitting parameters listed in Tables 7 and 8. In § 4.4, spectra from approximately one month after B maximum for SN 1991bg, SN 1997cn, and

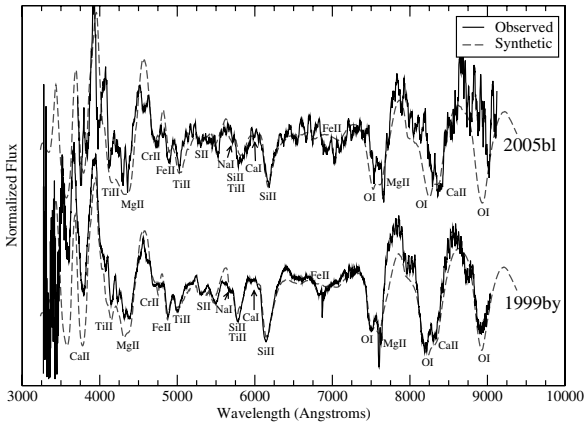

FIG. 4.—2005bl and 1999by day 3 before B maximum. The telluric oxygen feature at 7594 Å is not marked. See the electronic edition of the *PASP* for a color version of this figure.

SN 1999by are discussed. The spectra at this epoch are plotted in Figures 8 and 9, with fitting parameters displayed in Tables 9–13. A great deal of spectroscopic analysis has been performed on SN 1991bg by Filippenko et al. (1992a), Leibundgut et al. (1993), Turatto et al. (1996), Mazzali et al. (1997), and Branch et al. (2006, 2008, 2009). Turatto et al. (1998) have analyzed SN 1997cn. Garnavich et al. (2004) and Höflich et al. (2002) considered SN 1999by. Taubenberger et al. (2008) and Hachinger et al. (2009) performed an analysis of SN 2005bl.

4.1. Day 3 Before *B* Maximum Spectra

The day -3 spectra are presented in Figure 4. The SYNOW spectra for SN 1999by and SN 2005bl are overplotted with their respective observed spectra, and spectral absorptions are labeled. The synthetic spectra parameters are given in Tables 1 and 2.

TABLE 1
FITTING PARAMETERS FOR 1999BY DAY 3 BEFORE B MAXIMUM

Element	τ	$T_{\rm exc}$ (K)	$v_{\rm phot}$	v_e	$v_{\rm min}$	$v_{\rm max}$
HV_e O I	4.5	7000	11	1.1	0	40
O I	...	...	...	...	...	...
Na I	1.1	7000	11	0.5	12.5	15
Mg II	20	7000	11	1.0	0	40
Si II	550	7000	11	0.5	0	13.5
S II	12	7000	11	0.2	0	40
Ca I	8.0	7000	10	1.0	0	40
Ca II	800	7000	11	1.2	0	40
Ti II	2	7000	11	2.0	0	40
Cr II	600	7000	11	1.0	0	40
Fe II	3.0	5000	11	1.0	0	40

NOTE.—All velocities are given in 1000 km s^{-1}.

TABLE 2
FITTING PARAMETERS FOR 2005BL DAY 3 BEFORE B MAXIMUM

Element	τ	$T_{\rm exc}$ (K)	$v_{\rm phot}$	v_e	$v_{\rm min}$	$v_{\rm max}$
HV_e O I	4.5	7000	10	1.4	0	40
O I	...	...	...	...	...	...
Na I	0.9	7000	10	0.5	12.5	14.5
Mg II	40	7000	10	1.0	0	40
Si II	80	7000	10	0.5	0	40
S II	8.0	7000	10	0.2	0	40
Ca I	8.0	7000	10	1.0	0	40
Ca II	1000	7000	10	1.0	0	40
Ti II	6.0	7000	10	2.0	0	40
Cr II	1200	7000	10	1.0	0	40
Fe II	3.0	7000	10	1.0	0	40

NOTE.—All velocities are given in 1000 km s^{-1}.

The broad absorption trough at 4200 Å, characteristic of the CL subgroup, is well fit by a combination of Ti II and Mg II. This trough is continually fit by both Ti II and Mg II in all modeled spectra. Garnavich et al. (2004), while modeling SN 1999by with SYNOW, find the absorption at 5000 Å to be fit by Mg I, whereas we attribute this feature to Ti II and find no need of Mg I. Both Ti II and Mg I have an absorption at about 5000 Å; however, SYNOW fits with Ti II and without Mg I give accurate fits for this absorption. Mg I, while possibly present, when included is not the main contributor to this feature and has no other absorptions or emissions that can clearly be attributed to it. Thus, we consider the identification of Mg I to not be required. Ti II also contributes to the 5780 Å feature. The 7630 Å feature, blended into the O I triplet, belongs to Mg II. For these reasons Ti II and Mg II can be considered definite. Other definite

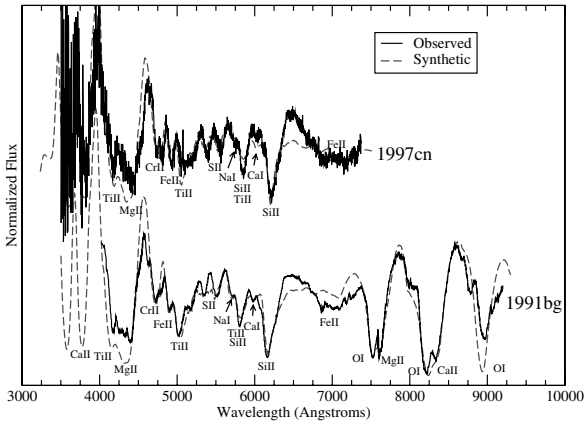

FIG. 5.—1997cn day 3 after B maximum and 1991bg day 2 after B maximum. The telluric oxygen feature at 7594 Å is not marked. See the electronic edition of the *PASP* for a color version of this figure.

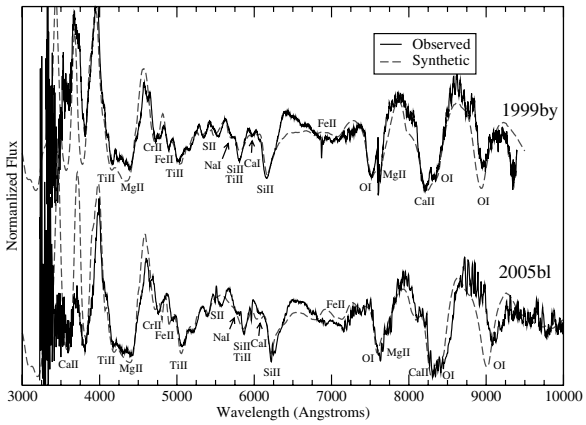

FIG. 6.—1999by day 3 after B maximum and 2005bl day 4 after B maximum. The telluric oxygen feature at 7594 Å is not marked. See the electronic edition of the *PASP* for a color version of this figure.

ions include Si II, Ca II, Fe II, and O I, which all contribute to multiple absorptions.

The other four ions, Ca I, Cr II, S II, and Na I, only contribute to one absorption each and, although quite likely, are not definite. The "W" feature at 5330 Å, often attributed to S II, may also be fit by features due to Sc II; Branch et al. (2006) have indeed produced SYNOW fits with this attribution. Although synthetic fits with Sc II are possible, S II is more likely in the SNe Ia scenario; we discuss this further subsequently. Na I creates a shoulder in the 5650 Å emission and, although very weak in the early spectra, becomes much more conspicuous later. Based on the evolution of multiple epochs, even though Na I is weak early, it is highly likely to be present. Na I is a common identification of this feature in CL SNe Ia (Filippenko et al. 1992a; Garnavich et al. 2004; Taubenberger et al. 2008); however, Mazzali et al. (1997) when using W7 cannot

TABLE 3
FITTING PARAMETERS FOR 1991BG DAY 2 AFTER B MAXIMUM

Element	τ	$T_{\rm exc}$ (K)	$v_{\rm phot}$	v_e	$v_{\rm min}$	$v_{\rm max}$
HV_e O I	5.0	7000	10	1.4	0	40
O I	...	...	...	...	...	...
Na I	0.5	7000	10	1.0	12.5	13.5
Mg II	40.0	7000	10	1.0	0	40
Si II	100	7000	10	0.5	0	40
S II	5.0	7000	10	0.2	0	40
Ca I	15.0	7000	10	1.0	0	40
Ca II	1100	7000	10	1.3	0	40
Ti II	6.0	7000	10	2.0	0	40
Cr II	1500	7000	10	1.0	0	40
Fe II	4.0	7000	10	1.0	0	40

NOTE.—All velocities are given in 1000 km s^{-1}.

TABLE 4
FITTING PARAMETERS FOR 1997CN DAY 3 AFTER B MAXIMUM

Element	τ	T_{exc} (K)	v_{phot}	v_e	v_{min}	v_{max}
HV_e O I	5.0	7000	7.6	1.4	0	40
O I	...	...	...	...	...	...
Na I	0.1	7000	7.6	1.0	10.5	17.5
Mg II	40.0	7000	7.6	1.0	0	40
Si II	30.0	7000	7.6	0.6	0	40
S II	5.0	7000	7.6	0.2	0	40
Ca I	8.0	7000	10	1.0	0	40
Ca II	1100	7000	7.6	1.3	0	40
Ti II	4.0	7000	7.6	2.0	0	40
Cr II	1000	7000	7.6	1.0	0	40
Fe II	6.0	7000	7.6	1.0	0	40

NOTE.—All velocities are given in 1000 km s^{-1}.

TABLE 6
FITTING PARAMETERS FOR 2005BL DAY 4 AFTER B MAXIMUM

Element	τ	T_{exc} K)	v_{phot}	v_e	v_{min}	v_{max}
HV_e O I	...	...	...	...	...	...
O I	4.5	7000	7.6	1.0	0	40
Na I	0.1	7000	7.6	1.0	10	12
Mg II	10.0	7000	7.6	1.0	0	40
Si II	10.0	7000	7.6	0.6	0	40
S II	1.0	7000	7.6	0.2	0	40
Ca I	8.0	7000	10	1.0	0	40
Ca II	800	7000	7.6	1.3	0	40
Ti II	7.0	7000	7.6	2.0	0	40
Cr II	600	7000	7.6	1.0	0	40
Fe II	6.0	7000	7.6	1.0	0	40

NOTE.—All velocities are given in 1000 km s^{-1}.

reproduce this feature without adding extra Na I and modifying their abundance distributions, while Leibundgut et al. (1993) identify it as a blend of Si II. Ca I matches the absorption at 5980 Å in these spectra, but disappears sometime after day 4 after B maximum and before day 18. Garnavich et al. (2004) identifies two Ca I absorptions as late as day 7 in SN 1999by, and Taubenberger et al. (2008) make no Ca I identifications for SN 2005bl. The remaining ion, Cr II, is found at the 4700 Å absorption and further helps to block the emission at 4600 Å, in agreement with Taubenberger et al. (2008), but unidentified by Garnavich et al. (2004).

Aside from Garnavich et al. (2004) identifying Mg I in SN 1999by at 5000 Å instead of Cr II, our other line identifications are in good agreement. An analysis performed by Hachinger et al. (2009) on SN 2005bl identifies small amounts (less than 10% of the mass fraction) of C II, in agreement with Taubenberger et al. (2008), who also find C II. C II is possible, but does not add any benefits to our synthetic fits and, as noted by Hachinger et al. (2009), is a break from other CL SNe Ia such as SN 1991bg and SN 1999by in which C II has not been identified. In fact, C II is more often associated with superluminous, rather than subluminous, SNe Ia (Howell et al. 2006; Hicken et al. 2007; Parrent et al. 2011).

TABLE 5
FITTING PARAMETERS FOR 1999BY DAY 3 AFTER B MAXIMUM

Element	τ	T_{exc} (K)	v_{phot}	v_e	v_{min}	v_{max}
HV_e O I	5.0	7000	10	1.4	0	40
O I	...	...	...	...	...	...
Na I	0.5	7000	10	1.0	12.5	13.5
Mg II	40.0	7000	10	1.0	0	40
Si II	100	7000	10	0.5	0	40
S II	5.0	7000	10	0.2	0	40
Ca I	12.0	7000	10	1.0	0	40
Ca II	1100	7000	10	1.3	0	40
Ti II	6.0	7000	10	2.0	0	40
Cr II	1500	7000	10	1.0	0	40
Fe II	4.0	7000	10	1.0	0	40

NOTE.—All velocities are given in 1000 km s^{-1}.

4.2. Days 2, 3, and 4 After *B* Maximum Spectra

Figures 5 and 6 show the observed and synthetic spectra for SN 1991bg, SN 1997cn, SN 1999by, and SN 2005bl at days 2, 3, 3, and 4, respectively. The spectrum for SN 1997cn ends at 7400 Å, which is before the O I feature and Mg II absorption at 7630 Å; however, these ions are still used in the SYNOW fits, as they contribute to the overall shape of the spectra. The fitting parameters used for these synthetic spectra are given in Tables 3–6.

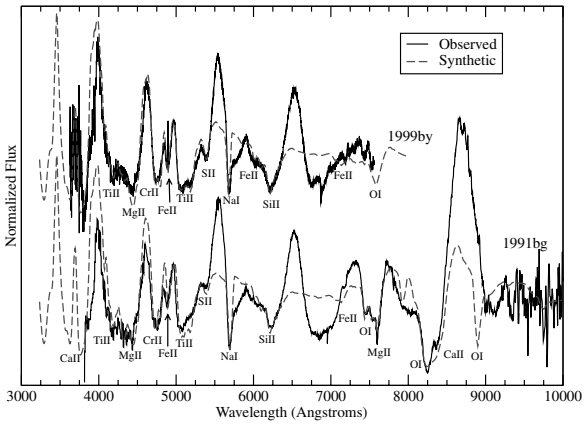

FIG. 7.—1999by day 3 after B maximum with the feature usually attributed to S II fit with both S II and Sc II. The telluric oxygen feature at 7594 Å is not marked. See the electronic edition of the *PASP* for a color version of this figure.

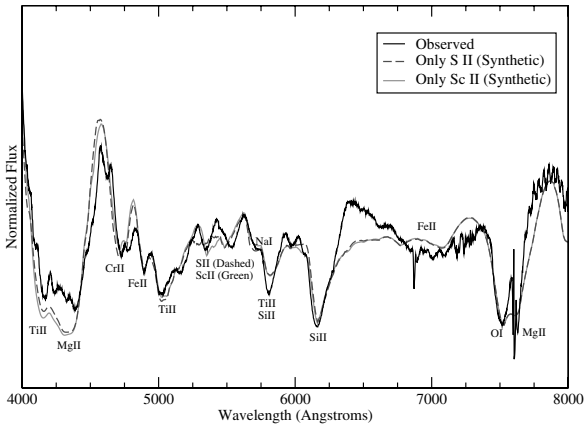

FIG. 8.—2005bl day 19 after B maximum, and 1991bg day 18 after B maximum. See the electronic edition of the *PASP* for a color version of this figure.

As usual, we consider Si II, Ca II, Fe II, and O I to be definitely present for their contribution to multiple spectral features. Also, Ti II and Mg II are definite ions, except in the case of 1997cn, where the Mg II feature at 7630 Å is not available to be modeled. Due to the attribution of Mg II to the absorption trough in SN 1997cn, we still consider it highly likely. Again, Cr II continues to be present at 4700 Å and helps to reduce the emission just blueward of its absorption. We consider the presence of Cr II to be not only plausible, but likely. Further, during these early spectra Ca I fits the absorption at 5980 Å.

In comparison with the analysis by Turatto et al. (1998) on SN 1997cn, we continue to see good agreement, with the primary differences being Ca I and Cr II, which they do not identify. Turatto et al. (1998) also identify Ni II at 4067 Å, which is possible, but we find no benefit in the inclusion of Ni II in our fits.

TABLE 7
FITTING PARAMETERS FOR 1991BG DAY 18 AFTER B MAXIMUM

Element	τ	$T_{\rm exc}$ (K)	$v_{\rm phot}$	v_e	$v_{\rm min}$	$v_{\rm max}$
HV_e O I	2.0	7000	8	1.6	0	40
O I	0.7	7000	8	1.0	15.2	16
Na I	9.0	7000	8	0.5	11	12
Mg II	3.5	7000	8	1.0	12	40
Si II	50	7000	8	0.5	0	40
S II	0.8	7000	8	1.0	14.5	40
Ca II	4000	7000	8	1.3	0	40
Ti II	12	7000	8	1.0	0	40
Cr II	2500	7000	8	1.0	0	40
Fe II	70	7000	8	0.7	0	40

NOTE.—All velocities are given in 1000 km s^{-1}.

TABLE 8
FITTING PARAMETERS FOR 2005BL DAY 19 AFTER B MAXIMUM

Element	τ	$T_{\rm exc}$ (K)	$v_{\rm phot}$	v_e	$v_{\rm min}$	$v_{\rm max}$
HV_e O I	1.0	7000	7.5	1.6	0	40
O I	...	...	...	...	...	...
Na I	3.0	7000	7.5	0.5	11	12
Mg II	2.0	7000	7.5	1.0	12	40
Si II	40	7000	7.5	0.5	0	40
S II	0.7	7000	7.5	1.0	14.5	40
Ca II	4000	7000	7.5	1.0	0	40
Ti II	17	7000	7.5	1.0	0	40
Cr II	2800	7000	7.5	1.0	0	40
Fe II	30	7000	7.5	0.8	0	40

NOTE.—All velocities are given in 1000 km s^{-1}.

Close examination of the fitting parameters given for these SNe in Tables 3–6 will show that both 1997cn and 2005bl have photospheric velocities ($v_{\rm phot}$) of 7600 km s^{-1}, which is significantly lower than 1991bg at 11,000 km s^{-1} and 1999by at 10,000 km s^{-1}. Looking forward to days 18 and 19 we see that 2005bl has a lower gradient in $v_{\rm phot}$ than does 1991bg and differs by only 100 km s^{-1}. By days 28 and 29, the differences in $v_{\rm phot}$ between the SNe are insignificant.

Figure 10 compares the fit of SN 1999by at day +3, using S II and Sc II to fit the "W" feature usually attributed to S II. It is hard to definitively decide between the two fits, and without the strong S II λ6355 line, the identification of SN 1999by as a SNe Ia becomes weaker. This effect is important but needs to be followed up in future work with more detailed spectral modeling.

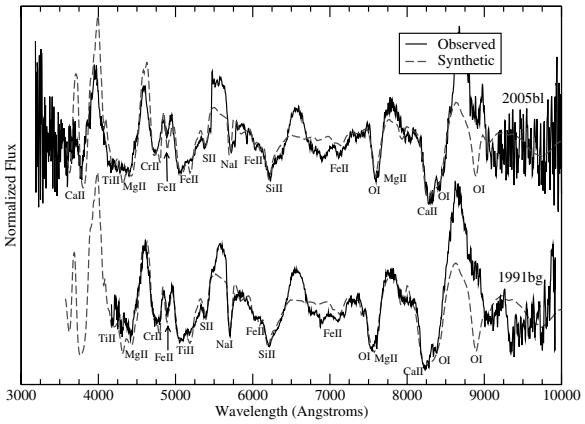

FIG. 9.—1997cn dDay 28 after B maximum, 1999by day 29 after B maximum, and 1991bg day 29 after B maximum. See the electronic edition of the *PASP* for a color version of this figure.

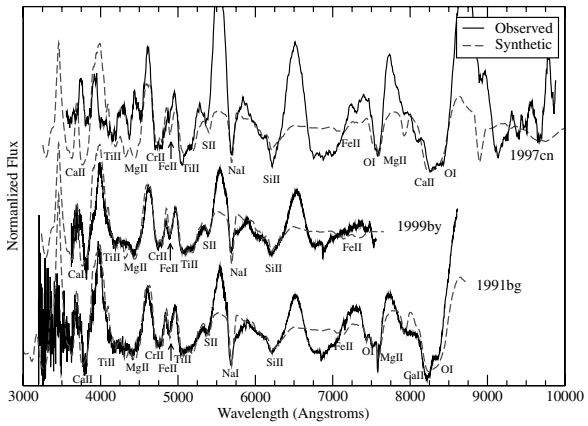

FIG. 10.—1999by day 31 after B maximum and 1991bg day 32 before B maximum. See the electronic edition of the *PASP* for a color version of this figure.

4.3. Days 18 and 19 After *B* Maximum Spectra

All the same ions as discussed in §§ 4.1 and 4.2, except Ca I, are still present by days 18 and 19, but the spectra have several noticeable differences from the early time spectra. (Synthetic and observed spectra for SN 1991bg and SN 2005bl can be seen in Fig. 7.) Primarily, the differences include the ions having deeper absorptions, higher emissions, and lower $v_{\rm phot}$. The most obvious difference is the Na I absorption at 5700 Å, which is no longer just a shoulder in an emission, but a rather strong and sharp absorption. We still find Si II, Ca II, Fe II, Ti II, Mg II, and O I to be definite, whereas Na I is now much more likely. Cr II and S II are plausible for the same reasons as before, and Ca I is no longer used in the synthetic spectra.

4.4. Days 28, 29, 31, and 32 After *B* Maximum Spectra

Figures 8 and 9 have the synthetic and observed spectra for SN 1991bg, SN 1997cn, and SN 1999by, where the absorptions are well fit; however, in the red, the synthetic emissions are weak. This lack of strong emissions can be explained by the assumptions of SYNOW itself. SYNOW assumes a perfect blackbody emitter and absorber with a sharp photosphere surrounded by a homologous and spherically expanding ion cloud, where lines form by resonance scattering treated in the Sobolev approximation. These assumptions do not allow for net emission profiles. Once ions begin to enter net emission, SYNOW can no longer reproduce the strong emission peaks well. To overcome this issue it is possible to greatly increase the optical depth and rescale, but better fits are often obtained simply by leaving these emissions alone and focusing on the absorptions.

The same nine ions are present in these spectra as in the previous, but O I has been strongly stratified to fit the three separate absorptions at about 7530 Å. Furthermore, a deep and wide absorption at around 6700 Å to 7000 Å has appeared. Despite our best efforts, we were unable to fit this trough in a reasonable way. We tried a variety of ions, including C I and O II, which could fill some of the trough, but not without heavy restriction in $v_{\rm min}$ and $v_{\rm max}$. None of the attempts proved successful and we do not find any of these ions to be likely.

TABLE 9
FITTING PARAMETERS FOR 1997CN DAY 28 AFTER B MAXIMUM

Element	τ	$T_{\rm exc}$ (K)	$v_{\rm phot}$	v_e	$v_{\rm min}$	$v_{\rm max}$
HV_e O I	0.6	7000	7.4	1.6	0	40
O I	0.4	7000	7.4	1.0	14	16
Na I	6.0	7000	7.4	0.7	11	40
Mg II	7.0	7000	7.4	1.0	12	13
Si II	10	7000	7.4	0.5	0	40
S II	0.4	7000	7.4	1.0	14	40
Ca II	4000	7000	7.4	1.3	0	40
Ti II	8.0	7000	7.4	1.0	0	40
Cr II	3000	7000	7.4	1.0	0	40
Fe II	50	7000	7.4	0.6	0	40

NOTE.—All velocities are given in 1000 km s^{-1}.

TABLE 10
FITTING PARAMETERS FOR 1991BG DAY 29 AFTER B MAXIMUM

Element	τ	$T_{\rm exc}$ (K)	$v_{\rm phot}$	v_e	$v_{\rm min}$	$v_{\rm max}$
HV_e O I	0.6	7000	7.6	1.6	0	40
O I	0.4	7000	7.6	1.0	14	16
Na I	6.0	7000	7.6	0.7	11	40
Mg II	7.0	7000	7.6	1.0	12	13
Si II	10	7000	7.6	0.5	0	40
S II	0.4	7000	7.6	1.0	14	40
Ca II	4000	7000	7.6	1.3	0	40
Ti II	8.0	7000	7.6	1.0	0	40
Cr II	3000	7000	7.6	1.0	0	40
Fe II	50	7000	7.6	0.6	0	40

NOTE.—All velocities are given in 1000 km s^{-1}.

TABLE 11
FITTING PARAMETERS FOR 1999BY DAY 29 AFTER B MAXIMUM

Element	τ	$T_{\rm exc}$ (K)	$v_{\rm phot}$	v_e	$v_{\rm min}$	$v_{\rm max}$
HV_e O I	0.6	7000	7.6	1.6	0	40
O I	0.4	7000	7.6	1.0	14	16
Na I	3.0	7000	7.6	0.7	11	40
Mg II	7.0	7000	7.6	1.0	12	13
Si II	15	7000	7.6	0.5	0	40
S II	0.4	7000	7.6	1.0	14	40
Ca II	4000	7000	7.6	1.3	0	40
Ti II	8.0	7000	7.6	1.0	0	40
Cr II	3000	7000	7.6	1.0	0	40
Fe II	50	7000	7.6	0.6	0	40

NOTE.—All velocities are given in 1000 km s^{-1}.

TABLE 12
FITTING PARAMETERS FOR 1999BY DAY 31 AFTER B MAXIMUM

Element	τ	T_{exc} (K)	v_{phot}	v_e	v_{min}	v_{max}
HV$_e$ O I	0.6	7000	7.5	1.6	0	40
O I	0.1	7000	7.5	1.0	0	40
Na I	3.5	7000	7.5	0.6	12	40
Mg II	0.1	7000	7.5	1.0	12	13
Si II	10	7000	7.5	0.6	0	40
S II	0.4	7000	7.5	1.0	14.5	40
Ca II	4000	7000	7.5	1.3	0	40
Ti II	7.0	7000	7.5	1.0	0	40
Cr II	3300	7000	7.5	1.0	0	40
Fe II	35	7000	7.5	0.8	0	40

NOTE.—All velocities are given in 1000 km s^{-1}.

5. INTERMEDIATE TYPE Ia SUPERNOVAE

Figure 11 is another W-W plot that is very similar to Figure 1, but in this W-W plot, intermediates are included. Intermediates are SNe Ia that do not necessarily fall into any particular subgroup; instead, they fall in-between, sharing properties of the different subgroups. What we find when including the intermediates is that the subgroups begin to blend, indicating that rather than being discrete, SNe Ia subgroups, as delineated by Branch et al. (2006), are a continuous distribution based on multiple parameters. Branch et al. (2006, 2009) did extensive work on spectroscopic subclassification of SNe Ia and came to a similar conclusion.

Recent work of Maeda et al. (2010) indicates that some of the spectral diversity of SNe Ia is a result of the viewing angle on an asymmetrically exploding WD progenitor. Maeda et al. (2010) used the Benetti classification scheme of faint, HVG, and LVG. Using the emission lines Fe II λ7155 and Ni II λ7378 lines, which occur during the nebular phase, they measured the Doppler shift in the ejecta. Blueshifted lines will be on the near side and redshifted will be on the far side of an exploding SN. They found a diversity in the velocities of the blueshifted and

TABLE 13
FITTING PARAMETERS FOR 1991BG DAY 32 AFTER B MAXIMUM

Element	τ	T_{exc} (K)	v_{phot}	v_e	v_{min}	v_{max}
HV$_e$ O I	0.6	7000	7.6	1.6	0	40
O I	0.5	7000	7.6	1.0	14	16
Na I	6.0	7000	7.6	0.6	11	40
Mg II	4.0	7000	7.6	1.0	12	14
Si II	10	7000	7.6	0.5	0	40
S II	0.1	7000	7.6	1.0	14.5	40
Ca II	4000	7000	7.6	1.3	0	40
Ti II	7.0	7000	7.6	1.0	0	40
Cr II	3500	7000	7.6	1.0	0	40
Fe II	40	7000	7.6	0.6	0	40

NOTE.—All velocities are given in 1000 km s^{-1}.

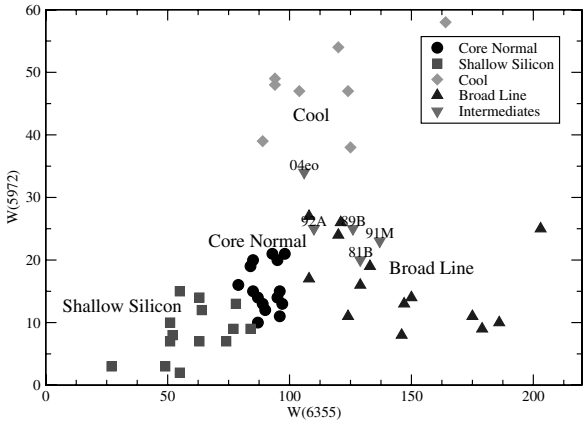

FIG. 11.—Pseudo-equivalent widths of λ5972 vs. λ6355, including intermediates. Data come from Branch et al. (2009) and Branch (2011, private communication). See the electronic edition of the *PASP* for a color version of this figure.

redshifted lines, implying that the initial SN ignition occurred off-center. Measurement of redshift and blueshift in HVG and LVG SNe Ia show that HVGs are preferentially redshifted and LVGs blueshifted. Maeda et al. (2010) concluded that LVGs are viewed in the direction of the initial spark and HVGs are viewed opposite the spark. Statistical treatment of this result indicates a high probability that the differences of the two groups are entirely an effect of viewing angle. The work of Maeda et al. (2010) explained why the differences between the HVG and LVG groups occurred, but did little to address the faint group, which they acknowledge may arise from a completely different explosion mechanism than HVGs and LVGs.

6. DISCUSSION

Due to the high level of importance placed on SNe Ia, a complete understanding of their physical nature is paramount. One method to probe this nature is examination of their differences. Thus, we analyzed the spectroscopically CL subgroup of SNe Ia. In summary, SNe in this subgroup are underluminous, rapid decliners, and poor ^{56}Ni producers, with deep and wide absorption troughs at around 4200 Å due to Ti II and unusually strong Si II λ5972 absorptions. The path leading to subluminous SNe Ia is presently uncertain. SD scenarios in which a delayed detonation, where a subsonic deflagration front transitions into a detonation, are strong theoretically and account well for observations (Höflich et al. 2010). There also exist competing DD scenarios such as that presented by Pakmor et al. (2011), which indicate that SNe Ia potentially originate from the merger of two CO WDs. Each scenario has its own strengths and weaknesses, and the question of progenitors remains open. Furthermore, population synthesis studies tell us that neither scenario alone can account for the total number of observed SNe Ia.

We have modeled the spectra of several CL SNe Ia with the fast and highly parameterized synthetic spectrum code SYNOW and compared our findings with those of similar studies. We find good agreement with other studies. Our work indicates that many ions are potentially present in cool SNe, and line identifications are complicated for this reason. We show that Si II, Ca II, Fe II, Ti II, Mg II, and O I are the most definite ions present in the cool spectra. It is also very likely that Na I is present. Three other ions, Ca I, Cr II, and S II, are considered as possibilities. S II is quite likely, but Ca I and Cr II only occur in one location in our synthetic spectra, and they have not been definitively explained in other studies. Therefore, we consider these ions to be possible but not definite.

Examining the velocity evolution of Si II λ6355 shows the primary difference among this subgroup. From our models we see that SN 2005bl and SN 1999by have lower Si II λ6355 velocities than SN 1991bg and SN 1997cn in early time spectra, but have lower velocity gradients, and so by about day 18 after B maximum, all four cool SNe have approximately the same velocity. Si II λ6355 velocities are plotted in Figure 12 for several CL and CN SNe. Comparing our velocities with those of other studies shows insignificant differences. Overall, the appearance of the velocity distribution for all SNe Ia is quite continuous.

Our examination of this subgroup indicates that 1991bg-like SNe Ia are fairly homogeneous among themselves (albeit somewhat due to construction) and not only share the same ions, but fitting parameters and properties as well. Upon consideration of

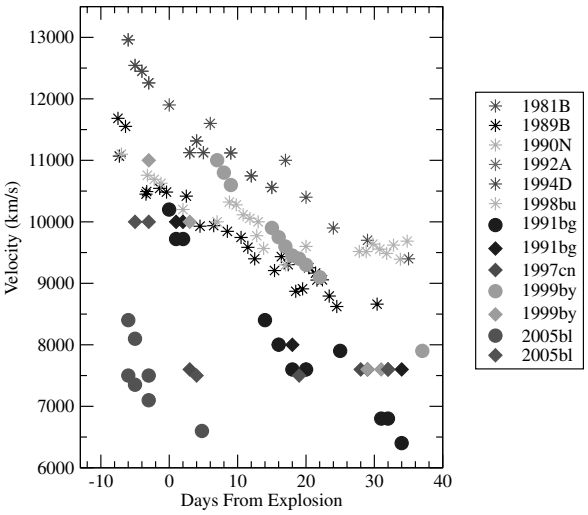

FIG. 12.—Si II λ6355 velocities. Filled symbols are CL SNe Ia and diamond symbols represent velocities from our data. Other line-velocity data come from Turatto et al. (1996), Jha et al. (1999), Garnavich et al. (2004), and Taubenberger et al. (2008). See the electronic edition of the *PASP* for a color version of this figure.

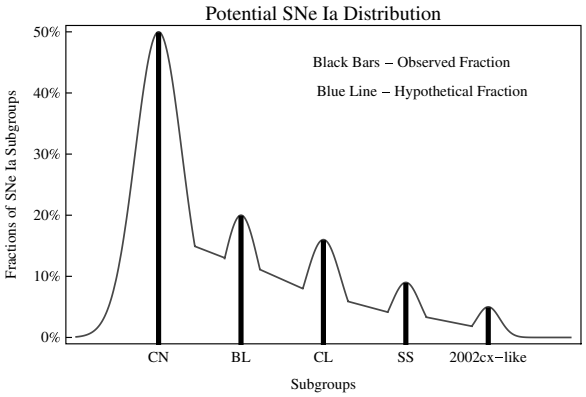

FIG. 13.—Schematic of SNe Ia distribution. The observed subgroup fraction data come from Li et al. (2010). See the electronic edition of the *PASP* for a color version of this figure.

intermediates the distinctions among the subgroups begin to blur even more and the distribution of SNe Ia seems increasingly continuous. With a large and well-observed sample this distribution may take a form similar to the hypothetical distribution displayed in Figure 13.

A continuous distribution of SNe Ia could have regions of high density and low density in the W-W plots, but the difference in density should be fairly small. These dense regions would contain the subgroups. The highest-density region would contain the most common SNe Ia, the CNs. The lowest density regions would contain SNe Ia that are steps away from one subgroup toward another: intermediates. The reason for different regions of high density and low density, i.e., the subgroups, could indicate sets of secondary parameters that are slightly more stable and thus more likely to be reproduced for WDs transitioning into SNe Ia, rather than fundamentally different processes.

Present work on the diversity of SNe Ia is incomplete but is leading to the conclusion that rather than being made of discrete subgroups, SNe Ia are a continuous distribution of the same phenomenon. However, for more definitive conclusions it is necessary to have a much larger and well-observed sample coupled with more robust explosion models.

We thank David Branch for many helpful discussions, Saurabh Jha for providing his data, and Stefano Benetti for providing his data. We thank the anonymous referee for improving our presentation and bringing the S II versus Sc II identification question into clearer focus. This work was supported in part by National Science Foundation grant AST-0707704, US Department of Energy grant DE-FG02-07ER41517, and NASA grant HST-GO-12298.05-A. Support for program HST-GO-12298.05-A was provided by NASA through a grant from the Space Telescope Science Institute, which is operated by the Association of Universities for Research in Astronomy, Inc., under NASA contract NAS5-26555.

REFERENCES

Abell, P. A., Allison, J., Anderson, S. F., Andrew, J. R., Angel, J. R. P., Armus, L., Arnett, D., Asztalos, S. J., et al., et al. 2009, preprint (arXiv:0912.0201)

Arnett, W. D., Branch, D., & Wheeler, J. C. 1985, Nature, 314, 337

Baade, W. 1938, ApJ, 88, 285

Benetti, S. 2005, in ASP Conf. Ser. 342, 1604-2004: Supernovae as Cosmological Lighthouses, ed. M. Turatto, S. Benetti, L. Zampieri, et al. (San Francisco: ASP), 235

Benetti, S., Cappellaro, E., Mazzali, P. A., Turatto, M., Altavilla, G., Bufano, F., Elias-Rosa, N., Kotak, R., et al. 2005, ApJ, 623, 1011

Branch, D., Benetti, S., Kasen, D., Baron, E., Jeffery, D. J., Hatano, K., Stathakis, R. A., Filippenko, A. V., et al. 2002, ApJ, 566, 1005

Branch, D., Dang, L. C., & Baron, E. 2009, PASP, 121, 238

Branch, D., Dang, L. C., Hall, N., Ketchum, W., Melakayil, M., Parrent, J., Troxel, M. A., Casebeer, D., et al. 2006, PASP, 118, 560

Branch, D., Garnavich, P., Matheson, T., Baron, E., Thomas, R. C., Hatano, K., Challis, P., Jha, S., et al. 2003, AJ, 126, 1489

Branch, D., Jeffery, D. J., Parrent, J., Baron, E., Troxel, M. A., Stanishev, V., Keithley, M., Harrison, J., et al. 2008, PASP, 120, 135

Branch, D., Parrent, J., Troxel, M. A., Casebeer, D., Jeffery, D. J., Baron, E., Ketchum, W., & Hall, N. 2007, in AIP Conf. Ser., 924, The Multicolored Landscape of Compact Objects and Their Explosive Origins, ed. T. di Salvo, G. L. Israel, L. Piersant, et al. (New York: AIP), 342

Branch, D., & Tammann, G. A. 1992, ARA&A, 30, 359

Chuang, C., & Wang, Y. 2011, preprint (arXiv:1102.2251)

Conley, A., Guy, J., Sullivan, M., Regnault, N., Astier, P., Balland, C., Basa, S., Carlberg, R. G., et al. 2011, ApJS, 192, 1

Copin, Y., Blanc, N., Bongard, S., Gangler, E., Saugé, L., Smadja, G., Antilogus, P., Garavini, G., et al. 2006, NewA Rev., 50, 436

Filippenko, A. V., Richmond, M. W., Branch, D., Gaskell, M., Herbst, W., Ford, C. H., Treffers, R. R., Matheson, T., et al. 1992a, AJ, 104, 1543

Filippenko, A. V., Richmond, M. W., Matheson, T., Shields, J. C., Burbidge, E. M., Cohen, R. D., Dickinson, M., Malkan, M. A., et al. 1992b, ApJ, 384, L15

Fisher, A. K. 2000, Ph.D. thesis, Univ. Oklahoma

Garnavich, P. M., Bonanos, A. Z., Krisciunas, K., Jha, S., Kirshner, R. P., Schlegel, E. M., Challis, P., Macri, L. M., et al. 2004, ApJ, 613, 1120

Goobar, A., Perlmutter, S., Aldering, G., Goldhaber, G., Knop, R. A., Nugent, P., Castro, P. G., Deustua, S., et al. 2000, Phys. Scr. T, 85, 47

Hachinger, S., Mazzali, P. A., Taubenberger, S., Pakmor, R., & Hillebrandt, W. 2009, MNRAS, 399, 1238

Hicken, M., Garnavich, P. M., Prieto, J. L., Blondin, S., DePoy, D. L., Kirshner, R. P., & Parrent, J. 2007, ApJ, 669, L17

Hicken, M., Wood-Vasey, W. M., Blondin, S., Challis, P., Jha, S., Kelly, P. L., Rest, A., & Kirshner, R. P. 2009, ApJ, 700, 1097

Hillebrandt, W., & Niemeyer, J. C. 2000, ARA&A, 38, 191

Hoeflich, P., Mueller, E., & Khokhlov, A. 1993, A&A, 268, 570

Höflich, P. 2006, Nucl. Phys. A, 777, 579

Höflich, P., Gerardy, C. L., Fesen, R. A., & Sakai, S. 2002, ApJ, 568, 791

Höflich, P., Krisciunas, K., Khokhlov, A. M., Baron, E., Folatelli, G., Hamuy, M., Phillips, M. M., Suntzeff, N., et al. 2010, ApJ, 710, 444

Howell, D. A., Sullivan, M., Nugent, P. E., Ellis, R. S., Conley, A. J., Le Borgne, D., Carlberg, R. G., Guy, J., et al. 2006, Nature, 443, 308

Iben, Jr., I., & Tutukov, A. V. 1984, ApJS, 54, 335

Jeffery, D. J., Ketchum, W., Branch, D., Baron, E., Elmhamdi, A., & Danziger, I. J. 2007, ApJS, 171, 493

Jha, S., Garnavich, P. M., Kirshner, R. P., Challis, P., Soderberg, A. M., Macri, L. M., Huchra, J. P., Barmby, P., et al. 1999, ApJS, 125, 73

Khokhlov, A. M. 1991, A&A, 245, 114

Law, N. M., Kulkarni, S. R., Dekany, R. G., Ofek, E. O., Quimby, R. M., Nugent, P. E., Surace, J., Grillmair, C. C., 2009, PASP, 121, 1395

Leibundgut, B., Kirshner, R. P., Phillips, M. M., Wells, L. A., Suntzeff, N. B., Hamuy, M., Schommer, R. A., Walker, A. R., et al. 1993, AJ, 105, 301

Li, W., Filippenko, A. V., Treffers, R. R., Riess, A. G., Hu, J., & Qiu, Y. 2001, ApJ, 546, 734

Li, W., Leaman, J., Chornock, R., Filippenko, A. V., Poznanski, D., Ganeshalingam, M., Wang, X., Modjaz, M., et al. 2010, MNRAS, 412, 1441

Maeda, K., Benetti, S., Stritzinger, M., Röpke, F. K., Folatelli, G., Sollerman, J., Taubenberger, S., Nomoto, K., et al. 2010, Nature, 466, 82

Maoz, D., & Badenes, C. 2010, MNRAS, 407, 1314

Maoz, D., Mannucci, F., Li, W., Filippenko, A. V., Della Valle, M., & Panagia, N. 2011, MNRAS, 307

Mazzali, P. A., Chugai, N., Turatto, M., Lucy, L. B., Danziger, I. J., Cappellaro, E., della Valle, M., & Benetti, S. 1997, MNRAS, 284, 151

Mennekens, N., Vanbeveren, D., De Greve, J. P., & De Donder, E. 2010, A&A, 515, A89

Miknaitis, G., et al. 2007, ApJ, 666, 674

Nugent, P., Phillips, M., Baron, E., Branch, D., & Hauschildt, P. 1995, ApJ, 455, L147

Pakmor, R., Hachinger, S., Röpke, F. K., & Hillebrandt, W. 2010, Nature, 463, 61

———. 2011, A&A, 528, A117

Parkinson, D., Kunz, M., Liddle, A. R., Bassett, B. A., Nichol, R. C., & Vardanyan, M. 2010, MNRAS, 401, 2169

Parrent, J. T., Thomas, R. C., Fesen, R. A., Marion, G. H., Challis, P., Garnavich, P. M., Milisavljevic, D., Vinkò, J., & Wheeler, J. C. 2011, ApJ, 732, 30

Pastorello, A., Mazzali, P. A., Pignata, G., Benetti, S., Cappellaro, E., Filippenko, A. V., Li, W., Meikle, W. P. S., et al. 2007, MNRAS, 377, 1531

Patat, F., Benetti, S., Cappellaro, E., Danziger, I. J., della Valle, M., Mazzali, P. A., & Turatto, M. 1996, MNRAS, 278, 111

Perlmutter, S., Aldering, G., Goldhaber, G., Knop, R. A., Nugent, P., Castro, P. G., Deustua, S., Fabbro, S., et al. 1999, ApJ, 517, 565

Phillips, M. M. 1993, ApJ, 413, L105

Riess, A. G., Filippenko, A. V., Challis, P., Clocchiatti, A., Diercks, A., Garnavich, P. M., Gilliland, R. L., Hogan, C. J., et al. 1998, AJ, 116, 1009

Riess, A. G., Macri, L., Casertano, S., Sosey, M., Lampeitl, H., Ferguson, H. C., Filippenko, A. V., Jha, S. W., et al. 2009, ApJ, 699, 539
Ruiter, A. J., Belczynski, K., & Fryer, C. 2009, ApJ, 699, 2026
Taubenberger, S., Hachinger, S., Pignata, G., Mazzali, P. A., Contreras, C., Valenti, S., Pastorello, A., Elias-Rosa, N., et al. 2008, MNRAS, 385, 75
Timmes, F. X., & Woosley, S. E. 1992, ApJ, 396, 649
Turatto, M., Benetti, S., Cappellaro, E., Danziger, I. J., Della Valle, M., Gouiffes, C., Mazzali, P. A., & Patat, F. 1996, MNRAS, 283, 1
Turatto, M., Piemonte, A., Benetti, S., Cappellaro, E., Mazzali, P. A., Danziger, I. J., & Patat, F. 1998, AJ, 116, 2431
Waagen, E., Evans, R. O., Villi, M., Cortini, G., Johnson, W., McNaught, R. H., Mueller, J., Cappellaro, E., et al. 1991, IAU Circ., 5239, 1
Webbink, R. F. 1984, ApJ, 277, 355
Whelan, J., & Iben, Jr., I. 1973, ApJ, 186, 1007
Wood-Vasey, W. M., Miknaitis, G., Stubbs, C. W., Jha, S., Riess, A. G., Garnavich, P. M., Kirshner, R. P., Aguilera, C., et al. 2007, ApJ, 666, 694

Hydrogen in SNe Ib

Eddie Baron

University of Oklahoma, USA

June 28, 2010

Collaborators

- Usual Suspects
  - David Branch
  - Peter Hauschildt
- Good Undergraduates
  - Wesley Ketchum
  - Spencer James

SN Taxonomy

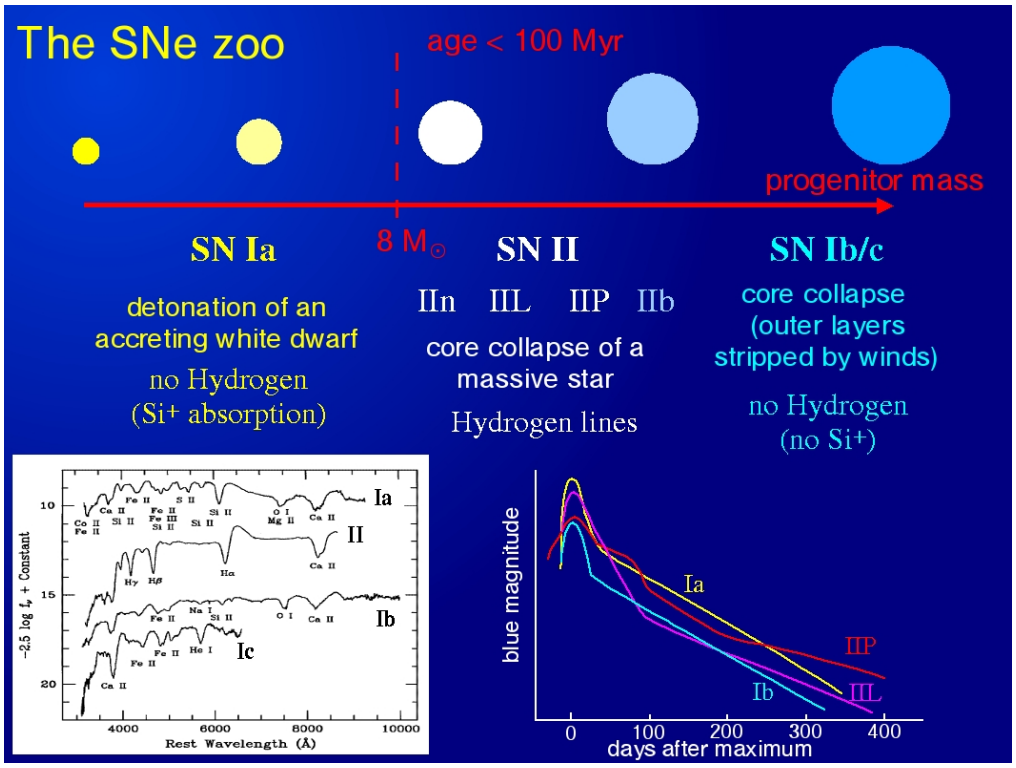
The SNe zoo
age < 100 Myr
progenitor mass
SN Ia
8 M⊙
SN II
SN Ib/c
detonation of an accreting white dwarf
no Hydrogen (Si+ absorption)
IIn IIL IIP IIb
core collapse of a massive star
Hydrogen lines
core collapse (outer layers stripped by winds)
no Hydrogen (no Si+)
Ia
II
Ib
Ic
−2.5 log fλ + Constant
Rest Wavelength (Å)
blue magnitude
days after maximum
IIP
IIL

3 Classes of Ixb SNe

- Most if not all in Binary Systems
- SNe IIb $M_H \sim 0.3\ \mathrm{M}_\odot$
  - Progenitor: Stable Case C, Critical mass $\sim 0.3\ \mathrm{M}_\odot$ Roche lobe shrinks
- Hydrogen Rich Ib $M_H \sim 0.1\ \mathrm{M}_\odot$
  - Progenitor: Stable Case C, followed by wind loss? (Posiadlowski et al.)
- Hydrogen Poor Ib $M_H \sim 0.001\ \mathrm{M}_\odot$
  - Progenitor: UnStable Case C, Common Envelope Formation (Posiadlowski et al.)
  - Progenitor: Rotation + Nonconservative Case A or B, Followed by Wind loss (Yoon et al.)

SN IIb

SN 1993J: Days +25, 48

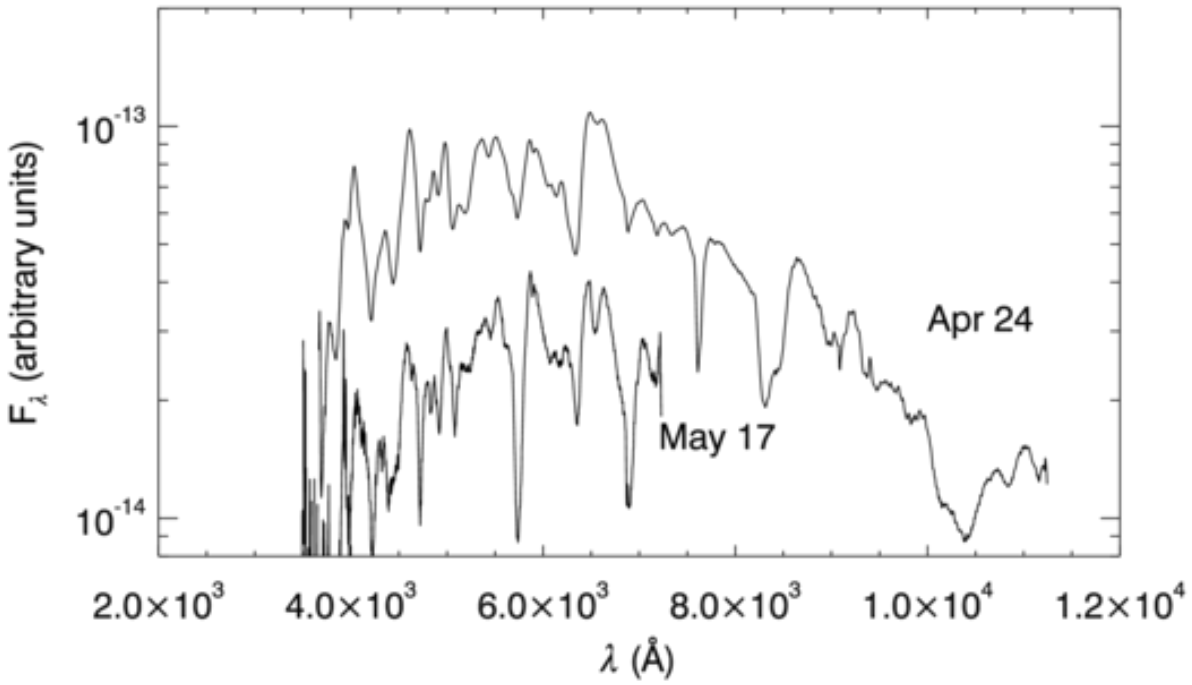

SYNOW Analyses

- Highly parametrized
- Good for line IDs
- Can't determine abundances or masses

Hydrogen Rich SN Ib
SN 2000H

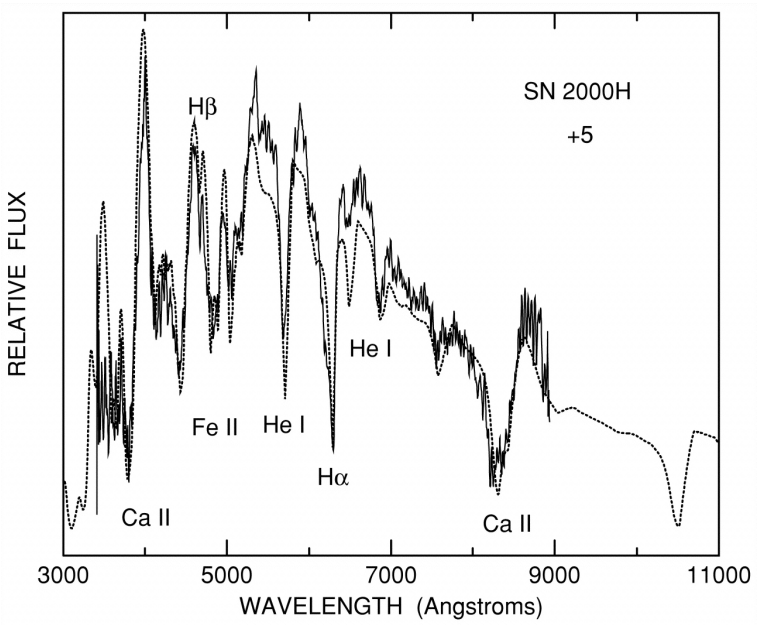

Hydrogen in Typical SN Ib?

SN 1999dn

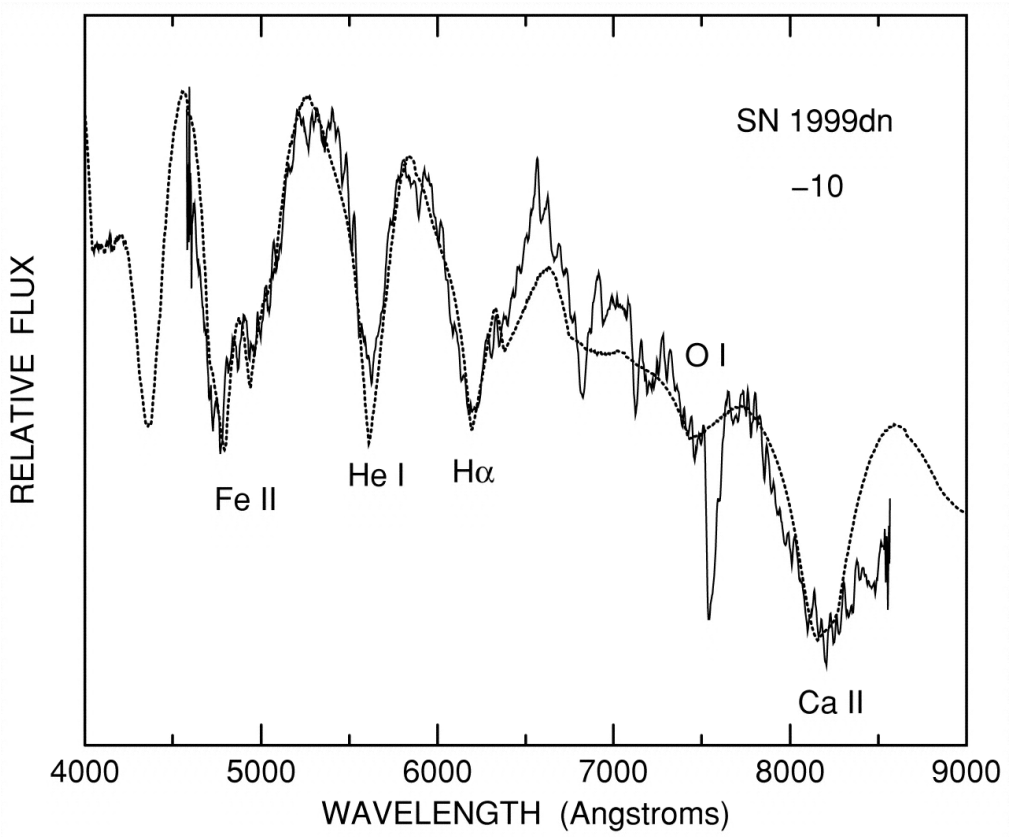

PHOENIX Analysis

- PHOENIX: Generalized Stellar Atmospheres Code
- Try to use “best phyics”

Hydrogen Free Models

- Parametrized Model
- Powerlaw Density
- Helium Core
- Vary Metallicity

SN 1999dn
Maximum Light

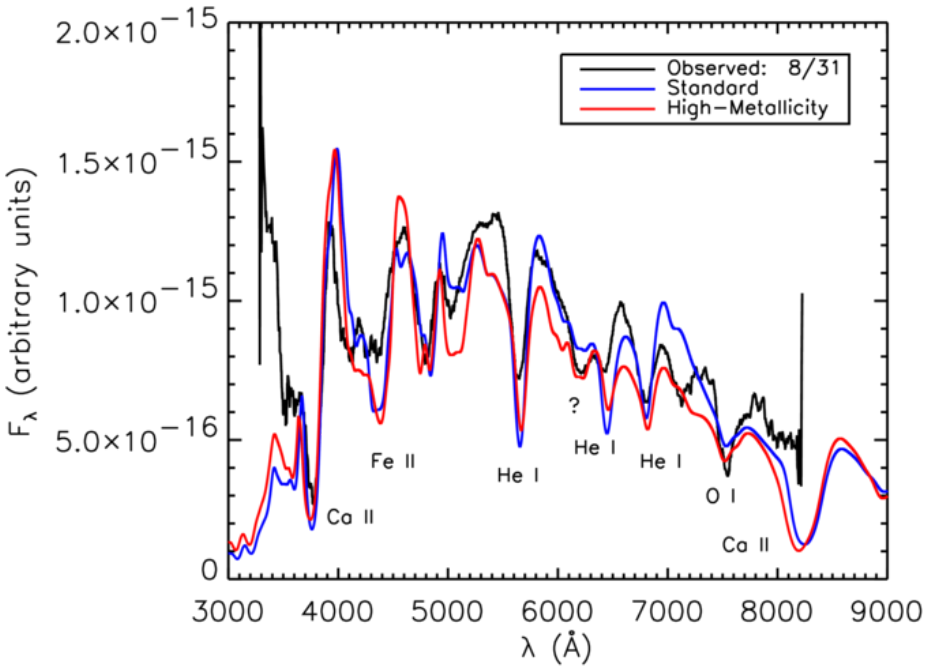

Hydrogen Skin Models

- Parametrized Model
- Solar Compositions
- Powerlaw Density
- Helium Core with hydrogen (solar) skin
- Self-consistent

SN 1999dn
Day -10

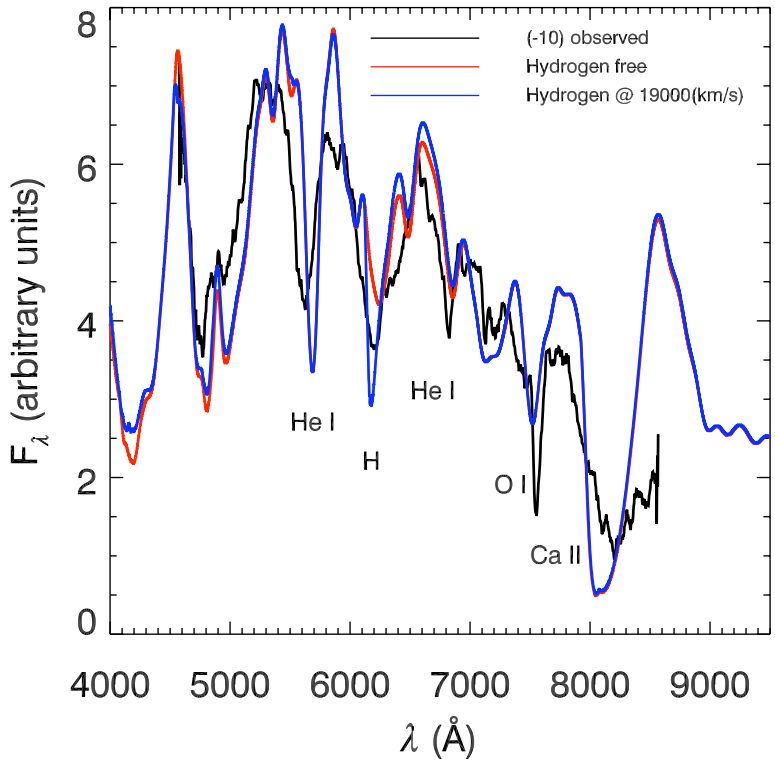

SN 1999dn
Day 0

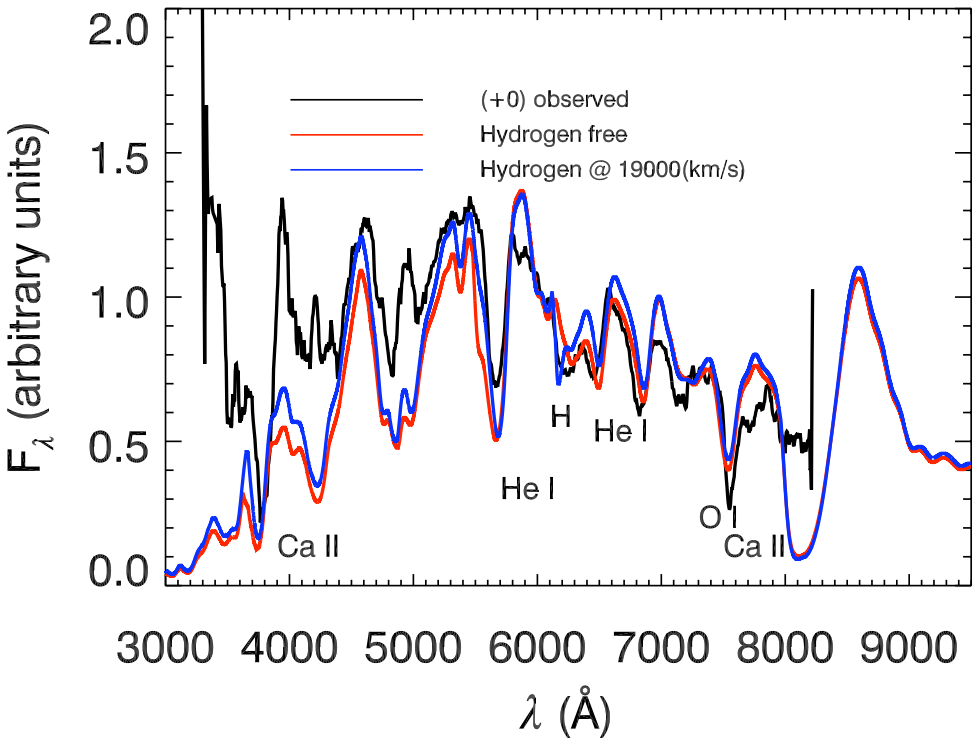

SN 2000H
Day 0

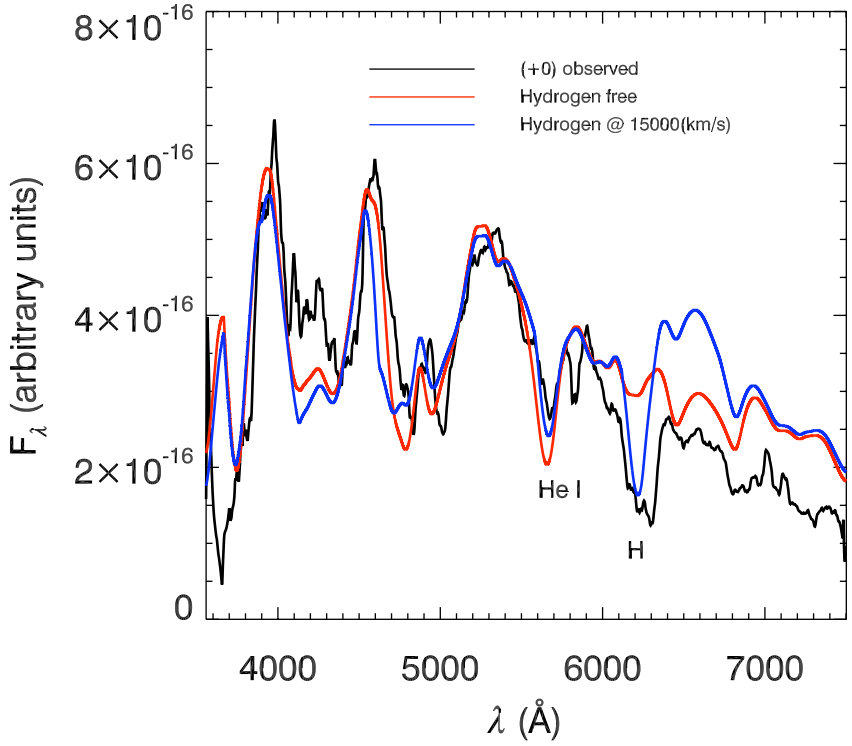

SN 2000H
Day 6

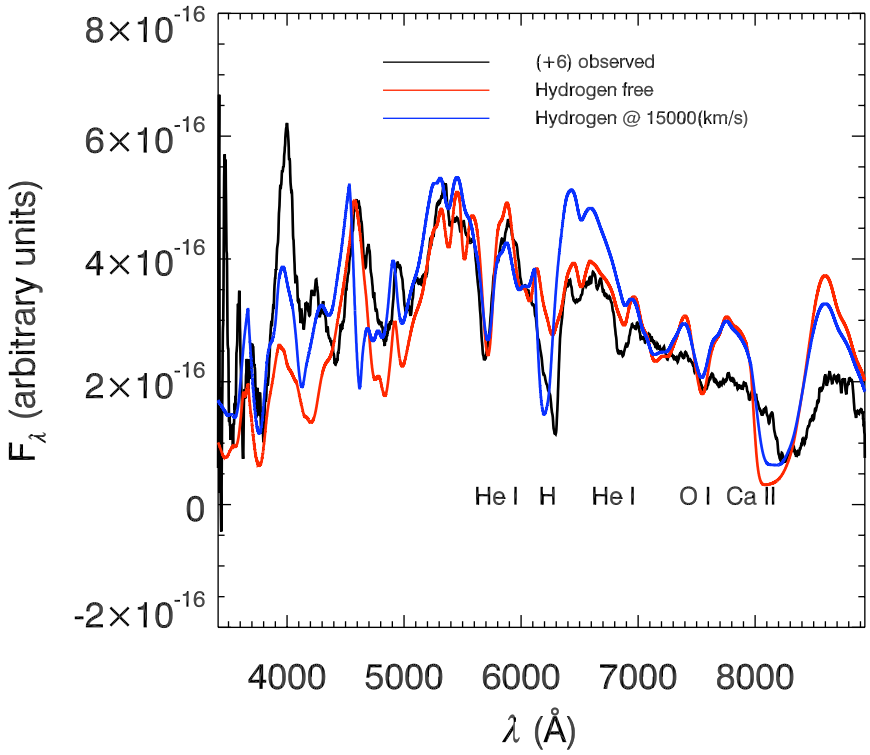

SN 2000H CSM

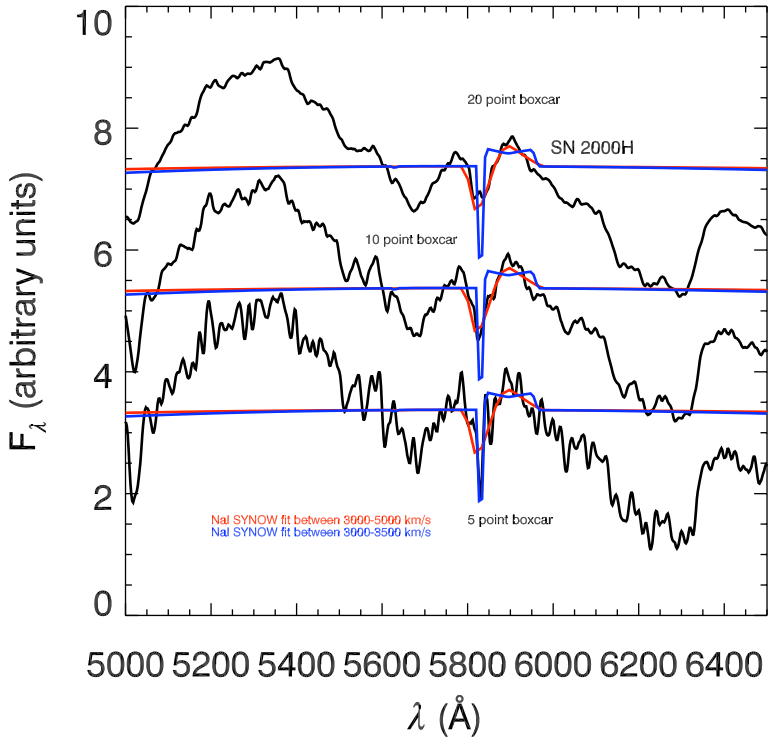
20 point boxcar
SN 2000H
10 point boxcar
5 point boxcar
NaI SYNOW fit between 3000-5000 km/s
NaI SYNOW fit between 3000-3500 km/s
F_λ (arbitrary units)
λ (Å)
0
2
4
6
8
10
5000 5200 5400 5600 5800 6000 6200 6400

Conclusions

- Hydrogen is common in SNe Ib
- May be two classes of SNe Ib
  - Class I: Closely Related to SNe IIb
  - Class II: Very thin hydrogen envelope
  - Class III: Hydrogen free?

A&A 502, 1043–1049 (2009)
DOI: 10.1051/0004-6361/200810982

Astronomy & Astrophysics

Time-dependent radiative transfer with PHOENIX

D. Jack[1], P. H. Hauschildt[1], and E. Baron[1,2]

[1] Hamburger Sternwarte, Gojenbergsweg 112, 21029 Hamburg, Germany
e-mail: [djack@;yeti]@hs.uni-hamburg.de; baron@ou.edu
[2] Homer L. Dodge Department of Physics and Astronomy, University of Oklahoma, 440 W Brooks, Rm 100, Norman, OK 73019-2061, USA

Received 18 September 2008 / Accepted 3 April 2009

ABSTRACT

Aims. We present first results and tests of a time-dependent extension to the general purpose model atmosphere code PHOENIX. We aim to produce light curves and spectra of hydro models for all types of supernovae.
Methods. We extend our model atmosphere code PHOENIX to solve time-dependent non-grey, NLTE, radiative transfer in a special relativistic framework. A simple hydrodynamics solver was implemented to keep track of the energy conservation of the atmosphere during free expansion.
Results. The correct operation of the new additions to PHOENIX were verified in test calculations.
Conclusions. We have shown the correct operation of our extension to time-dependent radiative transfer and will be able to calculate supernova light curves and spectra in future work.

Key words. stars: supernovae: general – radiative transfer – methods: numerical

1. Introduction

All types of supernovae are important for the role that they play in understanding stellar evolution and galactic nucleosynthesis and as cosmological probes. Type Ia supernovae are of particular cosmological interest, e.g., because the dark energy was discovered with type Ia supernovae (Riess et al. 1998; Perlmutter et al. 1999).

In dark energy studies, the goal now is to characterize the nature of the dark energy as a function of redshift. While there are other probes that will be used (gravitational lensing, baryon acoustic oscillations), a JDEM or Euclid mission will likely consider supernovae in some form. In planning for future dark energy studies both from space and from the ground, it is important to know whether the mission will require spectroscopy of modest resolution, or whether pure imaging or grism spectroscopy will be adequate. Several purely spectral indicators of peak luminosity have been proposed (Nugent et al. 1995; Hachinger et al. 2006; Bongard et al. 2006; Bronder et al. 2008; Foley et al. 2008; Le Du et al. 2009). What is required is an empirical and theoretical comparison of both light curve shape luminosity indicators (Pskovskii 1977; Phillips 1993; Riess et al. 1996; Goldhaber et al. 2001) and spectral indicators.

To make this comparison one needs to know more about the physics going on in a supernova explosion and to be able to calculate light curves and spectra self-consistently. Thus, we need to extend our code to time-dependent problems. While our primary focus is on type Ia supernovae, the time-dependent radiative transfer code is applicable to all types of supernovae, as well as to other objects, e.g., stellar pulsations.

In the following we present the methods we used to implement time dependence. First we focus on solving the energy equation (first law) and then turn our attention to time-dependent radiative transfer.

2. Equation of energy conservation

To compute light curves we extended PHOENIX with a time-dependent solution of the non-grey, NLTE radiative transfer problem in special relativistic environments and a simple hydrodynamic code to solve the free expanding case relevant to supernova light curves. The idea is to keep track of the conservation of energy for the gas and radiation together and to allow for different time scales for the gas and the radiation.

For the time-dependent radiative transfer problem we extended our existing radiative transfer code PHOENIX (Hauschildt & Baron 1999, 2004b). The change in the energy density of a radiating material is given by Eq. (96.15) in Mihalas & Mihalas (1984)

$$\frac{D}{Dt}E = -\frac{\partial}{\partial M_r}(L_r + P_r) + \varepsilon, \tag{1}$$

where E is the total energy density. All quantities are considered in the comoving frame. P_r is not the pressure, but rather mechanical power on the sphere of a radius r. Equation (1) is only valid to first order in v/c, and thus lacks the full special relativistic accuracy of PHOENIX. This is adequate for the velocities found in supernovae. The total energy density of a radiating fluid consists of the sum of the energy density of the material, the energy density of the radiation field, the kinetic energy density of the material, and the gravitational energy density:

$$E = E_{\rm gas} + \frac{E_0}{\rho} + E_{\rm kin} + E_{\rm grav}. \tag{2}$$

For supernovae in the free expansion phase, the gravitational energy density $E_{\rm grav}$ is negligible since the potential is small in absolute value with the standard choice of zero at infinity. Homologous expansion is a reasonably good assumption for supernovae. The energy release by the decay of ^{56}Ni can influence the dynamics of the expansion (Pinto & Eastman 2000).

Woosley et al. (2007) compared a study following this energy release to the results from assuming homologous expansion. Figure 2 in their paper shows the deviation and density variations can be as large as 10%. However, this is probably an upper limit due to the simple burning parameterization used in that study. Ultimately, when the deflagration to detonation transition is understood, it will be important to revisit this issue and replace 1-D calculations with full 3-D calculations, which include the effects of clumps, as well as nickel bubble expansion. For now the accuracy of homologous expansion should be adequate, given the other uncertainties in the problem.

With the assumption of homology, the velocity of a given matter element is then constant as is the kinetic energy density. Thus, we can neglect the kinetic energy term $\frac{DE_{\rm kin}}{Dt}$. So for our approach, we only have to consider the energy densities of the radiation field and the material. For the material, this includes effects such as an energy deposition due to radioactive decay of nickel and cobalt in an SN Ia envelope.

The other possible cause of a change in the energy density is the structure term. This term is given by (Cooperstein et al. 1986)

$$\frac{\partial}{\partial M_r}\left(P_r + L_r\right) = \frac{\partial}{\partial M_r}\left\{4\pi r^2\left[u\left(p + P_0\right) + F_0\right]\right\} \tag{3}$$

where p is the pressure of the material and P_0 the radiation pressure, u the velocity of the expanding gas, the radiative flux is represented by F_0, and the mass inside of the radius r of a layer is given by M_r. The radiation pressure is a result of the solution of the detailed radiative transfer equation and given by

$$P_0 = \frac{4\pi}{c}K, \tag{4}$$

with K the second moment of the radiation field. The change of the energy density is given by the two quantities

$$L_r = 4\pi r^2 F_0 \tag{5}$$

and

$$P_r = 4\pi r^2 u\left(p + P_0\right). \tag{6}$$

If the atmosphere is in radiative equilibrium, the structure term is zero and the energy density stays constant if there is no additional energy source and the atmosphere is not expanding.

All the quantities required for the structure term can be derived from thermodynamics or the solution of the radiative transfer problem. We need the energy density of the material $E_{\rm gas}$ and the energy density of the radiation field $\frac{E_0}{\rho}$. For the latter, we have to solve the radiative transfer equation for the radiation field and the radiative energy. We use our radiative transfer code PHOENIX to solve the time-independent radiative transfer equation. The energy of the radiation field is given by

$$E_0 = \frac{4\pi}{c}J, \tag{7}$$

where J is the mean intensity and c the speed of light.

The energy density of the material is given by

$$E_{\rm gas} = \frac{3}{2}\frac{p}{\rho} = \frac{3}{2}\frac{R}{m_{\rm u}}T, \tag{8}$$

with the mean molecular weigh $m_{\rm u}$ and the universal gas constant R. The gas pressure is represented by p and the density by ρ. T stands for the temperature of the gas. The sum of the radiation and material energy density is then the total energy density

$$E_{\rm total} = E_{\rm gas} + \frac{E_0}{\rho}\,. \tag{9}$$

The change in this total energy density is given by Eq. (1). So the equation to calculate the new energy density $E_{\rm new}$ is given by

$$E_{\rm new} = E_{\rm old} - \frac{\partial}{\partial M_r}\left(L_r + P_r\right)\Delta t + \varepsilon\Delta t. \tag{10}$$

We now have all the needed equations to calculate a simple light curve. One problem for the calculation is that we can only determine the change in the *total* energy density for the next time step. However, the total energy change is divided into a change in the gas energy density and the energy density of the radiation field. To obtain the correct distribution of the gas and radiative energy, one has to iterate for each time step by solving the radiative transfer equation to compute the correct new temperature at the next time step.

To get the correct new temperature we apply the following iteration scheme. The error in the energy density, $E_{\rm err}$ is given by

$$E_{\rm err} = \frac{E_{\rm current} - E_{\rm target}}{E_{\rm target}}\,. \tag{11}$$

Here, $E_{\rm target}$ is the desired new total energy density, which is known from Eq. (10), and $E_{\rm current}$ is the total energy density obtained by Eq. (9) with the current temperature guess and the radiative transfer solution. Tests have shown that the error is almost linearly proportional to the temperature T. Therefore, a new temperature guess can be calculated for the next iteration step. The new temperature guess $T_{\rm new}$ is obtained by

$$T_{\rm new} = \frac{E_{\rm err}T_{\rm old} - E_{{\rm err}_{\rm old}}T_{\rm cur}}{E_{\rm err} - E_{{\rm err}_{\rm old}}}, \tag{12}$$

where $T_{\rm cur}$ and $E_{\rm err}$ are the current temperature guess and energy error. The variables $T_{\rm old}$ and $E_{{\rm err}_{\rm old}}$ are the temperature and energy error of the temperature iteration step before. With the new temperature guess we solve the radiative transfer equation again and check whether the total energy density is the desired one. It takes approximately four or five iteration steps to get the correct new temperature for a typical time step. The energy density is correct within an accuracy of 10^{-5}.

3. Test light curves

For the first test calculations we have solved the radiative transfer equation for a grey test atmosphere. Test model atmospheres are divided in 100 layers and we consider here time independent radiative transfer (in Sect. 4 below we discuss time dependent radiative transfer).

As a first test we applied our time evolution code to a static atmosphere. The test atmosphere is not expanding and no energy sources are present. Inside the test atmosphere we used a "lightbulb" radiating with a constant luminosity to simulate the internal energy flow from a star. We assumed an approximate temperature structure for $t = 0$ and then let the atmosphere evolve towards radiative equilibrium. The atmosphere changed until it reaches steady state and the luminosity is constant in both space and time. The resulting final temperature structure should

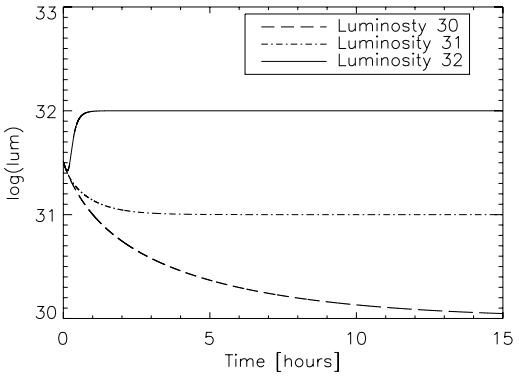

Fig. 1. Three different light curves for the evolution to a stationary state. The three models have different luminosities produced by different inner "lightbulbs".

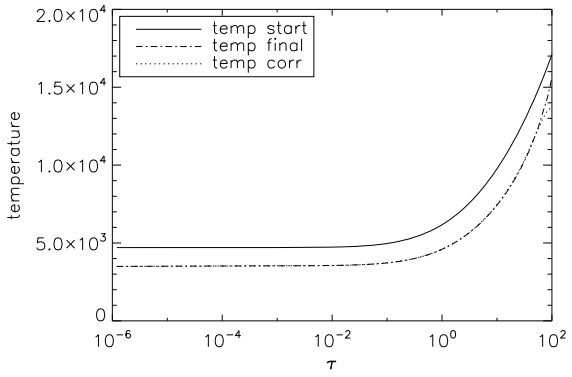

Fig. 2. The final temperature structures of the time evolution calculations.

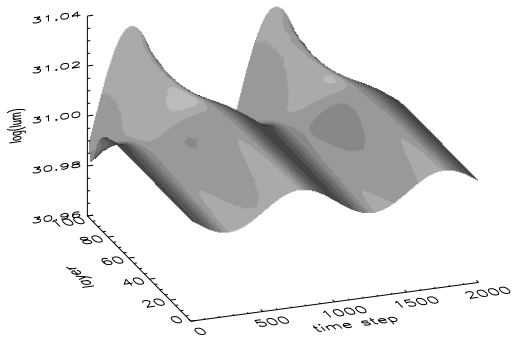

Fig. 3. The flux in every layer at each time step.

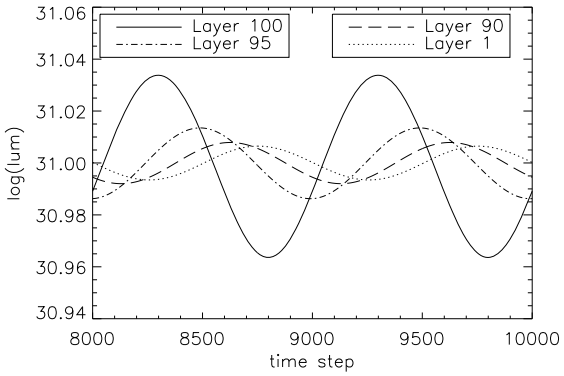

Fig. 4. The result for a sinusoidal varying lightbulb. Shown here is the luminosity in different layers. The phase shift between the lightbulb and the emergent flux is roughly π.

be identical to the structure for radiative equilibrium computed directly.

In Fig. 1 we show the light curves for three different static models. We can observe the model on its way towards radiative equilibrium. All calculations were started from the same temperature structure. After a certain time, the radiative relaxation time scale, each atmosphere has the (constant) luminosity of the lightbulb throughout the configuration.

The final temperature structure of the model atmosphere with the lightbulb with a luminosity of 10^{31} erg/s is displayed in Fig. 2. Also shown is the result of a calculation using the temperature correction procedure of PHOENIX (Hauschildt et al. 2003) to directly compute the radiative equilibrium structure of the configuration. As one can clearly see, the resulting temperature structure of both methods agrees very well, and the maximum deviation of the temperature structure is less than one percent. Only the inner three layers have a deviation of up to 10 percent due to the implicit assumption of a diffusion approximation (and not a lightbulb) in the static calculation.

The next test is to look at time varying atmospheres. As an example we considered an atmosphere with a sinusoidally varying lightbulb inside. The resulting luminosity in each layer at each time point is plotted in Fig. 3. The luminosity in each layer is sinusoidal. It takes some time for the radiation to reach the outside boundary of the atmosphere and this results in a phase shift compared to the lightbulb.

We now take a look at the luminosity in different layers. These are plotted in Fig. 4. One can see the phase shift of the sine in each layer. As expected, the luminosity from the central source needs time to move through the atmosphere.

One can also see that the amplitude of the sine decreases with increasing radius. What one would expect is that the amplitude is the same in every layer. The radiation is moving outwards and the incoming varying luminosity from the lightbulb should move through every layer and therefore the amplitude is supposed to be the same in each layer. If we integrate the luminosity over a whole sine, it stays constant in every layer. In the plot one can see that the mean luminosity is at the same level, so the luminosity is preserved. But why does the amplitude decrease? A possible explanation is that the radiation moving through the atmosphere is going backwards when the sine is declining, so this smears out the amplitude. If the sine varying radiation is moving through a very thick atmosphere, the amplitude at the top of the atmosphere is finally flat. An observer sees the mean luminosity.

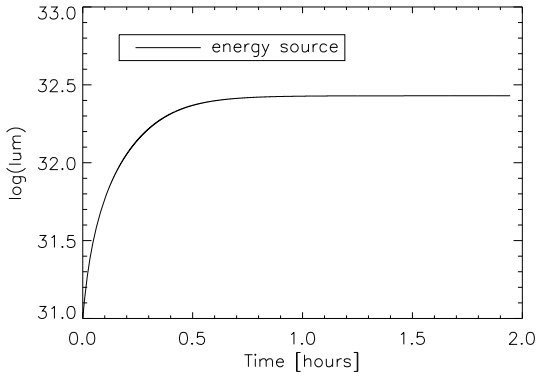

Fig. 5. The light curve of an lightbulb with an additional energy source. An energy source in each layer causes an increasing luminosity of the model atmosphere.

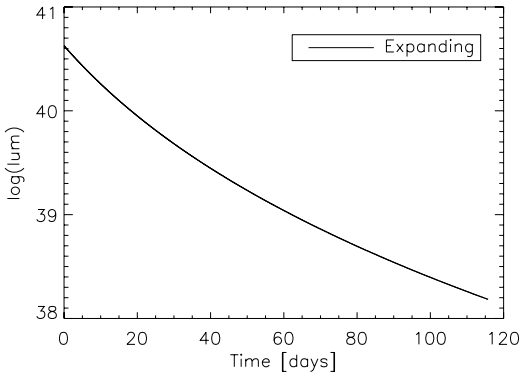

Fig. 6. Light curve of an atmosphere that is just expanding.

For the next test we consider an atmosphere with an internal energy source. The initial structure is the radiative equilibrium structure of the static model with the lightbulb with a luminosity of 10^{31} erg/s. We assume a constant energy deposition rate in each layer of the model atmosphere. The luminosity is expected to increase over time and towards the outside. Figure 5 shows a plot of the light curve of this test atmosphere. The luminosity increases in time because of the energy deposition.

3.1. Expansion

In the case of SN Ia, homologous expansion is a good assumption after the initial breakout. In our test model each layer has a constant velocity, $u \propto r$, to simulate a freely expanding envelope. The new radius $r_{\rm new}$ of a layer is, therefore, determined by

$$r_{\rm new} = u \cdot \Delta t + r_{\rm old} \tag{13}$$

for a time step Δt, while the layer is expanding with a velocity u. The radius before the new time step is $r_{\rm old}$. With the same assumption of homologous expansion the new density $\rho_{\rm new}$ of a layer after at the new time step is determined by

$$\rho_{\rm new} = \rho_{\rm old} \cdot \left(\frac{r_{\rm old}}{r_{\rm new}}\right)^3 \tag{14}$$

where $\rho_{\rm old}$ is the old density. With the new radius and density, we are now able to calculate the new thermodynamics of the atmosphere. We assume the expansion of the supernova is an adiabatic process. The internal energy of the material changes due to work dW done during the expansion

$$\mathrm{d}E = \mathrm{d}W = -p\mathrm{d}V, \tag{15}$$

where p is the pressure and dV a volume change. The energy conservation equation considers the energy density. The change in the energy density for the adiabatic expansion is given by

$$\mathrm{d}E_{\rm adia} = \frac{\mathrm{d}W}{m} = -\frac{p}{m}\mathrm{d}V. \tag{16}$$

The mass m of a layer is given by its volume and density

$$m = V \cdot \rho. \tag{17}$$

In our approach to a homologous expanding supernova of the type Ia, we consider each layer has a constant mass, so the derivative dV is given by

$$\mathrm{d}V = -\frac{m}{\rho^2}\mathrm{d}\rho. \tag{18}$$

Together with the equation of state

$$p = \frac{R}{\mu}T\rho, \tag{19}$$

we obtain the work for the adiabatic expansion as

$$\frac{\mathrm{d}W}{m} = \frac{R}{\mu}T\frac{\mathrm{d}\rho}{\rho}\,. \tag{20}$$

For differences in a time step Δt, the work is

$$W_{\rm adia} = \Delta\frac{W}{m} = \frac{R}{\mu}T\ln\left(\frac{\rho_2}{\rho_1}\right). \tag{21}$$

For the first test of a light curve for a supernova with an expanding atmosphere, we neglect the interaction between the layers, meaning the structure term is equal to the work of the adiabatic expansion so that

$$\frac{\mathrm{D}}{\mathrm{D}t}E = \frac{\mathrm{D}}{\mathrm{D}t}\left(\frac{E_0}{\rho} + e\right) = W_{\rm adia}. \tag{22}$$

As we now consider expanding atmospheres, we use more supernova-like structures for the tests. We set the maximum velocity to 30 000 km s^{-1} and use a radius of 5×10^{15} cm. With this setup, we calculated a light curve for the expanding atmosphere.

Figure 6 shows a plot of the light curve of supernova test atmosphere that is simply expanding. We considered time-independent radiative transfer and a grey atmosphere. As one can see, the luminosity is decreasing, because the atmosphere is cooling down adiabatically.

Now we test a setup more closely resembling a real supernova light curve. Therefore, we take an initial atmosphere structure and add an energy source (radioactive decay) in each layer. The energy source exponentially decreases to simulate declining activity of the radioactive species. Figure 7 shows the plot of the light curve of this test, resulting in a light curve with a supernova-like shape. We have a rising part of the light curve at

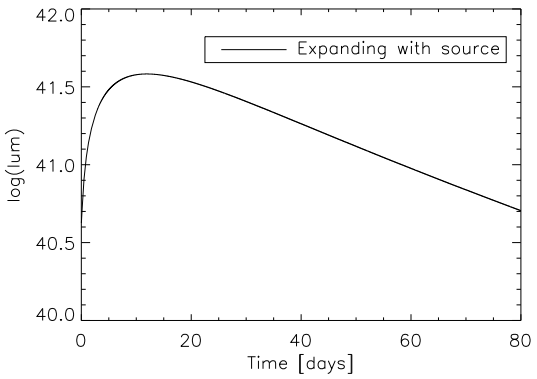

Fig. 7. Light curve of an atmosphere that is expanding and has an energy source. It has the typical shape of a light curve of a SN Ia. The luminosity rises due to the energy deposition. After the maximum we see the decline resulting from the expansion.

the beginning because of the energy deposition. After the maximum, the luminosity decreases due to the ongoing expansion and decreasing energy deposition. Of course this light curve is far from correct because the assumption of a grey atmosphere is a bad assumption for an SN Ia. But the tests show that the code behaves as expected.

3.2. Entropy

We calculated the entropy to test the code. Because energy is moving through the atmosphere, entropy is not conserved. Nevertheless, testing entropy conservation is an important test of the correctness of the code. Therefore, we calculated the entropy change in the case of pure adiabatic expansion. For testing, we neglected interaction between layers and gamma ray deposition and calculated the entropy change for a time step for the just expanding case.

To be consistent with our hydrodynamics equations, we deduced the entropy from the first law of thermodynamics. A change in the entropy during a time step is therefore given by

$$\frac{\Delta S}{mR} = \frac{3}{2}\frac{1}{\mu}\ln\left(\frac{T_2}{T_1}\right) + \frac{3}{2}\left(\frac{1}{\mu_2} - \frac{1}{\mu_1}\right) - \frac{1}{\mu}\ln\left(\frac{\rho_2}{\rho_1}\right) \tag{23}$$

where 2 is the index of quantities at the new time and 1 the one of the old. For the integration of the temperature and the density term, we kept μ fixed. This is not correct, but it is simpler to solve and the resulting differences for the entropy are small.

The entropy given here is only the entropy of the gas, so to check that the expansion worked right we had to neglect the radiation energy density in our energy density conservation equation. Furthermore we ignored the interaction between the layers and neglected the structure term. We now have only a change in the energy due to the adiabatic expansion.

With this setup we calculated a few time steps and checked the entropy. Even for a long time step of 1000 s the entropy stays almost constant. The relative change of the entropy was $\approx 10^{-6}$.

4. Time-dependent radiative transfer

So far, our radiative transfer code only solves the time-independent radiative transfer equation. For an implementation of the time dependence in the radiative transfer itself, the spherical symmetric special relativistic radiative transfer equation (SSRTE) for expanding atmospheres (Hauschildt & Baron 1999) is extended so that the additional time dependent term is given by

$$\frac{\gamma}{c}(1+\beta\mu)\frac{\partial I}{\partial t} \tag{24}$$

where $\beta = \frac{v}{c}$ is the velocity in units of the speed of light c and $\gamma = (1-\beta^2)^{-1/2}$ is the usual Lorentz factor. Here, I is the intensity, μ the cosine of the angle between the radial direction and the propagation vector of the light. Using the notation of Hauschildt & Baron (2004a), the comoving frame SSRTE with the additional time dependent term is given by

$$a_t\frac{\partial I}{\partial t} + a_r\frac{\partial I}{\partial r} + a_\mu\frac{\partial I}{\partial \mu} + a_\lambda\frac{\partial \lambda I}{\partial \lambda} + 4a_\lambda I = \eta - \chi I \tag{25}$$

where η is the emissivity and χ the extinction coefficient. The wavelength is represented by λ. The additional time dependent coefficient is given by

$$a_t = \frac{\gamma}{c}(1+\beta\mu)\,. \tag{26}$$

Along the characteristics the equation has the form

$$\frac{\mathrm{d}I_l}{\mathrm{d}s} + a_t\frac{\partial I}{\partial t} + a_l\frac{\partial \lambda I}{\partial \lambda} = \eta_l - (\chi_l + 4a_l)I_l \tag{27}$$

where $\mathrm{d}s$ is a line element along a (curved) characteristic and $I_l()$ is the specific intensity along the characteristic at point $s \geq 0$ ($s = 0$ denotes the beginning of the characteristic). For a definition of the other coefficients see Hauschildt & Baron (2004a).

4.1. Discretization of the time derivative

We used the first discretization as described in Hauschildt & Baron (2004a) and added the time dependent term. We discretized the time-dependent, as well as the wavelength, derivative in the SSRTE with an fully implicit method. The discretization of the time dependent term is given by

$$\left.\frac{\partial I}{\partial t}\right|_{t=t_j} = \frac{I_{t_j} - I_{t_{j-1}}}{t_j - t_{j-1}}, \tag{28}$$

so the SSRTE including the time discretization can be written as

$$\frac{\mathrm{d}I}{\mathrm{d}s} + a_\lambda\frac{\lambda_l I - \lambda_{l-1}I_{\lambda_{l-1}}}{\lambda_l - \lambda_{l-1}} + a_t\frac{I - I_{t_{j-1}}}{t_j - t_{j-1}} = \eta_{\lambda_l} - (\chi_{\lambda_l} + 4a_\lambda)I, \tag{29}$$

where I is the intensity at wavelength point λ_l and time point t_j. We define the optical depth scale along the ray as

$$\mathrm{d}\tau = \chi + a_\lambda\left(4 + \frac{\lambda_l}{\lambda_l - \lambda_{l-1}}\right) + \frac{a_t}{\Delta t} = -\hat{\chi}\mathrm{d}s. \tag{30}$$

Introducing the source function $S = \eta/\chi$, we get

$$\frac{\mathrm{d}I}{\mathrm{d}\tau} = I - \frac{\chi}{\hat{\chi}}\left(S + \frac{a_\lambda}{\chi}\frac{\lambda_{l-1}}{\lambda_l - \lambda_{l-1}}I_{\lambda_{l-1}} + \frac{a_t}{\chi}\frac{1}{\Delta t}I_{t_{j-1}}\right) \equiv I - \hat{S}\,. \tag{31}$$

We now have a modification of the source function and a new definition of the optical depth scale along a ray. With this redefinition of the optical depth and the source function, one can now proceed with the formal solution as described in Hauschildt & Baron (2004a).

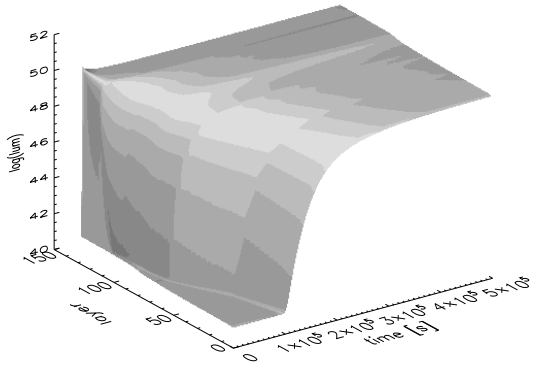

Fig. 8. Luminosity of each layer and time step of our test atmosphere.

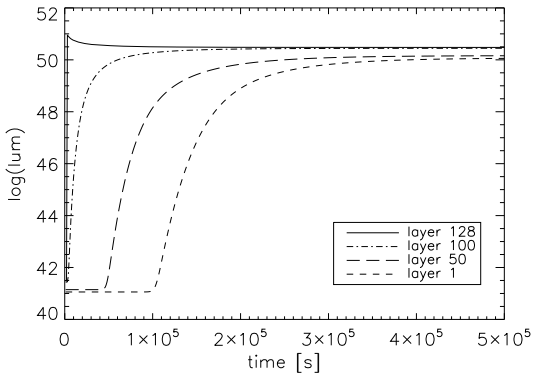

Fig. 9. The light curves of a few layers. In this case the atmosphere has an additional light source switching on inside. The radiation needs time to get to the outer layers.

4.2. Test calculations: time-dependent radiative transfer

For the test of the time-dependent radiative transfer, we used a static atmosphere structure to see the direct effects of the time dependence of the radiative transfer. Therefore, the temperature, radius, and density are all constant in time. For the test we then changed the inner boundary condition for the radiation (the "lightbulb") to initiate a perturbation of the radiation field, which then moves through the atmosphere via the time-dependent radiation transfer.

For the first test we switched on an additional light source inside the atmosphere. This light source has a luminosity of 10^9 times higher then the inner lightbulb.

In Fig. 8 we show the result of the time-dependent radiative transfer calculation. One can see that the light propagates outwards through the atmosphere. It takes a while before the additional light has propagated everywhere throughout the atmosphere. In Fig. 9 the light curves of a few layers are shown. One can see that the radiation needs time to get to the outer layers.

We compared our time scale to the radiation diffusion time scale. Assuming a random-walk process the mean free path for a photon is given by $\lambda_p = \frac{1}{\bar{\chi}}$, where $\bar{\chi}$ is the mean opacity. For a travel distance l the time t_p a photon needs is given by

$$t_p \approx \frac{1}{3}\frac{l^2}{c\lambda_p} = \frac{1}{3}\frac{l^2}{c}\bar{\chi}, \tag{32}$$

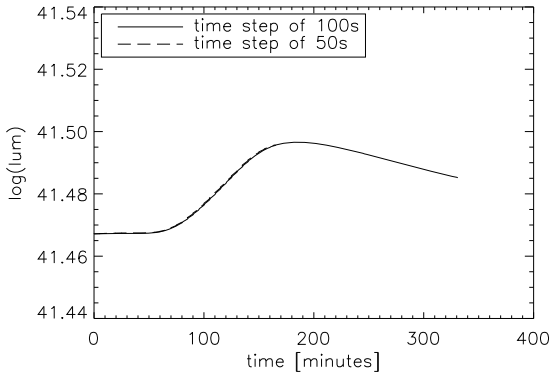

Fig. 10. The light curve of an atmosphere where a small perturbation moves outwards. The two plotted light curves of layer 110 were calculated with different time steps.

where c is the speed of light. For the mean opacity $\bar{\chi}$ we used the Rosseland mean. In our test case the atmosphere was divided into 128 layers. The mean opacity $\bar{\chi}$ ranges from 3×10^{-19} cm^{-1} in the outer parts to 3×10^{-14} cm^{-1} in the inner parts of the atmosphere. The distance l is the thickness of each layer, and it ranges between 6×10^{12} cm and 3×10^{13} cm. The result is that the diffusion time for a photon through the whole model atmosphere is about 3×10^3 s. As one can see in our plots our time scale is roughly 10^5. The assumption of a diffusion through the atmosphere is only valid for optically thick regions. Another problem is the choice of the right mean opacity. Considering this our estimate of the time scale is reasonable.

An important test is also to check that the results of the time-dependent radiative transfer calculation depend on the size of the time step. We tested this with a model that has a small perturbation inside that is moving outwards. This was calculated with two different time steps. In Fig. 10 the results of calculations with two different time steps are shown. As one can see, the result does not depend on the size of the time step.

In the next test we put a sinusoidally varying light bulb inside of our test atmosphere. In Fig. 11, we show a plot of the luminosity for each time step. After a while, the luminosity of the whole atmosphere varies sinusoidally and steady state is reached. The luminosities in different layers are shown in Fig. 12. One can see a phase shift of the sine curve, due to the time required for the radiation field to propagate through the atmosphere.

5. Conclusion

We have implemented a time evolution code into our general-purpose model atmosphere code PHOENIX, which keeps track of the energy conservation. Because a homologous expansion is a good assumption for supernovae in general and particularly for type Ia supernovae, we considered adiabatic free expansion for our code. With first test calculations, we reproduced the expected behavior of the test cases. Static atmospheres adopted the luminosity of an internal lightbulb and perturbations of the lightbulb moved outwards in time. We also calculated a light curve that had the shape of a typical supernovae Ia light curve.

To complete the physics of time-dependent processes in a supernova atmosphere, we extended our code even further. PHOENIX now solves the time dependent radiative transfer

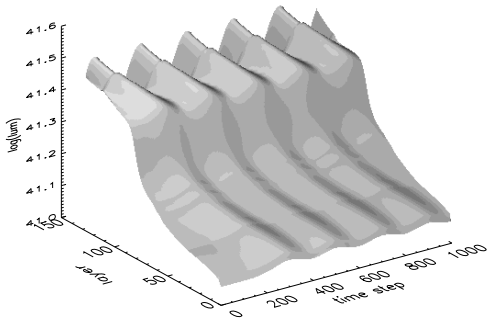

Fig. 11. Luminosity in each layer and time step. The light source inside the atmosphere varies sinusoidally.

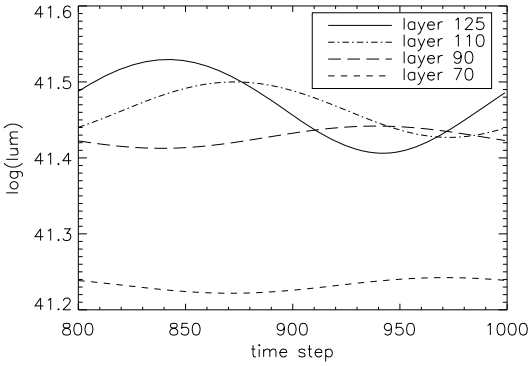

Fig. 12. Flux at different radii of a sinusoidally varying atmosphere.

equation. We presented the new discretization scheme of the time dependent $\frac{\partial}{\partial t}$ term. We checked our code with a series of tests. A perturbation can be followed on its way through the atmosphere. We ran a test model with a sinusoidal source. In steady state the whole atmosphere was varying sinusoidally, responding to the source. A phase shift between the inner and outer layers could also be observed. All tests indicate that our extended code works fine.

Future work is to calculate realistic light curves for type Ia supernova hydro models. As a first step we can consider the atmosphere to be in LTE, but including detailed opacities and treating full line blanketing.

Also with our time-dependent radiative transfer, we can address a longstanding debate about the importance of time dependence in calculating the spectra of type Ia supernovae (Eastman & Pinto 1993; Baron et al. 1996). One challenge is the computation time needed for a whole light curve with more complex NLTE radiative transfer.

Acknowledgements. This work was supported in part by the Deutsche Forschungsgemeinschaft (DFG) via the SFB 676, NASA grant NAG5-12127, NSF grant AST-0707704, and US DOE Grant DE-FG02-07ER41517. This research used resources of the National Energy Research Scientific Computing Center (NERSC), which is supported by the Office of Science of the U.S. Department of Energy under Contract No. DE-AC02-05CH11231, and the Höchstleistungs Rechenzentrum Nord (HLRN). We thank all these institutions for generous allocations of computer time.

References

Baron, E., Hauschildt, P. H., & Mezzacappa, A. 1996, MNRAS, 278, 763
Bongard, S., Baron, E., Smadja, G., Branch, D., & Hauschildt, P. 2006, ApJ, 647, 480
Bronder, T. J., Hook, I. M., Astier, P., et al. 2008, A&A, 477, 717
Cooperstein, J., van den Horn, L. J., & Baron, E. 1986, ApJ, 309, 653
Eastman, R., & Pinto, P. 1993, ApJ, 412, 731
Foley, R. J., Filippenko, A. V., & Jha, S. W. 2008, A&A [ArXiv:0803.1181]
Goldhaber, G., Groom, D. E., Kim, A., et al. 2001, ApJ, 558, 359
Hachinger, S., Mazzali, P. A., & Benetti, S. 2006, MNRAS, 370, 299
Hauschildt, P. H., & Baron, E. 1999, J. Comp. Appl. Math., 109, 41
Hauschildt, P. H., & Baron, E. 2004a, A&A, 417, 317
Hauschildt, P. H., & Baron, E. 2004b, Mitteilungen der Mathematischen Gesellschaft in Hamburg, 24, 1
Hauschildt, P. H., Barman, T. S., Baron, E., & Allard, F. 2003, in Stellar Atmospheric Modeling, ed. I. Hubeny, D. Mihalas, & K. Werner (San Francisco: ASP), 227
Le Du, J., et al. 2009, preprint
Mihalas, D., & Mihalas, B. W. 1984, Foundations of Radiation Hydrodynamics (Oxford: Oxford University)
Nugent, P., Phillips, M., Baron, E., Branch, D., & Hauschildt, P. 1995, ApJ, 455, L147
Perlmutter, S., Aldering, G., Goldhaber, G., et al. 1999, ApJ, 517, 565
Phillips, M. M. 1993, ApJ, 413, L105
Pinto, P. A., & Eastman, R. G. 2000, ApJ, 530, 744
Pskovskii, I. P. 1977, Sov. Astron., 21, 675
Riess, A., Filippenko, A. V., Challis, P., et al. 1998, AJ, 116, 1009
Riess, A. G., Press, W. H., & Kirshner, R. P. 1996, ApJ, 473, 88
Woosley, S. E., Kasen, D., Blinnikov, S., & Sorokina, E. 2007, ApJ, 662, 487

A&A 509, A36 (2010)
DOI: 10.1051/0004-6361/200913064

Astronomy & Astrophysics

A 3D radiative transfer framework

VI. PHOENIX/3D example applications

P. H. Hauschildt[1] and E. Baron[1,2,3]

[1] Hamburger Sternwarte, Gojenbergsweg 112, 21029 Hamburg, Germany
e-mail: yeti@hs.uni-hamburg.de
[2] Homer L. Dodge Dept. of Physics and Astronomy, University of Oklahoma, 440 W. Brooks, Rm 100, Norman, OK 73019, USA
e-mail: baron@ou.edu
[3] Computational Research Division, Lawrence Berkeley National Laboratory, MS 50F-1650, 1 Cyclotron Rd, Berkeley, CA 94720-8139, USA

Received 5 August 2009 / Accepted 10 November 2009

ABSTRACT

Aims. We demonstrate the application of our 3D radiative transfer framework in the model atmosphere code PHOENIX for a number of spectrum synthesis calculations for very different conditions.
Methods. The 3DRT framework discussed in the previous papers of this series was added to our general-purpose model atmosphere code PHOENIX/1D and an extended 3D version PHOENIX/3D was created. The PHOENIX/3D code is parallelized via the MPI library using a hierarchical domain decomposition and displays very good strong scaling.
Results. We present the results of several test cases for widely different atmosphere conditions and compare the 3D calculations with equivalent 1D models to assess the internal accuracy of the 3D modeling. In addition, we show the results for a number of parameterized 3D structures.
Conclusions. With presently available computational resources it is possible to solve the full 3D radiative transfer (including scattering) problem with the same micro-physics as included in 1D modeling.

Key words. radiative transfer – methods: numerical – stars: atmospheres

1. Introduction

In a series of papers (Hauschildt & Baron 2006; Baron & Hauschildt 2007; Hauschildt & Baron 2008, 2009; Baron et al. 2009, hereafter: Papers I–V), we have described a framework for the solution of the radiative transfer equation in 3D systems (3DRT), including a detailed treatment of scattering in continua and lines with a non-local operator splitting method. These papers deal solely with the radiation transport problem and its numerical solution for test cases designed to stress-test the algorithms and codes. It is important, however, to apply the radiative transfer codes to "real" problems, e.g., model atmosphere simulations and to compare the results to 1D equivalents. We have extended our general purpose model atmosphere code PHOENIX to use the 3DRT framework so that the new version of PHOENIX can calculate both 1D (PHOENIX/1D) and 3D (PHOENIX/3D) models and spectra. In this paper we will describe the implementation and the results of PHOENIX calculations comparing the results of 1D and 3D spectrum syntheses for different model parameters.

2. Method

In the following discussion we use notation of Papers I–V. The basic framework and the methods used for the formal solution and the solution of the scattering problem via non-local operator splitting are discussed in detail in these papers and will not be repeated here.

3. PHOENIX/3D implementation and micro-physics

We have implemented PHOENIX/3D to use as much as possible of the micro-physics of PHOENIX/1D. This applies to the ACES equation of state (Barman, in preparation), to the b-f and f-f opacities, to dust opacities, and to the line opacities (PHOENIX/3D is presently restricted to LTE population densities). This includes individual line profiles (Gauss profiles for weak lines and Voigt profiles for strong lines depending on user-selectable selection criteria) for atomic and molecular lines with the same physics that is implemented in PHOENIX/1D, so that the results of the opacity calculations are equal for the same physical conditions for the two modes of PHOENIX.

The important considerations of PHOENIX/3D implementation are memory and CPU time consumption. The memory requirements of PHOENIX/3D compared to PHOENIX/1D are mostly due the the much larger number of voxels in the 3D case (typically 10^6 voxels) compared to the 1D case (usually 64–128 layers). As the memory required to store (and to compute) physical data such as the partial pressures of close to 900 species or the opacities scales linearly with the number of cells (or layers in 1D), it is obvious that only very small tests can be run without using domain decomposition methods on large scale parallel supercomputers. The domain decomposition implementation of PHOENIX/3D distributes the task of solving (and storing) the equation of state data and the wavelength dependent opacities to sets of processes each with its private

memory. This linearly (with number of processes used) reduces the amount of memory and time required for these tasks. For 1024 processes, this reduces the memory requirements to just a few MB per process to store the full equation of state results. The 3DRT requires, in comparison, a total of about 450 MB for the same problem (due to the storage requirements of the non-local Łstar-operator). Including the storage required for the computation of the line opacities, this is still just about 0.5GB/process, which is small compared to the typically available 4–16 GB/core (CPU) on modern parallel supercomputers. In order to fully utilize the available memory per core and to increase flexibility we have implemented a hierarchical scheme similar to the parallel PHOENIX/1D implementation discussed in Hauschildt et al. (1997) and in Baron & Hauschildt (1998) and to the 3DRT parallelization in Paper II: We use a number of "clusters" of processes where every cluster works on a different wavelength. Each cluster internally uses (on its subset of processes) the domain decomposition discussed above and the 3DRT parallelizations discussed in Paper I. This scheme can be adjusted to (a) fit the problem in the memory available for each core and (b) to optimize overall performances (e.g., depending on the number of solid angle points for the 3DRT solution or the coordinate system used). In the calculations presented here, we typically use clusters with 256–1024 processes, the number of clusters is limited only by the number of available CPUs.

4. Results

We have calculated a number of test models to compare the results of PHOENIX/1D calculations with PHOENIX/3D results. This comparison can be used to adjust the parameters of the 3D calculations (number of voxels or solid angle points) to give an accuracy that is acceptable for a given investment in computer time. The models that we show here were taken from the latest PHOENIX/1D grid (in preparation) of model atmospheres. In all stellar models (1D and 3D) we have used the set of solar abundances given in Asplund et al. (2005).

4.1. Stellar models

We have computed synthetic spectra for stellar model atmospheres with the parameters $T_{\rm eff} = 3000\ K$, $\log(g) = 5.0$ (M dwarf), $T_{\rm eff} = 5700\ K$, $\log(g) = 4.5$ (solar type star) and $T_{\rm eff} = 9000\ K$, $\log(g) = 4.5$ (A star). The PHOENIX/1D models were computed with the latest setup in the input physics, including the ACES equation of state and the latest version of the atomic and molecular line databases. The model structures were then used as inputs to PHOENIX/3D to calculate synthetic spectra with the same sampling rates as the spectra from the PHOENIX/1D calculations. In the PHOENIX/3D calculations we have used a 3D spherical coordinate system with $n_{\rm r} = 129$, $n_{\theta_{\rm c}} = 65$ and $n_{\phi_{\rm c}} = 129$ points for a total of about 1M voxels. The calculations used (if not specified otherwise) 64^2 solid angle points. For each object we calculated synthetic spectra with PHOENIX/1D and PHOENIX/3D and compare the fluxes of the 1D spectra to the flux vectors of the 3D results. As in paper IV we can use the $(\theta_{\rm c}, \phi_{\rm c})$ components of the 3D flux vector in 3D spherical coordinates to estimate the internal accuracy of the solution (as the $F_{\theta_{\rm c}}$ and $F_{\phi_{\rm c}}$ components are zero for spherically symmetric configurations). Figures 1 to 7 show selected results for the different models. In these cases, the error due to the number of solid angle points is about 3% and in all tests run the differences between the PHOENIX/1D fluxes and the $F_{\rm r}$ component of the PHOENIX/3D calculation is of the same order. The differences between the 1D and 3D calculations are within the accuracy set by the number of solid angles in the 3D model. In order to verify that the errors get smaller with larger number of solid angles (as shown in Paper IV for simple test cases), we have run test models with 256^2 angles. Three example plots are shown in Figs. 8 to 10 The results show clearly that the higher solid angle resolution reduces the errors in $F_{\theta_{\rm c}}$ and $F_{\phi_{\rm c}}$ considerably and also improves the comparison for $F_{\rm r}$ to the 1D result, as the higher internal accuracy due to more solid angle points also increases the internal accuracy of $F_{\rm r}$. This also shows that in 3D radiative transfer calculations the spatial resolution is not the only factor governing the quality of the solution, the solid angle resolution may in fact be more important, depending on the coordinate system used and the details of the problem that isve calculated a number of test models to compare the results of PHOENIX/1D calculations with PHOENIX/3D results. This comparison can be used to adjust the parameters of the 3D calculations (number of voxels or solid angle points) to give an accuracy that is acceptable for a given investment in computer time. The models that we show here were taken from the latest PHOENIX/1D grid (in preparation) of model atmospheres. In all stellar models (1D and 3D) we have used the set of solar abundances given in Asplund et al. (2005). We have calculated a number of test models to compare the results of PHOENIX/1D calculations with PHOENIX/3D results. This comparison can be used to adjust the parameters of the 3D calculations (number of voxels or solid angle points) to give an accuracy that is acceptable for a given investment in computer time. The models that we show here were taken from the latest PHOENIX/1D grid (in preparation) of model atmospheres. In all stellar models (1D and 3D) we have used the set of solar abundances given in Asplund et al. (2005).

4.2. Scaling

In order to investigate the strong scaling properties of PHOENIX/3D we have constructed a small test case for a M dwarf model with 1000 wavelength points in a 3D spherical coordinate system with $n_{\rm r} = 129$, $n_{\theta_{\rm c}} = 65$ and $n_{\phi_{\rm c}} = 129$ points for a total of about 1M voxels and 64^2 solid angle points and ran the calculations with different configurations of the domain decomposition and different total numbers of processes. The total workload remains constant in these calculations, so this is a strong scaling test where the workload per CPU drops as the number of processes increase (in contrast to a weak scaling test where the workload per process remains constant). The results are given in Table 1. In this table, "n(MPI)" is the total number of MPI processes used, "cluster size" is the number of processes that collaboratively work on a single wavelength (spatial domain decomposition) and "n(cluster)" is the number of such clusters, each working on a different wavelength (energy domain decomposition). The product "cluster size" × "n(cluster)" is always equal to "n(MPI)". The column "Comm" gives the time spent in MPI communication to collect the opacities from the different processes before the 3DRT calculation starts. The communication requirements of the 3DRT calculations are included in the 3DRT column. The columns "line opacity" give the time in seconds and scaling efficiency for all line opacity calculations, respectively, The columns "total" give the total time and scaling efficiency, respectively, of the overall time spent in the computation of the 3D spectrum, this time does not include (small) contributions from the EOS solution and the line selection procedures. In the

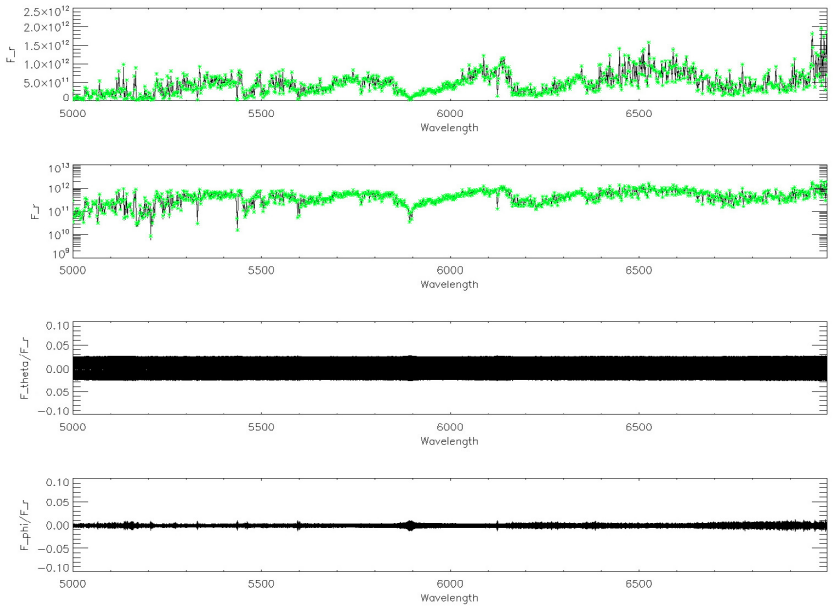

Fig. 1. Comparison between the PHOENIX/1D optical spectrum and the flux vectors across the outermost voxels for the PHOENIX/3D spectra computed for the M dwarf test model ($T_{\rm eff}$ = 3000 K, $\log(g)$ = 5.0, "$*$" symbols). In the PHOENIX/3D calculations we have used a 3D spherical coordinate system with $n_{\rm r}$ = 129, $n_{\theta_{\rm c}}$ = 65 and $n_{\phi_{\rm c}}$ = 129 points for a total of about 1M voxels. The calculations used 64^2 solid angle points. The *top panels* show the $F_{\rm r}$ component of all outer voxels in linear and logarithmic scales, respectively. The *bottom panels* show the corresponding runs of $F_\theta/F_{\rm r}$ and $F_\phi/F_{\rm r}$, respectively. The should be identically zero and the deviations measure the internal accuracy. See Figs. 8 to 10 for high-accuracy solutions for comparison. The wavelengths are given in Å and the fluxes are in cgs units.

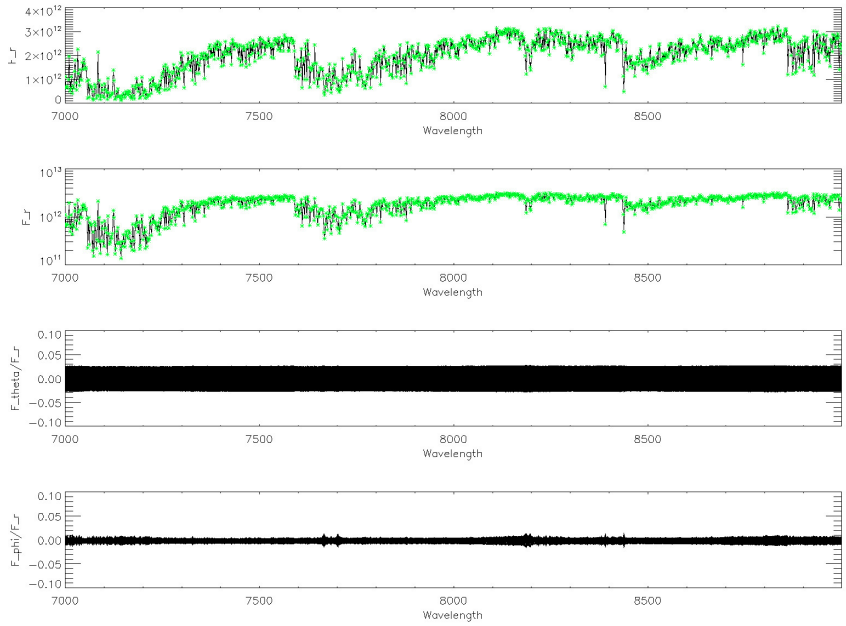

Fig. 2. Comparison between the PHOENIX/1D near infrared spectrum and the flux vectors across the outermost voxels for the PHOENIX/3D spectra computed for the M dwarf test model ($T_{\rm eff}$ = 3000 K, $\log(g)$ = 5.0, "$*$" symbols). In the PHOENIX/3D calculations we have used a 3D spherical coordinate system with $n_{\rm r}$ = 129, $n_{\theta_{\rm c}}$ = 65 and $n_{\phi_{\rm c}}$ = 129 points for a total of about 1M voxels. The calculations used 64^2 solid angle points. The *top panels* show the $F_{\rm r}$ component of all outer voxels in linear and logarithmic scales, respectively. The *bottom panels* show the corresponding runs of $F_\theta/F_{\rm r}$ and $F_\phi/F_{\rm r}$, respectively. The should be identically zero and the deviations measure the internal accuracy. See Figs. 8 and 10 for high-accuracy solutions for comparison. The wavelengths are given in Å and the fluxes are in cgs units.

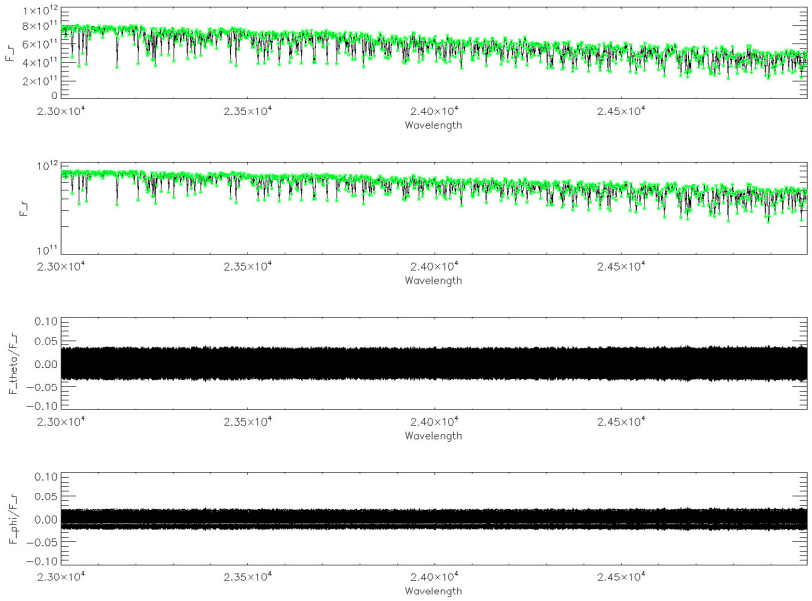

Fig. 3. Comparison between the PHOENIX/1D infrared spectrum and the flux vectors across the outermost voxels for the PHOENIX/3D spectra computed for the M dwarf test model ($T_{\rm eff}$ = 3000 K, $\log(g)$ = 5.0, "∗" symbols). In the PHOENIX/3D calculations we have used a 3D spherical coordinate system with $n_{\rm r}$ = 129, $n_{\theta_{\rm c}}$ = 65 and $n_{\phi_{\rm c}}$ = 129 points for a total of about 1M voxels. The calculations used 64^2 solid angle points. The *top panels* show the $F_{\rm r}$ component of all outer voxels in linear and logarithmic scales, respectively. The *bottom panels* show the corresponding runs of $F_\theta/F_{\rm r}$ and $F_\phi/F_{\rm r}$, respectively. The should be identically zero and the deviations measure the internal accuracy. See Figs. 8 and 10 for high-accuracy solutions for comparison. The wavelengths are given in Å and the fluxes are in cgs units.

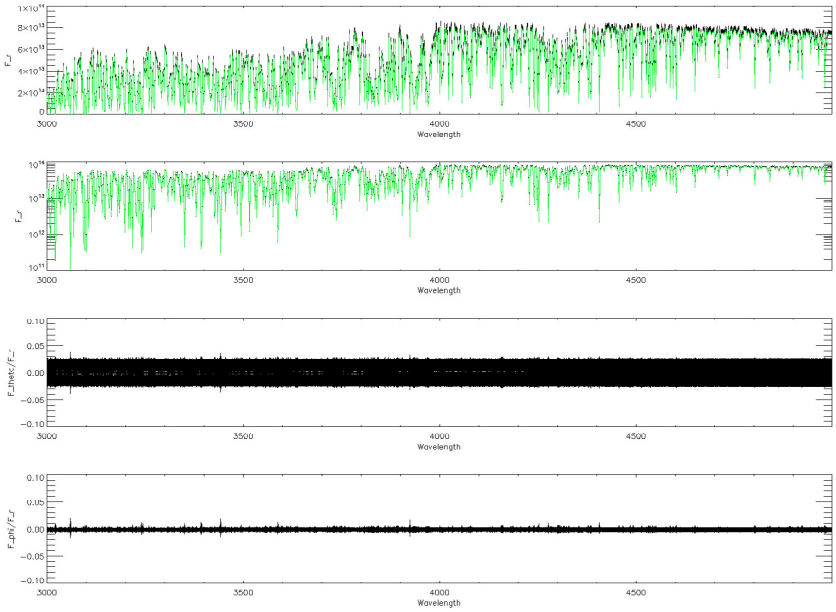

Fig. 4. Comparison between the PHOENIX/1D near UV spectrum and the flux vectors across the outermost voxels for the PHOENIX/3D spectra computed for the G2V dwarf test model ($T_{\rm eff}$ = 5700 K, $\log(g)$ = 4.5, "∗" symbols). In the PHOENIX/3D calculations we have used a 3D spherical coordinate system with $n_{\rm r}$ = 129, $n_{\theta_{\rm c}}$ = 65 and $n_{\phi_{\rm c}}$ = 129 points for a total of about 1M voxels. The calculations used 64^2 solid angle points. The *top panels* show the $F_{\rm r}$ component of all outer voxels in linear and logarithmic scales, respectively. The *bottom panels* show the corresponding runs of $F_\theta/F_{\rm r}$ and $F_\phi/F_{\rm r}$, respectively. The should be identically zero and the deviations measure the internal accuracy. See Figs. 8 and 10 for high-accuracy solutions for comparison. The wavelengths are given in Å and the fluxes are in cgs units.

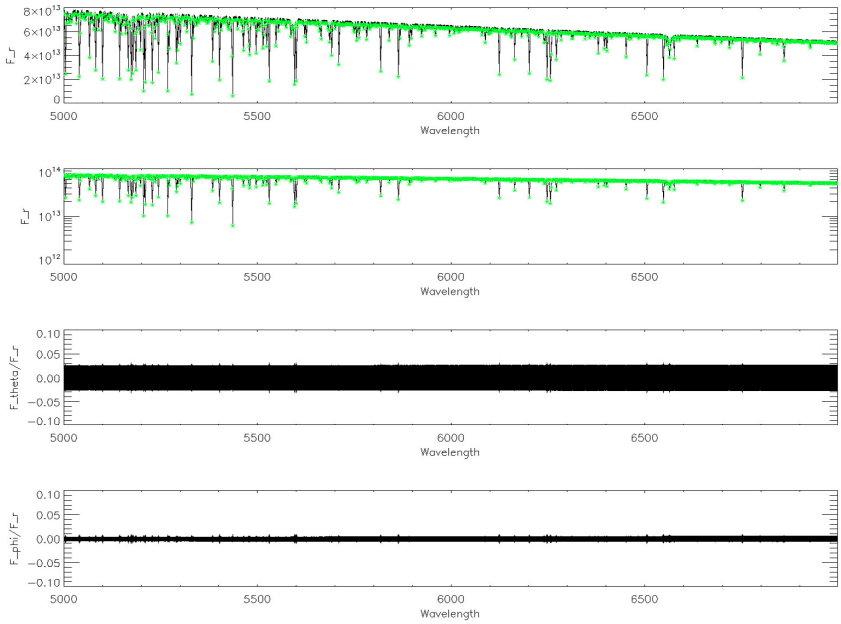

Fig. 5. Comparison between the PHOENIX/1D optical spectrum and the flux vectors across the outermost voxels for the PHOENIX/3D spectra computed for the G2V dwarf test model ($T_{\rm eff}$ = 5700 K, $\log(g)$ = 4.5, "$*$" symbols). In the PHOENIX/3D calculations we have used a 3D spherical coordinate system with $n_{\rm r}$ = 129, n_{θ_c} = 65 and n_{ϕ_c} = 129 points for a total of about 1M voxels. The calculations used 64^2 solid angle points. The *top panels* show the $F_{\rm r}$ component of all outer voxels in linear and logarithmic scales, respectively. The *bottom panels* show the corresponding runs of $F_\theta/F_{\rm r}$ and $F_\phi/F_{\rm r}$, respectively. The should be identically zero and the deviations measure the internal accuracy. See Figs. 8 and 10 for high-accuracy solutions for comparison. The wavelengths are given in Å and the fluxes are in cgs units.

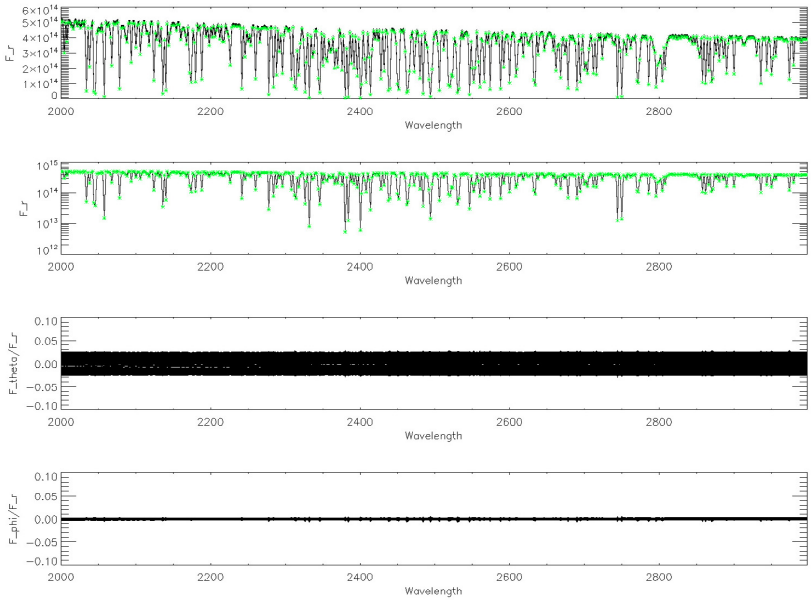

Fig. 6. Comparison between the PHOENIX/1D optical spectrum and the flux vectors across the outermost voxels for the PHOENIX/3D spectra computed for the A dwarf test model ($T_{\rm eff}$ = 9000 K, $\log(g)$ = 4.5, "$*$" symbols). In the PHOENIX/3D calculations we have used a 3D spherical coordinate system with $n_{\rm r}$ = 129, n_{θ_c} = 65 and n_{ϕ_c} = 129 points for a total of about 1M voxels. The calculations used 64^2 solid angle points. The *top panels* show the $F_{\rm r}$ component of all outer voxels in linear and logarithmic scales, respectively. The *bottom panels* show the corresponding runs of $F_\theta/F_{\rm r}$ and $F_\phi/F_{\rm r}$, respectively. The should be identically zero and the deviations measure the internal accuracy. See Figs. 8 and 10 for high-accuracy solutions for comparison. The wavelengths are given in Å and the fluxes are in cgs units.

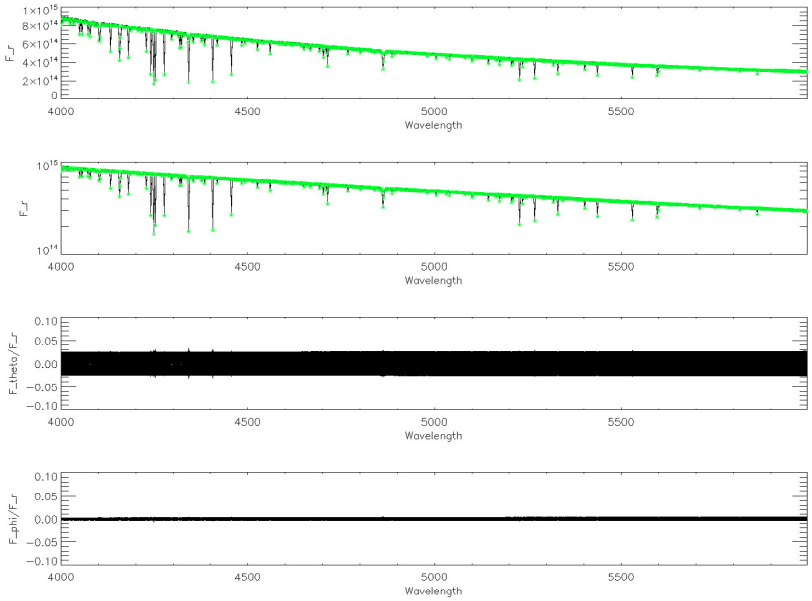

Fig. 7. Comparison between the PHOENIX/1D UV spectrum and the flux vectors across the outermost voxels for the PHOENIX/3D spectra computed for the A dwarf test model ($T_{\rm eff}$ = 9000 K, $\log(g)$ = 4.5, "$*$" symbols). In the PHOENIX/3D calculations we have used a 3D spherical coordinate system with $n_{\rm r}$ = 129, $n_{\theta_{\rm c}}$ = 65 and $n_{\phi_{\rm c}}$ = 129 points for a total of about 1M voxels. The calculations used 64^2 solid angle points. The *top panels* show the $F_{\rm r}$ component of all outer voxels in linear and logarithmic scales, respectively. The *bottom panels* show the corresponding runs of $F_\theta/F_{\rm r}$ and $F_\phi/F_{\rm r}$, respectively. The should be identically zero and the deviations measure the internal accuracy. See Figs. 8 and 10 for high-accuracy solutions for comparison. The wavelengths are given in Å and the fluxes are in cgs units.

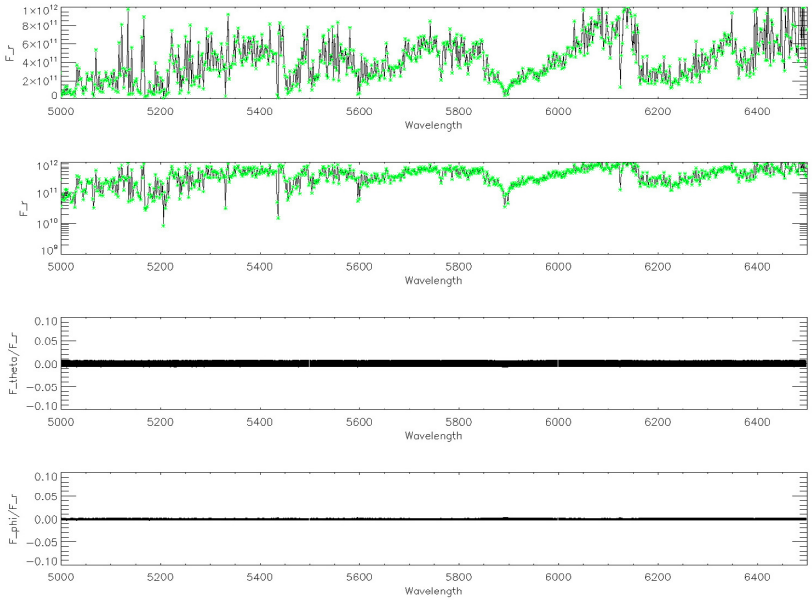

Fig. 8. Comparison between the PHOENIX/1D optical spectrum and the flux vectors across the outermost voxels for the higher resolution PHOENIX/3D spectra computed for the M dwarf test model ($T_{\rm eff}$ = 3000 K, $\log(g)$ = 5.0, "$*$" symbols). In the PHOENIX/3D calculations we have used a 3D spherical coordinate system with $n_{\rm r}$ = 129, $n_{\theta_{\rm c}}$ = 65 and $n_{\phi_{\rm c}}$ = 129 points for a total of about 1M voxels. The calculations used 256^2 solid angle points. The *top panels* show the $F_{\rm r}$ component of all outer voxels in linear and logarithmic scales, respectively. The *bottom panels* show the corresponding runs of $F_\theta/F_{\rm r}$ and $F_\phi/F_{\rm r}$, respectively. The should be identically zero and the deviations measure the internal accuracy. The wavelengths are given in Å and the fluxes are in cgs units.

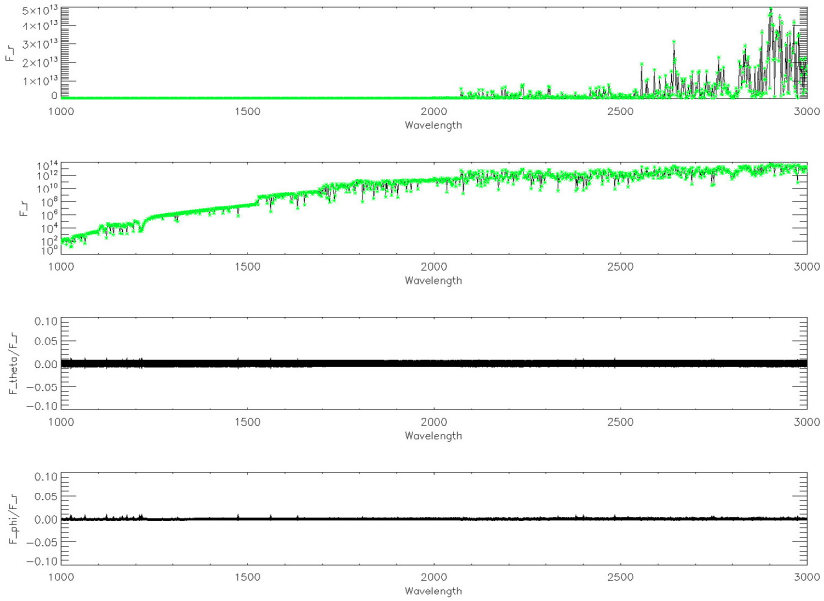

Fig. 9. Comparison between the PHOENIX/1D UV spectrum and the flux vectors across the outermost voxels for the higher resolution PHOENIX/3D spectra computed for the G2V dwarf test model ($T_{\rm eff}$ = 5700 K, $\log(g)$ = 4.5, "$*$" symbols). In the PHOENIX/3D calculations we have used a 3D spherical coordinate system with $n_{\rm r}$ = 129, $n_{\theta_{\rm c}}$ = 65 and $n_{\phi_{\rm c}}$ = 129 points for a total of about 1M voxels. The calculations used 256^2 solid angle points. The *top panels* show the $F_{\rm r}$ component of all outer voxels in linear and logarithmic scales, respectively. The *bottom panels* show the corresponding runs of $F_\theta/F_{\rm r}$ and $F_\phi/F_{\rm r}$, respectively. The should be identically zero and the deviations measure the internal accuracy. The wavelengths are given in Å and the fluxes are in cgs units.

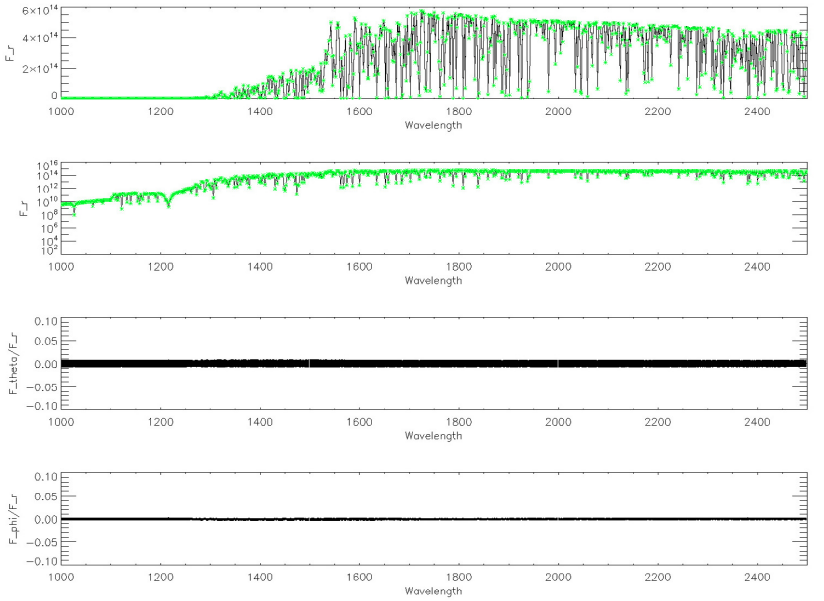

Fig. 10. Comparison between the optical PHOENIX/1D spectrum and the flux vectors across the outermost voxels for the higher resolution PHOENIX/3D spectra computed for the A dwarf test model ($T_{\rm eff}$ = 5700 K, $\log(g)$ = 4.5, "$*$" symbols). In the PHOENIX/3D calculations we have used a 3D spherical coordinate system with $n_{\rm r}$ = 129, $n_{\theta_{\rm c}}$ = 65 and $n_{\phi_{\rm c}}$ = 129 points for a total of about 1M voxels. The calculations used 256^2 solid angle points. The *top panels* show the $F_{\rm r}$ component of all outer voxels in linear and logarithmic scales, respectively. The *bottom panels* show the corresponding runs of $F_\theta/F_{\rm r}$ and $F_\phi/F_{\rm r}$, respectively. The should be identically zero and the deviations measure the internal accuracy. The wavelengths are given in Å and the fluxes are in cgs units.

Table 1. Strong scaling behavior of a M dwarf model test case for different configurations and total number of processors used. (See text for details).

			Timing:				Scaling:		
n(MPI)	Cluster size	n(cluster)	Line opacity	3DRT	Comm	Total	Line opacity	3DRT	Total
2048	512	4	2473	9942	436	12 909	96.7%	79.3%	81.9%
2048	256	8	2414	8054	285	10 789	99.1%	97.9%	98.0%
1024	512	2	4900	20 103	754	25 872	97.6%	78.4%	81.7%
1024	256	4	4741	15 966	604	21 385	100.9%	98.7%	98.9%
1024	128	8	4681	14 275	471	19 483	102.2%	110.4%	108.6%
512	512	1	9780	39 793	1539	51 341	97.8%	79.2%	82.4%
512	256	2	9566	31 524	1061	42 300	100.0%	100.0%	100.0%

largest cluster size of 512 processes each process only works on 8 solid angles, whereas in the smallest cluster size (128) each process works on 32 solid angles. The work per solid angle is not perfectly constant and the amount of communication increases linearly as more processes collaborate, therefore, the scaling efficiency drops if more than about 512 processes are used for this problem size (i.e., number of solid angles). The scaling efficiency for the overall problem is quite good, the optimal value is about 98%. The drop-off for cluster sizes of 512 (and more) is due to (a) the relatively small number of solid angles leading to very little work for each 3DRT process and relatively more internal communication time in the 3DRT and (b) the small effect of the communication related to the spatial domain decomposition. We could not test setups with more than (the maximum available) 2048 processes; however, the test case should scale to 256 k processes (number of wavelength points times cluster size), although for such a setup the overheads for, e.g., the solution of the equation of state and the line selection would be very noticeable.

4.3. 3D hydro model of solar convection

For a test with a computed 3D structure, we use the same example snapshot structure from Ludwig (Caffau et al. 2007; Wedemeyer et al. 2004) of a radiation-hydrodynamical simulation of convection in the solar atmosphere as in Paper III. The radiation transport calculations were performed with a total of $141 \times 141 \times 151$ Cartesian grid points in x, y, and z, respectively, for a total of 3 002 031 voxels, the periodic boundary conditions are set in the (horizontal) x, y plane. The 3D radiative transport equation is solved for $n_\theta = 64$ and $n_\phi = 64$ solid angle points, so that a total of about 12×9 intensities are calculated for each 3DRT iteration and wavelength point. For the tests described here, we are only using the temperature–pressure structure of the hydro model and ignore the velocity field.

We show example results in Figs. 11 to 14 in terms of the x, y, and z components of the flux vectors of each outer boundary voxel. The F_z components are, in addition, compared to the 1D model for the G2V star with the parameters $T_{\rm eff} = 5700\ K$, $\log(g) = 4.5$ ($*$ symbols in the figures). The general shape of the 3D spectra compare well to the 1D solar type model, of course there are large variations across the horizontal plane. In the UV the differences are largest, a number of voxel flux vectors show strong line emission, whereas the radiative+convective equilibrium 1D model only shows absorption features. This is to be expected as the 3D simulation of convection gives significant temperature variations across the volume considered, in particular in the horizontal plane. These variations have considerable effect on the radiative transfer solution: The horizontal components of the flux vectors of each voxel compared to the length of the flux vector $F = |\boldsymbol{F}|$, F_x/F and F_y/F, show quite substantial variations for different wavelengths. The variations are much larger for smaller wavelengths (e.g., in the UV), due to the larger temperature dependence of the source functions for smaller wavelengths which translates to larger horizontal flux components for small wavelengths compared to longer wavelengths.

The components of the flux vectors in the $x - y$ plane can be larger than the z component, strongly dependent on the wavelength and on the location of the voxel. This is illustrated in Figs. 15–22, which show the flowlines of the $x - y$ components of the flux vector at the surface. The flow distances are much larger at optical wavelengths than in the UV due to the larger UV opacities. The "pattern" of the horizontal energy flow depends strongly on the wavelength, it is also significantly different in the cores of strong lines compared to the surrounding continuum. The horizontal heat exchange could have in turn noticeable effects on the gas flow pattern.

4.4. Supernovae

The modeling of supernova spectra is a very important application of `PHOENIX/3D` modeling as it is expected, and explosion models show, that supernova explosions are intrinsically 3D driven. For the calculations shown here we use the Lagrangian frame 3DRT in spherical 3D coordinates as discussed in paper V. The test model is a simplified model for a type II supernova atmosphere with a maximum expansion speed of about $0.13c$. The model is a simple uniform composition model with the density parameterized as $\rho \propto r^{-9}$, and a "photospheric velocity" of $v_0 = 7600$ km s^{-1}, and a model temperature of $T_{\rm model} = 17\,000$ K. These conditions correspond roughly to those of SN 1999em seven days after explosion. In Fig. 23 we show the CMF spectrum of the `PHOENIX/3D` run compared to the corresponding `PHOENIX/1D` synthetic spectrum. Due to computer time limitations we could only run a relatively small 3D model with $n_{\rm r} = 129$, $n_{\theta_{\rm c}} = 33$ and $n_{\phi_{\rm c}} = 65$ points and 128^2 solid angle points. The small angular resolution causes the scatter in the $F_{\rm r}$ plots and the errors in the $F_{\theta_{\rm c}}$ and $F_{\phi_{\rm c}}$ components. In general the agreement is acceptable for this test run, for a full scale 3D SN spectrum the resolution in $(\theta_{\rm c}, \phi_{\rm c})$ should be increased to (65, 129) at least and the angular resolution should be at least 512^2 (which reduces the bandwidth dramatically, see Paper V).

5. Summary and conclusions

We have described first results we have obtained by incorporating the 3D radiative transfer framework we have discussed in

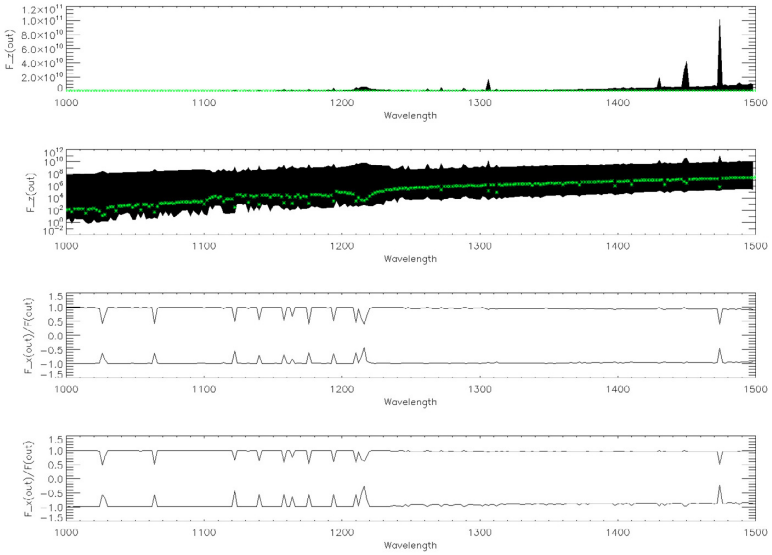

Fig. 11. Comparison between the flux vectors across the outermost voxels for the PHOENIX/3D UV spectra computed for the 3D hydro structure and the PHOENIX/1D spectrum for the G2V dwarf test model ($T_{\rm eff}$ = 5700 K, $\log(g)$ = 4.5). In the PHOENIX/3D calculations we have used a 3D coordinate system with a total of 141 × 141 × 151 Cartesian grid points in x, y, and z, respectively, the periodic boundary conditions are set in the (horizontal) x, y plane. The 3D radiative transport equation is solved for n_θ = 64 and n_ϕ = 64 solid angle points. The *top panels* show the F_z component of all outer voxels in linear and logarithmic scales, respectively, compared to the results of the 1D comparison model. The *bottom panels* show the corresponding maxima and minima of $F_x/|\boldsymbol{F}|$ and $F_y/|\boldsymbol{F}|$, respectively, over all surface voxels for each wavelength. These panels show that in the 3D structure even at the surface a substantial horizontal energy flow takes place, see also Figs. 15–22. See text for details. The wavelengths are given in Å and the fluxes are in cgs units.

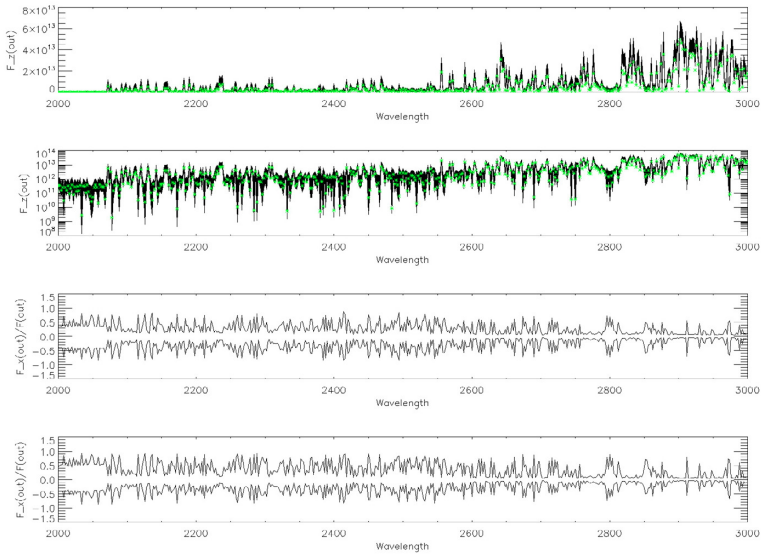

Fig. 12. Comparison between the flux vectors across the outermost voxels for the PHOENIX/3D near UV spectra computed for the 3D hydro structure and the PHOENIX/1D spectrum for the G2V dwarf test model ($T_{\rm eff}$ = 5700 K, $\log(g)$ = 4.5). In the PHOENIX/3D calculations we have used a 3D coordinate system with a total of 141 × 141 × 151 Cartesian grid points in x, y, and z, respectively, the periodic boundary conditions are set in the (horizontal) x, y plane. The 3D radiative transport equation is solved for n_θ = 64 and n_ϕ = 64 solid angle points. The *top panels* show the F_z component of all outer voxels in linear and logarithmic scales, respectively, compared to the results of the 1D comparison model. The *bottom panels* show the corresponding maxima and minima of $F_x/|\boldsymbol{F}|$ and $F_y/|\boldsymbol{F}|$, respectively, over all surface voxels for each wavelength. Note the difference between this result and that shown in the bottom two panels of Fig. 11. See text for details. The wavelengths are given in Å and the fluxes are in cgs units.

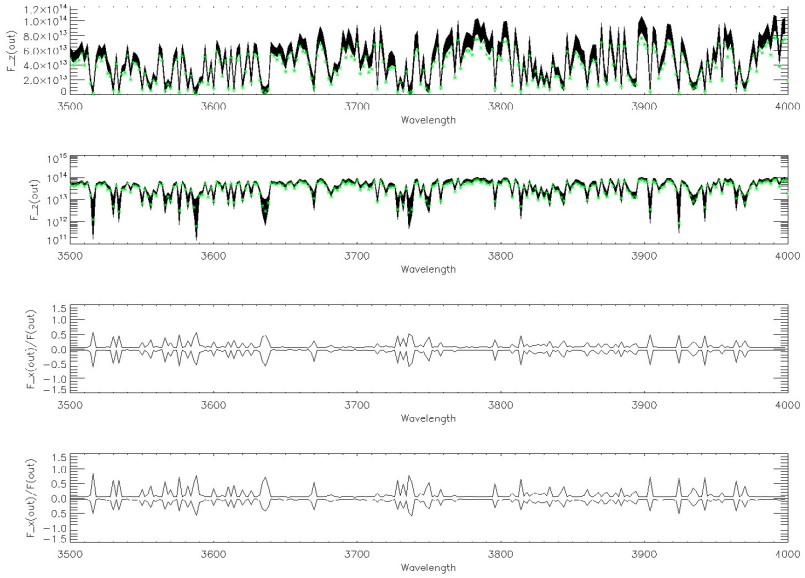

Fig. 13. Comparison between the flux vectors across the outermost voxels for the PHOENIX/3D UV spectra computed for the 3D hydro structure and the PHOENIX/1D spectrum for the G2V dwarf test model ($T_{\rm eff}$ = 5700 K, $\log(g)$ = 4.5). In the PHOENIX/3D calculations we have used a 3D coordinate system with a total of 141 × 141 × 151 Cartesian grid points in x, y, and z, respectively, the periodic boundary conditions are set in the (horizontal) x, y plane. The 3D radiative transport equation is solved for n_θ = 64 and n_ϕ = 64 solid angle points. The *top panels* show the F_z component of all outer voxels in linear and logarithmic scales, respectively, compared to the results of the 1D comparison model. The *bottom panels* show the corresponding maxima and minima of $F_x/|\boldsymbol{F}|$ and $F_y/|\boldsymbol{F}|$, respectively, over all surface voxels for each wavelength. Note the difference between this result and that shown in the bottom two panels of Fig. 11. See text for details. The wavelengths are given in Å and the fluxes are in cgs units.

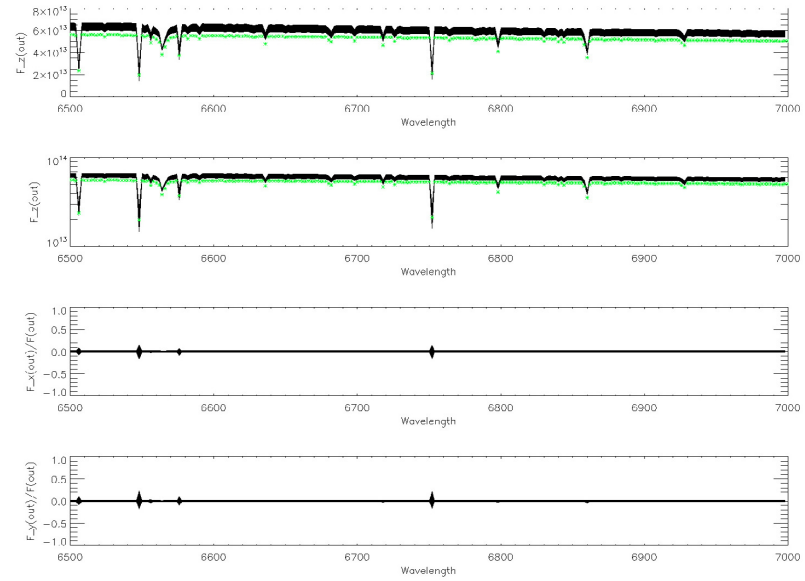

Fig. 14. Comparison between the flux vectors across the outermost voxels for the PHOENIX/3D optical spectra computed for the 3D hydro structure and the PHOENIX/1D spectrum for the G2V dwarf test model ($T_{\rm eff}$ = 5700 K, $\log(g)$ = 4.5). In the PHOENIX/3D calculations we have used a 3D coordinate system with a total of 141 × 141 × 151 Cartesian grid points in x, y, and z, respectively, the periodic boundary conditions are set in the (horizontal) x, y plane. The 3D radiative transport equation is solved for n_θ = 64 and n_ϕ = 64 solid angle points. The *top panels* show the F_z component of all outer voxels in linear and logarithmic scales, respectively, compared to the results of the 1D comparison model. The *bottom panels* show the corresponding runs of $F_x/|\boldsymbol{F}|$ and $F_y/|\boldsymbol{F}|$, respectively. See text for details. The wavelengths are given in Å and the fluxes are in cgs units.

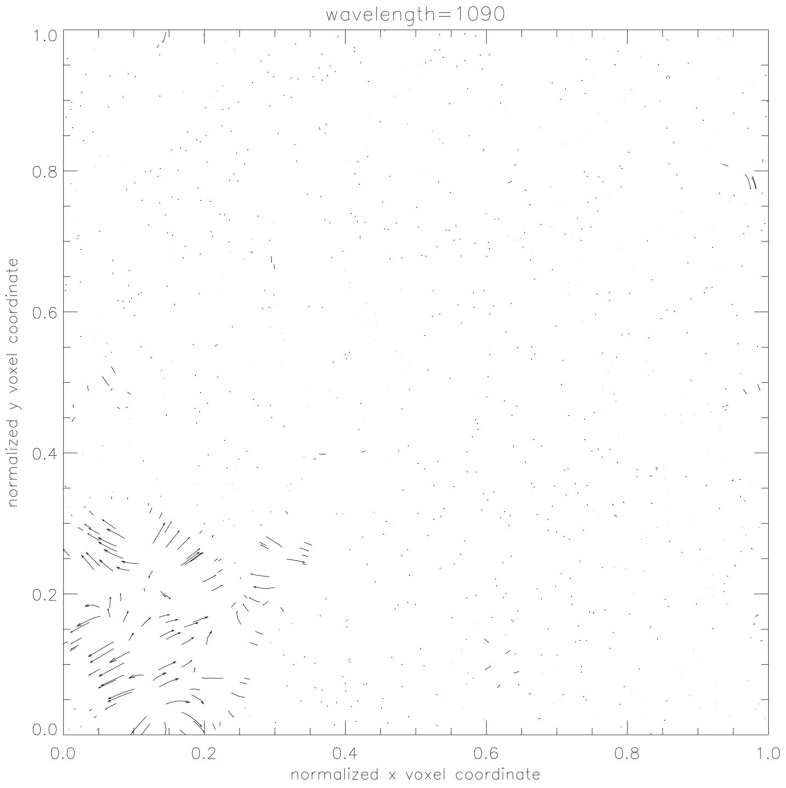

Fig. 15. Illustration of horizontal energy flow for the outermost voxels of the the 3D hydro structure for the red spectral range. The graphics shows the flowlines of the x and y components of the flux vector $\boldsymbol{F}$. Here, a flowline connects points of constant $|(F_x, F_y)|$ following the direction of (F_x, F_y). The 3D radiative transport equation is solved for $n_\theta = 64$ and $n_\phi = 64$ solid angle points. The wavelengths are given in Å. The normalized x and y voxel coordinates are shown on the x and y axes, respectively.

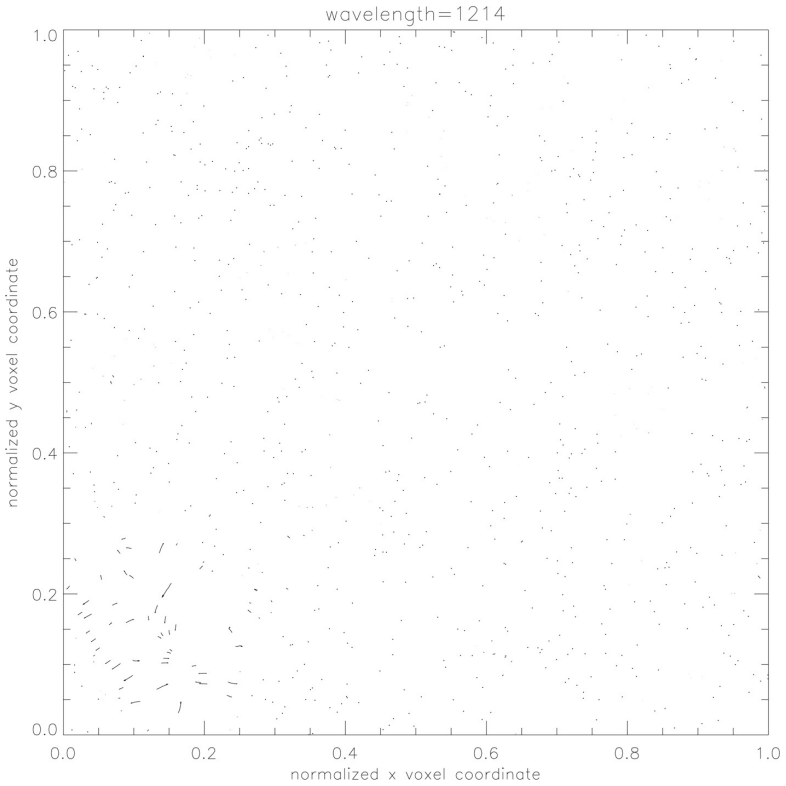

Fig. 16. Illustration of horizontal energy flow for the outermost voxels of the the 3D hydro structure for the red spectral range. The graphics shows the flowlines of the x and y components of the flux vector $\boldsymbol{F}$. Here, a flowline connects points of constant $|(F_x, F_y)|$ following the direction of (F_x, F_y). The 3D radiative transport equation is solved for $n_\theta = 64$ and $n_\phi = 64$ solid angle points. The wavelengths are given in Å. The normalized x and y voxel coordinates are shown on the x and y axes, respectively.

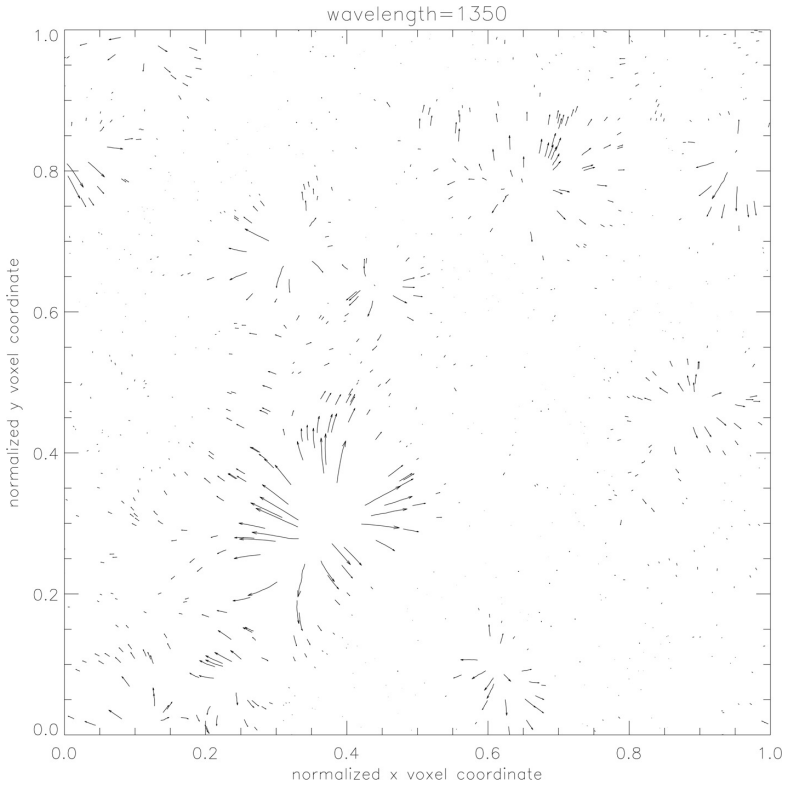

Fig. 17. Illustration of horizontal energy flow for the outermost voxels of the the 3D hydro structure for the red spectral range. The graphics shows the flowlines of the x and y components of the flux vector $\boldsymbol{F}$. Here, a flowline connects points of constant $|(F_x, F_y)|$ following the direction of (F_x, F_y). The 3D radiative transport equation is solved for $n_\theta = 64$ and $n_\phi = 64$ solid angle points. The wavelengths are given in Å. The normalized x and y voxel coordinates are shown on the x and y axes, respectively.

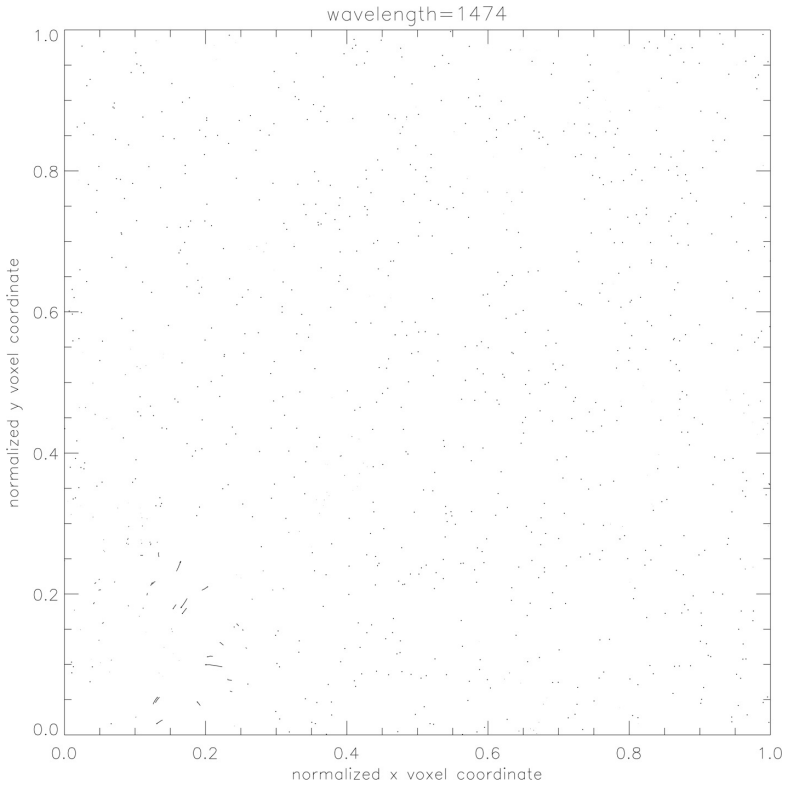

Fig. 18. Illustration of horizontal energy flow for the outermost voxels of the the 3D hydro structure for the red spectral range. The graphics shows the flowlines of the x and y components of the flux vector $\boldsymbol{F}$. Here, a flowline connects points of constant $|(F_x, F_y)|$ following the direction of (F_x, F_y). The 3D radiative transport equation is solved for $n_\theta = 64$ and $n_\phi = 64$ solid angle points. The wavelengths are given in Å. The normalized x and y voxel coordinates are shown on the x and y axes, respectively.

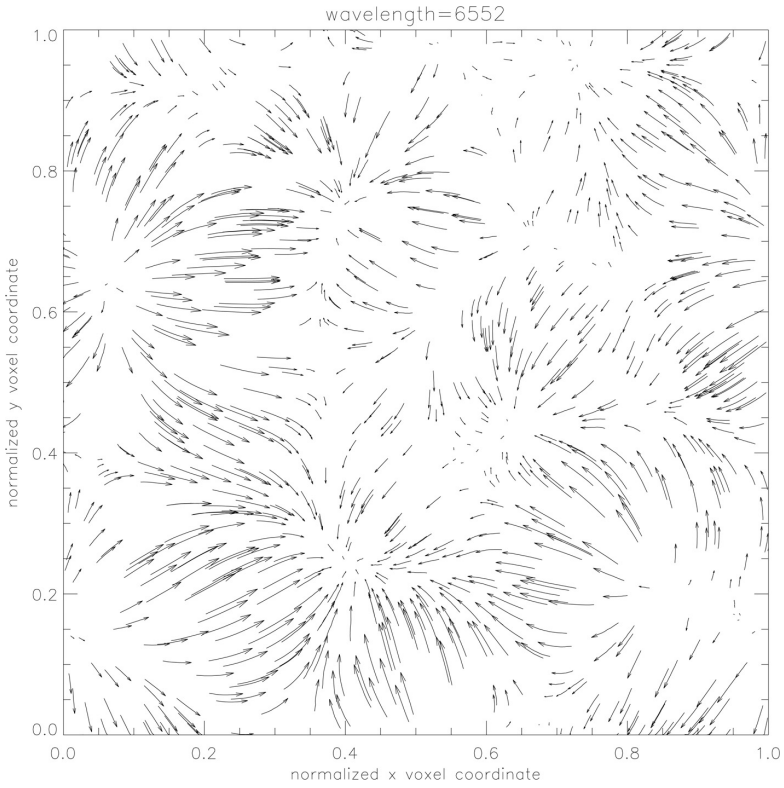

Fig. 19. Illustration of horizontal energy flow for the outermost voxels of the the 3D hydro structure for the red spectral range. The graphics shows the flowlines of the x and y components of the flux vector $\boldsymbol{F}$. Here, a flowline connects points of constant $|(F_x, F_y)|$ following the direction of (F_x, F_y). The 3D radiative transport equation is solved for $n_\theta = 64$ and $n_\phi = 64$ solid angle points. The wavelengths are given in Å. The normalized x and y voxel coordinates are shown on the x and y axes, respectively.

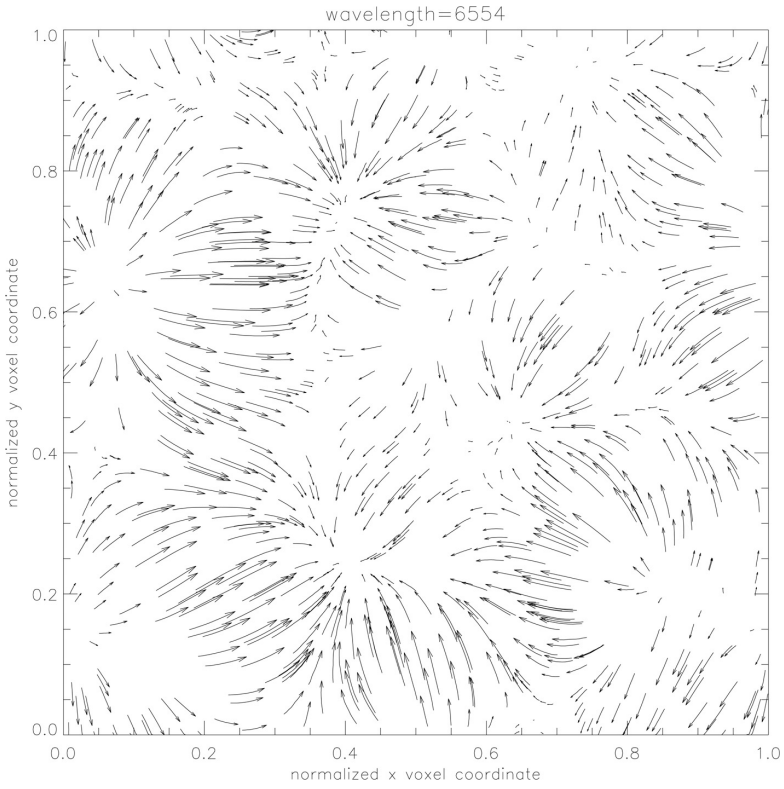

Fig. 20. Illustration of horizontal energy flow for the outermost voxels of the the 3D hydro structure for the red spectral range. The graphics shows the flowlines of the x and y components of the flux vector $\boldsymbol{F}$. Here, a flowline connects points of constant $|(F_x, F_y)|$ following the direction of (F_x, F_y). The 3D radiative transport equation is solved for $n_\theta = 64$ and $n_\phi = 64$ solid angle points. The wavelengths are given in Å. The normalized x and y voxel coordinates are shown on the x and y axes, respectively.

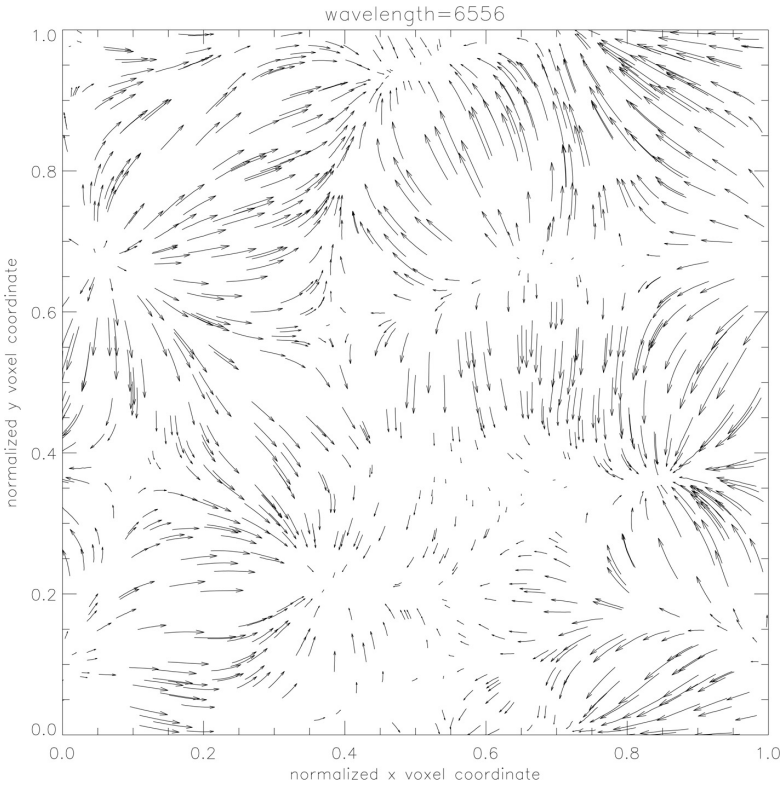

Fig. 21. Illustration of horizontal energy flow for the outermost voxels of the the 3D hydro structure for the red spectral range. The graphics shows the flowlines of the x and y components of the flux vector $\boldsymbol{F}$. Here, a flowline connects points of constant $|(F_x, F_y)|$ following the direction of (F_x, F_y). The 3D radiative transport equation is solved for $n_\theta = 64$ and $n_\phi = 64$ solid angle points. The wavelengths are given in Å. The normalized x and y voxel coordinates are shown on the x and y axes, respectively.

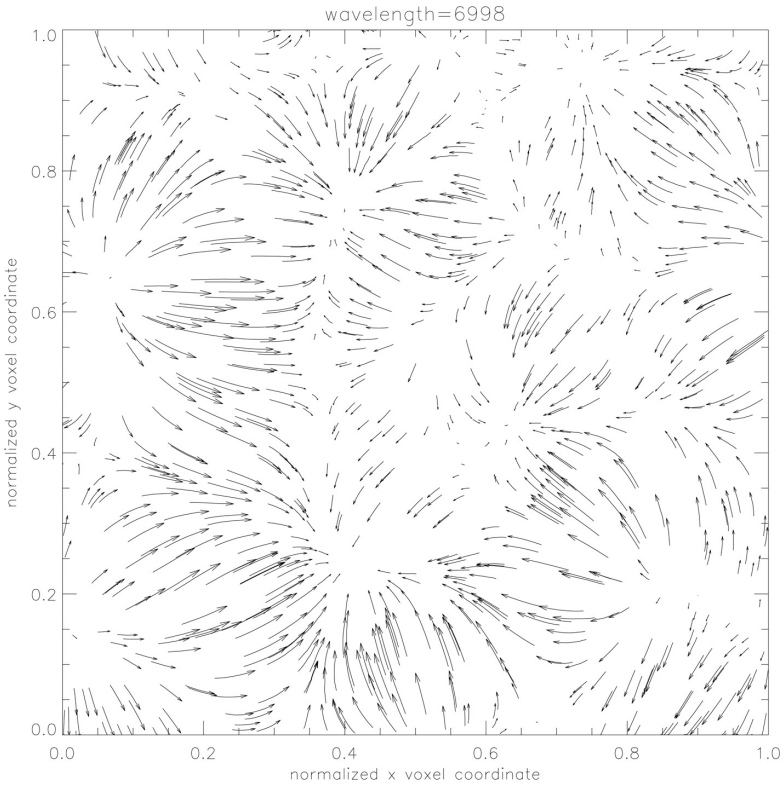

Fig. 22. Illustration of horizontal energy flow for the outermost voxels of the the 3D hydro structure for the red spectral range. The graphics shows the flowlines of the x and y components of the flux vector $\boldsymbol{F}$. Here, a flowline connects points of constant $|(F_x, F_y)|$ following the direction of (F_x, F_y). The 3D radiative transport equation is solved for $n_\theta = 64$ and $n_\phi = 64$ solid angle points. The wavelengths are given in Å. The normalized x and y voxel coordinates are shown on the x and y axes, respectively.

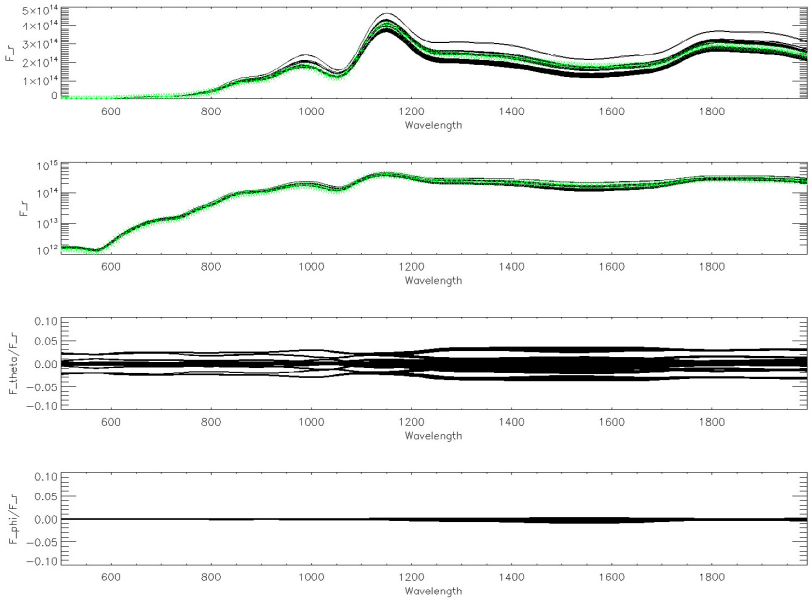

Fig. 23. Comparison between the PHOENIX/1D co-moving frame UV spectrum (computed with 256 layers, $*$ symbols) and the co-moving frame flux vectors across the outermost voxels for the PHOENIX/3D spectra computed for the Supernova test model. In the PHOENIX/3D calculations we have used a 3D spherical coordinate system with $n_{\rm r} = 129$, $n_{\theta_{\rm c}} = 33$ and $n_{\phi_{\rm c}} = 65$ points for a total of about 275 k voxels. The calculations used 128^2 solid angle points. The *top panels* show the $F_{\rm r}$ component of all outer voxels in linear and logarithmic scales, respectively. The *bottom panels* show the corresponding runs of $F_\theta/F_{\rm r}$ and $F_\phi/F_{\rm r}$, respectively. The should be identically zero and the deviations measure the internal accuracy. The wavelengths are given in Å and the fluxes are in cgs units.

Papers I-V into our general purpose model atmosphere package PHOENIX, thus allowing both 1D models (PHOENIX/1D) and 3D models (PHOENIX/3D) with the same micro-physics. We have verified and tested PHOENIX/3D by computing a number of test spectra for 1D conditions and comparing the results to the corresponding PHOENIX/1D calculations. The conditions range from M dwarfs, solar type stars to A stars and type II supernovae with relativistic expansions speeds. In addition, we have calculated spectra for a 3D hydrodynamical simulation of solar atmosphere convection. These tests demonstrate the it is now possible to calculate realistic spectra for 3D configurations including complex micro-physics. PHOENIX/3D can be used to calculate synthetic spectra for a number of complex 3D atmosphere model, including irradiated stars or planets, novae, and supernovae. We are currently working on extensions of the 3D radiative transfer framework to arbitrary velocity fields in the Euler (for low velocities, e.g., in convection simulations or planetary winds) and the Lagrangian (for Supernovae, accretion disks and matter flow in the vicinity of black holes) frames, which will extend the applications of PHOENIX/3D significantly.

Acknowledgements. This work was supported in part by DFG GrK 1351 and SFB 676, as well as NSF grant AST-0707704, and US DOE Grant DE-FG02-07ER41517. The calculations presented here were performed at the Höchstleistungs Rechenzentrum Nord (HLRN); at the Hamburger Sternwarte IBM Regatta Systems, Apple G5, and Delta Opteron clusters financially supported by the DFG and the State of Hamburg; and at the National Energy Research Supercomputer Center (NERSC), which is supported by the Office of Science of the US Department of Energy under Contract No. DE-AC03-76SF00098. We thank all these institutions for a generous allocation of computer time.

References

Asplund, M., Grevesse, N., & Sauval, A. J. 2005, in Cosmic Abundances as Records of Stellar Evolution and Nucleosynthesis, ed. T. G. Barnes, III, & F. N. Bash, ASP Conf. Ser., 336, 25
Baron, E., & Hauschildt, P. H. 1998, ApJ, 495, 370
Baron, E. & Hauschildt, P. H. 2007, A&A, 468, 255
Baron, E., Hauschildt, P. H., & Chen, B. 2009, A&A, 498, 987
Caffau, E., Steffen, M., Sbordone, L., Ludwig, H.-G., & Bonifacio, P. 2007, A&A, 473, L9
Hauschildt, P. H. & Baron, E. 2006, A&A, 451, 273
Hauschildt, P. H. & Baron, E. 2008, A&A, 490, 873
Hauschildt, P. H. & Baron, E. 2009, A&A, 498, 981
Hauschildt, P. H., Baron, E., & Allard, F. 1997, ApJ, 483, 390
Wedemeyer, S., Freytag, B., Steffen, M., Ludwig, H.-G., & Holweger, H. 2004, A&A, 414, 1121

A&A 522, A102 (2010)
DOI: 10.1051/0004-6361/201014278

Astronomy & Astrophysics

A 3D radiative transfer framework
VII. Arbitrary velocity fields in the Eulerian frame

A. M. Seelmann[1], P. H. Hauschildt[1], and E. Baron[1,2,3]

[1] Hamburger Sternwarte, Gojenbergsweg 112, 21029 Hamburg, Germany
e-mail: [aseelmann;yeti]@hs.uni-hamburg.de
[2] Dept. of Physics and Astronomy, University of Oklahoma, 440 W. Brooks, Rm 100, Norman, OK 73019, USA
e-mail: baron@ou.edu
[3] Computational Research Division, Lawrence Berkeley National Laboratory, MS 50F-1650, 1 Cyclotron Road, CA 94720-8139, USA

Received 17 February 2010 / Accepted 17 July 2010

ABSTRACT

Aims. A solution of the radiative-transfer problem in 3D with arbitrary velocity fields in the Eulerian frame is presented. The method is implemented in our 3D radiative transfer framework and used in the PHOENIX/3D code. It is tested by comparison to our well-tested 1D co-moving frame radiative transfer code, where the treatment of a monotonic velocity field is implemented in the Lagrangian frame. The Eulerian formulation does not need much additional memory and is useable on state-of-the-art computers, even large-scale applications with 1000's of wavelength points are feasible.
Methods. In the Eulerian formulation of the problem, the photon is seen by the atom at a Doppler-shifted wavelength depending on its propagation direction, which leads to a Doppler-shifted absorption and emission. This leads to a different source function and a different Λ^* operator in the radiative transfer equations compared to the static case.
Results. The results of the Eulerian 3D spherical calculations are compared to our well-tested 1D Lagrangian spherical calculations, the agreement is, up to $v_{\max} = 1 \times 10^3$ km s^{-1} very good. Test calculation in other geometries are also shown.

Key words. radiative transfer

1. Introduction

A solution of the 1D radiative transfer problem in arbitrary velocity fields in the Lagrangian frame has been developed by Baron & Hauschildt (2004). Knop et al. (2009) optimized their method by reducing the memory footprint of the algorithm (using domain decomposition), and also introduced a new method which speeds up the formal solution by developing an iterative Gauss-Seidel (GS) type solver where the solution becomes quasi-analytic when the source function is interpolated linearly. However, in a 3D setup the limiting factor is the memory footprint which already stretches the limits of modern supercomputers. The memory requirements of a 3D calculation in the Lagrangian frame are very high because one has to store additional wavelength information in every volume element (hereafter voxel) for every solid angle, whereas the 3D Eulerian frame calculation needs more computing time in multi-level applications due to the explicit computing of the opacity for every solid angle point.

In Sect. 2 we describe the Eulerian formulation of the problem, in Sect. 3 the comparison to our well-tested 1D code is presented and application examples in other geometrical setups are shown. In Sect. 4 we describe expected and discovered limitations with the formalism in the Eulerian frame.

2. Method

The 3D radiative transfer framework uses the full-characteristics method to solve the radiative transfer equations (Hauschildt & Baron 2006). The intensity along a characteristic, which are straight lines with given direction (θ, ϕ) in the Eulerian frame, is simply given by

$$\frac{\mathrm{d}I}{\mathrm{d}\tau} = I - S. \tag{1}$$

With this definition, the formal solution for a given characteristic (θ, ϕ) can be written as

$$I(\tau_i) = I(\tau_{i-1})\exp(\tau_{i-1} - \tau_i) + \int_{\tau_{i-1}}^{\tau_i} S(\tau)\exp(\tau - \tau_i)\mathrm{d}\tau \tag{2}$$

$$\equiv I_{i-1}(-\Delta\tau_{i-1}) + \Delta I_i \tag{3}$$

where i labels the points along the characteristic, S is the source function and $\Delta\tau_i$ is the optical depth, computed, e.g., by using piecewise linear interpolation of the opacity χ along the characteristic:

$$\Delta\tau_{i-1} = (\chi_{i-1}(\lambda) + \chi_i(\lambda))|s_{i-1} - s_i|/2. \tag{4}$$

Hauschildt & Baron (2006) give a more detailed explanation of the general method.

Due to the movement of the atom in the Eulerian frame, the atom "sees" the photon (on the characteristic) at a wavelength shifted according to

$$\lambda_{\mathrm{atom},i} = \lambda_{\mathrm{observer},i} \cdot \left(1 + \frac{\boldsymbol{e}_{\mathbf{char}} \cdot \boldsymbol{v}_i}{c}\right) \tag{5}$$

where $\boldsymbol{e}_{\mathbf{char}}$ is the unit vector in the direction of the characteristic, c the speed of light and $\boldsymbol{v}$ the velocity of the atom. This leads to a different opacity seen by the characteristic depending on its direction:

$$\chi_i(\lambda) = \chi_i(\lambda, \theta, \phi). \tag{6}$$

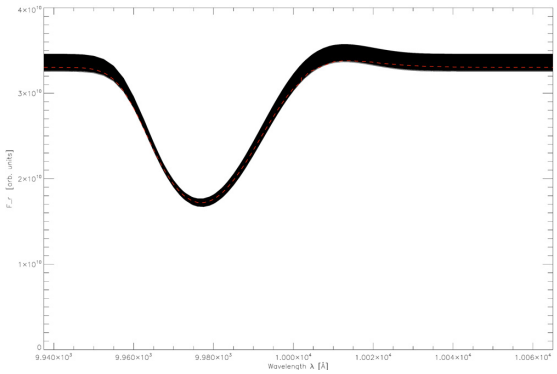

Fig. 1. Comparison of the Eulerian 3D and the Lagrangian 1D code with a linear increasing velocity field with $v_{\max} = 1 \times 10^3$ km s^{-1} and scattering $\epsilon_{\rm line} = 10^{-2}$. Solid: spectra from all outermost voxels in the 3D spherical coordinate grid, dashed: spectrum from the 1D code.

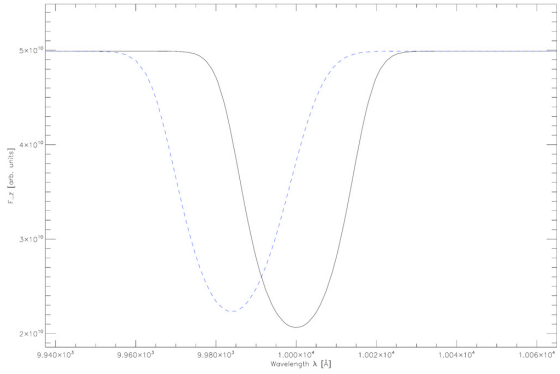

Fig. 2. Spectra from all outermost voxels in the 3D Cartesian geometry with periodic boundary conditions, a linearly increasing velocity field with $v_{\max} = 1{\times}10^3$ km s^{-1} and line scattering $\epsilon_{\rm line} = 10^{-2}$. Solid: without the treatment of the velocity field, dashed: with the treatment of the velocity field. This plot shows the influence of the velocity field on the line.

In the case of line transfer, the profile of the line becomes anisotropic in the Eulerian frame:

$$\Phi(\lambda) = \Phi(\lambda, \theta, \phi). \tag{7}$$

The solution for the line transfer then proceeds with the Eulerian profile function $\Phi(\lambda, \theta, \phi)$ and following Baron & Hauschildt (2007), we obtain

$$\bar{J} = \iiint \Phi(\lambda, \mu, \phi) J_\lambda \mathrm{d}\lambda \mathrm{d}\mu \mathrm{d}\phi \tag{8}$$

and

$$\bar{\Lambda^*} = \iiint \Phi(\lambda, \mu, \phi) \Lambda^* \mathrm{d}\lambda \mathrm{d}\mu \mathrm{d}\phi \tag{9}$$

where λ is the wavelength in the observers frame, $\mu = \cos\theta$ and ϕ the solid angle under which the voxel is hit by the characteristic.

Relativistic corrections are neglected in the Eulerian frame, as we are working on a implementation of the co-moving frame method into our 3D code (Chen et al. 2007, Baron et al., in prep.).

3. Application examples

A simple two-level-atom approach was used to test the code, the physical atmosphere setup presented in Sects. 3.1–3.2 is similar to the one used in Hauschildt & Baron (2009), remarks about the numerical resolution of our spherical 3D code can also be found there.

3.1. 3D spherical coordinates

Our well-tested Lagrangian 1D spherical code was used to compare its results to the new Eulerian formalisms in the 3D RT code to verify the 3D Eulerian Code.

For this, many test calculations were made with linearly increasing velocity fields up to $v_{\max} = 1 \times 10^3$ km s^{-1}. Figure 1 shows the corresponding spectra from a calculation with $v_{\max} = 1 \times 10^3$ km s^{-1}, the agreement to the 1D Lagrangian code is very good, the variation of the 3D lines is due to numerical resolution. The 3D model was computed using $(n_r, n_\theta, n_\phi) = (197 \times 99 \times 197) = 3.842.091$ voxels and a solid angle resolution of $(\theta_c, \phi_c) = (64, 64)$ (computing time: ca. 18h on 2048 CPUs)[1].

3.2. 3D Cartesian coordinates with and without periodic boundary conditions

In Fig. 2 a test calculation of the 3D Cartesian code with periodic boundary conditions in a $(n_x, n_y, n_z) = (157 \times 157 \times 157) = 3.869.893$ voxel grid with $(\theta_c, \phi_c) = (64, 64)$ is shown (computing time: ca. 6h on 2048 CPUs)[1]. The difference between the calculation with and without velocity field is clearly visible. Similar results can be obtained in the Cartesian mode without periodic boundary conditions, the spectra are not shown here.

3.3. 3D hydro-structure

To test the new method with a 3D hydro-dynamical structure with an inherent arbitrary velocity field, we obtained a computed snapshot of convection in the solar atmosphere from Ludwig (Caffau et al. 2007; Wedemeyer et al. 2004), which was used as input for the code. The spectra from a few outermost voxels in a calculation ($(n_x, n_y, n_z) = (140 \times 150 \times 140) = 2.940.000$, $(\theta_c, \phi_c) = (64, 64)$, computing time: ca. 11h on 1024 CPUs[1]) with and without velocity field is shown in Fig. 3. The plot show that the use of velocity fields in such calculations is mandatory.

4. Limitations of the Eulerian formalisms

4.1. Solid angle points

In static line transfer problems it is necessary that the profile of the line is covered by the discretized wavelength grid used in the calculation, as the profile does only depend on the wavelength $\Phi = \Phi(\lambda)$. In Eulerian moving atmospheres the profile depends on Eq. (7) and therefore also on the solid angle discretization.

In Fig. 4 the profile in the (observer's frame) line center is plotted: the plus signs show the profile in the static case, as it is not solid angle depend it is everywhere 1. The asterisks show the

[1] Intel Xeon Harpertown CPU's, 92 wavelength points.

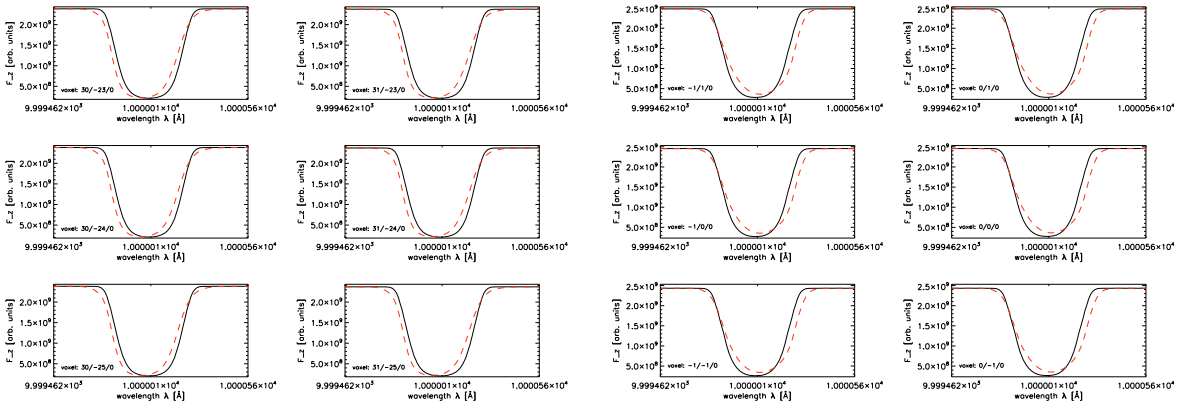

Fig. 3. Spectra from selected voxels on top of the 3D hydro-dynamical Cartesian atmosphere to show the influence of the inherent velocity field on the line, the calculations include line scattering ($\epsilon_{\rm line} = 10^{-2}$). Solid: without velocity field, dashed: with the inherent velocity field.

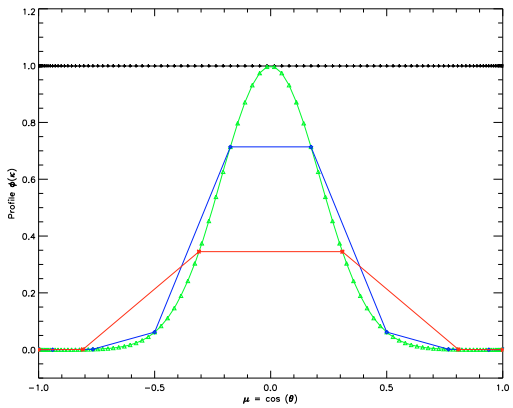

Fig. 4. Plot to illustrate the problem of a poor solid angle discretization. The plus signs show the profile in the line center of a static atmosphere. The asterisks and the diamonds show a poor/medium solid angle discretization, the triangles good solid angle discretization in the Eulerian moving atmosphere where the anisotropic Eulerian profile has good coverage. See text for a more detailed explanation.

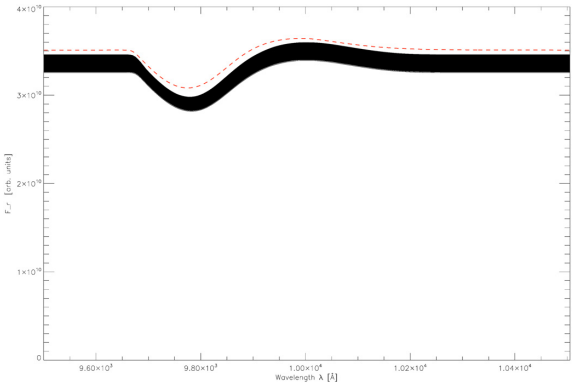

Fig. 5. Example of a calculation with a linearly increasing velocity field with $v_{\rm max} = 1 \times 10^4$ km s^{-1}. Solid: spectra from all outermost voxels in the 3D spherical grid, dashed: spectra from the 1D code. The Lorentz boost drives the continuum up as v gets closer to c.

anisotropic profile of a poor quality, the diamonds of a medium quality solid angle discretization in the moving Eulerian atmosphere: the profile in the line center is not hit at all, this causes a wiggly or even no spectral line. The triangles show a good quality solid angle discretization, the anisotropic profile in the Eulerian moving atmosphere hits the line center and the profile is well covered.

Various test show that a solid angle resolution of $(\theta_{\rm c}, \phi_{\rm c}) = (64, 64)$ is sufficient for velocity fields up to $v_{\rm max} = 10^3$ km s^{-1}.

4.2. Relativistic velocities

The formulation of the Eulerian method in the observers frame is inherently non-relativistic, which leads to differences between the 1D Lagrangian code and the new method presented here when the velocity field is greater then about 5×10^3 km s^{-1}. When the velocity is getting close to the speed of light, the Lorentz boost drives the continuum of the radiation field higher, what is clearly visible in Fig. 5. As v gets closer to c this effect increases, the error in the Eulerian solutions increases rapidly.

Various tests show that the agreement between the well-tested Lagrangian 1D and the Eulerian 3D code is excellent with velocity fields up to 1×10^3 km s^{-1}, this is enough to do 3D radiative transfer in convection or global circulation models. We have extended the method described in Knop et al. (2009) into our 3D code, which then allows exact, full relativistic radiative transfer in 3D (Chen et al. 2007, Baron et al., in prep.)

5. Conclusion

With our new Eulerian method it is now possible to do 3D radiative transfer in non-relativistic, arbitrary velocity fields in spherical, Cartesian, and cylindrical (while not described in detail, the method is also implemented in this part of the code) coordinates. The memory footprint and the computing time of the new algorithm in the two-level-atom setup presented here is negligible compared to the general requirements of the 3D code. In multi-level applications the time needed to calculate the opacity for

every solid angle must be considered. The velocity field limitations must also be kept in mind when using the method.

Acknowledgements. Some of the calculations presented here were performed at the Höchstleistungs Rechenzentrum Nord (HLRN); at the Hamburger Sternwarte Apple G5 and Delta Opteron clusters financially supported by the DFG and the State of Hamburg; and at the National Energy Research Supercomputer Center (NERSC), which is supported by the Office of Science of the U.S. Department of Energy under Contract No. DE-AC03-76SF00098. We thank all these institutions for a generous allocation of computer time. AS thanks the Research Training Group GrK 1351 of the German Research Foundation for funding. This work was supported in part by NSF grant AST-0707704 and by US DOE Award Number DE-FG02-07ER41517.

References

Baron, E., & Hauschildt, P. H. 2004, A&A, 427, 987
Baron, E., & Hauschildt, P. H. 2007, A&A, 468, 255
Caffau, E., Steffen, M., Sbordone, L., Ludwig, H., & Bonifacio, P. 2007, A&A, 473, L9
Chen, B., Kantowski, R., Baron, E., Knop, S., & Hauschildt, P. H. 2007, MNRAS, 380, 104
Hauschildt, P. H., & Baron, E. 2006, A&A, 451, 273
Hauschildt, P. H., & Baron, E. 2009, A&A, 498, 981
Knop, S., Hauschildt, P. H., & Baron, E. 2009, A&A, 501, 813
Wedemeyer, S., Freytag, B., Steffen, M., Ludwig, H., & Holweger, H. 2004, A&A, 414, 1121

A&A 528, A141 (2011)
DOI: 10.1051/0004-6361/201014778

Astronomy & Astrophysics

Theoretical light curves of type Ia supernovae

D. Jack[1], P. H. Hauschildt[1], and E. Baron[1,2]

[1] Hamburger Sternwarte, Gojenbergsweg 112, 21029 Hamburg, Germany
e-mail: [djack;yeti]@hs.uni-hamburg.de
[2] Homer L. Dodge Department of Physics and Astronomy, University of Oklahoma, 440 W Brooks, Rm 100, Norman, OK 73019-2061, USA
e-mail: baron@ou.edu

Received 13 April 2010 / Accepted 9 February 2011

ABSTRACT

Aims. We present the first theoretical SN Ia light curves calculated with the time-dependent version of the general purpose model atmosphere code PHOENIX. Our goal is to produce light curves and spectra of hydro models of all types of supernovae.
Methods. We extend our model atmosphere code PHOENIX to calculate type Ia supernovae light curves. A simple solver was implemented which keeps track of energy conservation in the atmosphere during the free expansion phase.
Results. The correct operation of the new additions to PHOENIX were verified in test calculations. Furthermore, we calculated theoretical light curves and compared them to the observed SN Ia light curves of SN 1999ee and SN 2002bo. We obtained LTE as well as NLTE model light curves.
Conclusions. We have verified the correct operation of our extension into the time domain. We have calculated the first SN Ia model light curves using PHOENIX in both LTE and NLTE. For future work the infrared model light curves need to be further investigated.

Key words. supernovae: general – radiative transfer – methods: numerical

1. Introduction

All types of supernovae are important for the role that they play in understanding stellar evolution, galactic nucleosynthesis, and as cosmological probes. Type Ia supernovae are of particular cosmological interest, e.g., because the dark energy was discovered with type Ia supernovae (Riess et al. 1998; Perlmutter et al. 1999).

In dark energy studies, the goal now is to characterize the nature of the dark energy as a function of redshift. While there are other probes that will be used (gravitational lensing, baryon acoustic oscillations), a JDEM or Euclid mission will likely consider supernovae in some form. In planning for future dark energy studies both from space and from the ground, it is important to know whether the mission will require spectroscopy of modest resolution, or whether pure imaging or grism spectroscopy will be adequate. Several purely spectral indicators of peak luminosity have been proposed (Nugent et al. 1995; Hachinger et al. 2006; Bongard et al. 2006; Bronder et al. 2008; Foley et al. 2008; Chotard et al. 2011). What is required is an empirical and theoretical comparison of both light curve shape luminosity indicators (Pskovskii 1977; Phillips 1993; Riess et al. 1996; Goldhaber et al. 2001) and spectral indicators.

To make this comparison one needs to know more about the physics going on in a supernova explosion and to be able to calculate light curves and spectra self-consistently. Thus, we need to extend our code to time-dependent problems. While our primary focus is on type Ia supernovae, the time-dependent radiative transfer code is applicable to all types of supernovae, as well as to other objects, e.g., stellar pulsations.

In the following we present the methods we used to implement time dependence. First we focus on solving the energy equation (first law) and then present our first theoretical LTE light curves of type Ia supernova events. In a further section, we present results of NLTE model light curve calculations.

2. Energy solver

In our previous paper (Jack et al. 2009), we presented our approach to calculate light curves of type Ia supernovae events. We implemented a simple energy solver into our general purpose model atmosphere code PHOENIX where we kept track of the overall energy change of the radiating fluid and the energy exchange between the matter and radiation. Simple test light curves confirmed that our approach worked correctly. We now present a new approach to calculate theoretical light curves of SNe Ia. Again, we are using a simple solver where we keep track of the energy conservation. In the new approach, we consider only the energy density of the material. We assume free expansion and do not solve the equations of hydrodynamics. In order to obtain the result for the new time step, we use an explicit scheme. We apply this scheme and compute time steps until radiative equilibrium is reached. These are the points in our light curves.

The direct change of the energy density of the material considering absorption and emission of radiation and energy deposition by gamma rays is given by Eq. (96.7) in Mihalas & Mihalas (1984)

$$\rho \left[\frac{\mathrm{d}e}{\mathrm{d}t} + p \frac{\mathrm{d}}{\mathrm{d}t} \left(\frac{1}{\rho} \right) \right] = \int (c\chi E - 4\pi\eta) + \rho\epsilon, \tag{1}$$

where ρ is the density, p the gas pressure and e is the energy density of the material. The quantities of the radiation field are χ which is the absorption coefficient, η is the emission coefficient and $E = \frac{4\pi}{c} J$ is the radiation energy density with the mean intensity J. To obtain E, the radiative transfer equation in spherical symmetry is solved including special relativity. All additional

energy sources are put in ϵ such as the energy input from gamma ray deposition. This equation represents the first law of thermodynamics for the material. The change of the energy density of the material depends on the coupling of matter and radiation field, the absorption of gamma-radiation and positron annihilation energy, the expansion work and the change of the ionization and excitation of matter.

Dividing equation 1 by the material density ρ we obtain

$$\frac{\mathrm{d}e}{\mathrm{d}t} = \frac{1}{\rho}\int (c\chi E - 4\pi\eta)\,\mathrm{d}\lambda - p\frac{\mathrm{d}}{\mathrm{d}t}\frac{1}{\rho} + \epsilon. \quad (2)$$

The radiation energy density is given by $E = \frac{4\pi}{c}J$, where J is the mean intensity. Using this, we obtain for the radiation term

$$\int (c\chi E - 4\pi\eta)\mathrm{d}\lambda = 4\pi\int(\chi J - \eta)\mathrm{d}\lambda = 4\pi\int(\chi(J-S))\mathrm{d}\lambda, \quad (3)$$

where $S = \frac{\eta}{\chi}$ is the source function. All these quantities can be derived from the solution of the radiative transfer equation. The term of the change of the energy density by the radiation is therefore given by

$$Q = \int \chi_\lambda(J_\lambda - S_\lambda)\mathrm{d}\lambda. \quad (4)$$

Another change of the energy density is due to the work W done by the adiabatic expansion of the SN Ia atmosphere. For a discrete step this work is given by

$$W = p\left(\frac{1}{\rho_2} - \frac{1}{\rho_1}\right). \quad (5)$$

The expansion is assumed to be homologous. Since we solve the energy equation for the matter, we do not include the radiation pressure work. Since the system is radiation dominated there is the possibility of numerical inaccuracies in coupling the matter and radiation only by Q. For the calculation of the new radii and densities as well as a discussion about the accuracy of this assumption see Jack et al. (2009).

Including all energy changing effects, the new energy density of the material e_2 after a discrete time step Δt is explicitly given by

$$e_2 = e_1 - p\left(\frac{1}{\rho_2} - \frac{1}{\rho_1}\right) + \frac{4\pi}{\rho}\Delta t\int\chi(J-S)\mathrm{d}\lambda + \epsilon\Delta t, \quad (6)$$

where e_1 is the old energy density.

To obtain all the needed quantities we have to solve the spherically symmetric special relativistic radiative transfer equation. The advantage of our new approach is that we do not have to iterate for each time step. In our previous paper the calculation of each time step involved an iteration process to obtain the new matter temperature. With the new approach we can calculate the new temperature for the next time step directly from all the known quantities.

The translational energy density of the material is given by

$$e_{\mathrm{trans}} = \frac{3}{2}\frac{p}{\rho} = \frac{3}{2}\frac{R}{\mu}T = \frac{3}{2}\frac{N_\mathrm{A}kT}{m}, \quad (7)$$

with the mean molecular weigh μ and the universal gas constant R. The gas pressure is represented by p and the density by ρ. T stands for the temperature of the material. This equation of the energy density is now used to determine the new temperature after the next time step.

During the first phase of the SN Ia envelope evolution, the material of the atmosphere is hot and, therefore, highly ionized. The energy change due to ionization and excitation changes of the atoms present in the SN Ia atmosphere cannot be neglected. `PHOENIX` already solves the equation of state (EOS), where all the excitation and ionization stages of the present atoms and molecules are included. Using the EOS, we obtain the overall energy density of the material by the sum of the ionization energy e_{ions} and the translational energy e_{trans}

$$e = e_{\mathrm{trans}} + e_{\mathrm{ions}}. \quad (8)$$

Hence, the energy density change of the material goes into a change of the translational energy and the ionization energy, which both depend on the temperature. Therefore, we obtain the new temperature by an iteration scheme. The matter density at the next point in time is determined by homologous expansion. A first temperature guess is used, and the EOS is solved to obtain the ionization energy density. Combined with the translational energy density, the overall energy density is computed. This is checked against the target energy density, which we obtained Eq. (6). If the obtained energy density is incorrect, a new temperature guess is made. This new temperature guess is obtained by assuming a linear dependence of the energy density and temperature. The current temperature guess is iterated to the target energy density. It takes about 5–10 iteration steps to determine the new temperature. If the EOS delivers the correct target energy density, the new temperature of the next time step has been found. The accuracy relative of the energy density in this iteration process is set to 10^{-5}.

2.1. γ-ray deposition

The maximum of the light curve of an SN Ia event is observed around 20 days after explosion. Causing this later maximum of the light curve of an SN Ia event is the energy release into the envelope caused by the radioactive decay of ^{56}Ni and its also radioactive decay product ^{56}Co. Therefore, this energy deposition has a strong influence on the energy change of the SN Ia envelope structure. Hence, the energy deposition due to radioactive decay has to be taken into account for the calculation of the SN Ia envelope evolution.

The energy deposition due to the γ-rays emitted by radioactive isotopes needs to be computed by a radiative transfer solver for the γ-rays. In this work, we solve the γ-ray deposition with the assumption of a gray atmosphere for the γ-rays. Jeffery (1998) did a detailed study of the γ-ray deposition and pointed out that this is an adequate approach to calculate γ-ray deposition in SN Ia atmospheres. In the decay of a ^{56}Ni nucleus, a γ-photon is emitted with an energy of 2.136 MeV. The ^{56}Co nucleus decays to an ^{56}Fe nucleus and emits a γ-photon, which has an energy of 4.566 MeV. In the decay of ^{56}Co about 19% of the energy is released by positrons. The positrons are assumed to be locally trapped. They annihilate by emitting two photons each with an energy of 512 keV, which has to be taken into account for the energy deposition calculation. The opacity is considered to be constant and a pure absorption opacity, meaning that no scattering is assumed. As in Jeffery (1998), $\kappa_\gamma = 0.06\langle Z/A\rangle\,\mathrm{cm}^2\,\mathrm{g}^{-1}$ was chosen as the opacity. $\langle Z/A\rangle$ is the proton fraction, which is counts both bound and free electrons, since the electron binding energy is small compared to the energy of gamma rays. The energy deposition into the atmosphere per unit time is given by

$$\epsilon = 4\pi\frac{\chi}{\rho}J, \quad (9)$$

where J is the mean intensity, which has been obtained by solving the gray radiative transfer for the γ-rays. This obtained energy deposition has to be taken into account for the calculation of the overall energy change.

2.2. Adaptive time step procedure

The timescale for energy changes in the SN Ia envelope will change during the evolution of the light curve. In order to save computation time, the light curves have to be calculated with the optimal time step size for each phase of light curve evolution. Therefore, we implemented an adaptive time step routine to determine the optimal time step size for the current time step.

The energy change Δe of the energy of the material e may be approximated by

$$\Delta e = x \cdot e = \Delta t \cdot (Q + \epsilon)\,, \tag{10}$$

where Q is the energy change of the interaction with the radiation, and ϵ is the energy deposition by the gamma rays. The energy change due to the expansion is ignored in this case. On the one hand, this energy change depends on the new matter density after the time step, which is unknown because it depends on the size of the time step itself. Furthermore, the energy change because of the expansion is small compared to the changes caused by the energy transport and the energy deposition by γ-rays. The idea of the adaptive time step procedure is to limit the energy change to a prescribed amount of the energy of the material. Thus, rewriting Eq. (10), we obtain the time step size Δt for the current time step by

$$\Delta t = \frac{e}{Q + \epsilon} \cdot x, \tag{11}$$

where x is the introduced limiting energy change factor. The factor x ranges between $x_{\min}$ and $x_{\max}$, which mark the largest and smallest allowed energy change. These are input parameters for the adaptive time step procedure. The time step size is calculated for every layer, and the minimum time step size of all layers is used for the energy solver.

Each time the adaptive time step procedure is called, it checks if the energy changes of the time step before were too big or could have been bigger. If the minimum time step size is in a different layer, the same value of x is kept for the next time step. If the minimum is in the same layer and the sign of the energy change does not change, the previous time step might have been too small. Thus, the factor x is increased for the following time step. If the sign changes, the last time step might have been too large, therefore, the factor x is decreased. This means that for each time step, the allowed energy change is adapted and the factor x is updated to get the optimal time step during the whole evolution of the SN Ia atmosphere.

3. Test calculations

All new implemented physical processes of the simple energy solver have to be tested. For the test atmosphere, the atmosphere structure and abundances of the W7 deflagration model (Nomoto 1984) are used. The atmosphere structure is expanded to a point in time of 10 days after the explosion. The densities and radii are determined by free homologous expansion and can be computed easily. To perform the test calculations, we obtained an initial temperature structure with the PHOENIX temperature correction procedure (Hauschildt et al. 2003). This temperature structure is the result of a simple approach that does not represent the temperature structure of an SN Ia precisely. However, for the test calculations for our energy solver, this simple temperature structure is sufficient. With this initial atmosphere structure, the energy solver is applied for different test cases. All contributions to the energy change are tested separately.

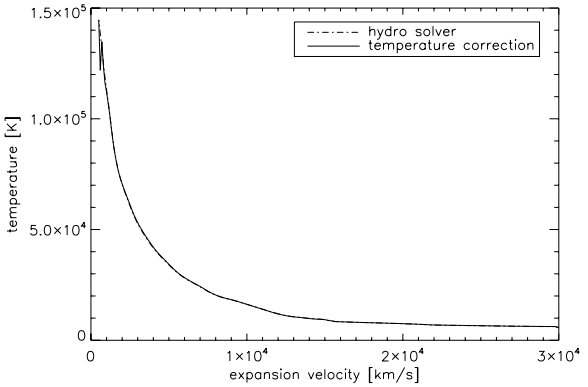

Fig. 1. Temperature structures of a test atmosphere obtained with the energy solver and the PHOENIX temperature correction procedure.

3.1. Energy transport

In this section, the energy transport through the atmosphere is tested. The energy solver considers only the energy change caused by emission and absorption of radiation, where the result of the radiative transfer equation is needed. All other influences are neglected. As a first test, we check how the initial temperature structure changes if the energy solver is changing the SN Ia envelope. As the initial atmosphere structure is already in radiative equilibrium, the energy solver should not change the temperature structure significantly, because it also pushes the atmosphere towards a radiative equilibrium state.

In Fig. 1, a comparison of the temperature structure of the energy solver to the result of the temperature correction procedure is shown. The differences in the temperature structure for most layers are less than 1%. But the temperature differences of the inner layers are clearly higher. These differences arise in the PHOENIX temperature correction result which produces a spike in the temperature structure. This is likely due to the boundary condition in the temperature correction. Hence, the resulting temperature structure obtained with the energy solver is more accurate. Here, the temperature structure is smooth. In order to obtain an atmosphere in radiative equilibrium, the energy transport part of the energy solver can be used instead of the temperature correction procedure. The main problem is that about a few hundred time steps are needed to obtain the resulting atmosphere structure in radiative equilibrium, while the temperature correction needs fewer iteration steps and is, therefore, significantly faster.

3.2. Expansion

In a further test calculation, the expansion part of the energy solver is checked. The only energy change considered is the adiabatic cooling due to free expansion of the SN Ia envelope. The energy deposition by γ-rays or an energy change due to energy transport is disabled. For this test case, the expectation is that the atmosphere should just cool down, so the temperature of the atmosphere and the observed luminosity should be decreasing.

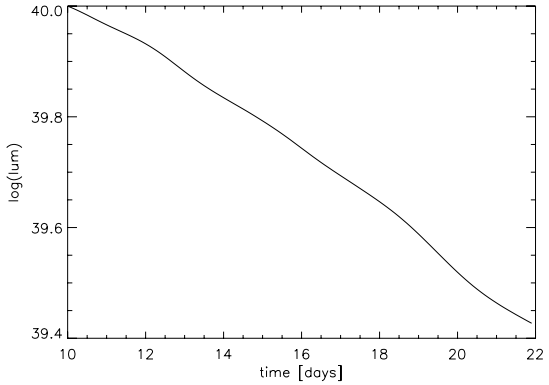

Fig. 2. Light curve of a test atmosphere that is just expanding and adiabatically cooling.

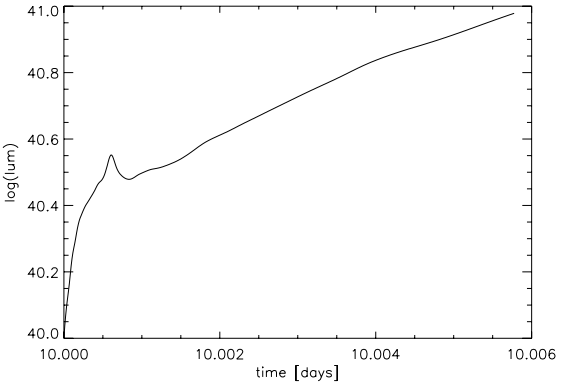

Fig. 4. Light curve of a test atmosphere with energy deposition. Because of the additional energy, the luminosity increases with time.

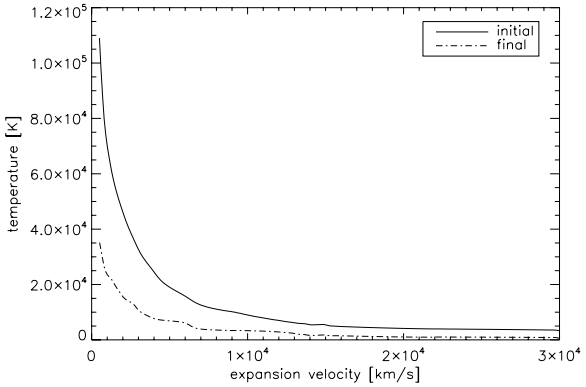

Fig. 3. Initial and final temperature structure of a test atmosphere which is just expanding and adiabatically cooling.

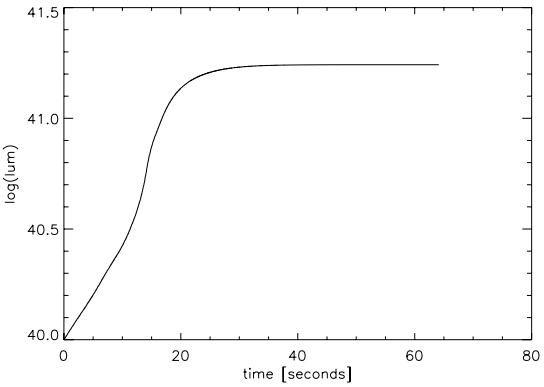

Fig. 5. Model light curve of a realistic test scenario.

The observed luminosity is shown in Fig. 2. The observed luminosity of the SN Ia atmosphere decreases in time. The temperature structure of the first and the last time step is plotted in Fig. 3. The adiabatic expansion has cooled the atmosphere everywhere, and the new temperature structure is now significantly lower than the initial one.

3.3. Energy deposition

To test the energy deposition by the radioactive decay of nickel and cobalt into the SN Ia atmosphere, a test case is considered, where only this γ-ray deposition is calculated with the energy solver. The energy change due to free expansion and energy transport are neglected to see the direct effect of the additional energy put into the test SN Ia atmosphere.

The results of the energy deposition by γ-rays calculation with the energy solver is shown in Fig. 4, where the light curve is plotted. Due to the energy added to the atmosphere, the luminosity seen by an observer increases with time.

3.4. Realistic test scenario

After all single effects have been tested, we now calculate a test case where all effects are considered for the solution of the energy solver. Again, the same initial temperature structure is used and we start our calculation at day 10 after the explosion. Free expansion as well as energy deposition and energy transport are active for this computation.

The observed light curve is shown in Fig. 5. The luminosity increases because of the energy input from deposition of energy from the γ-rays produced by decay of nickel and cobalt. It takes a certain time, until the whole atmosphere has relaxed to this new condition. The atmosphere is then in radiative equilibrium state, and the luminosity stays constant. The initial and final temperature structure are plotted in Fig. 6. The energy input caused by radioactive decay has increased the temperature of the whole atmosphere. The atmosphere is heated by γ-ray deposition in the inner part of the atmosphere. Due to this additional energy, the luminosity of these layers increases and the heat is radiated away and absorbed by the surrounding layers. This energy transport takes care that the deposited energy is moving through the whole atmosphere so that the temperature increases everywhere and the additional energy from the radioactive decay is radiated away towards the observer. The atmosphere is then in radiative equilibrium.

4. SN Ia model light curves

We now present our first theoretical SN Ia light curves obtained with our extensions to the general purpose model atmosphere code `PHOENIX` and compare them to observed SN Ia light

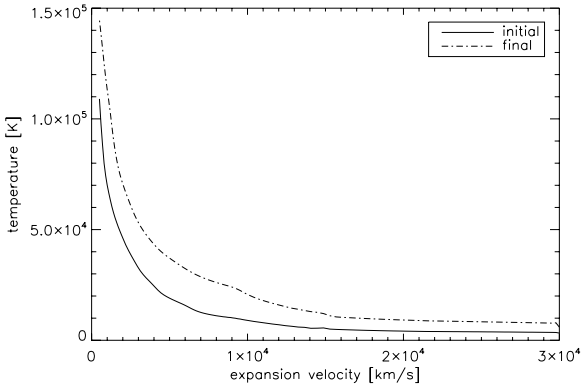

Fig. 6. The initial temperature structure for the static solution of the equation of radiative equilibrium and the relaxed temperature structure obtained 1 min later by advancing the energy solver in the test scenario. All influences on the SN Ia atmosphere are considered.

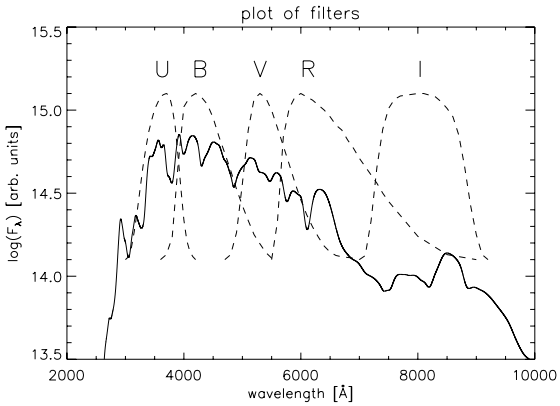

Fig. 7. A typical model spectrum of an SN Ia together with the filter functions for the U, B, V, R and I band. These are used to determine the luminosity in each band for the model light curves.

curves. The online supernova spectrum archive (SUSPECT) (Richardson et al. 2001, 2002)[1] provides numerous of observations of different types of supernovae. For this work, the observed light curves of SN 2002bo and SN 1999ee are used to compare them to our results of model light curves. Photometric light curve observations of SN 2002bo in different photometric bands (Benetti et al. 2004) have been obtained. SN 1999ee also has observed spectra (Hamuy et al. 2002) and photometry (Stritzinger et al. 2002).

4.1. Method

The energy solver is now applied to calculate synthetic light curves of SNe Ia. The SN Ia light curve evolution is calculated during the free expansion phase. For the initial model atmosphere structure, the results of the explosion calculation of other groups are used as the input structure. Each layer has a certain expansion velocity, which does not change during the evolution, because homologous expansion is assumed. We start the model light curve calculation a few days after explosion. In the first few days the SN Ia envelope is optically thick and compact. Another point is, in the first few days the SNe Ia light curves are quite faint, and there are almost no observations of this early time phase that have been obtained. Thus, for the model light curve calculation, it is adequate to start the light curve calculation a few days after the explosion. The initial structure is given by the result of the explosion model simulation. The results of the explosion model give the expansion velocities, density structure and the non-homogeneous abundances of all chemical elements present in the SN Ia envelope. The envelope expands for the first few days by assuming homologous expansion. The radii are determined by the expansion velocities and time after explosion. For the first temperature structure guess, the PHOENIX temperature correction procedure is used to obtain an initial temperature structure, which is in radiative equilibrium. Alternatively we could calculate RE models starting at day one.

For the computation of an SN Ia model light curve, we let the energy solver change the obtained initial model atmosphere structure. The atmosphere structure adapts to the new conditions caused by γ-ray deposition and other energy effects. After a certain time, the atmosphere eventually reaches the radiative equilibrium state. A typical time step of an energy change in the model atmosphere is about 0.1 s. It takes about 500 time steps to reach radiative equilibrium depending on in which evolution phase the SN Ia is. For the later phase after the maximum of the SN Ia light curve, fewer time steps are needed. We use this first radiative equilibrium atmosphere structure to calculate a more detailed spectrum, where more wavelength points are used. This model spectrum is then used to obtain the first point of the model light curve for each band by using the filter functions described below. It certainly would require too much computation time to calculate a whole light curve evolution by using the typical time steps of about 0.1 s. Therefore, to obtain the next point of the light curve, big time steps are computed. For these big time steps, the atmosphere is only expanding. This means that neither energy deposition by γ-rays or energy transport through the atmosphere is considered for the solution of the energy solver. After half a day computed with big time steps, the whole energy solver changes the atmosphere structure again and the next point in the light curve is obtained after the atmosphere structure moves back to radiative equilibrium. Even with the use of these big time steps, the radiative transfer for a light curve of 50 days has to be solved about 10 000 times. For normal model atmosphere calculation in PHOENIX with the temperature correction procedure, the radiative transfer equation has to be solved about 100 times, at most. Therefore, the computation of a whole SN Ia model light curve is very computationally expensive, because the solution of the radiative transfer equation has to be obtained too many times. It takes a huge amount of computation time to calculate even simple SN Ia model light curves, even when using only a few wavelength points. Basically, the SN Ia model light curve is a curve consisting of half day points, where the atmosphere is in radiative equilibrium. During the later phase after maximum light, the big time steps have been performed for one or even two days, as the energy changes is the SN Ia atmosphere become smaller.

As described above, a model spectrum is calculated with the obtained atmosphere structure, which is in radiative equilibrium at each half day point of the light curve. To obtain a model light curve for different photometric bands, filter functions were used to calculate the luminosity in different bands. In Fig. 7, an SN Ia model spectrum and the filter functions for the U, B, V, R and I bands are shown. These filter functions are described in Hamuy et al. (1992). With these filter functions, SNe Ia model light

[1] http://suspect.nhn.ou.edu/

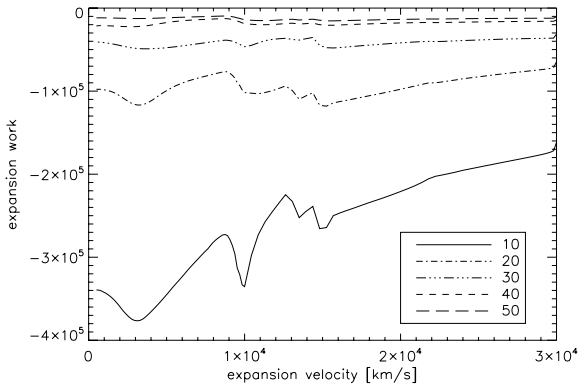

Fig. 8. The energy change due to the expansion for several days.

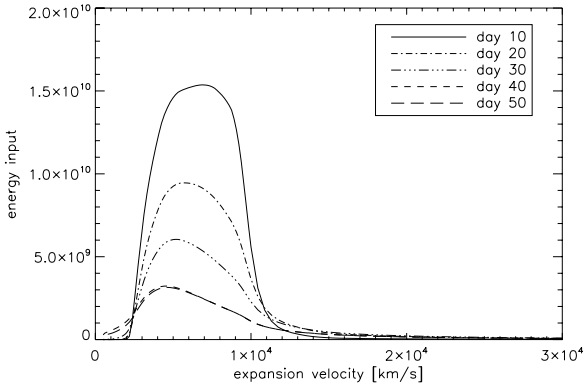

Fig. 9. The energy change due to the additional energy input for several days.

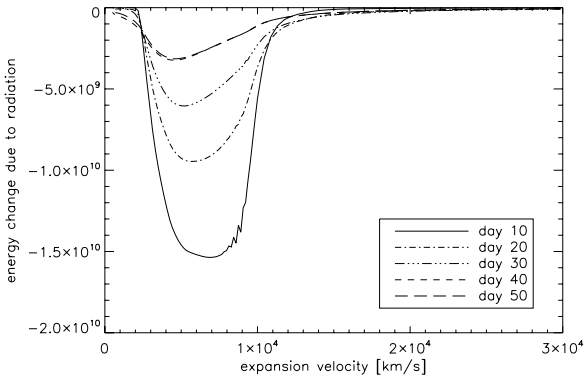

Fig. 10. The energy change due to the radiation for several days.

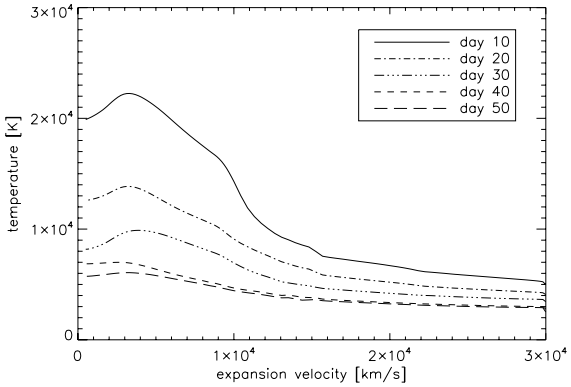

Fig. 11. Temperature profiles as a function of time.

curves can now be obtained for these five different photometric bands.

4.2. Light curves of LTE models

For the first calculations of theoretical light curves, the model atmosphere of the SN Ia is considered to be in LTE. For a first approach to obtain model light curves this is adequate. Another reason for the assumption of LTE is that model light curve calculations with an atmosphere treated in NLTE use more computation time. In order to obtain an SN Ia model light curve in reasonable computation time, a model atmosphere in LTE is a necessary assumption. For the model light curve calculations presented in this section the following parameters were chosen. The model atmosphere is divided into 128 layers. The radiative transfer is solved including atomic lines of the Kurucz atomic data line list. The number of wavelength points used for the solution of the radiative transfer is about 2400. For the inner boundary condition of the radiation, we use the nebular boundary condition, which means that the radiation is just passing through the inner empty region, therefore all the radiation is produced by the ejecta itself, there is no inner lightbulb. The outer boundary condition is zero.

For the first LTE light curve calculation, the W7 deflagration explosion model is used to obtain model light curves of SNe Ia in different photometric bands. The first point of the light curve was calculated at three days after the explosion. The method to obtain the theoretical light curves is described in Sect. 4.1.

Before we present our resulting model light curves, we present plots of various terms that change the energy density for several moments in time. In Fig. 8, the energy change due to the expansion is shown for several moments in time. The energy change is decreasing for later days in the light evolution. The additional energy input due to the radioactive decay is shown in Fig. 9. With increasing time, the amount of energy input into the atmosphere decreases. It also shows, that the additional energy is located in the inner part of the envelope, where the ^{56}Ni has been produced. Figure 10 shows the energy loss due to the emission of radiation. The temperature structures of the atmosphere for several moments in time are shown in Fig. 11.

Figure 12 shows the LTE SN Ia model light curve of the W7-based explosion model in the optical V band. The theoretical light curve accurately reproduces the observed light curves of two SNe Ia. The steep rise of the model light curve beginning at three days after explosion is in agreement with the observed light curves. The maximum of the W7-based model light curve seems to be later than that of the observed light curves. At 20 days after the explosion, the model light curve has its maximum, while the maximum of the observed light curves is around 17 days after the explosion. After maximum, the decline of the light curve of the W7-based model well reproduces the observed light curve. Even up to the later phase at 50 days after the explosion, where the atmosphere becomes significantly thinner, the fit to the observed light curves is quite accurate.

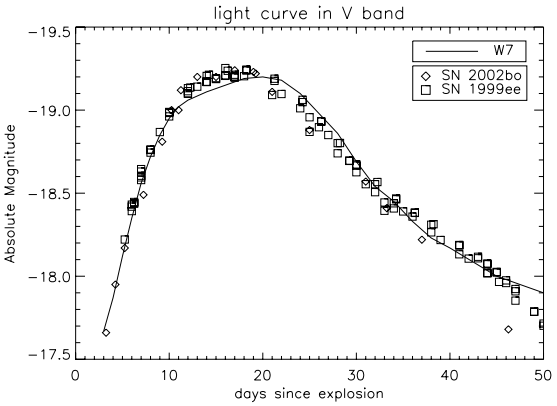

Fig. 12. LTE model light curve of the W7 explosion model in the *V* band compared to two observed SN Ia light curves of SN 1999ee and SN 2002bo.

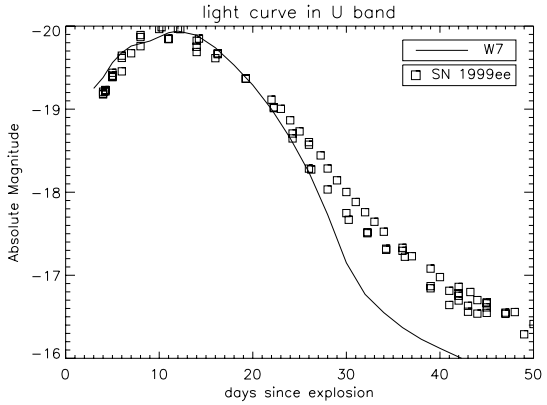

Fig. 13. *U* band light curve of the LTE model light curve compared to SN 1999ee.

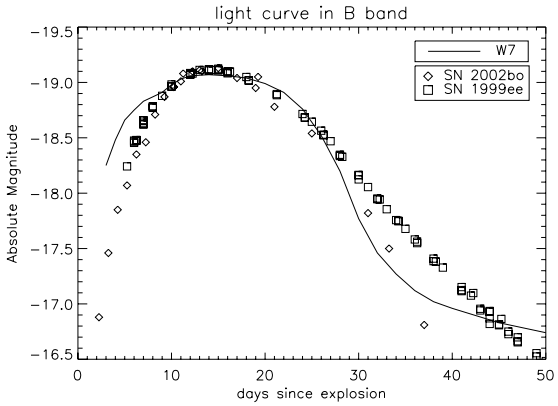

Fig. 14. LTE light curves of the W7 explosion model. The *B* band model light curve is too bright during the first few days.

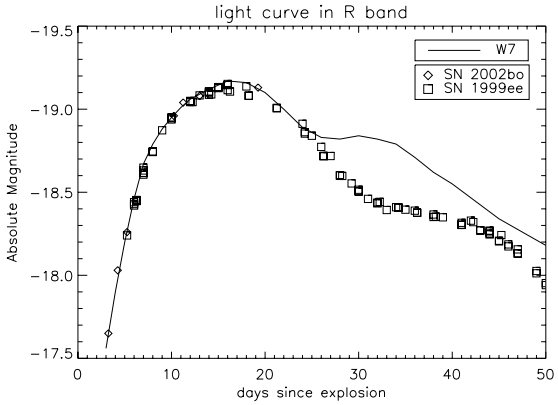

Fig. 15. The theoretical light curve in the *R* band seems to rise after a first decline after the maximum phase.

The theoretical light curve in the ultraviolet *U* band is shown in Fig. 13. Only an observed light curve of SN 1999ee is available. The observational data are scattered. The rise in the beginning as well as the maximum phase is well represented by the model light curve. However, the decline of the theoretical light curve seems to be too steep. This same effect is present in the model light curve of the *B* band, which is shown in Fig. 14. The first days of the model light curve are too bright compared to both observed SN Ia light curves. The maximum phase of the model light curve is in good agreement with the observed ones. At day 50, the model light curve becomes brighter than the observed light curves.

In Fig. 15, a plot of the model light curve of the *R* band is shown. The steep rise in the beginning and the maximum phase of the observed SN Ia light curves is well represented by the computed model light curve. However, the theoretical light curve fit becomes worse for later phases. The luminosity of the model light curve seems to rise again at around day 25 after the explosion. Up to day 45, the model light curve has a second bump, which is not observed in the light curves of SN 1999ee and SN 2002bo. In the infrared *I* band, the decline after the maximum phase is missing, as shown in Fig. 16. As in the *R* band, the rise in the beginning and maximum are well represented in the model light curve. However, at maximum, the luminosity of the SN Ia model light curve rises further, which is not seen in the observed light curves of SN 2002bo and 1999ee. Around day 30, the difference between model and observed light curve in the I band are about 1 mag. Up to day 50, the model light curve declines, while the observed light curves show their second maximum around 40 days after explosion.

In Fig. 17, we compared the relation $U - B$ of the theoretical and observed light curves. The same comparision for the $B - V$ relation is shown in Fig. 18.

4.3. Dynamical models

We have three different results of explosion calculations of SN Ia events. The structure of these models are results from hydrodynamical explosion calculations. One is the W7 deflagration model of Nomoto et al. (1984). The W7 dynamical model assumes that the ongoing explosion is a deflagration. The flame propagates with a velocity lower than the speed of sound outwards. Another possible explosion model is the delayed detonation model. The explosion starts with a deflagration which eventually proceeds to a detonation. We used two different dynamical models named as DD25 and DD16. For more detailed information about the used delayed detonation models see Höflich et al. (2002).

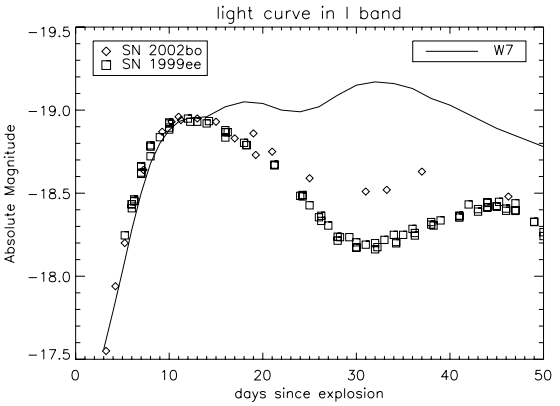

Fig. 16. LTE light curves of the W7 explosion model. For the I band the model light curve has no distinctive maximum. At 30 days after the explosion the model light curve is way too bright in comparison to the observed ones.

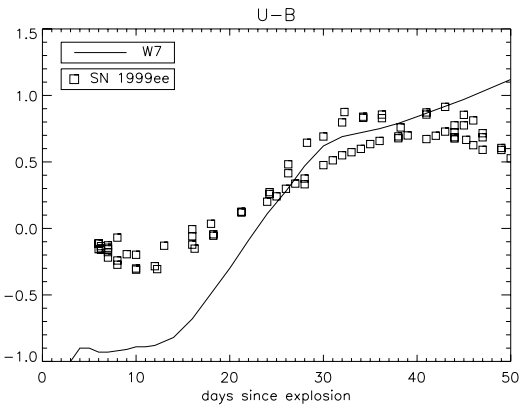

Fig. 17. Comparison of $U - B$ for the theoretical and observed light curves.

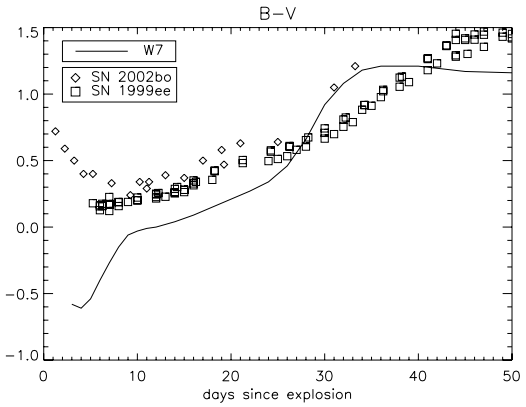

Fig. 18. Comparison of $B - V$ for the theoretical and observed light curves.

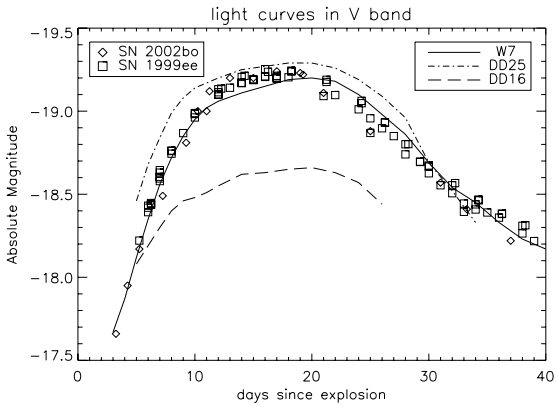

Fig. 19. V band light curves for three different dynamical models W7, DD16 and DD25. The DD25 dynamical model is fainter because less nickel was produced during the explosion. The W7 and DD15 dynamical model light curves are quite similar.

The resulting optical model light curves of the V band are plotted in Fig. 19. The light curve of the DD16 is fainter than the other ones. This is due to the fact that in this explosion model less ^{56}Ni is produced. The W7 and DD25 model are quite similar. DD25 is slightly brighter than W7. The shape of the light curves are in good agreement with the observed ones. The maximum of the DD16 is later than the one of the W7 and DD25.

In Fig. 20 the light curves in the I band of the three dynamical models are shown. The infrared light curves deviate strongly from the observations. As in the optical light curve, the DD16 light curve is fainter than W7 and DD25. DD16 also has only one maximum and a decline. However, this maximum is later than the observed ones. The DD25 and W7 light curves are still rising after the observed light curves have reached their maximum and are declining. The theoretical light curves in the infrared must be improved for all explosion models.

5. Light curves of NLTE models

The LTE model light curves in the V Band and most other bands are in quite good agreement with observed SN Ia light curves. However, in the near-infrared of the I band, the model light curves need improvements especially for the later phase to fit the observational light curves more accurately. So far, the SN Ia model atmosphere is considered to be in LTE during the whole evolution time. In this section, we calculate the model light curves with the assumption of an atmosphere which is not in LTE. The computation of model light curves with SN Ia model atmospheres in NLTE requires a huge amount of computation time. At first, we model light curves with atmospheres in NLTE that are computed with LTE temperature structures. More realistic NLTE model light curves with a temperature structure that adapts to NLTE conditions are computed to investigate the NLTE effects on the model light curves.

The first approach to compute NLTE model light curves is to consider the atmosphere to be in NLTE, but use a fixed LTE temperature structure. For this computation of NLTE model light curves, we used the calculated radiative equilibrium LTE temperature structure of the W7 deflagration model. We keep this temperature structure constant and perform 20 iterations to let the NLTE converge, which is mainly the occupation numbers of the species that are considered for the NLTE calculation. We considered the following species for the calculations in NLTE: H I, He I, He II, C I-III, O I-III, Ne I, Na I, Mg I-III, Si I-III,

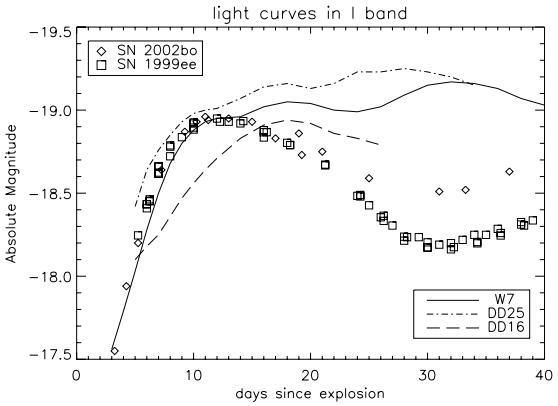

Fig. 20. *I* band light curves for the dynamical models W7, DD16 and DD25 are compared to the two observed SN Ia light curves.

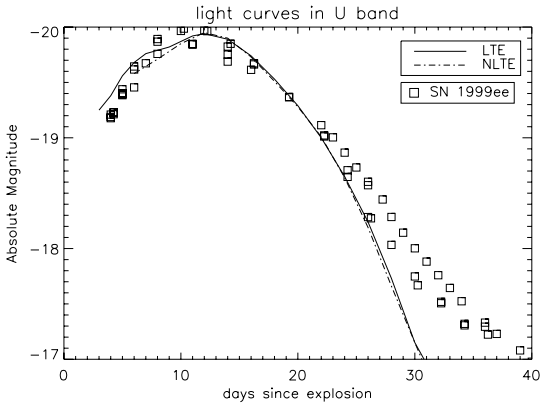

Fig. 22. Model light curves of the W7 model in the *U* band. The NLTE model atmosphere has an LTE temperature structure.

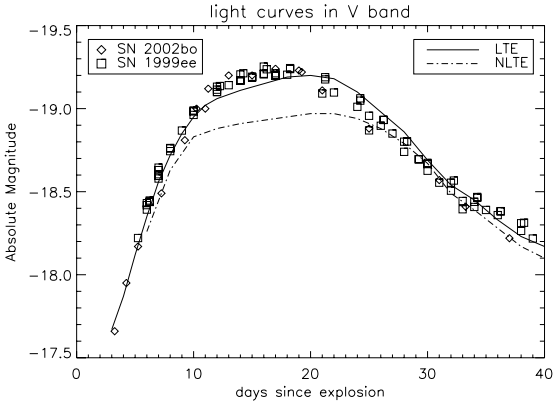

Fig. 21. Model light curves of the W7 explosion model in the *V* band. The NLTE model atmosphere has an LTE temperature structure.

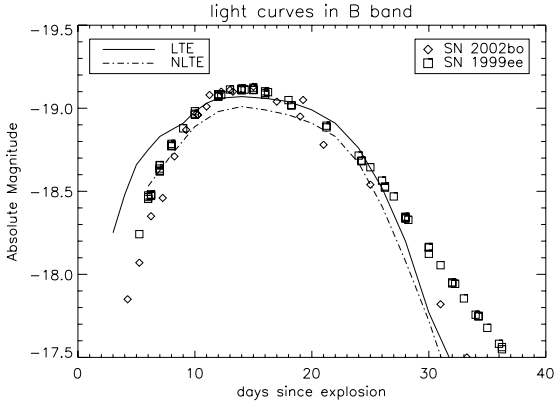

Fig. 23. Model light curves of the W7 model in the *B* band. The NLTE model atmosphere has an LTE temperature structure.

S I-III, Ca II, Ti II, Fe I-III and Co II. These are the species that are most abundant in SN Ia atmospheres and mainly contribute to the spectrum. There is only little H and He in SN Ia, and in W7, there is none. However, considering H I, He I and He II in NLTE does not cost much computation time. The advantage of this approach to an NLTE model light curve is that no temperature iterations have to be performed. This reduces the computation time significantly, although about 200 000 wavelength points are calculated instead of 2400 in case of LTE.

In Fig. 21, the SN Ia model light curve in the *V* band of an NLTE calculation with an LTE temperature structure is shown. The NLTE light curve is fainter than the LTE light curve. During the maximum phase there is about 0.4 mag difference between both light curves. We have to point out that for our NLTE models, the energy is not conserved because the radiation does not thermalize within the envelope. After maximum the NLTE model light curve approaches the LTE light curve and agrees with the observed light curves as well as the LTE light curve. However, the NLTE model light curve in the *V* band does not agree with the observed light curves very accurately. With the assumption of an atmosphere in LTE, a better fit is obtained, although NLTE is more accurate.

The NLTE model light curve of the *U* band is shown in Fig. 22. The NLTE light curve shows almost no deviations from the LTE light curve. During the later phase the steep decline is also present in the NLTE model light curves. In Fig. 23, the NLTE model light curve in the B band is presented. The NLTE model light curve is slightly fainter than the LTE light curve. The shape of the NLTE light curve seems to be the same as for the LTE light curve. The NLTE model light curve is also an accurate fit to the observed light curves.

In Fig. 24, the NLTE model light curve of the *R* band is shown. The luminosity of the NLTE light curve is fainter than the LTE light curve. It has almost the same shape. But for the phase after 25 days after the explosion, the NLTE model light curve rises again. The assumption of NLTE does not improve the fit to the observed light curves of SN 1999ee and SN 2002bo. The infrared NLTE light curve for the *I* band is shown in Fig. 25. During the maximum phase, the NLTE light curve is fainter than the LTE light curve. A distinctive maximum is missing in the NLTE model light curve. For the phase between day 15 and day 25, the NLTE model light curve fits the observed SN Ia light curves very accurately. Here, there is a significant improvement compared to the light curve of the LTE model atmosphere. But, after day 25 the NLTE model light curve starts to

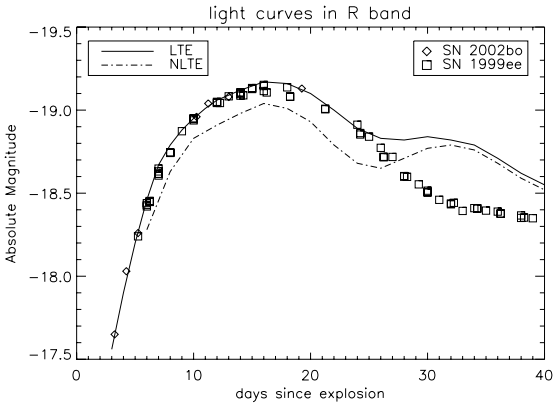

Fig. 24. NLTE and LTE model light curves in the *R* band of the W7 model. The NLTE model atmosphere has an LTE temperature structure.

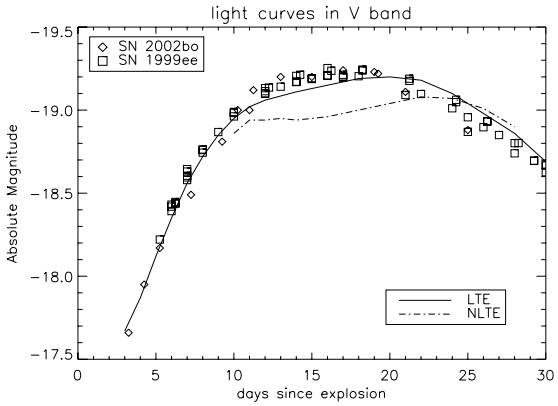

Fig. 26. NLTE and LTE model light curves of the W7 explosion model in the *V* band.

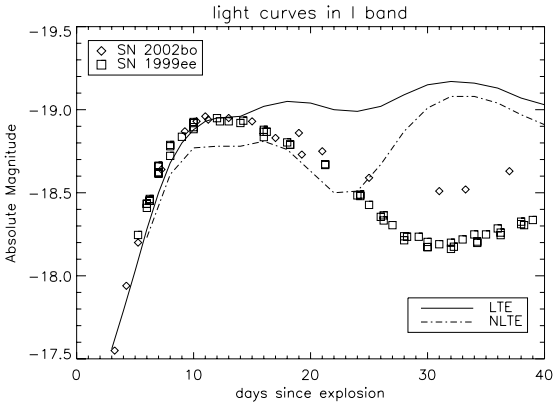

Fig. 25. NLTE and LTE model light curves of the W7 model. The NLTE model atmosphere has an LTE temperature structure. In the *I* band the NLTE light curve is somewhat of an improvement.

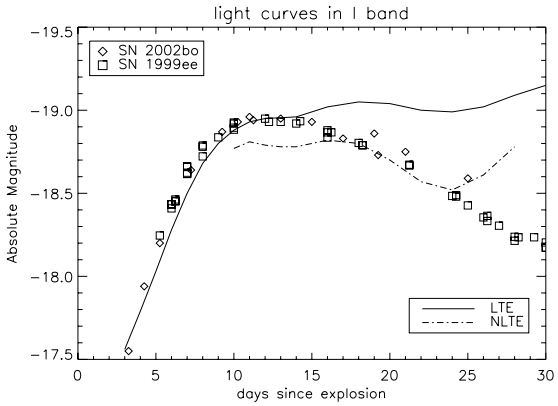

Fig. 27. NLTE and LTE model light curves of the W7 explosion model in the *I* band.

rise and becomes too bright. This is the same problem that already emerged in the LTE light curve.

5.1. NLTE atmosphere structures

We perform a more realistic NLTE calculation of the SN Ia model atmosphere evolution. The temperature structure is now changing and adapting to the new conditions of NLTE. The calculation of an NLTE model light curve takes a huge amount of computation time. Considerably more wavelength points are needed for the calculation of the solution of the radiative transfer. For all the species considered in NLTE, the rate equations have to be solved. Note that a time step in the NLTE calculation is not a real time step. The rate equation changes the energy of the atmosphere, but this is not included in the energy solver. However, it is adequate as the goal is to obtain a temperature structure, where the atmosphere is in radiative equilibrium.

In a first try to calculate a more realistic NLTE light curve, numerous species up to calcium are considered to be in NLTE. These are the species H I, He I, He II, C I-III, O I-III, Ne I, Na I, Mg I-III, Si I-III, S I-III and Ca II. Higher species are neglected because they have more levels, which would increase the computation time significantly. Nevertheless, the computation of an NLTE light curve needs significantly more time than LTE. For this computation of NLTE model light curves, about 200 000 wavelength points need to be calculated, compared to about 2400 wavelength points for a pure LTE light curve calculation. To obtain an NLTE model light curve in a reasonable time, we started the calculation at day 10 after the explosion and used the LTE temperature structure as the initial atmosphere structure. The main focus is to check if the infrared light curves during the later phase can be further improved.

In Fig. 26, the NLTE and LTE light curves of the W7 deflagration model in the V band are shown. The maximum phase is not well fitted by the NLTE model light curve. The LTE light curve fits the observed light curves better. At day 20 the NLTE and LTE light curves are almost the same. Compared to the NLTE light curve obtained with the LTE temperature structure, there are only small differences to the NLTE calculation where the temperature structure adapts to the NLTE conditions.

In Fig. 27, the *I* band model light curves of NLTE and LTE are shown. During the maximum phase, the NLTE light curve is fainter than the LTE light curve. Between day 15 and day 25 the NLTE model light curve fits the observed light curves quite accurately. Here, the use of NLTE improves the fit to the observed

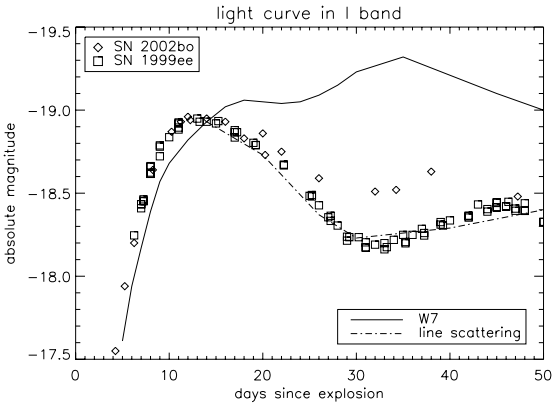

Fig. 28. Light curves in the *I* band. The light curve with variable scattering is fainter than the LTE light curve.

light curves. However, we obtained this improvement also with the NLTE model light curve calculated with the LTE temperature structure. At day 25 the NLTE model light curve starts to rise again. Although the consideration of NLTE improves the model light curve in the *I* band, the problem with a rise in brightness after the maximum remains.

5.2. Line scattering

The fits to the infrared light curves need to be improved, as they are too bright during the phase of 20 to 50 days after the explosion in all models. We found that a change in the ratio of line scattering to absorption in the LTE case improves the fits to the *I* band light curve. The resulting light curve is shown in Fig. 28. The line scattering is here roughly inversely proportional to the density and was for the figure "hand tuned" to produce a good match. As the density becomes lower due to the ongoing expansion, the scattering becomes more important, as expected. A more detailed investigation of the IR line scattering and its effects on SN Ia light curve modeling will be a topic of future work. To treat this effect more accurately, very detailed NLTE model atoms are required that include the important infrared lines. In the atomic data we have presently available, these lines are mostly "predicted" lines and were not included in the our current NLTE model atoms. This result indicates that an accurate treatment of line scattering and NLTE effects in the IR lines is very important to model and interpret the IR light curves of SNe.

6. Conclusion

We have presented a new approach for an energy solver which can be applied to expanding SN Ia envelopes to compute SN Ia model light curves. Test calculations confirm that the implemented code works properly. We applied the energy solver to calculate SN Ia model light curves during the free expansion phase.

We present the first PHOENIX light curves of type Ia supernovae in different photometric bands. At first, we solved the radiative transfer equation with the assumption of the atmosphere being in LTE. The model light curves were in decent agreement with the observed ones at early times. However, in the infrared *I* band, the theoretical light curves do not fit the observed light curves. Blinnikov et al. (2006) had the same deviations in their model light curves compared to observations. Their light curve in the *I* band is also too bright and further rising, even after the maximum in observed light curves. Kasen (2006) presented a detailed study of SN Ia light curves in the near IR. His *I* band light curve fits the observations better. He also showed how variable and dependent on different parameters the light curves in the near infrared can be.

Three different dynamical models were compared to observed SN Ia light curves. The delayed detonation model DD 16 is unlikely to be the best explosion model because the model light curves are too faint to fit the observed light curves due to the low ^{56}Ni mass. The results of the W7 model are the best fit to the observed light curves.

For the later phase of the light curves, especially in the infrared, we need the atmosphere to be considered in NLTE. We showed that NLTE model light curves computed with an LTE temperature structure leads to improvements in the model light curves. For future work more investigation of the infrared model light curves and the NLTE needs to be performed. The focus has to lie on the influence of line scattering on the shape of the light curves. It would also be interesting to look in detail on the spectral evolution during the free expansion phase. Further improvements may be achieved with a full 3D radiative transfer and energy solver.

Acknowledgements. This work was supported in part by the Deutsche Forschungsgemeinschaft (DFG) via the SFB 676, NSF grant AST-0707704, and US DOE Grant DE-FG02-07ER41517. This research used resources of the National Energy Research Scientific Computing Center (NERSC), which is supported by the Office of Science of the US Department of Energy under Contract No. DE-AC02-05CH11231, and the Höchstleistungs Rechenzentrum Nord (HLRN). We thank all these institutions for generous allocations of computation time.

References

Benetti, S., Meikle, P., Stehle, M., et al. 2004, MNRAS, 348, 261
Blinnikov, S. I., Roepke, F. K., Sorokina, E. I., et al. 2006, A&A, 453, 229
Bongard, S., Baron, E., Smadja, G., Branch, D., & Hauschildt, P. 2006, ApJ, 647, 480
Bronder, T. J., Hook, I. M., Astier, P., et al. 2008, A&A, 477, 717
Chotard, N., et al. 2011, A&A, submitted
Foley, R. J., Filippenko, A. V., & Jha, S. W. 2008, ApJ, 686, 117
Goldhaber, G., Groom, D. E., Kim, A., et al. 2001, ApJ, 558, 359
Hachinger, S., Mazzali, P. A., & Benetti, S. 2006, MNRAS, 370, 299
Hamuy, M., Walker, A. R., Suntzeff, N. B., et al. 1992, PASP, 104, 533
Hamuy, M., Maza, J., Pinto, P. A., et al. 2002, AJ, 124, 417
Hauschildt, P. H., Barman, T. S., Baron, E., & Allard, F. 2003, in Stellar Atmospheric Modeling, ed. I. Hubeny, D. Mihalas, & K. Werner (San Francisco: ASP), 227
Höflich, P., Gerardy, C., Fesen, R., & Sakai, S. 2002, ApJ, 568, 791
Jack, D., Hauschildt, P. H., & Baron, E. 2009, A&A, 502, 1043
Jeffery, D. J. 1998 [arXiv:astro-ph/9811356]
Kasen, D. 2006, ApJ, 649, 939
Mihalas, D., & Mihalas, B. W. 1984, Foundations of Radiation Hydrodynamics (Oxford: Oxford University)
Nomoto, K. 1984, ApJ, 277, 791
Nomoto, K., Thielemann, F.-K., & Yokoi, K. 1984, ApJ, 286, 644
Nugent, P., Phillips, M., Baron, E., Branch, D., & Hauschildt, P. 1995, ApJ, 455, L147
Perlmutter, S., Aldering, G., Goldhaber, G., et al. 1999, ApJ, 517, 565
Phillips, M. M. 1993, ApJ, 413, L105
Pskovskii, I. P. 1977, SvA, 21, 675
Richardson, D., Thomas, R. C., Casebeer, D., et al. 2001, BAAS, 33, 1428
Richardson, D., Thomas, R., Casebeer, D., Branch, D., & Baron, E. 2002, BAAS, 34, 1205
Riess, A. G., Press, W. H., & Kirshner, R. P. 1996, ApJ, 473, 88
Riess, A. G., Filippenko, A. V., Challis, P., et al. 1998, AJ, 116, 1009
Stritzinger, M., Hamuy, M., Suntzeff, N. B., et al. 2002, AJ, 124, 2100

A&A 533, A127 (2011)
DOI: 10.1051/0004-6361/201117051

Astronomy & Astrophysics

A 3D radiative transfer framework

VIII. OpenCL implementation

P. H. Hauschildt[1] and E. Baron[1,2,3]

[1] Hamburger Sternwarte, Gojenbergsweg 112, 21029 Hamburg, Germany
e-mail: yeti@hs.uni-hamburg.de
[2] Homer L. Dodge Dept. of Physics and Astronomy, University of Oklahoma, 440 W. Brooks, Rm 100, Norman, OK 73019, USA
e-mail: baron@ou.edu
[3] Computational Research Division, Lawrence Berkeley National Laboratory, MS 50F-1650, 1 Cyclotron Rd, Berkeley, CA 94720-8139, USA

Received 8 April 2011 / Accepted 18 July 2011

ABSTRACT

Aims. We discuss an implementation of our 3D radiative transfer (3DRT) framework with the OpenCL paradigm for general GPU computing.
Methods. We implemented the kernel for solving the 3DRT problem in Cartesian coordinates with periodic boundary conditions in the horizontal (x, y) plane, including the construction of the nearest neighbor Λ^* and the operator splitting step.
Results. We present the results of both a small and a large test case and compare the timing of the 3DRT calculations for serial CPUs and various GPUs.
Conclusions. The latest available GPUs can lead to significant speedups for both small and large grids compared to serial (single core) computations.

Key words. radiative transfer – methods: numerical

1. Introduction

In a series of papers (Hauschildt & Baron 2006; Baron & Hauschildt 2007; Hauschildt & Baron 2008, 2009; Baron et al. 2009; Hauschildt & Baron 2010; Seelmann et al. 2010, hereafter: Papers I–VII), we have described a framework for solving the radiative transfer equation in 3D systems (3DRT), including a detailed treatment of scattering in continua and lines with a nonlocal operator splitting method and its use in the general model atmosphere package PHOENIX.

The 3DRT framework discussed in the previous papers of this series requires very substantial amounts of computing time owing to the complexity of the radiative transfer problem in strongly scattering environments. The standard method of speeding up these calculations is to implement parallel algorithms for distributed memory machines using the MPI library (Hauschildt & Baron 2006; Baron & Hauschildt 2007). The development of relatively inexpensive graphic processing units (GPUs) with large numbers of cores and the development of relatively easily used programming models, OpenCL and CUDA has made the use of GPUs attractive for accelerating scientific simulations. GPUs are built to handle numerous lightweight parallel threads simultaneously and to offer theoretical peak performance far beyond that of current CPUs. However, using them efficiently requires different programming methods and algorithms than those employed on standard CPUs. We describe our first results of implementing our 3DRT framework for a single geometry within the OpenCL (Munshi 2009) paradigm for generalized GPU and CPU computing.

2. Method

In the following discussion we use the notation in Papers I–VII. The basic framework and the methods used for the formal solution and the solution of the scattering problem via nonlocal operator splitting are discussed in detail in these papers and are not repeated here. Our implementation of the 3DRT framework considers the most time-consuming parts of the process – the formal solution and the solution of the operator splitting equations – to obtain the updated values of the mean intensities, whereas less time-consuming parts of the code (set-up, Ng acceleration, etc.) are left to Fortran95 or C implementations. The OpenCL implementation of the 3DRT framework minimizes data transfer between the host computer (CPU) and the GPU and keeps most of the data locally on the GPU memory. Only the relevant input data (e.g., opacities) and the results, e.g., the mean intensities J for all voxels, need to be transferred to and from the GPU device.

2.1. General purpose computing on graphic processors

Using a GPU for numerical calculations requires special programming environments. While GPU manufacturers have provided programming environments for vendor-special hardware, e.g., CUDA (NVIDIA 2007) for NVIDIA produced GPUs and ATI Stream SDK (AMD 2009) (which has now been replaced by AMD APP (AMD 2011) which uses OpenCL) for AMD/ATI produced GPUs. The differences between these environments make programs specific to systems from their respective vendors. Our applications need to be extremely portable, so having to code for multiple vendor-specific environments is not

acceptable. Fortunately, the open standard OpenCL (Munshi 2009) was designed to efficiently use not only GPUs but also modern multicore CPUs and other accelerators using a thread-centered programming model. With OpenCL it is possible to run the same code on many different CPU and GPU architectures. There is a relatively minor cost with some loss of performance when using OpenCL rather than CUDA specific programming models (Komatsu et al. 2011). This is insignificant for our application where portability is far more important than the fraction of the theoretical peak performance attained for a specific piece of hardware. At the present time, OpenCL is available for all types of GPUs and CPUs, including accelerators such as the Cell Broadband Engine (CBE), whereas CUDA is only available for NIVIA GPUs. This is a major concern for us with the technology progressing rapidly and new hardware released frequently. Using a defined standard is, therefore, already important for building a reliable code base that can be used easily in the future. Maintaining several different codes for the same tasks in different programming languages is, on the other hand, costly in terms of human time and is also error prone. The disadvantage of this use of general standards is a small loss of performance. We consider this a low price for the portability because hardware features and performance increase dramatically with new hardware. Therefore, we implemented our 3DRT framework in OpenCL for portability reasons.

The design of GPUs differs considerably from the design of CPUs, focusing much more on simultaneous execution of many threads to hide memory access latencies. In contrast to CPUs, branching is costly on GPUs and should therefore be limited as much as possible. It is in many cases faster to compute both branches of a decision and then select the correct one afterwards rather than using conditional execution. This is not an uncommon strategy and it was used, for example, on the original CRAY vector machines in the 1980s. In addition, GPUs provide better performance for regular memory-access patterns. The preferred programming model for these GPU systems is a single-program, multiple-data (SPMD) type scheme that is directly supported by OpenCL. Branching within a program is allowed in this model, but often drastically reduces performance and thus should be avoided.

2.2. Implementation of the formal solution and Λ^* computation

As a first step, we have implemented the "simplest" formal solution kernel in OpenCL. This is the kernel for Cartesian coordinates with periodic boundary conditions in the (horizontal) $x - y$ plane discussed in Hauschildt & Baron (2008). An OpenCL implementation of the formal solution is in principle straightforward: For any given direction of photon propagation, all characteristics can be tracked simultaneously through the voxel grid, which corresponds to a 2D kernel in the OpenCL paradigm. The characteristics are started on the inner or outer $x - y$ planes. The only substantial hurdle in the problem is that OpenCL (version 1.0 or 1.1) does not have facilities for atomic updates of floating point variables. This is, however, necessary for the numerically correct operation of a straightforward implementation of the formal solution for the calculation of the mean intensities and the Λ^* operator. Therefore, we have implemented a 2-pass kernel, where in the first pass the intensities (etc.) are computed and stored along the characteristics that can be implemented with atomic operations on integer variables when the results are stored per voxel rather than per characteristic. In a second pass, these data are collected on a per voxel (3D) OpenCL kernel. With this method, the results are identical (to the precision used in the OpenCL implementation) to the Fortran95 implementation. However, the 2-pass method requires additional memory on the GPU to store the intermediate results and the first pass generates complex memory access patterns that are likely to limit performance on GPU based systems.

2.3. Implementation of the operator splitting step

The second very time-consuming part of the 3DRT framework is the solution of the operator splitting equations for computing the new values of the mean intensities J for all voxels. The Fortran95 code solves these equations by Jordan or Gauss-Seidel iterations. In OpenCL, it is much simpler to implement the Jordan method since it requires less synchronization between threads than does the Gauss-Seidel method. The OpenCL implementation uses a 3D kernel (all voxels simultaneously) and locally buffers the Λ^* during the iterations, which dramatically speeds up the calculations.

3. Results

3.1. Test case setup

The test cases we have investigated follow the continuum tests used in Hauschildt & Baron (2008). In detail, we used the configuration for the testing where periodic boundary conditions (PBCs) are realized in a plane parallel slab. We used PBCs on the x and y axes and $z_{\max}$ is at the outside boundary, $z_{\min}$ the inside boundary. The slab has a finite optical depth in the z axis. The gray continuum opacity is parameterized by a power law in the continuum optical depth $\tau_{\rm std}$ in the z axis. The basic model parameters are

1. the total thickness of the slab, $z_{\max} - z_{\min} = 10^7$ cm;
2. the minimum optical depth in the continuum, $\tau_{\rm std}^{\min} = 10^{-4}$ and the maximum optical depth in the continuum, $\tau_{\rm std}^{\max} = 10^8$;
3. an isothermal slab, $T = 10^4$ K;
4. boundary conditions with outer boundary condition $I_{\rm bc}^- \equiv 0$ and inner boundary condition LTE diffusion for all wavelengths;
5. parameterized coherent & isotropic continuum scattering given by

   $$\chi_{\rm c} = \epsilon_{\rm c}\kappa_{\rm c} + (1 - \epsilon_{\rm c})\sigma_{\rm c}$$

   with $0 \le \epsilon_{\rm c} \le 1$. $\kappa_{\rm c}$ and $\sigma_{\rm c}$ are the continuum absorption and scattering coefficients.

For the tests presented here, we used $\epsilon_{\rm c} = 10^{-2}$ in order to allow single-precision runs, and double-precision is required for smaller epsilons for the solution of the operator splitting equations.

We have verified that the OpenCL calculations give the same result as the Fortran95 CPU calculations for the formal solution (intensities), the mean intensities, and the Λ^*. Likewise the solution of the 3D radiative transfer problem is the same for both OpenCL and Fortran95. For OpenCL single-precision calculations, the relative accuracy is about 10^{-5}, which is acceptable for most calculations.

3.2. Timing results

In Figs. 1–4 we show the timing and speed-up results for small and large test cases. The difference between the tests is

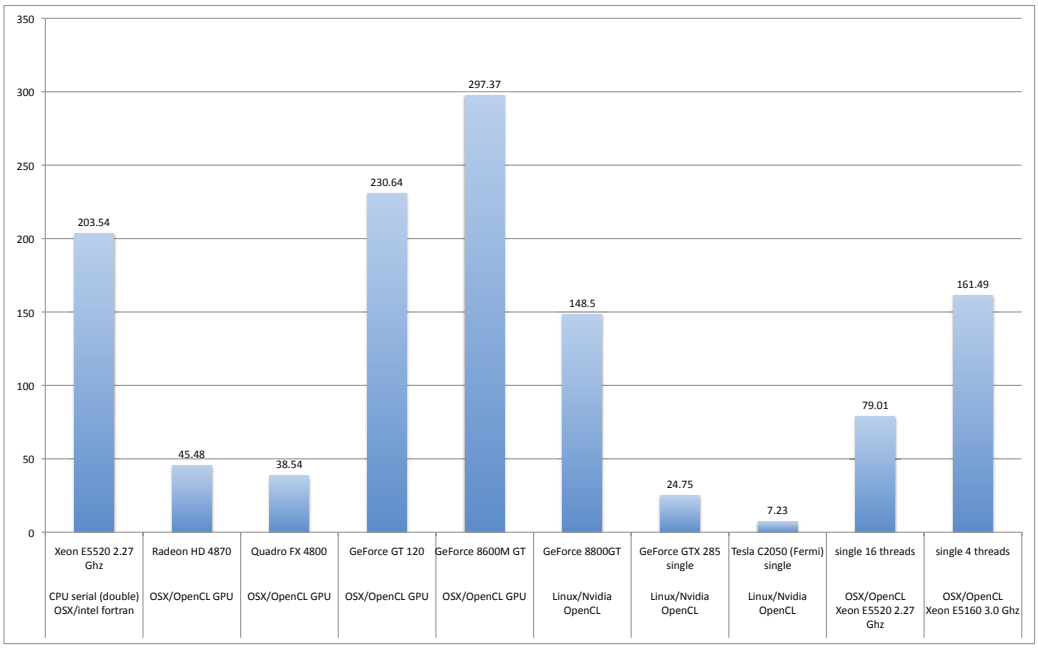

Fig. 1. Timing of the small 3D radiative transfer test calculation on CPUs (leftmost column), various GPUs with OpenCL, and multicore CPUs using OpenCL. The times are given in seconds of wallclock time.

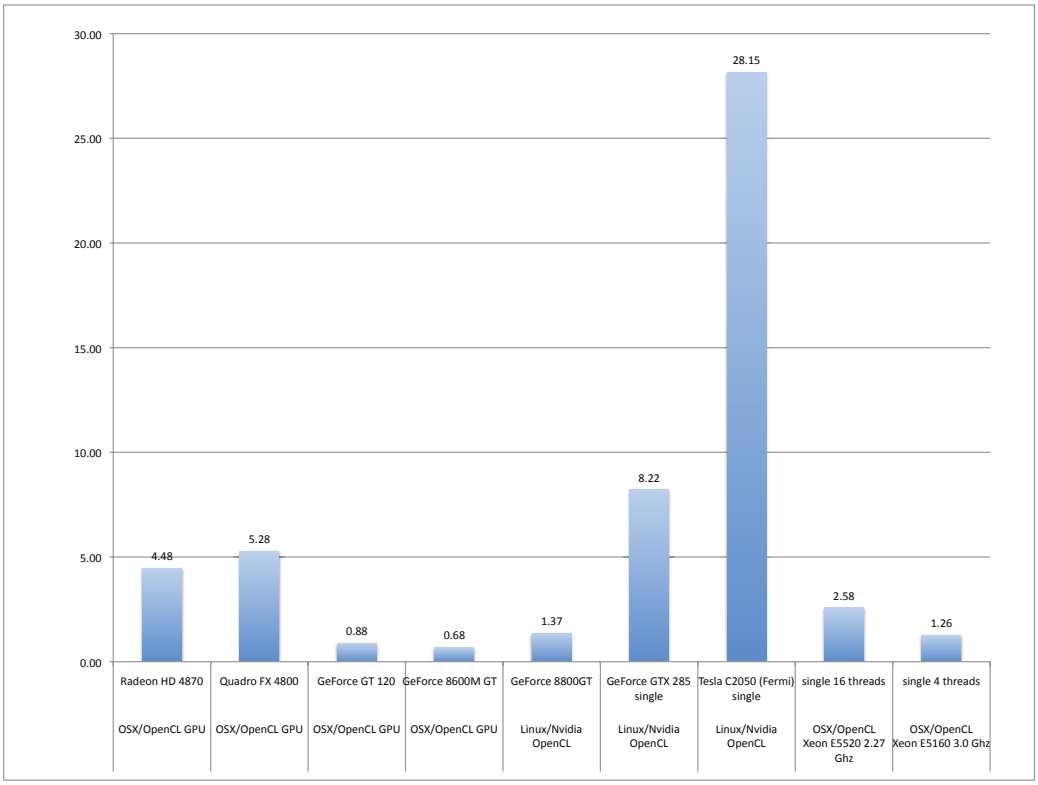

Fig. 2. Speed-ups of the small 3D radiative transfer test calculation for the OpenCL implementation relative to the serial CPU run.

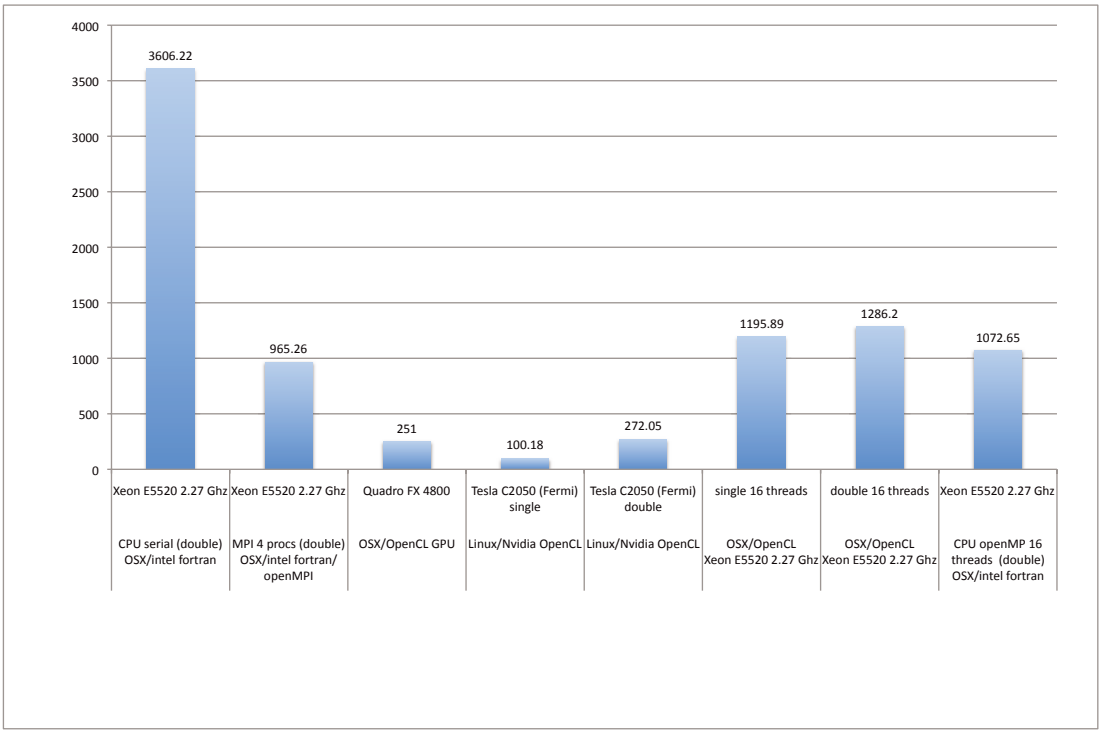

Fig. 3. Timing of the large 3D radiative transfer test calculation on CPUs (leftmost column), various GPUs with OpenCL, and multicore CPUs using OpenCL, MPI and OpenMP. The MPI calculation was run on 4 cores (1 CPU), the OpenMP run used 16 threads (8 cores, incl. hyperthreading) to be comparable to the OpenCL CPU run. The times are given in seconds of wallclock time.

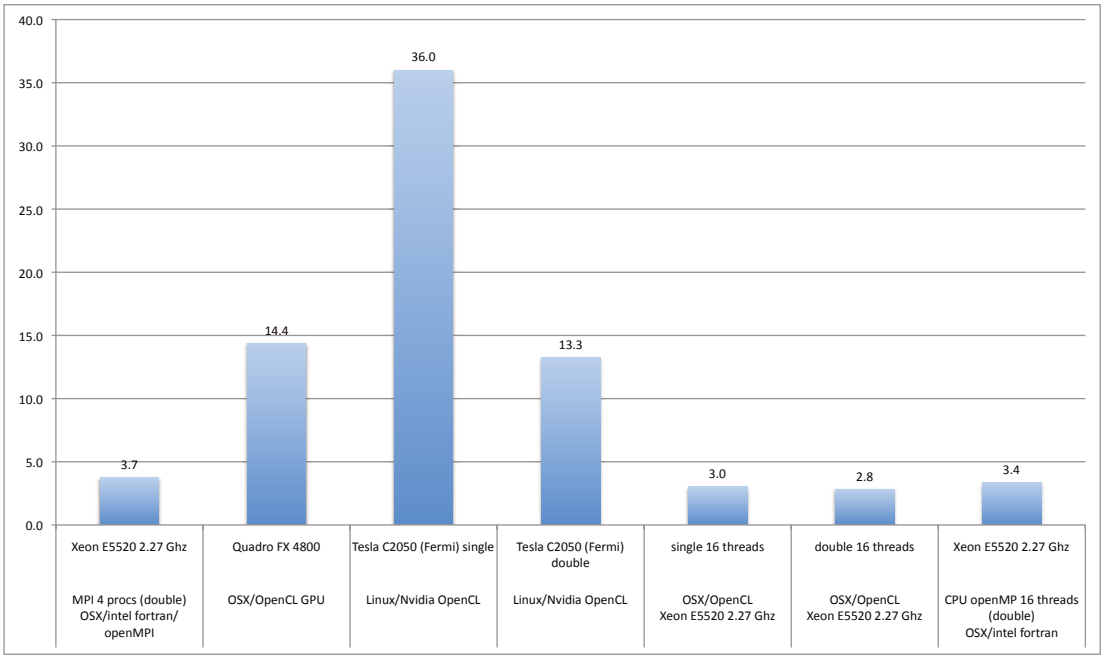

Fig. 4. Speed-ups of the large 3D radiative transfer test calculation for the OpenCL, OpenMP, and MPI implementations relative to the serial CPU run. The MPI calculation was run on 4 cores (1 CPU), and the OpenMP run used 16 threads (8 cores, incl. hyperthreading) to be comparable to the OpenCL CPU run.

simply the size of the voxel grid. In the small case, we use $65^3 = 274\,625$ voxels, whereas the large test case uses a grid with $129^2 * 193 = 3\,211\,713$ voxels. The small test cases uses 95.3 MB OpenCL memory in single-precision (165.5 MB double-precision) and thus fits easily in GPU devices with little memory, whereas the large test case uses 1.1 GB OpenCL memory in single-precision (1.9 GB in double-precision) and can thus only be used on high-end GPU devices. The tests were run on a variety of systems, from laptops with low-end GPUs to Xeon-based systems with dedicated GPU based numerical accelerator boards. For the comparisons in the figures, we have selected the fastest CPU run as the serial baseline for all comparisons. The systems used in the tests are:

1. serial CPU: Mac Pro with OSX 10.6.4 and Intel Fortran 11.1, the CPU is a Xeon E5520 with 2.27 GHz clock-speed;
2. MPI: 4 processes on Mac Pro with OSX 10.6.4 and Intel Fortran 11.1, the CPU is a Xeon E5520 (4 cores) with 2.27 GHz clock-speed;
3. AMD/ATI Radeon HD 4870 GPU with 512 MB RAM on a Mac Pro with OSX 10.6.4 OpenCL;
4. NVIDIA GeForce 8600M GT GPU with 512 MB RAM on a MacBook Pro laptop with OSX 10.6.4 OpenCL;
5. NVIDIA GeForce GT 120 GPU with 512 MB RAM on a Mac Pro with OSX 10.6.4 OpenCL;
6. NVIDIA Quadro FX 4800 GPU with 1536 MB RAM on a Mac Pro with OSX 10.6.4 OpenCL;
7. NVIDIA GeForce 8800GT GPU with 512 MB RAM on a Linux PC with NVIDIA OpenCL (OpenCL 1.1, CUDA 3.2.1);
8. NVIDIA GeForce GTX 285 GPU with 1024 MB RAM on a Linux PC with NVIDIA OpenCL (OpenCL 1.0, CUDA 3.0.1);
9. NVIDIA Tesla C2050 Fermi-GPU with 2687 MB RAM on a Linux PC with NVIDIA OpenCL (OpenCL 1.1, CUDA 3.2.1);
10. Intel Xeon E5520 at 2.27 GHz clock-speed on a Mac Pro with OSX 10.6.4, OpenCL (16 OpenCL threads);
11. Intel Xeon E5520 at 2.27 GHz clock-speed on a Mac Pro with OSX 10.6.4, Intel Fortran 11.1 OpenMP (16 OpenMP threads).

All these system were used for the small test case, since the large test case could only be run on the serial CPU, the 2 OpenCL CPU runs, and on the Quadro FX 4800 and Tesla C2050 GPUs due to memory constraints.

The results for the small test case show that low-end GPUs (GeForce GT 120, GeForce 8xxx) do not provide significant speed-up compared to serial CPU calculations. However, compared to a laptop class CPU, they can be useful (the GeForce 8600M GT reaches about the speed of the serial CPU of the laptop, an Intel T9300 CPU at 2.5 GHz) because they can be used in parallel with the CPU (e.g., to offload formal solutions for visualizations from the CPU). Medium-grade GPUs (Radeon HD 4870 or Quadro FX 4800) give speed-ups ranging between four and five compared to CPUs, which is already quite useful for small-scale calculations on workstations. High-end GPUs (GeForce GTX 285, Tesla C2050) deliver substantially larger speed-ups for the small test case, and a factor of 28 for the Fermi-GPU based accelerator is very significant for calculations.

For the large case, which is close to the size of a real production calculation, we show the timing results in Figs. 3 and 4. The memory requirements of the calculations now limit the tests to the CPUs (serial and OpenCL) and the Quadro FX 4800 and Tesla C2050 devices. For the OpenCL runs on CPUs and the Tesla C2050 runs, we also include the results for double-precision OpenCL calculations. In this test, the GPUs deliver larger speed-ups, up to a factor of 36 for the Tesla C2050 device. Using double-precision reduces the speed-up to about a factor of 13 (a factor of about 2.7 slower than single-precision), which is presumably due to more complex memory accesses and less efficient double-precision hardware on the Fermi GPU. Running OpenCL on CPUs is still not efficient compared to running MPI code, but the timings are essentially the same regardless of single or double-precision. OpenCL is about as efficient as using OpenMP shared memory parallelization with the same number of threads. Therefore, OpenCL can be used as a more versatile replacement for OpenMP code. It has been suggested that ultimately GPUs may be only a factor of 2−3 faster than multicore CPUs (Lee et al. 2010); therefore, a careful split of the computational work between CPUs and GPUs is probably the most efficient way to use these systems.

Comparing our results to others in the literature is not easy, since most other physics and astronomy applications solve problems that have very different computational characteristics with different levels of difficulty in their parallelization on SMP machines, e.g. *N*-body problems (Capuzzo-Dolcetta et al. 2011; Gaburov et al. 2010) where speedups can be a factor of 100 or more when a clever strategy is adopted for evaluating of the pairwise force in the system by direct summation. On the other hand, in molecular dynamics problems, speedups of 20–60 are considered acceptable (Chen et al. 2009). The highly nonlocal nature of the radiative transfer problem makes the kernels extremely complex. Therefore, to retain numerical accuracy and portability, some fraction of the theoretical speedup must be sacrificed.

We note that we have chosen OpenCL for its portability and have so far not tried to fully optimize our kernels for the specific architecture, because new features and fundamental changes are introduced very frequently into new hardware, and better OpenCL compilers will reduce the importance of hand-tuning the OpenCL code reported by Komatsu et al. (2011). Studies have shown that hand-tuned optimizations can lead to OpenCL performance approaching that of vendor specific software (Weber et al. 2011; Komatsu et al. 2011), but in this still early state of general computing on GPUs, this will change with new versions of the OpenCL framework and better OpenCL compilers. One of the main issues concerning further optimization is an inherent problem of the formal solution: for each solid angle (direction) any characteristic passes through a large fraction of the voxel grid, resulting in highly complex memory access patterns that also vary from one direction to another and from one characteristic to another. This is a basic feature of radiative transfer. Using approaches that maximize data locality work on CPUs (with a small number of cores) but are very inefficient on GPUs because many PEs may be idle at any given time (again, depending on the direction). We did a number of experiments with different approaches and found that the parallel tracking implementation described above is a good overall compromise that keeps many OpenCL threads active and allows the GPU hardware to mask many memory latencies. On CPUs, the impact is even less because the number of cores tends to be small and complex memory access patterns are handled more efficiently than for a single thread on a GPU. With this the algorithm performs best on newer GPU hardware than on older hardware, which is encouraging for future devices. A promising venue for further optimization requires the availability of atomic updates for floating point numbers in OpenCL, and this could remove the need for a two pass approach in the formal solution and may improve performance.

4. Summary and conclusions

We have described first results we obtained by implementing our 3DRT framework in OpenCL for use on GPUs and similar accelerators. The results for 3D radiative transfer in Cartesian coordinates with periodic boundary conditions show that high-end GPUs can result in quite large speed-ups compared to serial CPUs and are thus useful for accelerating complex calculations. This is in particular useful for clusters where each node has one GPU device and where calculations can be domain-decompositioned with one-node granularity. Large-scale calculations that require a domain-decomposition greater than one node are more efficient on large scale supercomputers with thousands of cores, because data transfer required for simultaneous use of multiple GPUs on multiple nodes will dramatically reduce performance. Even medium-end or low-end GPUs can be useful for offloading calculations from the CPU to speed up the overall calculations.

Acknowledgements. This work was supported in part by DFG GrK 1351 and SFB 676, as well as by the NSF grant AST-0707704, US DOE Grant DE-FG02-07ER41517, and NASA Grant HST-GO-12298.05-A. Support for program number HST-GO-12298.05-A was provided by NASA through a grant from the Space Telescope Science Institute, which is operated by the Association of Universities for Research in Astronomy, Incorporated, under NASA contract NAS5-26555. The calculations presented here were performed at the Höchstleistungs Rechenzentrum Nord (HLRN) and at the National Energy Research Supercomputer Center (NERSC), which is supported by the Office of Science of the US Department of Energy under Contract No. DE-AC03-76SF00098. We thank all these institutions for generous allocation of computer time.

References

AMD 2009, AMD Stream Computing User Guide version 1.4-Beta, Tech. Rep., AMD Corp, http://ati.amd.com/technology/streamcomputing/Stream_Computing_user_Guide.pdf

AMD 2011, AMD Accelerated Parallel Processing (APP) SDK (formerly ATI Stream), Tech. Rep., AMD Corp, http://developer.amd.com/sdks/AMDAPPSDK/Pages/default.aspx

Baron, E., & Hauschildt, P. H. 2007, A&A, 468, 255

Baron, E., Hauschildt, P. H., & Chen, B. 2009, A&A, 498, 987

Capuzzo-Dolcetta, R., Mastrobuono-Battisti, A., & Maschietti, D. 2011, New A, 16, 284

Chen, F., Ge, W., & Li, J. 2009, in Many-core and Accelerator-based Computing for Physics and Astronomy Applications, ed. H. Shukla, T. Abel, & J. Shalf, http://www.lbl.gov/html/manycore.html

Gaburov, E., Bédorf, J., & Portegies Zwart, S. 2010 [arXiv:1005.5384]

Hauschildt, P. H., & Baron, E. 2006, A&A, 451, 273

Hauschildt, P. H., & Baron, E. 2008, A&A, 490, 873

Hauschildt, P. H., & Baron, E. 2009, A&A, 498, 981

Hauschildt, P. H., & Baron, E. 2010, A&A, 509, A36

Komatsu, K., Sato, K., Arai, Y., et al. 2011, in High Performance Computing for Computational Science – VECPAR 2010 – 9th International conference, Berkeley, CA, USA, June 22–25, 2010, Revised Selected Papers, ed. J. L. Palma, M. Daydé, O. Marques, & J. C. Lopes (Springer), Lect. Not. Comp. Sci., 6449

Lee, V. W., Kim, C., Chhugani, J., et al. 2010, in ISCA10, ACM

Munshi, A. 2009, The OpenCL Specification, Tech. Rep., Khronos Group, http://www.khronos.org/registry/cl/specs/opencl-1.0.29.pdf

NVIDIA 2007, NVIDIA CUDA: Compute Unified Device Architecture, Tech. Rep., NVIDIA Corp

Seelmann, A. M., Hauschildt, P. H., & Baron, E. 2010, A&A, 522, A102

Weber, R., Gothandaraman, A., Hinde, R. J., & Peterson, G. D. 2011, IEEE Transactions on Parallel and Distributed Systems, 22, 58

A&A 538, A132 (2012)
DOI: 10.1051/0004-6361/201117271

Astronomy & Astrophysics

Near-infrared light curves of type Ia supernovae *(Research Note)*

D. Jack[1], P. H. Hauschildt[1], and E. Baron[1,2]

[1] Hamburger Sternwarte, Gojenbergsweg 112, 21029 Hamburg, Germany
e-mail: [djack;yeti]@hs.uni-hamburg.de
[2] Homer L. Dodge Department of Physics and Astronomy, University of Oklahoma, 440 W Brooks, Rm 100, Norman, OK 73019-2061, USA

Received 17 May 2011 /Accepted 3 January 2012

ABSTRACT

Aims. With our time-dependent model atmosphere code PHOENIX, our goal is to simulate light curves and spectra of hydrodynamical models of all types of supernovae. In this work, we simulate near-infrared light curves of SNe Ia and confirm the cause of the secondary maximum.
Methods. We apply a simple energy solver to compute the evolution of an SN Ia envelope during the free expansion phase. Included in the solver are energy changes due to expansion, the energy deposition of γ-rays and interaction of radiation with the material.
Results. We computed theoretical light curves of several SN Ia hydrodynamical models in the I, J, H, and K bands and compared them to the observed SN Ia light curves of SN 1999ee and SN 2002bo. By changing a line scattering parameter in time, we obtained quite reasonable fits to the observed near-infrared light curves. This is a strong hint that detailed NLTE effects in IR lines have to be modeled, which will be a future focus of our work.
Conclusions. We found that IR line scattering is very important for the near-infrared SN Ia light curve modeling. In addition, the recombination of Fe III to Fe II and of Co III to Co II is responsible for the secondary maximum in the near-infrared bands. For future work the consideration of NLTE for all lines (including the IR subordinate lines) will be crucial.

Key words. radiative transfer – methods: numerical – stars: atmospheres – supernovae: general

1. Introduction

We focus on the near-infrared light curves of type Ia supernovae (SNe Ia). The light curves in the near-infrared are of particular interest, because they have been claimed to be near standard candles at the time of B-band maximum in the IR (Krisciunas et al. 2004a). In addition, many, but not all SNe Ia exhibit a secondary maximum in the IR bands. The secondary maximum was first noted by Elias et al. (1981). Höflich et al. (1995) explained the secondary maximum as due to the expansion of the IR pseudo-photosphere, whereas Suntzeff (1996) suggested that it was due to a global shift of radiation from blue to red. Pinto & Eastman (2000) suggested that the transition from Fe III to Fe II as the dominant ionization stage was important although they implied that the secondary maximum occurs when the photosphere has receded into the non-radioactive center. Kasen (2006) performed a detailed study of SN Ia light curves in the near-infrared and obtained reasonable fits to observations. He also finds that the secondary maximum is an effect of the ionization evolution of iron group elements in the expanding envelope. We apply our time-dependent model atmosphere code PHOENIX and investigate SNe Ia by comparing model light curves in the near-infrared to observed light curves. We will also focus on the origin of the secondary maximum.

We present model light curves of SNe Ia in the near-infrared. In Sect. 2 we present the methods we used in some detail. In Sect. 3 we present light curves of SNe Ia for different hydrodynamical models in the I, J, H, and K bands. We consider a parametrized IR line scattering in the solution of the radiative transfer to improve our fits to observed light curves. An investigation of the secondary maximum that has been observed in near-infrared light curves is discussed in a final section.

2. Methods

We use our time dependent model atmosphere code PHOENIX, version 16, to compute model light curves of type Ia supernovae. We use the time dependent extension and the method as described in Jack et al. (2009, 2011). We calculate SN Ia model light curves for different hydrodynamic (explosion) models. In our previous work, we presented model light curves in the optical bands with reasonable fits to observations. In this work, we focus on the near-infrared wavelength region and model the light curves in the I, J, H, and K bands.

To compute SN Ia light curves, our approach is a simple energy solver that solves for an energy change of the material during a time step of the envelope evolution. The energy can change due to the free adiabatic expansion, the deposition of energy from γ-rays from the radioactive decay of ^{56}Ni and ^{56}Co, and the interaction of radiation with the material. In our calculations, we assume homologous expansion. The γ-ray deposition is solved with the assumption of a gray atmosphere. Changes of ionization state are also included in our solver.

To determine the energy change of the material due to the interaction with the radiation, we have to solve the radiative transfer. For each time step, we solve the non-gray spherical symmetric radiative transfer equation for expanding atmospheres including special relativistic effects. We typically use

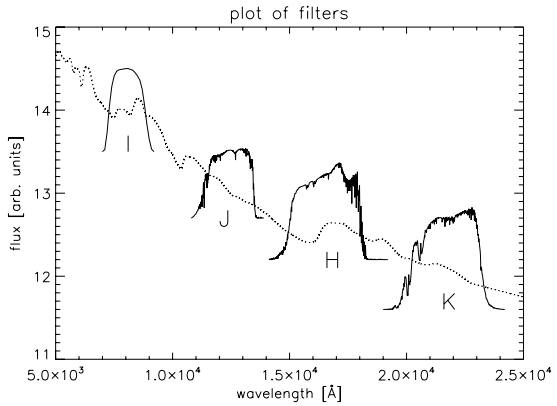

Fig. 1. Synthetic spectrum of a SN Ia at day 20 plotted with the filter functions of the I, J, H, and K band.

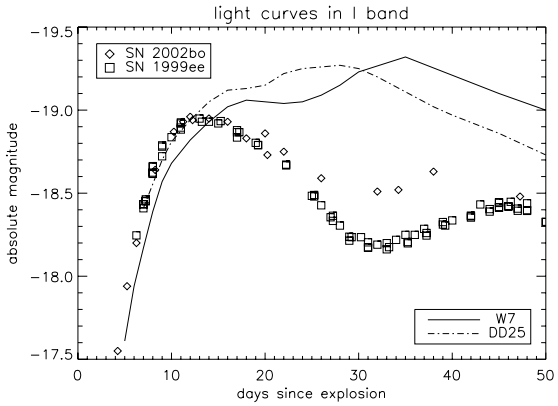

Fig. 2. Model and observed light curves in the I band. Two different explosion models were used to compute the model light curves.

about 2000 wavelength points to keep the computation time reasonable.

Given the problems with the simple LTE treatment of line scattering as shown in Jack et al. (2011), we investigate the effects of IR line scattering on SN Ia light curves in the near-infrared. In our previous paper (Jack et al. 2011), we indicated how important UV/optical line scattering is during the later phases of the light curve evolution. Here, we study this effect in more detail.

The source function of the radiative transfer equation including scattering for an equivalent two level atom can be written as

$$S_\lambda = (1 - \epsilon_\lambda)J_\lambda + \epsilon_\lambda B_\lambda. \quad (1)$$

The source function is represented by S_λ, the Planck function by B_λ and the mean intensity by J_λ. All these quantities depend on the wavelength λ. Here, we used ϵ_λ as the line thermal coupling parameter. For $\epsilon_\lambda = 1$ there is only true absorption and no line scattering takes place. The source function is then given by $S_\lambda = B_\lambda$ (pure LTE). In reality, the thermal coupling parameter ϵ_λ will vary over the whole wavelength range. For the calculation with PHOENIX, it is possible to set a wavelength independent factor $\epsilon = \epsilon_\lambda = \text{const.}$ to approximate LTE line scattering over the whole wavelength range.

For our approach to model light curves of SNe Ia, we use the results of hydrodynamical explosion simulations, as our initial atmosphere structures which we then evolve in time. In this work, we use the explosion model results of the deflagration model W7 (Nomoto 1984). We also used one delayed detonation model, the model DD25 calculated by Höflich et al. (2002). Model DD16 (Höflich et al. 2002) which we studied in previous work is not considered here, because its low yield of ^{56}Ni makes it too dim to account for normal SNe Ia. We used our hydrodynamic solver to obtain detailed spectra at certain days in the light curve evolution, (see Jack et al. 2011, for details). Light curves are calculated by convolving the appropriate filter functions with the theoretical spectra. We compare our synthetic light curves to observed light curves of two SN Ia events: SN 1999ee and SN 2002bo. The filter functions we used here are shown in Fig. 1. The photometric observations of SN 1999ee in the J and H band are presented in Krisciunas et al. (2004b). For SN 2002bo photometric observations in the J, H, and K band have been obtained by Krisciunas et al. (2004c).

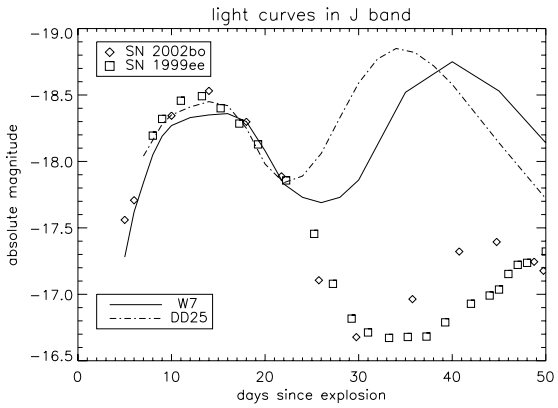

Fig. 3. Light curves in the J band. Two different explosion models were used to compute the model light curves and to compare them to observations.

3. Near-infrared light curves of SNe Ia

We first present the results of an approach of a constant line scattering factor $\epsilon = 0.8$ to the light curve modeling, where we compare the results of two different hydrodynamical models. Figure 2 shows the calculated model light curves of two hydrodynamical models in the I band. They are compared to two observed light curves of SN 1999ee and SN 2002bo. Both model light curves produce the steep rise during the first days after the explosion reasonably well. However, the model light curve rises further, although the observed light curves show a decline after maximum at around 13 days after explosion. During the later phase around 30 days after the explosion, the model light curves are much too bright compared to the observed light curves. There is also no indication of a secondary maximum in the model light curves. In Fig. 3, the model light curves in the J band are shown together with the observed light curves. Again, the first phase is well represented by the model light curves. The model light curves rise after a first maximum to a secondary maximum, which is much brighter and earlier than the secondary maximum in the observed light curves. Furthermore, the secondary maximum of the DD25 model is earlier than the one of hydrodynamical model W7. However, the difference of 2.5 mag around

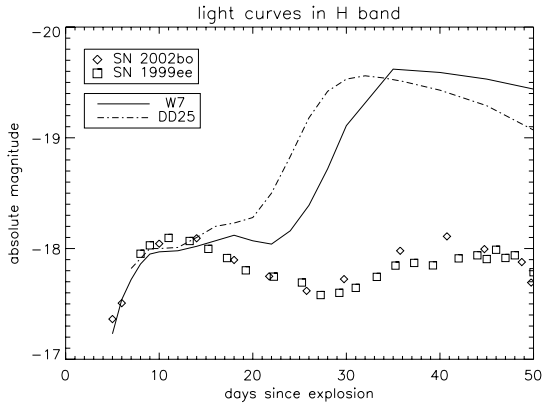

Fig. 4. Light curves in the *H* band. Two different explosion models were used to compute the model light curves.

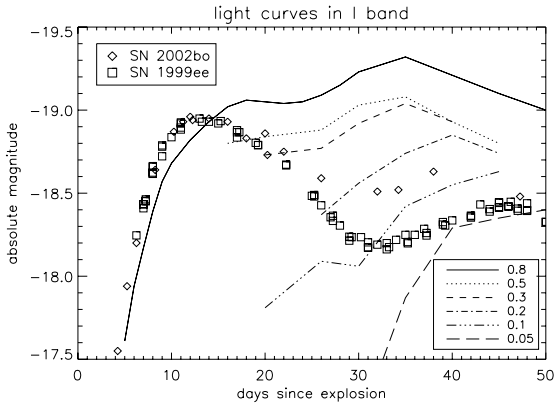

Fig. 6. Light curves in the *I* band computed with different values of the line scattering factor ϵ.

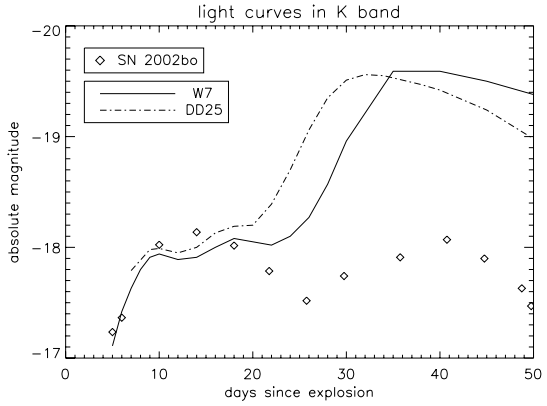

Fig. 5. Light curves in the *K* band. The model light curves of W7 and DD25 are significantly brighter than the observations during the later phase.

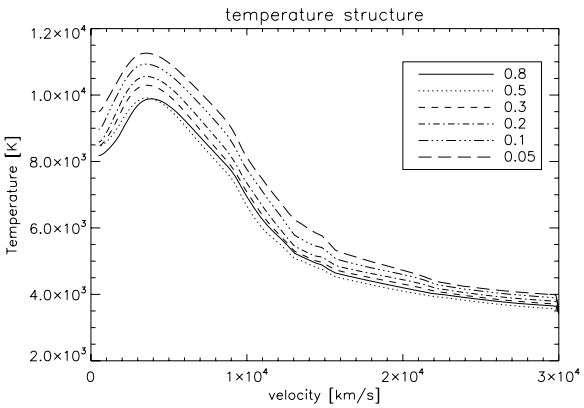

Fig. 7. Temperature structure of the envelope at day 30. A smaller line scattering factor ϵ leads to a hotter atmosphere.

day 35 between models and observations is enormous. A similar picture is seen in the *H* and *K* band as shown in Figs. 4 and 5.

So far, we used for the calculations of our LTE model light curves a constant time independent factor of $\epsilon = 0.8$. We now use this LTE line scattering factor to approximate the effect of line scattering on the shape of the light curves in the near-infrared. We calculated several model light curves each with a different LTE line scattering factor, ϵ. At each point of the light curve, we let the atmosphere structure adapt to the new conditions with its ϵ until a radiative equilibrium state is reached. This led to different resulting atmosphere structures or more precisely temperature structures at each day and thus to differences in the shapes of the model light curves.

Figure 6 shows the *I* band light curves obtained with different values of ϵ. With a smaller ϵ, the light curve becomes fainter. A look at the temperature structure in Fig. 7 reveals that decreased ϵ leads to a hotter atmosphere. In the hotter atmosphere, the iron and cobalt are mostly doubly ionized. As the atmosphere cools down, the iron and cobalt recombine to Fe II and Co II, and the flux increases due to numerous lines of these species in the near-infrared. This recombination effect in the near-infrared light curve has also been found by Kasen (2006) and Höflich et al. (1995). The intersection of the model light curves with the observed light curves shows that the best value of ϵ changes during the evolution of the light curve. ϵ decreases with time (i.e., line scattering becomes more and more important) in order to fit the observed light curves. This is reasonable, because the ongoing expansion leads to lower densities at later times, and line scattering becomes more important because of the thinner atmosphere. However, during the early phase near maximum light, ϵ has to be closer to pure LTE (Baron et al. 1996).

We now seek to fit the entire light curve with a single function for ϵ, that is we choose $\epsilon = \epsilon_0 f(t)$ where $f(t)$ is a function of time. Our model light curves now reproduce the observed light curves much more faithfully. Even the secondary maximum is well reproduced for each band. For instance, we show in Fig. 12 the new best fitting light curve in the *I* band. The solid line shows the W7 model light curve, which has an ϵ that decreases with time. We chose the light curve of SN 1999ee to obtain the best fit. It is clear that different values of $f(t)$ can be used to obtain a better fit to the light curve of SN 2002bo.

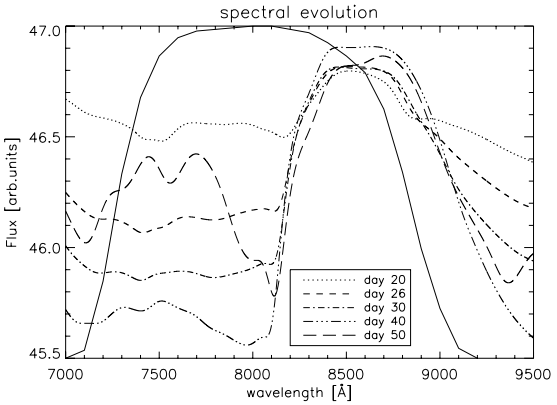

Fig. 8. Spectral evolution in the *I* band from day 20 to day 50 after the explosion. The solid line displays the filter function.

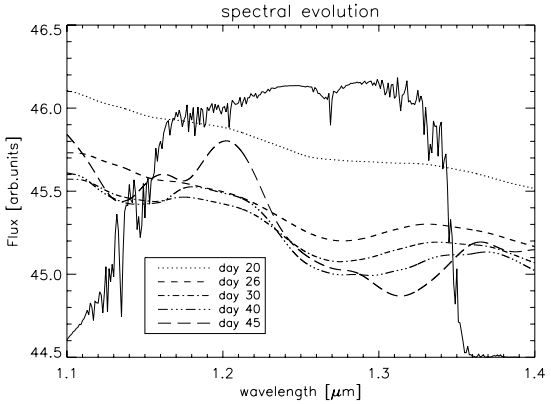

Fig. 9. Spectral evolution in the *J* band from day 20 to day 45 after the explosion. The solid line shows the filter function.

4. Secondary maximum in the near-infrared SN Ia light curves

In all bands in the near-infrared, the observed light curves show a secondary maximum around 30 to 40 days after explosion. Since with a time-dependent ϵ our model light curves reproduce the observed light curves pretty well, we will focus on the specific cause of the secondary maximum in each *IR* band. We investigate the cause of the secondary maximum in each of the near-infrared bands by looking at the spectral evolution of the model light curves in the respective band. Basically, we confirm the results of Kasen (2006). However, we can additionally assign features of certain elements to the individual bands and show detailed spectra.

The *I* band is known to be dominated by the Ca IR triplet. In Fig. 8 the spectral evolution in the *I* band is shown. The broad feature at 8500 Å is the Ca triplet. This feature stays present as the flux outside of the feature declines while the SN Ia envelope evolves. This leads to the decline in the light curve after the first maximum. Starting at day 40 a new "W-shaped" feature emerges at around 7500 Å. These are lines of Fe II, and the feature is even more significant in the spectrum at day 50. From day 30 to day 50 the temperature in the expanding envelope is decreasing. The temperature eventually reaches the temperature/pressure regime where Fe III recombines to Fe II. This increases the brightness in the *I* band due to *emission* lines of Fe II present in this wavelength region. Thus, emission lines of Fe II are responsible for the rise to a secondary maximum in the *I* band.

We now examine the secondary maximum in the *J* band. The spectral evolution in that wavelength range is shown in Fig. 9. With the SN Ia evolving, the flux is decreasing in the *J* band because the temperature of the envelope decreases. At day 30, new features arise, which increase the brightness in the *J* band. These features are caused by lines of Fe II and Co II. Therefore, the recombination of Fe III to Fe II is responsible for the rise in the *J* band. Additionally, Co III recombines to Co II at about the same temperature and therefore time in the light curve evolution. Thus, Co II lines emerge in the *J* band due to this recombination. The secondary maximum in the *J* band is caused by both emerging Fe II and Co II lines.

The spectral evolution in the *H* band is shown in Fig. 10. In the spectrum at day 26, two broad features emerge in this wavelength range. In the spectrum of days 35 and 45, these two features are clearly visible. They cause the rise in the brightness of the *H* band to a secondary maximum. We found that these features are caused by lines of Co II. Thus, the recombination of Co III to Co II causes the rise to a secondary maximum in the light curve of the *H* band.

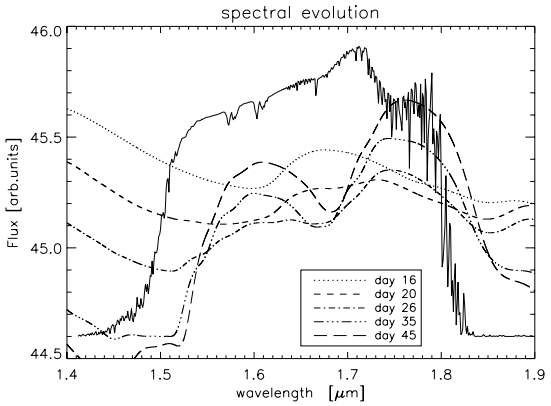

Fig. 10. Spectral evolution in the *H* band from day 16 to day 45 after the explosion. The solid line shows the filter function.

In the *K* band, the spectral evolution of our SN Ia model is shown in Fig. 11. The flux is decreasing as the envelope expands and cools down. However, at days 40 and 45 features emerge and cause a rise in the brightness of the *K* band. These features are again lines of Co II. The recombination of Co III to Co II causes the secondary maximum in the *K* band.

4.1. Non-radioactive core

The W7 model has a non-radioactive iron core. Pinto & Eastman (2000) showed that the consequent negative temperature gradient leads to a further reduction in the mean opacity. This may have an influence on the duration or magnitude of the IR secondary maximum. Therefore, it is worthwhile checking wether the non-radioactive center affects the shape of the secondary maximum in the near-infrared. We replaced the iron core of the W7 model with radioactive ^{56}Ni and computed the light curve. This increases the total mass of ^{56}Ni from 0.56 to 0.66 solar

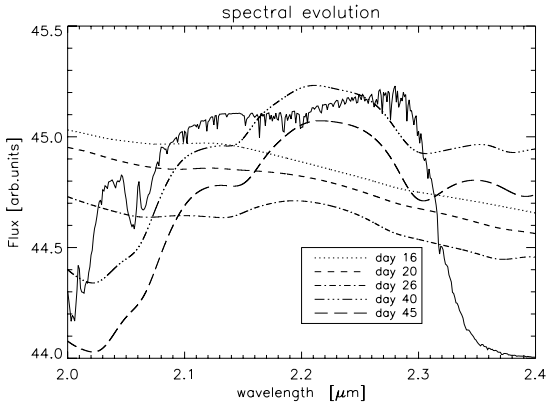

Fig. 11. Spectral evolution in the *K* band from day 16 to day 45 after the explosion. The solid line shows the filter function.

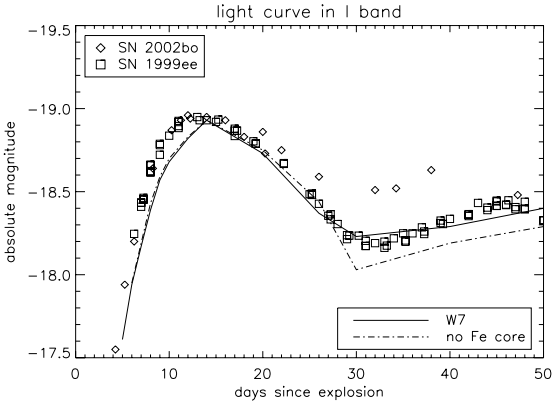

Fig. 12. Light curve in the *I* band with and without the non-radioactive iron core.

masses. As shown in Fig. 12, there are only small difference between the light curves with and without the non-radioactive iron core. This simple variation does not capture the full effect of the presence or absence of a non-radioactive core, since a shift in the nickel distribution can have important effects on the light curve (Baron et al., in prep.). Additionally, late time spectra show that that a non-radioactive core seems to be required in most SNe Ia (Höflich et al. 2004; Motohara et al. 2006; Fesen et al. 2007; Gerardy et al. 2007; Maeda et al. 2010).

5. Conclusion

We applied our time-dependent model atmosphere code PHOENIX to model light curves of type Ia supernovae in the near-infrared wavelength range. In a first approach with a constant LTE line scattering parameter ϵ in the radiative transfer, we reproduced the observed light curves during the first phase quite well. However, the model light curves during the later phase were too bright, and we could not reproduce the secondary maximum.

We show that a more detailed treatment of IR line scattering is very important for the modeling of the later phase of the near-infrared light curves of SNe Ia. We used as an approximation an LTE line scattering parameter that decreases in time. This is a good approach, because the atmosphere becomes thinner as expansion goes on and scattering becomes more important. We use this approximation to obtain fits to the observed light curves of SN 1999ee and SN 2002bo, improving our model light curves significantly. The next step is to treat the atmosphere in full non-LTE, where the temperature needs to adapt to the non-LTE condition, which requires substantial time on parallel supercomputers. Kasen (2006) also found that his models overshot the observed secondary maximum in *H* and *K*, while he mainly attributed this to incomplete line lists in the IR, he also suggested that his treatment of LTE might be a possible cause.

The secondary maximum in each band of the near-infrared was quite accurately reproduced by our model light curves with time-dependent ϵ. We investigated the spectral evolution and found that the *I* band secondary maximum arises due to recombination of Fe III to Fe II. An Fe II feature emerges in this band and increases the brightness. For the secondary maximum in the *J* band, a mix of Fe II and Co II lines emerges and causes the rise to a secondary maximum in the model light curve. The bands *H* and *K* also show a secondary maximum. This is caused by the recombination of Co III to Co II. We confirmed that ionization stage changes in iron group elements are responsible for the secondary maximum as previously found (Kasen 2006). In fact, since we use neither expansion opacities, nor the Sobolev approximation, our results robustly indicate the need for a full NLTE treatment. Furthermore, we can explicitly assign lines of different elements to different bands. These results also show how important the treatment of Fe and Co in non-LTE is and should be used in future work, when faster computers are available.

Acknowledgements. This work was supported in part by the Deutsche Forschungsgemeinschaft (DFG) via the SFB 676, NSF grant AST-0707704, US DOE Grant DE-FG02-07ER41517, and by program number HST-GO-12298.05-A which is supported by NASA through a grant from the Space Telescope Science Institute, which is operated by the Association of Universities for Research in Astronomy, Incorporated, under NASA contract NAS5-26555. This research used resources of the National Energy Research Scientific Computing Center (NERSC), which is supported by the Office of Science of the US Department of Energy under Contract No. DE-AC02-05CH11231, and the Höchstleistungs Rechenzentrum Nord (HLRN). We thank all these institutions for generous allocations of computation time.

References

Baron, E., Hauschildt, P. H., Nugent, P., & Branch, D. 1996, MNRAS, 283, 297
Elias, J. H., Frogel, J. A., Hackwell, J. A., & Persson, S. E. 1981, ApJ, 251, L13
Fesen, R. A., Höflich, P. A., Hamilton, A. J. S., et al. 2007, ApJ, 658, 396
Gerardy, C. L., Meikle, W. P. S., Kotak, R., et al. 2007, ApJ, 661, 995
Höflich, P., Khokhlov, A., & Wheeler, J. C. 1995, ApJ, 444, 831
Höflich, P., Gerardy, C., Fesen, R., & Sakai, S. 2002, ApJ, 568, 791
Höflich, P., Gerardy, C. L., Nomoto, K., et al. 2004, ApJ, 617, 1258
Jack, D., Hauschildt, P. H., & Baron, E. 2009, A&A, 502, 1043
Jack, D., Hauschildt, P. H., & Baron, E. 2011, A&A, 528, A141
Kasen, D. 2006, ApJ, 649, 939
Krisciunas, K., Phillips, M. M., & Suntzeff, N. B. 2004a, ApJ, 602, L81
Krisciunas, K., Phillips, M. M., Suntzeff, N. B., et al. 2004b, AJ, 127, 1664
Krisciunas, K., Suntzeff, N. B., Phillips, M. M., et al. 2004c, AJ, 128, 3034
Maeda, K., Benetti, S., Stritzinger, M., et al. 2010, Nature, 466, 82
Motohara, K., Maeda, K., Gerardy, C. L., et al. 2006, ApJ, 652, L101
Nomoto, K. 1984, ApJ, 277, 791
Pinto, P. A., & Eastman, R. G. 2000, ApJ, 530, 757
Suntzeff, N. B. 1996, in Supernovae and Supernova Remnants, ed. T. S. Kuhn (Cambridge, UK: Cambridge University Press), IAU Colloq., 145, 41

A&A 546, A39 (2012)
DOI: 10.1051/0004-6361/201118152

Astronomy & Astrophysics

A 3D radiative transfer framework

IX. Time dependence

D. Jack[1,2], P. H. Hauschildt[1], and E. Baron[1,3]

[1] Hamburger Sternwarte, Gojenbergsweg 112, 21029 Hamburg, Germany
e-mail: [djack;yeti]@hs.uni-hamburg.de
[2] Departamento de Astronomía, Universidad de Guanajuato, Apartado Postal 144, 36000 Guanajuato, Mexico
[3] Homer L. Dodge Department of Physics and Astronomy, University of Oklahoma, 440 W Brooks, Rm 100, Norman, OK 73019-2061, USA
e-mail: baron@ou.edu

Received 26 September 2011 / Accepted 29 August 2012

ABSTRACT

Context. Time-dependent, 3D radiation transfer calculations are important for the modeling of a variety of objects, from supernovae and novae to simulations of stellar variability and activity. Furthermore, time-dependent calculations can be used to obtain a 3D radiative equilibrium model structure via relaxation in time.
Aims. We extend our 3D radiative transfer framework to include direct time dependence of the radiation field; i.e., the $\partial I/\partial t$ terms are fully considered in the solution of radiative transfer problems.
Methods. We build on the framework that we have described in previous papers in this series and develop a subvoxel method for the $\partial I/\partial t$ terms.
Results. We test the implementation by comparing the 3D results to our well tested 1D time dependent radiative transfer code in spherical symmetry. A simple 3D test model is also presented.
Conclusions. The 3D time dependent radiative transfer method is now included in our 3D RT framework and in PHOENIX/3D.

Key words. radiative transfer – methods: numerical – supernovae: general

1. Introduction

Supernovae of all types undergo a rather rapid evolution after their explosion. During the free-expansion phase, observations show fast evolving light curves and changing spectral features. In type Ia supernovae, the radioactive decay of ^{56}Ni heats the envelope, causing a peak in the optical light curve about 20 days after the explosion. We have already modeled light curves of SNe Ia with our 1D spherically symmetric model atmosphere code PHOENIX/1D (Jack et al. 2011, 2012; Wang et al. 2012). To compute more accurate model light curves, the hydrodynamical evolution during the free expansion phase needs to be calculated in 3D, including the time dependence of the radiation field. This requires a time-dependent solution of the 3D radiative transfer equation, including the velocity field. In addition, even for the calculation of static and stationary 3D atmospheres, time relaxation to radiative equilibrium is a possible method for modelling 3D atmospheres in energy equilibrium.

In a series of papers presenting a 3D radiative transfer framework (Hauschildt & Baron 2006; Baron & Hauschildt 2007; Hauschildt & Baron 2008, 2009; Baron et al. 2009; Hauschildt & Baron 2010; Seelmann et al. 2010; Hauschildt & Baron 2011), several radiative-transfer test problems for several scenarios were considered, always under the assumption of time independence. In this paper, we extend our framework to include direct time dependence in the solution of radiative transfer by considering the $\partial I/\partial t$ terms in the 3D radiative transfer equation. We used our 1D time-dependent radiative transfer code (Jack et al. 2009) to verify the implementation of time dependence in the 3D RT framework using a number of test calculations that are discussed below.

In the following section, we describe the method we use to solve the time-dependent 3D radiative transfer. The test calculations are presented in Sect. 3 to verify that the implementation functions correctly. In the tests, we include scattering and investigate atmospheres with time-dependent inner boundary conditions.

2. Transfer equation

Chen et al. (2007) present an approach to solve the radiative transfer equation in a flat space time and in the comoving frame. The radiative transfer equation written in terms of an affine parameter ξ, Eq. (18) from Chen et al. (2007), is given by

$$\frac{\partial I_\lambda}{\partial \xi} + \left(\frac{\mathrm{d}\lambda}{\mathrm{d}\xi}\right)\frac{\partial I_\lambda}{\partial \lambda} = -\left(\chi_\lambda \frac{h}{\lambda} + \frac{5}{\lambda}\frac{\mathrm{d}\lambda}{\mathrm{d}\xi}\right) I_\lambda + \eta_\lambda \frac{h}{\lambda}. \tag{1}$$

The description of the $\partial I/\partial\lambda$-discretization for homologous velocity fields has been presented in Baron et al. (2009). We use this discretization method and extend it to include the $\partial I/\partial t$ time dependence in the solution of the radiative transfer.

The time-dependent 3D radiative transfer equation along a characteristic is a modification of Eq. (15) in Baron et al. (2009) and given by

$$\frac{\partial I_{\lambda,t}}{\partial s} + a(s)\frac{\partial}{\partial \lambda}(\lambda I_{\lambda,t}) + a(t)\frac{\partial}{\partial t} I_{\lambda,t} + 4a(s) I_{\lambda,t} = -\chi_\lambda f(s) I_{\lambda,t} + \eta_\lambda f(s), \tag{2}$$

where the factor $a(t)$ is simply

$$a(t) = \frac{1}{c}. \tag{3}$$

The path length along a characteristic is represented by s, the intensity $I_{\lambda,t}$ is a function of the wavelength λ and time t along the characteristic. For the detailed derivation of $f(s)$ and $a(s)$ see Baron et al. (2009).

The fully implicit discretization of Eq. (1) in both wavelength and time is given by

$$\frac{\mathrm{d}I_\lambda}{\mathrm{d}s} + \left[a(s)\frac{\lambda_l}{\lambda_l - \lambda_{l-1}} + \frac{a(t)}{\Delta t} + 4a(s) + \chi_\lambda f(s)\right] I_{\lambda,t}$$

$$= a(s)\frac{\lambda_{l-1} I_{\lambda_{l-1}}}{\lambda_l - \lambda_{l-1}} + \eta_\lambda f(s). \tag{4}$$

Following Baron et al. (2009), this leads to a modification of the effective optical length $\hat{\chi}$, which is now defined by

$$\mathrm{d}\tau = -\left(\chi_\lambda f(s) + 4a(s) + \frac{a(s)\lambda_l}{\lambda_l - \lambda_{l-1}} + \frac{a(t)}{\Delta t}\right)\mathrm{d}s \equiv -\hat{\chi}\mathrm{d}s. \tag{5}$$

Baron et al. (2009) chose an unusual sign convention for $\hat{\chi}$, which we have restored to its conventional choice. The modified source function $\hat{S}_\lambda$ is then defined by

$$\frac{\mathrm{d}I_\lambda}{\mathrm{d}\tau} = I_\lambda + \frac{\chi_\lambda}{\hat{\chi}_\lambda}\left(S_\lambda f(s) + \frac{a(s)}{\chi_\lambda}\frac{\lambda_{l-1} I_{\lambda_{l-1}}}{\lambda_l - \lambda_{l-1}} + \frac{a(t)}{\chi_\lambda}\frac{1}{\Delta t} I_{t-1}\right) \tag{6}$$

$$\equiv I_\lambda - \hat{S}_\lambda. \tag{7}$$

Our restoration of the conventional sign choice for $\hat{\chi}$ alters the sign of Eq. (7) as compared to Eq. (21) of Baron et al. (2009).

This approach of including time dependence in the 3D RT framework is similar to the first discretization method for the 1D case as described in Jack et al. (2009). The discretization of the $\partial I/\partial t$ term modifies the generalized optical depth and adds an additional term to the generalized source function. Please note that the underlying frame differs in the 1D and 3D cases. In the 1D case all momentum quantities are measured by a comoving observer, whereas in the 3D case, only the wavelength is measured by a comoving observer, the momentum angles are measured in the observer's frame. Additionally as noted in Baron et al. (2009), the path length differs in the 3D case and the 1D case. In the 1D case the path length ds_M is that defined by Mihalas (1980), which is not a true distance, whereas our ds is a true distance (Chen et al. 2007). These differences lead to the differences in the equations and in the factor $a(t)$.

3. Test of the implementation

The new extension for time dependence in the solution of the 3D radiative transfer needs to be tested and compared to the results of our time-dependent, 1D spherically symmetric radiative transfer code. We implemented the extension as described above into our MPI parallelized Fortran 95 code described in the previous papers of this series. For all our test calculations, we use a sphere with a gray continuum opacity parameterized by a power law in the continuum optical depth τ_std. We interpolate the τ_std profile from the 1D grid onto the 3D grid using two-point power-law interpolation. The opacity on the 3D grid is then given by $\chi = -\Delta\tau/\Delta r$. We use a 3D spherical coordinate system because the results can be directly compared to our 1D spherically symmetric radiation transport code (Hauschildt 1992). The basic model parameters are

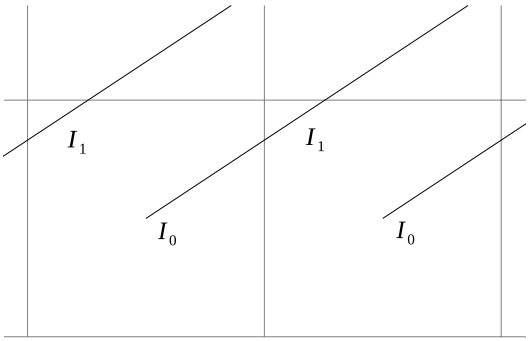

Fig. 1. A sketch of two inner voxels and the characteristics of one particular angle, I_0 and I_1 represent the resulting specific intensities of two characteristics that hit the same voxel.

1. Inner radius of $R_\mathrm{c} = 5 \times 10^{10}$ cm and an outer radius of $R_\mathrm{out} = 1 \times 10^{11}$ cm,
2. Optical depth in the range of $\tau_\mathrm{min} = 10^{-6}$ to $\tau_\mathrm{max} = 5$,
3. Gray temperature structure with $T_\mathrm{model} = 10^4$ K,
4. Outer boundary condition $I_\mathrm{bc}^- = 0$ and diffusive inner boundary condition.
5. We assume an atmosphere in LTE,
6. The atmosphere is static.

For our test calculations, we use a moderately sized 3D grid with $n_r = 2 * 128 + 1$, $n_\phi = 2 * 8 + 1$ and $n_\theta = 2 * 4 + 1$ points along each axis, for a total of $257 * 9 * 17 \approx 2 \times 10^4$ voxels. See Sect. 3.2 for a detailed explanation why this voxel setup is used. In all tests, we use the full characteristic method for the 3D time-dependent RT solution (Hauschildt & Baron 2006). For the solid angle sampling (θ, ϕ), we chose a grid of 64^2 points, which is a reasonable resolution of the spherical coordinate system (Hauschildt & Baron 2009). The time-dependent test calculations are performed with a time step of 10^{-2} s, unless stated otherwise.

3.1. Constant atmosphere

First, we verify the results for the case of a model atmosphere completely constant in time. The results of the time-dependent RT solution should relax in time to be equal to the time-independent solution.

To obtain a numerically accurate solution, it is necessary to follow the time derivative of the intensities for each characteristic individually (hereafter: subvoxel method). Previously, the mean intensity of each voxel is a voxel average of the intensities of all characteristics that go through the particular voxel. The characteristics are started either from the innermost or outermost voxels. One specific inner voxel can be hit by many characteristics of the same angle. Figure 1 shows an example of two innermost voxels with the characteristics of one particular angle. Clearly, the voxels are hit by the characteristic that started at the neighboring voxel. This second hit gives an additional and different result for specific intensity for the particular voxel. The intensities are taken at a point of the characteristic that is closest to the center of the voxel. Previously, the mean of all of these intensities has been used to compute the intensity of this particular voxel, $I_\mathrm{mean} = \sum I_i/n$. Using the average of the intensities

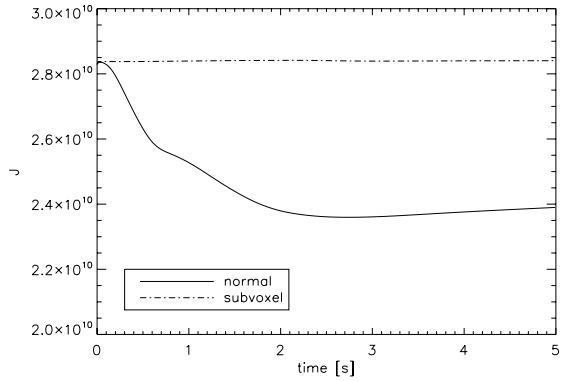

Fig. 2. Demonstration of numerical errors. The solid line shows the mean intensity of one outermost voxel for a method that tracks the intensity time derivatives by averaging over a voxel. The mean intensity is inaccurate and then relaxes to the wrong solution. The dot-dashed line shows the results of the subvoxel method, which is numerically much more accurate.

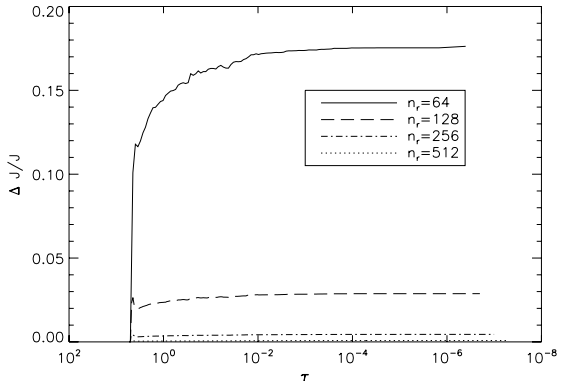

Fig. 3. The error of the mean intensity versus τ for different numbers of radial voxels, n_r, of a model atmosphere with a light bulb at the inner boundary that has been switched on at the start of the calculations.

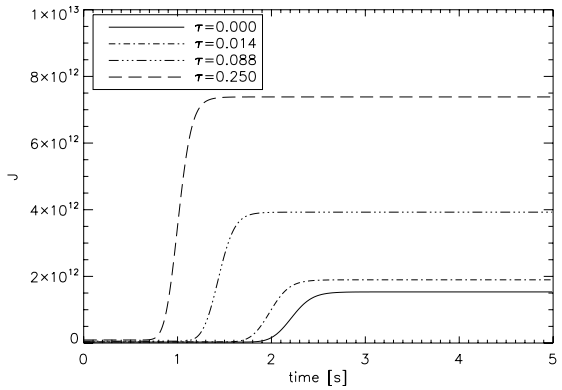

Fig. 4. The mean intensity versus time for voxels at different optical depth, τ, of a model atmosphere with a light bulb at the inner boundary that has been switched on at the start of the calculations.

passing through a given voxel to model the time-dependent intensities results in significant numerical errors, and must therefore be avoided. The explanation is that the difference between the averaged intensity and the individual intensity of a characteristic adds an additional term to the source function. This is completely analogous to the correct treatment of the wavelength derivative in Lagrange frame radiative transfer calculations. In the subvoxel method, all the intensities are saved and used for the individual characteristics. The subvoxel method increases the storage requirements, but this is addressed with a solid-angle domain decomposition method so that the storage requirements per process remain limited.

Figure 2 shows the mean intensity J of one outermost voxel as function of time. Although the atmosphere structure is time independent, the mean intensity changes in time and relaxes to a wrong solution if a numerical method with voxel-averaged time derivatives is used. The errors are on the order of 15% compared to the time independent solution. The mean intensity obtained with the subvoxel method is constant in time and identical to the 3D time-independent solution. Thus, we only use the subvoxel method.

3.2. Perturbations

To see direct effects of the time dependence in the solution of 3D RT problems, we use a setup with a time variable inner boundary condition of our test model atmosphere. These perturbations will then propagate through the model atmosphere by radiation transport in time and finally emerge at the surface of the sphere. We perform the same calculations with our 1D spherically symmetric code and compare the results to the time-dependent 3D spherically symmetric RT.

For all our perturbation tests, we place a "light bulb" at the center of the model atmosphere. This light bulb is just a central source of light inside of the atmosphere. For the first test, the light bulb is switched on and set to (arbitrarily) radiate at 10^5 times the initial inner boundary intensity. The calculations then track the changes in the 3D (or 1D) radiation field in time.

First, we compare the resulting mean intensity J of the time-independent solution to the relaxed time-dependent solution, which should be identical. In Fig. 3, the error in the resulting mean intensity, $(J_{\rm dep} - J_{\rm indep})/J_{\rm indep}$, is shown after the atmosphere has relaxed to the new inner boundary condition. Clearly the error is lower when a higher resolution in the radial voxels n_r is used. This is equivalent to a higher resolution in the optical depth τ. With $n_r = 2{*}512{+}1$, the error is reduced to below 0.1%. Therefore, we use a large number of voxels for the radial coordinate. Changing the number of voxels for the other coordinates does not affect the resulting mean intensity in this spherically symmetric test.

The test model run with $n_r = 2{*}512{+}1$ has been computed on a supercomputer, where we used 2,048 CPUs. The computation time for this calculation with 500 time steps is about two hours. The storage requirement is about 11 GB and is mainly required for saving all the intensities at a time step. By using a solid-angle domain decomposition, the memory per process required is kept small. For true 3D models the resolution in both the other coordinates n_θ and n_ϕ likely also needs to be significantly higher. These calculations are beyond the scope of this work. In future work, we will test our code with a higher resolution in n_θ and n_ϕ and apply realistic 3D models to further test our time-dependent extension.

In Fig. 4, the mean intensity at different layers (radii in the 3D atmosphere) is shown versus time. The additional radiation of the inner light bulb needs time to propagate through the

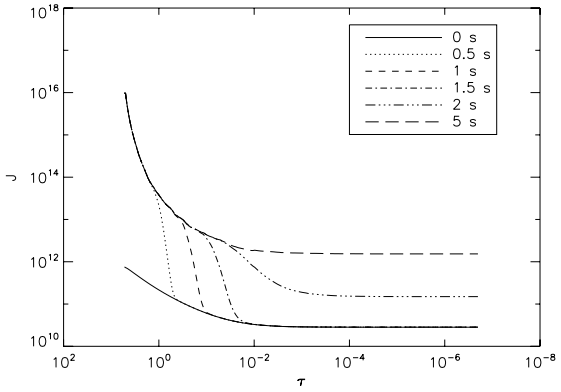

Fig. 5. Snapshots of the mean intensity of the atmosphere at different points instants in time.

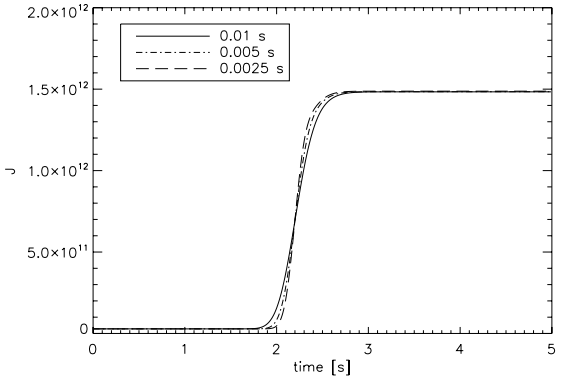

Fig. 6. Mean intensity of the outermost radius versus time computed with three different time step choices.

atmosphere. One simple test is to calculate the time the radiation would need at the speed of light to move from the inner to the outermost layer. For the distance of $R_{\rm out} - R_{\rm c} \approx 5 \times 10^{10}$ cm, the radiation needs about ≈1.7 s, which is consistent with the result of the 3D radiative transfer as seen in Fig. 4. Figure 5 illustrates the propagation of the radiation "wave" throughout the atmosphere. Here, the mean intensity is plotted against radius for a few snapshots at different times.

Another test is to check if the time relaxed result of the time-dependent 3D RT depends on the size of the time steps. The results of this test are shown in Fig. 6, the resulting mean intensities of the outermost layer are plotted for the test case with the light bulb inside computed with three different time step sizes. The change in the mean intensity emerges at the same point in time for all sizes of the time step. However, the shape of the change is different. The explanation is that with a shorter time step, the step function that moves through the atmosphere is better resolved in time.

Another important check is to compare the results of the time-dependent 3D radiative transfer to the results of our 1D spherically symmetric radiative transfer results. The mean intensity of the outermost layer of the 3D and the 1D RT time-dependent calculation is shown in Fig. 7. The test case simulates a light bulb at the inner boundary that has been switched on. The change in the mean intensity emerges at the same point in time, and the final mean intensity is the same.

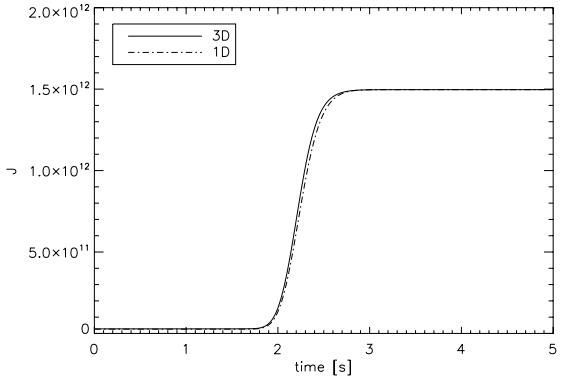

Fig. 7. The mean intensity of the outermost radius versus time computed with 3D and 1D time-dependent radiative transfer.

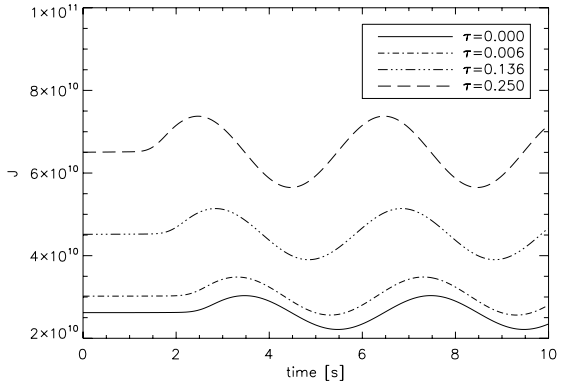

Fig. 8. The mean intensity at different optical depths, τ, with a sinusoidally varying light bulb at the center of the sphere.

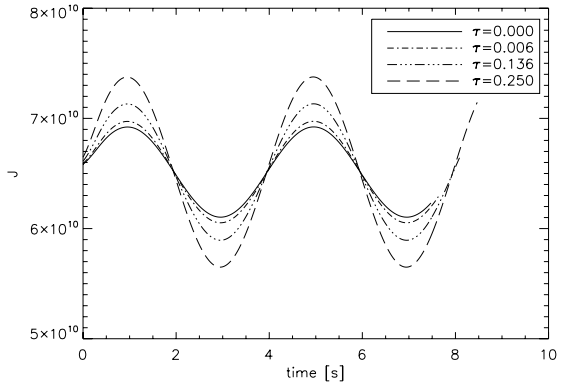

Fig. 9. The mean intensity at different optical depths, τ, corrected for the radial time delay. The mean intensities are shifted arbitrarily to better illustrate the smoothing.

The next interesting test case is to place a sinusoidally varying light bulb at the center of the sphere and to follow the radiation field in time. This leads to an atmosphere where the mean intensity should vary sinusoidally everywhere. For this test we used a sine wave with a full period of 4 s. In Fig. 8, the resulting mean intensities for different radii are plotted versus time. It takes about 2 s before the perturbation has moved outwards to

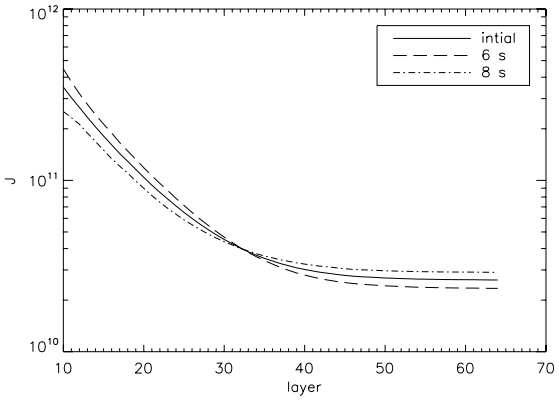

Fig. 10. Snapshot of the mean intensity at different phases of the sine wave.

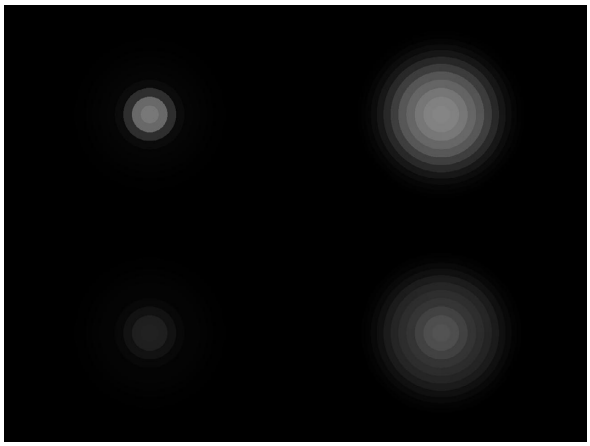

Fig. 11. Snapshots of the sphere looking down the pole of the coordinate system. In the *right panel* side no scattering is considered, while in the *left panel* the results with scattering are shown. The *upper row* shows a snapshot at time $t = 0$ s, and the *lower row* is at the time of minimum of the sine wave.

affect the outermost layers. The sinusoidally varying mean intensity is then observed in every layer. The phase shift between the inner and outer radii is approximately π, which is about 2 s in time. In Fig. 9, we corrected the resulting sine waves at each optical depth for the radial time delay. We also shifted the mean intensity arbitrarily to directly overlay the sine waves. With this correction for the travel time of the light, there is no additional phase shift. The smoothing of the sine wave as it moves through the atmosphere is also clearly illustrated. A snapshot of the mean intensity at different moments in time is shown in Fig. 10. The phase difference between the two snapshots is π.

3.3. Continuum scattering

In this section, we investigate the effects of continuum scattering on the solution of the 3D time dependent radiative transfer. For that, we use a model atmosphere with a low optical depth, so that we can more easily "see" the light bulb at the center. Therefore, we chose for this test: $\tau_{\rm min} = 10^{-2}$ and $\tau_{\rm max} = 5$.

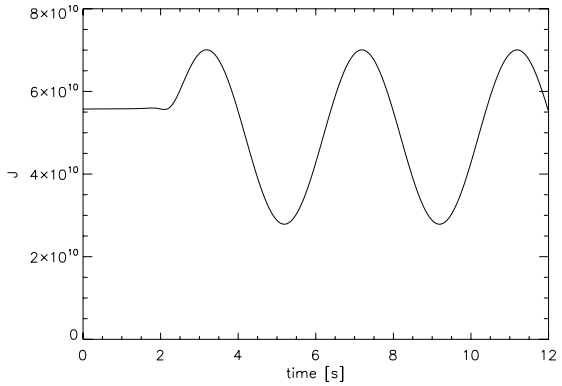

Fig. 12. The mean intensity at one outer voxel as a function of time for a sinusoidally varying light bulb at the center of the sphere.

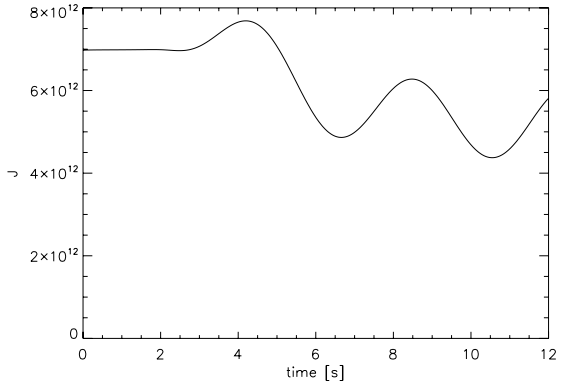

Fig. 13. Illustration of the time-dependent mean intensity at the outer boundary for a model with a sinusoidally varying light bulb at the center. In this solution, scattering is considered with $\epsilon = 10^{-4}$.

We solved the radiative transfer problem for this model atmosphere both without scattering and for a scattering dominated atmosphere with $\epsilon = 10^{-4}$. A visualization of both spheres is shown in Fig. 11. It shows the image for an observer looking down one pole of the coordinate system. The lefthand panel displays the solution for an atmosphere where no scattering is considered. The outer voxels are dark and not visible to the observer, and the sphere shows strong limb darkening. The righthand panel shows the results with scattering included in the solution of the radiative transfer. The outer voxels of the disk are significantly brighter as the radiation from the light bulb is scattered towards the observer, thus the model showing less limb darkening.

We now let the light bulb inside of the sphere vary sinusoidally. The resulting mean intensity versus time is shown in Fig. 12 for one outermost voxel. The mean intensity is varying sinusoidally, as expected. It takes about 2 s for the radiation to travel from the light bulb to the surface. The resulting mean intensity for the solution of radiative transfer considering scattering with $\epsilon = 10^{-4}$ is shown in Fig. 13. Again a sinusoidal variation in intensity is seen at the surface, but it has a smaller amplitude than without scattering. In the presence of scattering, it also takes more time for the radiation to move through the atmosphere. A visualization is shown at Fig. 11. The lower row shows the apparent disk at a minimum of the sine. For the atmosphere

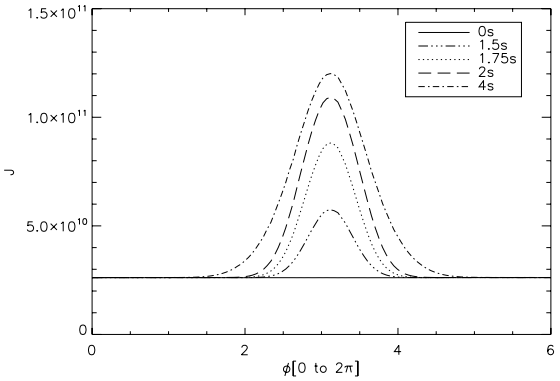

Fig. 14. The mean intensity, J, at a ring of outermost voxels ($\theta = 0$) at different times for a test case with an off-center perturbation.

where scattering is included, the intensity of the voxels at the outer disk also varies in time.

3.4. A 3D test model

All comparisons with our well-tested 1D spherically symmetric code show that the results of the test models for our implemented time-dependent 3D radiative transfer framework are in good agreement. We now want to verify that our 3D time-dependent extension also works for test cases of a fully 3D test model atmosphere. Unfortunately, we cannot compare these results to our 1D code, but we can discuss whether the results are reasonable.

We again use a spherically symmetric setup in the opacity and radius for the test model atmosphere. For the optical depth, we use a range of $\tau_{\rm min} = 10^{-6}$ to $\tau_{\rm max} = 5$. For the inner radius we chose $R_{\rm c} = 5 \times 10^{10}$ cm and for the outer radius $R_{\rm out} = 1 \times 10^{11}$ cm. In this 3D test model, no scattering is considered ($\epsilon = 1$).

Since we now want to examine 3D effects, we had to increase our angular resolution. For the following test calculation, we used a setup of $n_r = 2 * 64 + 1$, $n_\theta = 2 * 32 + 1$, and $n_\phi = 2 * 64 + 1$ voxels. We now place a Gaussian perturbation of the temperature and, therefore, the local source function at an off-center position in the sphere. The center of the Gaussian has a value for the source function 50 times higher than the value of the source function at the center of the sphere and is located 20 voxels away from the center at a radius of 5.69×10^{10}cm. The source function is, therefore, given by

$$S = S(r) + 50S(r) \exp\left\{-\left[(x - x_0)^2 + (y - y_0)^2 + (z - z_0)^2\right]/40\right\}, \quad (8)$$

with a width for the Gaussian perturbation of $\sigma^2 = 40$. For the first time step, the time-independent model without the perturbation is solved. After the first time step, the perturbation is introduced and remains constant for the rest of the calculation. This means that the resulting mean intensities J will be constant in time after the relaxation process. In Fig. 14, the mean intensity J of one ring of the outermost voxels around the sphere is shown for different times. The perturbation is located inside the sphere at $\phi = \pi$ and $\theta = 0$. The mean intensity J at the initial time $t = 0$ s is also the result for the non-perturbed model. As expected, the voxels closer to the perturbation have a higher mean intensity J. The intensity then decreases, the farther away the voxel is from the perturbation. On the other side of the sphere, there is no effect on the mean intensities of the outer voxels. It is also clear that it takes more time for the radiation to reach voxels that are farther away from the perturbation.

The calculation for this 3D test model atmosphere run needed about 7000 CPUh. This shows how demanding a fully 3D time-dependent atmosphere computation is, especially for more realistic models in the future. So far, we have only been able to test our time-dependent extension with a gray atmosphere. For realistic models, we need to solve the non-gray radiative transfer equation. For a type Ia supernova model atmosphere in LTE, on the order of 10 000 wavelength points are needed in the computations. The computation time scales roughly linearly with the number of wavelength points.

4. Conclusion

We have implemented direct time dependence into our 3D radiative transfer framework. For best numerical accuracy we used a subvoxel method for the discretized time derivative. We have also shown that it is important to use high resolution in the radial direction. To verify the code, we have calculated the solution for a number of simple parameterized 1D test cases. The inner boundary condition was made time dependent to simulate radiation waves traveling through an atmosphere. All these perturbations move through the atmosphere as expected. We also computed a test case with a sinusoidally varying inner light bulbs. We compared the results of the 3D time-dependent radiative transfer to the results of our well tested 1D spherically symmetric radiative transfer program and found excellent agreement. In a scattering dominated atmosphere, it takes more time for the radiation to move through an atmosphere. We also calculated a fully 3D test case. All tests indicate that the new implementations work as intended.

Acknowledgements. This work was supported in part by the Deutsche Forschungsgemeinschaft (DFG) via the SFB 676, NSF grant AST-0707704, and US DOE Grant DE-FG02-07ER41517. This research used resources of the National Energy Research Scientific Computing Center (NERSC), which is supported by the Office of Science of the US Department of Energy under Contract No. DE-AC02-05CH11231. The computations were carried out at the Höchstleistungs Rechenzentrum Nord (HLRN). We thank all these institutions for generous allocations of computer time. We also thank the anonymous referee for improving the presentation of this work.

References

Baron, E., & Hauschildt, P. H. 2007, A&A, 468, 255
Baron, E., Hauschildt, P. H., & Chen, B. 2009, A&A, 498, 987
Chen, B., Kantowski, R., Baron, E., Knop, S., & Hauschildt, P. H. 2007, MNRAS, 380, 104
Hauschildt, P. H. 1992, JQSRT, 47, 433
Hauschildt, P. H., & Baron, E. 2006, A&A, 451, 273
Hauschildt, P. H., & Baron, E. 2008, A&A, 490, 873
Hauschildt, P. H., & Baron, E. 2009, A&A, 498, 981
Hauschildt, P. H., & Baron, E. 2010, A&A, 509, A36
Hauschildt, P. H., & Baron, E. 2011, A&A, 533, A127
Jack, D., Hauschildt, P. H., & Baron, E. 2009, A&A, 502, 1043
Jack, D., Hauschildt, P. H., & Baron, E. 2011, A&A, 528, A141
Jack, D., Hauschildt, P. H., & Baron, E. 2012, A&A, 538, A132
Mihalas, D. 1980, ApJ, 237, 574
Seelmann, A. M., Hauschildt, P. H., & Baron, E. 2010, A&A, 522, A102
Wang, X., Wang, L., Filippenko, A. V., et al. 2012, ApJ, 749, 126

A&A 548, A67 (2012)
DOI: 10.1051/0004-6361/201219343

Astronomy & Astrophysics

A 3D radiative transfer framework

X. Arbitrary velocity fields in the comoving frame

E. Baron[1,2,3,4], P. H. Hauschildt[1], B. Chen[2], and S. Knop[1]

[1] Hamburger Sternwarte, Gojenbergsweg 112, 21029 Hamburg, Germany
e-mail: [sknop;yeti]@hs.uni-hamburg.de
[2] Homer L. Dodge Department of Physics and Astronomy, University of Oklahoma, 440 W Brooks, Rm 100, Norman, OK 73019, USA
e-mail: [baron;bchen]@ou.edu
[3] Computational Research Division, Lawrence Berkeley National Laboratory, MS 50F-1650, 1 Cyclotron Rd, Berkeley, CA 94720, USA
e-mail: eabaron@lbl.gov
[4] Physics Department, Univ. of California, Berkeley, CA 94720, USA

Received 4 April 2012 / Accepted 20 October 2012

ABSTRACT

Aims. General 3D astrophysical atmospheres will have random velocity fields. We seek to combine the methods we have developed for solving the 1D problem with arbitrary flows to those that we have developed for solving the fully 3D relativistic radiative transfer problem for monotonic flows.
Methods. The methods developed for 3D atmospheres with monotonic flows, solving the fully relativistic problem along curves defined by an affine parameter, are very flexible and can be extended to the case of arbitrary velocity fields in 3D. Simultaneously, the techniques we developed for treating the 1D problem with arbitrary velocity fields are easily adapted to the 3D problem.
Results. The algorithm we present can be used to solve 3D radiative transfer problems that include arbitrary wavelength couplings. We use a quasi-analytic formal solution of the radiative transfer equation that significantly improves the overall computation speed. We show that the approximate lambda operator developed in previous work gives good convergence, even neglecting wavelength coupling. Ng acceleration also gives good results. We present tests that are of similar resolution to what has been presented using Monte-Carlo techniques, thus our methods will be applicable to problems outside of our test setup. Additional domain decomposition parallelization strategies will be explored in future work.

Key words. radiative transfer

1. Introduction

In a series of papers (Hauschildt & Baron 2006, 2008, 2009, 2010; Baron & Hauschildt 2007; Baron et al. 2009b; Seelmann et al. 2010) we have developed a general framework for solving 3D radiative transfer problems in Cartesian, cylindrical, and spherical coordinates for both static and monotonic velocity fields in the comoving frame. We have also developed an Eulerian code for velocities $\lesssim$1000 km s^{-1} (Seelmann et al. 2010). The neglect of relativistic effects and resolution constraints limits the applicability of the Eulerian approach to $v/c \lesssim 0.01$. Our affine method for solving the fully relativistic transfer equation is exact to all orders in v/c (Chen et al. 2007; Baron et al. 2009a). In a parallel series of papers we have introduced methods for solving the fully relativistic transfer equation in 1D spherical coordinates with arbitrary velocity fields (Baron & Hauschildt 2004; Knop et al. 2009a,b).

2. Basic formalism

Using the general formalism developed in Chen et al. (2007) we can derive the transfer equation in flat spacetime with arbitrary flows. We choose to work in spherical coordinates without loss of generality.

The photon's four-momentum can be written

$$p^a \equiv \frac{\mathrm{d}x^a}{\mathrm{d}\xi} = \frac{h}{\lambda_\infty}(1, \hat{\boldsymbol{n}}), \tag{1}$$

where h is Planck's constant, ξ is the affine parameter, λ_∞ is the rest frame wavelength, and $\hat{\boldsymbol{n}}$ is the 3D direction of the photon as seen by a distant, stationary, observer. The four-velocity of the comoving observer in an arbitrary flow can be written

$$u^a = \gamma(\boldsymbol{r}, t)[1, \boldsymbol{\beta}(\boldsymbol{r}, t)], \tag{2}$$

and the comoving wavelength λ can be obtained using

$$\frac{h}{\lambda} = -(u \cdot p). \tag{3}$$

Here, $\boldsymbol{\beta} = \boldsymbol{v}/c$, and $\gamma = (1 - \beta^2)^{-1/2}$, are the usual quantities of special relativity. The 3D geodesic in the flat spacetime can be parametrized as

$$\boldsymbol{r}(s) = \boldsymbol{r}_0 + \hat{\boldsymbol{n}}\, s, \tag{4}$$

where $\boldsymbol{r}_0$ is the starting point of the characteristics, and s is the rest frame physical distance related to the affine parameter ξ by

$$s \equiv \frac{h}{\lambda_\infty}\xi. \tag{5}$$

The radiative transfer equation can be written in terms of the affine parameter ξ as (see Eq. (10) of Chen et al. 2007):

$$\left.\frac{\partial I_\lambda}{\partial \xi}\right|_\lambda + \frac{\mathrm{d}\lambda}{\mathrm{d}\xi}\frac{\partial I_\lambda}{\partial \lambda} = -\left(\chi_\lambda \frac{h}{\lambda} + \frac{5}{\lambda}\frac{\mathrm{d}\lambda}{\mathrm{d}\xi}\right) I_\lambda + \eta_\lambda \frac{h}{\lambda}, \tag{6}$$

where $I_\lambda(\boldsymbol{r}, t; \hat{\boldsymbol{n}})$ is the specific intensity measured by a comoving observer (note that $I_\lambda \lambda^5$ is observer-independent) at the (global) rest frame space-time point (r, t), toward the rest frame direction $\hat{\boldsymbol{n}}$, and at the comoving wavelength λ. When expressing the 7D phase-space dependence of the comoving specific intensity, the only comoving variable we used was the wavelength λ, in particular, we did not use angles measured by a comoving observer to specify the direction of the photons. The advantages for this at first sight odd phase-space configuration have been explained in detail in Chen et al. (2007), and we applied this technique in Baron et al. (2009a).

We can rewrite Eq. (6) as

$$\frac{\mathrm{d}(ct)}{\mathrm{d}\xi}\frac{1}{c}\left.\frac{\partial I_\lambda}{\partial t}\right|_\lambda + \frac{\mathrm{d}\boldsymbol{r}}{\mathrm{d}\xi}\cdot\nabla I_\lambda + \frac{\mathrm{d}\lambda}{\mathrm{d}\xi}\frac{\partial I_\lambda}{\partial \lambda} = -\left(\chi_\lambda \frac{h}{\lambda} + \frac{5}{\lambda}\frac{\mathrm{d}\lambda}{\mathrm{d}\xi}\right) I_\lambda + \eta_\lambda \frac{h}{\lambda}, \tag{7}$$

or equivalently

$$\frac{\mathrm{d}(ct)}{\mathrm{d}\xi}\frac{1}{c}\left.\frac{\partial I_\lambda}{\partial t}\right|_\lambda + \frac{\mathrm{d}s}{\mathrm{d}\xi}\frac{\mathrm{d}\boldsymbol{r}}{\mathrm{d}s}\cdot\nabla I_\lambda + \frac{\mathrm{d}s}{\mathrm{d}\xi}\frac{\mathrm{d}\lambda}{\mathrm{d}s}\frac{\partial I_\lambda}{\partial \lambda} = -\left(\chi_\lambda \frac{h}{\lambda} + \frac{5}{\lambda}\frac{\mathrm{d}s}{\mathrm{d}\xi}\frac{\mathrm{d}\lambda}{\mathrm{d}s}\right) I_\lambda + \eta_\lambda \frac{h}{\lambda}. \tag{8}$$

Then using the definition of s from Eq. (5) and the fact that

$$\frac{\mathrm{d}(ct)}{\mathrm{d}\xi} = cp^t = \frac{h}{\lambda_\infty}, \tag{9}$$

we find

$$\frac{1}{c}\left.\frac{\partial I_\lambda}{\partial t}\right|_\lambda + \left.\frac{\partial I_\lambda}{\partial s}\right|_\lambda + \frac{\mathrm{d}\lambda}{\mathrm{d}s}\frac{\partial I_\lambda}{\partial \lambda} = -\left(\chi_\lambda \frac{\lambda_\infty}{\lambda} + \frac{5}{\lambda}\frac{\mathrm{d}\lambda}{\mathrm{d}s}\right) I_\lambda + \eta_\lambda \frac{\lambda_\infty}{\lambda}. \tag{10}$$

Equation (10) can be put into our standard form:

$$\frac{1}{c}\left.\frac{\partial I_\lambda}{\partial t}\right|_\lambda + \frac{\partial I_\lambda}{\partial s} + a(s)\frac{\partial}{\partial \lambda}(\lambda I_\lambda) + 4a(s) I_\lambda = -\chi_\lambda f(s) I_\lambda + \eta_\lambda f(s), \tag{11}$$

where

$$f(s) \equiv \frac{\lambda_\infty}{\lambda} = \gamma(\boldsymbol{r}, t)[1 - \hat{\boldsymbol{n}}\cdot\boldsymbol{\beta}(\boldsymbol{r}, t)] \tag{12}$$

is simply the Doppler factor, and

$$a(s) \equiv \frac{1}{\lambda}\frac{\mathrm{d}\lambda}{\mathrm{d}s}. \tag{13}$$

Using Eqs. (4) and (12), $a(s)$ is found to be

$$a(s) = \frac{1}{1 - \hat{\boldsymbol{n}}\cdot\boldsymbol{\beta}}\left[\frac{\mathrm{d}}{\mathrm{d}s}(\hat{\boldsymbol{n}}\cdot\boldsymbol{\beta}) - \gamma^2\beta(1 - \hat{\boldsymbol{n}}\cdot\boldsymbol{\beta})\frac{\mathrm{d}\beta}{\mathrm{d}s}\right], \tag{14}$$

where β is the magnitude of $\boldsymbol{\beta}$, and

$$\frac{\mathrm{d}}{\mathrm{d}s} = \frac{1}{c}\frac{\partial}{\partial t} + \hat{\boldsymbol{n}}\cdot\nabla = \frac{1}{c}\frac{\partial}{\partial t} + \frac{\partial}{\partial s}. \tag{15}$$

When we numerically integrate the radiation transfer equation, $a(s)$ can be approximated as

$$a(s) \approx \frac{\delta(\hat{\boldsymbol{n}}\cdot\boldsymbol{\beta}) - \gamma^2\beta(1 - \hat{\boldsymbol{n}}\cdot\boldsymbol{\beta})\,\delta\beta}{\delta s(1 - \hat{\boldsymbol{n}}\cdot\boldsymbol{\beta})}, \tag{16}$$

where δs is the differential step size (physical distance) along the characteristics, $\delta(\hat{\boldsymbol{n}}\cdot\boldsymbol{\beta})$ and $\delta\beta$ are the changes of $\hat{\boldsymbol{n}}\cdot\boldsymbol{\beta}$ and β, respectively, when we move one step forward, which includes the changes induced by both time and spatial advances, for instance

$$\delta\beta = \beta(s_{i+1}, t_{i+1}) - \beta(s_i, t_i). \tag{17}$$

Since few numerical schemes will be able to provide the fully implicit derivative, $\delta\beta$, will often be obtained for example by the backward difference

$$\delta\beta = (\beta(s_i, t_i) - \beta(s_i, t_{i-1}) + (\beta(s_i, t_i) - \beta(s_{i-1}, t_i). \tag{18}$$

In the stationary case, both β and $f(s)$ are independent of time and specializing Eqs. (4) and (12) to that case, $a(s)$ becomes

$$\begin{aligned} a(s) &= \frac{\hat{\boldsymbol{n}}\cdot\nabla(\hat{\boldsymbol{n}}\cdot\boldsymbol{\beta}) - \gamma^2\beta(1 - \hat{\boldsymbol{n}}\cdot\boldsymbol{\beta})(\hat{\boldsymbol{n}}\cdot\nabla\beta)}{1 - \hat{\boldsymbol{n}}\cdot\boldsymbol{\beta}} \\ &= -(\hat{\boldsymbol{n}}\cdot\nabla)\ln(1 - \hat{\boldsymbol{n}}\cdot\boldsymbol{\beta}) - \gamma^2\beta(\hat{\boldsymbol{n}}\cdot\nabla\beta), \end{aligned} \tag{19}$$

where we have used the fact that along the characteristics, $\mathrm{d}/\mathrm{d}s$ no longer contains the time derivative and is thus the directional derivative operator, that is, $\mathrm{d}/\mathrm{d}s = \hat{\boldsymbol{n}}\cdot\nabla$. We recall that in the flat spacetime that we are considering, our characteristics are straight lines for all velocity flows.

In terms of its spherical components, $\boldsymbol{\beta}$ can be written

$$\boldsymbol{\beta} = \beta_r\hat{\boldsymbol{e}}_r + \beta_\theta\hat{\boldsymbol{e}}_\theta + \beta_\phi\hat{\boldsymbol{e}}_\phi, \tag{20}$$

where $\hat{\boldsymbol{e}}_r, \hat{\boldsymbol{e}}_\theta, \hat{\boldsymbol{e}}_\phi$ are the spherical orthonormal basis vectors at point $\boldsymbol{r}(r, \theta, \phi)$, i.e.

$$\begin{aligned} \hat{\boldsymbol{e}}_r &= (\sin\theta\cos\phi, \sin\theta\sin\phi, \cos\theta), \\ \hat{\boldsymbol{e}}_\theta &= (\cos\theta\cos\phi, \cos\theta\sin\phi, -\sin\theta), \\ \hat{\boldsymbol{e}}_\phi &= (-\sin\phi, \cos\phi, 0), \end{aligned} \tag{21}$$

and consequently the $\hat{\boldsymbol{n}}\cdot\boldsymbol{\beta}$ in Eq. (16) can be calculated using

$$\begin{aligned} \hat{\boldsymbol{n}}\cdot\boldsymbol{\beta} &= \beta_r\hat{\boldsymbol{n}}\cdot\hat{\boldsymbol{e}}_r + \beta_\theta\hat{\boldsymbol{n}}\cdot\hat{\boldsymbol{e}}_\theta + \beta_\phi\hat{\boldsymbol{n}}\cdot\hat{\boldsymbol{e}}_\phi \\ &\equiv \beta_r n_r + \beta_\theta n_\theta + \beta_\phi n_\phi \end{aligned} \tag{22}$$

(note that along the characteristics, $\hat{\boldsymbol{n}}$ has constant Cartesian components, n_x, n_y, n_z, but changing spherical components, n_r, n_θ, n_ϕ). Writing $\hat{\boldsymbol{n}} = (n_x, n_y, n_z)$, the spherical components n_r, n_θ, n_ϕ can be easily computed using Eq. (21).

2.1. Comparison with Mihalas

At first glance, comparing Eq. (11) with Eq. (2.12) of Mihalas (1980) something seems amiss. Like Mihalas (1980), we work in the frame where spatial coordinates and clocks are measured by an observer at rest. However, Mihalas' time derivative contains a Doppler factor, whereas ours does not. Also, our terms on the right-hand side contain Doppler factors, $f(s)$, whereas those of Mihalas do not. The discrepency has been noted in passing by Chen et al. (2007) and arises because our s is a true distance

measured in the observer's frame, whereas that of Mihalas, $s_{\rm M}$, contains an extra Doppler factor:

$$\mathrm{d}s_{\rm M} = \frac{\lambda_\infty}{\lambda}\mathrm{d}s = f(s)\mathrm{d}s$$

(note that $f(s)$ is not a constant along the characteristics, and therefore $s_{\rm M}$ is not related to the physical distance s by a simple affine transformation). Thus, we can transform from s to $s_{\rm M}$ in Eq. (10) to find

$$\frac{\lambda}{\lambda_\infty}\frac{1}{c}\frac{\partial I_\lambda}{\partial t}\bigg|_\lambda + \frac{\partial I_\lambda}{\partial s_{\rm M}}\bigg|_\lambda + \frac{\mathrm{d}\lambda}{\mathrm{d}s_{\rm M}}\frac{\partial I_\lambda}{\partial\lambda} = -\left(\chi_\lambda + \frac{5}{\lambda}\frac{\mathrm{d}\lambda}{\mathrm{d}s_{\rm M}}\right)I_\lambda + \eta_\lambda, \quad (23)$$

which is very similar to the equation of Mihalas, except that the coefficient multiplying the time derivative term is the inverse Doppler factor $f(s)^{-1}$, since we are working with I_λ instead of I_ν, as did Mihalas. Jack et al. (2009) accidentally forgot to convert the time derivative from I_ν to I_λ and thus their Eqs. (24), (25) have a coefficient of the time derivative with the Doppler factor in the numerator, rather than in the denominator. Thus, the time derivative terms in their Eqs. (24), (25) should be multiplied by $f(s)^{-2}$ to give the correct equations.

2.2. Nonmonotonic flows

We are now in a position to tie together the work of Baron & Hauschildt (2004), Knop et al. (2009a) and Baron et al. (2009b). The formal solution in the monotonic case is an initial value problem in wavelength, but in the arbitrary flow case *both* spatial coordinates and wavelengths are *fully* coupled. This poses a significant memory cost, since the matrix obtained by finite-differencing the equations now contains every wavelength and not just the spatial points along the characteristic. The computational cost is surprisingly low because the linear system can be solved using the semi-analytic method of Knop et al. (2009a). While the framework that was given in Baron & Hauschildt (2004) and Baron et al. (2009b) was formulated for just one wavelength discretization, we included here the fully implicit discretization developed in Hauschildt & Baron (2004). Furthermore, we used the new formal solution that avoids negative generalized opacities (Knop et al. 2009b).

The stationary equation of radiative transfer in its characteristic form for the specific intensity I along a path s reads

$$\frac{\mathrm{d}I_l}{\mathrm{d}s} = f(s)\eta_l - f(s)\chi_l I_l - 4a_l I_l - a_l\frac{\partial(\lambda I_l)}{\partial\lambda}, \quad (24)$$

where η is the emissivity, χ the opacity, and the subscript l indicates dependence on wavelength. The $\frac{\partial}{\partial\lambda}$-term is the coupling term between the wavelengths and depends on the structure of the atmosphere and on the mechanism of the coupling (Mihalas 1980).

The wavelength derivative can be discretized in two ways as described in Hauschildt & Baron (2004). The different discretizations can be mixed via a Crank-Nicholson-like scheme with a mixing parameter $\xi \in [0, 1]$. The wavelength discretized equation of radiative transfer can then be written as

$$\begin{aligned}\frac{\mathrm{d}I_l}{\mathrm{d}s} &= f(s)\eta_l - f(s)\chi_l I_l - a_l\left(4 + \xi\, p_l^{\vert}\right)I_l \\ &\quad -\xi\, a_l\left(p_l^- I_{l-1} + p_l^+ I_{l+1}\right) \\ &\quad -[1-\xi]\, a_l\left(p_l^- I_{l-1} + p_l^{\vert} I_l + p_l^+ I_{l+1}\right), \end{aligned} \quad (25)$$

where the $p_l^\bullet$ coefficients in an ordered wavelength grid $\lambda_{l-1} < \lambda_l < \lambda_{l+1}$ are defined as

$$\left.\begin{aligned} p_l^- &= -\frac{\lambda_{l-1}}{\lambda_l - \lambda_{l-1}} \\ p_l^{\vert} &= \frac{\lambda_l}{\lambda_l - \lambda_{l-1}} \\ p_l^+ &= 0 \end{aligned}\right\} \quad \text{for} \quad a_{\lambda_l} \geq 0 \quad (26)$$

$$\left.\begin{aligned} p_l^- &= 0 \\ p_l^{\vert} &= \frac{\lambda_l}{\lambda_l - \lambda_{l+1}} \\ p_l^+ &= -\frac{\lambda_{l+1}}{\lambda_l - \lambda_{l+1}} \end{aligned}\right\} \quad \text{for} \quad a_{\lambda_l} < 0. \quad (27)$$

The dependence on the sign of a_λ is introduced to define local upwind schemes (see Baron & Hauschildt 2004).

After introducing a generalized opacity (see Knop et al. 2009a,b)

$$\hat{\chi}_l = f(s)\chi_l + \xi\, a_l p_l^{\vert}, \quad (28)$$

defining the source functions

$$S_l = \frac{\eta_l}{\chi_l} \quad (29)$$

$$\hat{S}_l = \frac{\chi_l}{\hat{\chi}_l}\left\{f(s)S_l - \xi\,\frac{a_l}{\chi_l}\left(p_l^- I_{l-1} + p_l^+ I_{l+1}\right)\right\} \quad (30)$$

$$\tilde{S}_l = -\frac{a_l}{\hat{\chi}_l}\left\{[1-\xi]\,\left(p_l^- I_{l-1} + p_l^+ I_{l+1}\right) + \left(4 + [1-\xi]\,p_l^{\vert}\right)I_l\right\}, \quad (31)$$

a formal solution of the radiative transfer problem can be formulated. We used a full characteristic method throughout the atmosphere. The spatial position on a characteristic is then discretized on a spatial grid. In the following a pair of subscript indices will mark the position in the spatial grid and in the wavelength grid. Commonly the spatial grid is mapped locally onto an optical depth grid via the relation $\mathrm{d}\tau_l = \hat{\chi}_l \mathrm{d}s$. The formal solution of the radiative transfer Eq. (25) between two points s_{i-1} and s_i on a spatial grid along the photon path can be written in terms of the optical depth as follows:

$$I_{i,l} = I_{i-1,l}\mathrm{e}^{-\Delta\tau} + \delta\hat{I}_{i,l} + \delta\tilde{I}_{i,l} \quad (32)$$

$$\delta\hat{I}_{i,l} = \int_{\tau_{i-1}}^{\tau_i}\hat{S}_l\mathrm{e}^{\tau-\tau_i}\mathrm{d}\tau = \alpha_{i,l}\hat{S}_{i-1,l} + \beta_{i,l}\hat{S}_{i,l} + \gamma_{i,l}\hat{S}_{i+1,l} \quad (33)$$

$$\delta\tilde{I}_{i,l} = \int_{\tau_{i-1}}^{\tau_i}\tilde{S}_l\mathrm{e}^{\tau-\tau_i}\mathrm{d}\tau = \tilde{\alpha}_{i,l}\tilde{S}_{i-1,l} + \tilde{\beta}_{i,l}\tilde{S}_{i,l}, \quad (34)$$

with $\Delta\tau = \tau_{i+1,l} - \tau_{i,l}$ and $\tau_{i,l} = \int^{s_i}\hat{\chi}_l(s)\mathrm{d}s$. The α-β-γ coefficients are described in Olson & Kunasz (1987) and Hauschildt (1992). $\delta\tilde{I}_l$ in Eq. (34) is linearly interpolated and in general different from the coefficients in Eq. (33) and is therefore marked with a tilde.

Equation (32) can be written in matrix notation for any given characteristic:

$$\mathbf{I} = \boldsymbol{A}\cdot\boldsymbol{I} + \boldsymbol{\Delta I}. \quad (35)$$

Here $\boldsymbol{I}$ is a vector with all intensities, $\boldsymbol{A}$ is a square matrix that describes the influence of the different intensities upon each other, and $\boldsymbol{\Delta I}$ is a vector with the thermal emission and scattering contribution of the source function. For a characteristic with n_i spatial points and n_l points in the wavelength grid, the intensity vector $\boldsymbol{I}$ has $n_i \times n_l$ entries. In the following a superscript of k will label the characteristic at hand. The components of the matrix $\mathbf{A}$

from Eq. (35) at the spatial point i and the wavelength point l are given by

$$A^{-,k}_{i,l} = -\left(\xi\alpha^k_{i,l} + [1-\xi]\,\tilde{\alpha}^k_{i,l}\right)\frac{a^k_{i-1,l}}{\hat{\chi}^k_{i-1,l}}p^{-,k}_{i-1,l} \quad (36)$$

$$B^{-,k}_{i,l} = -\left(\xi\beta^k_{i,l} + [1-\xi]\tilde{\beta}^k_{i,l}\right)\frac{a^k_{i,l}}{\hat{\chi}^k_{i,l}}p^{-,k}_{i,l} \quad (37)$$

$$C^{-,k}_{i,l} = -\xi\gamma^k_{i,l}\frac{a^k_{i+1,l}}{\hat{\chi}^k_{i+1,l}}p^{-,k}_{i+1,l} \quad (38)$$

$$A^{\searrow,k}_{i,l} = \exp\left(-\Delta\tau^k_{i-1,l}\right) - \tilde{\alpha}^k_{i,l}\frac{a^k_{i-1,l}}{\hat{\chi}^k_{i-1,l}}\left[4 + [1-\xi]p^{|,k}_{i-1,l}\right] \quad (39)$$

$$B^{\searrow,k}_{i,l} = -\tilde{\beta}^k_{i,l}\frac{a^k_{i,l}}{\hat{\chi}^k_{i,l}}\left[4 + [1-\xi]\,p^{|,k}_{i,l}\right] \quad (40)$$

$$C^{\searrow,k}_{i,l} = 0 \quad (41)$$

$$A^{+,k}_{i,l} = -\left(\xi\alpha^k_{i,l} + [1-\xi]\,\tilde{\alpha}^k_{i,l}\right)\frac{a^k_{i-1,l}}{\hat{\chi}^k_{i-1,l}}p^{+,k}_{i-1,l} \quad (42)$$

$$B^{+,k}_{i,l} = -\left(\xi\beta^k_{i,l} + [1-\xi]\tilde{\beta}^k_{i,l}\right)\frac{a^k_{i,l}}{\hat{\chi}^k_{i,l}}p^{+,k}_{i,l} \quad (43)$$

$$C^{+,k}_{i,l} = -\xi\gamma^k_{i,l}\frac{a^k_{i+1,l}}{\hat{\chi}^k_{i+1,l}}p^{+,k}_{i+1,l}. \quad (44)$$

Following Knop et al. (2009a), the naming scheme of the quantities in Eqs. (36)–(44) indicates with which specific intensity element they are associated. For an index pair i and l a $\bullet^-$ superscript refers to an intensity at wavelength $l-1$, a $\bullet^\searrow$ superscript to the same wavelength, and $\bullet^+$ to the next wavelength point $l+1$. The A, B, C terms refer to the spatial points $i-1, i, i+1$, respectively. Equations (25)–(44) are nearly identical to those of Knop et al. (2009a) except for the explicit Doppler factor $f(s)$, which arises because the photon direction is measured by a distant stationary observer here rather than by a comoving observer, as was the case in Knop et al. (2009a). We also clarified a problem with $C^{\searrow,k}_{i,l}$ that was confusing in Knop et al. (2009a). The formal solution matrix is therefore identical in form to that shown in Fig. 1 of Knop et al. (2009a).

An element of the source function vector $\Delta\boldsymbol{I}$ is given by (Knop et al. 2009a)

$$\Delta I^k_{i,l} = \alpha^k_{i,l}\hat{S}^k_{i-1,l} + \beta^k_{i,l}\hat{S}^k_{i,l} + \gamma^k_{i,l}\hat{S}^k_{i+1,l}. \quad (45)$$

Note that all Doppler factors are explicitly handled by including them in the opacity as $\chi_l * f(s)$.

From Eq. (35) the solution for the specific intensity for a given spatial point and wavelength reads

$$\begin{aligned} I^k_{i,l} = \left(1 - B^{\mathrm{diag},k}_{i,l}\right)^{-1}\cdot\Big(&\Delta I^k_{i,l} + B^{\mathrm{sub},k}_{i,l}I^k_{i,l-1} + B^{\mathrm{super},k}_{i,l}I^k_{i,l+1} \\ &+A^{\mathrm{sub},k}_{i,l}I^k_{i-1,l-1} + A^{\mathrm{diag},k}_{i,l}I^k_{i-1,l} + A^{\mathrm{super},k}_{i,l}I^k_{i-1,l+1} \\ &+C^{\mathrm{sub},k}_{i,l}I^k_{i+1,l-1} + \quad C^{\mathrm{super},k}_{i,l}I^k_{i+1,l+1}\Big). \end{aligned} \quad (46)$$

2.2.1. The operator splitting method

Now that we have the formal solution, the full scattering problem can be solved by using operator splitting. The mean intensity J_λ is obtained from the source function S_λ by a formal solution of the radiative transfer equation, which is symbolically written using the Λ-operator Λ_λ as

$$J_\lambda = \Lambda_\lambda S_\lambda. \quad (47)$$

For the transition of a two-level atom, we have

$$\bar{J} = \bar{\Lambda}S, \quad (48)$$

where $\bar{J} = \int\phi(\lambda)J_\lambda\,\mathrm{d}\lambda$, $\bar{\Lambda} = \int\phi(\lambda)\Lambda_\lambda\,\mathrm{d}\lambda$ with the normalized line profile $\phi(\lambda)$.

The Λ-iteration method, i.e. solving Eq. (48) by a fixed-point iteration scheme of the form

$$\bar{J}_{\mathrm{new}} = \bar{\Lambda}S_{\mathrm{old}}, \quad S_{\mathrm{new}} = (1-\epsilon)\bar{J}_{\mathrm{new}} + \epsilon B, \quad (49)$$

fails in the case of high optical depths and small ϵ. This is because the largest eigenvalue of the amplification matrix (for Doppler-profiles) is approximately $\lambda_{\max} \approx (1-\epsilon)(1-T^{-1})$, where T is the optical thickness of the medium (Mihalas et al. 1975). For small ϵ and high T, this is very close to unity and, therefore, the convergence rate of the Λ-iteration is very poor. A physical description of this effect can be found in Mihalas (1980).

The idea of the ALI or operator splitting method is to reduce the eigenvalues of the amplification matrix in the iteration scheme (Cannon 1973) by introducing an approximate $\bar{\Lambda}$-operator (ALO) Λ^* and to split $\bar{\Lambda}$ according to

$$\bar{\Lambda} = \Lambda^* + (\bar{\Lambda} - \Lambda^*) \quad (50)$$

and rewrite Eq. (48) as

$$\bar{J}_{\mathrm{new}} = \Lambda^* S_{\mathrm{new}} + (\bar{\Lambda} - \Lambda^*)S_{\mathrm{old}}. \quad (51)$$

This relation can be written as (Hamann 1987)

$$\left[1 - \Lambda^*(1-\epsilon)\right]\bar{J}_{\mathrm{new}} = \bar{J}_{\mathrm{fs}} - \Lambda^*(1-\epsilon)\bar{J}_{\mathrm{old}}, \quad (52)$$

where $\bar{J}_{\mathrm{fs}} = \bar{\Lambda}S_{\mathrm{old}}$. Equation (52) is solved to obtain the new values of $\bar{J}$, which are then used to compute the new source function for the next iteration cycle.

Mathematically, the ALI method belongs to the same family of iterative methods as the Jacobi or the Gauss-Seidel methods (Golub & Van Loan 1989). These methods have the general form

$$Mx^{k+1} = Nx^k + b \quad (53)$$

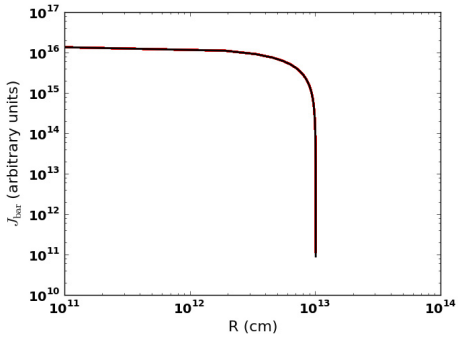

Fig. 1. Comparison of monotonic flow case with spherical symmetry solved using the full arbitrary velocity field method (red) to the well-tested 1D solution (black). The comoving mean intensity is plotted at each point in the computational volume. The agreement is at the 1% level.

for the iterative solution of a linear system $Ax = b$ where the system matrix A is split according to $A = M - N$. For the ALI method we have $M = 1 - \Lambda^*(1-\epsilon)$ and, accordingly, $N = (\bar{\Lambda} - \Lambda^*)(1-\epsilon)$ for the system matrix $A = 1 - \bar{\Lambda}(1-\epsilon)$. The convergence of the iterations depends on the spectral radius, $\rho(G)$, of the iteration matrix $G = M^{-1}N$. For convergence the condition $\rho(G) < 1$ must be fulfilled, this puts a restriction on the choice of Λ^*. In general, the iterations will converge faster for a smaller spectral radius. To achieve a significant improvement compared to the Λ-iteration, the operator Λ^* is constructed so that the eigenvalues of the iteration matrix G are much less than unity, resulting in swift convergence. Using parts of the exact $\bar{\Lambda}$ matrix (e.g., its diagonal or a tri-diagonal form) will optimally reduce the eigenvalues of the G. The calculation and the structure of Λ^* should be simple to make the construction of the linear system in Eq. (52) fast. For example, the choice $\Lambda^* = \bar{\Lambda}$ is best in view of the convergence rate (it is equivalent to a direct solution by matrix inversion) but the explicit construction of $\bar{\Lambda}$ is more time-consuming than the construction of a simpler Λ^*.

In the following discussion we use the notation of Hauschildt (1992) and Hauschildt & Baron (2006). The basic framework and the methods used for the formal solution and the solution of the scattering problem via operator splitting are discussed in detail in Hauschildt & Baron (2006) and will therefore not be repeated here. We have extended the framework to solve line transfer problems with a background continuum. The basic approach is similar to that of Hauschildt (1993). In the simple case of a two-level atom with background continuum that we consider here as a test case, we use a wavelength grid that covers the profile of the line including the surrounding continuum. We then use the wavelength-dependent mean intensities J_λ and approximate Λ operators Λ^* to compute the profile-integrated line mean intensities $\bar{J}$ and $\bar{\Lambda^*}$ via

$$\bar{J} = \int \phi(\lambda) J_\lambda \, \mathrm{d}\lambda$$

and

$$\bar{\Lambda^*} = \int \phi(\lambda) \Lambda^* \, \mathrm{d}\lambda.$$

$\bar{J}$ and $\bar{\Lambda^*}$ are then used to compute an updated value for $\bar{J}$ and the line source function

$$S = (1-\epsilon)\bar{J} + \epsilon B,$$

where ϵ is the line thermalization parameter (0 for a purely absorptive line, 1 for a purely scattering line). B is the Planck function, B_λ, profile averaged over the line

$$B = \int \phi(\lambda) B_\lambda \, \mathrm{d}\lambda$$

via the standard iteration method

$$\left[1 - \Lambda^*(1-\epsilon)\right] \bar{J}_{\mathrm{new}} = \bar{J}_{\mathrm{fs}} - \Lambda^*(1-\epsilon)\bar{J}_{\mathrm{old}}, \tag{54}$$

where $\bar{J}_{\mathrm{fs}} = \bar{\bar{\Lambda}} S_{\mathrm{old}}$. This equation is solved directly to obtain the new values of $\bar{J}$, which are then used to compute the new source function for the next iteration cycle.

We construct the line $\bar{\Lambda}$ directly from the wavelength-dependent Λ^* generated by the solution of the continuum transfer problems.

Given the form of Eq. (46) for the formal solution, the construction of the Λ^*-operator can proceed exactly as described in Baron & Hauschildt (2004). However, to conserve memory, we have implemented the Λ^*-operator, retaining the spatial off-diagonal terms, but *neglecting* the off-diagonal terms in wavelength. We still find good convergence at considerable savings in memory (see below).

3. Test calculations

In this section we present the results of test calculations we performed to test the new algorithm in terms of accuracy by regression testing. We compare these to results of the homologous case (Baron et al. 2009b), and to the spherical nonmonotonic cases (Baron & Hauschildt 2004).

The test calculations were performed on Opteron CPUs running Linux (Franklin and Hopper at NERSC), on Intel CPUs (Carver at NERSC, ICE2 at HLRN, and our own local Xserve clusters), and on IBM CPUs (PWR-4 and PWR-5). The code was compiled with Gfortran/gcc/g++, ifort/icc/icpc (versions 11 and 12), and xlf/xlc/xlC and with NAG f95/gcc/g++. Using the varied compiler suites and CPUs allowed us to find numerous errors.

3.1. Regression with monotonic case

Figure 1 shows the profile of the mean intensity J for homologous flow and spherical symmetry. The test problem is similar to that of Baron et al. (2009b). These are the basic model parameters:

1. An inner radius $R_{\mathrm{in}} = 10^{11}$ cm and an outer radius $R_{\mathrm{out}} = 1.01 \times 10^{13}$ cm.
2. A minimum optical depth in the continuum $\tau_{\mathrm{std}}^{\mathrm{min}} = 10^{-4}$ and a maximum optical depth in the continuum $\tau_{\mathrm{std}}^{\mathrm{max}} = 10^{4}$.
3. A gray temperature structure with $T_{\mathrm{model}} = 10^4$ K. That is the temperature solution of the spherical gray atmosphere problem with effective temperature T_{model} (Mihalas 1978).
4. An outer boundary condition $I_{\mathrm{bc}}^- \equiv 0$ and an inner boundary condition $I_\lambda = B_\lambda$ for all wavelengths.
5. For the initial wavelength the boundary condition is taken from that given by the 3D homologous calculation for homologous tests and set equal to the *Planck* function $B_{\lambda_{\mathrm{init}}}$ for non-homologous tests.
6. A continuum extinction $\chi_{\mathrm{c}} = C/r^2$, with the constant C fixed by the radius and optical depth grids.
7. A parametrized coherent and isotropic continuum scattering given by

$$\chi_{\mathrm{c}} = \epsilon_{\mathrm{c}}\kappa_{\mathrm{c}} + (1-\epsilon_{\mathrm{c}})\sigma_{\mathrm{c}} \tag{55}$$

with $0 \le \epsilon_{\mathrm{c}} \le 1$. κ_{c} and σ_{c} are the continuum absorption and scattering coefficients. In this work we have neglected scattering in the continuum.

The line of the simple two-level model atom is parameterized by the ratio of the profile-averaged line opacity χ_l to the continuum opacity χ_{c} and the line thermalization parameter ϵ_l. For the test cases presented below, we used $\epsilon_{\mathrm{c}} = 1$ and the line strength is given by $\Gamma \equiv \chi_l/\chi_{\mathrm{c}} = 10^2$ to simulate a strong line, with varying ϵ_l (see below).

The test model is just an optically thick sphere put into the 3D grid. The velocity at the outer radius was set to be relativistic, $v_{\mathrm{max}} = 8 \times 10^4$ km s^{-1}. The calculation was performed on a spherical grid with 33^3 spatial points, 33^2 solid angle directions, and 22 wavelength points. This and all calculations presented below were parallelized over characteristics and were run

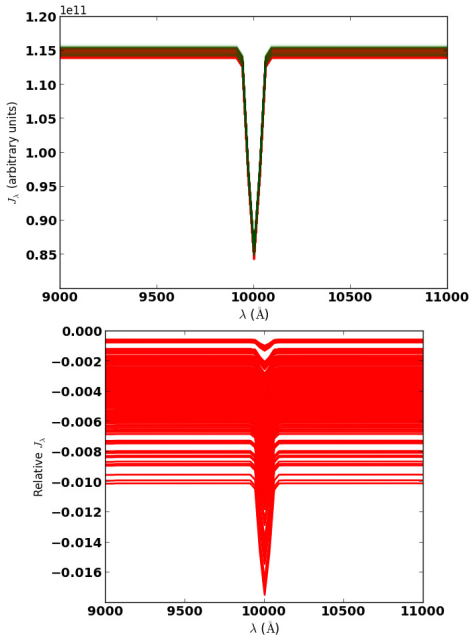

Fig. 2. Comparison of monotonic flow case with spherical symmetry solved using the full arbitrary velocity field method (green) to the 3D monotonic flow solution (red). The comoving mean intensity is plotted at the surface of the sphere. The test cases are identical, $v_{\max} = 8 \times 10^4$ km s^{-1}, $129 \times 17 \times 17$ spatial voxels, 114 wavelength points, and 256×256 directions. The thermalization parameter in the line is $\epsilon = 10^{-3}$ and the line strength is $\Gamma = 100$. The lower panel shows the relative difference, $\delta J_\lambda / J_\lambda$, as a function of wavelength.

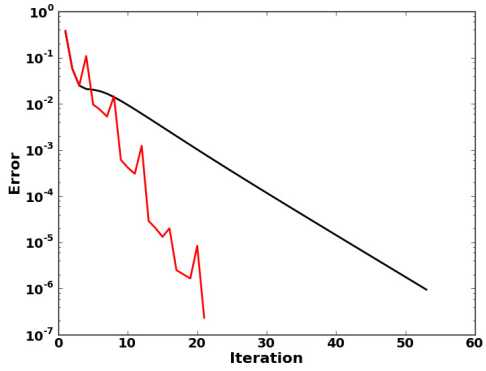

Fig. 3. Comparison of the convergence rate of a monotonic flow case with spherical symmetry with the thermalization parameter $\epsilon = 10^{-4}$ with and without Ng acceleration. The Ng acceleration is identical to that produced by the pure homologous 3D module.

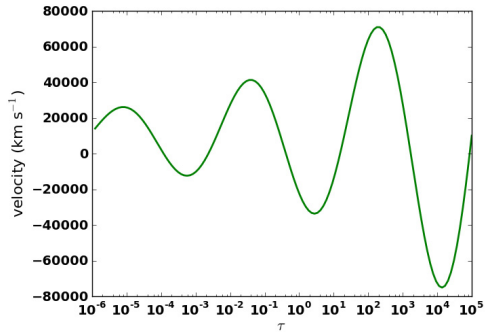

Fig. 4. Velocity profile used for the nonmonotonic velocity test with a damped sine wave.

on parallel clusters. Ng (Ng 1974; Auer 1987) acceleration was used to significantly speed up the operator splitting iterations for cases with scattering. Figure 2 shows the line profile at the surface, here we compare the 3D monotonic calculation (Baron et al. 2007) to the same calculation using the 3D arbitrary velocity algorithm. Because of the spatial resolution and the way that characteristics end at different points in a voxel (as opposed to always ending on a radial grid point in the 1D case), it is better to compare 3D cases to 3D cases.

Figure 3 shows the convergence rate of a monotonic flow case, with $\epsilon = 10^{-4}$, with and without Ng accleration. Not only does Ng acceleration clearly improve the convergence rate, it gives almost the exact same errors as the same test setup using both the 3D and 1D homologous algorithms.

3.2. Sine velocity flow

Here we again consider a spherically symmetric case with the same physical parameters as in Sect. 3.1, but the velocity, while still radial is now given modulated by a damped sine wave. We have also introduced a line into the opacity with thermalization parameter $\epsilon_l = 1$. The thermalization parameter in the continuum is $\epsilon_c = 1$. This case was calculated in 1D in Baron & Hauschildt (2004). Figure 4 shows the velocity as a function of radial optical depth in the continuum. The spatial grid was $129 \times 65 \times 17$ and the solid angle resolution was set to 512^2. The maximum velocity is $v \approx 10\,000$ km s^{-1} and the total number of wavelength points is 226. Figure 5 shows the comoving mean intensity J_λ from each surface voxel as a function of wavelength λ. The 1D result is plotted (the green curve) and the agreement is good to the sub-percent level. The variation in the velocity leads to an asymmetric line profile even in the comoving frame. But since this test has such a high spatial resolution, it requires a significant amount of memory per process. We explored the effects of lower spatial resolution, $129 \times 17 \times 17$, while keeping the high solid angle resolution 512×512. Figure 6 shows the mean intensity as a function of wavelength for the outmost part of the sphere. For computational expediency we set the line thermalization parameter $\epsilon_l = 1$. The spread in the results of 1.5% is indicative of the accuracy of these calculations, whereas the deviation of the envelope of the solution is indicative of the low spatial resolution of this calculation. While modern nodes may have 24 CPUs, but only about 1 GB of RAM per CPU, it is unfortunate that the evelope of the low spatial resolution calculation is offset from the 1D result. This shows that not only solid angle resolution is important, but spatial resolution is quite important as well. Figure 7 shows the same calculation with the spatial grid enhanced to $129 \times 65 \times 65$ and the solid angle grid reduced to 32×24 (Hauschildt & Baron 2010). As can be seen in Fig. 7, the reduced solid angle resolution increases the spread by roughly a factor of two, but now the 3D solution envelopes the 1D nonmonotonic result. With this higher spatial resolution, the spread can be further reduced by increasing the solid angle resolution, which shows near-perfect weak scaling, and thus does

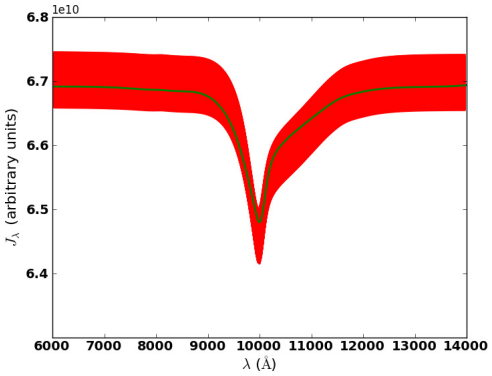

Fig. 5. Line profile for the damped sine-wave velocity case with high spatial $n_r = 129$, $n_\theta = 65$, and $n_\phi = 17$, and angular resolution $n_\Omega = 512 \times 512$. The comoving mean intensity J_λ for each voxel on the surface (there are $65 \times 17 = 1105$ of them) is plotted as a function of λ (red lines). The green curve is the 1D result using the methods of Baron & Hauschildt (2004) and Knop et al. (2009b,a). Here the scattering fraction is $\epsilon = 10^{-4}$ and the line strength is $\Gamma = 100$.

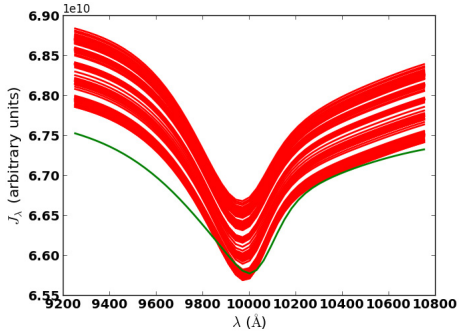

Fig. 6. Line profile for the damped sine-wave velocity case with lower spatial $n_r = 129$, $n_\theta = 17$, and $n_\phi = 17$, and higher angular resolution $n_\Omega = 512 \times 512$ than in Fig. 5. The comoving mean intensity J_λ for each voxel on the surface (there are $65 \times 17 = 1105$ of them) is plotted as a function of λ (red lines). The green curve is the 1D result using the methods of Baron & Hauschildt (2004) and Knop et al. (2009b,a). Here the scattering fraction is $\epsilon = 1$ for computational expediency, and the line strength is $\Gamma = 100$. With the very low spatial resolution, the 3D result no longer envelopes the 1D result (which by assuming spatial spherical symmetry has essentially infinite resolution in n_θ, and n_ϕ).

not increase the wallclock time required for these calculations (although it does require more CPUs).

3.3. Example of radial nonhomologous flows

The previous tests were all totally spherically symmetric, with radial variations in the velocity field. We now assume the flow to be radial and azimuthally symmetric, i.e.

$$\boldsymbol{\beta}(\boldsymbol{r}) = p(\theta)q(r)\hat{\boldsymbol{e}}_r. \tag{56}$$

For this case, we have

$$\hat{\boldsymbol{n}} \cdot \boldsymbol{\beta} = pqn_r, \tag{57}$$

$$(\hat{\boldsymbol{n}} \cdot \nabla)\beta = pn_r q'(r) + \frac{1}{r}p'(\theta)qn_\theta, \tag{58}$$

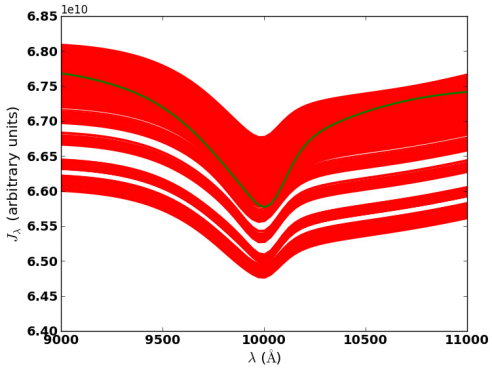

Fig. 7. Line profile for the damped sine-wave velocity case with higher spatial resolution, but lower angular resolution than in Fig. 5. The spatial resolution is $n_r = 129$, $n_\theta = 65$, and $n_\phi = 65$, and the angular resolution is reduced to $n_\Omega = 32 \times 24$. The comoving mean intensity J_λ for each voxel on the surface (there are $65 \times 17 = 1105$ of them) is plotted as a function of λ (red lines). The green curve is the 1D result using the methods of Baron & Hauschildt (2004) and Knop et al. (2009b,a). Here the scattering fraction is $\epsilon = 1$ for computational expediency, and the line strength is $\Gamma = 100$.

and

$$\hat{\boldsymbol{n}} \cdot \nabla(\hat{\boldsymbol{n}} \cdot \boldsymbol{\beta}) = \frac{1}{r}\left[p'qn_r n_\theta + p\,(q'r)\,n_r^2 + pq\left(1 - n_r^2\right)\right], \tag{59}$$

where we made use of

$$\dot{r} = n_r,\ \dot{\theta} = \frac{n_\theta}{r},\ \dot{\phi} = \frac{n_\phi}{r\sin\theta}, \tag{60}$$

and

$$\dot{n}_r = n_\theta\dot{\theta} + \sin\theta n_\phi\dot{\phi}. \tag{61}$$

Here an over dot implies $\frac{\mathrm{d}}{\mathrm{d}s}$, e.g., $\dot{r} \equiv \frac{\mathrm{d}r}{\mathrm{d}s}$, etc., and a prime denotes differentiation with respect to $\mu = \cos\theta$.

Inserting Eqs. (57)–(59) into Eq. (19), we find an analytic expression for $a(s)$:

$$a(s) = \frac{p'qn_r n_\theta + p(q'r)n_r^2 + pq(1 - n_r^2)}{r(1 - pqn_r)} - \gamma^2 pq\left[pn_r q'(r) + \frac{1}{r}p'(\theta)qn_\theta\right], \tag{62}$$

where the spherical components of the unit vector $\hat{\boldsymbol{n}} = (\sin\theta_n\cos\phi_n, \sin\theta_n\sin\phi_n, \cos\theta_n)$ are

$$\begin{aligned} n_r &= \sin\theta\sin\theta_n\cos(\phi - \phi_n) + \cos\theta\cos\theta_n, \\ n_\theta &= \cos\theta\sin\theta_n\cos(\phi - \phi_n) - \sin\theta\cos\theta_n, \\ n_\phi &= \cos\theta_n. \end{aligned} \tag{63}$$

For $p(\theta)$, we use an expansion in terms of Legendre polynomials (which form a complete and orthonormal basis for axially symmetric spherical functions)

$$p(\theta) = \sum_{n=0}^{k} c_n\mathcal{P}_n(\theta), \tag{64}$$

with $\mathcal{P}_0(\mu) = 1$, $\mathcal{P}_1(\mu) = \mu$, and $\mathcal{P}_2(\mu) = \frac{1}{2}(3\mu^2 - 1)$, etc., where $\mu = \cos\theta$. We consequently obtain

$$p'(\theta) = \sum_{n=1}^{k} c_n\mathcal{P}'_n(\theta) \tag{65}$$

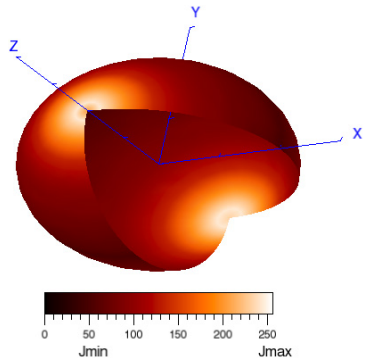

Fig. 8. Comoving mean intensity $J(\theta, \phi)$ plotted at the surface $R = R_{\rm out}$ for case where $\boldsymbol{\beta} = c_0 r p(\theta)\hat{\boldsymbol{e}}_r$, and $p(\theta) = 1 + \frac{1}{2}\mathcal{P}_2(\mu) = 1 + \frac{1}{2}(\frac{3}{2}\cos^2\theta - \frac{1}{2})$. The velocity flow is radial, but not spherically symmetric to approximate a jet-like flow in the $\pm z$ direction.

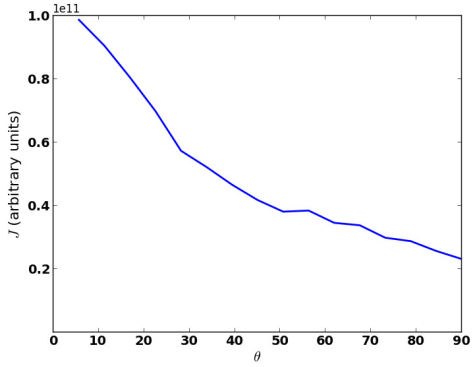

Fig. 9. Comoving mean intensity $J(\theta, \phi_0)$ plotted at the surface $R = R_{\rm out}$ for a fixed (arbitrarily chosen) value of $\phi = \phi_0$. The variation of nearly an order of magnitude from the pole to the equator is due to the fact the the continuum level is a function of the velocity.

with $\mathcal{P}'_1 = -\sin\theta$, and $\mathcal{P}'_2 = -\frac{3}{2}\sin 2\theta$, etc. (note that the case $c_n = c_0\delta^0_n$ degenerates to homologous flow). We can use this finite expansion in terms of the Legendre polynomial $\mathcal{P}_n(\theta)$ to construct azimuthally symmetric jets.

As a simple example of nonspherically symmetric flow, we run a test case where

$$\boldsymbol{\beta} = c_0 r p(\theta)\hat{\boldsymbol{e}}_r, \tag{66}$$

i.e. we take $q(r) = c_0 r$ (c_0 is a constant), which simplifies $a(s)$ to be

$$a(s) = c_0\left[\frac{p + p' n_r n_\theta}{1 - r n_r p} - \gamma^2\beta(p n_r + p' n_\theta)\right]. \tag{67}$$

Furthermore, we assume

$$p(\theta) = 1 + \frac{1}{2}\mathcal{P}_2(\mu) = 1 + \frac{1}{2}\left(\frac{3}{2}\cos^2\theta - \frac{1}{2}\right), \tag{68}$$

i.e., we perturb the homologous flow by adding a second-order Legendre polynomial with perturbation coefficient 0.5. We show the resulting mean intensity plot $J(\theta, \phi)$ at the boundary $R = R_{\rm out}$ in Fig. 8. We obtained perfect azimuthal symmetry as expected from the form of $\boldsymbol{\beta}$ in Eq. (66), although it was not explicitly enforced. Furthermore, we also recovered the symmetry with respect to the north/south pole (i.e., symmetry under a reflection with respect to the equatorial plane, $\theta \to \pi - \theta$), which is characteristic for Legendre polynomials of even order, see Eq. (68). Figure 9 shows a longitudinal slice of the comoving intensity, which shows that the comoving mean intensity varies by roughly a factor of ten from the pole to the equator. This is just due to the effect that the continuum level varies with the maximum velocity (Baron et al. 2009b).

3.4. Checkpointing

We implemented a checkpointing scheme that allows for restarts and new starts with higher resolution in solid angle. We simply write out (using stream I/O) the Λ^* operator once it has been calculated, and the value of J at each voxel after each ALO iteration. Since these calculations require significant numbers of processors, which may go down, or calculations may run out of time, this allows us to perform perfect restarts. We checked that restarting from the checkpoint files works perfectly and that the calculations are converged in a single iteration when restarting from a converged checkpoint file. We write Λ^* and J to separate files, since that allows us to read just J, and then recalculate Λ^* if we restart with a higher resolution. We checked this, and it allows us to use a low-resolution calculation (performed on fewer processors, for example) and then converge the higher resolution calculation with roughly half as many iterations for each resolution increase. Table 1 shows the rate of convergence for a test with homologous velocity fields (chosen for computational expedience), $v_{\rm max} = 10^5$ km s^{-1} and $\epsilon = 10^{-5}$. While the restart result still requires several iterations, this scheme allows for some speedup. The small ϵ and high maximum velocity make this test particularly demanding. The calculations were all restarted such that Ng acceleration cannot begin until the fourth iteration, and thus the restart calculations converge more slowly than they could. The scheme could indeed possibly be made more efficient by keeping the previous three values of $\bar{J}$, so that the restart iteration could immediately use Ng accleration.

Table 1. Convergence rate for homologous test with $v_{\rm max} = 10^5$ km s^{-1} and $\epsilon = 10^{-5}$, starting from the previous test.

Ω	Number of iterations
8×8	29
64×64	21
128×128	15
256×256	13

Notes. The first test with 8×8 solid angles is converged from the beginning. The spatial resolution is held fixed and Λ^* is recalculated at the beginning of each new resolution run.

4. Conclusion

We presented algorithm strategies and details for the solution of the radiative transfer problem in 3D atmospheres with arbitrary wavelength couplings.

Future possible applications are the velocity profiles of cool stellar winds, treating partial redistribution, calculating radiative transfer in shock fronts like in accretion shocks, calculating quasar jets, and general relativistic situations such as a rotating black hole.

Acknowledgements. This work was supported in part by SFB 676, GRK 1354 from the DFG, NSF grant AST-0707704, and US DOE Grant DE-FG02-07ER41517. Support for Program number HST-GO-12298.05-A was provided by NASA through a grant from the Space Telescope Science Institute, which is operated by the Association of Universities for Research in Astronomy, Incorporated, under NASA contract NAS5-26555. B.C. thanks the University of Okalahoma Foundation for a fellowship. This research used resources of the National Energy Research Scientific Computing Center (NERSC), which is supported by the Office of Science of the US Department of Energy under Contract No. DE-AC02-05CH11231; and the Höchstleistungs Rechenzentrum Nord (HLRN). We thank both these institutions for a generous allocation of computer time.

References

Auer, L. H. 1987, in Numerical Radiative Transfer, ed. W. Kalkofen (Cambridge: Cambridge Univ. Press), 101
Baron, E., & Hauschildt, P. H. 2004, A&A, 427, 987
Baron, E., & Hauschildt, P. H. 2007, A&A, 468, 255
Baron, E., Branch, D., & Hauschildt, P. H. 2007, ApJ, 662, 1148
Baron, E., Chen, B., & Hauschildt, P. H. 2009a, in Recent Directions In Astrophysical Quantitative Spectroscopy And Radiation Hydrodynamics, eds. I. Hubeny, J. M. Stone, K. MacGregor, & K. Werner (New York: AIP), 148
Baron, E., Hauschildt, P. H., & Chen, B. 2009b, A&A, 498, 987
Cannon, C. J. 1973, JQSRT, 13, 627
Chen, B., Kantowski, R., Baron, E., Knop, S., & Hauschildt, P. 2007, MNRAS, 380, 104
Golub, G. H., & Van Loan, C. F. 1989, Matrix computations (Baltimore: Johns Hopkins University Press)
Hamann, W.-R. 1987, in Numerical Radiative Transfer, ed. W. Kalkofen (Cambridge: Cambridge Univ. Press), 35
Hauschildt, P. H. 1992, JQSRT, 47, 433
Hauschildt, P. H. 1993, JQSRT, 50, 301
Hauschildt, P. H., & Baron, E. 2004, A&A, 417, 317
Hauschildt, P. H., & Baron, E. 2006, A&A, 451, 273
Hauschildt, P. H., & Baron, E. 2008, A&A, 490, 873
Hauschildt, P. H., & Baron, E. 2009, A&A, 498, 981
Hauschildt, P. H., & Baron, E. 2010, A&A, 509, A36
Jack, D., Hauschildt, P. H., & Baron, E. 2009, A&A, 502, 1043
Kalkofen, W., ed. 1987, Numerical Radiative Transfer (Cambridge: Cambridge Univ. Press)
Knop, S., Hauschildt, P. H., & Baron, E. 2009a, A&A, 501, 813
Knop, S., Hauschildt, P. H., & Baron, E. 2009b, A&A, 496, 295
Mihalas, D. 1978, Stellar Atmospheres (New York: W. H. Freeman)
Mihalas, D. 1980, ApJ, 237, 574
Mihalas, D., Kunasz, P., & Hummer, D. 1975, ApJ, 202, 465
Ng, K. C. 1974, J. Chem. Phys., 61, 2680
Olson, G. L., & Kunasz, P. B. 1987, JQSRT, 38, 325
Seelmann, A., Hauschildt, P. H., & Baron, E. 2010, A&A, 522, A102

The Astrophysical Journal, 710:444–455, 2010 February 10 doi:10.1088/0004-637X/710/1/444

SECONDARY PARAMETERS OF TYPE Ia SUPERNOVA LIGHT CURVES

P. Höflich[1], K. Krisciunas[2], A. M. Khokhlov[3], E. Baron[4], G. Folatelli[5], M. Hamuy[5], M. M. Phillips[6], N. Suntzeff[2], And L. Wang[2]
(NSF07-SNIa Collaboration)
[1] Department of Physics, Florida State University, Tallahassee, FL 32306, USA; pah@astro.physics.fsu.edu
[2] George P. and Cynthia Woods Mitchell Institute for Fundamental Physics & Astronomy, Texas A&M University, Department of Physics & Astronomy, 4242 TAMU, College Station, TX 77843, USA; krisciunas@physics.tamu.edu, suntzeff@physics.tamu.edu, lwang@physics.tamu.edu
[3] Department of Astronomy and Astrophysics, University of Chicago, Chicago, IL, USA; ajk@oddjob.uchicago.edu, vikram@oddjob.uchicago.edu
[4] Homer L. Dodge Department of Physics and Astronomy, University of Oklahoma, 440 W. Brooks, Rm 100, Norman, OK 73019-2061, USA; baron@ou.edu
[5] Departamento de Astronomia, Universidad de Chile, Casilla 36D, Santiago, Chile; mhamuy@das.uchile.cl, gfolatelli@das.uchile.edu
[6] Las Campanas Observatory, Casilla 601, La Serena, Chile; mmp@lcoeps1.lco.cl
Received 2009 July 3; accepted 2009 December 15; published 2010 January 19

ABSTRACT

High-quality observations of B and V light curves obtained at Las Campanas Observatory for local Type Ia Supernovae (SNe Ia) show clear evidence that SNe Ia with the same brightness decline or stretch may have systematic and independent deviations at times $t \lesssim 5$ days before and at times $t \gtrsim 30$ days after maximum light. This suggests the existence of two independent secondary parameters that control the shape of SN Ia light curves in addition to the primary light curve parameter, stretch s or Δm_{15}. The secondary parameters may reflect two independent physical effects caused by variations in the initial carbon-to-oxygen (C/O) profile in the progenitor and the initial central density ρ_c in a carbon–oxygen white dwarf exploding as an SN Ia. Theoretical light curves of delayed detonation SN Ia models with varying progenitor masses on the main sequence, varying accretion rates, and varying primordial metallicity reproduce two morphologically different and independent types of variations in observed visual light curves. These calculations predict small variations of ≈0.05 mag in the absolute brightness of SNe Ia which are correlated with the variations of progenitor mass on the main-sequence $M_{\rm MS}$, which changes the C/O profile, and ρ_c, which depends on the accretion rate. Such variations in real supernovae will induce systematic errors in SN Ia calibration at high redshifts. A physically motivated three-parameter, s, C/O, ρ_c, template for SNe Ia light curves might take these variations into account. Comparison between the theoretical predictions and the observational results agree qualitatively; however, the observations show variations between the B and V light curves that are not expected from the modeling and may indicate limitations in the details of the theoretical models.

Key words: distance scale – supernovae: general – supernovae: individual (2004ef, 2005al, 2005am, 2005el, 2005ki, 2005na)

Online-only material: color figures

1. INTRODUCTION

Type Ia Supernovae (SNe Ia) are thought to be thermonuclear explosions of massive carbon–oxygen white dwarfs (CO-WDs) in binary stellar systems. These supernovae are important tools ("standard candles") of modern physics and cosmology. Use of SNe Ia as standard candles has provided the first direct evidence of the accelerating expansion of the universe and the existence of dark energy (Riess et al. 1998; Perlmutter et al. 1999).

Maximum luminosity varies among SNe Ia and is not a constant. Essentially all supernova-based cosmology studies use methods of calibration of SNe Ia as standardizable candles (removing luminosity variations) which rely on empirical relations between the intrinsic brightness at maximum light and other observable characteristics of SNe Ia such as the shape of the light curve, or the rate of brightness decline after maximum light—the brightness–decline relation (Phillips 1993; Phillips et al. 1999). The present accuracy of calibration, $\sim 10\%$, has been sufficient for discovering dark energy, but it must be improved to perhaps $\simeq 1\%$–2% in order to study properties of dark energy quantitatively. This is a formidable task which requires increasing the accuracy of SN Ia light curve observations, accounting for effects of dust absorption, and so on. It also requires improving the calibration procedure itself, which involves two important interconnected issues.

1. If SN Ia light curves form a one-dimensional family characterized by a single parameter such as Δm_{15}, then the observed spread of individual SNe Ia around the average brightness–decline relation can be attributed to random statistical error, and the accuracy of cosmological measurements can be increased by simply increasing the number of observations of individual SNe Ia. On the other hand, if light curves are characterized, in addition to Δm_{15}, by some yet unknown independent "secondary" parameters, then improving the calibration is impossible without taking the dependence of the light curve on secondary parameters into account. So far, it is unknown if secondary parameters exist. Clear evidence for at least two independent secondary parameters will be provided in this paper.
2. Implicit in all SN Ia calibration procedures is a fundamental assumption that nearby and distant (cosmological) SNe Ia behave identically and that empirical brightness—decline or brightness—stretch relations established for local SNe Ia can be used for high-redshift cosmological supernovae as well. Obviously, empirical studies of nearby and distant SNe Ia alone cannot confirm or reject the existence of variations of brightness–decline relations with redshift. This requires independent accurate measurements of the intrinsic brightness of SNe Ia. Secondary parameters may hold a key to this difficult problem. If we understand the physical mechanisms and the relationship of secondary parameters to initial conditions of SN Ia explosions, e.g., metallicity and/or the parameters of binary progenitors, we may gain some insights into

systematic changes in SN Ia light curves with cosmological time.

The Carnegie Supernova Project (CSP) has recently obtained a highly uniform set of SNe Ia light curves with an accuracy of a few hundredths of a magnitude both for individual SNe Ia and in terms of variations between different objects (Contreras et al. 2010; Folatelli et al. 2010). These new data provide clear evidence for the existence of secondary variations in SNe Ia light curves which are independent of the primary Phillips relation, and thus, are evidence for the existence of independent secondary parameters. The CSP data allow us to begin addressing issues (1) and (2) outlined above.

SN Ia models predict a weak dependence of the early light curve on the carbon-to-oxygen (C/O) ratio of the progenitor. They also predict a weak dependence of the late-time light curve on the initial central density, ρ_c, of the exploding WD. A combined analysis of new observational data and theoretical predictions leads us to suggest the existence of two independent secondary parameters that, in addition to Δm_{15} or stretch, control the intrinsic brightness of SNe Ia.

The paper is organized as follows: Section 2 gives a short review of previous work on this subject; Section 3 describes new observational data used in this paper; Section 4 briefly summarizes the current theoretical understanding of SNe Ia and presents theoretical calculations of SNe Ia light curves; Section 5 analyzes the observational light curves which give the evidence for the existence of secondary parameters, compares observational and theoretical light curves, and discusses the theoretical interpretation and the mechanisms by which secondary parameters arise in SNe Ia; results of the paper are summarized and the discussion of the implications of the results to the calibration of SNe Ia is presented in Section 6.

2. PREVIOUS WORK

Over the last half decade, a number of observational and theoretical studies have sought to uncover secondary parameters. Much of this effort has been in attempts to find direct correlations between physical effects and peak luminosity. Examples include metallicity (Wang et al. 1997a; Höflich et al. 1998; Timmes et al. 2003; Ellis et al. 2008; Gallagher et al. 2008; Howell et al. 2009; Piro & Bildsten 2008; Chamulak et al. 2008), asymmetries of the explosion (Wang et al. 1997b; Howell et al. 2001; Kasen et al. 2003, 2004, 2009; Höflich et al. 2006; Wang & Wheeler 2008), central density and C/O ratio (Höflich et al. 1998, 2000; Domínguez et al. 2001; Röpke et al. 2006; Höflich 2006), age of the progenitor (Mannucci et al. 2006; Sullivan et al. 2006), neutron-rich isotope to ^{56}Ni ratio (Höflich et al. 2004; Mazzali & Podsiadlowski 2006), and the opacity of the overlying material (Mazzali et al. 2001; Kasen & Woosley 2007). Our approach here is different. Rather than focusing on a single physical effect on a specific observable or stage, we make use of detailed stellar evolution models that were calculated all the way through WD formation, accretion, and explosion (Domínguez et al. 2001; Höflich 2006) and focus on the effects that variations in the progenitor and accretion rate have on both the early and late parts of the light curve but using parameterizations when the underlying physics is uncertain. Both approaches are valid, and we must take care not to draw conclusions beyond the range of validity of our one-dimensional approach and rely on consistency checks using observations. At the present time, this approach makes sense since one-dimensional models do a reasonable job of reproducing observations. While current three-dimensional models are able to reproduce some of the observations, no three-dimensional model to date has begun with a configuration that was the result of detailed stellar evolution, nor is it understood what physical variations in three-dimensional models reproduce the tight brightness–decline relation. With or without constant mixing, one-dimensional models can reproduce the brightness–decline relation and its narrow width (Höflich et al. 1996, 2002; Umeda et al. 1999); a varying amount of mixing produces an "anti-correlation" and/or a huge spread comparable to the entire range of SNe Ia (Höflich et al. 1996; Pinto & Eastman 2000; Kasen et al. 2009).

Though details depend on the pre-conditioning of the WD (Höflich & Stein 2002; Livne et al. 2005; Kasen et al. 2009; Zingale et al. 2009), three-dimensional models of deflagrations and delayed detonations (DDs) predict strong mixing of the central region during the deflagration phase (Khokhlov 2000; Gamezo et al. 2003; Reinecke et al. 2002) in conflict with observations of late time spectra (Höflich et al. 2004; Gerardy et al. 2007) and remnants (Fesen et al. 2007). We note that recollapsing models (Bravo & Garcia-Senz 2006; Baron et al. 2008; Bravo et al. 2009a, 2009b) avoid central mixing, but produce only ^{56}Ni in the center. In these models, the center has expanded sufficiently prior to carbon ignition that the electron capture rates have dropped and so burning occurs without neutronization. The gravitational confined detonation (Plewa et al. 2004; Jordan et al. 2008; Meakin et al. 2009) model will produce neutronized material under some ignition conditions and avoid its production under others (Jordan et al. 2009).

3. OBSERVATIONS

The light curves of SNe are often stitched together from observations carried out on a variety of telescopes at a variety of sites. This has the advantage of filling in gaps in the light curves. However, there is a distinct disadvantage. The spectral energy distributions of SNe are considerably different than those of normal stars, and the spectra of SNe change on timescales of days. While some spectral features are easily associated with singly and doubly ionized metals such as silicon and iron, other absorption features are actually blends of many lines. The effective bandpasses of filters vary from camera to camera. The net result is that photometry of SNe carried out on different telescopes often exhibits systematic offsets, sometimes amounting to 0.2 mag. From synthetic photometry of spectra of normal stars and spectra of SNe at different times with respect to maximum light, we can compute "*S*-corrections" which largely resolve these differences (Stritzinger et al. 2002; Krisciunas et al. 2003). However, unless we have good sequences of spectra for all of our SNe, it is not possible to devise error-free *S*-corrections. Certainly, we wish to attribute variations in light curve morphology to the SNe themselves, not to some conspiracy of the telescopes, sites, and cameras.

The CSP, which began operation in September 2004, seeks to address this problem (Hamuy et al. 2006). The CSP endeavors to observe Type Ia and Type II-P SNe in the filters of the Sloan Digital Sky Survey ($u'g'r'i'$), the standard Johnson *B* and *V* filters, plus the near-infrared bands *Y*, *J*, and *H*. Roughly 50 SNe are being followed each year, for five years. Almost all of the optical photometry of nearby SNe is being obtained with the Swope 1 m telescope at Las Campanas Observatory (LCO). For higher redshift SNe, some *BVI* data are derived from images with the Wide Field CCD camera on the 2.5 m DuPont telescope at LCO, and a small amount of *BVR* data is from the 6.5 m Clay Telescope (Magellan 2). Based on high-quality CSP data, the

rms deviations of 0.025 mag have been achieved (Contreras et al. 2010).

We use 18 SNe Ia observed in 2004, 2005, and 2006 as part of the CSP. All these had well-sampled light curves. Many were observed a week or more prior to maximum light. Many were observed 60 or more days after maximum light. For the purposes of this paper we restrict ourselves to the *B*- and, in particular, *V*-band photometry because, based on theoretical models, *V* is expected to be least sensitive to additional variables.

The *BVRI* templates of SNe Ia are provided in Prieto et al. (2006). Sets of *BVRI* templates are characterized by the standard decline rate parameter $\Delta m_{15}(B)$ which serves as a morphological label for the set. While Prieto et al. (2006) provide *BVRI* templates only *BV* were used in this analysis. Prior to fitting the light curves with the templates of Prieto et al. (2006), we first estimated the time of *B*-band maximum and subtracted the redshift- and time-dependent *K*-corrections from the photometry by interpolating the *B*- and *V*-band corrections of Hamuy et al. (1993). If the subsequently determined time of maximum light was more than 0.5 days different than the value adopted for the calculation of the *K*-corrections, then they were recalculated. It was then checked that the newly determined time of maximum light was statistically consistent and thus there was no need to iterate further.

The range of $\Delta m_{15}(B)$ for the Prieto et al. (2006) templates is 0.83–1.93. For example, for a given object we chose *B*- and *V*-band templates from Prieto et al. (2006), stretched them by the time dilation factor (1+*z*), then shifted them by small increments over a range of dates and over a range of magnitudes to minimize the total χ^2 of the fit in each filter. Then we tried the other templates including all bands over a range of $\Delta m_{15}(B)$ to determine which templates give the lowest χ^2 of all. In this way, we determined the observed maximum magnitudes and the times of maximum light. For each of our SNe, we obtained functions that fit the *B*- and *V*-band light curves from roughly −5 until 25 days after the time of maximum light. This time interval for fitting the data was motivated by the theoretical models which predicted that, during this period, the visual light curves (LCs) should be least affected by variations in the central density and the progenitors (Höflich et al. 1998; Domínguez & Höflich 2000; Höflich 2006).

For a comparison of the fits to the photometry, we then subtracted off the derived maximum magnitudes in *B* and *V*, subtracted off the times of maximum light in the two filters, and divided the "time-since-maximum" by (1+*z*) to give "rest-frame days since maximum." The same normalization is applied to the photometric data.

4. MODELS OF SN Ia

4.1. Explosion

Current observations of SNe Ia favor a DD scenario of an SN Ia explosion in which the explosion begins as a subsonic deflagration which later turns into a supersonic detonation by the process of a deflagration-to-detonation transition (DDT) (Khokhlov 1991). The ensuing detonation incinerates the entire WD. In one-dimensional models the deflagration speed, *S*, and the transition density, $\rho_{\rm tr}$, at which the DDT occurs are free parameters. The value of $\rho_{\rm tr}$ determines the fraction of a WD that will burn to nuclear statistical equilibrium and produce ^{56}Ni. Therefore, $\rho_{\rm tr}$ is a critical parameter that controls the brightness of SNe Ia. DD models with $\rho_{\rm tr} \simeq (0.5\text{–}2.5) \times 10^7$ g cm^{-3} reproduce the observed range of SNe Ia luminosities, correct stratification of chemical elements in SNe Ia envelopes, and the correlation between maximum brightness and width of the light curve consistent with observations (Höflich 1995, 2006; Höflich et al. 1996, 2002; Mazzali et al. 1998, 2001, 2007; Quimby et al. 2007; Kasen et al. 2009; Marion et al. 2009). DD models appear to be in agreement with observations of SN Ia remnants (Fesen et al. 2007; Badenes et al. 2008).

The initial central density of a WD, ρ_c, its metallicity, and its C/O ratio also influence the production of ^{56}Ni and maximum brightness of SNe Ia during the explosion. Note that in our models, the free parameters are the main-sequence mass of the progenitor, $M_{\rm MS}$, the accretion rate, and the primordial metallicity *Z* (Domínguez et al. 2001; Höflich 2006). The fact that the brightness of an SN Ia is controlled, for the most part, by a single, primary parameter $\rho_{\rm tr}$, and that there exists an evolutionary bottleneck associated with the limiting Chandrasekhar mass of a WD provides a plausible explanation for a near one-dimensional sequence of SN Ia explosions. A crucial point is that ρ_c, primordial metallicity, and C/O ratio influence certain characteristics of the explosion *not associated* with the primary brightness–decline relation. In particular, the C/O ratio has an influence on the expansion velocity of SNe Ia. The dependence is caused by variations in the nuclear binding energy of the CO fuel. The larger the C/O ratio, the smaller the binding energy, and the faster the SN Ia envelope expands. This is a secondary effect since the bulk of the kinetic energy is determined by a much larger difference in binding energies of C/O and products of explosive burning (Fe-peak elements). On the other hand, ρ_c influences the distribution and amount of ^{56}Ni in the innermost parts of an SN Ia. SN Ia models based on explosions of Chandrasekhar-mass WDs predict a hole in the ^{56}Ni distribution near the center which is filled instead with highly neutronized isotopes of Fe-group elements. The hole is caused by electron captures and neutronization of matter at high densities. The size of the hole increases with ρ_c. These two effects influence the formation of both early and late portions of a light curve. As noted above the nickel hole is generally absent in all three-dimensional models, either because the core expands prior to ignition, or because in DD models mixing occurs during the deflagration phase, but the stratified structure is restored by the detonation. Because the flame is very topologically complex during the deflagration phase, the detonation will not produce a central neutronized hole.

The initial C/O ratio and profile and ρ_c in a supernova are a result of stellar and binary evolution. The C/O profile is produced during the central Helium burning and thin shell burning during the stellar evolution and the accretion to $M_{\rm Ch}$. The central He burning is initially dominated by carbon production via the 3α reaction in the convective core. When the He mass fraction becomes depleted, ^{12}C(α, γ)^{16}O mainly controls He-burning and most of the ^{16}O is produced during the late phases of central He-burning. Note that the final abundances depend on a combination of the ^{12}C(α, γ)^{16}O rate and chemical mixing which determines the duration of the phase of depleted He-core burning. Stellar evolution models which produce low C/O ratios of $\simeq$0.25–0.4 are in agreement with observational constraints, like the amount of oxygen found in the inner zone of pulsating WDs or the age of open clusters (Domínguez et al. 1999, 2001; Metcalfe et al. 2001; Straniero et al. 2003). The C/O ratio in the burning shell is greater, $\approx$ 1, because the shell helium source has lower density and higher temperature compared to helium burning in the core. The size of the convective core depends mainly on the progenitor mass $M_{\rm MS}$ on the main sequence and, to some

extent, on the primordial metallicity Z, namely the iron abundance, which dominates the opacity (Domínguez et al. 2001; Höflich et al. 2000). The dependence of $M_{\rm core}$ on $M_{\rm MS}$ is nonlinear, with the mass of the He convective core changing with $M_{\rm MS}$ slowly for low $M_{\rm MS}$ and more rapidly when $M_{\rm MS}$ approaches its maximum value. Approximately, $M_{\rm core}$ is 0.3, 0.4, 0.7 $M_\odot$ for $M_{\rm MS} = 1.5, 5, 7\ M_\odot$, respectively (Domínguez et al. 2001). The core's C/O ratio is smallest for small $M_{\rm MS}$, increases rapidly when $M_{\rm MS}$ increases from 1.5 to 3 $M_\odot$ and remains relatively constant for larger $M_{\rm MS}$. These two effects combine to make the mean C/O ratio in an exploding WD decrease with $M_{\rm MS}$ slowly for low-mass stars $M_{\rm MS} \simeq$ 1.5–5 $M_\odot$ and much more rapidly for higher mass stars with $M_{\rm MS} \simeq$ 5–7 $M_\odot$. In turn, this makes the explosion energy of a WD more sensitive to $M_{\rm MS}$ when $M_{\rm MS}$ is large.

The mass of the WD core is sensitive to the mass of the progenitor on the main sequence and is rather insensitive to the primordial metallicity. To first order, the C/O ratio and thus, the explosion energy decreases with $M_{\rm MS}$. This tendency is generally true for $M_{\rm MS}$ larger than 3 $M_\odot$ independent of assumptions about mixing and nuclear reaction rates. For lower mass progenitors, the total mean C/O ratio varies little with $M_{\rm MS}$. $M_{\rm core}$ decreases with $M_{\rm MS}$, but this effect is almost compensated by a decrease of the local C/O ratio which decreases with $M_{\rm MS}$. Both this effect and the high C/O ratio in shell burning can be understood by nuclear physics and chemical mixing. The local C/O ratio depends mostly on the competition between triple-α, $3\,^4{\rm He} \rightarrow {}^{12}$C, and α-capture on ^{12}C, i.e., $^{12}{\rm C}(\alpha,\gamma)^{16}{\rm O}$. As a three-body reaction, triple-α dominates at high α concentrations whereas $^{12}{\rm C}(\alpha,\gamma)^{16}{\rm O}$ dominates when ^{4}He is depleted (and at high temperature). During the early phases of helium core burning mostly ^{12}C is produced but, eventually it is depleted by $^{12}{\rm C}(\alpha,\gamma)^{16}{\rm O}$. For burning in small convective cores, even moderate chemical mixing keeps ^{4}He at a certain level and prolongs the phase of ^{4}He burning under depleted conditions, reducing carbon. In burning in thin radiative shells, the temperatures are higher and the burning timescales are shorter, therefore less carbon is depleted.

The central density ρ_c at which the WD ignites is controlled by the competition between adiabatic compression caused by accumulation of mass at the surface and energy losses in the center of the WD. As a result, ρ_c depends on a configuration of the binary system, that is on the rate of accretion onto the WD from the stellar companion.

The physics of the ignition process is multi-dimensional in nature. With the exception of Garcia-Senz & Woosley (1995) who find ignition occurs in rising plumes, all multi-dimensional simulations to date show ignition at or near the center due to the downward motion of plumes (Höflich & Stein 2002; Zingale et al. 2009) in the simmering phase. Though relevant for the pre-conditioning of the explosion, variations in the final stage of runaway are of the order of hours (Höflich & Stein 2002) and unlikely to affect the central density. As a result, ρ_c depends on the configuration of the binary system, the evolutionary state of the stellar companion, and the resulting accretion rate.

In what follows, we characterize the initial conditions by ρ_c, and the progenitor characterized by the initial metallicity Z and $M_{\rm MS}$. We use initial distributions of C and O in the core as predicted by the evolutionary calculations of a main-sequence star with appropriate $M_{\rm MS}$. Both during stellar shell burning and He burning during the accretion C/O $\simeq$ 1. Once the stellar and WD evolution has been calculated to the onset of the explosion, the explosion is calculated using one-dimensional DD models taking into account the progenitor evolution, the hydrodynamics of the explosion, detailed nuclear networks with 213 isotopes, the radiation transport, detailed atomic models, and γ-ray transport. Details of the actual models are described in Domínguez et al. (2001) and Höflich (2006).

Domínguez et al. (2001) described the effects of varying the $^{12}{\rm C}(\alpha,\gamma)^{16}{\rm O}$ rate from the high value (Caughlan et al. 1985) used in our calculations to the lower value of Caughlan & Fowler (1988). The effect on the final compositions is large, but we use the value that has been shown to agree with observational constraints (Domínguez et al. 1999, 2001; Metcalfe et al. 2001). Note, however, that the final C/O ratio depends on both the rate and the chemical mixing scheme adopted in the stellar models (see, for example, Straniero et al. 2003).

4.2. Theoretical Light Curves

We calculated B and V light curves of a series of DD models with fixed $\rho_{\rm tr} = 2.3 \times 10^7$ g cm^{-3} which produce explosions with spectral and light curve characteristics of normal bright SNe Ia. Our fiducial model has $\rho_c = 2 \times 10^9$ g cm^{-3}, primordial metallicity Z equal to the solar value $Z_\odot$ (Anders & Grevesse 1989), and $M_{\rm MS} = 5\ M_\odot$. The abundances in the WD are a result of the stellar evolution of a main-sequence star with metallicity, $Z_\odot$. When scaling Z, for elements up to Si, we adopted the [0/Fe] abundance suggested by Argast et al. (2000) which implies smaller variations with redshift for elements up to Si compared with Fe by a factor of 3. This is done because ^{22}Ne affects the explosive nucleosynthesis, whereas Fe determines the opacity, and therefore, the size of the convective He-burning core (for a given mass) and, to some extent, the B-band magnitudes. Note that the effect of primordial metallicity Z on the explosive nucleosynthesis is dominated by the ^{22}Ne abundance and not by the iron abundance because it is the reduction of the proton/nucleon ratio, Y_e, which changes the explosive equilibrium abundances. The light curves presented below illustrate the effects that variations of central density and progenitor mass, $M_{\rm MS}$, have on light curves of SNe Ia.

4.2.1. Influence of Progenitor Mass $M_{\rm MS}$ and Metallicity

Figure 1 presents B and V light curves and $B - V$ of four DD models with fixed $\rho_c = 2\times10^9$ g cm^{-3} and varying $M_{\rm MS}$ and primordial metallicity (upper panels). The lower panels present a differential comparison of light curves normalized to maximum light. The difference is defined as $dM(t) = M(t) - M_f(t)$, where M_f is the magnitude of the fiducial DD model. The figure shows that variations in the progenitor, i.e., the main-sequence mass $M_{\rm MS}$ and metallicity, strongly change the rise to maximum light. These variations are caused by variations in expansion velocity in models with various $M_{\rm MS}$ and hence with various C/O ratios. The expansion velocity decreases when $M_{\rm MS}$ increases and the overall C/O ratio decreases. At the same time, the chemical and density structure of the outer parts of the SN Ia envelope is similar for all DD models. Therefore, variations in the formation of the early light curve are mostly controlled by the rate at which the outer layers expand and become transparent. The faster the expansion rate, the faster the photosphere recedes, and the faster the light curve rises toward maximum (see the upper left panel of Figure 1). The light curve of the $M_{\rm MS} = 7\ M_\odot$ model in Figure 1 rises notably slower than the fiducial light curve while the light curve of $M_{\rm MS} = 1.5\ M_\odot$ model rises somewhat faster. This is reflected as the early time negative and positive dM in the left panels of Figure 1. The effect is more pronounced for

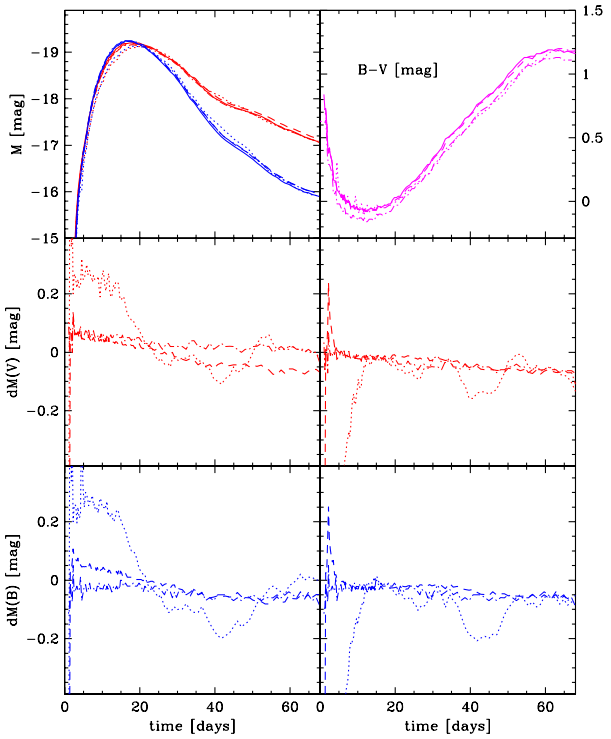

Figure 1. B (blue), V (red) and $B-V$ are given for a number of DD models with the same explosion parameters (Domínguez et al. 2001) and $\rho_c = 2 \times 10^9$ g cm^{-3} (see Section 4) but varying progenitor mass $M_{\rm MS}$ between 1.5 and 7.0 $M_\odot$ and metallicities Z between 0.002 and 0.02 (solar). Models are referenced by the pair of numbers [$M_{\rm MS}$, Z] for [1.5, 0.02] (dashed), [7.0, 0.02] (dotted), and [5.0, 0.002] (dash-dotted). The reference model has $M_{\rm MS} = 5\ M_\odot$, and $Z = 0.02$ (solid). The B (blue) and V (red) magnitudes and the color index $B-V$ are given in the upper right and left panel respectively. The Δm_{15} for both V and B light curves are close to within 0.03 mag but they are not identical. The lower panels show the B and V differentials without and with stretch-correction to the s_f of the reference model on the left and right, respectively (see Table 1).
(A color version of this figure is available in the online journal.)

higher $M_{\rm MS}$ due to the greater sensitivity of $M_{\rm core}$ on $M_{\rm MS}$ near the high end of $M_{\rm MS}$ interval. In particular, a strong secondary extremum develops when $M_{\rm core}$ extends to layers which only undergo incomplete silicon burning. As a consequence, we expect that differential effects are most pronounced in stellar populations with a mix of young and old stars, since these will contain a distribution of $M_{\rm MS}$. We notice also that variations of the progenitor lead to small variations on a 10% level in $B-V$ and its evolution with time (upper right panel). Changing the primordial Z will increase the primordial iron abundance in the outer layers, and, at the expense of ^{56}Ni, more ^{54}Fe will be produced from ^{22}Ne. Primordial metallicity plays a minor role for variations in V, but $B-V$ becomes bluer with decreasing primordial metallicity. This direct "photospheric" effect does not change the visual LCs but the B and UV light curves (Höflich et al. 1998). The evolution in $B-V$ is similar to and has been discussed in Krisciunas et al. (2003).

If we were to "observe" these four supernovae, match their light curves by applying the stretch correction, and *then* compare the residual differences we would get the result shown in the lower right panels of Figure 1. We show $dM(t)$ after matching the light curves around maximum and determining the stretch over the range up to $\simeq 15$ days past maximum light. The end result is essentially identical light curves near and past maximum with the exception of a strong deviation in the rise time for the light curve with the highest $M_{\rm MS} = 7\ M_\odot$ and a small deviation of the same light curve approximately 30 days past maximum. The pre-maximum deviation of the $M_{\rm MS} = 1.5\ M_\odot$ light curve is smaller but still visible at the level of $\simeq 0.1$ mag.

There has long been a suspicion that the metallicity of the progenitor should be associated with the luminosity at peak (Wang et al. 2001; Hamuy et al. 1995; Branch et al. 1996). Recently, attempts have been made to measure directly the average metallicity in the environment of the SN using either line indices or ratios (Hamuy et al. 2000; Gallagher et al. 2005, 2008) or by measuring the spectral energy distribution (SED) of the galaxy (Howell et al. 2009). These studies have failed to confirm the expected shift in peak luminosity with metallicity. Nuclear physics predicts that primarily due to increased amounts of the neutron-rich ^{22}Ne there should be a direct correlation between the amount of ^{56}Ni produced and the progenitor metallicity (Timmes et al. 2003). Recent results (Howell et al. 2009; Neill et al. 2010) find a weaker than expected dependence of metallicity on ^{56}Ni, whereas Gallagher et al. (2008) report a metallicity dependence in the Hubble residual, but not the peak luminosity. From the results of Argast et al. (2000), the variation of elements below Si (including Ne) varies less than Fe by about a factor of 3, thus the sensitivity of the peak brightness is smaller than would be found by just scaling all elements to the iron abundance. Theoretical attempts to find correlations between metallicity and peak luminosity (or light curve shape) have not followed the detailed stellar evolution through to explosion, but have rather just altered the nucleosynthetic yields post-explosion and calculated the light curve, scaling just on the iron abundance (Kasen et al. 2009).

4.2.2. *Influence of Central Density* ρ_c

Figure 2 shows the same type of comparison as Figure 1 but for a series of models with fixed $M_{\rm MS} = 5\ M_\odot$ and solar metallicity, and with varying accretion rate which leads to a central density $\rho_c = 1.5 \times 10^9$, 2×10^9, and 6×10^9 g cm^{-3} which, in our models, corresponds to late-time accretion rates of 1×10^{-7}–$2 \times 10^{-6}\ M_\odot$ yr^{-1}. Figure 2 shows small differences between the light curves prior to maximum light. They are virtually unnoticeable in the upper panels of Figure 2 but can be clearly seen on the differential plots (lower left panel). These differences arise due to small variations in the binding energy of WD models with different ρ_c. When ρ_c increases, so does the binding energy, and this translates into a somewhat smaller expansion velocity. As a result, light curves with larger/smaller ρ_c rise slower/faster and this results in a negative/positive pre-maximum differential dM.

We can also see that variations in ρ_c have a significant effect on the behavior of light curves which begin to show up at $\simeq$20–25 days after maximum light. Variations in ρ_c lead to a noticeable shift of the late time light curve with respect to the absolute magnitude at maximum light. The light curves shift up or down when ρ_c decreases or increases, respectively. This effect is related to the existence of the central hole in the distribution of ^{56}Ni in Chandrasekhar-mass models of SNe Ia. Due to increasing electron capture with density, the nuclear statistical equilibrium shifts away from ^{56}Ni to stable isotopes of the iron group when the central density of a WD increases. Near maximum and shortly past maximum light the envelope of an SN Ia is rather opaque and γ-rays emitted near the center are trapped and do not contribute to the formation of the light curve. The light curve around maximum light is controlled by

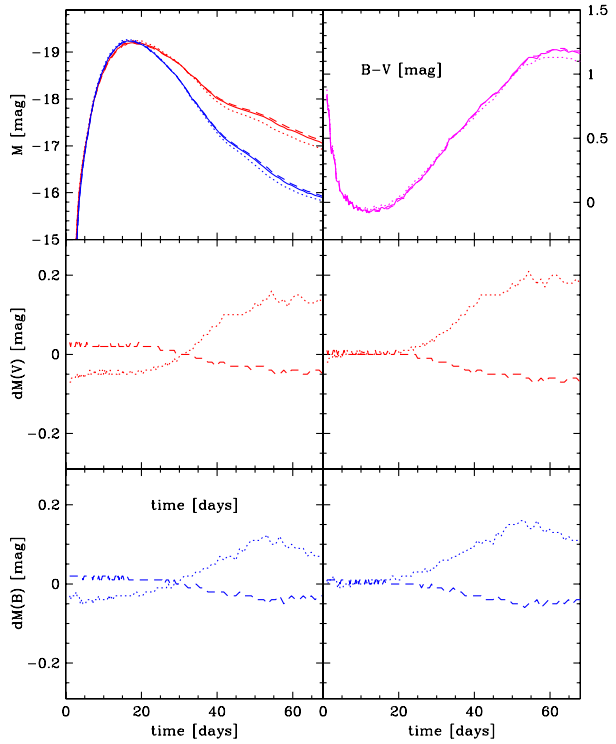

Figure 2. Same as in Figure 1 but compares models with fixed $M_{\rm MS} = 5\ M_\odot$ and $Z = 0.02$ and with varying central densities $\rho_c/(10^9$ g cm$^{-3})$ of 1.5 (dashed), 2.0 (solid), and 6 (dotted). The central density is due to variations in the accretion rate (see Figure 6 of Höflich 2006).

(A color version of this figure is available in the online journal.)

the distribution of ^{56}Ni in the outer parts of the supernova. As time goes on, the envelope expands and the distribution of ^{56}Ni near the center begins to influence the formation of the light curve. Larger central density means a larger hole and less ^{56}Ni. As a result, the light curve of an SN Ia with higher ρ_c becomes shifted down with respect to maximum. With decreasing ρ_c the hole is smaller which means more ^{56}Ni and the resulting shift of the light curve is positive. Note that $B - V$ is very similar but at late times differs from the "general blue shift" produced by variations in progenitors. The lower right panels of Figure 2 again show the differentials when a stretch correction has been applied. Small pre-maximum differences in the light curves have virtually disappeared. However, shifts in the late light curves caused by variations of ^{56}Ni near the center remain very pronounced.

Variations in some of the characteristics of light curves associated with variations in ρ_c and $M_{\rm MS}$ are summarized in Table 1. Table 1 shows that brightness of SNe Ia in both M_V and M_B increases monotonically from -19.25 to -19.11 and -19.32 to -19.18 mag, respectively, when $M_{\rm MS}$ decreases from 7 to 1.5 $M_\odot$ when other parameters, $\rho_{\rm tr}$, Z, and ρ_c, are kept constant. These variations are of the order $\simeq 0.1$ mag. Variations of M_V and M_B with ρ_c are smaller, ± 0.03 mag, because ρ_c mostly affects the electron-capture in the center of the SN Ia which hardly contributes to the SN Ia luminosity at maximum. The effect of metallicity Z can be seen by comparing the fiducial model (first model) of Table 1 with $Z = 0.02$ and the fifth model with $Z = 0.002$. Z affects both M_B and M_V and has a pronounced influence on the $B - V$ colors of SNe Ia.

Table 1
Properties of Calculated SNe Ia

Parameter	Model A	Model B	Model C	Model D	Model E	Model F	Model G
$M_{\rm MS}$	5.0	1.5	3.0	7.0	5.0	5.0	5.0
Z	0.02	0.02	0.02	0.02	0.002	0.02	0.02
ρ_c	2.0	2.0	2.0	2.0	2.0	1.5	6.0
M_V	−19.21	−19.25	−19.22	−19.11	−19.15	−19.19	−19.26
t_V	18.24	18.12	18.19	19.5	18.52	18.24	18.24
$B - V$	−0.02	−0.06	−0.03	−0.01	−0.13	0.03	0.01
M_B	−19.23	−19.32	−19.27	−19.18	−19.28	−19.22	−19.26
s/s_f	1.00	0.96	0.97	1.02	0.98	1.0	0.99

Notes. Characteristics of theoretical light curves of DD models with various progenitor mass $M_{\rm MS}/M_\odot$, metallicity Z, and central density ρ_c in units of 10^9 g cm^{-3}. Model A is the fiducial model with $M_{\rm MS} = 5.0\,M_\odot$, $Z = 0.02$ and $\rho_c = 2.0 \times 10^9$ g cm^{-3} with $\Delta m_{15} = 1.25$. Listed for all models are the absolute maximum brightness $M_{B/V}$, time of V maximum t_V (in days), and a correction to a stretch parameter, s/s_f, required for making the s-factor of the model equal to that of the fiducial model, s_f.

Variations in ρ_c and $M_{\rm MS}$ have pronounced secondary *differential* effects on stretch-matched light curves as illustrated in Figure 3. (1) $M_{\rm MS}$ influences the rise time of the light curves prior to maximum light. Larger $M_{\rm MS}$ leads to slower rise and vice versa. The upper right plot of Figure 3 shows secondary variations of the absolute visual magnitude of SNe Ia, M_V, and differentials in M_V as a function of $M_{\rm MS}$ for times 25, 42, and 55 days past maximum light. (2) On the other hand, ρ_c influences the light curve $\simeq 30$ days after maximum and later. Increases or decreases in ρ_c cause the later portion of the light curve to shift down or up with respect to maximum, respectively. The upper left plot of Figure 3 shows M_V, and differentials in M_V as a function of ρ_c at 20 and 40 days past maximum light. Secondary variations in $B - V$ for both series of models are given as a function of $M_{\rm MS}$ or ρ_c in the lower left plot of Figure 3. All the plots illustrate the point that there are noticeable secondary variations of color and absolute visual magnitude of stretch-matched supernovae which are associated with variations of secondary parameters.

Finally, the lower right plot of Figure 3 summarizes the relation of a predicted relative variation in absolute brightness of SNe Ia (the quantity which cannot be determined from observations unless the absolute brightness of SNe Ia has been measured using an independent method of calibration) and relative secondary variations (differentials) of stretch-matched light curves of SNe Ia which may be directly accessible to observations. This plot shows that secondary variations in M_V of stretch-matched supernovae may reach 0.2 mag.

5. ANALYSIS OF OBSERVATIONS

The above theoretical considerations guide us in our differential analysis of observed light curves of SNe Ia.

Below we present a differential comparison of V and B light curves of several SNe Ia obtained by the CSP survey (Figures 4–8). The basic LC properties are given in Table 2. These objects were selected because they were discovered well before maximum, have good time coverage for up to $\simeq 60$ days past maximum light, and very small observational errors. SN 2005na serves as the reference or fiducial model for the comparison. Stretch corrections for all SNe Ia are listed in Table 1. Left panels in each figure show a comparison of light curves with stretch corrections from Table 1. Right panels show the comparison of SNe Ia after we added an additional stretch to their light curves in order to match the s-factor of the fiducial

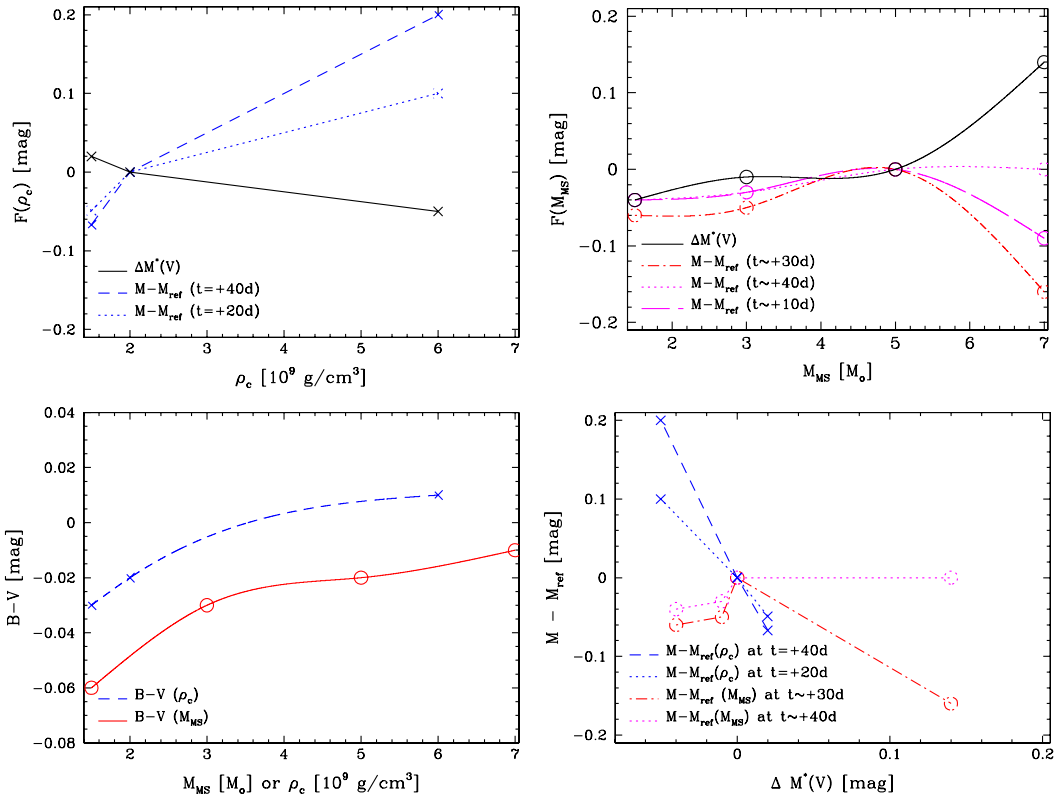

Figure 3. Basic observables in V for models with varying central densities ρ_c (crosses) and main-sequence progenitor masses $M_{\rm MS}$ (open circles) relative to the reference model. All quantities are normalized to the same fiducial s factor using the brightness–decline relation (Höflich et al. 2002). The change in absolute brightness at maximum light is $\Delta M^*(V)$, the differential brightness is $M - M_{\rm ref}$ at times $+t$ after maximum light for the ρ_c-series (crosses, upper left) and the 1st (≈+7 days), 2nd (≈ +35 days), and 3rd(≈ +10 days) for the $M_{\rm MS}$-series (open circles, upper right). The corresponding colors $B - V$ (lower left) and $M - M_{\rm ref}$ ($\Delta M^*(V)$; lower right) are shown. Note that the sign of the residual between two SNe Ia is arbitrary depending on the choice of a reference object.

(A color version of this figure is available in the online journal.)

model, SN 2005na. That is, rather than just making the Δm_{15} stretch correction using the formulae of Jha et al. (2006), the curves were stretched such that the luminosity was brought into coincidence with SN 2005na. The additional stretch is rather small since all these objects are in the range of normal bright SNe Ia. This procedure helps reduce primary differences due to the brightness–decline relation (see Section 4).

SN 2005al versus SN 2005na (Figure 4). These supernovae are well within the normal bright range. Early portions of their light curves, less than 25 days after maximum light, are very similar. This is also indicated by the very small difference in s-factors of these supernovae (Table 2). Exact matching gives only a marginal improvement in dispersion in $M - M_{\rm ref}$. Figure 4shows that $M - M_{\rm ref}$ is less than a few hundredths of a magnitude until $\simeq 25$ days after maximum. At later times the V light curves are shifted with respect to each other by $\simeq 0.2$ mag. There is no discernible systematic shift in B. This behavior in V might be explained by variations in ρ_c and the size of ^{56}Ni hole in the center of the SN Ia.

SN 2004ef versus SN 2005na (Figure 5). These two supernovae are different in their pre-maximum behavior and show an extremum between 20 and 40 days in V, both characteristics of variations in the progenitor. There might be a small systematic shift, $\simeq 0.05$ mag, in the late portions of the V light curves as well, although it is less pronounced compared to that of the previous pair SN 2005al and SN 2005na. Differences between SN 2004ef and SN 2005na may indicate both variations in progenitor masses and metallicity, and rather similar ρ_c in these two events.

SN 2005ki versus SN 2005na (Figure 6). Both supernovae are very similar early on with a very small shift in the late time light curves of less than 0.1 mag. They likely have similar values of ρ_c, $M_{\rm MS}$, and metallicity.

SN 2005el versus SN 2005na (Figure 7). These two supernovae show differences in the early light curves, a secondary extremum, and a significant shift in the late time light curves as well. Note that the stretches of SN 2005el and SN 2004ef are very similar, making it not very likely that the huge M(SN 2005el)$-M_{\rm ref}$ can be attributed to differences in s. In terms of SNe Ia models, the difference hints at variations in progenitor mass $M_{\rm MS}$ and ρ_c.

SN 2005am versus SN 2005el (Figure 8). Finally, we present a differential comparison of two supernovae with a large difference in s-values. SN 2005am is a steep decliner with $\Delta m_{15} = 1.61$, whereas SN 2005el is a normal SNe Ia with $\Delta m_{15} = 1.37$. After stretching (Figure 8), the values of M(SN 2004am) and $M_{\rm ref}$ are surprisingly similar. Within the framework of models, this suggests similar progenitor masses and ρ_c.

Contrary to theoretical calculations which predict similar behavior of $M - M_{\rm ref}$ in both B and V, observations show, depending on the example, variations in the B and V morphology. At the moment the reason is not clear. Several effects may play a role: (1) errors in s and the time of maximum $t_{\rm max}$, (2) differences

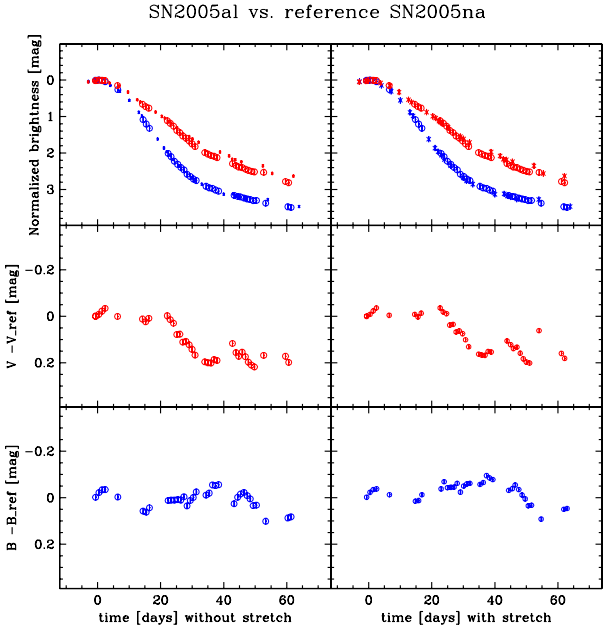

Figure 4. Comparison of SN 2005al to SN 2005na chosen as a reference supernova. Left column: comparison of un-normalized supernovae. Right column: comparison of supernovae normalized to the maximum brightness in V and with the s-factor of SN 2005al adjusted to be equal to the s-factors of SN 2005na. The original s-factors of all supernovae are listed in Table 2. Upper row: B and V light curves. Middle row: differential in V. Lower row: differential in B.

(A color version of this figure is available in the online journal.)

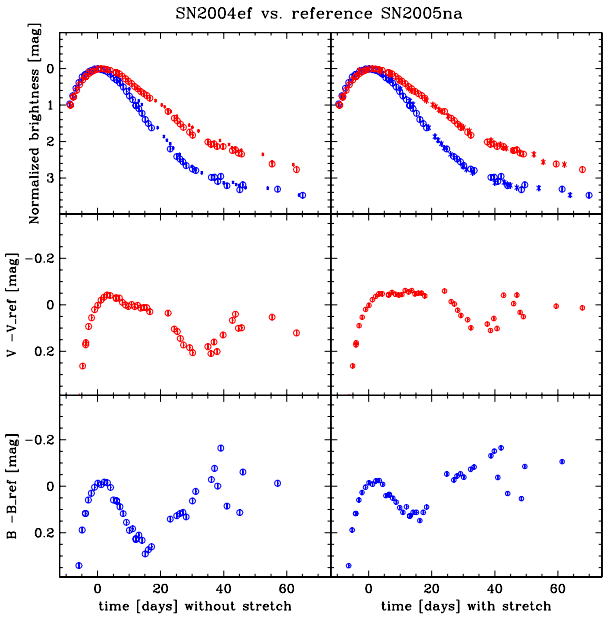

Figure 5. Same as Figure 4 but comparison of SN 2004ef to SN 2005na.

(A color version of this figure is available in the online journal.)

in the theoretical and observational filter functions B and V, and (3) limitations of the explosion models and progenitors.

First, we investigate the stability of differential comparisons of light curves. Matching the time of maximum light $t_{\max}$ of two supernovae may introduce an error in the differential

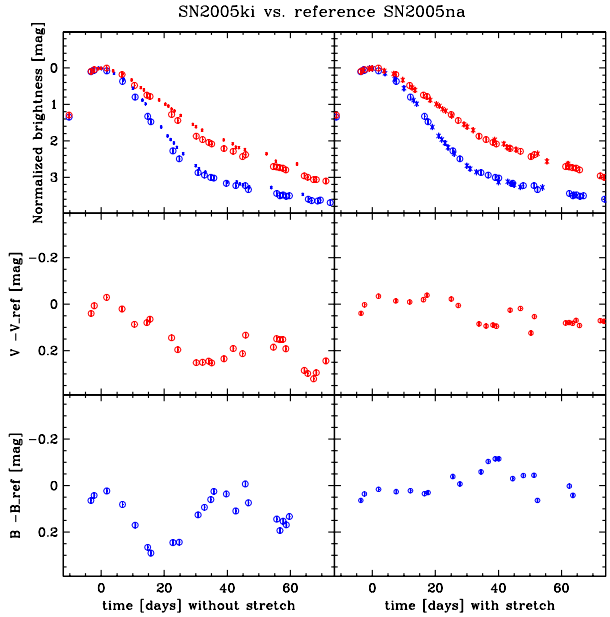

Figure 6. Same as Figure 4 but comparison of SN 2005ki to SN 2005na.

(A color version of this figure is available in the online journal.)

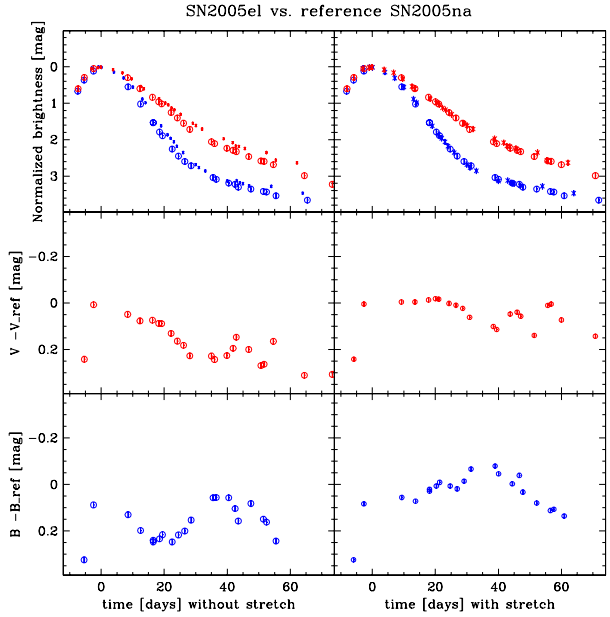

Figure 7. Same as Figure 4 but for SN 2005el. Note the S-shape in $M - M_{\rm ref}$ with a "spread" of about 0.15 mag.

(A color version of this figure is available in the online journal.)

comparison. Another source of the differential error may be small variations in Δm_{15} or s.

Figure 9 shows the effects of a relative shift of $t_{\max}$ and a variation of Δm_{15} of supernovae SN 2004am and SN 2004el. These two supernovae represent a pair with different rise times and a corresponding deviation at $\simeq 30$ days after maximum. As discussed in Section 4, this may be attributed to variations in the progenitor masses of these two objects. The differentials between supernovae of various progenitors are more sensitive to uncertainties in the observables than those with the ρ_c-signature because the former show variations at both early and late times.

Table 2
Properties of Observed SNe Ia

SN	Δm_{15}[a]	s[b]	t_B/m_B[c]	t_V/m_V[c]	δB(r/s)[d]	δV(r/s)[d]
2004ef	1.47		264.96	264.54	0.09/0.05	0.00/−0.03
	1.33	0.88	16.92	17.06	0.03/−0.07	0.14/0.04
2005al	1.19		429.47	430.96	−0.01/−0.02	−0.01/−0.01
	1.24	0.92	15.08	15.08	0.01/−0.03	0.16/0.13
2005am	1.56		437.10	437.53	0.12/−0.01	0.02/−0.07
	1.61	0.75	13.76	13.84	0.14/−0.09	0.29/−0.06
2005el	1.36		646.86	647.51	0.14/0.07	0.04/0.00
	1.37	0.86	15.24	15.22	0.13/0.02	0.24/0.08
2005ki	1.44		705.98	706.20	0.12/0.03	0.03/−0.01
	1.41	0.85	15.69	15.65	0.10/−0.04	0.24/0.07
2005na	1.19		740.32	741.79	0.00/0.00	0.00/0.00
	1.19	0.95	16.26	16.25	0.00/0.00	0.00/0.00

Notes.
[a] Top values of Δm_{15} are the values for a family of BV templates for which the B-band template gives the best fit to *all* B-band data. Bottom values are derived from the "early" subset of B data. This subset includes data which extends to the inflection point, some time 20–25 days after maximum light, where the second derivative of m_B changes sign.
[b] s-Factor is derived from the bottom value of Δm_{15} (for the early subset of B-data; see note (1)) using relation between s and Δm_{15} given in Jha et al. (2006).
[c] Time (top number) and apparent maximum brightness (bottom number) at the truncated Julian Date is "JD−2,453,000."
[d] Average difference (in mag) between B and V light curves relative to SN 2005el. Pairs of numbers are differences for raw (r) and stretched (s) data. Top pair is determined using the early subset of data. Bottom pair is determined using all data. See note (a).

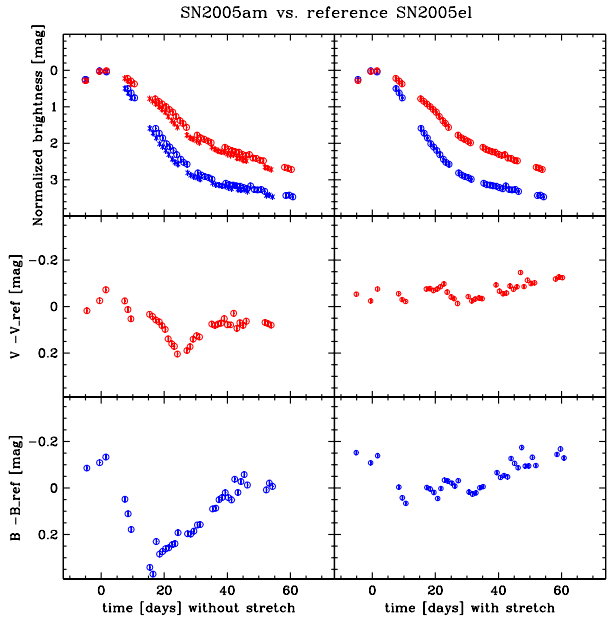

Figure 8. Same as Figure 7 but comparison of SN 2005am and SN 2005el. Here, we used an offset in stretch s and in t_B of 0.01 and 0.5 days compared to Table 2, respectively. The morphology of $M - M_{\rm ref}$ does not change, but the graph is "tilted" by about 0.1 mag.
(A color version of this figure is available in the online journal.)

Maxima were shifted by ±1 day and 2 days, and s by ±0.1. The figure clearly shows that the morphology of $M - M_{\rm ref}$ in V is stable, namely the rise, a rather flat part around maximum, and a dip at day 30. The variation of the differentials over the dip is less than 0.05 mag. For B, we still see that the main characteristics of $M - M_{\rm ref}$ in B are stable, namely extrema at ≈15 and 40 days, but they are larger than those in V in size, e.g., the first dip varies by almost 0.3 mag.

The difference in the shapes of B and V differentials appear to be real including the differences in B between observed and predicted morphology. In part, the size of the first B-dip may be caused by fringing, i.e., shifts of LCs with several maxima and minima, but hardly goes away.

One possible effect is a wavelength offset in the B filters. Another group of effects includes limitations inherent to the models: (1) Metallicity variations for stars with the same progenitor show differences of less than 0.05 mag (Figure 1), a value consistent with detailed spectral analyses (Lentz et al. 2001; Höflich 2006). However, uncertainties in our progenitor evolution during central He-burning may underestimate the variations in progenitors. (2) In B at this level of accuracy, we may be seeing limitations inherent in spherical models. After maximum light, B is very sensitive to temperature variations because it is formed by the Wien tail of the source function, $S \propto e^{-h\nu/kT}$, where S is the source function in the radiative transfer equation. For example, small variations of ^{56}Ni mixing will increase the temperature and, at the same time, the blocking in B. Indeed, off-center DDT models show spectral changes in B which are compatible to the size of the deviation we find (Höflich et al. 2006; Kasen et al. 2009). However, strong rotational mixing is rather unlikely because the impact on the brightness–decline relation and other observational constraints discussed in Section 1. As seen above, uncertainties in the determination of $t_{\rm max}$ and s have moderate influence on the differential in V, but may amplify differences in B.

6. DISCUSSION AND CONCLUSIONS

We analyzed a set of high-quality uniform V and B light curves of SNe Ia obtained by the CSP. These data provide clear evidence for the existence of secondary variations in SN Ia light curves which are independent of the primary Phillips relation and, thus, for the existence of at least two independent secondary parameters. Comparison of the data with a series of non-LTE light curve calculations of DD explosions indicates that these secondary parameters may be physically related to variations of central density, ρ_c of a Chandrasekhar-mass WD exploding as an SN Ia and to variations of the main-sequence mass, $M_{\rm MS}$, of the primary stellar companion in a progenitor binary stellar system.

It is generally accepted that the total amount of ^{56}Ni produced in the explosion is the primary parameter that controls the absolute brightness and the rate of post-maximum decline. Production of nickel depends mainly on the transition density $\rho_{\rm tr}$ at which subsonic burning turns into a supersonic detonation. However, if $\rho_{\rm tr}$ were the only parameter describing the explosion we would have a perfect one-dimensional sequence of SN Ia events and a one-dimensional family of light curves. Some previous attempts to find additional parameters were done by comparing the rise times of the nearby SNe Ia sample to that of the distant one. Riess et al. (1999) claimed to see a significant difference; however, Goldhaber et al. (2001) did not find the effect to be statistically significant.

The high-quality light curves of SNe Ia obtained by the CSP clearly show that one parameter is insufficient to characterize the light curve. Light curves of several CSP supernovae shown in Section 5 illustrate the fact that two supernovae with identical behavior at maximum light and the early portion of the

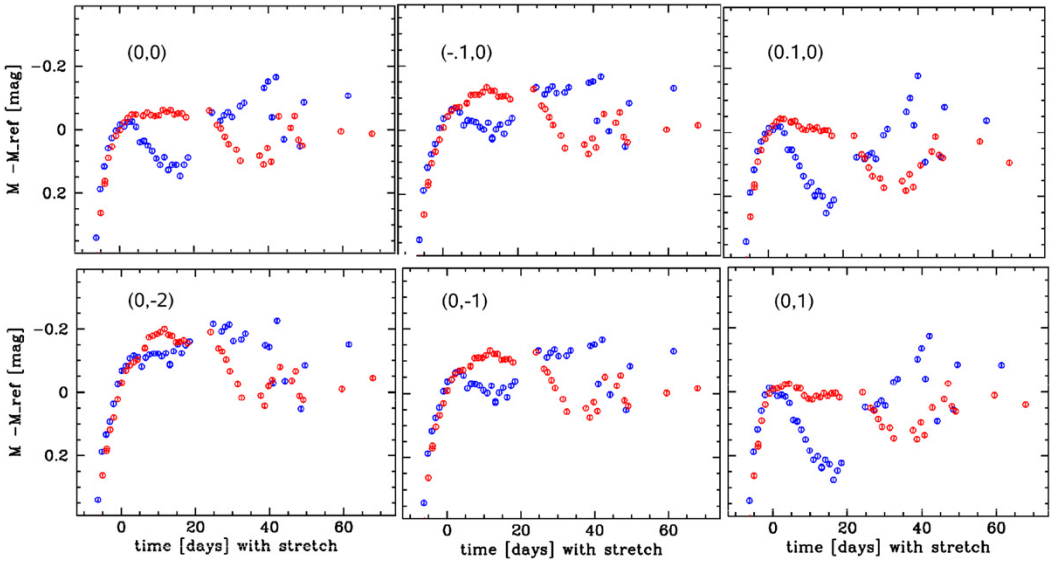

Figure 9. Influence of uncertainties in Δm_{15} and the time of maximum $t_{\max}$ on the differential comparison of SN2004ef and SN2005na (Figure 5). Panels are marked by the assumed variations in Δm_{15} and $t_{\max}$, $(\delta(\Delta m_{15}), \delta(t_{\max}))$. Time is in days. The functional form of the differential in V appears to be stable including the early rise, the extended plateau and the extremum at about 3 weeks past maximum. The functional form of the differential in B also appears to be stable although quantitatively the differential is more sensitive to the variations.

(A color version of this figure is available in the online journal.)

post-maximum light curve, 0–30 days past maximum, may behave differently prior to maximum as well as at late times (>30 days past maximum light). In particular, SNe Ia that are similar near maximum may have different pre-maximum rise and may have the late portion of the V light curve ($\geqslant$30 past maximum light) shifted up or down by different amounts with respect to maximum. Examples presented in Section 5 show that these differences may reach 0.2–0.3 mag.

Light curve modeling (Section 4) predicts that two supernovae with identical behavior of light curves near maximum may exhibit small differences in the rise time to maximum and small shifts of the light curves with respect to maximum luminosity at times $\geqslant$ 30 days after maximum. These variations may be traced to variations in initial central density, ρ_c, and the WD progenitor mass on the main sequence, $M_{\rm MS}$. Instead of $M_{\rm MS}$, one may consider the carbon–oxygen ratio (C/O) in the pre-exploding WD as a second parameter. As far as light curves of SNe Ia are concerned, these parameters, ρ_c and $M_{\rm MS}$ (or C/O), may be treated as "independent" secondary parameters characterizing the light curve in addition to its main characterization via Δm_{15} or stretch. Theoretical predictions seem to be qualitatively consistent with two distinct morphological types of deviations shown by observations in V (Section 5). The B light curves also show distinct morphological types of deviations but the morphology appears to be different from that of the V light curves. In contrast, light curve modeling predicts similar morphological behavior in V and B. We note that most of the energy flux is coming in the V band and thus the calculations of the V light curves should be more reliable. The reason for the discrepancy in B is not clear and requires further investigation.

The existence of independent secondary parameters in SNe Ia has several important implications. Obviously, any calibration of supernovae using a one-parameter set of light curve templates should lead to systematic errors in template matching and to calibration errors. The results of this paper indicate that a set of light curve templates should form at least a three-parameter family. Our analysis suggests that a physically motivated set of templates may be constructed by using a primary SN Ia template parameterized by Δm_{15} or stretch with (1) an additional correction of the slope of the pre-maximum light curve and (2) an additional offset of the late V light curve with respect to maximum. Physically, the primary parameter Δm_{15} should be thought of as a parameter which reflects variations in the amount and distribution of ^{56}Ni in the outer parts of the SNe Ia envelope responsible for the formation of the early post-maximum part of the light curve. The rise time correction might reflect the variation in the C/O ratio, and the offset of the light curve at later times might reflect variations in initial central density ρ_c and the amount and distribution of ^{56}Ni in the central parts of the envelope.

However, producing a multi-parameter set of light curve templates is not sufficient for improving the calibration procedure. The crucial point is that variations of initial conditions responsible for secondary parameters must also cause, according to theoretical predictions, small variations in absolute brightness of SNe Ia. The calibration must take the dependence of the absolute brightness on secondary parameters into account. By matching the proposed multi-parameter templates with high-quality observations, it should be possible to account for secondary variations in the intrinsic brightness and to reduce the calibration errors. High-quality data are not sufficient at this time for carrying out such a program systematically. However, this work clearly indicates the potential of high-quality uniform sets of observations for studying secondary variations in SN Ia light curves and for providing important theoretical clues about physical mechanisms of such variations. One may hope that with improvements in SN Ia theory, verified with observations of nearby supernovae, it would be possible to predict variations of absolute brightness of SNe Ia as a function of secondary parameters. This, in turn, may provide an opportunity to predict evolutionary effects in SNe Ia calibration related to systematic changes in initial conditions with redshift.

Finally, we have to address the promise and limitations of this study. Our quantitative theoretical predictions depend on our exact treatment of the explosion mechanism and stellar evolution. Thus, variations in the treatment of convection, the $^{12}C(\alpha, \gamma)^{16}O$ rate, rotation, and three-dimensional explosive effects could be important at some level. Nevertheless, we have tested the trends that we predict on a small number of SNe Ia and they should be tested on a large and homogeneous set of SNe Ia. Our preliminary results are promising. Light curves for a large number of SN are/will be available by projects such as the ESSENCE (ESSENCE 2009), CFH (SNLS 2009), Cfa3 (Hicken et al. 2009), NSNF (Aldering et al. 2002), PTF (Rau et al. 2010), and LSST (LSST 2009), and we will publish an extensive comparison. The properties of the components, i.e., the shape in $M - M_{\rm ref}$, may be based on theoretical models and optimized using large data sets. However, even if our results are confirmed fully, systematic theoretical studies including three-dimensional effects will be essential to go further. As discussed in Section 1, SN Ia physics is intrinsically three dimensional and thus those effects must be taken into account. However, the last decade or so of theoretical work indicates that the effect should not be dominant since it appears from the observations that three-dimensional effects, such as the rotation of the WD and the position of initial ignition, are reduced by the effects of the deflagration and DDT (e.g., Khokhlov 1995; Khokhlov et al. 1997; Niemeyer 1999; Reinecke et al. 2002; Gamezo et al. 2003, 2005; Plewa et al. 2004; Livne et al. 2005; Röpke & Hillebrandt 2005). For a review see Höflich (2006). Finally, we return to the implications of asymmetry for the use of SNe Ia for cosmology. A 10% asymmetry of the photosphere would not cause systematic difficulties for using SNe Ia as distance indicators at the current level of accuracy of about 20% (Wang et al. 2003) though it would require that most of the dispersion has to be attributed to asymmetry. We note that if such effects are present, then SNe Ia are even more homogeneous than they seem from current dispersions in peak brightness. This level of asymmetry would, however, cause a directional dependence of the luminosity of order $\sim$0.1 mag (Höflich 1991) and a corresponding, but smaller, dispersion in the brightness–decline relation of SNe Ia. This dispersion depends on the viewing angle dependence of the luminosity variation and, thus, the nature of the asymmetry. The angle dependence of the luminosity due to the viewing angle θ of a single SN Ia will not, in general, vary as the line of sight to the equator as $\cos\theta$. A more stringent limit comes from observations of individual supernovae. The first broadband survey by Wang et al. (1996) established that SNe Ia have very low polarization at a level of $P \sim 0.2\%$ whereas core-collapse SNe are generally more highly polarized $P \sim 1$ quality polarimetry measurements indicating that SNe Ia are more highly polarized before maximum, and a few weeks past maximum the polarization disappears (Wang et al. 2003). SN 2004dt showed that SNe Ia have spectral feature dependent polarization, implying different chemical species have different geometry (Wang et al. 2006; Patat et al. 2009). Since the continuum polarization at maximum light is observed to be $P < 0.2\%$ which, for scattering dominated atmospheres, translates into a directional dependence of the flux at the 0.05% level (Höflich 1991; Wang et al. 1997b, 2003; Howell et al. 2001; Wang & Wheeler 2004; Wang et al. 2006; Fesen et al. 2007; Patat et al. 2009), one expects that while three-dimensional effects are important for understanding the explosion mechanism, their observational effects are relatively small. However, as summarized in Wang & Wheeler (2008), asymmetries lead to a dispersion in the color terms which can be magnified significantly when extinction corrections are applied. Other independent factors will contribute to the error and dispersion such that the interaction within the progenitor system or the primordial metallicity require early time spectra, and/or a combination of optical and IR data.

We thank the anonymous referee for a very careful reading of the manuscript and critical comments that much improved the presentation. We thank Inma Dominguez for a careful reading of the manuscript and helpful discussions and comments. The work presented in this paper has been carried out within the NSF project "Collaborative research: Three-Dimensional Simulations of Type Ia Supernovae: Constraining Models with Observations" whose goal is to test and constrain the physics of supernovae by observations and improve SNe Ia as tools for high-precision cosmology. The project involves the University of Chicago (AST-0709181), the University of Oklahoma (AST-0707704), Florida State University (AST-0708855), Texas A&M (AST-0708873), the University of Chile in Santiago, and the Las Campanas Observatory, Chile. This research was also supported, in part, by the NSF grant AST-0703902 to P.A.H. and US Department of Energy Award Number DE-FG02-07ER41517 to E.B. M.H. and G.F. acknowledge support from Fondecyt (1060808 and 3090004), Programa Iniciativa Científica Milenio de MIDEPLAN' (P06-045-F), and CONICYT (FONDAP 15010003 and PFB 06). The authors are especially grateful to the members of the Carnegie Supernova Project team for the access to observational data prior to publication.

REFERENCES

Aldering, G., et al. 2002, Proc. SPIE, 4836, 61
Anders, E., & Grevesse, N. 1989, Geochim. Cosmochim. Acta, 53, 197
Argast, D., Samland, M., Gerhard, O. E., & Thielemann, F.-K. 2000, A&A, 356, 873
Badenes, C., Hughes, J. P., Cassam-Chenaï, G., & Bravo, E. 2008, ApJ, 680, 1149
Baron, E., Jeffery, D. J., Branch, D., Bravo, E., Garcia-Senz, D., & Hauschildt, P. H. 2008, ApJ, 672, 1038
Branch, D., Romanishin, W., & Baron, E. 1996, ApJ, 465, 73
Bravo, E., & Garcia-Senz, D. 2006, ApJ, 642, 457
Bravo, E., & Garcia-Senz, D. 2009, ApJ, 695, 1244
Bravo, E., Garcia-Senz, D., Caezon, R. M., & Dominguez, I. 2009b, ApJ, 695, 1257
Caughlan, G. R., & Fowler, W. A. 1988, At. Data Nucl. Data Tables, 40, 283
Caughlan, G. R., Fowler, W. A., Harris, M. J., & Zimmerman, B. A. 1985, At. Data Nucl. Data Tables, 32, 197
Chamulak, D. A., Brown, E. F., Timmes, F. X., & Dupczak, K. 2008, ApJ, 677, 160
Contreras, C., et al. 2010, AJ, in press (arXiv:0910.3330)
Domínguez, I., Chieffi, A., Limongi, M., & Straniero, O. 1999, ApJ, 524, 226
Domínguez, I., & Höflich, P. 2000, ApJ, 528, 854
Domínguez, I., Höflich, P., & Straniero, O. 2001, ApJ, 557, 279
Ellis, R. S., et al. 2008, ApJ, 674, 51
ESSENCE. 2009, ESSENCE Project, http://www.ctio.noao.edu/wproject/
Fesen, R. A., et al. 2007, ApJ, 658, 396
Folatelli, G., et al. 2010, AJ, 139, 120
Gallagher, J., et al. 2005, ApJ, 634, 210
Gallagher, J. S., et al. 2008, ApJ, 685, 752
Gamezo, V. N., Khokhlov, A. M., & Oran, E. S. 2005, ApJ, 623, 337
Gamezo, V. N., Khokhlov, A. M., Oran, E. S., Ctchelkanova, A. Y., & Rosenberg, R. O. 2003, Science, 299, 77
Garcia-Senz, D., & Woosley, S. E. 1995, ApJ, 454, 895
Gerardy, C. L., et al. 2007, ApJ, 661, 995
Goldhaber, G., et al. 2001, ApJ, 558, 359
Hamuy, M., Phillips, M. M., Wells, L. A., & Maza, J. 1993, PASP, 105, 787
Hamuy, M., et al. 1995, AJ, 109, 1
Hamuy, M., et al. 2000, AJ, 120, 1479

Hamuy, M., et al. 2006, PASP, 118, 2
Hicken, M., et al. 2009, ApJ, 700, 331
Höflich, P. 1991, A&A, 246, 481
Höflich, P. 1995, ApJ, 443, 89
Höflich, P. 2006, Nucl. Phys. A, 777, 579
Höflich, P., Gerardy, C., Fesen, R., & Sakai, S. 2002, ApJ, 568, 791
Höflich, P., Gerardy, C. L., Marion, H., & Quimby, R. 2006, New Astron. Rev., 50, 470
Höflich, P., Gerardy, C. L., Nomoto, K., Motohara, K., Fesen, R. A., Maeda, K., Ohkubo, T., & Tominaga, N. 2004, ApJ, 617, 1258
Höflich, P., Nomoto, K., Umeda, H., & Wheeler, J. C. 2000, ApJ, 528, 590
Höflich, P., & Stein, J. 2002, ApJ, 568, 779
Höflich, P., Wheeler, J. C., & Thielemann, F. K. 1998, ApJ, 495, 617
Höflich, P., et al. 1996, ApJ, 472, L81
Höflich, P., et al. 2004, ApJ, 617, 1258
Howell, D. A., Höflich, P., Wang, L., & Wheeler, J. C. 2001, ApJ, 556, 302
Howell, D. A., et al. 2009, ApJ, 691, 661
Jha, S., et al. 2006, AJ, 131, 527
Jordan, G. C., Meakin, C. A., Hearn, N., Fisher, R. T., Townstey, D. M., Lamb, D. Q., & Truran, J. W. 2009, in ASP Conf. Ser. 406, Numerical Modeling of Space Plasma Flows: ASTRONUM-2008 (San Francisco, CA: ASP), 92
Jordan IV, G. C., Fisher, R. T., Townsley, D. M., Calder, A. C., Graziani, C., Asida, S., Lamb, D. Q., & Truran, J. W. 2008, ApJ, 681, 1448
Kasen, D., Nugent, P., Thomas, R. C., & Wang, L. 2004, ApJ, 610, 876
Kasen, D., Röpke, F. K., & Woosley, S. E. 2009, Nature, 460, 869
Kasen, D., & Woosley, S. E. 2007, ApJ, 656, 661
Kasen, D., et al. 2003, ApJ, 593, 788
Khokhlov, A. 1991, A&A, 245, 114
Khokhlov, A. M. 1995, ApJ, 449, 695
Khokhlov, A. M. 2000, arXiv:astro-ph/0008463
Khokhlov, A. M., Oran, E. S., & Wheeler, J. C. 1997, ApJ, 478, 678
Krisciunas, K., et al. 2003, AJ, 125, 166
Lentz, E., Baron, E., Branch, D., & Hauschildt, P. H. 2001, ApJ, 547, 402
Livne, E., Asida, S. M., & Höflich, P. 2005, ApJ, 632, 443
LSST. 2009, Large Synoptic Survey Telescope, http://www.lsst.org/lsst
Mannucci, F., Della Valle, M., & Panagia, N. 2006, MNRAS, 370, 773
Marion, G. H., et al. 2009, AJ, 138, 727
Mazzali, P. A., Cappellaro, E., Danziger, I. J., Turatto, M., & Benetti, S. 1998, ApJ, 499, L49
Mazzali, P. A., & Podsiadlowski, P. 2006, MNRAS, 369, L19
Mazzali, P. A., Röpke, F. K., Benetti, S., & Hillebrandt, W. 2007, Science, 315, 825
Mazzali, P. A., et al. 2001, ApJ, 547, 988
Meakin, C. A., Seitenzahl, I., Townsley, D., Jordan, G. C., Truran, J., & Lamb, D. 2009, ApJ, 693, 1188
Metcalfe, T. S., Winget, D. E., & Charbonneau, P. 2001, ApJ, 557, 1021
Neill, J. D., et al. 2010, ApJ, in press (arXiv:0911.0690)
Niemeyer, J. C. 1999, ApJ, 523, L57
Patat, F., et al. 2009, A&A, 508, 229
Perlmutter, S., et al. 1999, ApJ, 517, 565
Phillips, M. M. 1993, ApJ, 413, L105
Phillips, M. M., et al. 1999, AJ, 118, 1766
Pinto, P. A., & Eastman, R. G. 2000, ApJ, 530, 744
Piro, A. L., & Bildsten, L. 2008, ApJ, 673, 1009
Plewa, T., Calder, A. C., & Lamb, D. Q. 2004, ApJ, 612, L37
Prieto, J. L., Rest, A., & Suntzeff, N. B. 2006, ApJ, 647, 501
Quimby, R., Höflich, P., & Wheeler, J. C. 2007, ApJ, 666, 1083
Rau, A., et al. 2010, ApJ, 708, 456
Reinecke, M., Hillebrandt, W., & Niemeyer, J. C. 2002, A&A, 391, 1167
Riess, A., Filippenko, A. V., Li, W., & Schmidt, B. P. 1999, AJ, 118, 2668
Riess, A., et al. 1998, AJ, 116, 1009
Röpke, F. K., Gieseler, M., Reinecke, M., Travaglio, C., & Hillebrandt, W. 2006, A&A, 453, 203
Röpke, F. K., & Hillebrandt, W. 2005, A&A, 429, L29
SNLS. 2009, Canada–France–Hawaii Telescope Legacy Survey, http://www.cfht.hawaii.edu/Science/CFHLS/
Straniero, O., Domínguez, I., Imbriani, G., & Piersanti, L. 2003, ApJ, 583, 878
Stritzinger, M., et al. 2002, AJ, 124, 2100
Sullivan, M., et al. 2006, ApJ, 648, 868
Timmes, F. X., Brown, E. F., & Truran, J. W. 2003, ApJ, 590, L83
Umeda, H., Nomoto, K., Kobayashi, C., Hachisu, I., & Kato, M. 1999, ApJ, 522, L43
Wang, L., Höflich, P., & Wheeler, J. C. 1997a, ApJ, 483, L29
Wang, L., Howell, D. A., Höflich, P., & Wheeler, J. C. 2001, ApJ, 550, 1030
Wang, L., & Wheeler, J. C. 2004, in AIP Conf. Ser. 743, The New Cosmology: Conference on Strings and Cosmology, ed. R. E. Allen, D. V. Nanopoulos, & C. N. Pope (Melville, NY: AIP), 77
Wang, L., & Wheeler, J. C. 2008, ARA&A, 46, 433
Wang, L., Wheeler, J. C., & Höflich, P. 1997b, ApJ, 476, L27
Wang, L., Wheeler, J. C., Li, Z., & Clocchiatti, A. 1996, ApJ, 467, 435
Wang, L., et al. 2003, ApJ, 591, 1110
Wang, L., et al. 2006, ApJ, 653, 490
Zingale, M., Almgren, A. S., Bell, J. B., Nonaka, A., & Woosley, S. E. 2009, ApJ, 704, 196

The Astrophysical Journal, 718:957–962, 2010 August 1 doi:10.1088/0004-637X/718/2/957

SEARCHING FOR HYDROGEN IN TYPE Ib SUPERNOVAE

Spencer James[1] and E. Baron[1,2]
[1] Homer L. Dodge Department of Physics and Astronomy, University of Oklahoma, 440 West Brooks, Rm. 100, Norman, OK 73019-2061, USA
[2] Computational Cosmology Center, Lawrence Berkeley National Laboratory, MS 50F-1650, 1 Cyclotron Rd, Berkeley, CA 94720-8139, USA
Received 2010 April 16; accepted 2010 June 7; published 2010 July 8

ABSTRACT

We present synthetic spectral fits of the typical Type Ib SN 1999dn and the hydrogen-rich Ib SN 2000H using the generalized non-local thermodynamic equilibrium stellar atmospheres code PHOENIX. We fit model spectra to five epochs of SN 1999dn ranging from 10 days pre-maximum light to 17 days post-maximum light and to the two earliest epochs of SN 2000H available, maximum light and six days post-maximum. Our goal is to investigate the possibility of hydrogen in Type Ib supernovae (SNe Ib), specifically a feature around 6200 Å which has previously been attributed to high-velocity Hα. In earlier work on SN 1999dn we found the most plausible alternative to Hα to be a blend of Si II and Fe II lines which can be adjusted to fit by increasing the metallicity. Our models are simple; they assume a power-law density profile with radius, homologous expansion, and solar compositions. The helium core is produced by "burning" 4H→He in order to conserve the nucleon number. For models with hydrogen the outer skin of the model consists of a shell of solar composition. The hydrogen mass of the standard solar composition shell is $M_H \lesssim 10^{-3}\,M_\odot$ in SN 1999dn and $M_H \lesssim 0.2\,M_\odot$ for SN 2000H. Our models fit the observed spectra reasonably well, successfully reproducing most features including the characteristic He I absorptions. The hydrogen feature in SN 1999dn is clear, but much more pronounced in SN 2000H. We discuss a possible evolutionary scenario that accounts for the dichotomy in the hydrogen shell mass between these two SNe.

Key words: supernovae: individual (1999dn, 2000H)

Online-only material: color figures

1. INTRODUCTION

1.1. Supernovae Nomenclature

Supernovae (SNe) are divided into two main subtypes, Type I and Type II, based on the presence of hydrogen in their spectra. SNe of Type I are then further subdivided into Types Ia, Ib, and Ic (Wheeler & Harkness 1990). SNe Ia are characterized by strong Si II absorption near 6100 Å and a characteristic sulfur "W"-shaped feature at 5400 Å. SNe Ib are classified by the presence of optical He I lines in their spectra, and SNe Ic are noted for their lack of helium and silicon. SNe Ia are thought to be caused by the thermonuclear explosion of a Chandrasekhar mass white dwarf star while SNe II, Ib, and Ic are caused by the core collapse of a massive star. The general consensus is that most SNe Ib/c result from mass loss due to interaction with a binary companion and that SNe IIb also result from binary interaction (Podsiadlowski et al. 1992, 1993; Nomoto et al. 1995; Heger et al. 2003).

SNe are classified by their spectra. As early spectra become more commonly available, trends in the variation of certain SNe types over the course of time have emerged. This is apparent in SN 1993J which was originally classified as an SN II for its conspicuous hydrogen but later showed helium absorptions characteristic of an SN Ib. SN 1993J is now classified as an SN IIb which is believed to be the explosion of a star that has undergone enough mass loss to lose a large portion of its hydrogen envelope (Filippenko et al. 1993). SN 1987K (Filippenko 1988) and SN 2008ax (Chornock et al. 2010) are other examples of this transitory class of SNe. This explains the distinct Balmer lines seen at early times which give way to significant helium features as time progresses. This type of transition-like object was first suggested by Woosley et al. (1987). It has been suggested that if mass loss from an SN II progenitor can produce SNe IIb, then an even larger mass loss would result in further stripping of the hydrogen envelope and would be characteristic of SNe Ib (Filippenko 1988). This suggests that we might see hydrogen in early spectra of SNe Ib if there was a large enough mass of hydrogen left prior to explosion. Nomoto et al. (1995) also suggest several binary mass loss scenarios that might lead to a spectroscopic sequence of SN types from IIn→IIb→Ib→Ic. By understanding the behavior of these transitory types of SNe we are able to better extrapolate back to the state of the progenitor star. We therefore investigate the early and late time spectra of a typical Type Ib SN 1999dn and the early spectra of a hydrogen-rich SNe Ib SN 2000H (Branch et al. 2002) in search of clues as to whether or not a thin hydrogen skin exists prior to the SN explosion.

1.2. Prior Investigations

The idea that there exists an underlying physical connection between SNe II and SNe Ib is not a new one. As more SNe are discovered at earlier times we see a number of these SNe IIb, which appear to be transition-like objects from Type II→Ib. The recent discovery of SN 2008ax (Chornock et al. 2010) has led to more detailed investigations into the connection between SNe IIb and SNe Ib, and Chornock et al. (2010) suggested that a full non-local thermodynamic equilibrium (NLTE) treatment is necessary for a conclusive analysis of the details of the hydrogen skin.

Branch et al. (2002) conducted a direct analysis of a selection of SN Ib spectra obtained by Matheson et al. (2001) using the SN spectrum synthesis code SYNOW. They concluded that a small amount of hydrogen is present in perhaps all SNe Ib spectra, specifically SN 1999dn, and that even more is seen in what they term hydrogen-rich SNe Ib: 2000H, 1999di, and 1954A. Others (Elmhamdi et al. 2006; Deng et al. 2000; Parrent et al. 2007)

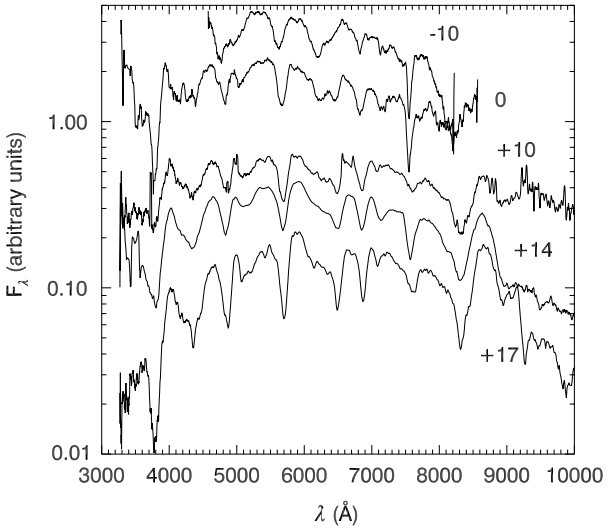

Figure 1. SN 1999dn epochs: emphasis is placed on the 6200 Å absorption feature that fades after maximum light. Observed spectra (Matheson et al. 2001; Deng et al. 2000) have been smoothed with a 10 point boxcar. These spectra were all obtained from the Supernovae Spectrum Repository (SUSPECT), http://suspect.nhn.ou.edu, maintained by the University of Oklahoma.

have also used SYNOW to investigate the presence of hydrogen in SNe Ib.

Because of the relative simplicity of SYNOW a first principle NLTE treatment is needed to analyze the presence of hydrogen in detail. While a SYNOW analysis can determine whether a particular ion is there or not and can also indicate the relative strength and velocity extent of that species, one cannot use SYNOW to determine quantitative abundances. We use the NLTE stellar atmospheres code PHOENIX (Hauschildt & Baron 2004, 1999) to accomplish this. We perform a time-series analysis of the spectra of SN 1999dn, a typical SN Ib, as well as some calculations of early time spectra of another SN Ib, SN 2000H. Benetti et al. (2000) originally classified SN 2000H as an SN IIb due to strong H_α and possible H_β absorptions.

We wish to accomplish the following: (1) produce hydrogen and hydrogen-free fits to relevant epochs of SN 1999dn and SN 2000H; and (2) constrain the possible ejection velocity and mass of the hydrogen skin.

2. METHODS

2.1. General Methods

We generate synthetic spectra of SNe Ib using the NLTE stellar atmospheres code PHOENIX (Hauschildt & Baron 2004, 1999, and references therein). The inclusion of NLTE calculations allows us to investigate the importance of non-thermal processes in reproducing SN Ib spectra. We explore the possibility of the existence of hydrogen in SNe Ib by adding a thin skin of solar composition material (Grevesse et al. 2007) to a helium core (which also has solar compositions of metals). The helium core is constructed by beginning with material at solar composition and then "burning" 4H→He. We then add the hydrogen skin with solar abundances by replacing the abundances above a specified velocity, v_H, which is varied to find the best fit without disturbing the helium core interior to v_H. Our models extend out to a maximum velocity of 21,000 km s^{-1} regardless of whether they are pure helium cores or include a hydrogen skin.

Table 1
Model Parameters: 1999dn

Epoch	$T_{\rm model}$(K)	v_0 (km s^{-1})	v_H (km s^{-1})	M_H ($M_\odot$)
−10	6000	11000	19000	2.95×10^{-4}
0	5250	10000	19000	2.94×10^{-3}
10	5400	7000	19000	2.63×10^{-4}
14	5000	7000	19000	2.63×10^{-4}
17	4600	7000	19000	3.38×10^{-4}

Note. Relevant model parameters for SN 1999dn.

Table 2
Model Parameters: 2000H

Epoch	$T_{\rm model}$(K)	v_0 (km s^{-1})	v_H (km s^{-1})	M_H ($M_\odot$)
0	6000	11000	15000	0.124
+6	5600	10000	15000	0.125

Note. Relevant model parameters for SN 2000H.

We approximate the gamma-ray deposition function by a constant parameter that is adjusted for each epoch. The assumption of a sharp boundary between the hydrogen and helium layers is not realistic, but is simple and eliminates the need to add extra parameters. This approximation should not significantly affect our conclusions.

The earliest model of SN 1999dn is only $M = 0.85\,M_\odot$ as compared with all the other days that are $M = 38\,M_\odot$. This difference in mass was necessary in order to deal with the large variation in the dynamic range of the atmosphere. Nevertheless our models are internally consistent. The very large mass of the progenitor is due to the straightforward extrapolation of the steep power-law density profile to low radii. Here, it is just a calculational expedient and does not imply that the progenitor was anywhere close to this massive.

3. RESULTS

3.1. SN 1999dn

Figure 1 shows the observed spectra for several epochs of SN 1999dn (Matheson et al. 2001; Deng et al. 2000). While we seek the overall best fit to the spectra, emphasis is placed on the absorption feature around 6200 Å which fades after maximum light. The observed spectra are smoothed with a 10 point boxcar average in order to remove some noise.

We explored variations in multiple parameters for each epoch adjusting the total bolometric luminosity in the observer's frame (specified by a temperature, $T_{\rm model}$), the photospheric velocity, the metallicity, the density profile, gamma-ray deposition, and hydrogen mass. By varying these parameters we have arrived at a set of parameters which we consider the best and we follow that model through each epoch. The relevant parameters for SN 1999dn are given in Table 1 and for SN 2000H in Table 2. The results of the NLTE PHOENIX calculations are shown in Figures 2–8. We treat the following species in NLTE: H I, He I–II, C I–III, N I–III, O I–III, Ne I, Na I–II, Mg I–III, Si I–III, Ca I–III, and Fe I–III. In all the spectra we successfully reproduce the characteristic He I absorptions at 5876 Å, 6678 Å, and 7065 Å.

Figure 2 shows the early epoch 1999 August 21 for SN 1999dn (Matheson et al. 2001, −10 days). The synthetic spectrum with hydrogen at 19,000 km s^{-1} fits the 6200 Å feature better than a pure helium core. In the maximum light spectrum, August 31, the hydrogen feature at 19,000 km s^{-1} does not properly blend with the feature just to the red (Figure 3), but this is likely

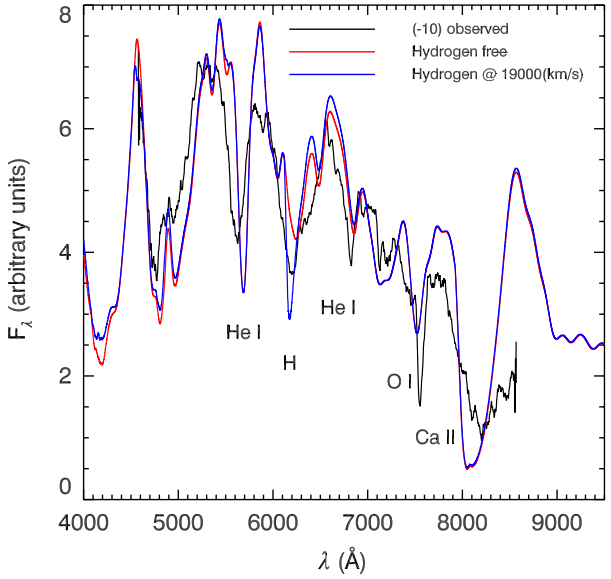

Figure 2. SN 1999dn (−10) observed spectrum (Deng et al. 2000) smoothed with a 10 point boxcar compared to synthetic spectra with and without hydrogen at $v_H = 19{,}000$ km s^{-1}.

(A color version of this figure is available in the online journal.)

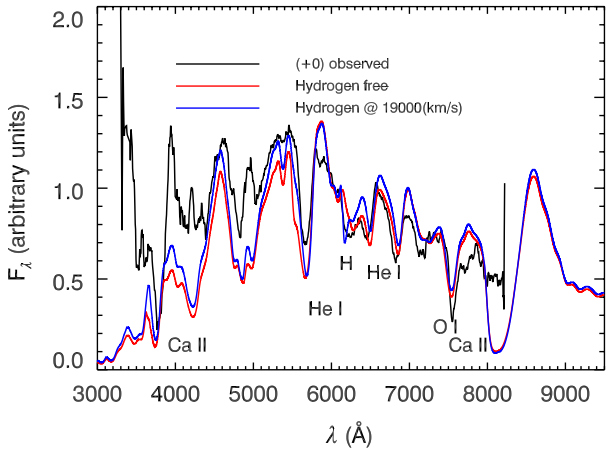

Figure 3. SN 1999dn (0) observed spectrum (Deng et al. 2000) smoothed with a 10 point boxcar compared to synthetic spectra with and without hydrogen at $v_H = 19{,}000$ km s^{-1}.

(A color version of this figure is available in the online journal.)

due to our assumption of a sharp abundance boundary. The detached-like profile (blueshifted absorption with flat topped emission) is a consequence of the abrupt cutoff of our model. The hydrogen velocity is 19,000 km s^{-1} and the outer velocity layer of our model is 21,000 km s^{-1}. A smoother variation in the abundances would reduce the sharp cutoff that leads to the detached profile.

By September 10 the hydrogen feature has faded in both the observed spectrum as well as the synthetic spectra as seen in Figure 4. This is reinforced by the lack of a feature in the later days of the observed spectra.

In Figures 5 and 6, on September 14 and 17, respectively, we find that the inclusion of hydrogen has little if any effect on the spectrum and so conclude that the thin skin of hydrogen is no longer visible due to geometric dilution.

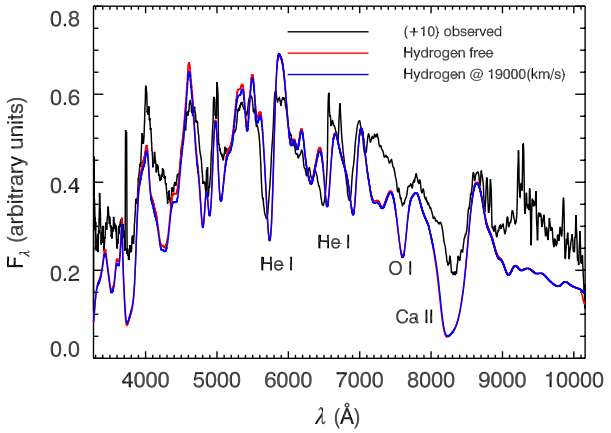

Figure 4. SN 1999dn (+10) observed spectrum (Matheson et al. 2001) smoothed with a 10 point boxcar compared to synthetic spectra with and without hydrogen at $v_H = 19{,}000$ km s^{-1}.

(A color version of this figure is available in the online journal.)

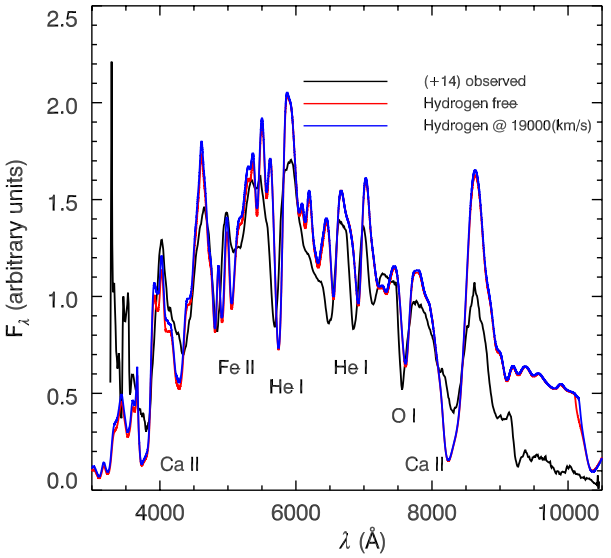

Figure 5. SN 1999dn (+14) observed spectrum (Deng et al. 2000) smoothed with an 8 point boxcar compared to synthetic spectra with and without hydrogen at $v_H = 19{,}000$ km s^{-1}.

(A color version of this figure is available in the online journal.)

The He I absorptions in many of the spectra appear to be slightly to the red of the observed absorptions. This is probably due to the assumption of a constant gamma-ray deposition parameter. By increasing the amount of gamma-ray deposition we increase the non-thermal components of the spectrum which increases the depth of the He I absorptions and also the speed of highly non-thermal lines. A more thorough treatment of the nickel distribution would likely improve this, but examining the exact amount of nickel mixing is beyond the scope of the present work.

3.2. SN 2000H

The earliest spectrum available of SN 2000H is at maximum light, 2000 April 21 (Barbon et al. 2009). Figure 7 shows a very deep and wide absorption trough in the region of H_α absorption. Part of the absorption feature could be due to blending with other

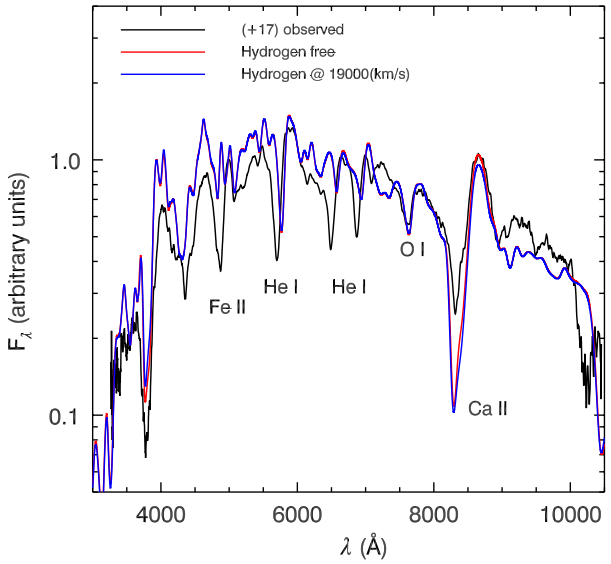

Figure 6. SN 1999dn (+17) observed spectrum (Matheson et al. 2001) smoothed with a 10 point boxcar compared to synthetic spectra with and without hydrogen at $v_H = 19{,}000$ km s^{-1}.

(A color version of this figure is available in the online journal.)

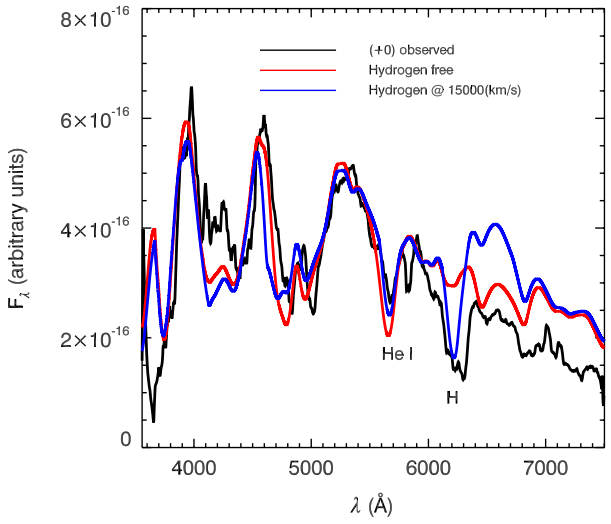

Figure 7. SN 2000H (0) observed spectrum (Barbon et al. 2009) smoothed with a 20 point boxcar compared to synthetic spectra with and without hydrogen at $v_H = 15{,}000$ km s^{-1}.

(A color version of this figure is available in the online journal.)

elements due to circumstellar interaction. Toward the end of this section we discuss the narrow Na D absorption near 5800 Å and the information we can gather about the circumstellar medium (CSM) from it.

Part of the line profile could be due to a low-velocity CSM region but the depth of the line would suggest that we should also see evidence of H_β, which is lacking. This SN is highly reddened. We adopt a reddening value of $E(B-V) = 0.61$ (Benetti et al. 2000) and a recession velocity of $v_{\rm rec} = 3945$ km s^{-1} taken from the NED[3] database.

[3] http://nedwww.ipac.caltech.edu/

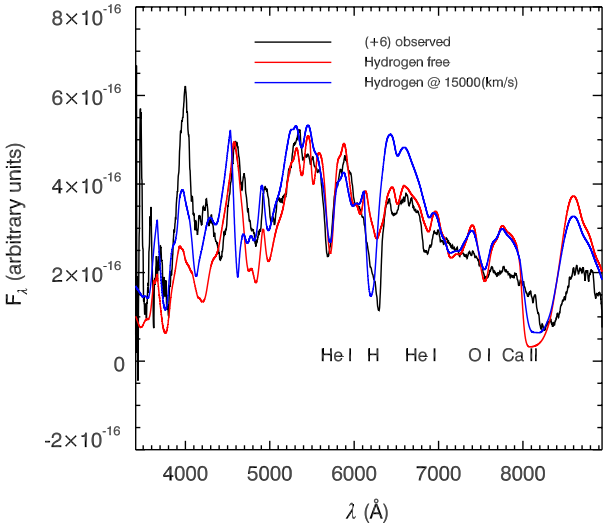

Figure 8. SN 2000H (+6) observed spectrum (Barbon et al. 2009) smoothed with a 20 point boxcar compared to synthetic spectra with and without hydrogen at $v_H = 15{,}000$ km s^{-1}.

(A color version of this figure is available in the online journal.)

We find that the spectrum of SN 2000H at +6 days post-maximum light (Barbon et al. 2009) can also be well reproduced by adding hydrogen to our models as is shown in Figure 8. We find that a hydrogen velocity of $v_H = 15{,}000$ km s^{-1} is necessary to fit the hydrogen feature around 6200 Å. The amount of hydrogen included in the 2000H model ($M_H \lesssim 0.2\,M_\odot$) is significantly greater than in our SN 1999dn models, ($M_H \lesssim 10^{-3}\,M_\odot$), which is consistent with the classification of a hydrogen-rich SN Ib by Branch et al. (2002). This is necessary to fit the hydrogen feature that persists to as late as +6 days post-maximum light. A larger amount of hydrogen suggests that SN 2000H is closer to the Type IIb subtype due to a lower degree of envelope stripping than in SN 1999dn (Benetti et al. 2000; Blondin & Tonry 2007; Chornock et al. 2010).

Figures 9 and 10 show two of the observed spectra of SN 2000H, both with and without a 20 point boxcar smoothing. The narrow Na D absorption around 5800 Å appears to fade quickly since it is not seen in the spectrum taken six days later. In Figure 11, we present a comparison of a SYNOW spectrum of only Na I constrained to 3000–5000 km s^{-1} as well as the case where the Na I is detached from the photosphere but constrained to 3000–3500 km s^{-1} with the maximum light spectrum of SN 2000H with 20, 10, and 5 point boxcar smoothing. The Na I and the 20 point boxcar spectrum look like the best fit, but since the SYNOW spectrum appears too broad to fit the 5 point boxcar the detached spectrum is a better fit in that case. In either case one finds a characteristic velocity of the Na D line to be about 3000 km s^{-1}.

While the Na D feature could be an artifact of the data reduction, it is possible that the feature formed in the surrounding CSM. The SYNOW velocity is large compared to typical wind velocities. Yoon et al. (2010) found wind velocities for different SN Ib/c progenitors ranging from $\sim$200 km s^{-1} to $\sim$2400 km s^{-1}, which at the upper limit could explain the high velocity we find for the Na D feature from the CSM; however, with a hydrogen shell of $\sim$0.1 $M_\odot$, the wind is more likely to be of order 500 km s^{-1}. The high velocity could also be due to radiative acceleration at shock breakout. We

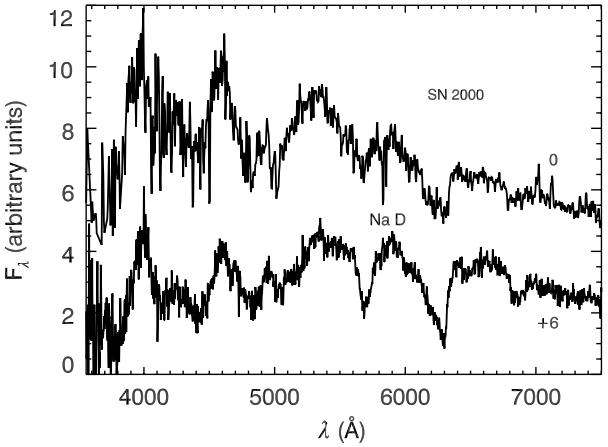

Figure 9. SN 2000H epochs (Barbon et al. 2009) without any smoothing.

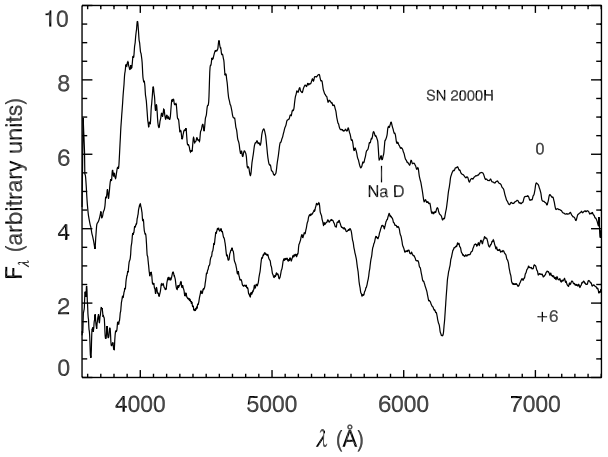

Figure 10. SN 2000H epochs (Barbon et al. 2009) smoothed with a 20 point boxcar.

find the total energy required to accelerate this mass to be $E_{\rm kin} = 2 \times 10^{47}$ erg$(\rho/10^{-15}$ g cm$^{-3})$, where the density is obtained from the SYNOW fit assuming an ionization fraction of 10^{-3}.

4. DISCUSSION

We find that the results from the PHOENIX calculations suggest a hydrogen mass of $M_H \lesssim 10^{-3}\,M_\odot$ for SN 1999dn. This corresponds to a hydrogen velocity $v_H \gtrsim 19{,}000$ km s^{-1}. Tanaka et al. (2009) placed a limit of $M_H \lesssim 5 \times 10^{-4}\,M_\odot$ on the hydrogen mass in SN 2008D and a limit on the Doppler velocity of approximately $v_H \approx 18{,}500$ km s^{-1}. Others have also suggested that hydrogen is responsible for this feature around 6200 Å. Deng et al. (2000) suggested a hydrogen velocity for SN 1999dn of 19,000 km s^{-1} on August 21, and 18,000 km s^{-1} on August 31, and that the feature becomes blended and then taken over by C II in later days. Ketchum et al. (2008) investigated C II, Si II, Fe II, and Ne I as possible candidates as well but found that without increasing the metallicity and abundances beyond physically reasonable amounts the 6200 Å feature was not easily reproduced in early epochs. This seems to be consistent with our calculations, reinforcing the existence of hydrogen in early spectra of SNe Ib.

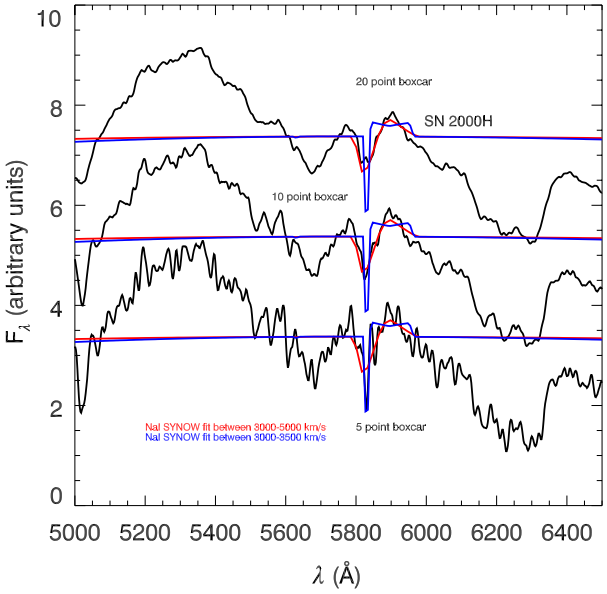

Figure 11. SN 2000H (0) (Barbon et al. 2009) with a 20, 10, and 5 point boxcar plotted with a SYNOW spectrum of Na I between 3000 and 5000 km s^{-1} and detached from the photosphere but constrained to a velocity between 3000 and 3500 km s^{-1}.

(A color version of this figure is available in the online journal.)

We also find that the results from the PHOENIX calculations suggest a hydrogen mass of $M_H \lesssim 0.2\,M_\odot$ for SN 2000H. This corresponds to a hydrogen velocity in our models of $v_H \approx 15{,}000$ km s^{-1}. This mass estimate is likely an upper limit since we assume a single power-law density profile for both the helium core and hydrogen shell. The width of the 6200 Å feature early on is likely due to some blending with some circumstellar material since it disappears in the spectrum six days later and the hydrogen feature is more clear. We know that circumstellar interaction was taking place at maximum light from the presence of the narrow Na D feature that quickly fades. The larger amount of hydrogen is more characteristic of that seen in an SN IIb such as SN 1993J or SN 2008ax with mass estimates on the order of $M_H \gtrsim 0.1\,M_\odot$ (Wheeler et al. 1994; Chornock et al. 2010).

The possibility of a hydrogen skin existing prior to the SN explosion is interesting. Podsiadlowski et al. (1992) first discussed the evolution of binary systems that would lead to mass stripping. Nomoto et al. (1995) discuss a continuum of SNe types from IIn→IIb→Ib→Ic which would be consistent with the idea of a varying degree of hydrogen mass loss due to a strong wind or binary interaction in a non-conservative mass transfer scenario. The energy released in a binary merger would be sufficient to eject some of the envelope. Wheeler et al. (1994) suggested that if hydrogen is present in SNe Ib then the amount of hydrogen in SNe Ib is less than that found in the Type IIb SN 1993J, which was about 0.1–0.5 $M_\odot$ (Filippenko et al. 1993). This is consistent with our results for SN 1999dn but suggests that SN 2000H is more accurately classified as an SN IIb. Chevalier & Fransson (2006) also suggest that there is a continuous distribution of SNe between SNe IIb where the hydrogen is clearly present and SNe Ib where the hydrogen is quite weak. This continuous distribution is likely to be the explanation for the sequence of SNe between type IIb and Ib, and the varied amounts of envelope stripping are a result of binary interaction and/or strong stellar winds. SN 1993J is

known to have been in a binary and as a result lost some of its hydrogen envelope due to the merging of the two stars in the binary (Podsiadlowski et al. 1993; Nomoto et al. 1995).

Recently, Yoon et al. (2010) studied binary progenitors of SNe Ib/c including the effects of rotation and various reduced wind-loss formulations. They found that even in the case of Case A and B mass transfer the mass transfer is non-conservative and for a limited range of helium cores ($3.5 \lesssim M \lesssim 4.5\ M_{\odot}$, for solar metallicity and $3.5 \lesssim M \lesssim 8\ M_{\odot}$, for $Z_{\odot}/20$) that the wind loss in the helium Wolf-Rayet stage is low enough that a hydrogen skin of the order of $M_H \sim 10^{-2}$–10^{-3} can be retained.

Even though there is a rather continuous distinction between SNe IIb and hydrogen-rich SNe Ib, the total hydrogen mass in the envelope is rather similar $M_H \sim 0.1$–$0.3\ M_{\odot}$. These objects are likely from binary progenitors with stable Case C mass transfer, which leads the donor to shrink below the Roche limit when the envelope reaches a critical mass of about $0.3\ M_{\odot}$ (Podsiadlowski et al. 1992, 1993). Further reduction of the envelope mass then follows via ablation of the hydrogen envelope from the wind of the secondary (Podsiadlowski et al. 1992, 1993). However, studies of SNe Ib suggest that many if not most have a much thinner skin of hydrogen similar to what we find here for SN 1999dn (Branch et al. 2002; Chornock et al. 2010). This could likely be explained by a binary scenario that leads to a common envelope that is ejected from the system (Podsiadlowski et al. 1992). As described in Podsiadlowski et al. (1992) this will lead to either a cataclysmic variable (if the core mass is less than $1.4\ M_{\odot}$) or to a low-mass helium core, which would explode as an SN Ib, but in the common envelope environment it would not be hard to keep a thin hydrogen skin. If this is a common channel for SNe Ib formation then one would expect many to have thin hydrogen envelopes which will be visible in early spectra. Since massive helium cores will blow strong winds that would quickly remove a $10^{-3}\ M_{\odot}$ envelope, this lends support to the idea that many SNe Ib progenitors are the result of relatively low-mass helium cores.

5. CONCLUSION

Our results indicate that hydrogen does exist in the Type Ib SN 1999dn and SN 2000H with an upper mass limit of $M_H \lesssim 10^{-3}\ M_{\odot}$ and $M_H \lesssim 10^{-1}\ M_{\odot}$, respectively. The existence of such a small amount of hydrogen is to be expected as suggested by the continuous spectrum of SN types from II to Ic. Further analysis of a more robust sample of SN Ib is needed for a definitive claim, but the existence of a hydrogen skin in SNe Ib is seen in the observed spectra as well as supported by synthetic calculations. This implies that the typing of core-collapse SNe is more useful as a means of determining the state of the ejecta at a given epoch as opposed to inferring the state of the progenitor at the time of explosion. While it is still useful to determine an SN type we need to set a uniform epoch, such as maximum light or later, in order to be consistent and conclusive when it comes to classification.

We thank Phillip Podsiadlowski for extensive discussions and tutelage on the nature of binary interactions in stripped envelope SNe. This work was supported in part by NSF grant AST-0707704 and US DOE grant DE-FG02-07ER41517. This research used resources of the National Energy Research Scientific Computing Center (NERSC), which is supported by the Office of Science of the U.S. Department of Energy under contract DE-AC02-05CH11231.

REFERENCES

Barbon, R., Buondi, V., Cappellaro, E., & Turatto, M. 2009, VizieR Online Data Catalog, 1
Benetti, S., Cappellaro, E., Turatto, M., & Pastorello, A. 2000, IAU Circ., 7375, 2
Blondin, S., & Tonry, J. L. , et al. 2007, in AIP Conf. Proc. 924, The Multicolored Landscape of Compact Objects and their Explosive Origins, ed. L. Burderi (Melville, NY: AIP), 312
Branch, D., et al. 2002, ApJ, 566, 1005
Chevalier, R. A., & Fransson, C. 2006, ApJ, 651, 381
Chornock, R., et al. 2010, ApJ, submitted (arXiv:1001.2775)
Deng, J. S., Qiu, Y. L., Hu, J. Y., Hatano, K., & Branch, D. 2000, ApJ, 540, 452
Elmhamdi, A., Danziger, I. J., Branch, D., Leibundgut, B., Baron, E., & Kirshner, R. P. 2006, A&A, 450, 305
Filippenko, A. V. 1988, AJ, 96, 1941
Filippenko, A. V., Matheson, T., & Ho, L. C. 1993, ApJ, 415, L103
Grevesse, N., Asplund, M., & Sauval, A. J. 2007, Space Sci. Rev., 130, 105
Hauschildt, P. H., & Baron, E. 1999, J. Comput. Appl. Math., 109, 41
Hauschildt, P. H., & Baron, E. 2004, Mitt. Math. Ges., 24, 1
Heger, A., Fryer, C. L., Woosley, S. E., Langer, N., & Hartmann, D. H. 2003, ApJ, 591, 288
Ketchum, W., Baron, E., & Branch, D. 2008, ApJ, 674, 371
Matheson, T., Filippenko, A. V., Li, W., Leonard, D., & Shields, J. 2001, AJ, 121, 1648
Nomoto, K. I., Iwamoto, K., & Suzuki, T. 1995, Phys. Rep., 256, 173
Parrent, J., et al. 2007, PASP, 119, 135
Podsiadlowski, P., Hsu, J. J. L., Joss, P. C., & Ross, R. R. 1993, Nature, 364, 509
Podsiadlowski, P., Joss, P. C., & Hsu, J. J. L. 1992, ApJ, 391, 245
Tanaka, M., et al. 2009, ApJ, 692, 1131
Wheeler, J. C., & Harkness, R. P. 1990, Rep. Prog. Phys., 53, 1467
Wheeler, J. C., Harkness, R. P., Clocchiatti, A., Benetti, S., Brotherton, M. S., Depoy, D. L., & Elias, J. 1994, ApJ, 436, L135
Woosley, S. E., Pinto, P., Martin, P. G., & Weaver, T. A. 1987, ApJ, 318, 664
Yoon, S., Woosley, S. E., & Langer, N. 2010, ApJ, in press (arXiv:1004.0843)

The Astrophysical Journal, 753:105 (10pp), 2012 July 10 doi:10.1088/0004-637X/753/2/105

A PHYSICAL MODEL FOR SN 2001ay, A NORMAL, BRIGHT, EXTREMELY SLOW DECLINING TYPE Ia SUPERNOVA

E. Baron[1,2,3,4], P. Höflich[5], K. Krisciunas[6], I. Dominguez[7], A. M. Khokhlov[8], M. M. Phillips[9], N. Suntzeff[6], and L. Wang[6]
[1] Homer L. Dodge Department of Physics and Astronomy, University of Oklahoma, 440 W. Brooks, Rm 100, Norman, OK 73019-2061, USA; baron@ou.edu
[2] Hamburger Sternwarte, Gojenbergsweg 112, 21029 Hamburg, Germany
[3] Computational Research Division, Lawrence Berkeley National Laboratory, MS 50B-4206, 1 Cyclotron Rd, Berkeley, CA 94720, USA
[4] Physics Department, University of California, Berkeley, CA 94720, USA
[5] Department of Physics, Florida State University, Tallahassee, FL 32306, USA; pah@astro.physics.fsu.edu
[6] George P. and Cynthia Woods Mitchell Institute for Fundamental Physics & Astronomy, Department of Physics & Astronomy, Texas A&M University, 4242 TAMU, College Station, TX 77843, USA; krisciunas@physics.tamu.edu, suntzeff@physics.tamu.edu, lwang@physics.tamu.edu
[7] Department of Physics, Universidad de Granada C/ Bajo de Huetor 24 Aptdo 3004, ES 18071, Granada, Spain; inma@ugr.es
[8] Department of Astronomy and Astrophysics, University of Chicago, Chicago, IL, USA; ajk@oddjob.uchicago.edu
[9] Las Campanas Observatory, Casilla 601, La Serena, Chile; mmp@lcoeps1.lco.cl
Received 2011 December 21; accepted 2012 May 2; published 2012 June 19

ABSTRACT

We present a study of the peculiar Type Ia supernova 2001ay (SN 2001ay). The defining features of its peculiarity are high velocity, broad lines, and a fast rising light curve, combined with the slowest known rate of decline. It is one magnitude dimmer than would be predicted from its observed Δm_{15}, and shows broad spectral features. We base our analysis on detailed calculations for the explosion, light curves, and spectra. We demonstrate that consistency is key for both validating the models and probing the underlying physics. We show that this SN can be understood within the physics underlying the Δm_{15} relation, and in the framework of pulsating delayed detonation models originating from a Chandrasekhar mass, $M_{\rm Ch}$, white dwarf, but with a progenitor core composed of 80% carbon. We suggest a possible scenario for stellar evolution which leads to such a progenitor. We show that the unusual light curve decline can be understood with the same physics as has been used to understand the Δm_{15} relation for normal SNe Ia. The decline relation can be explained by a combination of the temperature dependence of the opacity and excess or deficit of the peak luminosity, α, measured relative to the instantaneous rate of radiative decay energy generation. What differentiates SN 2001ay from normal SNe Ia is a higher explosion energy which leads to a shift of the ^{56}Ni distribution toward higher velocity and $\alpha < 1$. This result is responsible for the fast rise and slow decline. We define a class of SN 2001ay-like SNe Ia, which will show an anti-Phillips relation.

Key word: supernovae: individual: SN 2001ay

Online-only material: color figures

1. INTRODUCTION

While some progress has been made in the understanding of the Type Ia supernova (SN Ia) phenomenon in recent years, there does not yet exist an agreed upon standard model of the supernova explosion that can explain normal SNe Ia (Branch et al. 2005, 2009). For cosmology, the brightness decline relation plays a key role (Phillips 1993; Phillips et al. 1999; Goldhaber et al. 2001). From theory, Δm_{15} is well understood: the light curves (LCs) are powered by radioactive decay of ^{56}Ni (Colgate & McKee 1969). More ^{56}Ni increases the luminosity and causes the envelopes to be hotter. Higher temperature means higher opacity and, thus, longer diffusion timescales and slower decline rates after maximum light (Höflich et al. 1996; Nugent et al. 1997; Umeda et al. 1999; Kasen et al. 2009). The existence of a Δm_{15} relation holds for virtually all scenarios as long as there is an excess amount of stored energy to be released (Höflich et al. 1996). Although the tightness of the relation can be understood within the framework of the single degenerate scenario and spherical models (Höflich et al. 1996, 2002, 2010), it falls apart when taking into account burning instabilities during the deflagration phase (Kasen et al. 2009). This difficulty and the observation of a set of extremely bright SNe Ia may lend support for double degenerate (DD) scenarios (Tutukov & Yungelson 1979; Iben & Tutukov 1984; Webbink 1984) with progenitors well above the Chandrasekhar mass (Howell et al. 2006; Scalzo et al. 2010; Taubenberger et al. 2011; Howell 2011). We note, however, that the inferred brightness depends on a unique relation between the ^{56}Ni mass $M_{\rm Ni}$, and the intrinsic color: $B-V$ at maximum light. At least in a few cases, the apparent brightness can be understood within the framework of $M_{\rm Ch}$ mass white dwarfs (WDs) with intrinsically red color (Quimby et al. 2006).

Additionally, some progress has been made in understanding variations among the groups, with suggestions that some of the spectral diversity is due to metallicity, central density, and asymmetries (Höflich et al. 1998, 2010; Lentz et al. 2000; Maeda et al. 2010; Maund et al. 2010). The nature of the progenitor system is also controversial, with recent work on rates and the delay time distribution favoring the DD scenario (Yungelson & Livio 1998, 2000; Maoz 2008; Ruiter et al. 2009; Maoz et al. 2010, 2011; Mennekens et al. 2010; Ruiter et al. 2011). Nevertheless, theoretical work continues to favor the single degenerate scenario, with some contribution of DD scenario (Höflich & Khokhlov 1996; Saio & Nomoto 1998; Woosley & Weaver 1986; Mochkovitch & Livio 1990; Saio & Nomoto 1985; Shen et al. 2012).

Despite the uncertainties in theory, most of the known SNe Ia obey the brightness decline relation. The LCs are self-similar within ±0.3 mag (Goldhaber & Perlmutter 1998; Riess et al.

1999). Deviations of this order can be expected from variations of the progenitor (Höflich et al. 1998; Brachwitz et al. 2000; Thielemann et al. 2003; Seitenzahl et al. 2011). The stretching method works for both the local and high-z samples (Perlmutter et al. 1999; Riess et al. 1998). The self-similarity holds even for supernovae for which super-Chandrasekhar mass progenitors have been suggested.

The subject of this paper, SN 2001ay, shows that nature is even more diverse (Krisciunas et al. 2011). From the redshift of the host galaxy IC4423 (Freedman et al. 2001), the distance modulus $\mu = 35.55 \pm 0.1$ is well known. The reddening in our Galaxy is found to be $E(B-V) = 0.026 \pm 0.006$ mag, and interstellar absorption in Na I suggests low reddening in the host galaxy of about $E(B-V) = 0.072 \pm 0.008$ mag (Krisciunas et al. 2011). Together with the observed magnitude, the intrinsic brightness at maximum light is $M_V = -19.17$ mag with a $B-V$ color of -0.02 mag, which is comparable with typical core-normal supernovae.

However, the LC shape is unlike other SNe Ia: its measured decline rate of $\Delta m_B = 0.68$ is slower than any known SNe Ia, combined with a fast rise of some 16 days (Krisciunas et al. 2011). Based on its Δm_{15}, SN 2001ay should be brighter than observed by about 1 mag. Moreover, the line widths near maximum light put it solidly in the broad-line class of SNe Ia.

We show that SN 2001ay can be understood with the same physics underlying the Δm_{15} relation, and in the framework of parameterized pulsating delayed detonation (PDD) models similar to SN 1990N (Khokhlov et al. 1992), but with an unusual progenitor star. We consistently treat the explosion, LCs, and spectra (Höflich 1995). We show that consistent models reproduce the observed LCs and spectra reasonably well. Furthermore, we show that inconsistent calculations lead to spectral features which would lead to rejection of the explosion model. Finally, we summarize our findings and discuss possible implications for the understanding of SNe Ia and cosmology.

2. MOTIVATION FOR OUR MODEL FOR SN 2001ay

For our models, an understanding of the brightness decline relation is important. The Phillips relation (Phillips 1993; Phillips et al. 1999) provides an empirical link between peak brightness and decline of the LC after maximum. Most SNe Ia fall within 0.2 mag of this relation.

As discussed in the Introduction, the Δm_{15} relation can be understood as an opacity effect if energy in stored energy is available in excess of the instantaneous radioactive decay (Höflich et al. 1996; Nugent et al. 1997; Umeda et al. 1999; Kasen et al. 2009). The latter is a key to understand SN 2001ay. We will discuss that while the second condition is valid in most scenarios for SNe Ia, it is not guaranteed.

For our discussion, a useful quantity is the relation between instantaneous energy deposition by radioactive decay and the brightness at maximum:

$$L_{\rm bol}(t_{\rm max}) = \alpha \dot{S}(t_{\rm max}),$$

where α accounts for the fact that some of the γ-ray energy deposited prior to maximum light can be stored in the thermal energy and trapped radiation energy which cannot escape faster than a diffusion time. In a typical delayed detonation model the value of α is about 1.2 (Khokhlov et al. 1993; Höflich & Khokhlov 1996).

The role of the opacity condition can be seen from Arnett's analytic solution (Arnett 1980, 1982), which also provides further insights. Constant opacity in a polytropic model with homogeneous energy input does not produce a brightness decline relation. In this model, energy balance between radioactive decay and adiabatic expansion and cooling cancel exactly in a radiation dominated regime with pure geometrical dilution. At maximum, the ratio between maximum brightness and instantaneous energy input is $\alpha = 1$. Pinto & Eastman (2000) reconsidered Arnett's one-zone models and confirmed previous explanations. Declining opacity provide extra energy at maximum light because it accelerates the recession of the "photosphere" (Höflich et al. 1993) and results in a positive brightness decline relation in this case.

However, even an effective opacity declining with temperature may result in an anti-Δm_{15} relation, because Δm_{15} depends both on the opacity effect and the excess energy available. For example, the pure detonation model DET1 has an $\alpha \approx 0.73$ and Δm_{15} of 1.37 mag. In contrast, another pure detonation model DET2 has an $\alpha \approx 1.2$ and $\Delta m_{15} \approx 1.7$ (Khokhlov et al. 1993; Höflich & Khokhlov 1996). In DET1, the high central density leads to significant electron capture in the central region producing a ^{56}Ni free core. In contrast, lower central densities in DET2 produce ^{56}Ni in the center, and less ^{56}Ni in the outer region. In both models, the density structure is close to similar polytropes but the ^{56}Ni distribution is shifted outward and inward, respectively. The differences in α can be understood in terms of the deviation from Arnett's one-zone model with a flat ^{56}Ni distribution in mass. In DET1, this distribution is shifted outward leading to an increased escape probability of γ-rays and greater expansion work which leads to reduced α. In DET2, the shift of the ^{56}Ni distribution inward leads to a larger value of α.

From the above discussion, it is obvious that a narrow Δm_{15} relation requires similar abundance patterns and ^{56}Ni distributions for a given $M_{\rm Ni}$. The theoretical relation $\Delta m_{15}(M_{\rm Ni})$ depends on the explosion scenario. Self-similarity in the LCs requires a self-similar transformation between models of differing brightness. Within the delayed-detonation scenario, $M_{\rm Ni}$ depends mostly on the pre-expansion during the deflagration phase, since if the density is too high neutron-rich iron-group elements will be produced. However, as the nickel mass drops out of the standard 0.5–0.6 $M_\odot$ range, the ^{56}Ni distribution shifts inward with decreasing $M_{\rm Ni}$. This produces a $\Delta m_{15}(M_{\rm Ni})$ relation which is in agreement with observations (Höflich et al. 2002). For core-normal SNe Ia, the temperature and, with it the opacity, remains high well after maximum light, leading to a "shallow" $\Delta m_{15}(M_{\rm Ni})$. Below a certain $M_{\rm Ni}$, the nickel is very centrally condensed (there is no nickel hole) and the opacity drops rapidly soon after maximum leading to a steep $\Delta m_{15}(M_{\rm Ni})$ relation. In the case of fast decliners ^{56}Ni is only produced during the deflagration phase.

3. SCENARIOS FOR SN 2001ay

3.1. Models with an Increased Mass

SN 2001ay was suggested to fall within the class of "Super-Chandra" mass SNe Ia. Obviously, SN 2001ay does not obey the standard Δm_{15} relation. Within the framework of the empirical Δm_{15} relation, SN 2001ay should be brighter than observed by roughly 1.0 mag which can be ruled out (see Figure 10 of Krisciunas et al. 2011). In fact, compared to the putative super-Chandrasekhar SNe Ia, 2007if (Scalzo et al. 2010; Yuan et al. 2010) and SN 2009dc (Yamanaka et al. 2009; Tanaka et al. 2010; Silverman et al. 2011; Taubenberger et al. 2011) estimates of

$M_{\rm bol}$ at maximum light differ by about 1 mag. Estimates for the brightness of SN 2001ay imply 0.5 $M_{\rm Ni}$ (Krisciunas et al. 2011). We need an increase of the diffusion timescales by a factor of two from Δm_{15} of 1.25 for typical SNe Ia (Phillips et al. 1999) to $\Delta m_{15} = 0.68$. The diffusion times scale as, $t_{\rm diff} \propto \tau^2 \propto M^2$ and, for homologous expansion, $\tau \propto t^{-2}$. If we assume $M_{\rm Ch}$ for normal SNe Ia, this would imply a progenitor mass of 2 $M_\odot$ which is super-Chandra and in fact typical of the mass suggested for mergers, but then one must explain why some super-Chandras are extra bright and SN 2001ay is not.

A stronger argument against a high mass progenitor comes from the rise time to decline ratio. SN 2001ay rises quickly to maximum, whereas an increased timescale would unavoidably produce a slow rise to maximum light.

3.2. The Case for an $M_{\rm Ch}$ Mass WD with a Faster Expansion Rate

Here, we suggest another scenario outside the "classical" regime for SNe Ia, but within the delayed-detonation scenario of Chandrasekhar mass WD progenitors. To reproduce SN 2001ay, we require a fast rising LC followed by a decline slower than the slope of the instantaneous radioactive decay. We can produce models with $\alpha < 1$. This requires a model with ^{56}Ni shifted to high velocities. Since eventually, the luminosity is given by the rate of instantaneous energy deposition, such a model will show a slow decline by construction.

4. RESULTS

4.1. Explosion Models and Light Curves

We describe how a change of parameters can transform the results from that given by normal LCs to that of SN 2001ay, within the same physical picture.

Even in the absence of a well agreed upon model for SNe Ia most of the basic observational properties, that is, LCs and spectra, of core-normal SNe Ia can be understood within the framework of thermonuclear explosions of Chandrasekhar mass WDs and, in particular, the delayed-detonation scenario (Khokhlov 1989) which provides a natural explanation for the wide variety and range of the ^{56}Ni production. To first order, the amount of ^{56}Ni produced in the explosion depends on the pre-expansion of the WD during the deflagration phase, in which spherical models can be parameterized conveniently by the density at which the transition between deflagration to detonation occurs. For a recent review of the relation between observational properties and the underlying physical model, see, for example, Höflich (2006).

We base our analysis on a spherical explosion model within the framework of the PDD scenario. Our goal is to construct a model with reduced α and short diffusion timescales. We seek to obtain our goals by increasing the expansion ratio and shifting of the ^{56}Ni distribution to higher velocity.

4.1.1. Explosion Models

The spherical explosion model has been constructed to allow fits of optical LCs and spectra of SN 2001ay.

Within the DD scenario, the free model parameters are (1) the chemical structure of the exploding WD, (2) its central density, ρ_c at the time of the explosion, (3) the description of the deflagration front, and (4) the layer at which the transition from deflagration to detonation occurs.

As a reference, we started from the delayed detonation model 5p0y25z22.25, which has been found to be a good starting point for core-normal SNe Ia, with respect to both spectra and LCs (Domínguez et al. 2001; Höflich 2002; Quimby et al. 2006; Höflich et al. 2010). This base model originates from a star with a main-sequence mass of 5 $M_\odot$ and solar metallicity. Through accretion, the C+O core of the star has grown close to the Chandrasekhar limit. At the time of the explosion of the WD, its central density is 2.0×10^9 g cm^{-3} and its mass is close to 1.37 $M_\odot$. The transition density $\rho_{\rm tr}$ has been identified as the main factor which determines the ^{56}Ni production and, thus, the brightness of SNe Ia (Höflich 1995; Höflich et al. 1995, 2002; Iwamoto et al. 1999). The transition density $\rho_{\rm tr}$ from deflagration to detonation is 25×10^6 g cm^{-3}.

For SN 2001ay, we tuned the parameters. The reference model has been modified as follows. We reduced the central density, ρ_c to 1×10^9 g cm^{-3}, which decreased the potential energy, as always, and thus, increased the radius of the WD by ≈30% to 2320 km, and we increased the C/O ratio in the former He-burning core ($M < 0.56\ M_\odot$) to 4. Both modifications increase the explosion energy to 1.69×10^{51} erg (1.69 foe), leading to a more rapid expanding envelope, increasing the rate of geometrical dilution, and shifting the ^{56}Ni to higher velocity. These effects are responsible for both the fast rise and slower decline of SN 2001ay.

In classical DD models, the deflagration to detonation transition (DDT) occurs in a WD already unbound during the deflagration phase (Khokhlov 1989; Yamaoka et al. 1992). In contrast, in pulsating delayed models, PDD, the WD remains bound after the deflagration phase, and the DDT occurs during pulsation (Khokhlov 1993; Hoflich et al. 1995). Other authors have suggested variations on the PDD (Ivanova et al. 1974; Bravo & García-Senz 2006, 2009; Baron et al. 2008; Bravo et al. 2009), but here when we discuss the PDD model, we specifically refer to the model of Khokhlov (1993). Reducing the burning rate during the deflagration phase moves the model from the DD to the PDD regime in which the WD is bound at the end of the deflagration phase. We artificially reduced the Atwood number, which we approximate as a constant independent of density and composition (see the Appendix) from 0.2 to (0.14, 0.12, 0.10) for the series PDD_11a–c which all undergo weak pulsation—producing LCs with rise times between 14 and 16 days with a slow decline from maximum. The best fit to the observations is given by PDD_11b. Its details are described below. While some of the observed trends that we find with the PDD model may be obtained in a three-dimensional DD model, including the effects of rotation, exploring such models is beyond the scope of this work. We mention results from PDD_11a/c below when needed.

The density and abundance structure of PDD_11b is given in Figures 1 and 2. The pulsation leaves a shell of ≈0.06 $M_\odot$ of unburned C/O (with C/O ∼1, only the region of central helium burning has enhanced C/0), and 0.51 $M_\odot$ of ^{56}Ni. For PDD models, mixing during the pulsation may occur. In contrast to previous pulsating models (Hoflich et al. 1995; Höflich & Khokhlov 1996), we did not assume full mixing during the pulsation, but instead mixing was limited to one scale height from the position of the burning front during the pulsation. The mixed region between burned matter forms the layer where the detonation is born. As a result, the density and chemical structure are similar to spherical DD models and consistent with late time line profiles and SN remnants. We abandoned full mixing in order to preserve the inner, unmixed region as required by late time line profiles and the imaging of the supernova remnant S Andromedae (Höflich et al. 2004; Motohara et al.

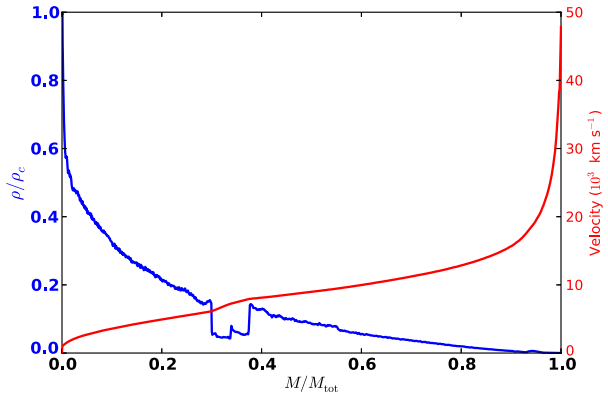

Figure 1. Density and velocity as a function of mass for model PDD_11b.
(A color version of this figure is available in the online journal.)

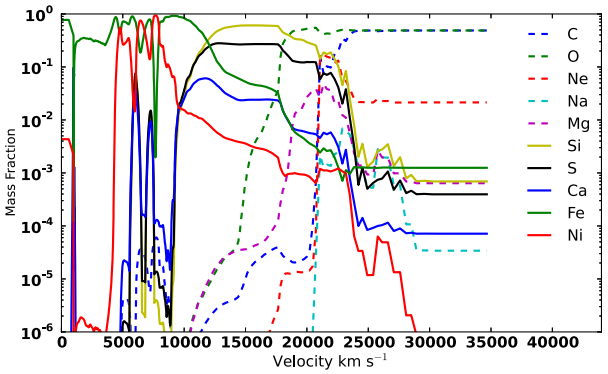

Figure 2. Abundances of stable isotopes as a function of the expansion velocity for model PDD_11b.
(A color version of this figure is available in the online journal.)

2006; Fesen et al. 2007; Gerardy et al. 2007; Maeda et al. 2010). Our models leave some unburned C/O. All modifications combined result in broader lines. We note that our model is highly parameterized. First, the deflagration phase depends critically on the initial condition and as discussed above, the problem of how to suppress strong mixing is still unsolved, though it may be related to high magnetic fields (Penney & Höflich 2012). Second, the amount of mixing will depend on Rayleigh–Taylor instabilities during the pulsation and possibly, rotation induced sheer instabilities.

4.1.2. Light Curves

Let us examine the formation of the LCs and the comparison with SN 2001ay. First, consider the energy input by γ-rays, positrons, and adiabatic cooling due to expansion. We contrast PDD_11b with our reference model. Both have a similar structure with respect to the chemical layering and, thus, similar opacities. Due to the higher explosion energy, the expansion rate of the inner layers is larger by about 25%–30%. PDD_11b shows an increased energy loss due to expansion work. The opacities for γ's depend only on the mass column height, τ_M, and the electron/nucleon ratio which is close to 0.5. τ_M scales as $v \times t^{-2}$ resulting in a 50% lower optical depth due to the higher velocity. The normalized energy deposition and escape fractions of γ-rays are shown in Figure 3. The high expansion rate results in strong heating by γ-rays in the outer region and a higher escape probability for γ-rays. Between 10 and 25 days, PDD_11b has an escape fraction larger than that of the reference model by about a factor of two.

In Figure 4, we give a comparison between LCs of PDD_11b and the reference model. PDD_11b rises faster and is brighter at early times. The higher escape of γ-rays and the increased expansion work leads to $\alpha < 1$ and, therefore, a lower peak relative to the rate of instantaneous γ-ray input. The second ingredient reducing the value of α is the opacity difference between optical photons and γ-rays. They are 0.1–0.2 and $1/35\,\mathrm{cm}^2\,\mathrm{g}^{-1}$, respectively. γ-rays leak into the center where the energy is trapped without contributing to the LC at maximum (Figure 3).

We therefore have a deficit in luminosity (with respect to the instantaneous γ-ray deposition rate), and the optical LCs approaches $\dot{E}_\gamma$ "from below." The same opacity mechanism responsible for the regular brightness decline relation results in an "anti-Phillips" relation. More ^{56}Ni and with it, larger opacities will lead to steeper declines.

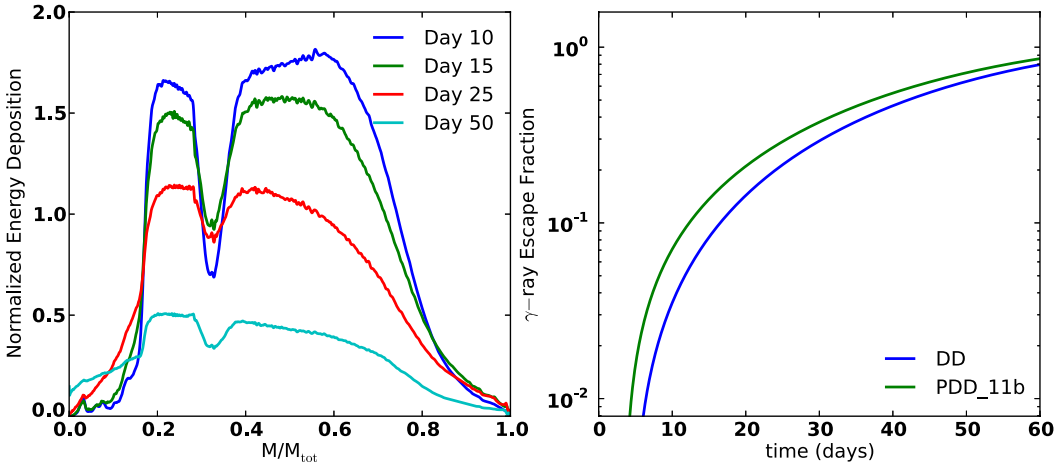

Figure 3. Normalized energy deposition by γ-ray and positrons in PDD_11b (left), and the escape fraction for PDD_11b and the reference model (right).
(A color version of this figure is available in the online journal.)

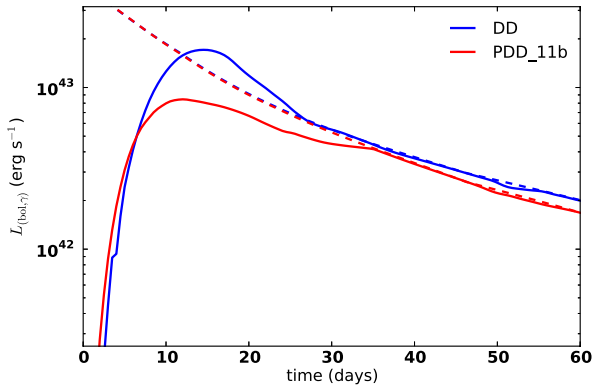

Figure 4. Instantaneous deposition rate due to radioactive decay (dashed) and bolometric luminosity (solid) for PDD_11b, a pulsating model with a carbon-rich core, and a "classical" DD model. The light curve of the DD model has been uniformly shifted by −0.037 dex and the light curve and γ-ray deposition of the PDD_11b model have been uniformly shifted by +0.05 dex to better illustrate the variation of the gradients.

(A color version of this figure is available in the online journal.)

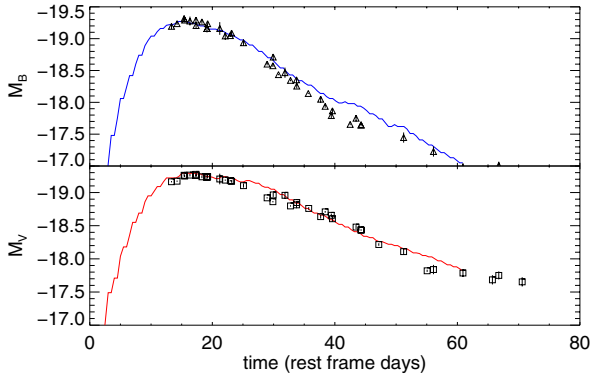

Figure 5. B and V LCs of SN 2001ay (Krisciunas et al. 2011) in comparison with theory. The comparison between SN 2001ay and PDD_11b in B (upper) and V (lower) as a function of time since maximum light in the V band. The model light curves have been corrected for reddening and redshift. We assume a distance modulus $m - M$ of 35.55 mag, and following Krisciunas et al. (2011), we take $A_V = 0.253$ and $A_B = 0.35$. The data include the photometric errors.

(A color version of this figure is available in the online journal.)

4.1.3. Comparison to SN 2001ay

In Figure 5, the theoretical LCs in B and V are compared with the observations. The agreement is reasonable, and they meet the brightness limit imposed by the early non-detection in R. The theoretical B and V have been corrected for the redshift z of the host galaxy. As discussed in the Introduction, the distance modulus of the host galaxy is 35.5 ± 0.1 mag, and the galactic foreground extinction $E(B - V) = 0.026$ mag. Krisciunas et al. (2011) use a reddening of the host galaxy of $E(B - V) = 0.072$ mag with an R_V of 3.1 and 2.4 for the Galaxy and host galaxy, respectively, giving $A_V = 0.253$ mag. Using our theoretical color, $(B - V)_{\max} = 0.0$ mag, and from an optimized fit, we find the host galaxy reddening $E(B - V) = 0.02$ mag with a global $R_V = 3.1$ for a total extinction $A_V = 0.144$ mag.

4.2. Spectral Analysis

Based on the explosion models, γ-ray transport, and LCs, we analyzed the spectrum of SN 2001ay at maximum light using the NLTE-code PHOENIX (see the Appendix).

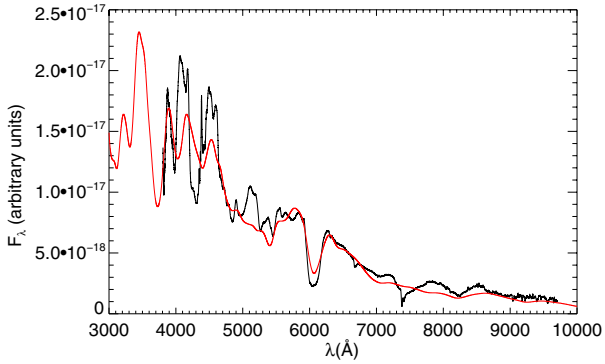

Figure 6. Synthetic spectrum at day 16 of PDD_11b in comparison with maximum spectrum of SN 2001ay. The density and abundance structure and the energy input by radioactive decay are taken from the explosion and light curve calculation (Figures 2, 3, and 5). Roughly consistent with the light curve, M_V was taken to be −19.07 mag, we have assumed standard reddening $R_V = 3.1$ and $E(B - V) = 0.096$.

(A color version of this figure is available in the online journal.)

We use the density, abundance structure, and γ-ray and positron deposition given by the explosion models and LC calculations. For the reddening and distance modulus, we use the values found from our LC fit. For the redshift, we use $z = 0.030244$. Converged models required 256 optical depth points.

For a consistent absolute M_V magnitude of −19.1 mag, the resulting synthetic spectrum is compared to the spectrum observed at maximum light in Figure 6. The continuum colors are well reproduced. The synthetic value of $B - V = -0.06$ mag, roughly consistent with 0 mag of SN 2001ay. In order to avoid the complications of two dust populations that was assumed by Krisciunas et al. (2011), we have taken $E(B - V) = 0.096$ and $R_V = 3.1$, so our reddening is a bit "bluer" that was assumed in the LC comparison, but it is well within the 0.1 mag error of the photometry.

The spectrum is dominated by single ionized lines of S II, Si II, Ca II, Fe II, Co II as well as blends of doubly ionized species in the blue. The synthetic and observed spectra show good agreement. The Doppler shifts of lines from elements undergoing incomplete oxygen burning include Si II λ6355, Si II λ5972 and S II λ5468 and λ5654, and the Ca II H+K and the IR triplet are reasonably well reproduced within 10, 20, and 30 Å, respectively, which corresponds to a velocity shift of 500–1000 km s^{-1} at the measured velocity of 14,400 km s^{-1}. The strength of the absorption components agrees well. A large number of weak lines form the quasi-continuum in the near IR. The feature due to blends of Fe II/Co II/Ni II which could possibly be misidentified as due to C II 6580 is reasonably strong, but the feature does not agree with the absorption notch identified as C II by Krisciunas et al. (2011). However, the evidence for C II claimed in Krisciunas et al. (2011) is stronger than warranted based on the analysis that were done for that paper (R. Thomas 2012, private communication). Some disagreement is evident. The S II W at about 5000 Å, blended with other lines, and the Si II λ5970 line are too weak. In the red, the Ca IR triplet is too weak, as is the O I λλ7773 line, which is, however, severely contaminated by Telluric absorption. The lack of O I is an indication that the outer part of our model is not correct, either in density structure or due to temperature effects.

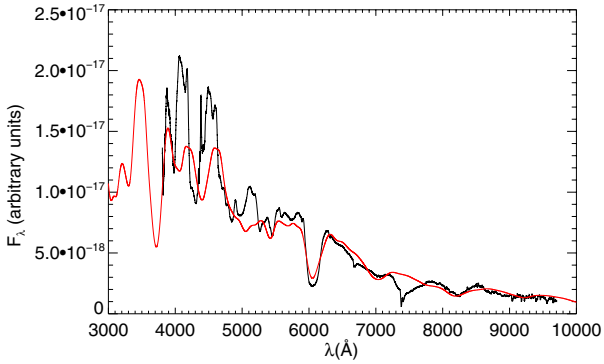

Figure 7. Same as Figure 6, but dimmer by 0.1 mag, i.e., M_V of −18.92 mag.
(A color version of this figure is available in the online journal.)

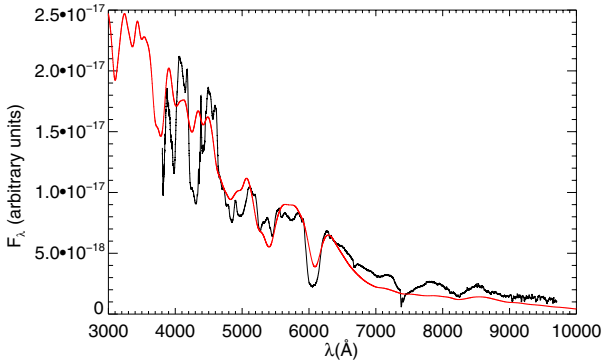

Figure 8. Same as Figure 6, but brighter by 0.15 mag, i.e., M_V of −19.23 mag.
(A color version of this figure is available in the online journal.)

To probe the importance of consistency and the sensitivity of the spectra, we calculated a series of maximum light spectra which are underluminous and overluminous, with M_V = (−18.92,−19.23,−19.35,−19.45) mag.

At +0.1 mag (Figure 7), the $B-V$ color becomes 0.03 mag. The Si II λ6355 line is well fit and the Ca II IR triplet is relatively well reproduced. In the blue, Co II lines dominate and a Co II line at 7400 Å appears. The feature at 6500 Å is weaker. The Doppler shift of the Si II and S II remains in good agreement because they are formed within the region of incomplete oxygen burning which produced nearly constant abundances due to burning in quasi-statistical equilibrium (QSE) conditions (Figure 2).

At −0.15 mag (Figure 8), $B-V$ equals −0.11 mag, but is clearly a little bit too blue as can be seen in the red part of the spectrum. However, the Si II λ5970 feature is too weak and S II lines are still significantly too weak. The Ca II IR triplet is much too weak. In the blue, Fe II lines are stronger and the fit is somewhat better. This could imply that the model should have had an initial metallicity somewhat higher, which would create more Fe II at the expense of Co II (from radioactive nickel).

At −0.25 mag (Figure 9), the spectrum becomes too blue, $B-V=-0.08$ mag, and the UV flux becomes too large. The Si II and S II lines are still significantly too weak and the IR flux is too low. The Ca H+K line is now too weak.

At −0.35 mag (Figure 10), the spectrum is much too blue, $B-V=-0.07$ mag and the Ca II features are completely absent. The Si II and S II features are now much too weak.

Figure 11 shows the model fit to the observed *Hubble Space Telescope* (*HST*)+Keck spectrum of April 29. The Si II line is

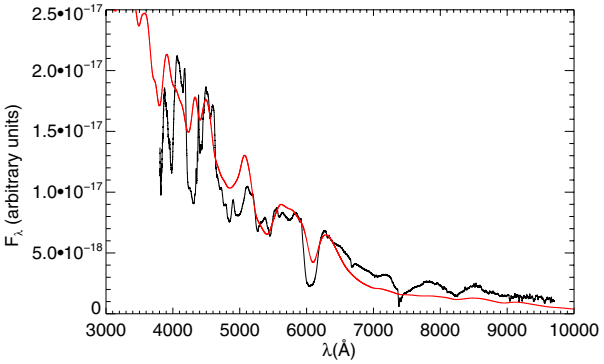

Figure 9. Same as Figure 6, but brighter by 0.25 mag, i.e., M_V of −19.35 mag.
(A color version of this figure is available in the online journal.)

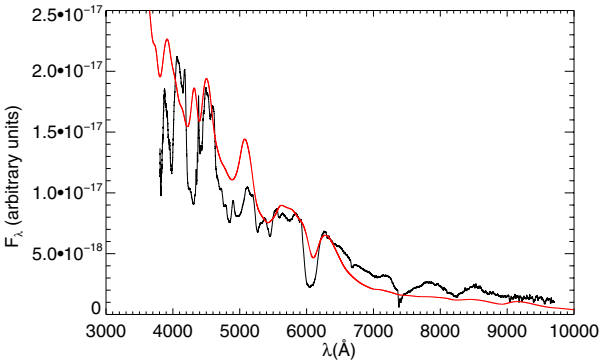

Figure 10. Same as Figure 6, but brighter by 0.35 mag, i.e., M_V of −19.45 mag.
(A color version of this figure is available in the online journal.)

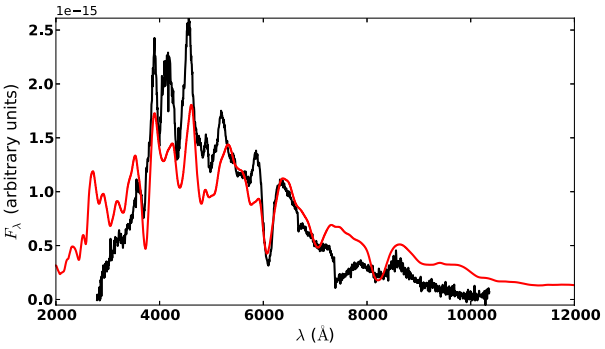

Figure 11. Synthetic spectrum (red) for 23 days after explosion compared with the observed spectrum obtained on 2001 April 29, from both *HST* and Keck. M_V is −18.97 mag and $B-V=0.43$.
(A color version of this figure is available in the online journal.)

very nicely fit, the S II "W" is well fit, although the blue line is a bit stronger in the model than in the observed spectrum. The rest of the blue is reasonably well fit, although the flux is about a factor of two too high in the UV, which may be an indication of the need for a higher metallicity, which would produce more line blanketing and reduce the UV flux. Both the Ca H+K and IR triplet are reasonably well fit, and the Co II + Fe II + Mn II feature at about 7350 Å is a bit too strong. The O I λλ7773 line is much too weak. Figure 12 shows the model fit for a somewhat brighter model $M_V=-19.22$ and $B-V=0.22$, still a bit too red, but the line features fit similarly well to the redder case.

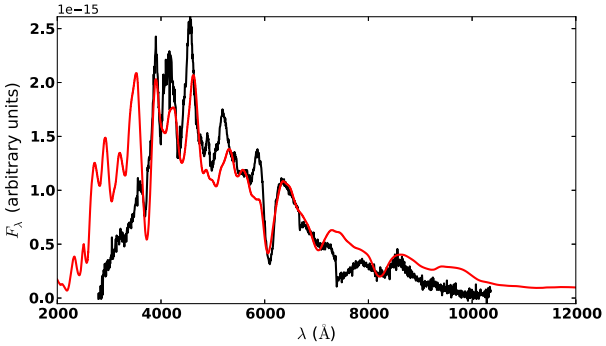

Figure 12. Same as Figure 11, but $M_V = -19.22$ mag and $B - V = 0.22$.
(A color version of this figure is available in the online journal.)

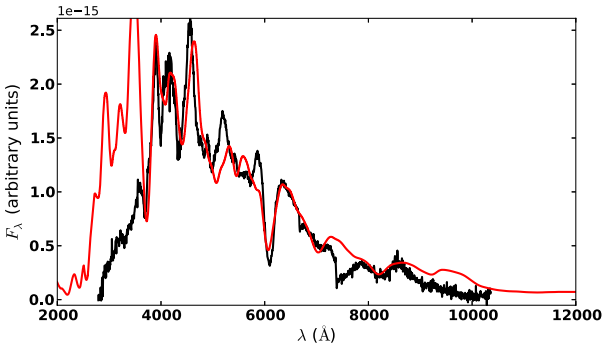

Figure 13. Same as Figure 11, but $M_V = -19.4$ mag and $B - V = 0.10$.
(A color version of this figure is available in the online journal.)

Figure 13 shows the model fit for a somewhat brighter model $M_V = -19.40$ and $B - V = 0.10$, a bit too bright, but about the right color. Again, the too high UV and the weak O I line are indications that the outer structure of our model is not quite correct, which could be due to primordial metallicity or our assumptions about mixing in the PDD.

Obviously, spectral synthesis is a very sensitive tool to probe the structure and luminosity on a level of $\Delta M_V \approx 0.1$ mag. Variations in excess of $\Delta M_V \approx 0.2$ lead to spectral fits which would lead to a rejection of even a valid, underlying explosion model. We note that our best fits give a "correct" velocity shift of, e.g., the Si II feature because, in PDD_11b, it is formed in the region of QSE for the Si/S group. Consistent treatment of explosion, LCs, and spectral formation is important. However, spectra lines are sensitive to both temperature effects and line blending and even a strong line like Si II λ6355 is not unblended. One can see a small blueward shift between Figures 6 and 11. Figure 14 shows the Si II λ6355 feature in velocity space, where two models at the same epoch (April 29) are plotted along with the data. The cooler model has an absorption minimum that is bluer than that of the hotter model and both are a bit bluer than the observed spectrum, although the noise in the spectrum makes a determination of the minimum a bit difficult.

In turn, LCs are mostly sensitive to the inner region and the large number of weak lines. Both in the LC and spectral calculation, $B - V$ is consistent, namely 0 and −0.06 mag. Only spectra show that the Si II line is too weak.

As discussed above, spherical models inherently suppress mixing by instabilities due to the deflagration phase at the inner layers, and the interaction between shells and the outer layers during the acceleration phase.

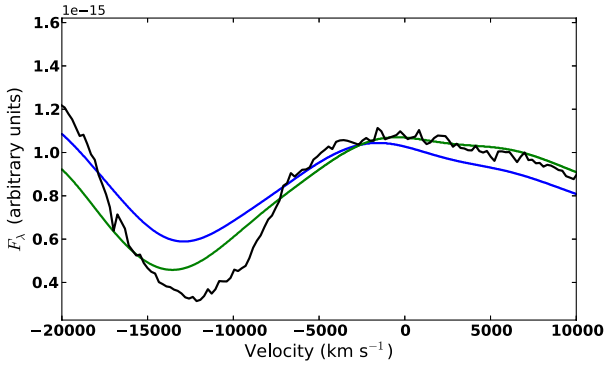

Figure 14. Si II λ6355 feature for 23 days after explosion compared with the observed spectrum obtained on 2001 April 29 (black) with the model shown in Figure 13 (green) and a somewhat hotter model (blue). The blueward shift in the absorption is clearly a temperature effect and is also due to blending.
(A color version of this figure is available in the online journal.)

Spectral analysis requires underlying models which are consistent including the luminosity. Then, however, they allow the study of secondary effects of individual spectral features.

5. DISCUSSION AND CONCLUSION

The peculiar Type Ia SN 2001ay is an important milestone for our understanding of the explosion, LCs, and spectra. Even with its extremely unusual LC shape and spectral features, we showed that it still can be accommodated within the framework of the explosion of a Chandrasekhar mass WD.

Although it does not follow the Δm_{15} relation, the LC can be reproduced within the physics of normal SNe Ia, and in the framework of PDD models. In our models, the key difference is a high, 80% carbon mass fraction, rather than the 15%–20% carbon mass fraction usual for stellar central He burning. The size of the carbon rich core is 0.56 $M_\odot$. The excess of carbon coupled with a lower central density of the initial WD results in an increase of the final kinetic energy by about 40% and, in turn, shifts the distribution of ^{56}Ni to larger velocities. These modifications are responsible for both the LC characteristics and the broad spectral features.

The peculiar LC shape is a consequence of the shift of the ^{56}Ni distribution in velocity space and higher rate of central expansion. Transport effects of γ-rays become more important and the escape probability is increased. This leads to a fast, early rise and a value of $\alpha < 1$, where α is the ratio between the luminosity and the instantaneous energy generation rate by radioactive decays at maximum. In normal SNe Ia, the Δm_{15} relation can be understood as a consequence of the temperature dependence of the opacity in combination with $\alpha > 1$. As discussed in Section 2, more ^{56}Ni causes higher luminosities and temperatures. Higher temperatures lead to larger opacities and therefore, a slower drop of the luminosity from the typical value of ≈1.2× the instantaneous energy input rate at maximum, to the instantaneous energy input rate at later times. Accordingly, for SN 2001ay with $\alpha \approx 0.55$, the LC approaches the instantaneous energy input rate from below which explains the unusually slow decline. Within our models and as a corollary, we expect that there exists a sub-class of supernovae which obeys an anti-Phillips relation. As discussed below, this sub-class should be rare.

The unusually broad spectral features can be understood by the overall shift of the overall element pattern to higher

velocities. However, this pattern remains similar to that found in normal SNe Ia (Figure 2). We demonstrated the power and sensitivity of spectral analysis. High sensitivity demands a consistent treatment with the explosion and LC models. Otherwise, even valid models may be rejected because of poor fits. However, since a good overall fit is achieved with a consistent treatment, individual features are a powerful tool to study details of the explosion physics.

We have shown that limiting the mixing during the pulsation to small scales produces a very similar abundance pattern to the one produced in standard DD models which have been shown to reproduce the observables for the majority of SNe Ia. PDD may be a promising mechanism for the DDT.

While our model fits the basic observed features of SN 2001ay, we do not mean to imply that other models are not possible. In particular, a DD model including three-dimensional effects as discussed above with a high central C/O ratio may also be a viable model and there may exist other models that fit the observed trends. Pursuing other explanations is beyond the scope of the present work.

Our model agrees reasonably well with the observations (Figure 5) but the high carbon abundance in the progenitor poses a challenge. The central region of the progenitor originates from central He burning in stars with less than 7–8 $M_{\odot}$ (Becker & Iben 1980). During the early stages of central He burning, high carbon abundances are produced by $^{4}\mathrm{He}(2\alpha, \gamma)^{12}\mathrm{C}$ burning. With time, the helium abundance is reduced in the core. Then, $^{12}\mathrm{C}(\alpha, \gamma)^{16}\mathrm{O}$ depletes ^{12}C to a typical value of 10%–25% (Umeda et al. 1999; Domínguez et al. 2001). The final amount of $^{12}\mathrm{C}/^{16}\mathrm{O}$ depends on the mass of the progenitor, and the $^{12}\mathrm{C}(\alpha, \gamma)^{16}\mathrm{O}$ rate (Buchmann 1997), and the amount chemical mixing assumed (Castellani et al. 1985; Caputo et al. 1989; Renzini & Fusi Pecci 1988; Domínguez et al. 2001). Increased chemical overshooting (or semiconvection) prolongs the phase of burning under helium depleted conditions, leading to a lower value of C/O. Although chemical overshooting prescriptions vary widely between various groups studying stellar evolution, the final outcome is a C-poor mixture. To reach high central carbon abundances, burning under He-depleted conditions must be avoided (see Straniero et al. 2003 and references therein). Straniero et al. (2003) found that they could increase the central carbon abundance somewhat by increasing mechanical overshooting. As a possible solution, we propose a common envelope phase with very strong mixing induced by a compact secondary such as a brown dwarf or planet. Common envelope evolution is generally assumed to be responsible for the formation of close binaries leading to cataclysmic variables, X-ray binaries, and supersoft-X-ray sources (Livio & Soker 1988; Ricker & Taam 2008). Moreover, close binary systems with planet or brown dwarfs have recently been detected (Neuhäuser & Posselt 2007; Hessman et al. 2011). Unfortunately, there are no systematic studies that allow one to estimate the amount of mixing. Detailed, numerical studies are few, and analytic models are insufficient to quantify the amount of chemical mixing (Meyer & Meyer-Hofmeister 1979). One observational clue may be SN 1987A, which is believed to be the result of a common envelope evolution (Podsiadlowski et al. 1990). Blue progenitors may also be a result of low metallicity (Brunish & Truran 1982; Chieffi et al. 2003), and very few SN 1987A-like events have been found (Pastorello et al. 2012; Taddia et al. 2012). Pastorello et al. (2012) estimate that SN 1987A-likes represent ∼1.5%–4% of SNe II; however, this is likely an extreme upper limit to our scenario, since the preponderance of these objects may be just from higher mass compact stars, rather than from systems in binaries that have undergone common envelope evolution. Similarly, one can use observations of WDs to provide another estimate. The number of WDs with sub-stellar companions is $\lesssim$0.5% (Farihi et al. 2005), and the number of WDs with debris disks from tidally disrupting minor planets is 1%–3% (Farihi et al. 2009). Therefore, our scenario should be quite rare, representing 0.05%–0.5% of all SNe Ia.

Finally, we want to mention the long list of limitations of our studies. We have suggested the existence of a rare subclass of SNe Ia which should obey an anti-Phillips relation. It is up to future systematic surveys, such as LSST, to find a sufficiently large statistical sample. Note that this sub-class may be hard to separate at the bright end of SNe Ia because the decline rates for both normal and "SN 2001ay-like" supernovae are low and similar. Chemical mixing during the common envelope phase needs to be studied in detail. Our model for SN 2001ay requires a shift of the ^{56}Ni distribution and a central hole in ^{56}Ni. Although verified for a number of normal SNe Ia, late time spectra for an SN 2001ay-like are required to confirm our assumptions of little mixing. Detailed time-series of early time spectra may help to probe whether PDDs provide a common mechanism for the transition from deflagration to detonation. Detailed three-dimensional models of the pulsation phase are required to test and quantify possible mixing.

The work presented in this paper has been carried out within the NSF project "Collaborative research: Three-Dimensional Simulations of Type Ia Supernovae: Constraining Models with Observations," whose goal is to test and constrain the physics of supernovae by observations and improve SNe Ia as tools for high-precision cosmology. The project involves The University of Chicago (AST-0709181), the University of Oklahoma (AST-0707704), Florida State University (AST-0708855), Texas A&M (AST-0708873), the University of Chile in Santiago, and the Las Campanas Observatory, Chile. This research was also supported, in part, by the NSF grant AST-0703902 to P.A.H. The work of E.B. was also supported in part by SFB 676, GRK 1354 from the DFG, and US DOE Grant DE-FG02-07ER41517. I.D. has been supported in part by the Spanish Ministry of Science and Innovation project AYA2008-04211-C02-02 (I.D.). Support for Program number HST-GO-12298.05-A was provided by NASA through a grant from the Space Telescope Science Institute, which is operated by the Association of Universities for Research in Astronomy, Incorporated, under NASA contract NAS5-26555. This research used resources of the National Energy Research Scientific Computing Center (NERSC), which is supported by the Office of Science of the U.S. Department of Energy under contract no. DE-AC02-05CH11231; and the Höchstleistungs Rechenzentrum Nord (HLRN). We thank both these institutions for a generous allocation of computer time.

APPENDIX

BRIEF DESCRIPTION OF NUMERICAL METHODS

A.1. Explosion

We have calculated explosion models and LCs using the one-dimensional radiation-hydro code HYDRA using computational modules for spherical geometry (Höflich 1995, 2003a, 2003b, 2009). We solve the hydrodynamical equations explicitly by the piecewise parabolic method on 910 depth points (Colella & Woodward 1984). Because a simple α network is insufficient

Table 1
Element Yields

Element	Yield ($M_\odot$)
He	0.01
C	0.021
O	0.043
Ne	3×10^{-3}
Na	7.8×10^{-5}
Mg	1×10^{-3}
Si	0.182
P	9×10^{-5}
S	0.104
Cl	4.2×10^{-5}
Ar	0.022
K	4.8×10^{-5}
Ca	0.022
Sc	3.1×10^{-7}
Ti	1.5×10^{-3}
V	0.022
Cr	0.106
Mn	0.024
Fe	0.661
Co	1.1×10^{-3}
Ni	0.146
^{56}Ni	0.515

Notes. The yield of the stable elements at time infinity along with the total mass of ^{56}Ni produced in the explosion.

to describe in sufficient detail the chemical boundary. Nuclear burning is taken into account using an extended network of 218 isotopes from *n, p* to ^{74}Kr (Thielemann et al. 1996; Hix & Thielemann 1996; Höflich et al. 1998 and references therein). The propagation of the nuclear burning front is given by the velocity of sound behind the burning front in the case of a detonation wave. We use the parameterization as described in Domínguez & Höflich (2000). For a deflagration front at distance $r_{\rm burn}$ from the center, we assume that the burning velocity is given by $v_{\rm burn} = \max(v_t, v_l)$, where v_l and v_t are the laminar and turbulent velocities with

$$v_t = \sqrt{\alpha_T g L_f}, \tag{A1}$$

with

$$\alpha_T = (\alpha - 1)/(\alpha + 1)$$

and

$$\alpha = \rho^+(r_{\rm burn})/\rho^-(r_{\rm burn}).$$

Here, α_T is the Atwood number, L_f is the characteristic length scale, and ρ^+ and ρ^- are the densities in front of and behind the burning front, respectively. The quantities α and L_f are directly taken from the hydrodynamical model at the location of the burning front and we take $L_f = r_{\rm burn}(t)$. The transition density is treated as a free parameter. Table 1 gives the yields of the stable elements as well as the total amount of ^{56}Ni produced in the explosion.

A.2. Light Curves

From these explosion models, the subsequent expansion, bolometric, and broadband LC are calculated using monochromatic radiation transport via the Eddington Tensor method. Both the Eddington tensor and the γ-ray transport are calculated via Monte Carlo as in the three-dimensional case. We include scattering, free–free, and bound–free opacities, and include the line transitions in the Sobolev approximation. For several elements, including C, O, Mg, Si, S, Ca, Fe, Co, and Ni, we solve the statistical equations for the three main ionization stages using detailed atomic models with 10–50 super-levels with ≈12,000 transitions using the databases of Kurucz (2002) and Cunto & Mendoza (1992). The levels closest to the continuum and of other elements are treated in local thermodynamical equilibrium with about 10^6 line transitions.

A.3. Spectra

The calculations were performed using the multi-purpose stellar atmospheres program `PHOENIX/1D` version `16` (Hauschildt & Baron 1999; Baron & Hauschildt 1998; Hauschildt et al. 1997a, 1997b, 1996). Version 16 incorporates many changes over previous versions used for supernova modeling (Baron et al. 2007, 2006) including many more species in the equation of state (83 versus 40), twice as many atomic lines, and many more species treated in full non-LTE (NLTE) and an improved equation of state. `PHOENIX/1D` solves the radiative transfer equation along characteristic rays in spherical symmetry including all special relativistic effects. The NLTE rate equations for many ionization states are solved including the effects of ionization due to non-thermal electrons from the γ-rays produced by the radiative decay of ^{56}Ni, which is produced in the supernova explosion. The atoms and ions calculated in NLTE are He I–II, C I–III, O I–III, Ne I, Na I–II, Mg I–III, Si I–III, S I–III, Ca II, Ti II, Cr I–III, Mn I–III, Fe I–III, Co I–III, and Ni I–III. These are all the elements whose features make important contributions to the observed spectral features in SNe Ia. γ-ray deposition was that calculated by the LC.

Each model atom includes primary NLTE transitions, which are used to calculate the level populations and opacity, and weaker secondary LTE transitions which are included in the opacity and implicitly affect the rate equations via their effect on the solution to the transport equation (Hauschildt & Baron 1999). In addition to the NLTE transitions, all other LTE line opacities for atomic species not treated in NLTE are treated with the equivalent two-level atom source function, using a thermalization parameter, $\alpha = 0.10$ (Baron et al. 1996). The atmospheres are iterated to energy balance in the comoving frame; while we neglect the explicit effects of time dependence in the radiation transport equation, we do implicitly include these effects, via explicitly including $p\,dV$ work and the rate of gamma-ray deposition in the generalized equation of radiative equilibrium and in the rate equations for the NLTE populations.

The outer boundary condition is the total bolometric luminosity in the observer's frame. The inner boundary condition is that the flux at the innermost zone ($v = 700$ km s^{-1}) is given by the diffusion equation. Converged models required 256 optical depth points to correctly obtain the Si II λ6355 profile.

`PHOENIX` and HYDRA have been well tested and compared on SNe Ia (Nugent et al. 1995a, 1995b, 1997; Lentz et al. 2001; Baron et al. 2006; Höflich 2002, 2005; Höflich et al. 1998) and, in particular, compared with observed LCs and spectra of SN 1994D and SN 2001ay.

REFERENCES

Arnett, W. D. 1980, ApJ, 237, 541
Arnett, W. D. 1982, ApJ, 253, 785
Baron, E., Bongard, S., Branch, D., & Hauschildt, P. 2006, ApJ, 645, 480
Baron, E., Branch, D., & Hauschildt, P. H. 2007, ApJ, 662, 1148

Baron, E., & Hauschildt, P. H. 1998, ApJ, 495, 370
Baron, E., Hauschildt, P. H., Nugent, P., & Branch, D. 1996, MNRAS, 283, 297
Baron, E., Jeffery, D. J., Branch, D., et al. 2008, ApJ, 672, 1038
Becker, S. A., & Iben, I., Jr. 1980, ApJ, 237, 111
Brachwitz, F., Dean, D., Hix, W. R., et al. 2000, ApJ, 536, 934
Branch, D., Baron, E., Hall, N., Melakayil, M., & Parrent, J. 2005, PASP, 117, 545
Branch, D., Dang, L. C., & Baron, E. 2009, PASP, 121, 238
Bravo, E., & García-Senz, D. 2006, ApJ, 642, L157
Bravo, E., & García-Senz, D. 2009, ApJ, 695, 1244
Bravo, E., García-Senz, D., Cabezón, R. M., & Domínguez, I. 2009, ApJ, 695, 1257
Brunish, W., & Truran, J. 1982, ApJ, 49, 447
Buchmann, L. 1997, ApJ, 479, L153
Caputo, F., Tornambe, A., & Castellani, V. 1989, A&A, 222, 121
Castellani, V., Chieffi, A., Tornambe, A., & Pulone, L. 1985, ApJ, 294, L31
Chieffi, A., Domínguez, I., Höflich, P., Limongi, M., & Straniero, O. 2003, MNRAS, 345, 111
Colella, P., & Woodward, P. R. 1984, J. Comput. Phys., 54, 174
Colgate, S. A., & McKee, C. 1969, ApJ, 157, 623
Cunto, W., & Mendoza, C. 1992, Topbase Users Guide, Tech. Rep. CSC-01-92, IBM Venezuela Scientific Center, Caracas, Venezuela
Domínguez, I., & Höflich, P. 2000, ApJ, 528, 854
Domínguez, I., Höflich, P., & Straniero, O. 2001, ApJ, 557, 279
Farihi, J., Becklin, E. E., & Zuckerman, B. 2005, ApJS, 161, 394
Farihi, J., Jura, M., & Zuckerman, B. 2009, ApJ, 694, 805
Fesen, R. A., Höflich, P. A., Hamilton, A. J. S., et al. 2007, ApJ, 658, 396
Freedman, W. L., Madore, B. F., Gibson, B. K., et al. 2001, ApJ, 553, 47
Gerardy, C. L., Meikle, W. P. S., Kotak, R., et al. 2007, ApJ, 661, 995
Goldhaber, G., Groom, D. E., Kim, A., et al. 2001, ApJ, 558, 359
Goldhaber, G., & Perlmutter, S. 1998, Phys. Rep., 307, 325
Hauschildt, P. H., & Baron, E. 1999, J. Comput. Appl. Math., 109, 41
Hauschildt, P. H., Baron, E., & Allard, F. 1997a, ApJ, 483, 390
Hauschildt, P. H., Baron, E., Starrfield, S., & Allard, F. 1996, ApJ, 462, 386
Hauschildt, P. H., Schwarz, G., Baron, E., et al. 1997b, ApJ, 490, 803
Hessman, F. V., Beuermann, K., Dreizler, S., et al. 2011, in AIP Conf. Ser. 1331, Planetary Systems Beyond the Main Sequence, ed. S. Schuh, H. Drechsel, & U. Heber (Melville, NY: AIP), 281
Hix, W. R., & Thielemann, F.-K. 1996, ApJ, 460, 869
Höflich, P. 1995, ApJ, 443, 89
Höflich, P. 2002, New Astron. Rev., 46, 475
Höflich, P. 2003a, in ASP Conf. Ser. 288, Stellar Atmosphere Modeling, ed. I. Hubeny, D. Mihalas, & K. Werner (San Francisco, CA: ASP), 185
Höflich, P. 2003b, in ASP Conf. Ser. 288, Stellar Atmosphere Modeling, ed. I. Hubeny, D. Mihalas, & K. Werner (San Francisco, CA: ASP), 371
Höflich, P. 2005, Ap&SS, 298, 87
Höflich, P. 2006, Nucl. Phys. A, 777, 579
Höflich, P. 2009, in Recent Directions In Astrophysical Quantitative Spectroscopy And Radiation Hydrodynamics, ed. I. Hubeny, J. M. Stone, K. MacGregor, & K. Werner (New York: AIP), 161
Höflich, P., Gerardy, C., Fesen, R., & Sakai, S. 2002, ApJ, 568, 791
Höflich, P., Gerardy, C. L., Nomoto, K., et al. 2004, ApJ, 617, 1258
Höflich, P., & Khokhlov, A. 1996, ApJ, 457, 500
Hoflich, P., Khokhlov, A. M., & Wheeler, J. C. 1995, ApJ, 444, 831
Höflich, P., Khokhlov, A., Wheeler, J. C., et al. 1996, ApJ, 472, L81
Höflich, P., Krisciunas, K., Khokhlov, A. M., et al. 2010, ApJ, 710, 444
Höflich, P., Müller, E., & Khokhlov, A. 1993, A&A, 268, 570
Höflich, P., Wheeler, J. C., & Thielemann, F.-K. 1998, ApJ, 495, 617
Howell, A., Sullivan, M., Nugent, P. E., et al. 2006, Nature, 443, 308
Howell, D. A. 2011, Nature Commun., 2, 350
Iben, I., & Tutukov, A. 1984, ApJS, 54, 335
Ivanova, L. N., Imshennik, V. S., & Chechetkin, V. M. 1974, Ap&SS, 31, 497
Iwamoto, K., Brachwitz, F., Nomoto, K., et al. 1999, ApJS, 125, 439
Kasen, D., Röpke, F. K., & Woosley, S. E. 2009, Nature, 460, 869
Khokhlov, A. M. 1989, MNRAS, 239, 785
Khokhlov, A. 1993, ApJ, 419, L77
Khokhlov, A., Müller, E., & Höflich, P. 1992, A&A, 253, L9
Khokhlov, A., Müller, E., & Höflich, P. 1993, A&A, 270, 223
Krisciunas, K., Li, W., Matheson, T., et al. 2011, AJ, 142, 74
Kurucz, R. L. 2002, in AIP Conf. Ser. 636, Atomic and Molecular Data and Their Applications, ed. D. R. Schultz, P. S. Krstic, & F. Ownby (Melville, NY: AIP), 134
Lentz, E., Baron, E., Branch, D., & Hauschildt, P. H. 2001, ApJ, 557, 266
Lentz, E., Baron, E., Branch, D., Hauschildt, P. H., & Nugent, P. 2000, ApJ, 530, 966
Livio, M., & Soker, N. 1988, ApJ, 329, 764
Maeda, K., Benetti, S., Stritzinger, M., et al. 2010, Nature, 466, 82
Maoz, D. 2008, MNRAS, 384, 267
Maoz, D., Mannucci, F., Li, W., et al. 2011, MNRAS, 412, 1508
Maoz, D., Sharon, K., & Gal-Yam, A. 2010, ApJ, 722, 1879
Maund, J. R., Höflich, P. A., Patat, F., et al. 2010, ApJ, 725, L167
Mennekens, N., Vanbeveren, D., De Greve, J. P., & De Donder, E. 2010, A&A, 515, A89
Meyer, F., & Meyer-Hofmeister, E. 1979, A&A, 78, 167
Mochkovitch, R., & Livio, M. 1990, A&A, 236, 378
Motohara, K., Maeda, K., Gerardy, C. L., et al. 2006, ApJ, 652, L101
Neuhäuser, R., & Posselt, B. 2007, Astron. Nachr., 328, 711
Nugent, P., Baron, E., Branch, D., Fisher, A., & Hauschildt, P. 1997, ApJ, 485, 812
Nugent, P., Baron, E., Hauschildt, P., & Branch, D. 1995a, ApJ, 441, L33
Nugent, P., Phillips, M., Baron, E., Branch, D., & Hauschildt, P. 1995b, ApJ, 455, L147
Pastorello, A., Pumo, M. L., Navasardyan, H., et al. 2012, A&A, 537, A141
Penney, B., & Höflich, P. 2012, ApJ, in press
Perlmutter, S., Aldering, G., Goldhaber, G., et al. 1999, ApJ, 517, 565
Phillips, M. M. 1993, ApJ, 413, L105
Phillips, M. M., Lira, P., Suntzeff, N. B., et al. 1999, AJ, 118, 1766
Pinto, P. A., & Eastman, R. G. 2000, ApJ, 530, 757
Podsiadlowski, P., Joss, P. C., & Rappaport, S. 1990, A&A, 227, L9
Quimby, R., Höflich, P., Kannappan, S., et al. 2006, ApJ, 636, 400
Renzini, A., & Fusi Pecci, F. 1988, ARA&A, 26, 199
Ricker, P. M., & Taam, R. E. 2008, ApJ, 672, L41
Riess, A., Filippenko, A. V., Challis, P., et al. 1998, AJ, 116, 1009
Riess, A., Filippenko, A. V., Li, W., & Schmidt, B. P. 1999, AJ, 118, 2668
Ruiter, A. J., Belczynski, K., & Fryer, C. 2009, ApJ, 699, 2026
Ruiter, A. J., Belczynski, K., Sim, S. A., et al. 2011, MNRAS, 417, 408
Saio, H., & Nomoto, K. 1985, A&A, 150, L21
Saio, H., & Nomoto, K. 1998, ApJ, 500, 388
Scalzo, R. A., Aldering, G., Antilogus, P., et al. 2010, ApJ, 713, 1073
Seitenzahl, I. R., Ciaraldi-Schoolmann, F., & Röpke, F. K. 2011, MNRAS, 414, 2709
Shen, K. J., Bildsten, L., Kasen, D., & Quataert, E. 2012, ApJ, 748, 35
Silverman, J. M., Ganeshalingam, M., Li, W., et al. 2011, MNRAS, 410, 585
Straniero, O., Domínguez, I., Imbriani, G., & Piersanti, L. 2003, ApJ, 583, 878
Taddia, F., Stritzinger, M. D., Sollerman, J., et al. 2012, A&A, 537, A140
Tanaka, M., Kawabata, K. S., Yamanaka, M., et al. 2010, ApJ, 714, 1209
Taubenberger, S., Benetti, S., Childress, M., et al. 2011, MNRAS, 412, 2735
Thielemann, F.-K., Argast, D., Brachwitz, F., et al. 2003, Nucl. Phys. A, 718, 139
Thielemann, F.-K., Nomoto, K., & Hashimoto, M.-A. 1996, ApJ, 460, 408
Tutukov, A. V., & Yungelson, L. R. 1979, ACTAA, 29, 665
Umeda, H., Nomoto, K., Kobayashi, C., Hachisu, I., & Kato, M. 1999, ApJ, 522, L43
Webbink, R. F. 1984, ApJ, 277, 355
Woosley, S. E., & Weaver, T. A. 1986, in NATO ASIC Proc. 163, Nucleosynthesis and its Implications on Nuclear and Particle Physics, ed. J. Audouze & N. Mathieu (Dordrecht: Reidel), 145
Yamanaka, M., Kawabata, K. S., Kinugasa, K., et al. 2009, ApJ, 707, L118
Yamaoka, H., Nomoto, K., Shigeyama, T., & Thielemann, F.-K. 1992, ApJ, 393, L55
Yuan, F., Quimby, R. M., Wheeler, J. C., et al. 2010, ApJ, 715, 1338
Yungelson, L., & Livio, M. 1998, ApJ, 497, 168
Yungelson, L. R., & Livio, M. 2000, ApJ, 528, 108

The Astrophysical Journal Supplement Series, 203:12 (15pp), 2012 November doi:10.1088/0067-0049/203/1/12

SUPERNOVA RESONANCE-SCATTERING LINE PROFILES IN THE ABSENCE OF A PHOTOSPHERE

Brian Friesen[1], E. Baron[1,2,3,4], David Branch[1], Bin Chen[1], Jerod T. Parrent[5,6], and R. C. Thomas[3]
[1] Homer L. Dodge Department of Physics & Astronomy, University of Oklahoma, 440 W. Brooks St., Rm. 100, Norman, OK 73019, USA
[2] Hamburger Sternwarte, Gojenbergsweg 112, D-21029 Hamburg, Germany
[3] Computational Cosmology Center, Computational Research Division, Lawrence Berkeley National Laboratory, MS 50B-4206, 1 Cyclotron Road, CA 94720, USA
[4] Department of Physics, University of California, Berkeley, CA 94720, USA
[5] 6127 Wilder Lab, Department of Physics & Astronomy, Dartmouth College, Hanover, NH 03755, USA
[6] Las Cumbres Observatory Global Telescope Network, Goleta, CA 93117, USA
Received 2012 May 29; accepted 2012 September 8; published 2012 November 1

ABSTRACT

In supernova (SN) spectroscopy relatively little attention has been given to the properties of optically thick spectral lines in epochs following the photosphere's recession. Most treatments and analyses of post-photospheric optical spectra of SNe assume that forbidden-line emission comprises most if not all spectral features. However, evidence exists that suggests that some spectra exhibit line profiles formed via optically thick resonance-scattering even months or years after the SN explosion. To explore this possibility, we present a geometrical approach to SN spectrum formation based on the "Elementary Supernova" model, wherein we investigate the characteristics of resonance-scattering in optically thick lines while replacing the photosphere with a transparent central core emitting non-blackbody continuum radiation, akin to the optical continuum provided by decaying ^{56}Co formed during the explosion. We develop the mathematical framework necessary for solving the radiative transfer equation under these conditions and calculate spectra for both isolated and blended lines. Our comparisons with analogous results from the Elementary Supernova code SYNOW reveal several marked differences in line formation. Most notably, resonance lines in these conditions form P Cygni-like profiles, but the emission peaks and absorption troughs shift redward and blueward, respectively, from the line's rest wavelength by a significant amount, despite the spherically symmetric distribution of the line optical depth in the ejecta. These properties and others that we find in this work could lead to misidentification of lines or misattribution of properties of line-forming material at post-photospheric times in SN optical spectra.

Key words: line: formation – line: profiles – radiative transfer – supernovae: general

Online-only material: color figures

1. INTRODUCTION

Many of the physical processes that contribute to spectrum formation in a supernova (SN) change dramatically as it ages. Given the difficulty and complexity of including all such processes, as well as their evolution in time, exploration into this computational frontier has begun only very recently (Pinto & Eastman 2000; Höflich 2003; Kasen et al. 2006; Jack et al. 2009; Kromer & Sim 2009; De et al. 2010; Dessart & Hillier 2010, 2011; Hillier & Dessart 2012). Most work in SN spectroscopy has focused on the early "photospheric" phase, comprising the time from explosion to a few weeks post-maximum light, where resonance-scattering from permitted lines dominates the spectrum (Branch et al. 1983, 1985, 2005; Jeffery et al. 1992; Mazzali & Lucy 1993; Mazzali et al. 1995, 1997, 2005; Fisher et al. 1997; Hatano et al. 1999a; Mazzali 2000, 2001; Dessart & Hillier 2005; Hachinger et al. 2006). Considerably less attention has been given to the "nebular" phase, several months or more after explosion, where emission from forbidden lines constitute most of the spectrum (Axelrod 1980; Ruiz-Lapuente & Lucy 1992; Kozma & Fransson 1998a, 1998b; Mazzali et al. 1998, 2011; Maeda et al. 2006; Jerkstrand et al. 2011). Finally, the intermediate phases, that is, a few months post-explosion, have received the least amount of scrutiny (Maurer et al. 2011). One reason so much attention focuses on either very early or very late times is that in these regimes one can reproduce with reasonable fidelity the physical processes that dominate spectrum formation through a number of simplifying assumptions. For example, in the early, photospheric phase the Sobolev approximation (Castor 1970) and a resonance-scattering source function (Jeffery & Branch 1990) are both accurate approximations due to the high densities and steep velocity gradients in the SN ejecta; at late times one typically assumes both that the ejecta are optically thin and that line emission arises exclusively from forbidden lines (Axelrod 1980). However these two groups of assumptions are generally incompatible with each other in the intermediate regime of an SN.

Complicating matters further is the possibility that the evolution of the different types of line-forming processes is asynchronous. Specifically, the emergence of forbidden emission lines in an SN spectrum may not herald the systematic withdrawal of resonance-scattering in optically thick permitted lines. Though this possibility has frequently been acknowledged (Bowers et al. 1997; Branch et al. 2005; Jerkstrand et al. 2011), it has to our knowledge never been pursued in detail until now. To illustrate this point we show in Figures 1 and 2 SYNOW fits to the day +87 optical spectrum of SN 2003du and the day +115 spectrum of SN 1994D, respectively. In the SN 2003du fit we use only three ions: Na I, Ca II, and Fe II. The photospheric velocity is 7000 km s^{-1}, and the photospheric temperature is 8000 K. The excitation temperature of all three ions is 7000 K. In the SN 1994D fit, we include five ions: Na I, Ca II, Cr II, Fe II, and Co II. Here, the photospheric velocity is 6000 km s^{-1} and the temperature is 10,000 K. The excitation temperature of all ions is 7000 K. The observed and synthetic spectra of both SN 1994D and SN 2003du have been flattened using the method of Jeffery et al. (2007).

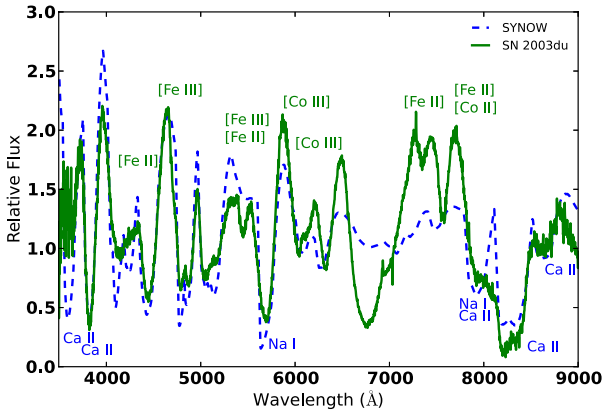

Figure 1. SYNOW fit to the +87 day spectrum of SN 2003du. The synthetic spectrum contains Na I, Ca II, and Fe II, each with an excitation temperature of 7000 K. The photospheric velocity is 7000 km s^{-1}, and the spectrum has been divided through by the blackbody continuum. The permitted line identifications (in blue) are from the SYNOW fit, with Fe II features unlabeled. The alternative forbidden-line IDs (in green) follow those in other SNe Ia made by Bowers et al. (1997).

(A color version of this figure is available in the online journal.)

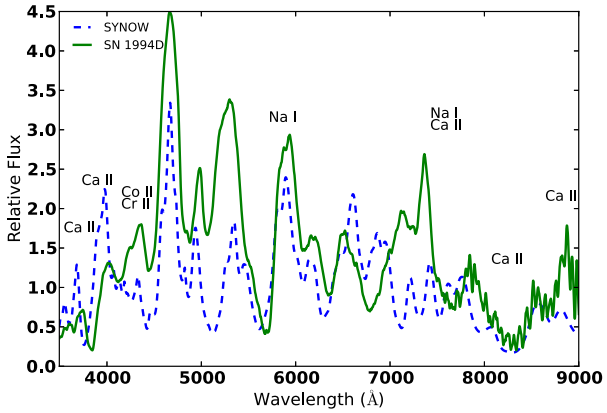

Figure 2. SYNOW fit to the +115 day spectrum of SN 1994D. The synthetic spectrum contains Na I, Ca II, Cr II, Fe II, and Co II, each with an excitation temperature of 7000 K. The photospheric velocity is 6000 km s^{-1}, and the spectrum has been divided through by the blackbody continuum. As in Figure 1 the unlabeled features in the SYNOW spectrum are due to Fe II.

(A color version of this figure is available in the online journal.)

The fits to the observed spectra in both of these figures are relatively good, and in both fits only permitted lines were considered. Even among the features that SYNOW cannot reproduce accurately, most of the emission peaks and absorption troughs in the synthetic spectra form at the same wavelengths as in the observed spectra, and only the strengths of the features are disparate. (The exceptions to this are the wavelength range 6600–7800 Å in SN 2003du and 6600–7500 Å in SN 1994D, throughout which SYNOW fails completely to reproduce the observed features.) It would therefore be a remarkable coincidence if the observed features in these two objects arise from purely forbidden emission (Branch et al. 2005).

In addition to the circumstantial evidence for persistent resonance-scattering provided by these reasonably good SYNOW fits to several-months-old Type Ia supernovae (SNe Ia), calculations by Hatano et al. (1999b) and Jerkstrand et al. (2011) further defend this claim. Hatano et al. (1999b) calculated the Sobolev optical depth (Equation (1) of that paper) for the most common ions observed in SN Ia optical spectra. In Figure 9(c) of that work they show the Sobolev local thermodynamic equilibrium (LTE) optical depth for Fe I & II and Co I & II for an iron-rich composition at 80 days post-explosion in an SN Ia model, and find that the optical depths for those ions can be as high as $\tau \sim 50{,}000$. Similarly, the simplified form of the Sobolev optical depth shown in Equation (39) of Jerkstrand et al. (2011) shows that the optical depths for some UV resonance lines (e.g., Mg II λ2798) can still be as high as $\tau \sim 1000$ even 8 *years* post-explosion.

In light of the evidence presented above for resonance-scattering at relatively late times in SNe Ia, we present a geometrical exploration of this phenomenon in the spirit of the Elementary Supernova approach of Jeffery & Branch (1990). Rather than attempt to discern exactly how late after an SN explosion resonance-scattering continues to contribute significantly to spectrum formation, we assume simply that the photosphere has receded and that the continuum opacity in the core of the SN is negligibly small. We replace the photosphere with a transparent core emitting non-blackbody continuum radiation and distribute ions both inside this "glowing" core and outside the core in a non-emitting shell. We then calculate emergent flux profiles for lines with parameterized optical depths in several different geometrical configurations. We scrutinize line formation and behavior in both isolated and blended cases. Because SYNOW inspired this model, the two naturally invite comparison, which we indulge throughout this work. In Section 2, we treat the case of pure continuum (no lines) in the core; in Section 3, we introduce a single line in the core; in Section 4, we surround the glowing core with a transparent, non-glowing shell and move the line to the shell; in Section 5, we account for the effects of multiple scattering by placing two lines in the core; Section 6 contains our discussion of the implications of our results on interpretation of late-time spectra of SNe; and in Section 7, we conclude our work. Finally, we include Appendices, which contain complete mathematical derivations so that all of our work may easily be reproduced.

2. A TRANSPARENT, UNIFORMLY EMITTING CORE

We begin by assuming that the SN is spherically symmetric. Under this circumstance it is natural to work in (p, z) coordinates, where p is the impact parameter of a ray relative to the center of the SN, such that the $p = 0$ ray exactly bisects the SN; and z is orthogonal to p, with the $z = 0$ line also exactly bisecting the SN. We will at times transform to spherical polar coordinates for computational expedience, where the radial coordinate r satisfies

$$r^2 = p^2 + z^2. \tag{1}$$

We also assume that the SN undergoes homologous expansion, $v = r/t$, so that surfaces of constant line-of-sight velocity are vertical planes, that is, planes of constant z. We further assume that the observer is located at $z \to -\infty$, in which case all rays incident on the observer are parallel. Next, we assume that the photosphere has receded and has been replaced by a transparent, spherically symmetric core with outer radius r_c, which emits continuum (but not blackbody) radiation. The post-photospheric spectra of many SNe Ia contain a flat and weak continuum, which is either thermal in nature or, as Bowers et al. (1997) suggest, due to the sea of weak optical lines of lowly ionized Fe and Co. At very late times when the spectrum becomes truly

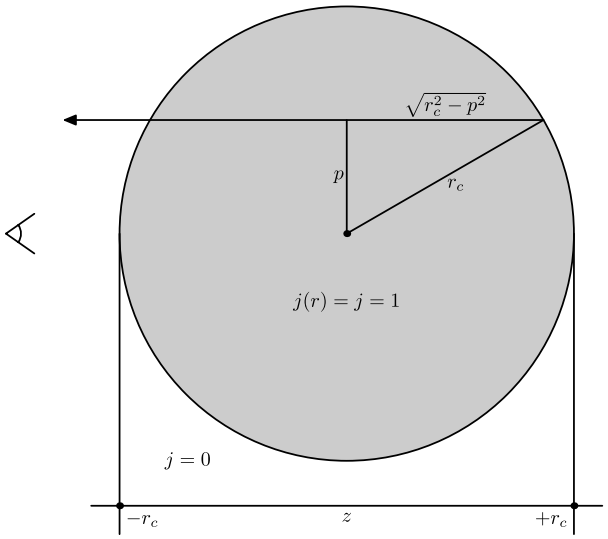

Figure 3. Continuum ray in the core of the SN. In this figure and all that follow, we use gray shading to label the continuum-emitting region.

nebular, there is no optical thermal continuum, but we do not seek to extend our methods into this very late regime. To mimic this pseudo-continuum we assign to the core a gray, spatially constant volume emissivity $j_\lambda(r) = j$ for all radii $r \leqslant r_c$ and all wavelengths λ. This assumption allows us to present simple analytic results; with only slight modification, our methods for calculating line profiles are amenable to chromatic emissivity.

2.1. Continuum Only

In general, to calculate the emergent flux from an SN atmosphere one must first calculate the source function at all locations in the SN, followed by the emergent intensity of rays exiting the ejecta toward the observer. However, since in this model we neglect all continuum opacity, the source function is not a well-defined quantity in the absence of lines. Therefore, we write down immediately the emergent intensity of a constant p ray originating at the back[7] of the core and traversing toward the observer, without calculating the source function. When no lines are present the intensity of a ray passing through the core is proportional to its geometric length:

$$I(p) = 2j\left(r_c^2 - p^2\right)^{1/2}. \tag{2}$$

A representative intensity ray is shown in Figure 3. If instead the emissivity has spatial dependence, $j = j(r)$, the result has a more general form:

$$\begin{aligned} I(p) &= \int_{-(r_c^2-p^2)^{1/2}}^{(r_c^2-p^2)^{1/2}} j((p^2+z^2)^{1/2})dz \\ &= 2\int_0^{(r_c^2-p^2)^{1/2}} j((p^2+z^2)^{1/2})dz, \end{aligned} \tag{3}$$

where we have transformed the argument of j since the intensity along a ray of constant p depends only on its z coordinate.

[7] In this discussion "front" and "back" refer to locations in the SN nearest to and farthest from the observer, respectively.

Already a physical peculiarity arises: limb darkening in the absence of scattering or absorption. The traditional interpretation of limb darkening in photospheric objects such as dwarf stars and young SNe is that intensity rays with large impact parameter p, that is, rays that emerge from the limb, reach an optical depth of $\tau \simeq 1$ at shallower layers in the atmosphere than low-impact parameter rays. Under the assumption of LTE, shallower locations in atmospheres have lower temperatures and thus weaker source functions, since LTE requires by definition that $S = B$ where B is the Planck function. A weaker source function in turn leads to a lower intensity emergent ray, the cumulative result of which is limb darkening.

In the case of this post-photospheric model, however, high-p rays accumulate less continuum as they proceed from the back of the object toward the observer. Such accumulation does not occur in photospheric-phase atmospheres of SNe except through lines in the atmosphere that scatter continuum photons from the blackbody photosphere into the ray; however, this contribution is small except when the line has an extraordinarily high optical depth.

Using Equation (2), the continuum flux at all wavelengths is given by

$$F_\lambda \equiv \int I_\lambda \cos\theta d\Omega = \frac{2\pi}{r_c^2}\int_0^{r_c} I_\lambda p dp = \frac{4\pi}{3} j r_c. \tag{4}$$

For clarity, and without loss of generality, hereafter we set $j \equiv 1$, so I_λ, J_λ, and F_λ have units of length and the geometric nature of our results becomes apparent. In addition, since in homologous expansion $v \propto r$, we interchange lengths and velocities where convenient.

2.2. Mean Intensity

We now calculate the mean intensity, J, both inside and outside the glowing core. Without any lines, J is not a particularly useful quantity in this model since we do not need it to calculate the emergent flux. However, when we add a single line to the core in Section 3 we require the source function to calculate the emergent intensity, and in the resonance-scattering approximation $S = J$.

By definition,

$$J_\lambda(r) \equiv \frac{1}{4\pi}\int I_\lambda(r) d\Omega = \frac{1}{2}\int_{-1}^{1} I_\lambda(r) d\mu, \tag{5}$$

where $\mu \equiv \cos\theta$, and we have applied to the radiation field the condition of azimuthal symmetry. Inside the core, $r \leqslant r_c$, so from Figure 4,

$$X = r\mu + \left(r^2\mu^2 + r_c^2 - r^2\right)^{1/2}. \tag{6}$$

Setting $I_\lambda(r) = X(r)$, plugging this into Equation (5), and using standard integral tables, we find

$$J(r) = \frac{1}{2r}\left\{ r r_c + \frac{\left(r_c^2 - r^2\right)}{2} \ln\left[\frac{r_c + r}{r_c - r}\right]\right\}. \tag{7}$$

Calculating the mean intensity outside the core (with the line still inside the core) is slightly more complicated and we include the derivation in Appendix A. The result is

$$J(r) = \frac{1}{2r}\left\{ r r_c + \frac{\left(r^2 - r_c^2\right)}{2} \ln\left[\frac{r - r_c}{r + r_c}\right]\right\}. \tag{8}$$

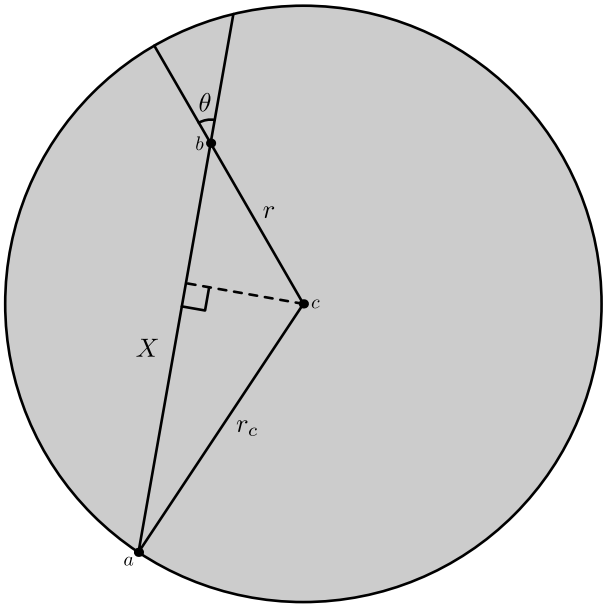

Figure 4. Geometric configuration used to calculate $J(r < r_c)$ both for pure continuum and for a single line in the core. X is the magnitude of the vector ***ab***, r_c is that of ***ac***, and r is that of ***bc***.

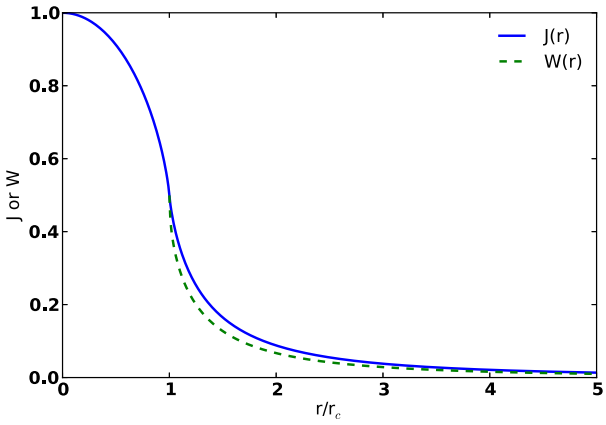

Figure 5. Profile of $J(r)$ and $W(r)$, where W is the dilution factor.
(A color version of this figure is available in the online journal.)

Figure 5 shows the behavior of $J(r)$ in units of r_c and for comparison the dilution factor $W(r)$ (Mihalas 1978) is also shown. The shape of J is vary similar to that of a Gaussian and it is larger than $W(r)$ until quite large r, where both functions behave as $(1/4)(r_c/r)^2$. We emphasize that J peaks strongly at $r = 0$, a result that affects line formation significantly, as we will discuss in Section 3.

3. A LINE IN THE CORE

We now treat the case of a single line, forming inside the core. We assume, for simplicity, a constant Sobolev optical depth τ in the line throughout the core. Before continuing, we note that the most profound effect of homologously expanding matter on the radiation field is that photons redshift with respect to the matter regardless of propagation direction. Therefore photons in a ray that starts at the back of the core and emerges toward the observer redshift continuously as they move along the ray. Referring to

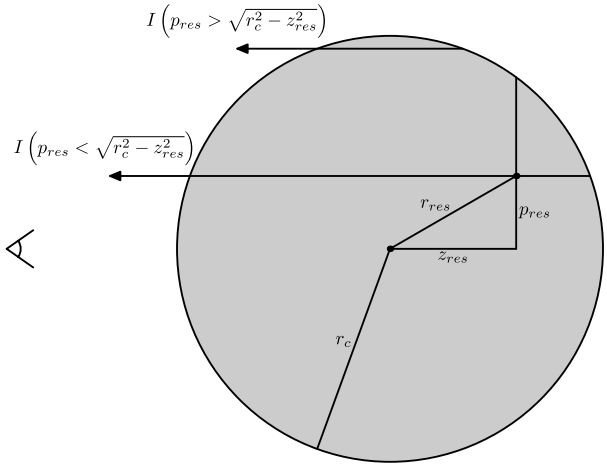

Figure 6. Intensity rays with a single line in the core.

Figure 6, if a ray originates in front of the plane of constant $z_{\rm res}$ corresponding to the location in the core $z = z_{\rm res}$ where the line Doppler shifts into resonance with a particular wavelength point—that is, if $p > (r_c^2 - z_{\rm res}^2)^{1/2}$—then the intensity of that ray is simply its continuum value, given by Equation (2). However, if the ray forms behind that plane—if $p < (r_c^2 - z_{\rm res}^2)^{1/2}$—the line attenuates some of the continuum intensity by scattering photons out of the ray and therefore out of the observer's line of sight. In the Sobolev approximation this attenuation manifests as an $e^{-\tau}$ term multiplying the continuum intensity at the location of the line. In addition to attenuating the intensity along a ray, the line also contributes to the intensity via its source function $S(r[z_{\rm res}])$. Specifically, the contribution is

$$I_{\rm line} = S(1 - e^{-\tau}). \tag{9}$$

The two different types of rays are depicted in Figure 6. Their emergent intensities are

$$I_{z_{\rm res}}(p) = \begin{cases} \left(\left(r_c^2 - p^2\right)^{1/2} - z_{\rm res}\right)e^{-\tau} + S(r)(1 - e^{-\tau}) \\ \quad + \left(r_c^2 - p^2\right)^{1/2} + z_{\rm res} & p < \left(r_c^2 - z_{\rm res}^2\right)^{1/2} \\ 2\left(r_c^2 - p^2\right)^{1/2} & p > \left(r_c^2 - z_{\rm res}^2\right)^{1/2}. \end{cases} \tag{10}$$

The integral over $I_{z_{\rm res}}(p)$ is straightforward except for the term containing the source function $S(r)$. To integrate this term we define

$$\begin{aligned} g(z_{\rm res}) &\equiv \int_0^{\sqrt{r_c^2 - z_{\rm res}^2}} S(r) p dp \\ &= \int_0^{\sqrt{r_c^2 - z_{\rm res}^2}} \frac{1}{2r}\left[r r_c + \frac{r_c^2 - r^2}{2} \ln\left[\frac{r_c + r}{r_c - r}\right]\right] p dp. \end{aligned} \tag{11}$$

We then transform the integration variable from p to r, which leads to

$$g(z_{\rm res}) = \int_{z_{\rm res}}^{r_c} \frac{1}{2r}\left[r r_c + \frac{r_c^2 - r^2}{2} \ln\left[\frac{r_c + r}{r_c - r}\right]\right] r dr.$$

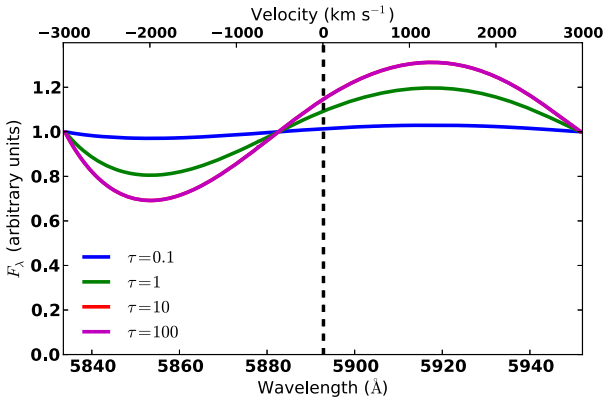

Figure 7. Flux profiles for Na I D, λ5892, in the post-photospheric model, with spatially constant optical depth and an outer core velocity of 3000 km s^{-1}. The vertical dashed line indicates the rest wavelength of the line. The $\tau = 10$ and $\tau = 100$ profiles overlap almost exactly and are indistinguishable in this figure. In contrast to SYNOW, the red emission peak does not occur at the rest wavelength, but rather is redshifted by an amount independent of optical depth.

(A color version of this figure is available in the online journal.)

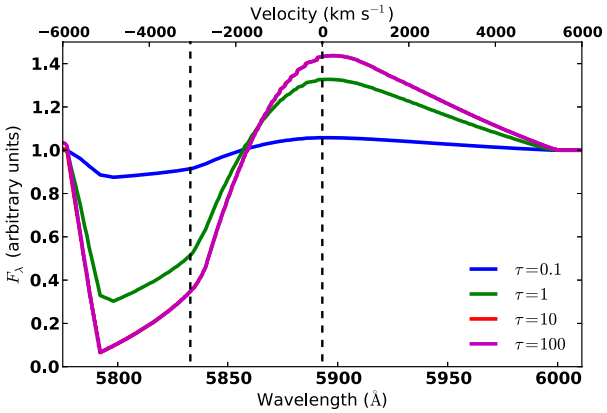

Figure 8. Flux profiles for Na I D in SYNOW, with photospheric velocity 3000 km s^{-1} and spatially constant optical depth. The maximum velocity of the line-forming region is 6000 km s^{-1}. The right dashed vertical line indicates the rest wavelength of the Na I D line (λ5892), and the left vertical line indicates the blueshifted rest wavelength of Na I D at the photospheric velocity. The $\tau = 10$ and $\tau = 100$ profiles overlap almost exactly and are indistinguishable in this figure. Unlike the profiles in Figure 7, the emission peak in the SYNOW case remains fixed at the line rest wavelength regardless of the optical depth.

(A color version of this figure is available in the online journal.)

This integral is still unwieldy, so we transform integration variables once again by defining

$$\mu \equiv \frac{z_{\rm res}}{r}$$

and

$$\mu_{\rm res} \equiv \frac{z_{\rm res}}{r_c}$$

from which we find

$$\frac{r}{r_c} = \frac{\mu_{\rm res}}{\mu}.$$

We then change the integration variable from r to μ, which yields

$$g(z_{\rm res}) = \frac{r_c^3}{2}\mu_{\rm res}^2 \int_{\mu_{\rm res}}^1 \left[1 + \frac{\mu^2 - \mu_{\rm res}^2}{2\mu\mu_{\rm res}} \ln\left[\frac{1+\mu_{\rm res}}{1-\mu_{\rm res}}\right]\right]\frac{d\mu}{\mu^3}.$$

The result is

$$g(z_{\rm res}) = \frac{r_c^3}{6}\left[1 + 2\ln 2 - \mu_{\rm res}^2 - \frac{\mu_{\rm res}}{2}\left(3 - \mu_{\rm res}^2\right)\ln\left[\frac{1+\mu_{\rm res}}{1-\mu_{\rm res}}\right] - \ln\left(1 - \mu_{\rm res}^2\right)\right]. \quad (12)$$

The remainder of Equation (4) poses little challenge and leads directly to an analytic result for the flux profile for the constant-τ case:

$$F(z_{\rm res}) = \frac{2\pi}{r_c^2}\left[\frac{2r_c^3}{3} + (1 - e^{-\tau})\left[g(z_{\rm res}) + \frac{z_{\rm res}\left(r_c^2 - z_{\rm res}^2\right)}{2} - \frac{r_c^3 - |z_{\rm res}|^3}{3}\right]\right]. \quad (13)$$

We remark here that, although Equation (4) defines the flux as a function of wavelength, we have derived Equation (13) in terms of the coordinate $z_{\rm res}$. One transforms between $z \leftrightarrow \lambda$ using the first-order Doppler formula,

$$z = r_{\rm max}\left(\frac{c}{v_{\rm max}}\right)\frac{\lambda - \lambda_0}{\lambda_0}, \quad (14)$$

where $r_{\rm max}$ ($v_{\rm max}$) is the maximum radius (velocity) of the ejecta. We show in Figure 7 the line profiles of Na I D, λ5892, with several different optical depths.[8] For comparison we show in Figure 8 the profile of Na I D as calculated by SYNOW, with the same optical depths as in Figure 7.

The profiles in both plots appear quite P Cygni-like, but differences do exist between them. We highlight two in particular. First, when a photosphere is present as in SYNOW, the emission peak of a line profile is located at its rest wavelength, regardless of the velocity of the material forming the line in the SN atmosphere. This fact enormously simplifies the task of identifying isolated lines in an SN spectrum (Jeffery & Branch 1990). In the post-photospheric model, however, the emission peak is *not* centered on the line rest wavelength; rather it is considerably redshifted. As Figure 7 shows, with a core outer edge velocity of only 3000 km s^{-1}, the emission peak is ∼15 Å redward of the line rest wavelength. Though the absorption component of a P Cygni profile is used more often than the corresponding emission to identify lines in a spectrum (since the former dominates the latter in overlapping lines; see Jeffery & Branch 1990), this redshift could lead to misidentification of lines in intermediate- or late-time SN spectra.

What is the origin of the emission peak redshift? This question is easier to answer in the limit $\tau \to \infty$, the line profile for which would look identical to that of $\tau = 100$ in Figure 7. In the $\tau \to \infty$ case the line at the resonance point $z_{\rm res}$ scatters *all* continuum photons forming in the ray segment $z > z_{\rm res}$ out of the ray, and the contribution of the line to the intensity along that ray is simply $I_{\rm line} = S(r[z_{\rm res}])$. Thus, only two sources of emission contribute to the flux at a given wavelength: (1) the continuum emission in front of the resonance plane at $z = z_{\rm res}$ and (2) the source function at the plane. If the plane is located near the back of the core, $z \lesssim r_c$, the portion of the core's volume that emits continuum photons will emit continuum photons that escape unscattered and reach the observer is large. However, because the surface area of the plane is small when z is close to r_c, and

[8] Examining Figures 1 and 2, identification of Na I is ubiquitous; we therefore use the Na I D line for illustrative purposes.

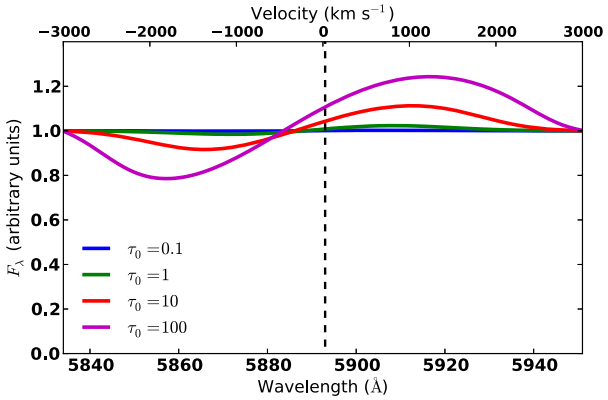

Figure 9. Flux profiles for Na I D, λ5892, in the post-photospheric model with outer edge core velocity 3000 km s^{-1} and a line optical depth following an exponential decay, $\tau(v) = \tau_0 \exp(-v/v_e)$, where $v_e = 500$ km s^{-1}. The vertical dashed line indicates the rest wavelength of the line. In contrast to SYNOW, the red emission peak does not occur at the rest wavelength, but is rather significantly redshifted by an amount that depends on the strength of the line. Also unlike SYNOW, the blue absorption minimum blueshifts continuously with increasing optical depth.

(A color version of this figure is available in the online journal.)

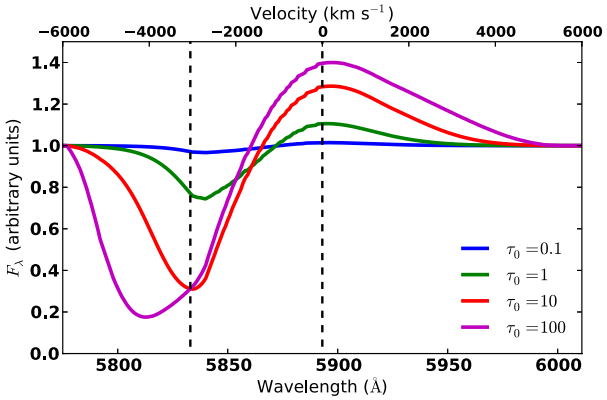

Figure 10. Flux profiles for Na I D, λ5892, in SYNOW, with photospheric velocity 3000 km s^{-1} and a line optical depth following an exponential decay, $\tau(v) = \tau_0 \exp(-v/v_e)$, where $v_e = 500$ km s^{-1}. The maximum velocity of the line-forming region is 6000 km s^{-1}. The right vertical dashed line indicates the rest wavelength of the line, and the left dashed line indicates the wavelength of Na I D blueshifted to the photospheric velocity. Except for extremely high optical depths, the blue edge of the absorption minimum remains fixed at the photospheric velocity; and for all optical depths, the red emission peak remains at the rest wavelength of the line.

(A color version of this figure is available in the online journal.)

because from Figure 5 we see that S is small at $r \sim r_c$—only half of its maximum value—the emission contribution from the source function on the plane is in turn relatively small.

As the resonance plane moves forward (to bluer wavelengths, smaller z), the volume of the emitting core in front of the plane decreases, but the surface area of the plane grows, and Figure 5 shows that the source function at the plane grows quickly as well. From $(1/3)r_c \lesssim z \lesssim r_c$ the scattering emission from the resonance plane more than compensates for the diminishing continuum emission from the core, causing the flux to increase monotonically as one moves blueward in that region, eventually reaching the emission peak, which in Figure 7 is ∼5915 Å. Blueward of this peak, despite the fact that S increases monotonically until reaching $z = 0$, the surface area of the plane increases only slightly when $z \gtrsim 0$ and the now very large resonance plane occults so much of the core over a small shift Δz that it can no longer compensate for the large amount of emission removed from the volume of the core behind it, causing the flux to decrease as z becomes smaller. This transition point exists *redward* of $z = 0$ and thus the emission peak of the P Cygni profile is redder than the rest wavelength of the line.

Blueward of $z = 0$, that is, $-r_c < z < 0$, the area of the resonance plane begins to decrease, now only obscuring a cylindrical volume of the glowing core. Even though the length of this occulted cylinder increases as z becomes more negative, its radius decreases, and the portion of the total volume of the core that this cylinder comprises decreases as well. The now-unocculted limbs of the core, emitting continuum that the resonance plane can no longer scatter away, grow in volume and eventually compensate once again for the cylindrical volume obscured by the plane, causing the flux to increase. This transition point manifests as the absorption minimum in the flux profile (∼5855 Å in Figure 7), blueward of which the flux increases until the resonance plane reaches $z = -r_c$ and we recover pure continuum.

The second difference between the line profiles with and without a photosphere is that, in the former, the flux in strong lines deviates from the continuum by a large amount, whereas in the latter the changes are small. The flux in the absorption minimum of the $\tau_0 = 100$ line in Figure 8, for example, is 80% lower than the continuum value. In our post-photospheric model, on the other hand, even the strongest line in Figure 7 departs by only up to 30% from the continuum. That the post-photospheric model exhibits such small departures from continuum is due to the ability of a small portion of the core to emit unscattered photons toward the observer even when the resonance plane is near the front. In the SYNOW case, the shell above the photosphere does not emit any continuum, so when the plane is close to the front of the ejecta, only scattering from the plane itself contributes to the flux, causing it to be extremely low at the absorption minimum.

The physical simplicity of constant τ line profiles such as those in Figures 7 and 8 readily facilitates analysis of line formation in SN ejecta, as we have just seen. However, one must also be aware of complicating effects such as the inhomogeneous structure of SNe, viz., the velocity-dependent density profile. In the Elementary Supernova framework, one assumes implicitly that $\tau = \tau(\rho)$, where ρ is the matter density, and accounts for this by writing τ as, e.g., an exponential or power-law function that decreases with increasing velocity. To illustrate how a variable optical depth affects line formation, we show in Figure 9 the line profile of Na I D in our post-photospheric model with $\tau(v) = \tau_0 \exp(-v/v_e)$, where τ_0 is a constant and $v_e = 500$ km s^{-1}. Again, for comparison, we show in Figure 10 a SYNOW plot of the same line with the same exponential τ profile.

In the post-photospheric case, shown in Figure 9, the relationship between velocities and the positions of the emission maximum and absorption minimum is not immediately obvious. Like the SYNOW line profiles, shown in Figure 10, the blue edge of the absorption component (not of the absorption *minimum*; see 5835 Å in Figure 9 and 5775 Å in Figure 10) indicates the maximum velocity of the line-forming material, although in blended cases this can be difficult to discern. Unlike SYNOW, in this model both the peak and trough continuously redshift and blueshift, respectively, as the line optical depth increases. In the SYNOW case, on the other hand, the separation

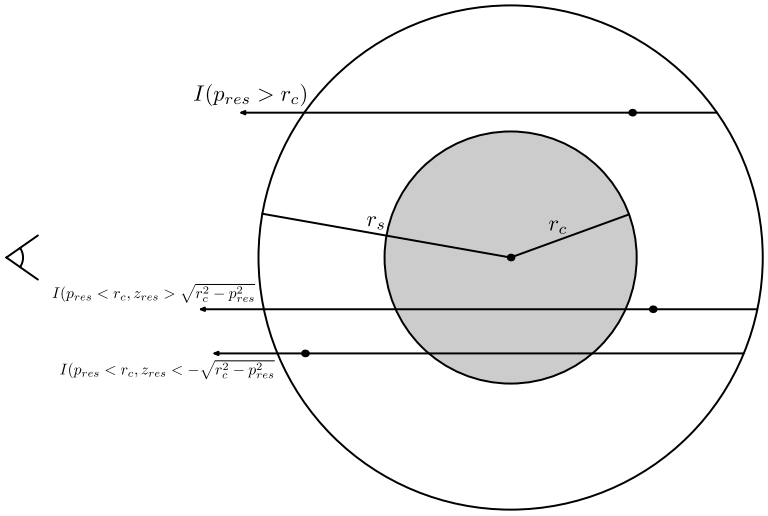

Figure 11. Three types of intensity rays for the core+shell configuration.

between the rest wavelength of the line and the minimum of the blueshifted absorption component indicates the velocity of the photosphere and thus the minimum velocity of the line-forming material itself (assuming the material is not "detached" above the photosphere; Jeffery & Branch 1990). Only when the line optical depth is extremely high does the location of the absorption minimum begin to move blueward of the photospheric blueshift, as in the $\tau_0 = 100$ line in Figure 10. For each of the three weaker lines in that figure, one can simply measure the blue edge of the absorption minimum, ∼5830 Å, then calculate the photospheric velocity, ∼3000 km s^{-1}.

We also note that the $\tau = 10$ and $\tau = 100$ line profiles in Figures 7 and 8 appear to be identical, whereas in Figures 9 and 10 the $\tau_0 = 10$ and $\tau_0 = 100$ profiles are distinct. This difference is due to the velocity dependence of τ: In the former pair of figures, the optical depth is constant everywhere, leading to a saturated profile throughout the line-forming region when $\tau \geqslant 10$. In the latter pair, on the other hand, τ decreases exponentially with increasing velocity, so the line samples such large optical depths at only very low velocities. This velocity dependence affects line formation outside the core in exactly the same way (cf. Section 4).

4. A LINE OUTSIDE THE CORE

Having explored in detail the geometric effects of continuum emission on line formation in the core, we now introduce a non-emitting, transparent shell around the core, with outer radius r_s, where $r_s > r_c$. In this region, there is no continuum emission and line formation occurs in exactly the same way as in SYNOW. Therefore, unlike the case discussed in Section 3, the line-forming region now exists *outside* the core, rather than inside. We include the shell in this model to account for the possibility of intermediate mass elements such as Ca II forming lines at late times above the material that has been burned all the way to the iron-peak.

4.1. Intensity for a Line Outside the Core

We must now consider a number of possible ways that the line and a particular ray can interact. First, if the ray has impact parameter $p > r_c$ then it never intersects the core and, regardless of the location of the line resonance point $z_{\rm res}$, the ray's emergent intensity is

$$I_{z_{\rm res}}(p) = S(r[z_{\rm res}])(1 - e^{-\tau}), \quad (15)$$

where $S(r)$ is now the source function *outside* the core, given by Equation (8), and

$$\tau = \tau(r[z_{\rm res}]). \quad (16)$$

If the line has $p < r_c$ but $z_{\rm res} < -\sqrt{r_c^2 - p_{\rm res}^2}$, then the line attenuates the continuum ray from the core:

$$I_{z_{\rm res}}(p) = S(r[z_{\rm res}])(1 - e^{-\tau}) + 2\left(r_c^2 - p^2\right)^{1/2} e^{-\tau}. \quad (17)$$

Finally, if the line has $p < r_c$ and $z_{\rm res} > \sqrt{r_c^2 - p_{\rm res}^2}$, then it does *not* attenuate the core continuum and the emergent intensity is

$$I_{z_{\rm res}}(p) = S(r[z_{\rm res}])(1 - e^{-\tau}) + 2\left(r_c^2 - p^2\right)^{1/2}. \quad (18)$$

These three cases are shown in Figure 11.

4.2. Flux for a Line Outside the Core

While F_λ proceeds simply from I_λ in the case $r \leqslant r_c$, its form is much more complicated in the $r > r_c$ regime. In particular the flux integral takes a unique form in five different regions. We show the five zones in Figure 12.

1. $-r_s < z < -\left(r_s^2 - r_c^2\right)^{1/2}$

$$F_z = \frac{4\pi}{r_c^2} e^{-\tau} \int_0^{(r_s^2 - z^2)^{1/2}} \left(r_c^2 - p^2\right)^{1/2} p dp + \frac{4\pi}{r_c^2} \int_{(r_s^2 - z^2)^{1/2}}^{r_c} \left(r_c^2 - p^2\right)^{1/2} p dp + \frac{2\pi}{r_c^2}(1 - e^{-\tau}) \int_0^{(r_s^2 - z^2)^{1/2}} S(r[p]) p dp.$$

2. $-\left(r_s^2 - r_c^2\right)^{1/2} < z < -r_c$

$$F_z = \frac{4\pi}{3} r_c e^{-\tau} + \frac{2\pi}{r_c^2}(1 - e^{-\tau}) \int_0^{(r_s^2 - z^2)^{1/2}} S(r[p]) p dp.$$

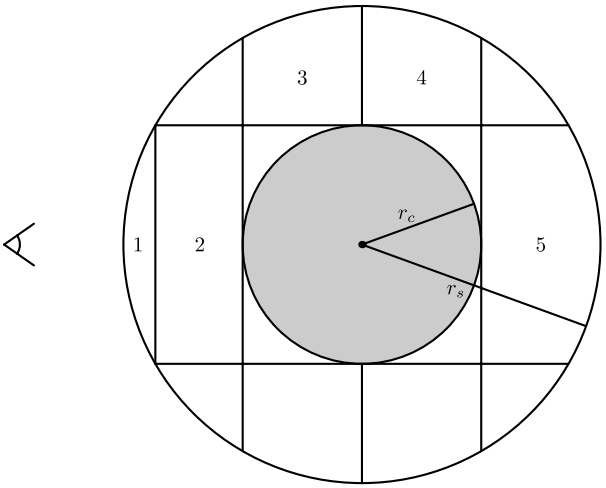

Figure 12. Five flux regions in the core+shell configuration.

3. $-r_c < z < 0$

$$F_z = \frac{4\pi}{r_c^2}\int_0^{(r_c^2-z^2)^{1/2}} \left(r_c^2 - p^2\right)^{1/2} pdp + \frac{4\pi}{r_c^2}e^{-\tau}\int_{(r_c^2-z^2)^{1/2}}^{r_c} \left(r_c^2 - p^2\right)^{1/2} pdp + \frac{2\pi}{r_c^2}(1-e^{-\tau})\int_{(r_c^2-z^2)^{1/2}}^{(r_s^2-z^2)^{1/2}} S(r[p])pdp.$$

4. $0 < z < r_c$

$$F_z = \frac{4\pi}{3}r_c + \frac{2\pi}{r_c^2}(1-e^{-\tau})\int_{(r_c^2-z^2)^{1/2}}^{\left(r_s^2-z^2\right)^{1/2}} S(r[p])pdp.$$

5. $r_c < z < r_s$

$$F_z = \frac{4\pi}{3}r_c + \frac{2\pi}{r_c^2}(1-e^{-\tau})\int_0^{(r_s^2-z^2)^{1/2}} S(r[p])pdp.$$

Figure 13 depicts single-line profiles with different values of τ. We first note the resemblance of these line profiles to those of SYNOW shown in Figure 8. This is not surprising, given that the only difference between the two models is that in SYNOW the core is opaque while in the post-photospheric model it is transparent. Both exhibit strong deviations from the continuum flux value, especially in the absorption component. We discussed in Section 3 the cause of this near-zero flux in the absorption component of the line.

The one major difference between the line profiles in Figures 8 and 13 is the flat-topped emission component in the latter. To discern the source of this plateau in the spectrum, we conduct a geometric analysis similar to that presented in Section 3, again studying the limit $\tau \to \infty$. Starting with the resonance plane at the back of the shell, $z = r_s$, we see that as it moves forward toward the observer, its surface area grows, which leads to the flux increase from 6010 Å blueward to 5950 Å in Figure 13.

When the resonance plane reaches the back edge of the core and begins to move forward through it, that is, when

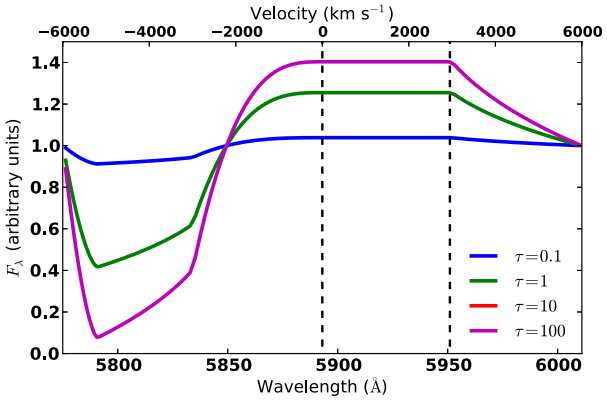

Figure 13. Flux for Na I D in the shell, with core velocity 3000 km s^{-1} and outer edge shell velocity 6000 km s^{-1}. The rest wavelength of the line is $\lambda_0 = 5892$ Å, indicated by the left vertical dashed line. The right dashed line indicates the rest wavelength of Na I D redshifted to the back edge of the core, at which point the emission peak forms a plateau. For $r_c \leqslant r \leqslant r_s$, τ = constant and for $r \leqslant r_c$, $\tau = 0$. The $\tau = 10$ and $\tau = 100$ profiles overlap almost exactly and are indistinguishable in this figure.

(A color version of this figure is available in the online journal.)

$0 < z_{\rm res} < r_c$, the core projects onto the plane a central circular region where $\tau = 0$ and continuum emission from the core is unattenuated. The component of the plane that samples the optical depth in the shell is a ring with area

$$A = \pi\left(r_s^2 - z_{\rm res}^2\right) - \pi\left(r_c^2 - z_{\rm res}^2\right) = \pi\left(r_s^2 - r_c^2\right). \quad (19)$$

From this equation, we see that A is constant when $0 < z_{\rm res} < r_c$; this constancy is the cause of the emission plateau in Figure 13.

When $-r_c < z_{\rm res} < 0$, the plane begins to obscure the core, starting at the core's limb, and scatters an increasing amount of the continuum emission out of the observer's line of sight. When $z_{\rm res} < -r_c$ the entire core is obscured and the only emission from the ejecta comes from the source function at $z_{\rm res}$. In the region $-r_s < z_{\rm res} < -r_c$, line formation occurs in exactly the same way as in SYNOW, leading to the absorption trough in Figure 13, which is almost identical to that of the SYNOW profile shown in Figure 8.

The constant-flux emission in the spectra in Figure 13 is the most distinguishing feature of our post-photospheric model. In Section 6, we will consider a nebular line-forming region with a "hole" devoid of line optical depth, and there we will encounter a geometric conspiracy similar to the one presented in this section, leading to similarly flat features in line profiles. We remark in addition that SYNOW can produce flat-topped emission features in a spectrum by detaching lines from the photosphere. Thus, we conclude that in general a plateau-shaped line emission feature indicates some kind of missing line opacity.

5. TWO LINES IN THE CORE

We now study the case of two resonance lines in the core. Understanding the ways in which multiple lines "interact" via their overlapping flux profiles, and in turn being able to identify them individually, is critical to interpreting observed spectra since, in all epochs of an SN, its optical spectrum exhibits severe line blending.

In the resonance-scattering approximation, for any number of lines in the core, the source function of the bluest line always has the single-line form given in Equation (7), since there are

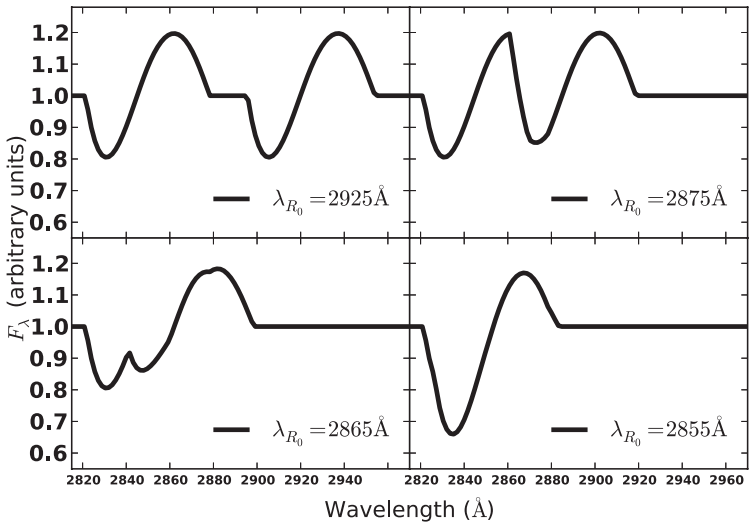

Figure 14. Interaction of two lines in the core as they blend together due to Doppler broadening. The rest wavelength of the blue line is fixed at $\lambda_{B_0} = 2850$ Å, while the rest wavelength of the red line moves blueward. The optical depths of both lines are fixed at $\tau_B = \tau_R = 1$.

no bluer photons in the radiation field that can redshift into resonance with it. The second bluest line then interacts only with its bluer neighbor, the third bluest line interacts with its two bluer neighbors, etc. In computational terms this means that one calculates the source function for each line starting with the bluest and moving redward. The details of the calculation are shown in Appendix B.

We first consider the case $v_{\rm core} = 3000$ km s^{-1}, and we hold the optical depths of both lines fixed everywhere in the core, $\tau_B = \tau_R = 1$. We then set the rest wavelength of the blue line to 2850 Å and decrement the rest wavelength of the red line from 3000 Å, where the lines are too far apart in wavelength space to blend in the spectrum, to 2855 Å, where the lines overlap completely. The result is shown in Figure 14. In this figure, we find that line blending in the post-photospheric case occurs in essentially the same way as in the SYNOW case (Jeffery & Branch 1990). Specifically, the absorption component of the red line completely overwhelms the emission of the blue line, and also, when the two lines overlap perfectly (the bottom-right panel of Figure 14), the redshifted emission component appears to be the same as the single-line case, but the absorption is much deeper.

One peculiar feature of Figure 14 is that, when the lines overlap only partially, the emission component of the blue line acquires a triangular shape. In fact, in the upper right panel of that figure, the triangular emission peak is nearly symmetrical. However the abrupt (perhaps unrealistic) drop in τ at the edge of the core in this calculation may somewhat exaggerate this triangular feature.

In this section, we have restricted our discussion to the interaction between two lines confined to the core. However, with the introduction of multiple lines, many other types of interactions are possible. As an example, in Appendix B.2 we construct the geometric framework for the two-line case where both lines are outside the core. However the situation is more complex due to the myriad combinations of line locations as well as their combined interaction with the core and shell. We thus defer a thorough examination of all the possible effects that can occur in this case, including the effects of the photosphere before it has receded completely, to a future work (B. Friesen & R. C. Thomas 2012, in preparation).

6. DISCUSSION

Much recent work analyzing SN Ia spectra has focused on the importance of asymmetries (Maeda et al. 2010, 2011; Maund et al. 2010; Foley & Kasen 2011; Foley et al. 2012). However, the spectra produced by this model illustrate a potentially significant complication in interpreting spectra at late times in SNe Ia, specifically in the interpretation of line emission in the absence of scattering. To illustrate this point, we refer to the work of Maeda et al. (2010, 2011), who interpret observed blueshifts and redshifts of Fe lines in nebular spectra as resulting from asymmetric clumps of iron-peak material moving toward and away from the observer, respectively, in the optically thin SN Ia ejecta. This interpretation implies that the explosion of a white dwarf resulting in an SN Ia is itself highly asymmetric, but relies heavily upon the assumption that spectral features at late times arise *only* through forbidden transitions of atomic lines due to the low gas density, and that the resulting emission profiles are distributed roughly symmetrically about the rest wavelength. Indeed, this assumption has become widespread in nebular spectrum synthesis since the pioneering work of Axelrod (1980). However, if an appreciable amount of resonance-scattering is present at this epoch, our results show that in the presence of significant continuum emission, a perfectly spherically symmetric distribution of matter produces a redshifted emission component. It remains unclear what effect, if any, that resonance-scattering has on the sample considered in Maeda et al. (2010) since the objects in their study were often several hundred days older than the objects we attempted to fit using SYNOW in Figures 1 and 2.

Maund et al. (2010) studied polarization measurements of the objects in Maeda et al. (2010) for which such data were available, and drew similar conclusions as Maeda et al. (2010), that is, that asymmetry alone may explain the diversity observed in SNe Ia. The survey in Maund et al. (2010) was biased in that polarization data existed only for SNe with redshifted emission

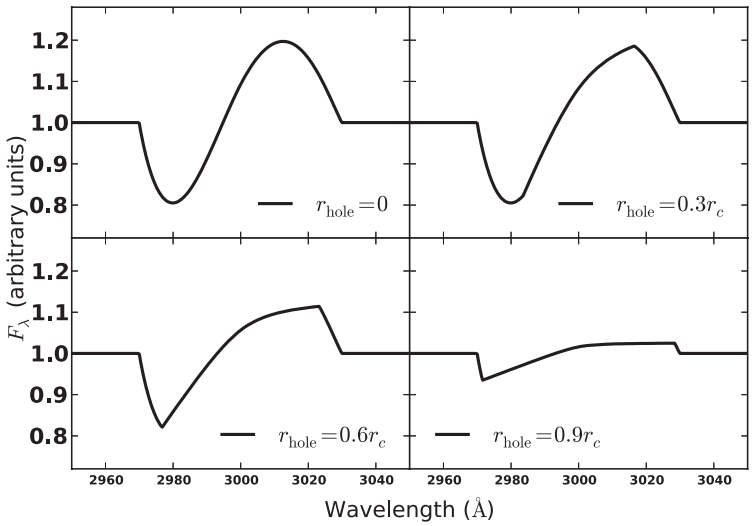

Figure 15. Post-photospheric line profile where the line is excluded from the various parts of the inner region of the core. The core has outer velocity 3000 km s^{-1}. The optical depth in the region $r > r_{\rm hole}$ is $\tau = 1$, whereas in $r < r_{\rm hole}$, $\tau = 0$. The rounded profile is replaced by a flattened profile, but there is still an emission peak and an absorption trough, both of which become more muted as $r_{\rm hole}$ increases.

peaks for particular lines of Fe II and Ni II, but nevertheless we note that, at intermediate times, for many features there are multiple possible line identifications, and redshifted emission can result from either optically thin, receding ejecta, or, as shown in Figure 7, from spherically symmetric ejecta with large line optical depth. While the very late data (Maeda et al. 2010; Maund et al. 2010) may indeed be showing the inferred asymmetry, our results show that one should indeed be cautious about the epoch of the data when interpreting redshifted emission profiles.

Finally, we consider another significant effect of resonance-scattering at late times in SNe. Studies of late-time line profiles and the imaging of the supernova remnant S Andromeda (Höflich et al. 2004; Motohara et al. 2006; Fesen et al. 2007; Gerardy et al. 2007; Maeda et al. 2010) have lead to the suggestion that a "nickel hole" exists in at least some SNe Ia. In optically thin media, a central region devoid of line-forming material manifests in a spectrum as a flat-topped emission feature in the spectrum; Höflich et al. (2004) find just this when studying the [Fe II] λ16, 440 line in a spectrum of SN 2003du taken ~300 days after explosion, suggesting that ^{56}Fe and therefore ^{56}Ni were absent in the central part of the SN ejecta. However, the IR observations in these studies are quite noisy, and if the same effect could be observed earlier, or in stronger lines, there would be more flux, allowing statistics to be built up on the existence of a nickel hole in SNe Ia, which would provide important constraints on the underlying explosion model.

With this in mind, we explore the possibility that one may observe a similar plateau feature inside the glowing core by carving out regions of zero optical depth in a resonance-scattering line. To study this, we return to the core-only model, with velocity 3000 km s^{-1}, and set the rest wavelength of a single line in the core to 3000 Å. We then set the optical depth of the line to $\tau = 1$ and proceed to exclude this optical depth from progressively larger portions of the core's central region. The resulting line profiles are shown in Figure 15. The classical rounded profile is replaced by a flat profile, but there still exists both an emission peak and an absorption trough. This result corroborates the plateau effects we studied in Section 4—Figure 13 already showed that when a region of large line optical depth surrounds a region of zero optical depth, flat-topped components can appear in the spectral line profiles.

7. CONCLUSIONS

We have presented the geometric framework for a post-photospheric model of an SN, making simple assumptions about its emissivity and source function, in an attempt to explore the effects of resonance-scattering in optically thick lines in SN atmospheres in epochs where such scattering processes are rarely considered. Our model is inspired by and similar to the Elementary Supernova model, but the substitution of a photosphere for a transparent but continuum-emitting core leads to significant differences in line formation. The most noticeable difference is that the emission peak of a line is redshifted from its rest wavelength, even though the model is spherically symmetric. This property may affect the interpretation of SN spectra in post-photospheric phases, when asymmetric effects on line formation become influential.

Our model remains mostly within the geometric confines of the Elementary Supernova model, and choices about its properties different than the ones made here are possible. For example, one may assume that severe line blending in the core creates a pseudo-continuum, leading to a source function in the shell exactly equal to that assumed in SYNOW:

$$S = W(r)J,$$

where $W(r)$ is the dilution factor. We have also chosen to parameterize all line optical depths rather than calculating them in any self-consistent manner, e.g., by solving rate equations. We believe our choices in these matters have resulted in a level of detail commensurate with the simplicity of this model.

To explore fully the other implications of resonance-scattering on line formation at post-photospheric times in SNe Ia, we are currently incorporating the formalism presented in this work into SYNAPPS (Thomas et al. 2011), whereby we

will be able to analyze the interaction of the receding photosphere with the emerging glowing core of ^{56}Co and its effects on the SN spectrum, a process that has so far received little attention.

The referee's careful eye vastly improved the content of this work, for which we are grateful. This work was supported in part by NSF grant AST-0707704, and US DOE Grant DE-FG02-07ER41517, and by SFB 676, GRK 1354 from the DFG. Support for Program No. HST-GO-12298.05-A was provided by NASA through a grant from the Space Telescope Science Institute, which is operated by the Association of Universities for Research in Astronomy, Incorporated, under NASA contract NAS5-26555. This research has made use of NASA's Astrophysics Data System.

APPENDIX A

$S(r)$ OUTSIDE THE CORE

In Section 4, we calculate sample spectra for lines forming outside the glowing core. Therefore, we calculate the source function in the region $r > r_c$. From Figure 16

$$Y = r\mu - \left(r^2\mu^2 + r_c^2 - r^2\right)^{1/2}.$$

Then

$$X = (X + Y) - Y = 2\left(r^2\mu^2 + r_c^2 - r^2\right)^{1/2}. \quad \text{(A1)}$$

We plug the expression for X into Equation (5), noting that, because the shell emits no continuum, the maximum value of θ is not 1, as in the $r \leqslant r_c$ case, but rather

$$\theta_{\max} = \cos^{-1}\left(\frac{\left(r^2 - r_c^2\right)^{1/2}}{r}\right).$$

Thus,

$$J(r) = \frac{1}{2}\int_{\mu_0}^{1} 2\left(r^2\mu^2 + r_c^2 - r^2\right)^{1/2} d\mu,$$

where μ_0 is the argument of the inverse cosine above. The result is

$$J(r) = \frac{1}{2r}\left\{rr_c + \left(r^2 - r_c^2\right)\ln\left[\frac{\sqrt{r^2 - r_c^2}}{r + r_c}\right]\right\}$$
$$= \frac{1}{2r}\left\{rr_c + \frac{\left(r^2 - r_c^2\right)}{2}\ln\left[\frac{r - r_c}{r + r_c}\right]\right\} \quad \text{(A2)}$$

The mean intensities inside and outside the core are identical except for two sign differences: one in the factor multiplying the logarithm and the other in the argument of the logarithm itself. We find that Equations (7) and (8) are continuous at the edge of the core, as they must be, each yielding $J(r = r_c) = 0.5r_c$.

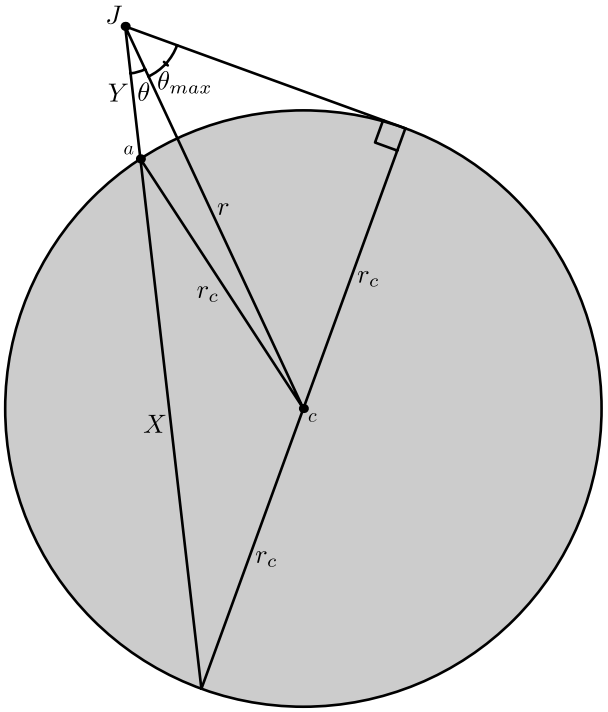

Figure 16. Geometric configuration used to calculate $S(r > r_c)$ in the absence of lines in the core.

APPENDIX B

TWO LINES

We now turn to the two-line case. We denote these lines as R and B, for "red" and "blue." First, as stated previously, the source function for the blue line, S_B, is given by Equation (7). The source function for the red line, $S_R(r)$, is equal to the mean intensity $J_\lambda(r)$, where λ is the rest wavelength of the line λ_{0_R}. The calculation of J is complicated by the fact that photons emitted by the blue line may be scattered into resonance with the red line, while some continuum photons from the glowing core that would, in the absence of the blue line, redshift into resonance with the red line are actually scattered away by the blue line. In velocity space, the region where the blue line interacts with the red line takes the form of a "scattering sphere" called the common point velocity surface (CPVS; Jeffery & Branch 1990). The radius of the CPVS, denoted Y in Figure 17, is given by the Doppler formula, Equation (14), where one replaces z in that equation with Y. In Appendix B.1, we study the interaction of two lines confined to the core and in Appendix B.2, we explore two lines in the shell.

B.1. Two Lines Inside the Core

When both lines are confined to the core, S_R contains three components:

1. the intensity of continuum photons that can redshift into resonance with R, but are scattered away when they reach the CPVS;
2. photons emitted by B along the CPVS, which redshift into resonance with R;
3. continuum photons that form *inside* the CPVS and therefore redshift into resonance with R without interacting with B.

Segments 1 and 3 are labeled X and Y, respectively, in Figure 17.

Mathematically we write this as

$$S_R = \frac{1}{2}\int_{-1}^{1} Xe^{-\tau_B} d\mu + \frac{1}{2}\int_{-1}^{1} S_B(1 - e^{-\tau_B}) d\mu + \frac{1}{2}\int_{-1}^{1} Y d\mu. \quad \text{(B1)}$$

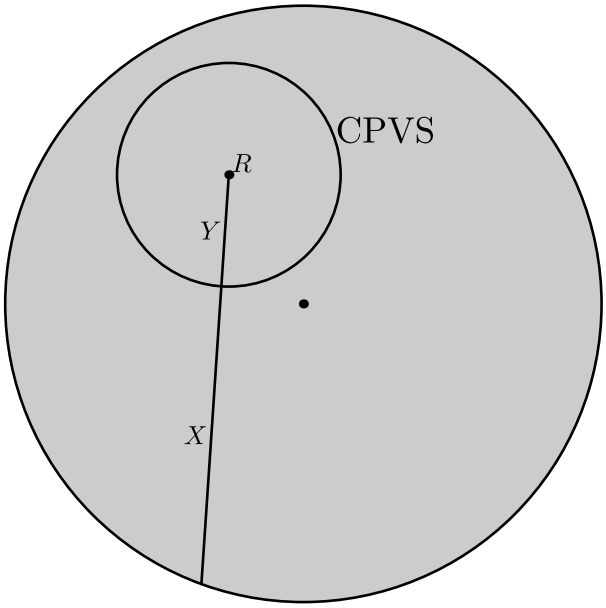

Figure 17. Different components of an intensity ray incident on the red line in the two-line case.

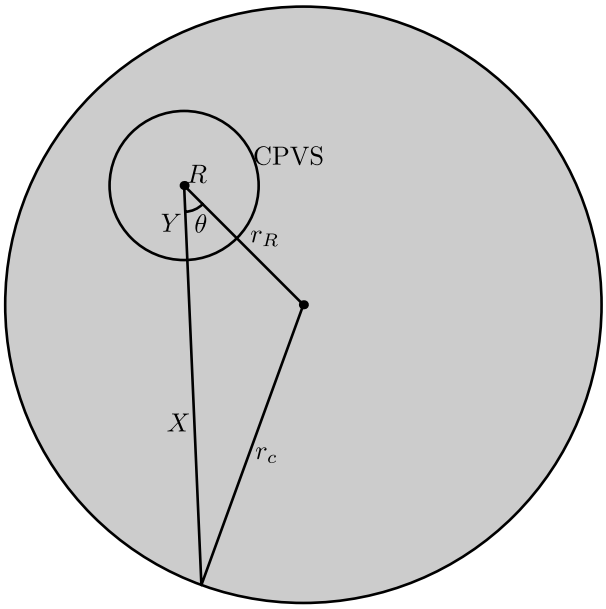

Figure 18. Explicit geometric construction of two-line configuration used to calculate $X = X(\mu)$.

To calculate $X = X(\mu)$ we refer to Figure 18. Defining the triangle ABC in Figure 18, we can use the law of cosines to find

$$r_c^2 = (X+Y)^2 + r_R^2 - 2(X+Y)r_R\mu, \tag{B2}$$

where we have used the fact that X and Y are co-linear and $\mu = \cos\theta$. Solving for X,

$$X = (r_R\mu - Y) \pm \sqrt{(r_R\mu - Y)^2 + r_c^2 - r_R^2 + 2Yr_R\mu}. \tag{B3}$$

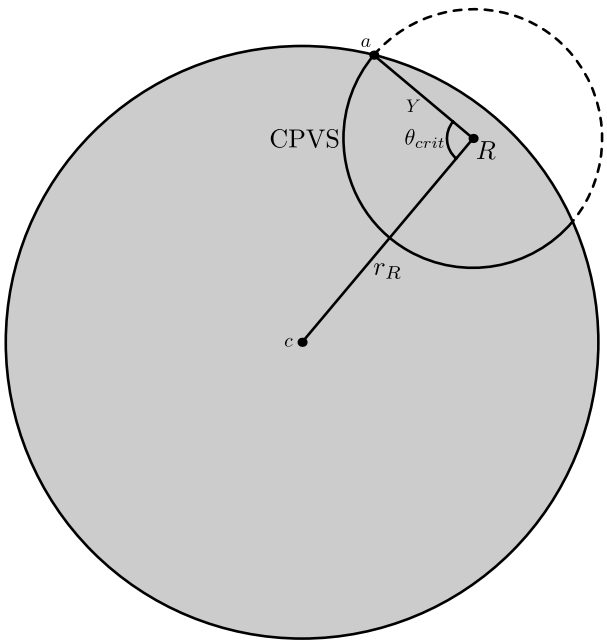

Figure 19. Geometric construction of angle $\theta_{\rm crit}$. The value r_R is the magnitude of the vector $\boldsymbol{cR}$ and Y is that of $\boldsymbol{aR}$.

Expanding the square root yields

$$\sqrt{(r_R\mu - Y)^2 + r_c^2 - r_R^2 + 2Yr_R\mu} = \sqrt{r_c^2 - r_R^2(1-\mu^2) + Y^2}. \tag{B4}$$

When $-1 \leqslant \mu \leqslant Y/r_R$, we see that $(r_R\mu - Y) < 0$ and we must take the positive root in Equation (B3). However, when $Y/r_R < \mu \leqslant 1$ we see from Equation (B3) that $\mu > 0$ and thus the term in the square root is larger than the expression $r_R\mu - Y$ and so the positive root is also correct. Hence,

$$X = (r_R\mu - Y) + \sqrt{r_c^2 - r_R^2(1-\mu^2) + Y^2}, \tag{B5}$$

for $-1 \leqslant \mu \leqslant 1$. Before proceeding we note that if the CPVS extends past the edge of the core, that is, if $r_R + Y > r_c$, then there exists a critical angle $\theta_{\rm crit}$ for which X becomes undefined if $\theta > \theta_{\rm crit}$. Its value is

$$\mu_{\rm crit} = \frac{Y^2 + r_R^2 - 1}{2Yr_R}, \tag{B6}$$

where $\mu_{\rm crit} \equiv \cos\theta_{\rm crit}$. When integrating to find the contribution of the CPVS to the source function of the red line, S_R, we must stop the integration at this angle. This limit is depicted in Figure 19.

Next, we must calculate $r_{S_B} = r_{S_B}(\mu)$, the location of the CPVS, as shown in Figure 20. Again through vector addition arguments, we find

$$r_{S_B}(\mu) = \left(r_R^2 + Y^2 - 2r_RY\mu\right)^{1/2}. \tag{B7}$$

It is at this location r_{S_B} that both τ_B and S_B in Equation (B1) are evaluated. Lastly we turn to the calculation of Y in Figure 17. If the entire CPVS fits inside the core, we may use the Doppler formula, Equation (14), to calculate Y for all θ. However,

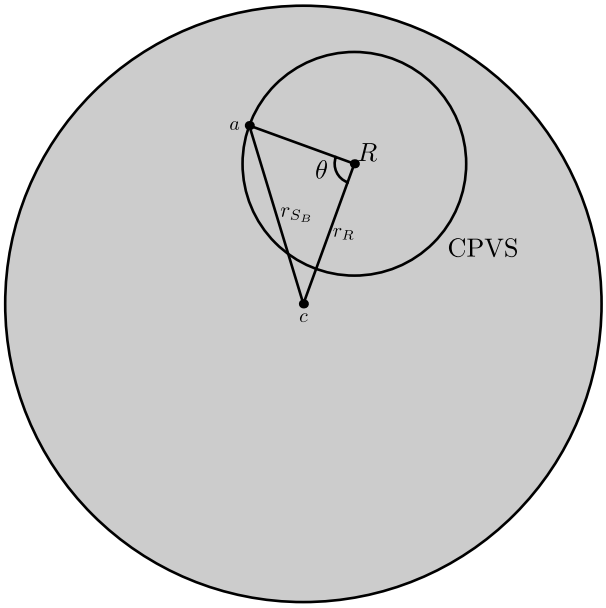

Figure 20. Calculation of location of CPVS, labeled r_{S_B}, with respect to the center of the SN. The quantity r_R is the magnitude of the vector $\boldsymbol{cR}$ and r_{S_B} is that of $\boldsymbol{ac}$.

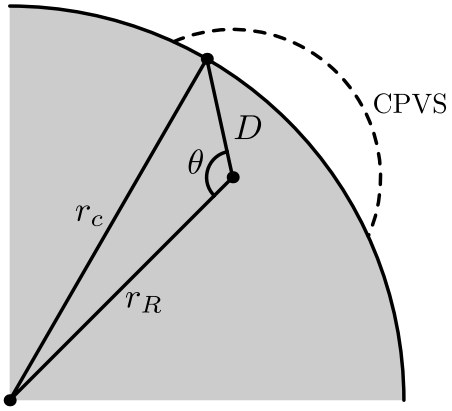

Figure 21. Geometric configuration of truncated intensity ray $D = D(\mu)$.

if part of the CPVS extends past the edge of the core then Y takes a slightly more complicated form. This latter case is shown in Figure 21, where $\theta_1 > \theta_{\rm crit}$. We calculated this angle in Equation (B6). If $\theta > \theta_{\rm crit}$ then, from Figure 21,

$$D(\mu) = r_R\mu \pm \left(r_R^2\mu^2 + r_c^2 - r_R^2\right)^{1/2}. \quad \text{(B8)}$$

Since D is a length and must always satisfy $D \geqslant 0$ we can rule out immediately the "minus" solution, since it is negative for all possible values of (r_R, Y, μ). Thus, we take the positive root:

$$D(\mu) = r_R\mu + \left(r_R^2\mu^2 + r_c^2 - r_R^2\right)^{1/2} \quad -1 \leqslant \mu \leqslant \mu_{\rm crit}. \quad \text{(B9)}$$

B.2. Two Lines Outside the Core

In the case that we have a resonance line that is strong under cold conditions, for example, certain lines of Ca II or Mg II, we may want to consider multiple lines forming outside the core. Figure 22 illustrates the most complex case. If $\theta > \theta_{\rm crit}$, where $\mu_{\rm crit} = \cos(\theta_{\rm crit}) = 1 - (r_c/r_R)^2$, then the characteristic

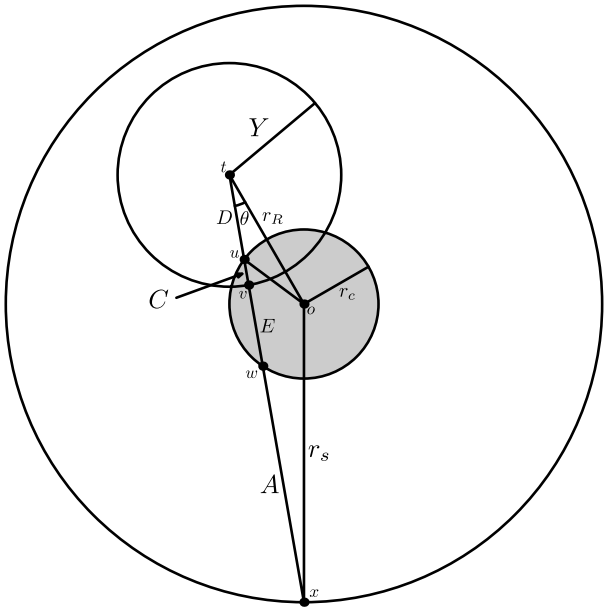

Figure 22. Case I geometry. The value of A corresponds to the magnitude of the vector $\boldsymbol{xw}$, E to $\boldsymbol{wv}$, C to $\boldsymbol{vu}$, D to $\boldsymbol{ut}$, r_c to $\boldsymbol{ou}$, and r_s to $\boldsymbol{xo}$. Only E and C contribute to the intensity of the ray since A and D lie outside the emitting core.

in that direction does not intersect the core and accumulates no intensity, but for the case that $\mu \geqslant \mu_{\rm crit}$ then the characteristic is given as shown in Cases I–III, (Figures 22–24).

For Case I, Figure 22, we find

$$D = r_R\cos\theta - \sqrt{r_c^2 - r_R^2\sin^2\theta}, \quad \text{(B10)}$$

$$C = Y - D = Y - r_R\cos\theta + \sqrt{r_c^2 - r_R^2\sin^2\theta}, \quad \text{(B11)}$$

$$E = 2(r_R\cos\theta - D) - C = \sqrt{r_c^2 - r_R^2\sin^2\theta} - Y + r_R\cos\theta, \quad \text{(B12)}$$

and

$$A = \sqrt{r_s^2 - r_R^2\sin^2\theta} - \sqrt{r_c^2 - r_R^2\sin^2\theta}. \quad \text{(B13)}$$

For Case II, Figure 23, we have

$$E = 2\sqrt{r_c^2 - r_R^2\sin^2\theta}, \quad \text{(B14)}$$

$$C = r_R\cos\theta - Y - \sqrt{r_c^2 - r_R^2\sin^2\theta}, \quad \text{(B15)}$$

$$A = \sqrt{r_s^2 - r_R^2\sin^2\theta} - \sqrt{r_c^2 - r_R^2\sin^2\theta}, \quad \text{(B16)}$$

and

$$D = Y. \quad \text{(B17)}$$

For Case III, Figure 24,

$$D = r_R\cos\theta - \sqrt{r_c^2 - r_R^2\sin^2\theta}, \quad \text{(B18)}$$

$$C = 2\sqrt{r_c^2 - r_R^2\sin^2\theta}, \quad \text{(B19)}$$

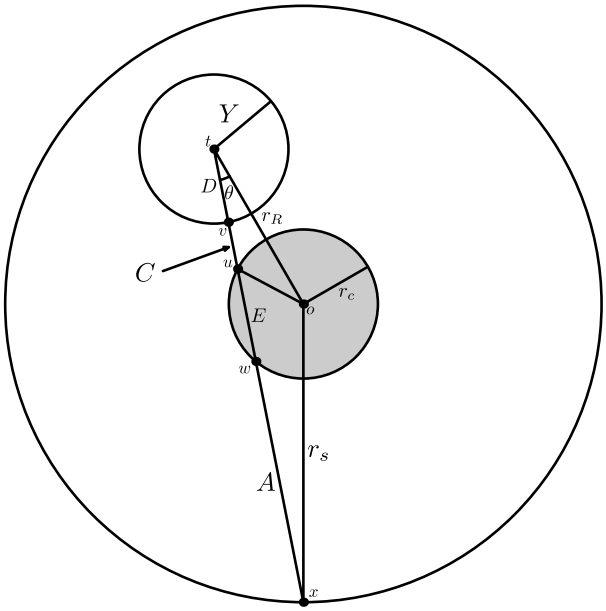

Figure 23. Case II geometry. The value of A corresponds to the magnitude of the vector $\boldsymbol{xw}$, E to $\boldsymbol{wu}$, C to $\boldsymbol{uv}$, D to $\boldsymbol{ut}$, r_c to $\boldsymbol{ou}$, and r_s to $\boldsymbol{xo}$. Only E contributes to the intensity of the ray since A, C, and D lie outside the emitting core.

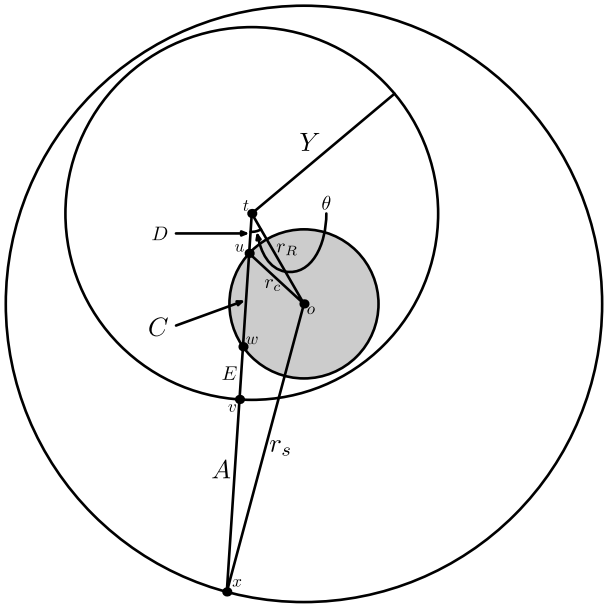

Figure 24. Case III geometry. The value of A corresponds to the magnitude of the vector $\boldsymbol{xv}$, E to $\boldsymbol{vw}$, C to $\boldsymbol{wu}$, D to $\boldsymbol{ut}$, r_c to $\boldsymbol{ou}$, and r_s to $\boldsymbol{xo}$. Only C contributes to the intensity of the ray since A, E, and D lie outside the emitting core.

$$E = Y - D - C = Y - \sqrt{r_c^2 - r_R^2 \sin^2\theta} - r_R \cos\theta, \quad \text{(B20)}$$

and

$$A = \sqrt{r_s^2 - r_R^2 \sin^2\theta} + r_R \cos\theta - Y. \quad \text{(B21)}$$

Then J for Case I is

$$J = \frac{1}{2}\left\{\int_{-1}^{\mu_{\rm crit}} S_B(1 - e^{-\tau_B})\, d\mu + \int_{\mu_{\rm crit}}^{1} \left[Ee^{-\tau_B} + S_B(1 - e^{-\tau_B}) + C\right] d\mu\right\}. \quad \text{(B22)}$$

For Case II, J is

$$J = \frac{1}{2}\left\{\int_{-1}^{\mu_{\rm crit}} S_B(1 - e^{-\tau_B})\, d\mu + \int_{\mu_{\rm crit}}^{1} \left[Ee^{-\tau_B} + S_B(1 - e^{-\tau_B})\right] d\mu\right\}. \quad \text{(B23)}$$

Finally, for Case III,

$$J = \frac{1}{2}\left\{\int_{-1}^{\mu_{\rm crit}} S_B(1 - e^{-\tau_B})\, d\mu + \int_{\mu_{\rm crit}}^{1} \left[E + S_B(1 - e^{-\tau_B})\right] d\mu\right\}. \quad \text{(B24)}$$

The extension of the two-line case to the N-line case is straightforward and is implemented most easily in a recursive fashion, moving along wavelength as the value of r_R increases.

B.3. Calculation of Emergent Intensity

Given that the flux integral in Equation (4) can be written as an integral over impact parameter p, we concern ourselves here with the calculation of the emergent intensity of rays with constant p, denoted $I_\lambda(p)$. We first calculate the domain $[z_{\rm min}, z_{\rm max}]$ over which a ray with given p exists:

$$z_{\rm min} = -\left(r_c^2 - p^2\right)^{1/2}$$
$$z_{\rm max} = +\left(r_c^2 - p^2\right)^{1/2}.$$

We then use the Doppler formula to establish the wavelength domain $[\lambda_{\rm min}, \lambda_{\rm max}]$ over which it is possible for a particular wavelength point λ to be in resonance in the core, given p:

$$\lambda_{\rm min} = \frac{\lambda}{1 + z_{\rm max}\left(\frac{v_{\rm core}}{c}\right)} \quad \text{(B25)}$$

$$\lambda_{\rm max} = \frac{\lambda}{1 + z_{\rm min}\left(\frac{v_{\rm core}}{c}\right)}. \quad \text{(B26)}$$

All lines with rest wavelength λ_0 that lie in this domain will be in resonance with the ray $I_\lambda(p)$ at some location in the core.

Now consider a ray with two lines that both fall in the domain $[\lambda_{\rm min}, \lambda_{\rm max}]$. The ray redshifts into resonance with the blue line "before" (at larger z, closer to the back of the core) redshifting into resonance with the red line; we denote these locations z_B and z_R, respectively, where $z_B > z_R$. The segment of the ray between the back edge of the core and z_B has intensity $(r_c^2 - p^2)^{1/2} - z_B$. However it will redshift into resonance with *both* lines before emerging from the core, so it acquires two attenuation terms, $e^{-\tau_B}$ and $e^{-\tau_R}$, where τ_B and τ_R are evaluated at z_B and z_R, respectively. The continuum segment between z_R and z_B has length $z_B - z_R$ and is attenuated only by the red line. The front-most continuum piece, between z_R and the front of the core, is unaffected by scattering and has intensity $(r_c^2 - p^2)^{1/2} + z_R$.

The source functions of the red and blue lines also contribute to the total emergent intensity. The contribution from each

is $S_i(1 - e^{-\tau_i})$, where $i \in \{R, B\}$. However the blue line's contribution will be attenuated when it redshifts into resonance with the red line, and so it receives the usual $e^{-\tau_R}$ multiplicative factor. Therefore, the total emergent intensity is

$$I_\lambda(p) = \left(\left(r_c^2 - p^2\right)^{1/2} - z_B\right)e^{-\tau_B}e^{-\tau_R} + S_B(1 - e^{-\tau_B})e^{-\tau_R} + (z_B - z_R)e^{-\tau_R} + S_R(1 - e^{-\tau_R}) + \left(r_c^2 - p^2\right)^{1/2} + z_R. \quad \text{(B27)}$$

If, for a particular ray, one of the two lines is outside $[\lambda_{\min}, \lambda_{\max}]$, the result for $I_\lambda(p)$ reduces to the one-line form for $I_\lambda(p)$ of Equation (10) or Equations (15), (17), and (18) for lines outside the core. It is important to understand that if, for some impact parameter p, the blue line has wavelength outside $[\lambda_{\min}, \lambda_{\max}]$, such that $I_\lambda(p)$ is given by Equation (10), the source function $S = S_R$ evaluated in that equation may nevertheless contain scattering effects of the blue line, as long as at least some portion of the CPVS for the blue line lines within the core.

If both lines fall outside this domain, the emergent intensity becomes the pure continuum result.

REFERENCES

Axelrod, T. S. 1980, PhD thesis, California Univ., Santa Cruz
Bowers, E. J. C., Meikle, W. P. S., Geballe, T. R., et al. 1997, MNRAS, 290, 663
Branch, D., Baron, E., Hall, N., Melakayil, M., & Parrent, J. 2005, PASP, 117, 545
Branch, D., Doggett, J. B., Nomoto, K., & Thielemann, F.-K. 1985, ApJ, 294, 619
Branch, D., Lacy, C. H., McCall, M. L., et al. 1983, ApJ, 270, 123
Castor, J. I. 1970, MNRAS, 149, 111
De, S., Baron, E., & Hauschildt, P. H. 2010, MNRAS, 401, 2081
Dessart, L., & Hillier, D. J. 2005, A&A, 437, 667
Dessart, L., & Hillier, D. J. 2010, MNRAS, 405, 2141
Dessart, L., & Hillier, D. J. 2011, MNRAS, 410, 1739
Fesen, R. A., Höflich, P. A., Hamilton, A. J. S., et al. 2007, ApJ, 658, 396
Fisher, A., Branch, D., Nugent, P., & Baron, E. 1997, ApJ, 481, L89
Foley, R. J., & Kasen, D. 2011, ApJ, 729, 55
Foley, R. J., Simon, J. D., Burns, C. R., et al. 2012, ApJ, 752, 101
Gerardy, C. L., Meikle, W. P. S., Kotak, R., et al. 2007, ApJ, 661, 995
Hachinger, S., Mazzali, P. A., & Benetti, S. 2006, MNRAS, 370, 299
Hatano, K., Branch, D., Fisher, A., Baron, E., & Filippenko, A. V. 1999a, ApJ, 525, 881
Hatano, K., Branch, D., Fisher, A., Deaton, J., & Baron, E. 1999b, ApJS, 121, 233
Hillier, D. J., & Dessart, L. 2012, MNRAS, 424, 252
Höflich, P. 2003, in ASP Conf. Ser. 288, Stellar Atmosphere Modeling, ed. I. Hubeny, D. Mihalas, & K. Werner (San Franciso, CA: ASP), 185
Höflich, P., Gerardy, C. L., Nomoto, K., et al. 2004, ApJ, 617, 1258
Jack, D., Hauschildt, P. H., & Baron, E. 2009, A&A, 502, 1043
Jeffery, D., & Branch, D. 1990, in Supernovae, ed. J. C. Wheeler & T. Piran (Singapore: World Scientific), 149
Jeffery, D., Leibundgut, B., Kirshner, R. P., et al. 1992, ApJ, 397, 304
Jeffery, D. J., Ketchum, W., Branch, D., et al. 2007, ApJS, 171, 493
Jerkstrand, A., Fransson, C., & Kozma, C. 2011, A&A, 530, A45
Kasen, D., Thomas, R. C., & Nugent, P. 2006, ApJ, 651, 366
Kozma, C., & Fransson, C. 1998a, ApJ, 496, 967
Kozma, C., & Fransson, C. 1998b, ApJ, 497, 431
Kromer, M., & Sim, S. A. 2009, MNRAS, 398, 1809
Maeda, K., Benetti, S., Stritzinger, M., et al. 2010, Nature, 466, 82
Maeda, K., Leloudas, G., Taubenberger, S., et al. 2011, MNRAS, 413, 3075
Maeda, K., Nomoto, K., Mazzali, P. A., & Deng, J. 2006, ApJ, 640, 854
Maund, J. R., Höflich, P. A., Patat, F., et al. 2010, ApJ, 725, L167
Maurer, I., Jerkstrand, A., Mazzali, P. A., et al. 2011, MNRAS, 418, 1517
Mazzali, P. A. 2000, A&A, 363, 705
Mazzali, P. A. 2001, MNRAS, 321, 341
Mazzali, P. A., Benetti, S., Altavilla, G., et al. 2005, ApJ, 623, L37
Mazzali, P. A., Cappellaro, E., Danziger, I., Turatto, M., & Benetti, S. 1998, ApJ, 499, L49
Mazzali, P. A., Chugai, N., Turatto, M., et al. 1997, MNRAS, 284, 151
Mazzali, P. A., Danziger, I. J., & Turatto, M. 1995, A&A, 297, 509
Mazzali, P. A., & Lucy, L. B. 1993, A&A, 279, 447
Mazzali, P. A., Maurer, I., Stritzinger, M., et al. 2011, MNRAS, 416, 881
Mihalas, D. 1978, Stellar Atmospheres (New York: W. H. Freeman)
Motohara, K., Maeda, K., Gerardy, C. L., et al. 2006, ApJ, 652, L101
Pinto, P. A., & Eastman, R. G. 2000, ApJ, 530, 757
Ruiz-Lapuente, P., & Lucy, L. B. 1992, ApJ, 400, 127
Thomas, R. C., Nugent, P. E., & Meza, J. C. 2011, PASP, 123, 237

Monthly Notices of the ROYAL ASTRONOMICAL SOCIETY

Mon. Not. R. Astron. Soc. **401,** 2081–2092 (2010) doi:10.1111/j.1365-2966.2009.15808.x

On the hydrogen recombination time in Type II supernova atmospheres

Soma De,[1] E. Baron[1,2]★ and P. H. Hauschildt[3]

[1]*Homer L. Dodge Department of Physics and Astronomy, University of Oklahoma, Norman, OK 73019, USA*
[2]*Computational Research Division, Lawrence Berkeley National Laboratory, MS 50F-1650, 1 Cyclotron Rd, Berkeley, CA 94720, USA*
[3]*Hamburger Sternwarte, Gojenbergsweg 112, 21029 Hamburg, Germany*

Accepted 2009 September 30. Received 2009 September 24; in original form 2009 July 16

ABSTRACT

Non-local thermodynamic equilibrium radiative transfer calculations of differentially expanding supernovae atmospheres are computationally intensive and are almost universally performed in a time-independent snapshot mode, where both the radiative transfer problem and the rate equations are solved assuming the steady-state approximation. The validity of the steady-state approximation in the rate equations has recently been questioned for Type II supernova (SN II) atmospheres after maximum light on to the plateau. We calculate the effective recombination time of hydrogen in SN II using our general purpose model atmosphere code PHOENIX. While we find that the recombination time for the conditions of SNe II at early times is increased over the classical value for the case of a simple hydrogen model atom with energy levels corresponding to just the first two principal quantum numbers, the classical value of the recombination time is recovered in the case of a multilevel hydrogen atom. We also find that the recombination time at most optical depths is smaller in the case of a multilevel atom than for a simple two-level hydrogen atom. We find that time dependence in the rate equations is important in the early epochs of a supernova's lifetime. The changes due to the time-dependent rate equation (at constant input luminosity) are manifested in physical parameters such as the level populations which directly affect the spectra. The Hα profile is affected by the time-dependent rate equations at early times. At later times, time dependence does not significantly modify the level populations and therefore the Hα profile is roughly independent of whether the steady-state or time-dependent approach is used.

Key words: line: formation – radiative transfer – supernova: individual: SN 1987A – supernova: individual: SN 1999em.

1 INTRODUCTION

Supernovae are one of the most widely researched objects in astrophysics. There has been much debate about the detailed physical nature of these objects, driven by the discovery of the dark energy using SNe Ia (Riess et al. 1998; Perlmutter et al. 1999). Supernovae add rich variety to the metal abundances in galaxies and are important to star formation theories. Supernova nucleosynthesis of heavy elements is responsible for galactic chemical evolution. Prior to the discovery of dark energy, supernova research was spurred on by the discovery of the peculiar Type II SN 1987A in the Large Magellanic Cloud (LMC; see Arnett et al. 1989, and references therein). Type II supernovae (SNe II) are classified by the presence of strong Balmer lines in their spectra in contrast with SNe I which lack strong Balmer lines. SNe II are due to core collapse of massive stars. SN 1987A was extremely well observed and much work has been done to explain all aspects of its spectra. The Balmer lines were not well reproduced at early times (especially about 8 d after explosion). At first, very large overabundances of the s-process elements Ba and Sc were suggested (Williams 1987a,b; Danziger et al. 1988; Höflich 1988). Further work showed that the Ba II and Sc II lines could be reproduced by assuming that the s-process abundances were enhanced by a factor of 5 compared to the LMC abundances (Mazzali, Lucy & Butler 1992).

The hydrogen Balmer line problem in many SNe II has not been accounted in a consistent manner. Dessart & Hillier (2008) summarizing their work using time-independent rate equations found that they were unable to reproduce the Hα line after 4 d in SN 1987A, 40 d in SN 1999em and 20 d in SN 1999br. Utrobin & Chugai (2005, henceforth UC05) point out the lack of a consistent physically motivated framework to explain the early epoch Balmer profile that matches with the observed line strength. Other authors followed different approaches to reproduce the observed line strengths with varying degrees of success (Schmutz et al. 1990; Hillier & Miller 1998; Höflich 2003; Dessart & Hillier 2005). UC05 argued that the

★E-mail: baron@ou.edu

poor fit of the Balmer lines could be overcome by including time dependence into the hydrogen rate equations. They argued that even in the intermediate layers, the recombination time increases due to Lyman α trapping or ionization from the first excited state. Consequently, the recombination time becomes comparable to the age of the supernova, making the validity of the steady-state approximation suspect. We numerically estimated the recombination time by directly calculating the recombination rate from the continuum into the bound states of hydrogen using H in non-local thermodynamic equilibrium (NLTE) with 31 bound states and all other metals in LTE. We use the general purpose model atmosphere code PHOENIX developed by Hauschildt & Baron (1999). We specify the density structure $\rho \propto r^{-7}$ and assume the ejecta mass to be $14.7\,\mathrm{M}_{\odot}$ as is appropriate for SN 1987A (Saio, Nomoto & Kato 1988). PHOENIX calculates the level populations, temperature and radiation field for successive epochs with a time interval of approximately 2 d. We generated our models and spectra using both time-dependent and time-independent rate equations. We calculated our recombination time for each epoch from the best-fitting spectra in each case. In Section 2, we outline the theoretical framework for the recombination time and motivation for our work. In Section 3, we discuss earlier work done to test the relevance of time dependence in SN II atmospheres. In Section 4, we describe the basic framework for our code and in Section 5 we present our approach to compute the recombination time. In Sections 6–8, we analyse our results and address the question of the necessity of incorporating time dependence in the rate equations due to the increased recombination time.

2 MOTIVATION

The recombination time is given by (Osterbrock 1989)

$$\tau_{\mathrm{rec}} = \frac{1}{n_{\mathrm{e}}\alpha_{\mathrm{A}}} = \frac{3 \times 10^{12}\,\mathrm{s}}{n_{\mathrm{e}}}, \tag{1}$$

where n_{e} is the number density of electrons and α_{A} is the recombination coefficient. The Case A recombination coefficient is used for convenient comparison with UC05 who also assume Case A. Hummer & Storey (1987) suggest that the Case B recombination coefficient is not appropriate for cases with Lyman α escape or with the electron densities as high as $10^8\,\mathrm{g\,cm^{-3}}$. Thus, Case A is more relevant here and since UC05 use the same coefficient we will use it to facilitate comparison.

It has been recently argued by UC05 that time dependence in the rate equations in a normal SN IIP atmosphere may be important due to a significant increase in the recombination time. It is well-known that in the early universe Lyman α trapping and ionization from the second level increases the effective recombination time in hydrogen (Zeldovich, Kurt & Syunyaev 1969; Peebles 1968). The net recombination rate is then determined by transitions that are not as highly resonant as Lyman α such as many non-resonant processes connecting the same parity states (e.g. the 2γ process) and the processes that are accompanied by the escape of the resonant photon. For a hydrogen model atom with $n = 2$ (consisting of only levels 1s, 2s, $2\mathrm{p}_{\frac{1}{2}}$ and $2\mathrm{p}_{\frac{3}{2}}$), the ionization from the second level dominates the Lyman α escape probability or the 2γ transition probability from the 2s to the 1s level. This delays the effective recombination or lengthens the recombination time. In the case of an atom with many excited levels, recombination into the upper levels followed by fluorescence can significantly alter the ionization fraction due to the well-known phenomena of 'photon suction' (Carlsson, Rutten & Shchukina 1992). The escape probability for the resonant Lyman lines increases as the energy of the bound state increases (De et al. in preparation). Thus, since these photons escape, the electrons end up in the ground state enhancing recombination. These two effects (in multilevel atoms) could affect the recombination process significantly, altering the physical conditions considered by UC05, so that there is once again efficient recombination and one should not necessarily expect any significant increase in recombination time over that given by equation (1). In the following sections, we briefly describe relevant earlier work and explain why it is important to check the numerical value of the recombination time in the system. To be able to correctly calculate the recombination rate for a multilevel atom, we use (Peebles 1968)

$$-\frac{\mathrm{d}}{\mathrm{d}t}\left(\frac{n_{\mathrm{e}}}{n}\right) = \sum \frac{(R_{nl} - P_{nl})}{n}, \tag{2}$$

where R_{nl} is the recombination rate into any bound level characterized by the principal quantum number n and angular quantum number l from the continuum and P_{nl} is the photoionization rate from any bound level into the continuum. This is similar to equation (23) of Peebles (1968). The difference is that instead of using simplified assumptions, we calculate the net recombination rate from the simultaneous solution to the rate equation and the radiative transfer equation. We then calculate the recombination time for a multilevel atom model by using

$$\tau_{\mathrm{rec}} = \frac{n_{\mathrm{e}}}{\sum(R_{nl} - P_{nl})}. \tag{3}$$

Equation (3) is an equivalent way of estimating the recombination time. UC05 used

$$\tau_{\mathrm{rec}} = \frac{n_{\mathrm{e}}}{\frac{\mathrm{d}n_{\mathrm{e}}}{\mathrm{d}t}} \tag{4}$$

to estimate the recombination time. In equations (3) and (4), when the Lagrangian derivative of the free electron density with respect to time goes to zero (in the case of ionization freeze-out), the recombination time goes to infinity. This contradiction is only apparent, since this equation only computes the time-scale associated with the variable part of the free electron density. When the free electron density is constant in the Lagrangian frame, this equation implies that the time associated with any variation in the free electron density is infinite or, in other words, it does not vary.

Since we are really considering just the recombination of hydrogen, in a solar mixture an alternative would be to define

$$\tau_{\mathrm{rec}} = \frac{n_{\mathrm{H}^+}}{R_{nl} - P_{nl}} \tag{5}$$

where n_{H^+} is the proton density in the system. The reason why the electron recombination time scales with hydrogen ion density is because we treat other elements except hydrogen in LTE or in other words the other elements do not have explicit time dependence in their ionic concentrations. Generally at the relevant optical depths, the ratio $n_{\mathrm{H}^+}/n_{\mathrm{e}}$ is very close to 1.0, so there is almost no difference between equations (3) and (5). We will therefore use equation (3).

3 EARLIER WORK

There have been different numerical models that treat the problem of recombination. This problem of recombination was addressed by Zeldovich et al. (1969) in the cosmological recombination epoch scenario. As noted above, UC05 have revived this for the case of SNe II. Dessart & Hillier (2008) calculated SNe IIP spectra obtained treating the rate equations including time-dependent effects. We try to carefully review the effect of time dependence in the results published by Dessart & Hillier (2008). The main idea is to check if the temporal nature of the rate equations is significantly supported by UC05's argument on the recombination time.

3.1 Utrobin and Chugai's calculation

UC05 used a two-level plus continuum approximation for the hydrogen atom to estimate the recombination probability and then estimate the recombination time. They argue that around $N_e > 10^8$ and neutral hydrogen number density $N_{HI} > 10^9$, a two-photon process dominates over other processes (collisional terms or the escape probability term) and the recombination probability is computed to be $<2.0 \times 10^{-3}$. The characteristic temperature was 5000 K, the photoionization probability was assumed to be $\sim 10^3\ s^{-1}$ and the dilution factor was taken as $W = 0.1$. Therefore, the classical recombination time $(\alpha N_e)^{-1}$ gets modified to $\frac{1}{\alpha N_e w_{21}}$ which is factor of 500 higher than the classical recombination time. For a typical SN II with an age of 10^6–10^7 s, the modified recombination time becomes of the order of 10^7 s. To test their numerical estimate and predictions about the importance of incorporating time dependence, UC05 treated the radiation field in the core-halo approximation and assumed the Sobolev approximation for line formation. Assuming that the SN atmosphere is very opaque in the Lyman continuum enabled them to fully determine the diffusive continuum in that frequency band by hydrogen recombinations and free–free emissions.

At lower frequencies, between the Balmer and the Lyman edges, there is a large optical depth owing to interaction with numerous metal lines. Under these conditions, UC05 assumed that absorption was given by the constant absorption coefficient from the solution of Chandrasekhar (1934).

In the visual band where the optical depth of the atmosphere is quite low, they adopted the free streaming approximation, which describes the average intensity of the continuum in the atmosphere as proportional to the specific intensity of photospheric radiation. The effective radius and temperature are given by their hydrodynamical model which was created after SN 1987A. UC05 incorporated gamma-ray deposition and included the time-dependent term in their rate equations for all species they considered.

They reproduced the Hα line that appears in the photospheric epoch in the first month of SN 1987A. They were unable to reproduce the additional blue peak that appears between days 20 and 29 which they argued was due to the Bochum event (Hanuschik & Dachs 1988). Also, they were able to reproduce the Ba II λ6142 line in SN 1987A between days 14 and 19 with LMC barium abundances. They argued that time-dependent hydrogen ionization provided higher electron densities in the atmosphere and thus made recombination of Ba III into Ba II more efficient.

3.2 Dessert and Hillier's work

Dessart & Hillier (2008) incorporated time-dependent terms into the statistical and radiation equilibrium calculations of the NLTE line-blanketed radiative transfer code CMFGEN. They allowed full interaction between the radiation field and level populations to study the effect on the full spectrum. Dessart & Hillier (2008) discuss their findings on the ejecta properties and spectroscopic signatures obtained from time-dependent simulations. They neglected time-dependent and relativistic terms in the radiative transfer equation. However, they argued that inclusion of those terms would not affect their results because the importance of the time-dependent terms arises primarily due to atomic physics and should not be sensitive to radiative transfer effects.

They compare their results with a sample of observations. They reported a strong and broad Hα line that closely matches the observed profile for SN 1999em in the hydrogen recombination epoch *without* the inclusion of non-thermal ionization/excitation due to gamma-ray deposition from the radioactive decay of ^{56}Ni. They were also able to reproduce the Hα, Na I D and Ca II IR triplet ($\sim$8500 Å) lines more satisfactorily.

Fig. 16 of Dessart & Hillier (2008) compares the observed spectra of SN 1999em for 48.7 d since explosion and the spectra calculated from both time-dependent and -independent models for the rate equations. One may note a significant mismatch between the time-dependent model and observed spectra in certain regions where the time-independent models match better. Around 4000 Å, the Fe I and Fe II lines are not reproduced well (Pastorello et al. 2004); similarly, the C I and Ca II line strengths around 8600 Å are underestimated using the time-dependent model and the line strengths are better reproduced by the time-independent model. Dessart & Hillier (2008) find that time dependence is better for later epochs, from their work on SN 1999em and SN 1999br, about 30 d after explosion.

4 DESCRIPTION OF PHOENIX

PHOENIX is a model atmosphere computer code that has been developed by Hauschildt, Baron and collaborators over the last two decades. Due to the coupling between the level populations and the radiation field, the radiation transport equation must be solved simultaneously with the rate equations. PHOENIX includes a large number of NLTE and LTE background spectral lines and solves the radiative transfer equation with a full characteristics piecewise parabolic method (Olson & Kunasz 1987; Hauschildt 1992) and *without* simple approximations such as the Sobolev approximation (Mihalas 1970). Hauschildt & Baron (1999) describe the numerical algorithms used in PHOENIX to solve the radiation transport equations, the NLTE rate equations and parallelization of the code. PHOENIX uses the total bolometric luminosity in the observer's frame, the density structure and element abundances as input parameters. The equation of radiative transfer in spherical geometry, the rate equations and the condition of radiative equilibrium are then solved. This process is repeated until the radiation field and the matter have converged to radiative equilibrium in the Lagrangian frame. In our model calculations, we have not taken into account the ionization by non-thermal electrons. Also, time dependence was incorporated only in the rate equations. The inclusion of time dependence in the thermal equilibrium equation is implicit. Since the time-dependent rate equations affect the opacities, the solution to the radiative transfer equation is affected as well. The explicit implementation of time dependence in the radiative transfer equation is beyond the scope of this work. Our goal was to specifically examine the effects of time dependence on the hydrogen Balmer lines, and therefore only hydrogen is treated in NLTE. This both speeds up the calculations significantly and isolates the effects of time dependence on hydrogen.

5 RECOMBINATION TIME CALCULATIONS

Our main motivation is to explore the recombination time in an SN II atmosphere. In order to obtain the correct electron densities and level populations, it is essential to make sure that the rate equations are correct even if the recombination time is actually longer than or comparable to the age of the supernova. We incorporated the time-dependent term in the rate equations and in our results we describe this as the time-dependent case. We have performed calculations assuming both the steady-state, time-independent approximation and the full time-dependent rate equations. In most of our models, we used a hydrogen model atom consisting of 31 levels. To save computing time and limit the time-dependent effects to the

Balmer lines, we treated all other elements in LTE for this work. We started with a known density profile typical of an SN II with mass similar to the progenitor mass of SN 1987A ($\sim$14.7 $M_\odot$) and luminosity (1.015×10^{43} erg) . We built a radial velocity grid with 128 layers. The location of the radial points was found from the assumption of homology, $r = vt$. PHOENIX then solves the radiative transfer equation and the rate equations simultaneously. This yields the temperature, radiation field and other physical parameters such as pressure, optical depth and electron density for each radial grid or layer. We choose the best model by tuning only the input luminosity and the input density profile by comparing the match between the synthetic and the observed spectra of SN 1987A.

We began with a time-independent model at day 2 and generated snapshots for both the time-dependent and -independent cases up to day 20 with intervals of 2 d. It is important for the time-dependent case to have the correct level populations at the previous time and consequently it was better to choose a smaller time interval (2 d) to generate snapshots of the physical profile of the supernova. Our analysis was done on a Lagrangian velocity grid. Right after the explosion, the optical depth is very high in the innermost layers that are expanding with low velocity. At very high optical depth, radiative diffusion is an excellent approximation. Thus, at high optical depths, we replace the innermost ejecta with an opaque core and the luminosity is given by the expression for radiative diffusion at this boundary. Our initial grid has a velocity of $\sim$3000 km s^{-1} and we gradually add deeper layers until at our final epoch of 20 d, the innermost layer has a velocity of around $\sim$1000 km s^{-1}. To add new layers in the inner core we merged the outer low density, high velocity layers keeping the total number of layers constant. This way we preserved the grid size but also made sure that we have the physically relevant velocity range at all epochs of evolution.

In order to recover the results of UC05 in a simple hydrogen model atom case and also to understand the difference between the simple and multilevel model atom framework, we repeated our calculations for a four-level hydrogen atom model case with solar compositions. In order to have the correct physical conditions, we held the structure of the atmosphere (temperature and density) fixed from what we had obtained with the time-dependent multilevel hydrogen atom case for that epoch. We then solved for the time-dependent level populations and the associated radiation field.

6 RESULTS

Our computations consist of three different systems at each epoch. They are the case when we have a four-level ($n = 2$) hydrogen model atom in NLTE (in absence of any other metals) and time-dependent rate equations. We refer to this model as Case 1. Cases 2 and 3 are full calculations with 31-level hydrogen model atoms, solar compositions and time-dependent and time-independent rate equations, respectively.

We measure the optical depth using the value $\tau_{\rm std}$ which is the optical depth in the continuum at 5000 Å.

6.1 Ionization fraction and electron density profile

The two most important physical parameters for the recombination time are the ionization fraction, $f_{\rm H}$, and the free electron density, $n_{\rm e}$. In Fig. 1, we present the electron density for the three different cases.

The upper panel shows the free electron density for Case 1 (where only hydrogen is present with $n = 2$ and rate equations are time dependent) over different epochs. Days 2–6 show a steady rise in the free electron density in the system as the optical depth becomes higher. The electron density declines at later epochs due to cooling and geometric dilution. These trends of high electron density at very early epochs and lower electron density at the later epochs are expected from the fact that the temperature is high at early times. At later epochs, the electron density at a given optical depth falls off due to the expansion and declining temperature. At epochs of 4–6 d, the hydrogen in the system is almost completely ionized and

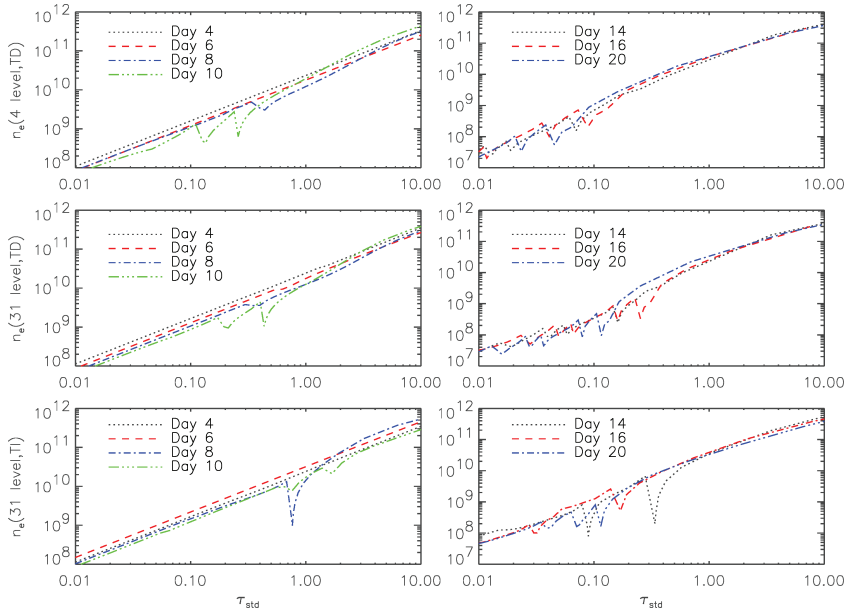

Figure 1. Comparison between the free electron densities at different systems. The upper panel has a four-level hydrogen atom case. The middle panel has the multilevel time-dependent case. The bottom panel has the multilevel time-independent case.

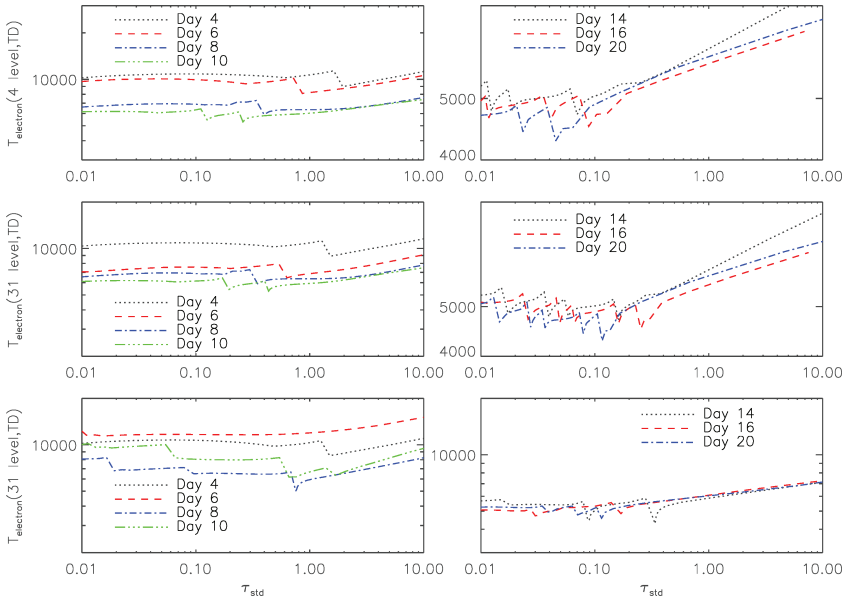

Figure 2. Comparison between electron temperatures at different systems. The upper panel has a four-level hydrogen atom case. The middle panel has the multilevel time-dependent case. The bottom panel has the multilevel time-independent case.

the free electron density is the highest at this epoch. In the right-hand plot of the top panel of Fig. 1, we display the electron density for the epochs of 14–20 d. At these epochs, hydrogen ionization is lower and recombination of hydrogen begins. This is evident from the corresponding temperature structure. Fig. 2 displays the electron temperature of the system, which controls the free electron density and the level of ionization. The top left-hand panel displays the temperatures for early epochs ($T \sim 8000$–$10\,000$ K for epochs <8 d). In the top right-hand panel, the temperature drops to around 5000 K and this is where the transition from the fully ionized to the partially ionized regime occurs. The recombination regime begins roughly at day 8. Between optical depths $\tau_{std} = 0.01$–0.1, the temperature is around 5000 K for epochs later than about 8 d since explosion; thus recombination starts to take place, reducing the free electron density. For optical depths higher than $\tau_{std} = 0.1$, the electron temperature is still high enough (even at later epochs) to maintain a high level of ionization. Using the values of the free electron density and the temperature structure, it is easy to understand the ionization fraction for hydrogen in the system which is displayed in Fig. 3. The optical depth is indicated using the value

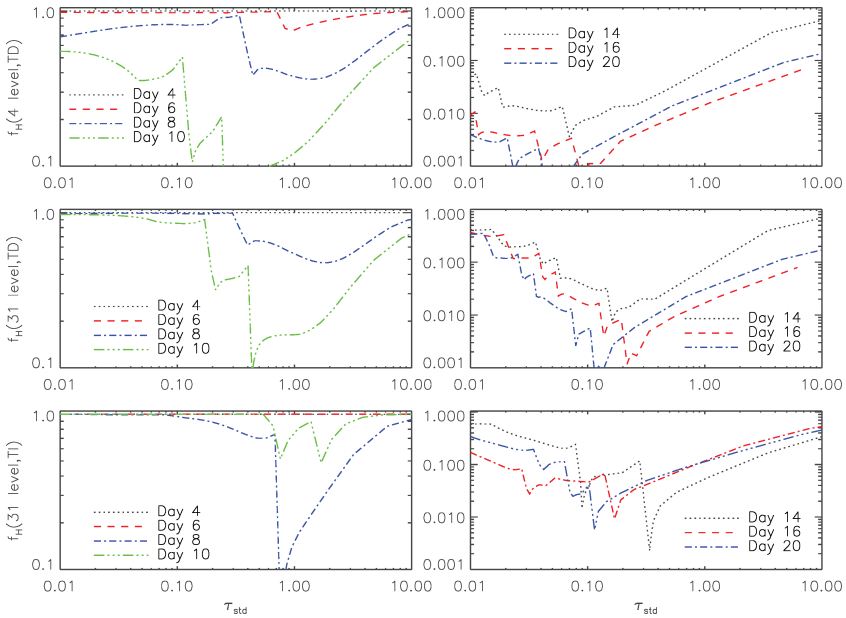

Figure 3. Comparison between ionization fractions at different systems. The upper panel has a four-level hydrogen atom case. The middle panel has the multilevel time-dependent case. The bottom panel has the multilevel time-independent case.

$\tau_{\rm std}$ which is the optical depth in the continuum at 5000 Å. Beginning at 6 d for Case 1, recombination starts to take place at optical depths $\tau_{\rm std} = 0.01$–0.1 causing a bumpy profile for the ionization fraction.

For Case 2 (time-dependent rate equations and multilevel hydrogen with 31 bound levels), results are displayed in the middle panel of our figures. We again refer to the middle panel of Figs 1–3. The basic nature of the temperature structure, free electron density and the ionization fraction is very similar to Case 1. The main difference in this case is that for the later epochs, the electron temperature is around 5000 K for optical depths $\tau_{\rm std} = 0.01$–0.3. Thus, the recombination front moves deeper into the expanding ejecta for the multilevel case with metals. This may be a cumulative effect due to the metals and the multiple bound levels. The metals tend to suppress the ionization of hydrogen at higher optical depths; hence, we would expect the ionization front for hydrogen to move deeper into the object. The multiple bound levels enhance the recombination at any optical depth. The ionization fraction for hydrogen follows the free electron density and the temperature profile by producing a bumpy profile for $\tau_{\rm std}$ between 0.01 and 0.3.

For Case 3, where the rate equations are time-independent with the 31-level hydrogen model atom, results are shown in the bottom panel of our plots. In this case, the recombination front moves deeper inside compared to Cases 1 and 2. Thus, the electron temperatures of about 5000 K are reached at optical depths $\tau_{\rm std} > 1.0$ for later epochs.

We summarize our results on the ionization fraction as follows. (1) In all three cases, we observed that the results from the free electron density, electron temperature and ionization fraction are consistent with each other. (2) As the supernova expands, the recombination front moves deeper inside. The span of the recombination front is different in all three cases, being largest in Case 3. Overall, the free electron densities are similar in all three cases. (3) In the recombining regime, the electron density drops, causing a drop in the ionization fraction as well. (4) All three cases (31-level time-dependent, 31-level time-independent and four-level time-dependent) have visibly different ionization fraction profiles, but the difference decreases between Cases 2 and 3 (31-level hydrogen model). In other words, Case 1 has an ionization profile that is different from Cases 2 and 3. The ionization fraction in these models after 10 d is higher than that in the four-level hydrogen atom time-dependent model (Case 1). (5) In the recombination regime, there are glitches at the recombination front which probably arise from the imperfect spatial resolution of the ionization front. It is clear from the figures that the glitches do not affect the overall qualitative results.

6.2 Spectral comparison

Spectra are important as they are the only observable. In our discussion, we emphasize the Hα profile of the spectra. In Fig. 4, we present the comparison between the Hα line profile of the spectra for Cases 2 and 3. In this plot, we have days 4, 6 and 8. We used *dotted* lines for Case 3 and solid lines for Case 2 in all our line profile and spectral comparison plots. The very early Hα profiles do not show any differences between Cases 2 and 3. From day 6 onwards, we notice that the line profile gets wider for Case 2 – the time-dependent case. Fig. 5 shows a spectral comparison between Cases 2 and 3. Overall, the spectral features for Case 2 are somewhat broader (especially between 4000 and 6500 Å).

We plot the Hα profile for days 10, 14, 16 and 20 for Cases 2 and 3 in Fig. 6. We see a similar broadening in the profile for Case 2 except at day 16. This broadening becomes more obvious if one looks at the spectral plot (Fig. 7). The spectra seem to have somewhat broader features for Case 2, especially in the regimes $\lambda < 4500$ Å and $\lambda > 8000$ Å. We emphasize that these spectral profiles for SN 1987A were generated by independently tuning their luminosity to obtain the best fit to the observed spectra. To summarize we find that the spectral features become somewhat broader with time-dependent

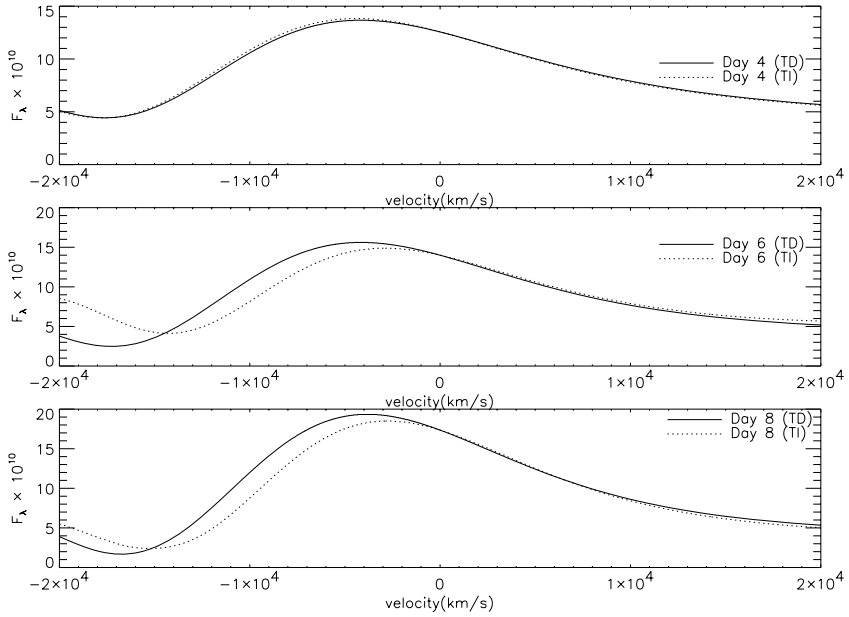

Figure 4. Comparison of the line profiles of Hα for days 4, 6, 8 in the time-dependent and time-independent cases for a model that is appropriate to SN 1987A. The luminosity in each case has been tuned to fit the observations.

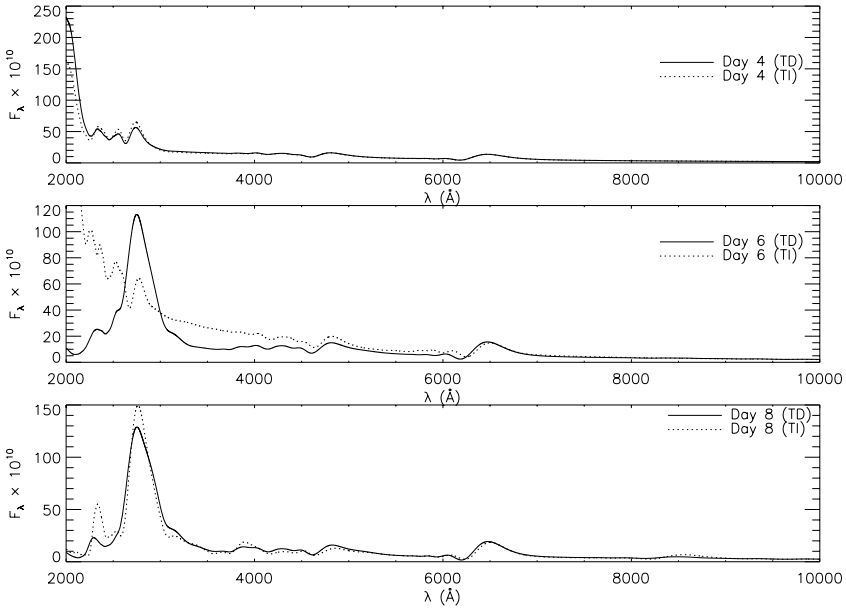

Figure 5. Comparison of the spectra for days 4, 6, 8 in the time-dependent and time-independent cases for a model that is appropriate to SN 1987A. The luminosity in each case has been tuned to fit the observations. The differences in the day 6 UV spectra are primarily due to variations in the opacity due to the exponential dependence of the Fe II populations on the temperature and not to time dependence in the hydrogen rate equations.

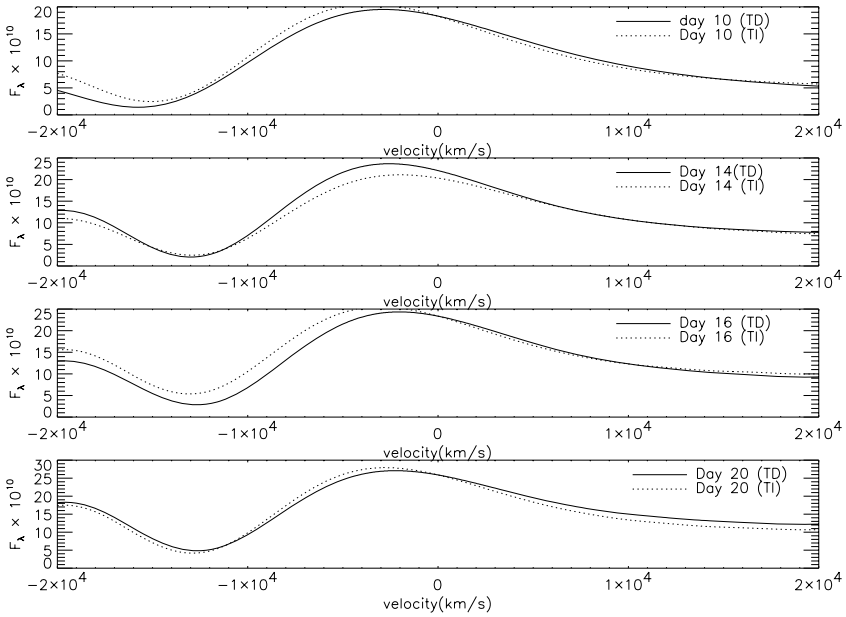

Figure 6. Comparison of the line profile of Hα for days 10, 14, 16, 20 in the time-dependent and time-independent cases for a model that is appropriate to SN 1987A. The luminosity has been tuned to fit the observations in each case.

treatment of the rate equations, but the effect is smaller than that found by Dessart & Hillier (2008).

Fig. 8 shows a comparison of the model spectra with observations for SN 1987A at days 4 and 6. There is a noticeable improvement in the Hα profile for the time-dependent case versus the time-independent case, although some of the effect is due to variations in the luminosity which is a parameter in our models. Thus, time-dependent effects can be important for the early epoch Hα profiles.

6.3 Results on the recombination time

The recombination time is a crucial quantity. The motivation for this paper was to study if the apparent importance of time

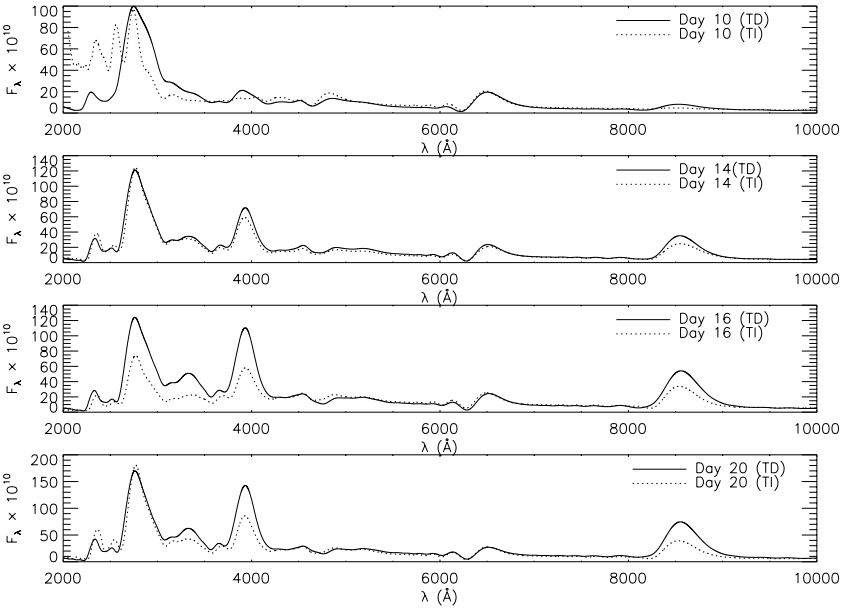

Figure 7. Comparison of the spectra for days 10, 14, 16, 20 in the time-dependent and time-independent cases for a model that is appropriate to SN 1987A. The luminosity in each case has been tuned to fit the observations.

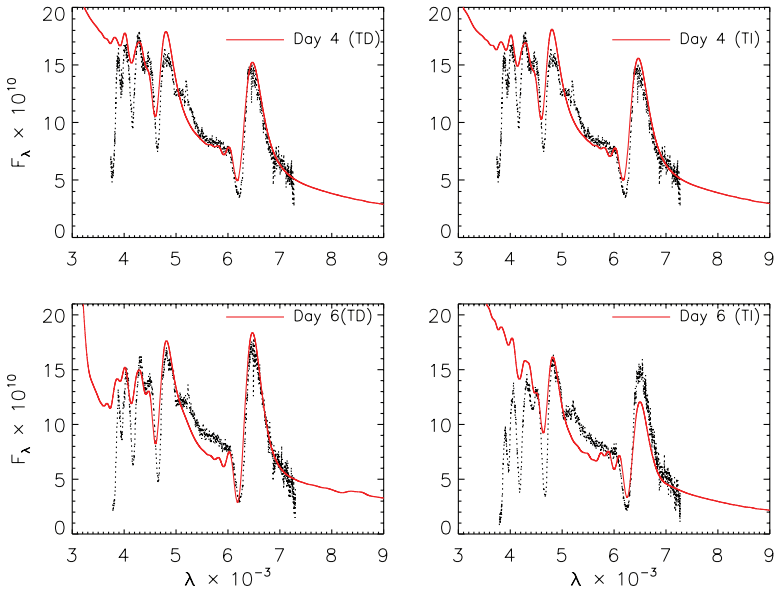

Figure 8. Comparison of the spectra for days 4 and 6 with time-dependent and time-independent cases with observed spectra of SN 1987A. The luminosity in each case has been tuned to fit the observations. The Hα profile is improved in the time-dependent case.

dependence could be verified from the numerical estimate of the effective recombination time. It is important to check if the effective recombination time is essentially comparable to the age of the supernova. Since our spectra were generated by independently tuning the luminosity, it is important to investigate the recombination time-scale to be able to conclude if the time dependence in the rate equations is indeed important. As noted above, the semi-analytic result is for a two-level atom and the effects of both non-resonant de-excitations and a reduction in the escape probability due to more channels could alter the numerical values compared to the simpler analysis. Fig. 9 shows the recombination time for Cases 1 and 2.

In Case 1, shown in the upper panel of Fig. 9, the recombination time (referred as $\tau_{\mathrm{H}(4)}$) follows an inverted profile compared to the ionization fraction (see Fig. 3). This is consistent with the fact that the low ionization fraction will reduce recombination, resulting in a longer recombination time. Similar to the profiles for the ionization fraction and the electron density, the recombination time also gives a bumpy structure in the recombining region. In Case 1, for epochs >6 d the recombination time is around 10^6–10^7 for $\tau_{\mathrm{std}} = 0.01$–$0.1$.

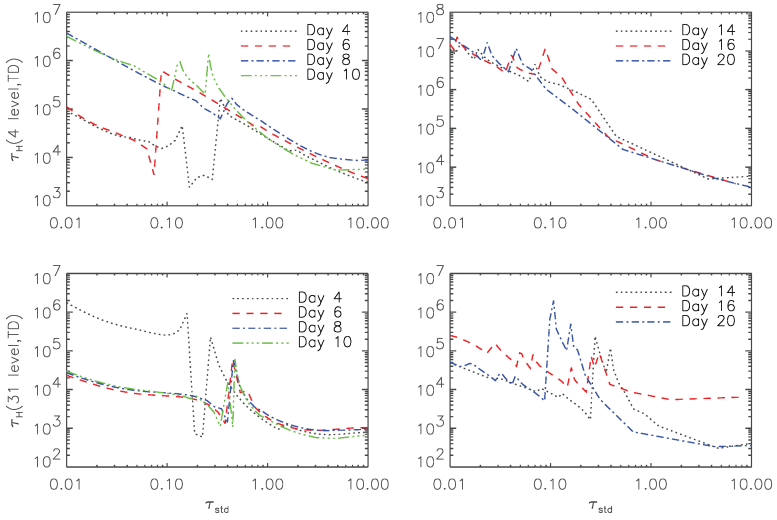

Figure 9. Comparison between recombination times at different systems. The upper panel has a four-level hydrogen atom case. The middle panel has the multilevel time-dependent case. The bottom panel has the multilevel time-independent case.

Below the recombining regime, the recombination time is lower. This is due to the increasing density. At lower τ_{std}, the recombination time increases because the electron density declines.

The bottom panel of Fig. 9 shows the recombination time for Case 2. The numerical value of the recombination time, $\tau_{H(31)}$, is highest for the earliest epochs. This is because there is barely any recombination since the temperature is $T > 10^4$ K (see Fig. 2). After the initial expansion, the electrons start to recombine. At the ionization front, due to the falling electron density, the recombination time increases at later epochs. Although outside of the ionization front, the recombination time decreases with the expansion of the supernova. This is the case for both $\tau_{H(4)}$ and $\tau_{H(31)}$ except that this effect is more evident at later epochs in the multilevel case (bottom panel of Fig. 9). We summarize as follows.

(1) $\tau_{H(31)}$ and $\tau_{H(4)}$ follow the profile expected from their respective free electron density and temperature profiles and almost follow an inverted profile compared to the ionization fraction profile. In other words, the recombination time is found to be proportional to the free electron density and temperature and inversely proportional to the ionization fraction.

(2) The recombination time is higher for low optical depths. There is a break in the monotonic decline in the recombination time (as it moves towards higher optical depth) in the recombining regime. There is a rise in the recombination time in this regime. For optical depths $\tau_{std} > 1.0$, both $\tau_{H(31)}$ and $\tau_{H(4)}$ decrease monotonically due to the increase in the free electron density.

(3) As the supernova expands, the recombination time at a given optical depth decreases at almost all optical depths (Fig. 9).

(4) Fig. 10 compares the time-dependent multilevel hydrogen atom and the classical recombination time, τ_{anal}. In the optically thin regime ($\tau_{std} < 0.10$), $\tau_{H(31)}$ is close to τ_{anal}. Only right at the ionization front does the ratio deviate significantly from unity and $\tau_{H(31)}$ is larger than τ_{anal}.

7 SN 1999em

SN1987A is one of the best observed astronomical objects. It is also a peculiar SN II. It has two maxima in its light curve and also has very steep rise to its maximum. On the other hand, SN 1999em has

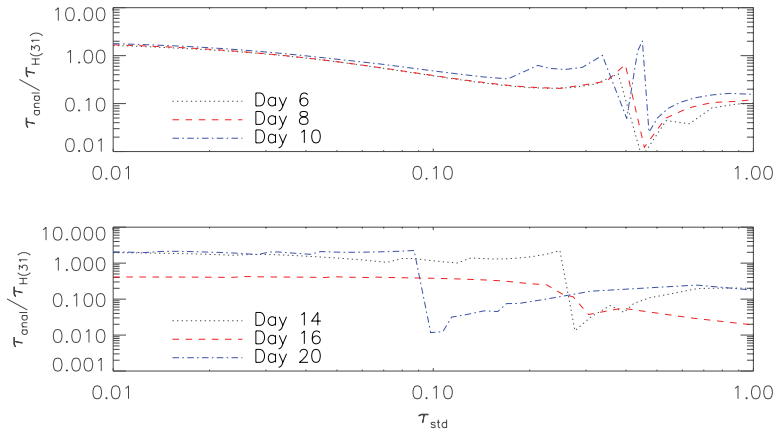

Figure 10. Ratio of recombination times for the analytical calculation and the 31-level hydrogen atom model calculated at different epochs. The upper panel shows the earlier epochs and the lower panel the later epochs.

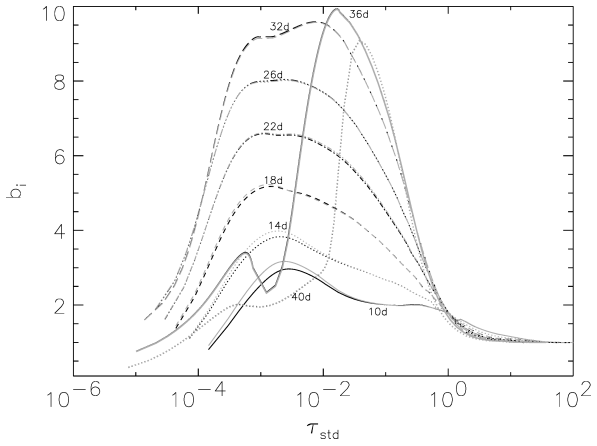

Figure 11. Departure coefficient, b_1, as a function of τ_{std} for the ground state of hydrogen. The black line is for the time-dependent case and grey line is the time-independent case for each day.

steady rise to the maximum and a well-defined plateau. Thus, we also studied the effects of time dependence in SN 1999em. We began with the day 7 spectrum and marched forwards in time until around day 40 (since explosion). We again considered a 31-level hydrogen atom and treated only hydrogen in NLTE. The departure coefficients (referred to as b_i) are the ratio of the real level population density to the expected LTE level population density (Menzel & Cillié 1937; Mihalas 1978). Figs 11–13 display the departure coefficients for the levels $n = 1$ (ground state), $n = 2$ and $n = 3$. It is evident from our plots that time dependence is important at early times although the effect is very small. This effect diminishes with time. Also, the effect is only relevant in the recombining regime. The explanation of this transient phenomenon is easier to understand in the Lagrangian frame. In a given mass element at very early times if the temperature is much higher than 5000 K, the hydrogen is nearly completely ionized and the $\frac{\mathrm{d}}{\mathrm{d}t}$ term is very small. At very late times when the temperature falls much below 5000 K, the hydrogen is mostly neutral and the $\frac{\mathrm{d}}{\mathrm{d}t}$ term is also small. Thus, the $\frac{\mathrm{d}}{\mathrm{d}t}$ term is important in the recombination regime. The effect decreases with time. Our results agree with those of UC05. The calculations are performed on a Lagrangian grid; however, the results are best presented on the τ_{std} grid. As an aid to interpreting these figures, Fig. 14 shows

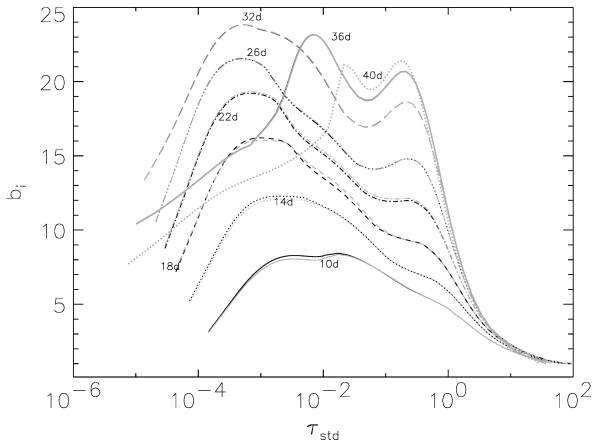

Figure 12. Departure coefficient, b_2, as a function of τ_{std} for the $n = 2$ state of hydrogen. The colours and line styles are the same as in Fig. 11.

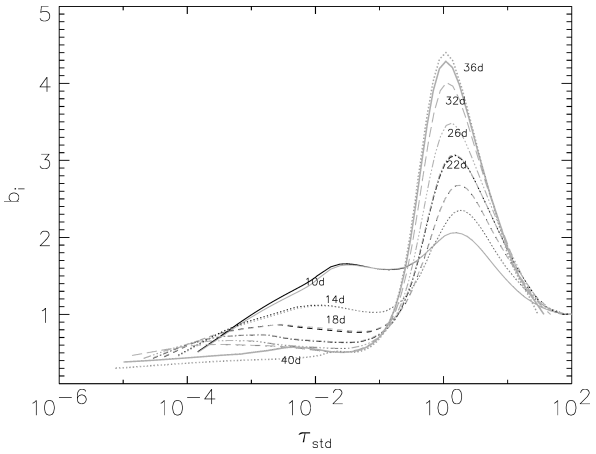

Figure 13. Departure coefficient, b_3, as a function of τ_{std} for the $n = 3$ state of hydrogen. The colours and line styles are the same as in Fig. 11.

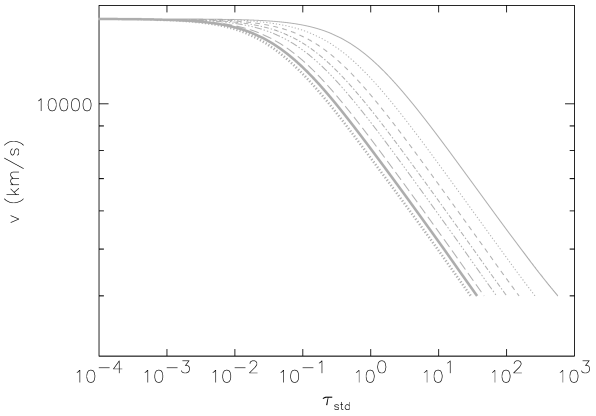

Figure 14. Expansion velocity of each layer as a function of τ_{std} for the SN 1999em model. The colours and line styles are the same as in Fig. 11.

the profile of velocity versus τ_{std}. We find that the change in the departure coefficients for the ground state is up to 12 per cent. For the first and second excited states, the change in the departure coefficients is up to 4 and 2 per cent, respectively. The change was found to be maximum at day 10. In order to test the sensitivity of our results to the time-step, we compared our results for SN 1999em for the case where we use a 4 d interval to that where we use a 1 d interval in the time-dependent rate equation for hydrogen. In the 14 d spectra, we find that the change in the departure coefficients (derived from two different time-steps) is within 3 per cent (for the ground state) in the line-forming region. This effect becomes even smaller at later times.

8 DISCUSSION AND CONCLUSIONS

We have studied the importance of time dependence in the rate equations in an SN II atmosphere due to the increase in the recombination time. We also explored the effects of having many angular momentum sub-states. In our description, we use $\tau_{H(4)}$ and $\tau_{H(31)}$ as the recombination time for a four-level hydrogen atom model and 31-level hydrogen atom model, respectively.

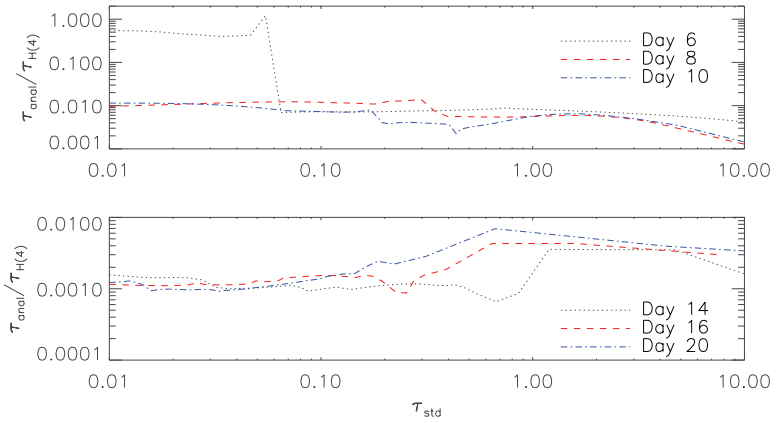

Figure 15. Ratio of recombination times for the analytical calculation and the four-level hydrogen atom model calculated at different epochs. The upper panel shows the earlier epochs and the lower panel the later epochs.

UC05 proposed that $\tau_{H(4)}$ is of the order of 10^7 s at $T \sim 5000$ K and $n_e = 10^8$ cm^{-3}. For epochs later than 6 d, we calculated $\tau_{H(4)}$ at similar electron density and temperature to be around 10^7 s ($\tau_{std} \sim 0.02$). Thus, we recover the recombination time-scale predicted by UC05 for the four-level hydrogen case. An important difference between our results and those of UC05 is that we find the electron densities and temperatures which they used as photospheric conditions to occur at $\tau_{std} \sim 0.02$ and not near $\tau_{std} = 1.0$. Around $\tau_{std} = 1.0$, the free electron density even for Case 1 is much higher and hence the recombination time is much smaller. This optical depth mismatch is due to the fact that we are looking at the continuum optical depth and not the line optical depth. The ratio of the Balmer line opacity to the continuum opacity is $\sim 10^3$ in the recombining region.

We also compare the classical recombination time (calculated using $1/\alpha n_e$) with our calculated $\tau_{H(4)}$ generated from the solution to the radiative transfer equation. We refer to the approximate classical recombination time as τ_{anal}. This allows us to determine the factor w_{21} (UC05). Fig. 15 displays the ratio $\tau_{anal}/\tau_{H(4)}$, a direct measure of w_{21} described by UC05.

In Fig. 16, we display the ratio of the recombination time for Case 2 to the recombination time from a simple hydrogen atom (Case 1) at the same epoch and at the same optical depth.

(1) For all epochs, $\tau_{H(31)}$ is smaller than $\tau_{H(4)}$ at almost all optical depths. For higher optical depths, the ratio increases and approaches unity because the ionization fraction for hydrogen and $\tau_{H(31)}$ becomes independent of the number of bound levels. At this point, the system is almost in LTE and the number of free electrons depends only on the temperature. (2) Fig. 15 shows that the simple hydrogen atom model (four-level) overestimates the recombination time by a factor of 100 or more at almost all epochs and optical depths. (3) Fig. 10 shows that the recombination time recovered from a multilevel hydrogen atom compares with the standard value (τ_{anal}) for $\tau_{std} < 1.0$. At the ionization front, $\tau_{H(31)}$ differs significantly from τ_{anal}. (4) Based on our work on SN 1999em, we find that the transient nature of the level population of hydrogen is not a crucial factor on the plateau, but it is important in the active recombining regime. This effect could be important for early features in the spectra but the steady-state approximation should be valid in the plateau phase. (5) In the early spectra of SN 1987A, we find that Hα is better fitted using the time-dependent formulation. (6) The recombination time jumps above the underlying trend only at the ionization front. This is just caused by the sudden reduction of the electron density driving the recombination time higher in the ionization front.

It is very difficult to decouple the effects of time-dependent rate equations in a radiative transfer framework and the effects

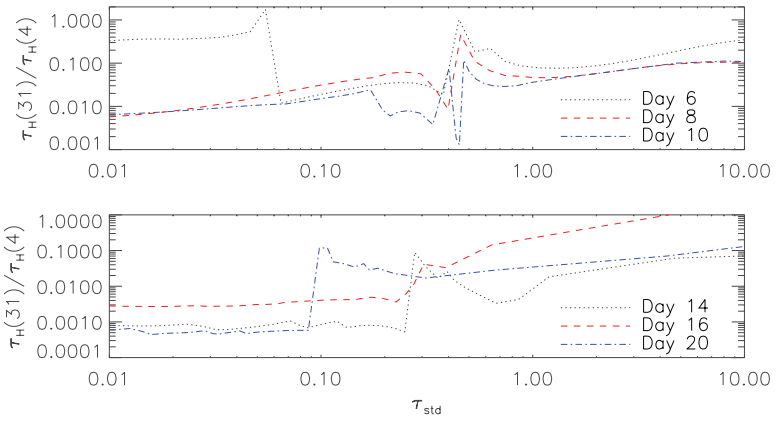

Figure 16. Ratio of recombination times for the time-dependent multilevel hydrogen atom case and the four-level hydrogen atom model calculated at different days. The upper panel shows the earlier epochs and the lower panel the later epochs.

of multilevel model atoms by only looking at spectra. The Balmer profile of the spectra of SN 1987A at early times (Fig. 8) and the level populations from our results on SN 1999em (Figs 11–13) indicate the effects of the time-dependent rate equations at early times. The increased recombination time (Fig. 9) at early times for SN 1987A also supports the importance of time-dependent rate equations. Therefore, we conclude that time dependence is more important at early times than later times. The effect of multilevel atoms can be seen in Fig. 9 which clearly shows than even at later times $\tau_{\mathrm{H}(4)}$ is much higher than $\tau_{\mathrm{H}(31)}$. Therefore, conclusions using only a four-level model may overestimate the importance of time dependence. Of course, including time dependence is not terribly costly numerically and thus it can be included when a time sequence is calculated.

ACKNOWLEDGMENTS

This work was supported in part by NSF grant AST-0707704, Department of Energy Award Number DE-FG02-07ER41517 and SFB grant 676 from the DFG. This research used resources of the National Energy Research Scientific Computing Center (NERSC), which is supported by the Office of Science of the U.S. Department of Energy under contract no. DE-AC02-05CH11231, and the Höchstleistungs Rechenzentrum Nord (HLRN). We thank both these institutions for a generous allocation of computer time.

REFERENCES

Arnett W. D., Bahcall J., Kirshner R. P., Woosley S. E., 1989, ARA&A, 27, 629
Carlsson M., Rutten R., Shchukina N., 1992, A&A, 253, 567
Chandrasekhar S., 1934, MNRAS, 94, 444
Danziger I. J., Bouchet P., Fosbury R. A. E., Gouiffes C., Lucy L. B., 1988, in Kafatos M., Michalitsianos A. G., eds, Supernova 1987A in the Large Magellanic Cloud. Cambridge Univ. Press, Cambridge, p. 37
Dessart L., Hillier D. J., 2005, A&A, 439, 671
Dessart L., Hillier D. J., 2008, MNRAS, 383, 57
Hanuschik R. W., Dachs J., 1988, A&A, 205, 135
Hauschildt P. H., 1992, J. Quant. Spectrosc. Radiat. Transf., 47, 433
Hauschildt P. H., Baron E., 1999, J. Comp. Applied Math., 109, 41
Hillier D. J., Miller D. L., 1998, ApJ, 496, 407
Höflich P., 1988, Proc. Astron. Soc. Australia, 7, 434
Höflich P., 2003, in Hubeny I., Mihalas D., Werner K., eds, ASP Conf. Ser. Vol. 288, Stellar Atmosphere Modelling. Astron. Soc. Pac., San Francisco, p. 185
Hummer D. G., Storey P. J., 1987, MNRAS, 224, 801
Mazzali P. A., Lucy L. B., Butler K., 1992, A&A, 258, 399
Menzel D. H., Cillié G. G., 1937, ApJ, 85, 88
Mihalas D., 1970, Stellar Atmospheres. Series of Books in Astronomy and Astrophysics. Freeman, San Francisco
Mihalas D., 1978, Stellar Atmospheres. Freeman, New York
Olson G. L., Kunasz P. B., 1987, J. Quant. Spectrosc. Radiat. Transf., 38, 325
Osterbrock D., 1989, Astrophysics of Gaseous Nebulae and Active Galactic Nuclei. Univ. Science Books, Mill Valley, CA
Pastorello A. et al., 2004, MNRAS, 347, 74
Peebles P. J. E., 1968, ApJ, 153, 1
Perlmutter S. et al., 1999, ApJ, 517, 565
Riess A. et al., 1998, AJ, 116, 1009
Saio H., Nomoto K., Kato M., 1988, ApJ, 331, 388
Schmutz W., Abbott D. C., Russell R. S., Hamann W.-R., Wessolowski U., 1990, ApJ, 355, 255
Utrobin V. P., Chugai N. N., 2005, A&A, 441, 271 (UC05)
Williams R. E., 1987a, ApJ, 320, L117
Williams R. E., 1987b, in Nomoto K., ed., Proc. IAU Colloq. 108, Atmospheric Diagnostics of Stellar Evolution: Chemical Peculiarities, Mass Loss and Explosion. Springer, Berlin, p. 118
Zeldovich Y. B., Kurt V. G., Syunyaev R. A., 1969, Soviet J. Exp. Theor. Phys., 28, 146

This paper has been typeset from a TEX/LATEX file prepared by the author.

Monthly Notices
of the
ROYAL ASTRONOMICAL SOCIETY

Mon. Not. R. Astron. Soc. **407,** 658–668 (2010) doi:10.1111/j.1365-2966.2010.16953.x

Hydrogen recombination with multilevel atoms

Soma De,[1] E. Baron[1,2]★ and P. H. Hauschildt[3]

[1]*Homer L. Dodge Department of Physics and Astronomy, University of Oklahoma, Norman, OK 73019, USA*
[2]*Computational Research Division, Lawrence Berkeley National Laboratory, MS 50F-1650, 1 Cyclotron Rd, Berkeley, CA 94720, USA*
[3]*Hamburger Sternwarte, Gojenbergsweg 112, 21029 Hamburg, Germany*

Accepted 2010 May 3. Received 2010 April 29; in original form 2009 December 23

ABSTRACT

Hydrogen recombination is one of the most important atomic processes in many astrophysical objects such as Type II supernova (SN II) atmospheres, the high redshift Universe during the cosmological recombination era and H II regions in the interstellar medium. Accurate predictions of the ionization fraction can be quite different from those given by a simple solution if one takes into account many angular momentum substates, non-resonant processes and calculates the rates of all atomic processes from the solution of the radiative transfer equation instead of using a Planck function under the assumption of thermal equilibrium. We use the general-purpose model atmosphere code PHOENIX 1D to compare how the fundamental probabilities such as the photoionization probability, the escape probability and the collisional de-excitation probability are affected by the presence of other metals in the environment, multiple angular momentum substates and non-resonant processes. Our comparisons are based on a model of SN 1999em, SNe Type II, 20 d after its explosion.

Key words: atomic processes – supernovae: general – cosmology: miscellaneous.

1 INTRODUCTION

Hydrogen recombination plays a very important role in many astrophysical phenomena such as Type II supernovae (SNe), the interstellar medium and cosmic recombination.

Time-dependent recombination has been studied for the case of cosmological recombination (Peebles 1968; Zeldovich, Kurt & Syunyaev 1969) and for SNe (Utrobin & Chugai 2005; Dessart & Hillier 2008; De, Baron & Hauschildt 2009). In SNe, this occurs when the hydrogen recombination time-scale becomes comparable to the age of the SN. This effect is found to be dominant in the early epochs of the SN's evolution (De et al. 2009). At later times, however, effects due to multilevel atom effects (the importance of having many angular momentum substates) become more important than time-dependent phenomena. De et al. (2009) discussed how the effective recombination time-scale can be different based on time-dependent rate equations using different hydrogen atom models. The primary goal of De et al. (2009) was to determine the epoch in the lifetime of an SN (during the photospheric phase), where time dependence in the rate equations is most important. In doing so, we found that at later times model atoms with significantly more energy levels (that is additional angular-momentum substates) have a strong effect in determining the effective recombination time-scale. This issue is also important for applications other than SNe. In fact, considering more complete atomic models is important to correctly estimate the electron density and recover subtle features in the spectra. Here, we study multilevel atomic systems for hydrogen alone using a non-local thermodynamic equilibrium (NLTE) treatment, which could alter the hydrogen ionization fraction and therefore produce a different temperature structure.

Cosmological recombination codes such as RECFAST (Seager, Sasselov & Scott 1999, 2000; Wong, Moss & Scott 2008) and RICO (Fendt et al. 2009) that deal with cosmological recombination and solve for the free electron fraction as a function of redshift do an excellent job. Nevertheless, there are assumptions about Saha equilibrium between higher angular momentum states. Grin & Hirata (2010) have presented their recombination code RECSPARSE, which is a highly detailed calculation but still uses the Sobolev approximation for line calculations. Recently, the cosmological recombination problem has been revisited by several authors, paying special attention to possibly neglected atomic physics effects. The processes studied have included two-photon decays in H I and He I (Dubrovich & Grachev 2005; Wong & Scott 2007; Chluba & Sunyaev 2008; Hirata 2008; Hirata & Switzer 2008; Karshenboim & Ivanov 2008), H I continuum absorption of the He I λ584 line photons (Kholupenko, Ivanchik & Varshalovich 2007; Rubiño-Martín, Chluba & Sunyaev 2008; Switzer & Hirata 2008a,b), stimulated two-photon decays and two-photon absorption (Chluba & Sunyaev 2006; Hirata 2008; Karshenboim & Ivanov 2008), Raman scattering (Hirata 2008; Hirata & Switzer 2008), a more complete set of angular momentum substates (Grin & Hirata 2010) and forbidden transitions in He I (Wong & Scott 2007; Rubiño-Martín et al. 2008; Switzer & Hirata 2008a,b). Hirata & Forbes (2009) studied the effects of

★E-mail: baron@nhn.ou.edu

partial frequency redistribution, line blanketing and time dependence in Lyα, but even then made use of the Sobolev approximation. Here we resolve all line profiles in the comoving frame and accurately treat line blanketing. We assume complete redistribution for the line profiles.

We focus primarily on estimating the photoionization rate, the escape probability and the collisional de-excitation rate. We show how these rates depend on the hydrogen model atom used and we also study the effects of the presence of metals on the results. These different rates ultimately lead to variations in the hydrogen ionization fraction. We also examine when the 2γ process plays the most significant role in controlling hydrogen recombination.

In Section 2, we outline the theoretical framework relating the photoionization rate, collisional de-excitation rate and escape probability to the effective hydrogen recombination time. In Section 3, we describe our approach and different test systems that we study. In Section 4, we present our results. In Section 5, we state our conclusions and describe a possible framework for future work.

2 THEORETICAL FRAMEWORK FOR HYDROGEN RECOMBINATION

The ionization fraction for hydrogen is defined as

$$f_{\rm H} = \frac{n_{\rm H^+}}{n_{\rm H^+} + n_{\rm H}} \, . \tag{1}$$

For any system, the ionization fraction depends on the net recombination rate in the system. For a system in LTE, the ionization fraction can be calculated using the Saha equation with knowledge of the electron density and temperature. On the other hand, for systems not in LTE, it is important to solve the radiative transfer equation and the rate equations simultaneously. The recombination rate of a system is dependent on the number of angular momentum substates of the system and also on the presence of other elements in the environment that can contribute to the free electron density. The recombination process in a system is determined by the net rate of photoionization and its inverse process (recombination), which are modified due to line transitions. The effectiveness (towards recombination) of a resonant transition depends on the escape probability of the line. Also, there are non-radiative transitions that take place such as the collisional de-excitation of electrons to lower energy levels. In addition to these, there is the downward 2γ process that connects states of the same parity while the corresponding upward transition rate is very low. Therefore, it is important to study all these quantities to determine the correct nature of recombination. We investigate the 2γ process, the photoionization rate, the escape probability and the collisional de-excitation rates of systems with different hydrogen atom models and metallicities of the environment. We denote P_n as the photoionization rate from a state with index n (which is not its principal quantum number). Similarly, we define the escape probability as $\beta_{n1,}$ which is the escape probability for the resonant line photon between the level 1s and the level characterized by index n. The collisional de-excitation rate is defined as the rate of de-excitation of the electron from level n into the 1s state. The analytical evaluation of each of these quantities is possible if the system is in LTE or if the system has a model atom which has just a very few angular momentum substates. But for a system with many angular momentum substates (we consider 921 bound levels for hydrogen) and in the presence of metals, it is necessary to evaluate these quantities numerically from a consistent solution of the radiative transfer equation and the rate equations.

The results presented in this paper are obtained by simultaneously solving the coupled radiative transfer equation and rate equations. The rate equations use multilevel atoms including a large set of line and continuum transitions. The upward radiative rate ($i \rightarrow j$) is given as $n_i R_{ij}$, where i is a bound state and j can be a bound or continuum state, n_i is the population for level i and R_{ij} is given as (Mihalas 1978)

$$R_{ij} = 4\pi \int_{\nu_0}^{\infty} \alpha_{ij}(\nu)(h\nu)^{-1} J_\nu \, {\rm d}\nu \, . \tag{2}$$

Similarly the downward rate ($j \rightarrow i$) is calculated as $n_j(\frac{n_i}{n_j})^* R_{ji}$, where R_{ji} is

$$R_{ji} = 4\pi \int_{\nu_0}^{\infty} \alpha_{ij}(\nu)(h\nu)^{-1} \left[\left(\frac{2h\nu^3}{c^2} \right) + J_\nu \right] {\rm e}^{-\frac{h\nu}{kT}} \, {\rm d}\nu \, . \tag{3}$$

In the above equations, J_ν is the angle-averaged radiation intensity at frequency ν. T is the temperature, k is Boltzmann's constant, α_{ij} is the photoionization cross-section for the $i \rightarrow j$ transition and ν_0 is the threshold frequency. The level populations denoted with $(*)$ are the equilibrium values as defined by Mihalas (1978). In our calculations, the Sobolev approximation has not been used. In order to compare our results with others, we plot the values of the Sobolev escape probability. All the level populations were calculated without assuming the Sobolev approximation.

Below, we give the equations that define P_n, β_{n1} (Mihalas 1978). First,

$$P_n = \left| n_n R_{n\kappa} - n_\kappa \left(\frac{n_n}{n_\kappa} \right)^* R_{\kappa n} \right| , \tag{4}$$

where κ stands for the continuum level.

The escape probability β_{n1} is defined using the Sobolev escape probability as

$$\beta_{n1} = \frac{1 - {\rm e}^{-\eta_{n1}}}{\eta_{n1}} \, , \tag{5}$$

$$\eta_{n1} = \frac{\pi {\rm e}^2}{m_{\rm e} c} f_{n1} \lambda_{n1} t \left(n_1 - \frac{g_1}{g_n} n_n \right) \, , \tag{6}$$

where f_{n1} is the oscillator strength of the line between excited level n and the ground state. n_1 and n_n are the number densities of the ground state and the excited state referred by index n, respectively. λ_{n1} is the wavelength of the line, t is the time since explosion in seconds. g_n is the degeneracy of level n and $\frac{g_1}{g_2} \sim \frac{1}{n^2}$ (Mihalas 1978). In Section 3, we discuss our approach to quantify the photoionization rate, the escape probability and the collisional de-excitation rate.

3 VARIATION OF HYDROGEN MODEL ATOMS AND COMPOSITION

3.1 Description of the test systems

To set up the physical structure of each system, we use the density profile and luminosity from a full NLTE calculation of a model atmosphere in homologous expansion, with a power-law density profile $\rho \propto v^{-7}$, 20 d after explosion, which is a reasonable fit to observed spectra of SN 1999em at that epoch. This underlying density profile and the total bolometric luminosity in the observer's frame are chosen to be representative of the conditions in SNe IIP near maximum light. Given this structure, we use our general-purpose model atmosphere code PHOENIX 1D to solve for the new temperature structure and level populations under the new conditions (such as the hydrogen model atom and the presence of

Table 1. Physical characteristics from our base model.

τ	ρ (g cm^{-3})	R (cm)	v (km s^{-1})	T (K)	n_e (cm^{-3})	μ
9.897E−05	1.823E−15	2.454E+15	14 200.00	3157.61	99 464.3	1.34
3.626	3.084E−13	1.242E+15	7187.50	7345.20	1.079E+11	0.75
804.480	6.533E−12	4.104E+14	2375.00	26 155.8	2.97E+12	0.67

Note. The columns give various quantities as a function of optical depth. ρ is the mass density, R is the radius, v is the velocity, T is the matter temperature, n_e is the electron density and μ is the mean molecular weight.

other metals). The initial model of SN 1999em at 20 d after explosion was generated using a 31-level hydrogen model atom, and solar metals were included. We call this starting model our base model. Our base model was generated treating hydrogen and other elements in NLTE. The details of our radiative transfer code are described in Hauschildt & Baron (1999, 2004, and references therein). The transfer equation and the rate equations were all time independent for the base model. The physical properties related to our base model are given in Table 1.

Now we define the different systems that we experimented upon to study the behaviour of the physical quantities affecting the recombination rate. For convenience, we name the different systems in the following way. We refer to model A as the system which has only hydrogen and the hydrogen model atom in this case has just four bound states (1s, 2s, $2p_{1/2}$, $2p_{3/2}$) and four lines that couple those states. Model C is the same as model A, except that it has a solar composition of metals present in the system in addition to hydrogen and all the other metals are treated in LTE. Model B has only hydrogen in the system but the hydrogen model atom has 921 bound levels and 995 lines that couple the bound states. Model D is the same as model B except that this has metals present and the metals are treated in LTE as in model C. The LTE treatment of metals was chosen to reduce computing time and in a hydrogen-rich environment the main role that metals play in continuum processes is to be a source of additional electrons. We did not focus on how their atomic structure affects hydrogen recombination.

For models A and C, there are primarily three major processes considered that couple the bound states:

$$\mathrm{H}_{1s} + \gamma \rightarrow e^- + \mathrm{H}^+,$$

$$\mathrm{H}_{1s} + \gamma \leftrightarrow \mathrm{H}_{2p},$$

$$\mathrm{H}_{2s} \rightarrow \mathrm{H}_{1s} + 2\gamma.$$

In addition to this, the 1s and 2p states are coupled by spontaneous transitions. In models B and D, the atomic line data were taken from Kurucz (1995).

4 RESULTS

We study the rates and the resulting hydrogen ionization fraction, f_H, among the four different systems that have been described in Section 3. These different systems can have different ionization fractions primarily because the solution to the transfer equation and the resulting temperature structure will be different than in the base model. The models that have metals (models C and D) are expected to have temperature structures similar to the base model. The four-level hydrogen atom model without metals is likely to have a different temperature structure than the base model. These differences could be subtle but important enough to change to the hydrogen ionization fraction. In our results, we have also studied whether the 2γ process has a significant effect on the recombination time-scale or the resulting ionization level or the consequent temperature structure of the system.

We define τ_{std} as the optical depth corresponding to the continuum opacity at 500 nm. We classify our results depending on whether the temperature structure was held fixed at the base model value or was allowed to reach radiative equilibrium under the particular assumptions of each case, in order to isolate the effect of temperature change on the level populations and the hydrogen ionization fraction.

4.1 Metal-rich models

We first discuss our results for the models where the composition included metals. We treat helium and metals in LTE. Hydrogen is always treated in NLTE. Recall that these systems are termed models C and D for the four-level and 921-level hydrogen atom models, respectively. Fig. 1 shows the hydrogen ionization fraction for models C and D. There is a significant change in the hydrogen ionization level, f_H, between models C and D. The quantity f_H decreases in the multilevel atom case in the lower optical depth regime. For $\tau_{std} > 0.1$, the ionization levels between models C and D are not very different. The quantitative difference is also tabulated in Table 2 which shows the physical parameters for models C and D when the 2γ process was or was not included. The reduction in f_H due to additional angular momentum substates was about a factor of 3 at an optical depth of about $\tau_{std} \sim 10^{-4}$ (when the 2γ process was included in both the models). The difference in f_H decreases as the optical depth increases. In metal-rich systems (models C and D), the exclusion of the 2γ process did not seem to have any significant effect for almost all optical depths of interest.

Fig. 2 displays the net photoionization rate from any bound state of the hydrogen atom, P_n, for the levels $2p_{1/2}$ and $2p_{3/2}$ for model C. The profile of P_n for model C is not monotonic, but there is an overall trend to increase with optical depth, τ_{std}. This increase in P_n is expected due to the fact that photoionization dominates over recombination at higher optical depths due to higher temperatures. Fig. 3 shows the net photoionization rate as a function of wavenumber of each energy level for model D. Different panels show different τ_{std} regimes. The P_n values increase with increasing τ_{std} for a given energy level. Also, the net photoionization rate does not change significantly with the change in the energy level of the bound state. There is a drop in the P_n profile at energy levels very close to the continuum. This may be due to the fact that very high energy bound states are not really distinguished from the continuum; therefore, the *net* photoionization rate falls off.

The escape probability (defined as the probability for the escape of the resonant line connecting the ground state and higher energy bound state) for models C and D is shown in Figs 4–5. Fig. 4 shows the escape probability for model C, for levels $2p_{1/2}$ and $2p_{3/2}$. The escape probability for model C decreases with increasing optical depth and also decreases with decreasing energy of the bound state.

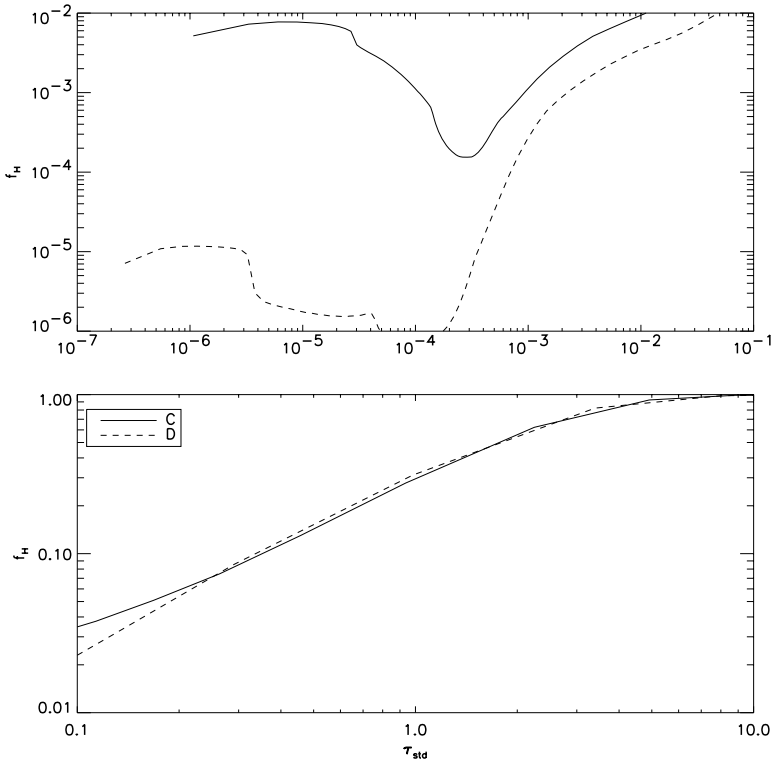

Figure 1. Comparison of the hydrogen ionization fraction found using the four-level (C) and 921-level (D) model atoms in a metal-rich environment. The upper panel shows the lower optical depth regime while the lower panel shows the higher optical depth regime. We define $\tau_{\rm std}$ as the optical depth corresponding to the continuum opacity at 500 nm.

For model D (Fig. 5), the escape probability increases with increasing energy of the bound state. Also the escape probability decreases very slowly with the increase in optical depth for model D, similar to that in model C. The apparent difference between models C and D is that the escape probability decreased for a higher energy level in model C as opposed to case D where the escape probability increased with the increased energy of the bound state. For model C, the levels in question are both 2p states and in model D for those two 2p states we also find a slight reduction in the escape probability with increasing energy of the bound state.

The reduction in the escape probability as a function of optical depth can be explained from equation (6). At higher optical depths (for a given excited state), when n_n, the population of the excited state, increases, this results in a decrease in the quantity η_{n1}. Following the decrease in η_{n1}, the escape probability β_{n1} decreases. On the other hand, at a given optical depth with increasing energy of the bound state, the escape probability increases. At a given $\tau_{\rm std}$, for an increase in the bound state energy, n_n and λ_{n1} decrease; hence, the overall effect almost always is to decrease β_{n1}.

Fig. 6 shows the collisional de-excitation rate (which is the collisional de-excitation coefficient $q_{\rm e}$ times the free electron density $n_{\rm e}$) for model C. In this model, there is an increase in the collisional de-excitation rate with increasing optical depth. For model D, the collisional de-excitation rate follows a similar pattern. The increase in the free electron density with increasing $\tau_{\rm std}$ explains the increased collisional de-excitation rate with $\tau_{\rm std}$. To summarize, the characteristics of the metal-rich models C and D are as follows. (1) The ionization fraction decreases for a multilevel hydrogen atom compared to a four-level hydrogen atom. (2) The net photoionization rate increases with optical depth for a given bound state. The photoionization rate also does not change significantly at a given $\tau_{\rm std}$ as the energy of the bound state increases. (3) The escape probability decreases with increasing $\tau_{\rm std}$, although this decrease is very small. The escape probability increases with increasing energy of the bound state except for the case of the 2p states. (4) The collisional rate increases with increasing optical depth. Also for the multilevel case, the rate is close to the equilibrium value. (5) The 2γ process did not seem to have any significant effects in models C and D.

4.2 Metal-deficient models

In this section, we focus on models A and B. Recall that models A and B are models where the atmosphere consists of pure hydrogen. Hydrogen was treated in NLTE in these models. In model A, we use a four-level hydrogen atom and in model B, we use a hydrogen atom model with 921 energy levels. We also study how the 2γ process affects these systems when the environment is metal-free. Fig. 7 displays the ionization fraction for models A and B. Interestingly, $f_{\rm H}$ does not change significantly between models A and B. This is quite different when compared to models C and D. Table 2 shows the changes due to the 2γ process. For model A, at low optical depths ($\tau_{\rm std} \sim 10^{-4}$) turning on the 2γ process produces about a 20 per cent change in the free electron density, but for $\tau_{\rm std} \gtrsim 10^{-3}$ no significant change is seen. For model B, there is a significant reduction in the free electron density due to the inclusion of the 2γ process. The electron density is five times higher with the inclusion of the 2γ process in model B, at low optical depths, $\tau_{\rm std} \sim 10^{-4}$.

Table 2. Physical characteristics from four different models, under radiative equilibrium.

Model name	Type	τ	T (K)	N_e (cm^{-3})	μ
		0.000 16	2820.75	105 236.	1.01
A	Four-level	0.023 43	4011.17	9.999E+07	1.01
		3.61	7564.24	2.351E+11	0.54
		1104.90	27 565.10	3.903E+12	0.50
		0.00 016	2820.61	121 450.0	1.01
A′	Four-level, no 2γ process	0.023 45	4011.18	9.999E+07	1.01
		3.61	7564.29	2.351E+11	0.54
		1106.10	26 840.2	3.9035E+12	0.50
		0.000 16	2801.08	3.946E+5	1.01
B	921-level	0.0272	4547.80	2.981E+8	1.01
		1.794	6779.06	1.087E+11	0.57
		1181.0	20 462.42	3.893E+12	0.50
		0.000 157	2826.28	6.709E+4	1.01
B′	921-level, no 2γ process	0.027 05	4547.69	2.983E+08	1.01
		1.794	6778.83	1.0864E+11	0.57
		1181	20 462.42	3.801E+12	0.50
		0.000 23	3564.79	271 828.	1.26
C	Four-level, metal-rich environment	4.912 80	7584.85	1.260E+11	0.68
		867.030	26 365.40	3.162E+12	0.625
		0.000 23	3564.78	271 808.	1.26
C′	Four-level, metal-rich environment	4.912 70	7584.84	1.260E+11	0.68
	no 2γ process	867.900	26 243.10	3.160E+12	0.625
		0.00 011	3099.54	84 640.4	1.26
D	921-level, metal-rich environment	0.98 338	6337.20	4.254E+10	0.98
		863.240	26 109.80	3.156E+12	0.63
		0.00 011	3099.46	84 638.0	1.26
D′	921-level, metal-rich environment	0.98 373	6337.44	4.256E+10	0.98
	no 2γ process	863.080	26 113.50	3.156E+12	0.63

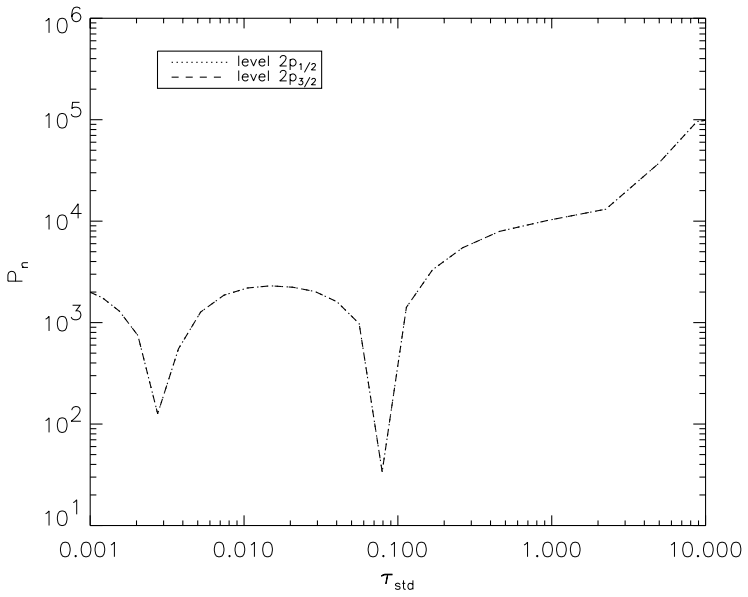

Figure 2. Photoionization rates of the 2p states versus optical depth for model C.

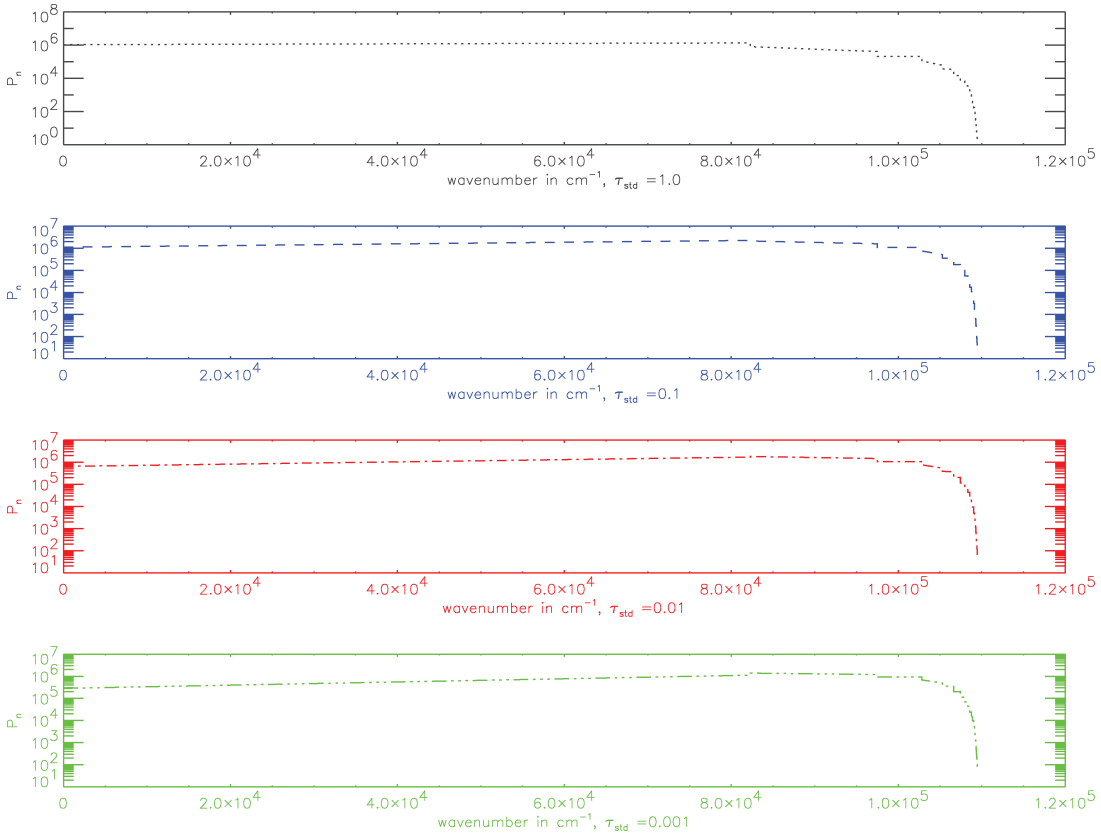

Figure 3. Photoionization rates versus energy level for model D at different optical depths. Each panel shows a particular optical depth.

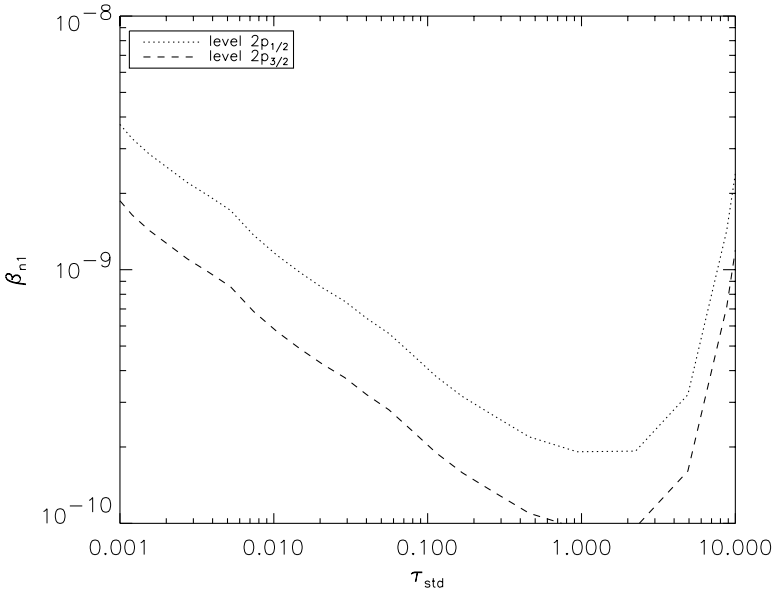

Figure 4. Escape probability versus optical depth for the 2p states for model C.

For higher optical depths, there is no significant effect due to the 2γ process. The decrease in the free electron density due to the 2γ process is expected since the upward process is suppressed by a factor of 1/137. The change is especially noticeable in model B. It is at a fairly low optical depth where the change in the rates is observed but this is also the optical depth where the optical depth of the Balmer line is high (De et al. 2009). This wavelength regime is similar to what is described in De et al. (2009).

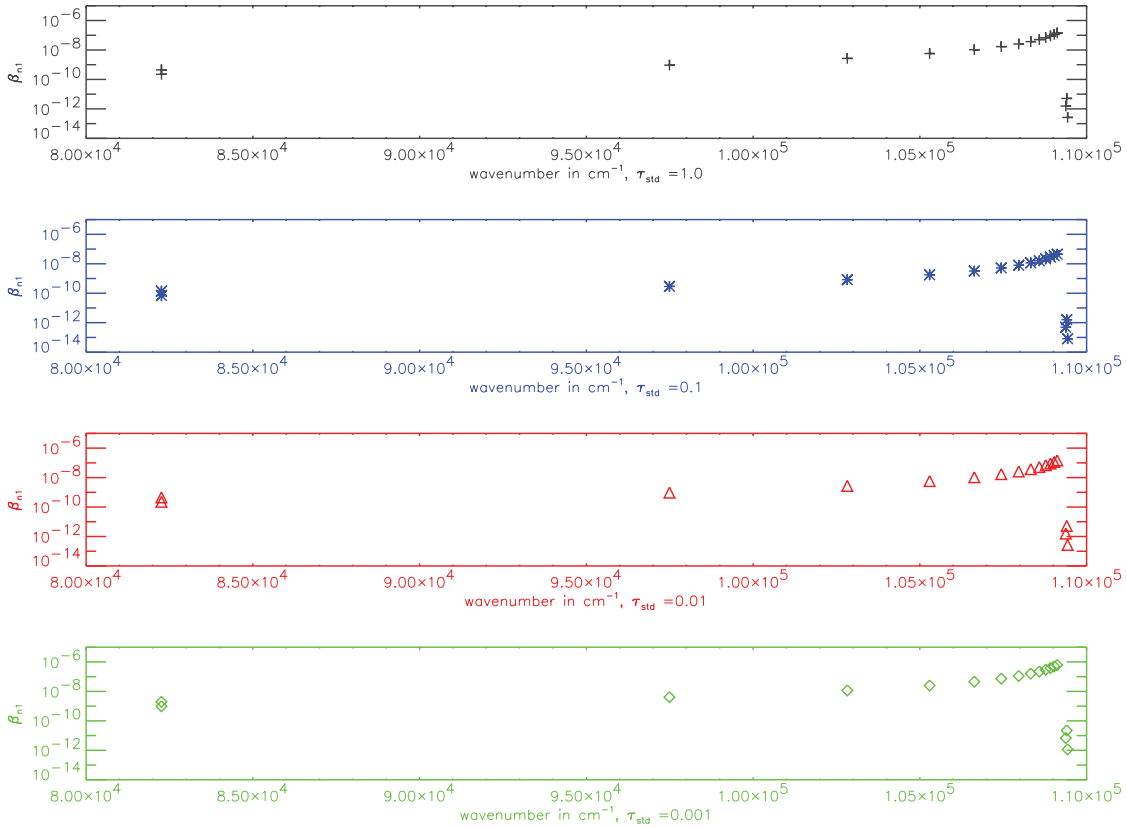

Figure 5. Escape probability versus energy levels for model D at different optical depths. Each panel shows a particular optical depth.

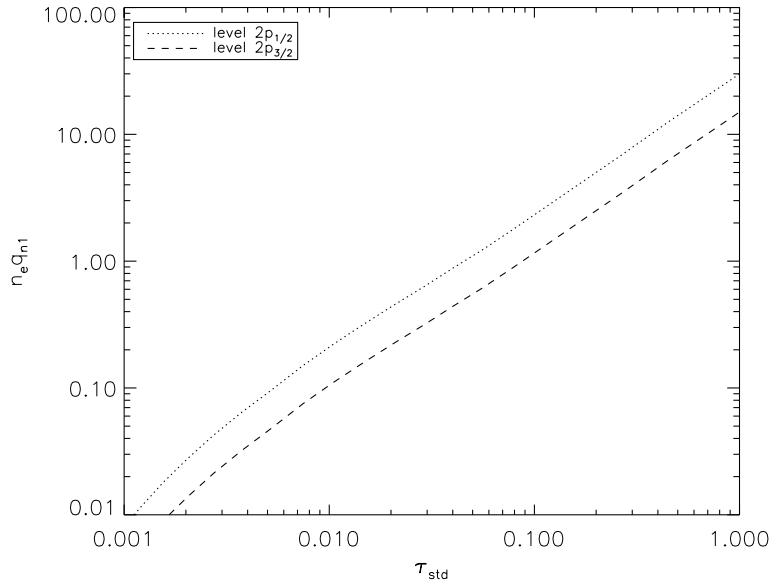

Figure 6. Collisional de-excitation coefficients of the 2p states versus optical depth for model C.

The net photoionization rate (P_n) does not change significantly between different bound states in both models A and B (see Figs 8 and 9). Although in the multilevel case (case B), P_n increases by almost a factor of 10 from the lowest energy bound state to the higher energy bound states (except for the states very close to the continuum) at low optical depths ($\tau_{std} < 0.01$). Figs 10 and 11 show the escape probability for models A and B, respectively. The trend is very similar to that of models C and D. The collisional de-excitation

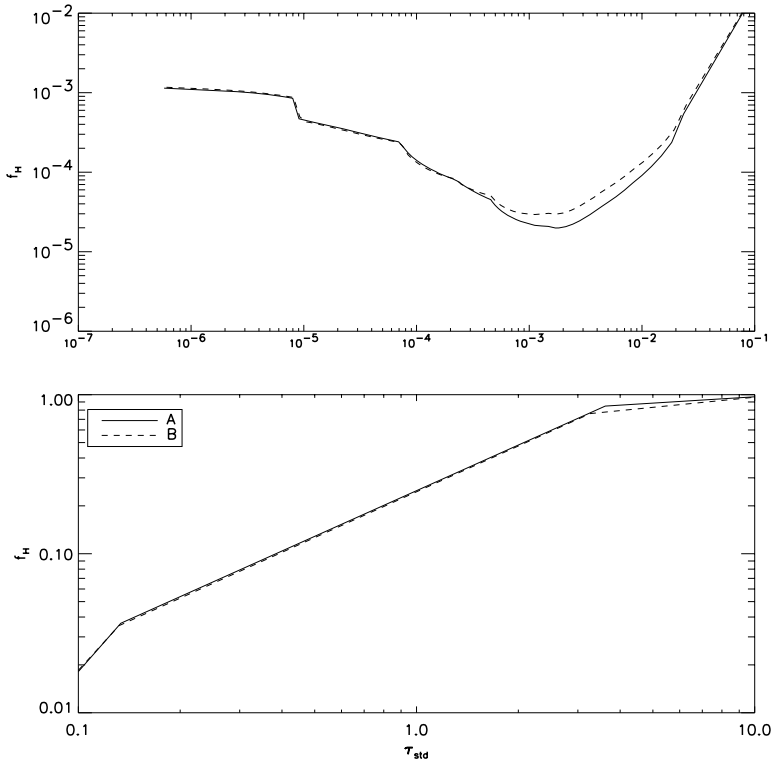

Figure 7. Comparison of hydrogen ionization fraction obtained using the four-level (A) and the 921-level model (B) hydrogen atom in pure hydrogen under radiative equilibrium. The upper panel shows the lower optical depth regime while the lower panel shows the higher optical depth regime.

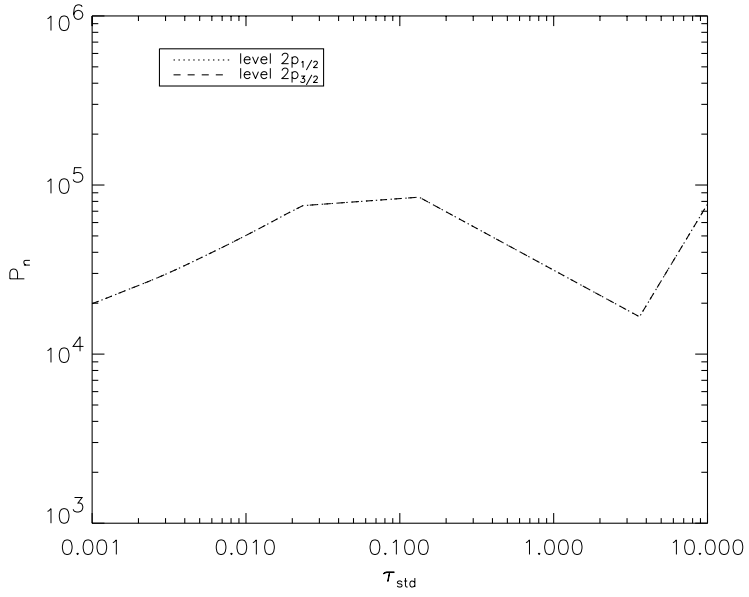

Figure 8. Photoionization rate versus optical depth for 2p states of model A under radiative equilibrium. The last point at $\tau_{\rm std} = 10$ is a numerical glitch caused by poor spatial resolution. The rate should continue to drop with depth.

rate increases with increasing optical depths in both the models C and D.

To summarize, our findings on models A and B (pure hydrogen models) are as follows. (1) For most optical depth regimes, the basic trend in the rates is similar to models C and D. (2) The 2γ process seems to have a significant effect in both models A and B (at lower $\tau_{\rm std}$). The effect is much larger for model B. This effect was not seen in models C and D.

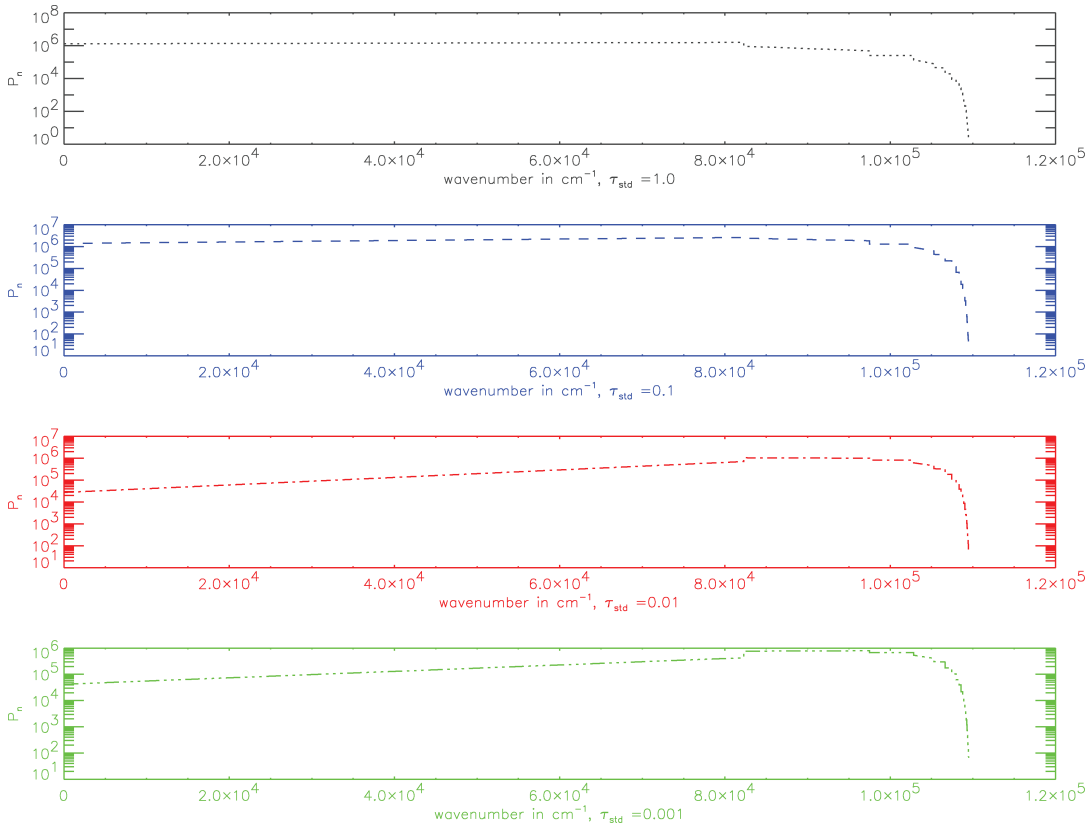

Figure 9. Photoionization rates versus energy level for model B in radiative equilibrium. Each panel shows a particular optical depth.

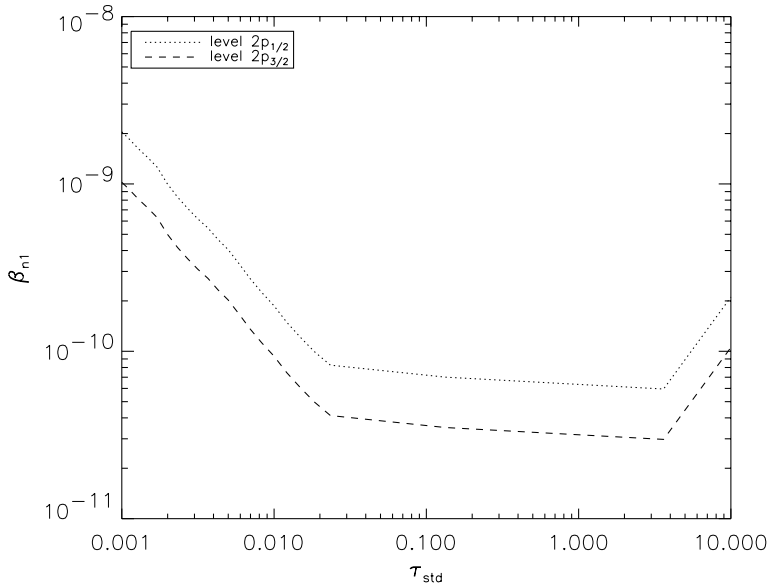

Figure 10. Escape probability versus optical depth for the 2p states of model A in radiative equilibrium.

We observe the following, for almost all optical depths:

$$P_n(A) > P_n(C),$$
$$\beta_{n1}(A) < \beta_{n1}(C),$$
$$n_e q_{n1}(A) < n_e q_{n1}(C).$$

For models B and D,

$$P_n(B) < P_n(D) \ (\tau < 0.01),$$
$$\beta_{n1}(B) \approx \beta_{n1}(D),$$
$$n_e q_{n1}(B) < n_e q_{n1}(D) \ (\tau < 0.01).$$

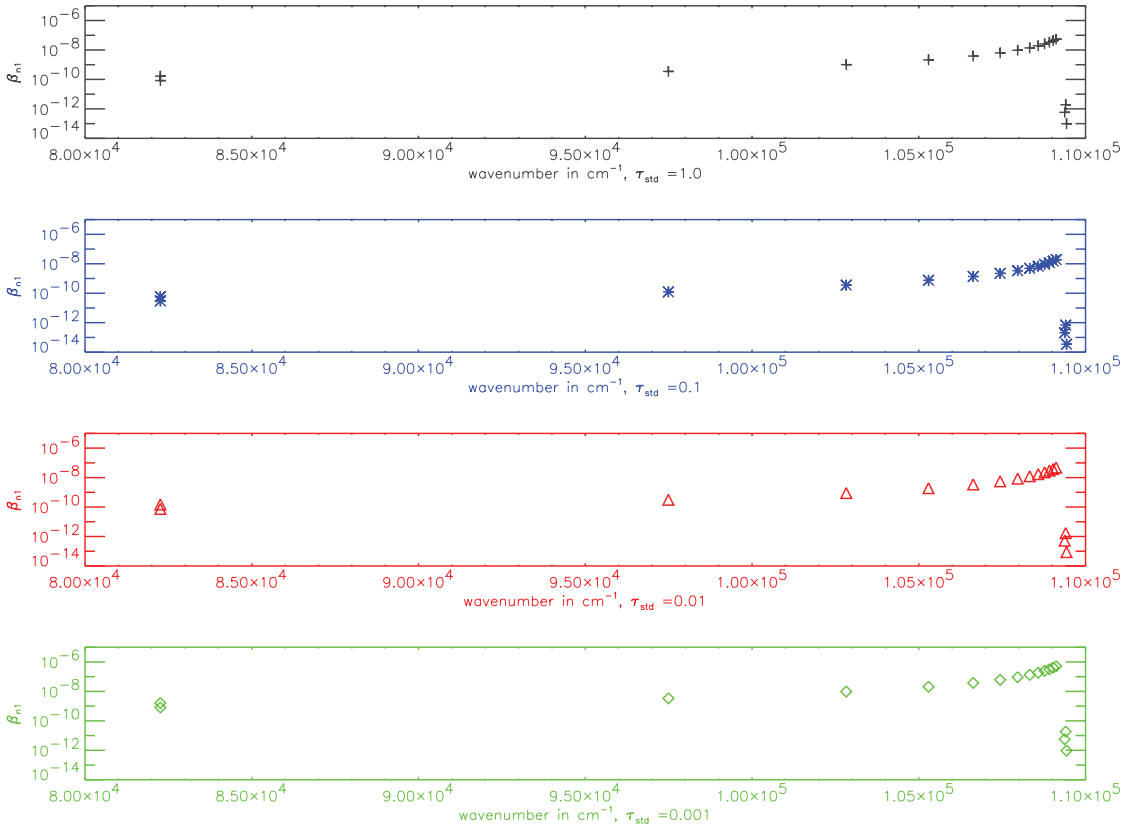

Figure 11. Escape probability versus energy level for model B in radiative equilibrium. Each panel refers to a specific optical depth.

The difference in the profiles of P_n, β_{n1} and $n_e q_{n1}$ between model A (or B) and model C (or D) can be attributed to their different temperature profiles.

4.3 Metal-deficient case without temperature corrections

In our previous models A–D, we allowed the system to reach radiative equilibrium for each assumption. It is useful to hold the temperature structure fixed and just examine the changes that are due to the variation in the compositions and model atoms. In the fixed temperature structure case, we do not find a large difference as compared to the radiative equilibrium case. The differences, compared to the radiative equilibrium case, occur in the optical depth region $10^{-3} < \tau < 10^{-2}$. There is a slight suppression in the ionization fraction for model B as compared to model A. The other rates are nearly identical.

5 DISCUSSION

The primary motivation for this paper was to investigate how the multilevel structure of the hydrogen model atom affects the hydrogen ionization fraction as well as the photoionization, escape and collisional de-excitation rates. We also investigated if the metals in the environment or if the 2γ process plays a significant role in the recombination process of the system. We find a multilevel hydrogen atom structure or, in other words, a more complete set of energy levels to be important in determining the ionization profile of the system. Recently, Grin & Hirata (2010) studied the effects of including a more complete set of angular momentum substates in the study of cosmological recombination and also found that including more substates is important. The need to have a more complete set of bound states in the hydrogen atom is found to be more important in a metal-rich environment. This is because of the fact that recombination is more effective in a multilevel framework. When there is a source of additional free electrons (such as metals), the suppression in f_H is larger than in pure hydrogen models. This is merely due to the fact that the larger free electron density drives recombination; thus, it is very important to use multilevel hydrogen atoms especially in realistic environments with solar compositions.

The enhancement of recombination is indicated by the increasing escape probability for the higher bound states (for both models B and D). This is also reinforced by the almost constant photoionization rate over different energy bound states.

The importance of the 2γ process is seen in the four-level pure hydrogen case (model A) as only a small reduction in the free electron density. In model B, the reduction in the free electron density due to the inclusion of the 2γ process is much larger. There was no significant effect due to the 2γ process in the solar composition models. The larger change in model B (at lower τ_{std}) can be explained from Fig. 12. At low optical depths, the relative population of the ground state to the first excited state is displayed. For the metal-free models (A and B), the ratio n_1/n_2 is not very high and about 4.0 for model B. Thus in model B, the first excited state population is not significantly lower than the ground state population. The relative first excited state population is much lower in

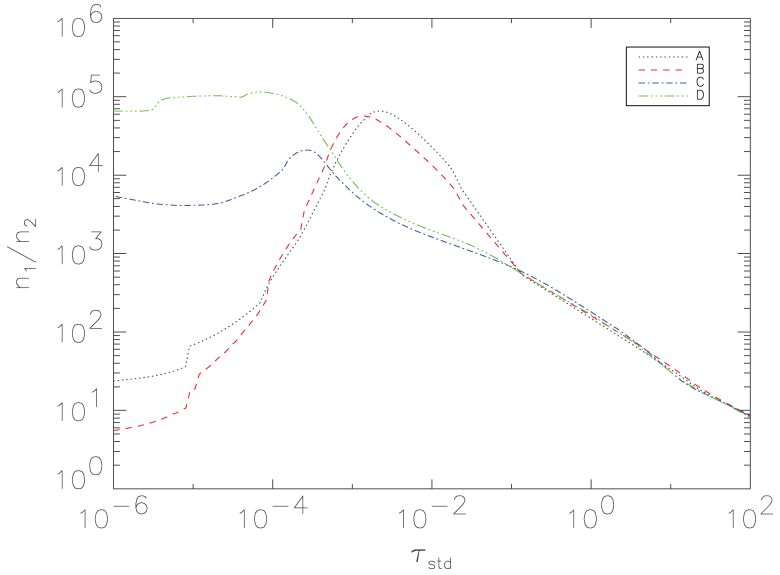

Figure 12. Ratio of the ground state to the first excited state population densities as a function of optical depth.

models C and D (where the ratio is around 10^4–10^5 at similar τ_{std}). The high level population of the first excited state (for model B) increases the importance of the 2γ process, due to the higher number of available electrons that can recombine into the ground state and the upward transition probability for this non-resonant process being low; thus, the recombination obtained is more effective. We find that it is essential to incorporate both multilevel atoms and the 2γ process. Our primary purpose was to do a simple calculation to emphasize the important factors in determining the recombination of hydrogen at typical free electron densities found in Type II SN atmospheres. Our results show that it is important to incorporate 2γ transitions and multiple angular momentum substates at low optical depths where the free electron density is small (typically $\sim 10^5$ cm^{-3}) and is also typical of the free electron density during the epoch of cosmological recombination (Peebles 1968). In H II regions, the electron density is much lower making the hydrogen recombination time-scale rise. Therefore, accurate treatment of hydrogen recombination is important in all of these scenarios. In the future, we plan to investigate hydrogen recombination in the context of cosmological recombination epoch.

ACKNOWLEDGMENTS

We thank the anonymous referee for helpful comments which significantly improved the presentation of this work. This work was supported in part by NSF grant AST-0707704, Department of Energy Award Number DE-FG02-07ER41517, and by SFB grant 676 from the DFG. This research used resources of the National Energy Research Scientific Computing Center (NERSC), which is supported by the Office of Science of the U.S. Department of Energy under contract no. DE-AC02-05CH11231, and the Höchstleistungs Rechenzentrum Nord (HLRN). We thank both these institutions for a generous allocation of computer time.

REFERENCES

Chluba J., Sunyaev R. A., 2006, A&A, 446, 39
Chluba J., Sunyaev R. A., 2008, A&A, 480, 629
De S., Baron E., Hauschildt P. H., 2009, MNRAS, 401, 2081
Dessart L., Hillier D. J., 2008, MNRAS, 383, 57
Dubrovich V. K., Grachev S. I., 2005, Astron. Lett., 31, 359
Fendt W. A., Chluba J., Rubiño-Martín J. A., Wandelt B. D., 2009, ApJS, 181, 627
Grin D., Hirata C. M., 2010, Phys. Rev. D, 81, 083005
Hauschildt P. H., Baron E., 1999, J. Comput. Applied Math., 109, 41
Hauschildt P. H., Baron E., 2004, Mitteilungen Mathematischen Ges. Hamburg, 24, 1
Hirata C. M., 2008, Phys. Rev. D, 78, 023001
Hirata C. M., Forbes J., 2009, Phys. Rev. D, 80, 023001
Hirata C. M., Switzer E. R., 2008, Phys. Rev. D, 77, 083007
Karshenboim S. G., Ivanov V. G., 2008, Astron. Lett., 34, 289
Kholupenko E. E., Ivanchik A. V., Varshalovich D. A., 2007, MNRAS, 378, L39
Kurucz R. L., 1995, Highlights Astron., 10, 579
Mihalas D., 1978, Stellar Atmospheres. Freeman & Co., New York
Peebles P. J. E., 1968, ApJ, 153, 1
Rubiño-Martín J. A., Chluba J., Sunyaev R. A., 2008, A&A, 485, 377
Seager S., Sasselov D. D., Scott D., 1999, ApJ, 523, L1
Seager S., Sasselov D. D., Scott D., 2000, ApJS, 128, 407
Switzer E. R., Hirata C. M., 2008a, Phys. Rev. D, 77, 083006
Switzer E. R., Hirata C. M., 2008b, Phys. Rev. D, 77, 083008
Utrobin V. P., Chugai N. N., 2005, A&A, 441, 271
Wong W. Y., Scott D., 2007, MNRAS, 375, 1441
Wong W. Y., Moss A., Scott D., 2008, MNRAS, 386, 1023
Zeldovich Y. B., Kurt V. G., Syunyaev R. A., 1969, Soviet J. Exp. Theor. Phys., 28, 146

This paper has been typeset from a TEX/LATEX file prepared by the author.

Monthly Notices
of the
ROYAL ASTRONOMICAL SOCIETY

Mon. Not. R. Astron. Soc. **422,** 1122–1139 (2012) doi:10.1111/j.1365-2966.2012.20685.x

The bright Type IIP SN 2009bw, showing signs of interaction⋆

C. Inserra,[1,2,3]† M. Turatto,[4] A. Pastorello,[5,6] M. L. Pumo,[6,7] E. Baron,[3,8] S. Benetti,[6] E. Cappellaro,[6] S. Taubenberger,[9] F. Bufano,[2,6] N. Elias-Rosa,[10] L. Zampieri,[6] A. Harutyunyan,[11] A. S. Moskvitin,[12] M. Nissinen,[13] V. Stanishev,[14] D. Y. Tsvetkov,[15] V. P. Hentunen,[13] V. N. Komarova,[12] N. N. Pavlyuk,[15] V. V. Sokolov[12] and T. N. Sokolova[12]

[1]*Dipartimento di Fisica ed Astronomia, Università di Catania, Sezione Astrofisica, Via S. Sofia 78, 95123 Catania, Italy*
[2]*INAF, Osservatorio Astrofisico di Catania, Via S. Sofia 78, 95123 Catania, Italy*
[3]*Department of Physics and Astronomy, University of Oklahoma, Norman, OK 73019, USA*
[4]*INAF, Osservatorio Astronomico di Trieste, Via Tiepolo 11, 34143 Trieste, Italy*
[5]*Astrophysics Research Centre, School of Mathematics and Physics, Queen's University Belfast, Belfast BT7 1NN*
[6]*INAF, Osservatorio Astronomico di Padova, Vicolo dell'Osservatotio 5, 35122 Padova, Italy*
[7]*Dipartimento di Astronomia, Università di Padova, Vicolo dell'Osservatorio 3, 35122 Padova, Italy*
[8]*Hamburger Sternwarte, Gojenbergsweg 112, 21029 Hamburg, Germany*
[9]*Max-Planck-Institut für Astrophysik, Karl-Schwarzschild-Str. 1, 85741 Garching, Germany*
[10]*Institut de Cincies de l'Espai (IEEC-CSIC), Campus UAB, 08193 Bellaterra, Spain*
[11]*Fundación Galileo Galilei-INAF, Telescopio Nazionale Galileo, Rambla José Ana Fernández Pérez 7, 38712 Breña Baja, TF, Spain*
[12]*Special Astrophysical Observatory of the Russian Academy of Sciences, Nizhnij Arkhyz 369167, Russia*
[13]*Taurus Hill Observatory, Härkämäentie 88, FI-79480 Kangaslampi, Finland*
[14]*CENTRA - Instituto Superior Tecnico, Av. Rovisco Pais, 1,1049-001 Lisbon, Portugal*
[15]*Sternberg Astronomical Institute of Lomonosov Moscow State University, University Avenue 13, 119992 Moscow, Russia*

Accepted 2012 February 2. Received 2012 January 30; in original form 2011 November 28

ABSTRACT

We present photometry and spectroscopy of the Type IIP supernova (SN IIP) 2009bw in UGC 2890 from a few days after the outburst to 241 d. The light curve of SN 2009bw during the photospheric phase is similar to that of normal SNe IIP but with a brighter peak and plateau ($M_R^{\rm max} = -17.82$ mag, $M_R^{\rm plateau} = -17.37$ mag). The luminosity drop from the photospheric to the nebular phase is one of the fastest ever observed, ∼2.2 mag in about 13 d. The radioactive tail of the bolometric light curve indicates that the amount of ejected ^{56}Ni is ≈0.022 $M_\odot$. The photospheric spectra reveal high-velocity lines of Hα and Hβ until about 105 d after the shock breakout, suggesting a possible early interaction between the SN ejecta and pre-existent circumstellar material, and the presence of CNO elements. By modelling the bolometric light curve, ejecta expansion velocity and photospheric temperature, we estimate a total ejected mass of ∼8–12 $M_\odot$, a kinetic energy of ∼0.3 foe and an initial radius of ∼3.6–7 × 10^{13} cm.

Key words: supernovae: general – supernovae: individual: SN 2009bw – galaxies: individual: UGC 2890.

1 INTRODUCTION

Type II supernovae (SNe II) are produced by the explosion following the gravitational collapse of massive stars ($M_{\rm ZAMS} \gtrsim$ 7–8 $M_\odot$; for details see Heger et al. 2003; Pumo et al. 2009; Smartt et al. 2009, and reference therein).

Those retaining part of their H envelope at the time of the explosion are called type II and, if they show a constant luminosity for a period ranging from about 30 d to a few months, are assigned to the 'Plateau' subclass (SNe IIP). Others present a steeper decline over the same period and are named 'Linear' (SNe IIL; Barbon, Ciatti

⋆Based on observations collected at the Italian 3.58-m Telescopio Nazionale Galileo, the Liverpool Telescope, the Nordic Optical Telescope (La Palma, Spain), the Calar Alto 2.2-m Telescope (Sierra de los Filabres, Spain), the orbital telescope *Swift*, the Copernico and Galileo Galilei telescopes (Asiago, Italy), the Special Astrophysical Observatory (Mt Pastukhov, Russia), the Taurus Hill Observatory (Hill Härkämäki, Finland), the 0.5-m Newton Telescope (Tatranska Lomnica, Slovakia), the 0.5- and 0.6-m telescopes of Sternberg Astronomical Institute Observatory (Nauchnyi, Crimea) and the 0.7-m Cassegrain Telescope (Moscow, Russia).

†E-mail: cosimo.inserra@oact.inaf.it

& Rosino 1979). A third subclass shows a slow decline and narrow emission lines in the spectra and hence forms the so-called group of 'narrow' SNe II (SNe IIn; Schlegel 1990). SNe IIP have been the subject of extensive analysis by Hamuy (2003) who pointed out a continuity in their properties and revealed several relations linking the observables to physical parameters. An independent analysis extending the sample to low- and high-luminosity SNe IIP confirmed these results (Pastorello 2003). Thanks to the direct identification of several SN precursors in deep pre-explosion images, recent studies support the idea that most SNe IIP are originated from explosions of stars with $M \lesssim 16$–$17\,M_{\odot}$ (Smartt et al. 2009) and are usually associated with red supergiant (RSG) progenitors (Smartt 2009). Such stars have 'extended', massive ($\gtrsim$5–7 $M_{\odot}$) hydrogen envelopes at the time of explosion. Variations in the explosion configurations (e.g. envelope mass, energy, radius, etc.) are thought to be responsible for the relatively 'large' variety of objects.

The configuration of the exploding stars and of the circumstellar matter (CSM), governed by the mass loss during the late evolutionary stages of the progenitor, can lead to different observables starting from stars of similar initial mass. Detailed studies at many different wavelengths show an almost unlimited variety of interaction scenarios between ejecta of different mass and CSM of various densities and distances from the exploding stars. As a recent example, SN 2007od (Inserra et al. 2011) shows evidence of weak interaction at early time and strong interaction at late times.

SN 2009bw is a good opportunity to explore the zoo of type IIP with early, weak interaction. It was discovered in UGC 2890 on 2009 March 27.87 UT (Nissinen, Heikkinen & Hentunen 2009). Stanishev, Adamo & Micheva (2009) classified it as a normal SN II soon after explosion, showing a spectrum with narrow Hα emission superimposed on a broader base.

The coordinates of SN 2009bw have been measured on our astrometrically calibrated images: $\alpha = 03^{\rm h}56^{\rm m}06\overset{\rm s}{.}92\ \pm 0\overset{\rm s}{.}05$, $\delta = +72^{\circ}55'40\overset{''}{.}90\ \pm 0\overset{''}{.}05$ (J2000). The object is located in the inner region of the highly ($i = 90$, LEDA) inclined UGC 2890, 11 arcsec east and 22 arcsec north of the centre of the galaxy (Fig. 1). This corresponds to a projected distance of $\sim$2.4 kpc from the nucleus assuming a distance to UGC 2890 of $\sim$20 Mpc (see Section 2.3).

In this paper we present and discuss optical and near-infrared (NIR) observations of SN 2009bw from 2009 March to 2010 August. In Section 2 we describe the photometric observations and give details on the reduction process, the reddening estimate and the photometric evolution. In Section 3 we describe and analyse the spectroscopic data. The explosion and progenitor parameters retrieved through the models are presented in Section 4. Discussion and conclusions follow in Sections 5 and 6.

2 PHOTOMETRY

The optical photometric monitoring of SN 2009bw started on 2009 March 30, the day after the discovery, and continued until 2009 late November. We attempted to recover the object at late time after the seasonal gap, but the object was already fainter than our instrument detection limit.

2.1 Data

Ground-based optical photometry was obtained with several telescopes (Table 1). Note that the *u*, *r* and *i* magnitudes of the Sloan filters of the Liverpool Telescope (LT) and the *i*-band filter of the Nordic Optical Telescope (NOT) have been reported in the Johnson–Cousins system. Optical data were reduced following standard procedures in the Image Reduction and Analysis Facility (IRAF)[1] environment. Instrumental magnitudes were measured on the final images, obtained after removal of the detector signature including overscan correction, bias subtraction, flat-field correction and trimming.

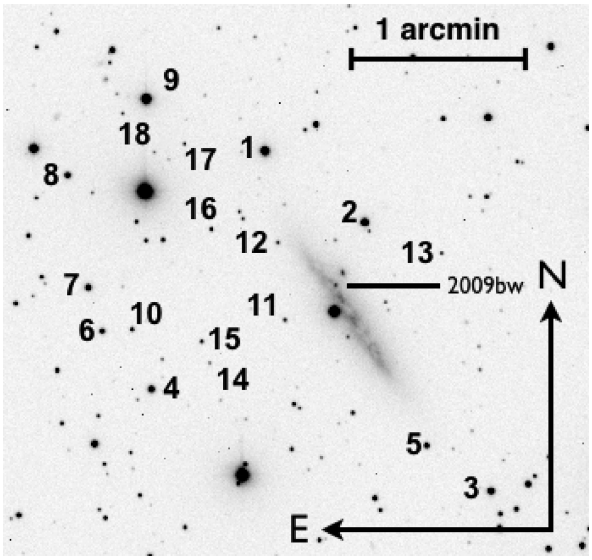

Figure 1. *R*-band image of SN 2009bw in UGC 2890 obtained with the Calar Alto 2.2-m Telescope + CAFOS (see Table 1) on 2009 August 30. The sequence of stars used to calibrate the optical and NIR magnitudes of SN 2009bw is indicated.

Photometric zero-points and colour terms were computed for all nights through observations of Landolt standard fields (Landolt 1992). 13 of the 49 nights were photometric. Using the photometry of these nights we calibrated the magnitudes of a local stellar sequence shown in Fig. 1. Magnitudes of the local-sequence stars are reported in Table 2 along with their rms (in brackets). Finally, the average magnitudes of the local-sequence stars were used to calibrate the photometric zero-points obtained in non-photometric nights. The sequence extends from bright ($V = 13.3$) to faint ($V = 19.4$) stars to allow a good calibration of the SN magnitudes from the luminous peak to the nebular phase. The brightest stars of the sequence were saturated on long-exposure frames with larger telescopes. Their calibration is based, therefore, on a fewer photometric nights. The calibrated optical magnitudes of the SN are reported in Table 3. The discovery magnitude reported in Nissinen et al. (2009) has been revised and reported in Table 3. There is no evidence of the SN presence on images obtained on 2010 August 24; the values in Table 3 are upper limits computed with artificial stars placed close to SN position. These values are not shown in Fig. 2 because they do not impose tight limits to the late phase decline.

Because of the complex background, SN magnitudes have been evaluated in two ways: (a) through the point spread function (PSF) fitting technique and (b) with the template subtraction and subsequent PSF fitting technique. The magnitudes calculated with both methods during the plateau period result in good agreement.

[1] IRAF is distributed by the National Optical Astronomy Observatories, which are operated by the Association of Universities for Research in Astronomy, Inc, under contract to the National Science Foundation.

Table 1. Instrument set-up used for the photometric follow-up.

Telescope	Primary mirror (m)	Camera	Array	CCD	Pixel scale (arcsec pixel^{-1})	Field of view (arcmin)	Filters
Copernico	1.82	AFOSC	1024 × 1024	TK1024AB	0.46	8.1	Bessell *B V R*, Gunn *i*
TNG	3.58	DOLORES	2048 × 2048	EEV 42-40	0.25	8.6	Johnson *U B V*, Cousins *R I*
		NICS	1024 × 1024	HgCdTe Hawaii	0.25	4.2	*J H K′*
LT	2.0	RATcam	2048 × 2048	EEV 42-40	0.13	4.6	Sloan *u*, Bessell *B V*, Sloan *r i*
NOT	2.5	ALFOSC	2048 × 2048	EEV 42-40	0.19	6.4	Johnson *U B V R*, interference *i*
CAHA	2.2	CAFOS	2048 × 2048	SITe	0.53	16	Johnson *U B V R I*
SWIFT	0.3	UVOT	2048 × 2048	Microchannel intensified CCD	0.48	17	*uvw2, uvm2, uvw1*
SAO-RAS	1.0	CCD phot.	530 × 580	EEV 42-40	0.48	2.38 × 3.53	Johnson *U B V*, Cousins *R I*
THO	0.4	ST-8XME	1530 × 1020	KAF-1603ME	0.9	24 × 16	Johnson *B V*, Cousins *R*
S50	0.5	ST-10XME	2184 × 1472	KAF-3200ME	1.12	20.6 × 13.9	Johnson *V*, Cousins *R I*
M70	0.7	Apogee AP-7p	512 × 512	SITe	0.64	5.5	Johnson *U B V I*, Cousins *R*
C60	0.6	Apogee AP-47p	1024 × 1024	EEV47-10	0.71	6.1	Johnson *B V I*, Cousins *R*
C50	0.5	Meade Pictor416	765 × 510	KAF-0400	0.92	11.7 × 7.8	Johnson *V*, Cousins *R*

Copernico = Copernico Telescope (Mt Ekar, Asiago, Italy); TNG = Telescopio Nazionale Galileo (La Palma, Spain); LT = Liverpool Telescope (La Palma, Spain); NOT = Nordic Optical Telescope (La Palma, Spain); CAHA = Calar Alto Observatory 2.2-m Telescope (Sierra de los Filabres, Andalucia, Spain); *Swift* orbiting telescope by NASA; SAO-RAS = Special Astrophysical Observatory 1-m Telescope (Mt Pastukhov, Russia); THO = Taurus Hill Observatory (Hill Härkämäki, Finland); S50 = 0.5-m Newton Telescope (Tatranska Lomnica, Slovakia); M70 = 0.7-m Cassegrain Telescope (Moscow, Russia); C60 = 0.6-m Cassegrain Telescope (Observatory of Sternberg Astronomical Institute, Nauchnyi, Crimea); C50 = 0.5-m Maksutov Telescope Meniscus (Observatory of SAI, Nauchnyi, Crimea).

Table 2. Magnitudes of the local-sequence stars in the field of SN 2009bw (cf. Fig. 1). The errors are reported in brackets.

ID	*U*	*B*	*V*	*R*	*I*
1	14.48 (0.03)	14.41 (0.02)	13.73 (0.01)	13.36 (0.01)	12.97 (0.01)
2	16.60 (0.03)	15.64 (0.02)	14.47 (0.02)	13.83 (0.01)	13.23 (0.01)
3	16.21 (0.02)	15.97 (0.02)	15.15 (0.01)	14.64 (0.01)	14.15 (0.01)
4	17.01 (0.02)	16.42 (0.02)	15.41 (0.01)	14.85 (0.01)	14.27 (0.01)
5	17.92 (0.02)	17.36 (0.02)	16.34 (0.01)	15.79 (0.02)	15.21 (0.02)
6	17.48 (0.02)	17.02 (0.02)	16.12 (0.02)	15.61 (0.02)	15.10 (0.03)
7	16.60 (0.02)	16.46 (0.02)	15.68 (0.01)	15.24 (0.01)	14.78 (0.01)
8	16.23 (0.02)	16.22 (0.02)	15.54 (0.01)	15.17 (0.02)	14.75 (0.01)
9	15.13 (0.02)	14.39 (0.02)	13.27 (0.02)	12.70 (0.02)	12.05 (0.01)
10	18.04 (0.01)	17.73 (0.02)	16.86 (0.02)	16.45 (0.01)	16.01 (0.02)
11	18.90:	18.86 (0.03)	18.07 (0.02)	17.64 (0.02)	17.24 (0.02)
12		19.85 (0.02)	18.40 (0.02)	17.39 (0.01)	16.57 (0.01)
13	19.27:	19.22 (0.02)	18.50 (0.03)	17.99 (0.02)	17.59 (0.02)
14		19.98 (0.02)	19.07 (0.03)	18.62 (0.02)	18.13 (0.03)
15	18.55:	18.76 (0.02)	17.94 (0.02)	17.55 (0.01)	17.09 (0.02)
16	18.80:	18.65 (0.01)	17.59 (0.02)	17.00 (0.01)	16.45 (0.01)
17	20.46:	19.51 (0.03)	18.47 (0.02)	17.82 (0.02)	17.26 (0.02)
18		20.94 (0.02)	19.36 (0.03)	18.34 (0.02)	17.52 (0.02)

However, the results differ by up to 0.5 mag during the radioactive tail phase (especially in bluer bands), and preference has been given to the reduction via the template subtraction. The values reported in Table 3 after 2009 June 26 have been obtained by the latter technique. The uncertainties reported in Table 3 were estimated by combining in quadrature the errors in the photometric calibration and the error in the PSF fitting through artificial stars.

NIR photometry was obtained at two epochs with NICS (cf. Table 1) mounted at the 3.5-m Telescopio Nazionale Galileo (TNG). The NIR images of the SN field were obtained combining several, sky-subtracted, dithered exposures. Photometric calibration was achieved relative to Two Micron All Sky Survey (2MASS) photometry of the same local-sequence stars as used for the optical calibration. The NIR magnitudes of SN 2009bw are listed in Table 4.

Ultraviolet (*uvw2, uvm2 and uvw1*; see Poole et al. 2008) observations obtained by UVOT on board of the *Swift* satellite are available for four epochs in a period of 9 d. We reduced these data using the HEASARC[2] software. For each epoch, all images were co-added and then reduced following the guidelines presented by Poole et al. (2008). Aperture magnitudes are reported in Table 5.

In Section 5 we will discuss also the implications of an 8-ks exposure obtained with *Swift*-XRT which has provided an upper limit of 7.9×10^{-14} erg cm^{-2} s^{-1} (over the energy range 0.3–10 keV) in an aperture of 9 XRT pixels (∼21 arcsec) centred at the position of SN 2009bw.

2.2 Photometric evolution

In Fig. 2, the *uvw2, uvm2, uvw1, U, B, V, R, I, J, H* and *K′* light curves of SN 2009bw are plotted. The *B*-, *V*-, *I*- and more clearly *R*-band light curves show a slow rise to the peak, estimated to have occurred around the JD 245 4923.5 ± 1.0 in the *B* band. It is likely that thus the discovery of the SN happened close to the shock breakout. The early discovery is also consistent with the phases derived for the first spectra of SN 2009bw as deduced from the comparison of the early spectra with a library of SN spectra performed with the 'GELATO' code (Harutyunyan et al. 2008). Therefore, hereafter we will adopt JD 245 4916.5 ± 3 (March 25.0 UT) as an estimate for the epoch of shock breakout.

An initial slow decline of ∼30 d, during which the SN decreases by about 0.5 mag in the *V* and *R* bands, is followed by a plateau lasting for 50–100 d. The plateau is flat from *V* to *I* ($m_R \sim 15.0$, i.e. $M_R \sim -17.4$; cf. Section 2.3), possibly shorter and inclined in blue bands. The plateau luminosity of SN 2009bw is more luminous than that of common SNe IIP (more than 1 mag; see Patat et al. 1994; Richardson et al. 2002) and similar to those of SN 1992H (Clocchiatti et al. 1996), SN 2004et (Maguire et al. 2010) and SN 2007od (Inserra et al. 2011).

[2] NASA's High Energy Astrophysics Science Archive Research Center.

Table 3. *UBVRI* magnitudes of SN 2009bw and assigned errors in brackets.

Date (yy/mm/dd)	JD (+240 0000)	*U*	*B*	*V*	*R*	*I*	Inst.
09/03/27	54918.42				15.88 (0.02)		7
09/03/30	54921.40		15.49 (0.02)	15.22 (0.01)	15.09 (0.01)		6
09/03/31	54922.24		15.38 (0.02)	15.01 (0.01)	14.90 (0.01)		6
09/04/01	54923.32		15.18 (0.01)	14.96 (0.01)	14.72 (0.01)		7
09/04/03	54925.31				14.55 (0.02)		7
09/04/03	54925.50		15.32 (0.10)	14.88 (0.06)	14.68 (0.01)	14.44 (0.02)	6
09/04/04	54926.24	14.51 (0.05)	15.30 (0.05)	14.95 (0.02)	14.65 (0.01)	14.37 (0.03)	9
09/04/07	54929.33			14.99 (0.02)	14.64 (0.02)	14.33 (0.01)	8
09/04/08	54930.46				14.65 (0.07)		7
09/04/09	54931.30	14.79 (0.07)	15.36 (0.03)	15.03 (0.02)	14.67 (0.02)	14.34 (0.03)	9
09/04/12	54934.25	14.95 (0.15)	15.57 (0.05)	15.08 (0.05)	14.72 (0.03)	14.40 (0.03)	9
09/04/12	54934.31	15.11 (0.03)	15.55 (0.02)	15.18 (0.02)	14.74 (0.02)	14.49 (0.02)	1
09/04/14	54936.40	15.49 (0.02)	15.73 (0.02)	15.20 (0.02)	14.77 (0.02)	14.50 (0.02)	2
09/04/14	54936.45				14.77 (0.18)		7
09/04/15	54937.39	15.52 (0.02)	15.82 (0.02)	15.17 (0.01)	14.78 (0.02)	14.50 (0.02)	4
09/04/19	54941.26	15.85 (0.11)	15.96 (0.03)	15.25 (0.02)	14.81 (0.02)	14.45 (0.03)	9
09/04/19	54941.39	16.05 (0.02)	15.98 (0.02)	15.28 (0.02)	14.80 (0.02)	14.48 (0.02)	4
09/04/22	54944.28	16.29 (0.13)	16.16 (0.05)	15.30 (0.03)	14.88 (0.02)	14.49 (0.03)	9
09/04/22	54944.34				14.81 (0.01)		7
09/04/23	54945.28	16.49 (0.03)	16.34 (0.05)	15.29 (0.02)	14.86 (0.02)	14.51 (0.02)	6
09/04/26	54948.28		16.36 (0.04)	15.40 (0.03)	14.94 (0.02)	14.53 (0.03)	9
09/04/28	54950.34	16.54 (0.19)	16.26 (0.10)	15.40 (0.20)	14.93 (0.12)	14.61 (0.12)	1
09/04/29	54951.29		16.44 (0.04)	15.47 (0.03)	15.02 (0.02)	14.58 (0.02)	9
09/04/30	54952.38				14.97 (0.25)		7
09/05/03	54955.33	17.27 (0.03)	16.70 (0.02)	15.57 (0.02)	15.03 (0.02)	14.65 (0.02)	1
09/05/03	54955.38	17.26 (0.04)	16.75 (0.02)	15.60 (0.02)	15.10 (0.04)	14.69 (0.02)	3
09/05/04	54956.28		16.81 (0.06)	15.61 (0.04)	15.03 (0.03)	14.57 (0.03)	9
09/05/08	54960.44				15.01 (0.13)		7
09/05/14	54966.45				15.11 (0.05)		7
09/05/18	54970.34		17.08 (0.07)	15.79 (0.03)	15.16 (0.03)	14.65 (0.03)	9
09/05/18	54970.44				15.20 (0.15)		7
09/05/21	54973.42	18.19 (0.15)	17.01 (0.05)	15.76 (0.02)	15.19 (0.02)	14.70 (0.03)	5
09/05/25	54977.39	18.26 (0.19)	17.27 (0.04)	15.83 (0.02)	15.17 (0.02)	14.74 (0.02)	5
09/05/25	54977.42				15.17 (0.30)		7
09/05/26	54978.33			15.78 (0.15)	15.17 (0.10)	14.66 (0.15)	9
09/05/30	54982.63	18.28 (0.09)	17.29 (0.02)	15.75 (0.02)	15.17 (0.02)	14.73 (0.02)	1
09/05/31	54983.32				15.22 (0.15)	14.70 (0.16)	9
09/06/26	55009.58		17.63 (0.02)	15.94 (0.02)	15.31 (0.02)	14.82 (0.02)	1
09/07/04	55017.46			16.04 (0.15)	15.31 (0.12)		10
09/07/19	55032.68		18.15 (0.04)	16.29 (0.02)	15.60 (0.02)	15.12 (0.02)	3
09/07/23	55036.58		18.26 (0.08)	16.38 (0.02)	15.62 (0.02)	15.13 (0.02)	5
09/07/26	55039.43				15.71 (0.05)		7
09/07/30	55043.42		18.32 (0.17)	16.57 (0.10)	15.76 (0.10)	15.30 (0.10)	9
09/07/30	55043.65		18.43 (0.03)	16.52 (0.03)	15.74 (0.03)	15.23 (0.03)	1
09/08/05	55049.35		18.62 (0.30)	16.93 (0.10)	16.11 (0.10)	15.61 (0.10)	9
09/08/10	55054.40			18.52 (0.30)	17.54 (0.16)	17.00 (0.15)	9
09/08/12	55056.43			18.78 (0.20)	17.90 (0.18)	17.35 (0.30)	9
09/08/12	55056.54	20.04 (0.40)	20.79 (0.09)	18.90 (0.10)	17.93 (0.06)	17.36 (0.08)	1
09/08/13	55057.59	21.18 (0.38)	20.74 (0.09)	18.96 (0.12)	18.01 (0.04)	17.41 (0.07)	2
09/08/20	55063.61		20.80 (0.21)	19.23 (0.11)	18.12 (0.17)	17.47 (0.13)	5
09/08/23	55067.29				18.03 (0.15)	17.59 (0.30)	9
09/08/29	55073.55			19.06 (0.15)	18.05 (0.10)		11
09/08/30	55074.52				18.05 (0.15)		11
09/08/30	55074.57		20.81 (0.04)	19.14 (0.13)	18.19 (0.08)	17.57 (0.08)	1
09/09/04	55079.44		21.02 (0.05)	19.19 (0.04)	18.14 (0.04)	17.55 (0.07)	1
09/09/04	55079.53			19.15 (0.16)	18.14 (0.12)	17.51 (0.27)	11
09/09/05	55080.47				18.12 (0.12)		11
09/09/06	55081.43				18.15 (0.12)		11
09/10/12	55116.74		21.03 (0.11)	19.48 (0.29)	18.51 (.57)	18.10 (0.15)	3
09/10/18	55123.62			19.62 (0.13)	18.70 (0.11)	18.20 (0.12)	5
09/11/07	55143.50			20.09 (0.27)	19.01 (0.15)		11
09/11/09	55145.47			20.13 (0.21)	19.05 (0.18)		11
09/11/10	55146.46		21.41 (0.12)	20.11 (0.19)	19.05 (0.56)	18.68 (0.22)	3
09/11/17	55153.42			20.36 (0.21)	19.22 (0.12)		11
09/11/22	55157.85			20.40 (0.21)	19.36 (0.24)	18.78 (0.25)	1
10/08/24	55433.69			>21.9	>20.3	>19.5	3

1 = CAHA; 2 = NOT; 3 = TNG; 4 = LT; 5 = Copernico; 6 = SAO-RAS; 7 = THO; 8 = S50; 9 = M70; 10 = C50 and 11 = C60. The telescopes abbreviations are the same as in Table 1.

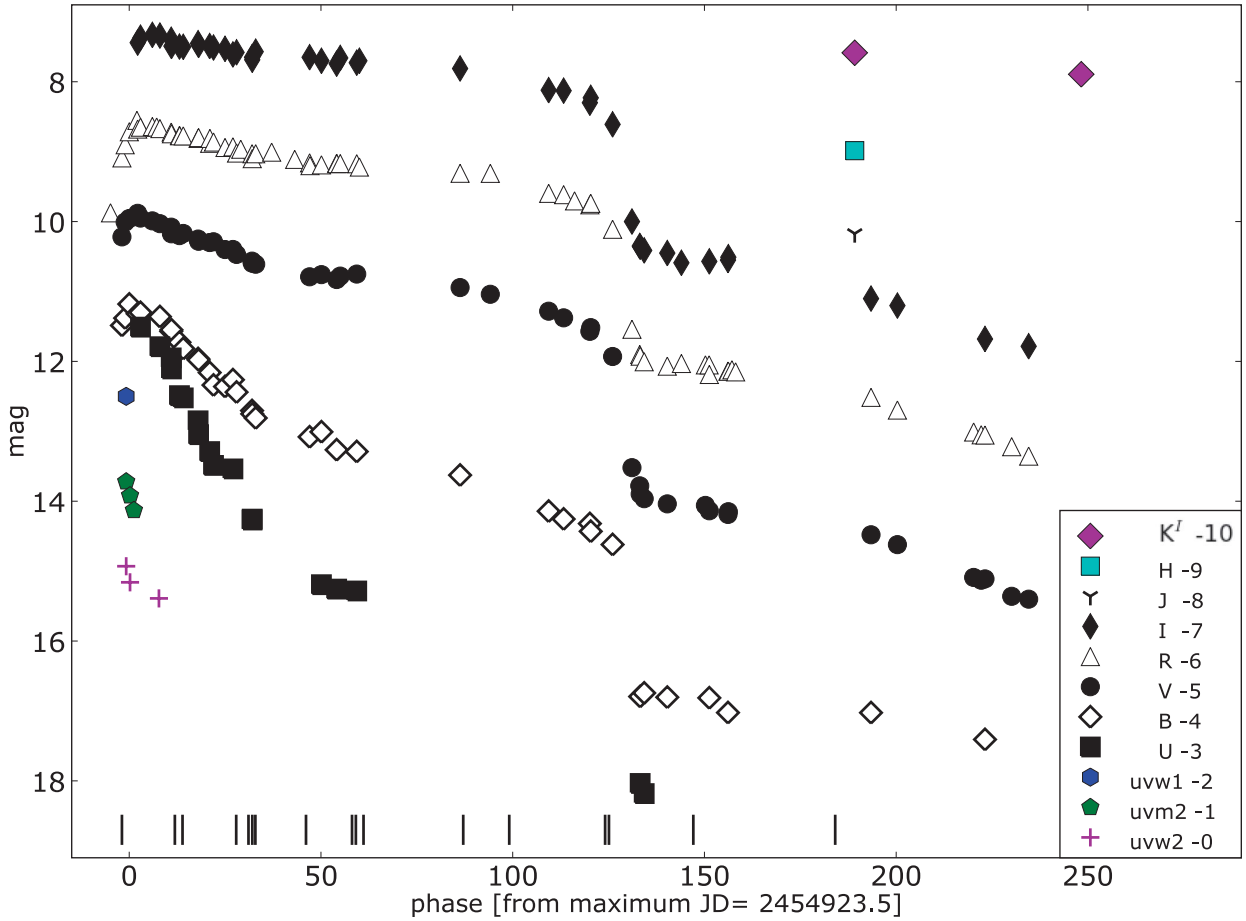

Figure 2. Synoptic view of the light curves of SN 2009bw in all available bands. The shifts from the original values reported in Table 3 are in the legend. Vertical marks at the bottom indicate the epochs of available spectra (cf. Table 8).

Table 4. *JHK′* TNG magnitudes of SN 2009bw and assigned errors.

Date (yy/mm/dd)	JD (+240 0000)	*J*	*H*	*K′*
09/10/07	55112.49	18.17 (0.18)	17.99 (0.15)	17.59 (0.13)
09/12/05	55171.50			17.89 (0.08)

Table 5. *Swift* magnitudes of SN 2009bw and assigned errors.

Date (yy/mm/dd)	JD (+240 0000)	*uvw2*	*uvm2*	*uvw1*
09/04/01	54922.51	14.93 (0.06)	14.72 (0.07)	14.50 (0.10)
09/04/02	54923.51	15.16 (0.06)	14.92 (0.08)	
09/04/03	54924.52		15.13 (0.09)	
09/04/09	54931.05	15.39 (0.06)		

As shown in Fig. 2, after ∼110d *BVRI* light curves show a decline from the plateau. Though very fast (∼2.2 mag in only 13 d), the jump is less pronounced than in other SNe IIP, e.g. 6 mag in SN 2007od (Inserra et al. 2011), >3.5 mag in SN 1994W (Sollerman, Cumming & Lundqvist 1998) and 3.6 mag in the low-luminosity SN 2005cs (Pastorello et al. 2009).

After the drop, the light curve settles on to the radioactive tail. The late time decline rates in various bands are reported in Table 6. Although with some variations, these share an overall similarity with those of most SNe IIP (e.g. Turatto et al. 1990; Patat et al. 1994) and are close to 0.98 mag (100 d)$^{-1}$, the decay rate of ^{56}Co to ^{56}Fe (corresponding to a lifetime of 111.26 d).

In Fig. 3 we show the time evolution of the $B - V$ and $V - I$ colour curves of SN 2009bw together with those of SN 1987A, SN 2005cs, SN 2004et, SN 1999em and SN 2007od, dereddened according to the values of Table 7.

All typical SNe IIP show a similar colour evolution with a rapid increase of $B - V$ as the SN envelope expands and cools. After about 40 d, the colour changes more slowly as the rate of cooling decreases. SN 2009bw follows the general behaviour. The only exception to this smooth trend is SN 2005cs that shows a red jump at about 120 d, which seems to be a characteristic of low-luminosity SNe II (Pastorello et al. 2004). The $B - V$ trend of SN 2009bw during the early days seems redder than that of normal SNe IIP such as SN 1999em and closer to that of SN 2007od. The last two points suggest a blue excess, as does the SN 2007od, but the errors of these points are large and we will not consider it any further.

Table 6. Main data of SN 2009bw.

Position (2000.0)	$03^h56^m02\overset{s}{.}92$	$+72^\circ55^m40\overset{s}{.}9$
Parent galaxy morphology	UGC 2890, Sdm pec:	
Offset with respect to nucleus	11 arcsec east	22 arcsec north
Adopted distance modulus	$\mu = 31.53 \pm 0.15$	
SN heliocentric velocity	$1155 \pm 6\,\mathrm{km\,s^{-1}}$	
Adopted reddening	$E_g(B-V) = 0.23$	$E_{tot}(B-V) = 0.31$

	Peak time (JD 245 4000+)	Peak observed magnitude	Peak absolute magnitude
B	923 ± 1	15.18 ± 0.01	-17.70 ± 0.15
V	925 ± 1	14.88 ± 0.06	-17.67 ± 0.16
R	925 ± 1	14.55 ± 0.02	-17.82 ± 0.15
I	929 ± 1	14.33 ± 0.01	-17.83 ± 0.15
UBVRI	925 ± 2	$L_{bol} = 2.6 \times 10^{42}\,\mathrm{erg\,s^{-1}}$	
Rise to *R* max	∼8 d		
Explosion day	$\sim 916.5 \pm 3$	∼2009 March 25	

	Late time decline [mag (100d)$^{-1}$]	Interval (d)
V	1.00	139–239
R	1.09	139–239
I	1.13	139–239
UBVRI (tot)	1.06	139–239
UBVRI (seg 1)	0.70	139–156
UBVRI (seg 2)	1.16	161–239
$M(^{56}\mathrm{Ni})$	$0.022\,M_\odot$	
M(ejecta)	$8.3–12\,M_\odot$	
Explosion energy	0.3×10^{51} erg	

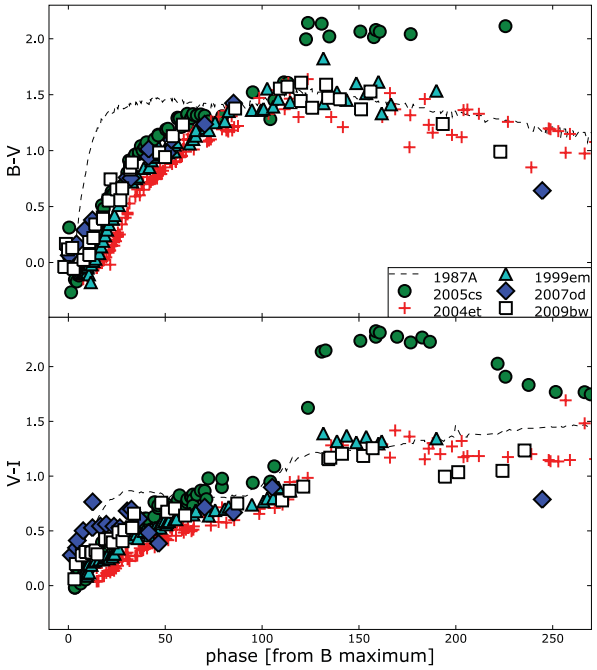

Figure 3. Comparison of the dereddened colours of SN 2009bw and those of SN 1987A, SN 2005cs, SN 1999em, SN 2004et and SN 2007od. The phase of SN 1987A is with respect to the explosion date.

Table 7. Main parameters of SNe II used in the comparisons with SN 2009bw.

SN	μ^a	$E(B-V)$	Parent galaxy	References
1987A	18.49	0.195	LMC	1
1992H	32.38	0.027	NGC 5377	2
1998S	31.08	0.232	NGC 3877	3
1999em	29.47	0.1	NGC 1637	4,5
2004et	28.85	0.41	NGC 6946	6
2005cs	29.62	0.05	M 51	7
2006bp	31.44	0.031	NGC 3953	8
2007od	32.05	0.038	UGC 12846	9

[a]In the $H_0 = 73\,\mathrm{km\,s^{-1}\,Mpc^{-1}}$ distance scale.
References: 1 – Arnett et al. (1989), 2 – Clocchiatti et al. (1996), 3 – Fassia et al. (2001), 4 – Elmhamdi et al. (2003), 5 – Baron et al. (2000), 6 – Maguire et al. (2010), 7 – Pastorello et al. (2009), 8 – Quimby et al. (2007) and 9 – Inserra et al. (2011).

The $V-I$ colour evolution of SN 2009bw is similar to that of other SNe IIP (cf. Fig. 3).

2.3 Reddening and absolute magnitude

The Galactic reddening to UGC 2890 is $E_g(B-V) = 0.231$ mag [$A_g(B) = 0.996$ mag] according to Schlegel, Finkbeiner & Davis (1998), a relatively large value consistent with the low Galactic latitude of UGC 2890 (b_2=14.°7; LEDA). In the optical spectra of SN 2009bw, the absorption features due to interstellar Na I D (λλ5890, 5896) of the Galaxy are present, with an average $\mathrm{EW_g(Na\,I\,D)} \sim 1.37$ Å, as determined by our best resolution spectra (cf. Section 3). According to Turatto, Benetti & Cappellaro (2003), this corresponds to a Galactic reddening $E_g(B-V) \sim 0.22$ mag [$A_g(B) \sim 0.92$ mag]. This is in good agreement with Schlegel et al. (1998). With the same method, we can estimate the reddening inside the parent galaxy. Interstellar Na I D components within the host galaxy have been measured with an average $\mathrm{EW_i(Na\,I\,D)} \sim 0.52$ Å that corresponds to a low internal reddening $E_i(B-V) \sim 0.08$ mag or $A_i(B) \sim 0.35$ mag. We should warn the reader that recently Poznanski et al. (2011) have suggested that Na I D lines in SN Ia spectra are poor tracers of dust extinction. However, having no alternative throughout this paper we have adopted a total reddening $E_{tot}(B-V) = 0.31 \pm 0.03$ mag.

NASA/IPAC Extragalactic Database (NED) provides a heliocentric radial velocity of $v_{hel}(\mathrm{UGC2890}) = 1155 \pm 6\,\mathrm{km\,s^{-1}}$. Adopting $H_0 = 73\,\mathrm{km\,s^{-1}\,Mpc^{-1}}$ and a velocity corrected for the Virgo infall of $v_{Virgo} = 1473 \pm 16\,\mathrm{km\,s^{-1}}$ (Mould et al. 2000), we obtain a distance modulus $\mu = 31.53 \pm 0.15$ mag which will be used throughout this paper. Tully et al. (2009) provided a $\mu = 30.23 \pm 0.40$ mag ($H_0 = 72\,\mathrm{km\,s^{-1}\,Mpc^{-1}}$). This would make SN 2009bw more than 1 mag fainter; however, it is inconsistent with the identified galaxy lines.

Assuming the above distance and extinction values, we find $M_B^{max} = -17.72 \pm 0.15$, $M_V^{max} = -17.67 \pm 0.16$, $M_R^{max} = -17.82 \pm 0.15$ and $M_I^{max} = -17.83 \pm 0.15$, where the reported errors include the uncertainties on the adopted distance modulus, reddening and magnitude measurements.

2.4 Bolometric light curve and ^{56}Ni mass

Unfortunately, because of the lack of simultaneous optical–NIR observations, it is impossible to obtain a true bolometric light curve

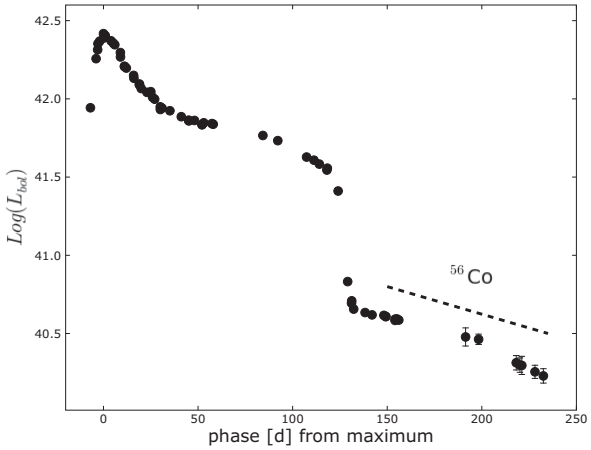

Figure 4. *UBVRI* bolometric light curve of SN 2009bw. The slope of ^{56}Co to ^{56}Fe decay is also displayed for comparison. Distance modulus and reddening are reported in Table 6.

for SN 2009bw. In fact, extended coverage from B to K' is available only in the late radioactive tail. In order to obtain the bolometric light curve, we convert only *UBVRI* broad-band magnitudes (corrected for the adopted extinction; cf. Section 2.3) into fluxes at the effective wavelengths and integrate them over the entire range (flux integration limits equal to zero).

Flux was then converted to luminosity using the distance adopted in Section 2.3. The emitted flux was computed at phases in which *R* observations were available. When simultaneous observations in a bandpass were unavailable, the magnitudes were interpolated from the light curves using low-order polynomials or were extrapolated. The peak of the bolometric light curve is reached close to the *R*-band maximum on $\mathrm{JD}^{\mathrm{bol}}_{\mathrm{max}} = 245\,4925.3 \pm 2.0$ at a luminosity $L_{\mathrm{bol}} = 2.6 \times 10^{42}\,\mathrm{erg\,s^{-1}}$.

The nebular tail of the bolometric light curve declines at a rate of $\gamma \sim 1.06\,\mathrm{mag}\,(100\,\mathrm{d})^{-1}$, measured from 138–239 d since explosion, which matches the decay of ^{56}Co to ^{56}Fe, suggesting complete γ-ray trapping (see Fig. 4). However, we noted that the tail can be divided into two different segments: a flatter one from 138 to 156 d with $\gamma \sim 0.70\,\mathrm{mag}\,(100\,\mathrm{d})^{-1}$ resembling that of the early tail of SN 1999em and present in many SNe, and a second one (161–239 d) with $\gamma \sim 1.16\,\mathrm{mag}\,(100\,\mathrm{d})^{-1}$. The last two points at ∼234–240 d seem to suggest a further increase of the decline rate, maybe due to dust formation. However, due to the relatively large errors this is not significant, and we will not elaborate it any further.

In Fig. 5 we compare the bolometric (*UBVRI*) light curve of SN 2009bw with those of other SNe reported in Table 7. The early luminosity of SN 2009bw is slightly smaller than those of the luminous SN 2007od, SN 2004et, SN 1992H. The duration of the plateau

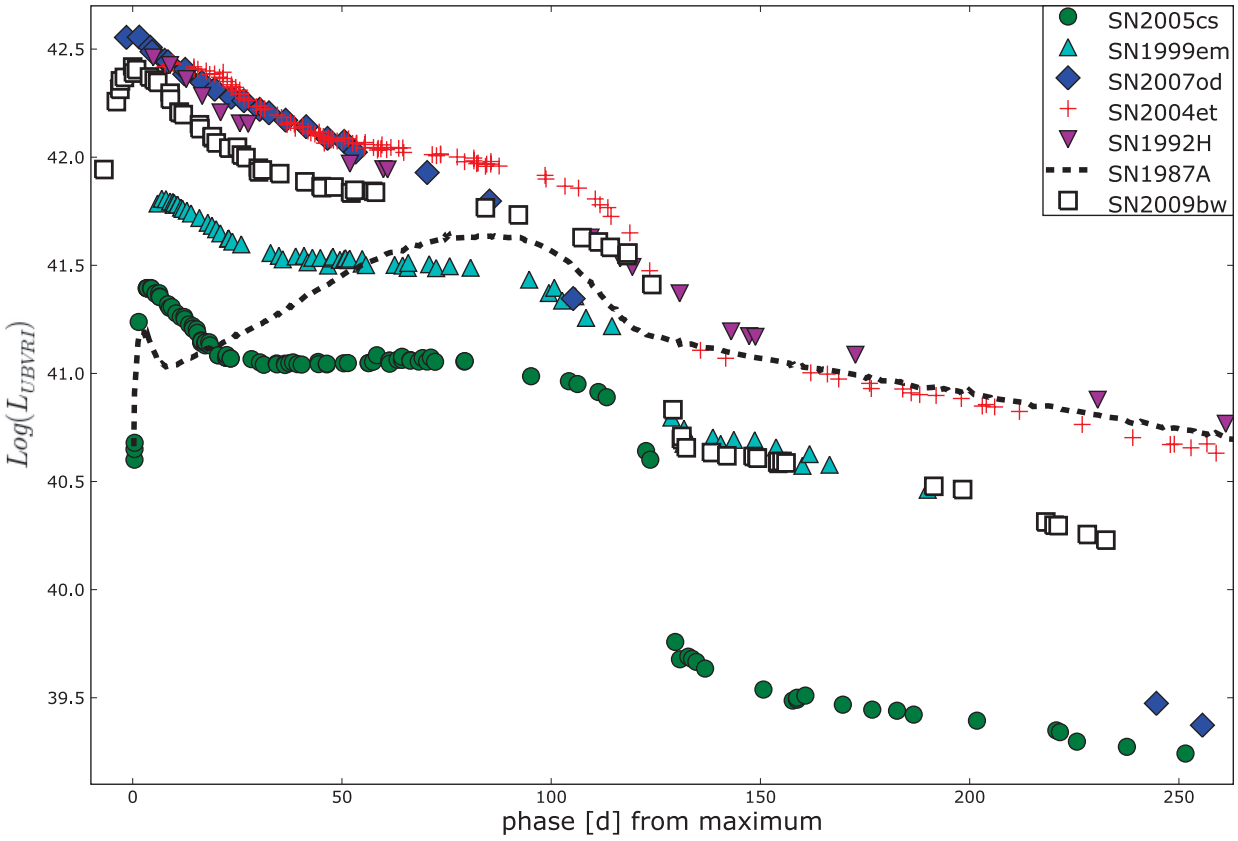

Figure 5. Comparison of bolometric (*UBVRI*) light curves of SN 2009bw with those of other SNe II. The distances and reddenings for the various objects are reported in Table 7. Small misalignments in the epoch of the maximum are due to different shifts between the maxima of the band adopted as reference and the bolometric one.

Table 8. Journal of spectroscopic observations of SN 2009bw.

Date	JD (+240 0000)	Phase[a] (d)	Instrumental configuration	Range (Å)	Resolution[b] (Å)
09/03/29	54920.5	4.0	NOT+ALFOSC+gm4	3600–9000	13
09/04/12	54934.3	17.8	CAHA+CAFOS+b200,r200	3380–10 000	10
09/04/14	54936.3	19.8	NOT+ALFOSC+gm4	3480–10 000	13
09/04/15	54937.3	20.8	TNG+NICS+ij,hk	8750–24 600	18,36
09/04/28	54950.3	33.8	CAHA+CAFOS+b200	3480–8730	10
09/05/01	54953.5	37.0	TNG+DOLORES+LRB	3500–7900	15
09/05/02	54954.5	38.0	TNG+DOLORES+LRR	5000–9600	15
09/05/03	54955.3	39.0	CAHA+CAFOS+b200	3500–8760	10
09/05/16	54968.5	52.0	BTA+SCORPIO+G400	3870–9830	13
09/05/28	54980.5	64.0	Copernico +AFOSC+gm4	4500–7760	25
09/05/29	54981.5	65.0	Copernico +AFOSC+gm2	5330–9020	37
09/05/31	54983.5	67.0	CAHA+CAFOS+g200	3780–10 000	9
09/06/26	54509.5	93.0	CAHA+CAFOS+g200	4000–10 000	10
09/07/18	55021.5	105.0	CAHA+CAFOS+g200	4800–10 000	14
09/08/12	55046.5	130.0	CAHA+CAFOS+g200	4000–9650	12
09/08/13	55047.5	131.0	NOT+ALFOSC+gm4	4200–9100	18
09/09/04	55069.5	153.0	CAHA+CAFOS+g200	4000–10 000	9
09/10/11	55106.5	190.0	TNG+DOLORES+LRR	5260–10 000	16

[a]With respect to the explosion epoch (JD 245 4916.5).
[b]As measured from the FWHM of the night sky lines.
The abbreviations are the same as in Table 1; in addition, BTA = the 6-m Big Telescope Alt-azimutal (Mt Pastukhova, Russia).

resembles those of SN 1992H and SN 2004et, whilst it is longer than that of the peculiar SN 2007od. The peak seems slightly broader than those of other SNe IIP including SN 2007od. The luminosity drop from the plateau to the tail of SN 2009bw appears intermediate between the high value for SN 2007od and the small value for SN 1999em.

The ^{56}Ni mass ejected by SN 2009bw has been derived by comparing its bolometric light curve to that of SN 1987A assuming similar γ-ray deposition fraction:

$$M\left(^{56}\mathrm{Ni}\right)_{09\mathrm{bw}} = M\left(^{56}\mathrm{Ni}\right)_{87\mathrm{A}} \frac{L_{09\mathrm{bw}}}{L_{87\mathrm{A}}}\,\mathrm{M}_{\odot}, \quad (1)$$

where $M(^{56}\mathrm{Ni})_{87\mathrm{A}} = 0.075 \pm 0.005\,\mathrm{M}_{\odot}$ is the mass of ^{56}Ni produced by SN 1987A (Arnett 1996) and $L_{87\mathrm{A}}$ is the *UBVRI* luminosity of 1987A at a comparable epoch. The comparison, performed between 161 and 205 d from explosion, gives $M(^{56}\mathrm{Ni})_{09\mathrm{bw}} \sim 0.022\,\mathrm{M}_{\odot}$. Indeed, L_{bol}(09bw) on the tail is similar to that of SN 1999em that ejected $\sim$0.022 $\mathrm{M}_{\odot}$ of ^{56}Ni (Elmhamdi et al. 2003). We have cross-checked this result by using the formula from Hamuy (2003) and assuming that γ-rays resulting from the ^{56}Co decay are fully thermalized at this epoch:

$$M\left(^{56}\mathrm{Ni}\right)_{09\mathrm{bw}} = \left(7.866 \times 10^{-44}\right) \times L_{\mathrm{t}} \exp\left[\frac{(t-t_0)/(1+z) - 6.1}{111.26}\right] \mathrm{M}_{\odot}, \quad (2)$$

where t_0 is the explosion time, 6.1 d is the half-life of ^{56}Ni and 111.26 d is the e-folding time of the ^{56}Co decay, which releases 1.71 and 3.57 MeV in the form of γ-rays (Woosley, Hartmann & Pinto 1989; Cappellaro et al. 1997). This method provides $M(^{56}\mathrm{Ni}) \sim 0.021\,\mathrm{M}_{\odot}$, consistent with the preceding value within the uncertainties. The single epoch (161 d) of NIR observations shows a NIR contribution of $\sim$20 per cent, which is similar to that of the other SNe IIP (see fig. 7 of Inserra et al. 2011).

Good sampling of the end of the plateau phase and the beginning of the radioactive tail allow us to estimate the steepness function S (maximum value at the transition phase of the first derivative of the plateau absolute visual magnitude) and in turn the ^{56}Ni mass using the method devised by Elmhamdi, Chugai & Danziger (2003). We evaluated $S = 0.57$ corresponding to $0.002\,\mathrm{M}_{\odot}$ of ^{56}Ni, typical of faint core collapse supernovae and very different from the previous estimates. The S value is larger than in all SNe of the sample of Elmhamdi et al. (2003) and extremely different to those of similar luminosity SN 1992H ($S = 0.048$) and SN 1999em ($S = 0.118$). This result suggests that in this case, the anticorrelation between steepness function and ^{56}Ni mass does not work, implying something uncommon in the high photospheric luminosity or a transition masked by some effect. We will address this issue in Section 5.

3 SPECTROSCOPY

The spectroscopic monitoring of SN 2009bw was carried out with several telescopes over a period of six months. The journal of spectroscopic observations is reported in Table 8.

3.1 Spectra reduction

Spectra were reduced (including trimming, overscan, bias correction and flat-fielding) using standard routines of IRAF. An optimal extraction of the spectra was adopted to improve the signal-to-noise ratio (S/N). Wavelength calibration was performed through spectra of comparison lamps acquired with the same configurations as the SN observations. Atmospheric extinction correction was based on tabulated extinction coefficients for each telescope site. Flux calibration was done using spectrophotometric standard stars observed with the same set-up as SN in the same nights. Absolute flux calibration was checked by comparison with the photometry, integrating the spectral flux transmitted by standard *BVRI* filters and, when necessary, adjusting it by a multiplicative factor. The resulting flux calibration is accurate to within approximately 0.1 mag. The spectral resolutions in Table 8 were estimated from the full width at half-maximum (FWHM) of the night sky lines. We used the spectra of standard stars to remove when possible telluric features in the

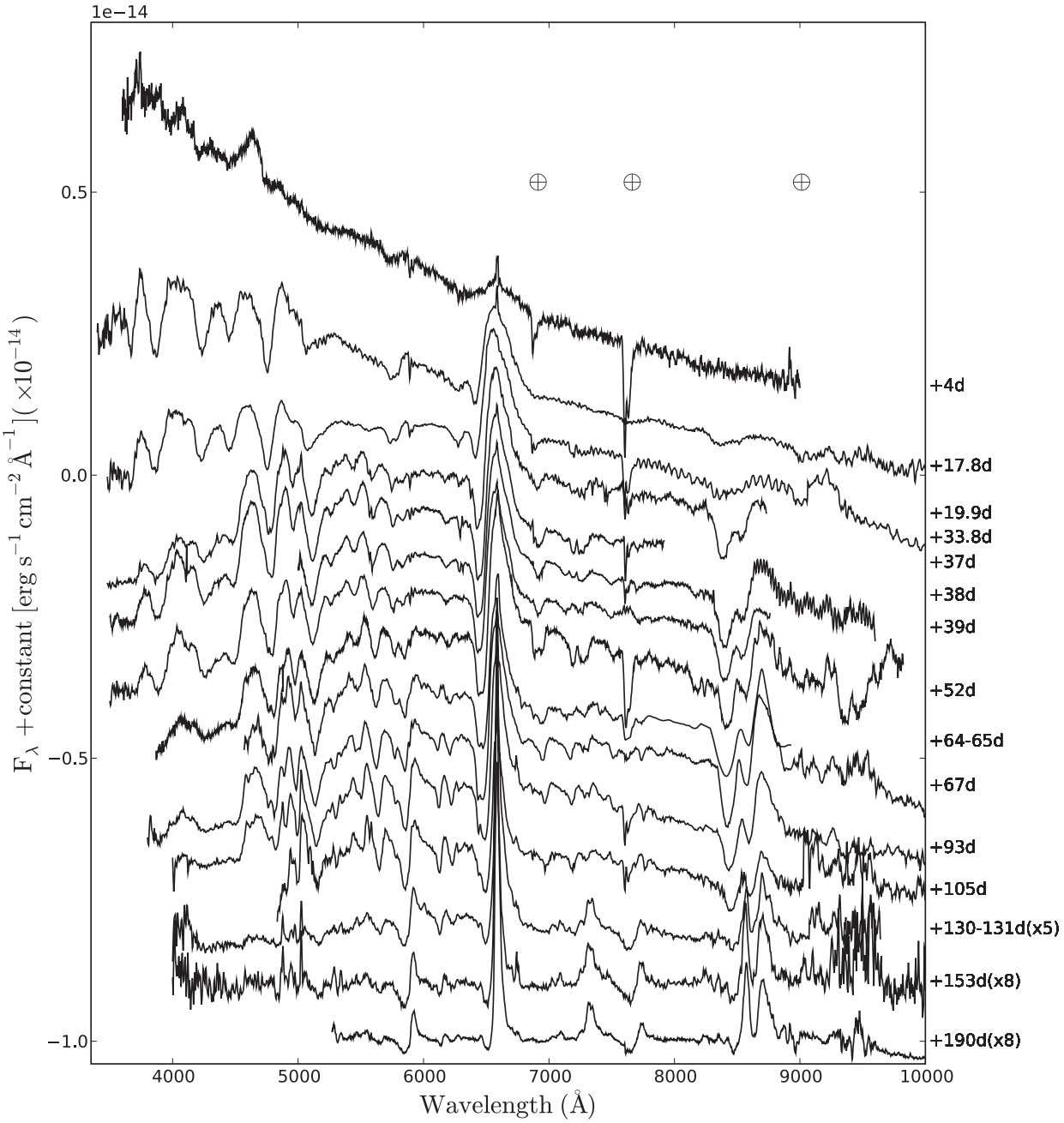

Figure 6. The overall spectral evolution of SN 2009bw. Wavelengths are in the observer rest frame. The phase reported for each spectrum is relative to the explosion date (JD 245 4916.5). The ⊕ symbols mark the positions of the most important telluric absorptions. The ordinate refers to the first spectrum. The second spectrum is shifted downwards by 2×10^{-15} units, the third by 3.3×10^{-15} units with respect to the second, others by 1.5×10^{-15} erg s^{-1} cm^{-2} Å^{-1} with respect to the previous.

SN spectra. The regions of the strongest atmosphere features are marked in Fig. 6. Spectra of similar quality obtained in the same night with the same telescope have been combined to increase the S/N.

The spectrum of May 28 (64 d) revealed some problems in the flux calibration of the blue side. The spectral continuum was forced to follow the spectral energy distribution (SED) derived fitting, with a low-order polynomial function the photometry obtained in the same night. This spectrum has not been used in the estimate of the temperature in Section 3.3. Since no significant evolution is expected, the spectra at 64 and 65 d, as well as those at 130 and 131 d, have been combined in Fig. 6.

For SN 2009bw a single NIR spectrum was collected at a phase at 20 d, which was reduced and extracted through standard

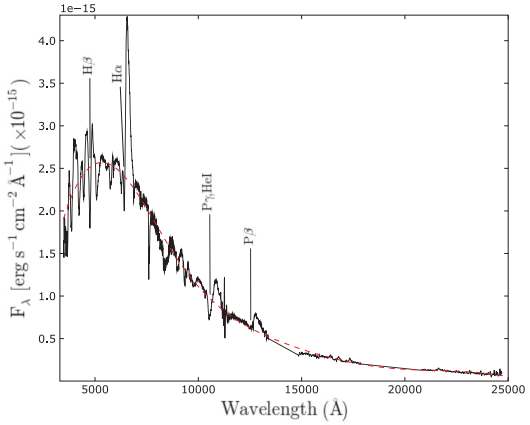

Figure 7. Composed spectrum of SN 2009bw, from optical to NIR wavelengths, at ∼20 d past explosion (JD 245 4916.5). Wavelengths are in the observer rest frame. A blackbody fit at ∼7900 K is overplotted. The regions of the strongest atmospheric features are not shown.

routines of IRAF. As for the optical, the spectrum was calibrated in wavelength through spectra of comparison lamps acquired with the same configuration of the SN observation. First-order flux calibration was obtained using telluric A0 standard stars taken in the same night with the SN set-up. The prominent telluric bands were identified through the spectra of the standard star and thus removed. The combined optical and NIR spectrum on day 20 is shown in Fig. 7.

3.2 Spectra analysis

Fig. 6 shows the spectral evolution of SN 2009bw from ∼2 d before maximum to over six months past peak, well sampled both in the photospheric and early nebular stages.

The first spectrum, used for classification by Stanishev et al. (2009), shows a blue continuum typical of SNe II at the same age. An unusual, prominent feature at 4600 Å appears near maximum. The feature is not present in the subsequent spectrum (18 d) and is most likely related to the SN since it is relatively broad (FWHM ∼ 140 Å) and has a short life. No significant emission of the underlying H II region, well seen at other wavelengths, is present in this range even in the latest spectra at 190 d (N II, N III, O II and forbidden Fe III lines are present in the spectra of typical H II regions at about 4600 Å; cf. Tsamis et al. 2003). The FWHM of the 4600-Å feature corresponds to a velocity $v \sim 9100\,\mathrm{km\,s^{-1}}$, larger than the velocity of Hα (∼7000 km s^{-1}), leading us to explore the possibility of a unusual line formation mechanism or to a very peculiar line blending. Similar features seen in ultraluminous SNe Ic (Pastorello et al. 2010; Quimby et al. 2011) have been identified as O II, but at wavelengths slightly bluer than this (λ4414). Concerning the opacity, its component related to the bound-free process has a sawtooth behaviour. If we consider a complex atmosphere, formed by H+He+heavy elements (e.g. Fe, Si) with temperature of the order of $T \sim 10^4$, the opacity in a window of the order of 10^2 Å around this wavelength is in a minimum with little dependence on T (Rutten 2003). In this hypothesis, the emission from lines due to highly ionized elements like N III, N IV and C V is allowed. On the other hand, we can not exclude the possibility of an extreme top lighting effect (concerning a flip of the P Cygni profile; see Branch et al. 2000) relative to Hβ and not observed in Hα due to a difference in the optical depth (maybe due to the interaction). However, to observe this effect, the interaction should be really strong, while nothing in the light curve suggests such strong interaction. Actually, the comparison with SN 2006bp and SN 1998S shown in panel (a) of Fig. 8 suggests the identification of this feature as a blend of highly ionized N and C. Indeed, the feature is closer in wavelength to that observed in SN 1998S, identified by Fassia et al. (2001) as C III/N III emission, rather than that in SN 2006bp attributed to He II λ4686 by Quimby et al. (2007). Note, however, that the difference between the FWHM of our feature (140 Å) and the C III/N III of SN 1998S (∼20 Å) is remarkable. The similarity with SN 1998S becomes more convincing if one compares a spectrum of 2–3 weeks after the explosion (FWHM of the blended feature ∼180 Å, cf. Fig. 8, panel a).

The spectra at 18 and 20 d are characterized by a blue continuum, comparable to that of SN 1992H and slightly bluer than that of SN 1999em at a similar age (cf. Fig. 8 panel b and Fig. 11). In the optical domain, we identified H Balmer lines, He I 5876 Å and some Fe II multiplet lines. In this set of spectra a narrow Hα emission due to an underline H II region is visible.

In order to perform a detailed line identification, we computed a synthetic photospheric spectrum model using SYNOW (Fisher 2000) and matching the properties of our observed +18 d spectrum. We adopted a blackbody temperature $T_{\rm bb} \sim 12000$ K, an expansion velocity at the photosphere $v_{\rm phot} \sim 7000\,\mathrm{km\,s^{-1}}$ (cf. Section 3.3), an optical depth $\tau(v)$ parametrized as a power law of index $n = 9$ and an excitation temperature $T_{\rm exc} = 10000$ K, constant for all ions. The most relevant spectral features are reproduced using only six ions (Fig. 9). The P Cygni profiles of the Balmer lines are clearly visible, as well as He I λ5876, but there is also contribution from Ca II, Fe II, Fe I and Si II. Detached H lines better match the line troughs. The poor fit of the Ca II IR triplet is due to low optical depth, which is, however, necessary to reproduce the Ca II H&K lines. We excluded the O I ion because of the early phase of the spectrum.

The line at about 6250 Å has been identified as Si II λ6355 with an expansion velocity comparable to those of the other metal ions. The presence of Si II has been identified in several SNe II, such as SN 2007od (Inserra et al. 2011), SN 2005cs (Pastorello et al. 2006), SN 1992H (Clocchiatti et al. 1996), SN 1999em (Dessart & Hillier 2005) and SN 1990E (Schmidt et al. 1993).

In the NIR spectrum (20 d), having a photospheric temperature derived from a blackbody fit of ∼7900 K (cf. Fig. 7), the P Cygni profiles of the Paschen series are detected, in particular Paschen β and Paschen γ. The latter is blended with He I λ10830 and has a velocity which is higher by $\Delta v \sim 2200\,\mathrm{km\,s^{-1}}$ than that of He I λ5876.

The subsequent set of spectra (33–39 d) shows well-developed P Cygni profiles of Balmer and metal lines. Sc II λ5031 on the red side and Sc II λ4670 on the blue side of Hβ are visible, as well as the Fe II multiplet 42 lines (λλ4924, 5018, 5169), Fe II at about 4500 Å, Fe I and Sc II in the region between 5200 and 5500 Å. Starting from day ∼34, the He I λ5876 forms a blend with the Na I D. The Ca II IR triplet (λλ8498, 8542, 8662) is well developed, while the Ca II H&K feature blends with Ti II. O I at about 7700 Å starts to be visible. Si II λ6355 has now disappeared, and the bottom of the Hα absorption shows a flat profile. We will discuss in detail the line profiles in Section 5.

In the late plateau phase, the spectra continue to show the elements identified at earlier phases, complemented by Ba II and Ti II, whose presence indicate a temperature of ∼5000 K. Both ions are required for explaining several features between 4000 and 5000 Å. In particular, Ba II λ6142 is clearly visible. At this phase Ba I may

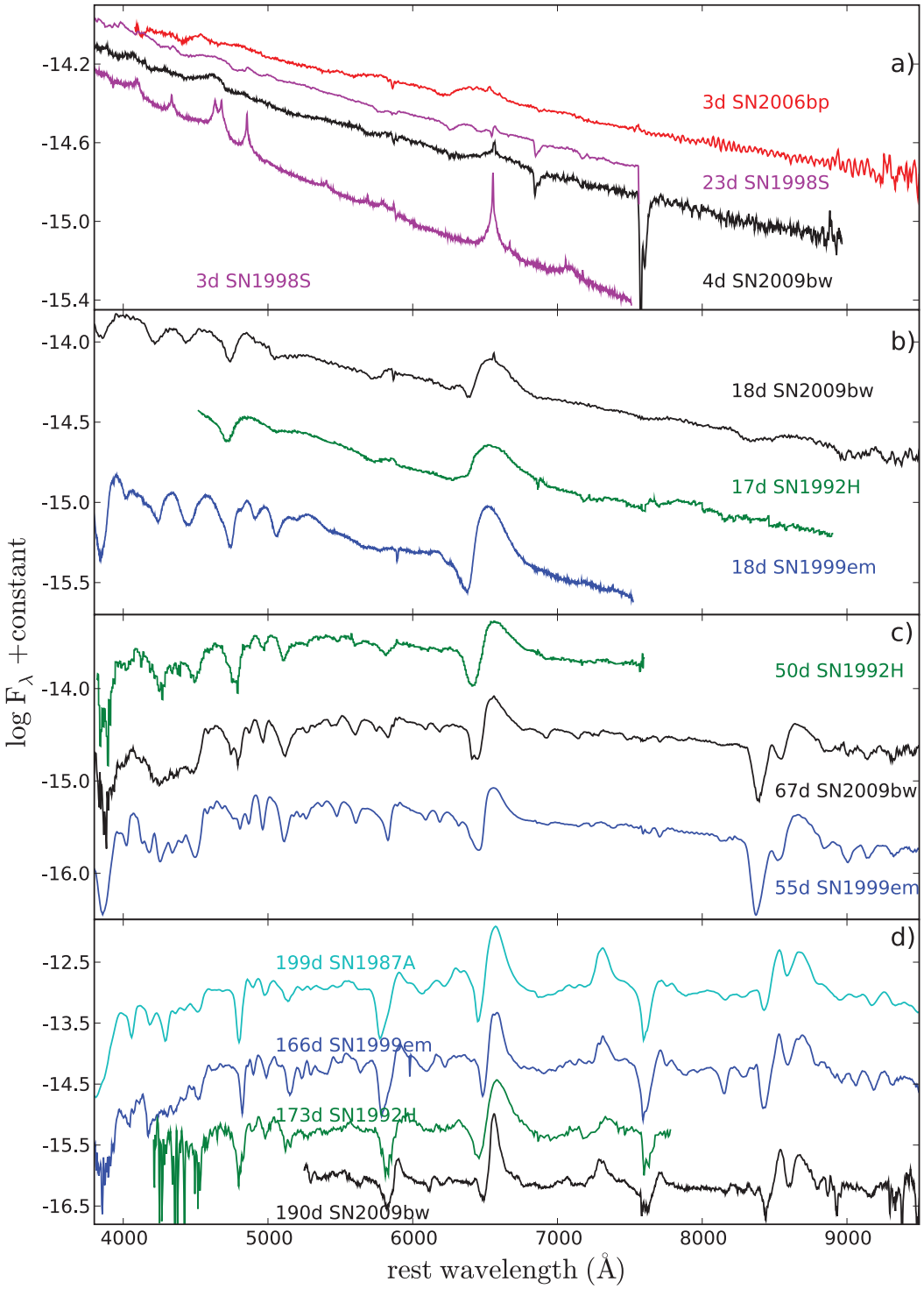

Figure 8. Panel (a): comparison among spectra of SN 2009bw, SN 1998S and SN2006bp about ∼4 d past explosion, plus the spectrum of SN 1998S at 23 d. Panel (b): comparison between spectra of SN 2009bw, SN 1999em and SN 1992H about 18 d past explosion. In panel (c) spectra of SN 2009bw, SN 1999em and SN 1992H in the plateau phase are compared, and in panel (d) spectra of SN 2009bw, SN 1987A, SN 1999em and SN 1992H during the nebular phase are shown. For references, see the text and Table 7, except for the SN 1987A spectrum (Suntzeff & Bouchet 1990).

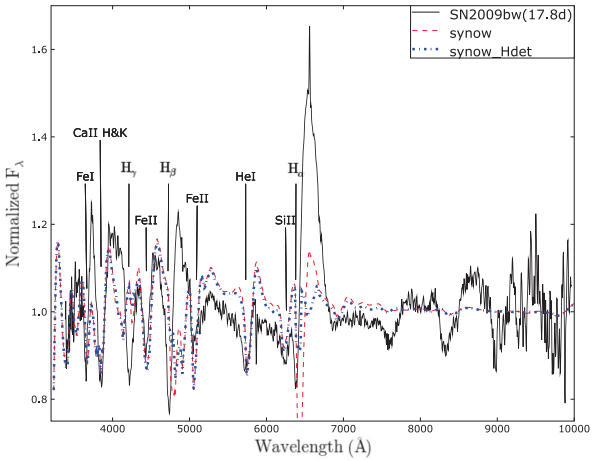

Figure 9. Comparison between the optical spectrum of SN 2009bw at 17.8 d after the explosion (JD 245 4916.5) and SYNOW synthetic spectra (for the composition of the synthetic spectra, see the text). Two models are plotted having H detached (blue dot–dashed line) or undetached (red dashed line). The observed spectrum has been corrected for extinction in the Galaxy, reported to the local rest frame and normalized to its continuum. The most prominent absorptions are labelled.

contribute to the blends of lines in the wavelength range 5000–6000 Å and Mg II around 9140 Å.

SYNOW fairly reproduces the characteristics of the best S/N spectrum obtained in the late plateau phase (∼67 d) with the following parameters: $T_{\rm bb} \sim 5400$ K, $v_{\rm phot} \sim 3050$ km s^{-1} (cf. Section 3.3), optical depth $\tau(v)$ parametrized as a power law of index $n = 7$ and $T_{\rm exc} = 5000$–8000 K for neutral atoms and 10 000 K for ionized species. The SYNOW spectrum (Fig. 10) has been obtained by considering 11 different contributing ions (red dashed line): H I, C I, N I, O I, Na I, Ca II, Sc II, Ti II, Fe I, Fe II and Ba II. The inclusion of two additional ions (blue dot–dashed line), Ba I and Mg II, allows for a better fit of the absorption on the blue wing of Na I D at 5745 Å and the absorption at 9145 Å as a blend of O I and Mg II. The absorption feature visible around 7100 Å and poorly fitted by both the synthetic spectra could be Ti II with a different optical depth. However, because of the noise and the presence of telluric absorptions in this range, it is difficult to draw a firm conclusion. The discrepancy in the emission between the SYNOW fits and observed spectra at about 4500 Å is perhaps due to a high optical depth of Ti II that masks the emission of nearby lines. Other discrepancies between observed and synthetic spectra may be attributed to non-local thermodynamic equilibrium (NLTE) effects ignored in our computation. H I and Ca II are detached to improve the line fit, but this causes problems in fitting the red wings. Interesting lines are identified on the red side

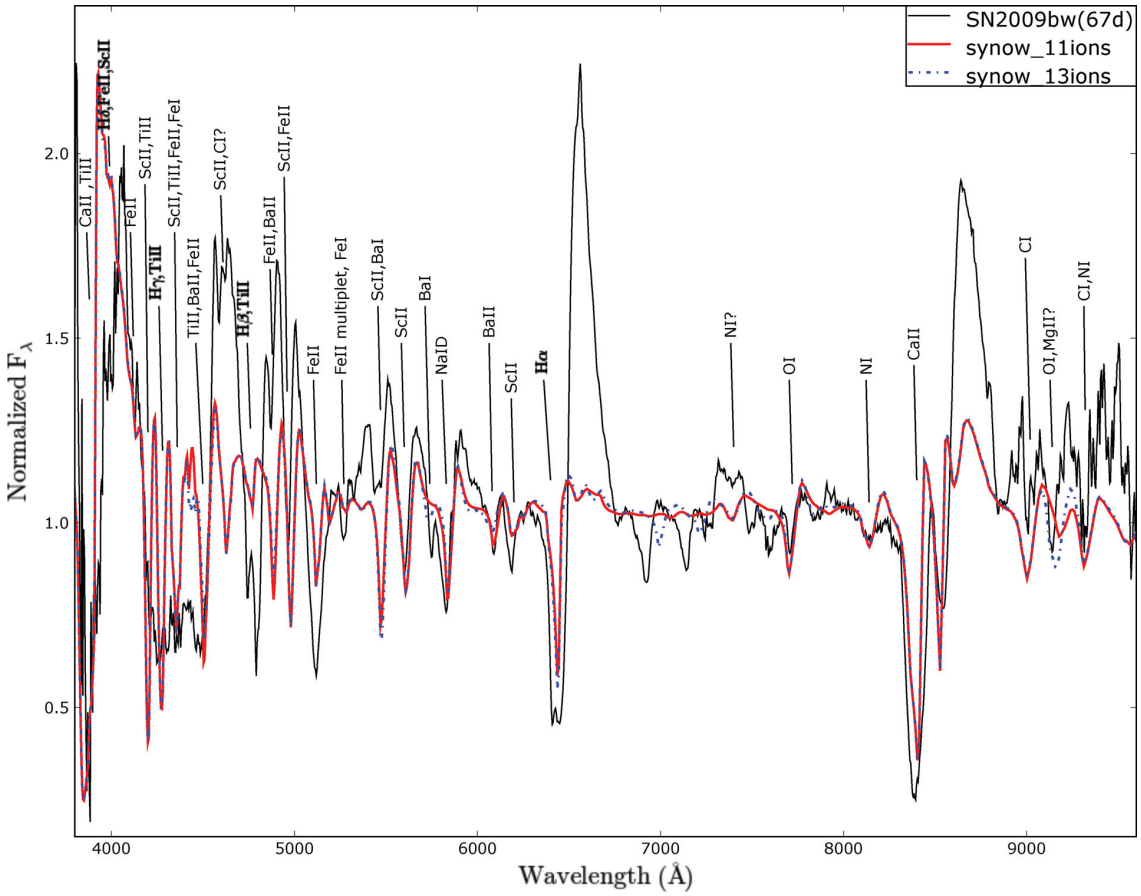

Figure 10. Comparison between the optical spectrum of SN 2009bw at ∼67 d after explosion (JD 245 4916.5) and two SYNOW analytical spectra. The difference between the SYNOW spectra is the presence of Ba I and Mg II ions (blue). The spectrum has been corrected for extinction in the Galaxy and reported to the SN rest frame. The most prominent absorptions are labelled.

(>7000 Å) of the spectrum, where absorptions due to the elements of the CNO cycle appear. In particular, O I λ7774 is present, and possibly also O I λ9260, blended with Mg II. N I has been identified around 7400 and 8130 Å. C I appears around 9010 and 9310 Å and possibly around 4615 Å close to the Sc II line, but in this region the fit is affected by the emission profile of detached hydrogen. O I and N I have been identified at this phase in other SNe, e.g. SN 1999em (Pastorello 2003), but the presence of C I lines in spectra of SNe IIP has only occasionally been claimed, e.g. in SN 1995V (Fassia et al. 1998) and SN 1999em (Pastorello 2003).

Fig. 8 (panel c) shows the comparison of spectra of several SNe II in the plateau phase. The spectrum of SN 2009bw appears similar to that of SN 1992H, sharing features commonly present in SNe IIP during the plateau phase. The comparison is interesting with SN 1999em around 9000 Å, where SYNOW has identified C I lines. Unfortunately, the other SN 2009bw spectra do not cover this wavelength range. The flat absorption profile of Hα resembles that observed in SN 1999em. In Section 5 we will discuss this feature arguing that this is due to weak CSM interaction.

Three early nebular spectra of SN 2009bw have been collected between 130 and 190 d. A narrow component appears at the host galaxy rest position, confirming that it is due to an underlying H II region. The broad Hα emission, attributed to the SN ejecta, is also centred at the rest wavelength and shows a residual absorption. Na I D and Ca II IR triplet absorptions are clearly visible. The spectra also show evidence of the forbidden emission of the [Ca II] λλ7291, 7324 doublet. Compared to other SNe IIP (panel d of Fig. 8), the complete absence of [O I] λλ6300, 6363 is noticeable even in the latest available SN 2009bw spectrum, and the relatively narrow FWHM of the emission lines [FWHM(Hα) ∼1900 km s^{-1}].

.

3.3 Expansion velocity and temperature

The photospheric expansion velocities of Hα, Hβ, He I λ5876, Fe II λ5169 and Sc II λ6246 are reported in Table 9 and plotted in Fig. 11 (top panel). They have been derived through the minima of P Cygni profiles. Error estimates have been derived from the scatter of several independent measurements. Hα is always the strongest line, and the derived velocities are systematically the largest. During the first 20 d when He I λ5876 dominates over Na I D, the He I velocity is comparable with that of Hβ. The Fe II velocity, which is considered to be a good indicator for the photospheric velocity because of the small optical depth, is lower than those of H and He, reaching 3000 km s^{-1} at about two months. Sc II is also a good indicator of the photospheric velocity and indeed its velocity is very close to that of Fe II, supporting the identification of the lines of both ions.

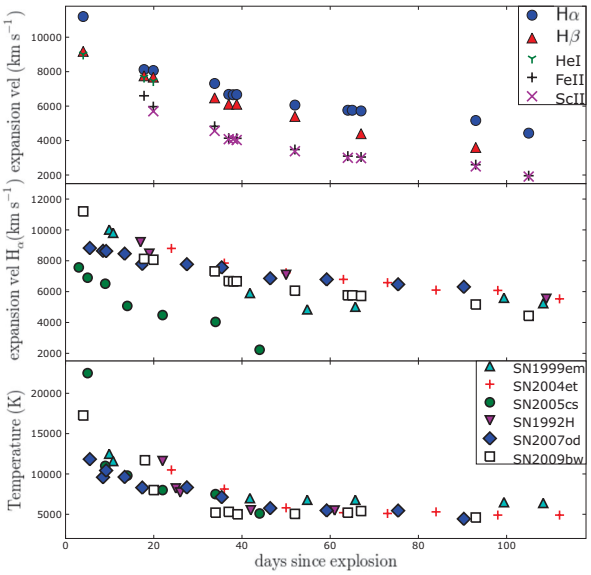

Figure 11. Top: expansion velocity of Hα, Hβ, He I λ5876, Fe II λ5169 and Sc II λ6246 measured from the minima of P Cygni profiles. Middle: comparison of the Hα velocity of SN 2009bw with those of other SNe II. Bottom: evolution of the continuum temperature of SN 2009bw, SN 2007od, SN 1999em, SN 2004et, SN 2005cs and SN 1992H.

In Fig. 11 (middle) we compare the Hα velocity evolution of SN 2009bw with those of other SNe IIP. The velocity of SN 2009bw in the first two months is close to those of SNe IIP like SN 1999em, SN 2004et, SN 1992H and SN 2007od, and higher than that of SN 2005cs, which is known to have an exceptionally slow photospheric expansion. Afterwards, the photospheric velocity of SN 2009bw slowly decreases, showing a trend that is slightly different from that of other SNe II. This may be attributed to the presence of a

Table 9. Observed blackbody temperature and expansion velocities in SN 2009bw. For the Balmer lines, the velocities were measured on the red wing component.

JD (+240 0000)	Phase[a] (d)	T (K)	v(Hα) (km s^{-1})	v(Hβ) (km s^{-1})	v(He I) (km s^{-1})	v(Fe II) (km s^{-1})	v(Sc II) (km s^{-1})
54920.5	4.0	17250 ± 1000	11200 ± 2000	9180 ± 1000	9000 ± 500		
54934.3	17.8	11700 ± 700	8122 ± 200	7760 ± 120	7658 ± 122	6600 ± 400	
54936.3	19.8	8000 ± 500	8067 ± 80	7682 ± 150	7454 ± 100	5970 ± 400	5700 ± 600
54950.3	33.8	5200 ± 400	7313 ± 300	6480 ± 300		4828 ± 300	4560 ± 200
54953.5	37.0	5300 ± 500	6680 ± 200	6110 ± 200		4138 ± 100	4080 ± 140
54954.5	38.0	5200 ± 400	6660 ± 300				4080 ± 140
54955.3	39.0	5000 ± 500	6670 ± 200	6109 ± 130		4130 ± 100	4030 ± 200
54968.5	52.0	5050 ± 250	6060 ± 60	5400 ± 400		3480 ± 100	3380 ± 120
54980.5	64.0	5200 ± 300	5760 ± 300			3097 ± 80	3000 ± 200
54981.5	65.0	5250 ± 250	5759 ± 180			3000 ± 200	
54983.5	67.0	5400 ± 300	5720 ± 300	4400 ± 230		3045 ± 150	2980 ± 200
54509.5	93.0	4600 ± 200	5165 ± 150	3600 ± 180		2600 ± 300	2500 ± 150
55021.5	105.0		4430 ± 100			1960 ± 300	1910 ± 110

[a]With respect to the explosion epoch (JD 245 4916.5).

moderate/low-density CSM that changes the shape of the absorption profile of Hα (see Section 5).

In Fig. 11 (bottom) the evolution of the photospheric temperature, derived from a blackbody fit to the spectral continuum, is shown and is compared to those of the reference sample. We already mentioned that the first spectrum of SN 2009bw is quite blue, indicating high blackbody temperatures ($1.7 \pm 0.1 \times 10^4$ K). The temperature remains high also at the second epoch ($\sim$18 d). Nevertheless, the temperature evolution of SN 2009bw is normal and not so different from those of the other SNe in the sample: its ejecta is probably hotter in the first month (similar to SN 1992H) and marginally cooler than average from the plateau onwards.

4 EXPLOSION AND PROGENITOR PARAMETERS

We have inferred the physical properties of the SN 2009bw progenitor (namely, the ejected mass, the progenitor radius and the explosion energy) by performing a model/data comparison based on a simultaneous χ^2 fit of the main observables (i.e. the bolometric light curve, the evolution of line velocities and the continuum temperature at the photosphere), using the same procedure adopted for SN 2007od in Inserra et al. (2011).

According to this procedure, we employ two codes, the semi-analytic code presented in Zampieri et al. (2003) to perform a preparatory study in order to constrain the parameter space, and a new code which includes an accurate treatment of the radiative transfer and radiation hydrodynamics (Pumo, Zampieri & Turatto 2010; Pumo & Zampieri 2011), to narrower grid of models.

The application of these two codes is appropriate if the SN emission is dominated by the expanding ejecta. For SN 2009bw the contamination from interaction may in part affect the observables (cf. Section 5), and the possibility to reproduce the observed features is to be taken with caution. However, since there is no evidence that the ejecta–CSM interaction is a strong effect during most of the post-explosive evolution, our modelling can still be applied to SN 2009bw, returning a reliable estimate of the physical parameters of the explosion that can be useful to characterize its progenitor.

The distance and shock breakout epoch are taken from Table 6. In order to evaluate the *uvoir* (from optical to NIR) bolometric luminosity, we further assume that the SN has the same SED evolution as SN 1999em, and hence

$$L_{09\mathrm{bw}} = \left(L_{99\mathrm{em}}/L_{99\mathrm{em}}^{UBVRI}\right) L_{09\mathrm{bw}}^{UBVRI},$$

where $L_{09\mathrm{bw}}/L_{99\mathrm{em}}$ and $L_{09\mathrm{bw}}^{UBVRI}/L_{99\mathrm{em}}^{UBVRI}$ are the *uvoir* bolometric and quasi-bolometric luminosity of SN 2009bw and SN 1999em (Elmhamdi et al. 2003), respectively.

Assuming a ^{56}Ni mass of 0.022 $M_\odot$ (see Section 2.4), the best fits of the semi-analytic and numerical models are in fair agreement and return values for the total (kinetic plus thermal) energy of $\sim$0.3 foe, an initial radius of 3.6–7 $\times$ 10^{13} cm, and an envelope mass of 8.3–12 $M_\odot$.

The agreement between our modelling and the observed luminosity and temperature evolution is reasonably good, except at early epochs ($\lesssim$33 d, cf. Fig. 12). These discrepancies may in part be caused by some ejecta–CSM interaction (see discussion in Section 5), leading to an excess of the observed luminosity, and to the approximate initial density profile used in our simulations, which does not reproduce correctly the radial profile of the outermost high-velocity (HV) shell of the ejecta formed after shock breakout (cf. Pumo & Zampieri 2011).

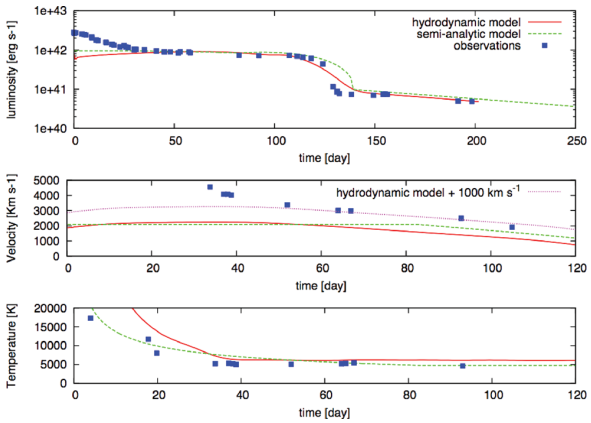

Figure 12. Comparison of the evolution of the main observables of SN 2009bw with the best-fitting models computed with the semi-analytic code (total energy $\sim$0.3 foe, initial radius 3.6 $\times$ 10^{13} cm and envelope mass 8.3 $M_\odot$) and with the relativistic, radiation-hydrodynamics code (total energy $\sim$0.3 foe, initial radius 7 $\times$ 10^{13} cm and envelope mass 12 $M_\odot$). Top, middle and bottom panels show the bolometric light curve, the photospheric velocity and the photospheric temperature as a function of time, respectively. To estimate the photospheric velocity from the observations, we used the value inferred from the Sc II lines (often considered to be a good tracer of the photosphere velocity in SNe II). The dotted purple line is the radiation-hydrodynamics model shifted by 1000 km s^{-1} to reproduce the later epochs of data (see text).

During the entire photospheric phase the best fit of the velocity is unsatisfactory. This is unusual for the Pumo and Zampieri code that has proved to work well for standard SNe II, reinforcing the idea that for SN 2009bw the ejecta–CSM interaction could be at work. Indeed, the discrepancies between the simulated photospheric velocity and the data could be related to the interaction creating a pseudo-photosphere at a larger radius, hence at a higher velocity ($\Delta v \sim 1000$ km s^{-1}), than expected by the model (cf. Fig. 12, middle panel, purple-dotted line). This effect has been found in luminous and interacting SNe as shown by Agnoletto et al. (2009).

The model parameters reported above are consistent with both a superasymptotic giant branch (SAGB) star, with a mass close to the upper limit of this class, and a progenitor of a small Fe core collapse SN with a mass close to the lower limit. They are reliable progenitors even if, through the first one is difficult to explain the amount of ^{56}Ni (e.g. Wanajo et al. 2009), instead the second one poorly explains the mass loss and the probable mixing related to the CNO elements (e.g. Maeder & Meynet 2008). However, in both scenarios, the progenitors are expected to have a radius of $\sim$1000 $R_\odot$ (Garcia-Berro & Iben 1994; Ritossa, García-Berro & Iben 1999; Woosley, Heger & Weaver 2002) and hence to fall into the RSG category (200 $< R <$ 1500 $R_\odot$).

5 DISCUSSION

In the previous sections we have presented and discussed the photometric and spectroscopic data of SN 2009bw in UGC 2890 from the photospheric to the early nebular stages.

The analysis reported in Section 2.4 indicates that SN 2009bw was a relatively luminous SN IIP with a peak magnitude similar to that of SN 1992H ($M_V = -17.67$) and an extended plateau in *V, R* and *I*. The duration of the plateau suggests an envelope mass not dissimilar from that of standard SNe IIP such as SN 1999em,

which in the nebular phase shows strong similarity with SN 2009bw both in photometry and spectroscopy. The rise to maximum seems relatively slow for an SN IIP (∼8 d) and the peak somehow broad. The light curves show a steep but shallow drop of ∼2.2 mag in ∼13 d from the end of the plateau to the tail. The tail is flat for the first couple of months, then declines with the canonical ^{56}Co decline rate of 0.98 mag (100 d)$^{-1}$. The luminosity of the radioactive tail indicates an ejected mass of ^{56}Ni of $M(^{56}\mathrm{Ni}) \sim 2.2 \times 10^{-2}\ \mathrm{M}_{\odot}$ (cf. Table 6), which is comparable to that estimated for SN 1999em (Elmhamdi et al. 2003).

The spectral evolution is quite similar to that observed in canonical SNe IIP, although an unidentified, broad feature is present in the first photospheric spectrum, at about 4600 Å. A plausible interpretation is that the feature is due to emission emerging in a region of low opacity.

The host galaxy has been classified as a highly inclined peculiar Magellanic Spiral (Sdm pec:). In the spectra, an unresolved component due to an underlying H II region is clearly visible. A reasonable assumption is to consider that the SN has the same metallicity of the H II region. From the spectra obtained at Calar Alto on 2009 September 4 and at TNG on October 11, we have measured the N2 and (only for the CAHA spectrum) the O3N2 indices (Pettini & Pagel 2004) of the H II region extracted close to the SN along the slit of the spectrograph. The average relations of Pettini & Pagel (2004) then provide the O abundances which turn out to be $12+\log(\mathrm{O/H}) = 8.66 \pm 0.06 \pm 0.41$ (where the first error is statistical and the second one is the 95 per cent spread of the N2 index calibration relation). While the projected distance from the galaxy nucleus is relatively small (2.4 kpc), we were unable to determine the deprojected one because of the very high inclination ($i = 90^{\circ}$) of the parent galaxy (Section 1). Pilyugin, Vílchez & Contini (2004) have shown that the central oxygen abundances of spiral galaxies is typically $8.3 < [12 + \log \mathrm{O/H}] < 9.1$, similar to solar abundance (8.69; Asplund et al. 2009). Therefore, the estimated progenitor metallicity is close to solar and in line with the expected metallicity at the position inside the parent galaxy.

No information is available in the literature about the X-ray and radio emission of the SN. An observation (8 ks) with *Swift*-XRT has been obtained generating a single combined and astrometrically corrected event file. In an aperture of 9 XRT pixels (∼21 arcsec) centred at the position of SN 2009bw we obtained a limit on total source counts of $n < 5$. Considering a column density of $N_{\mathrm{H}} = 1.9 \times 10^{21}$ cm^{-2} (Dickey & Lockman 1990; Predehl & Schmitt 1995), we have measured an upper limit to the X-ray flux (over the energy range 0.3–10 keV) 7.9×10^{-14} erg cm^{-2} s^{-1} corresponding to upper limits of the X-ray luminosity of $L_{\mathrm{X}} < 3.77 \times 10^{39}$ erg s^{-1} (thermal bremsstrahlung model with $kT = 10$ keV) and 1.6×10^{-13} erg cm^{-2} s^{-1} corresponding to $L_{\mathrm{X}} < 7.65 \times 10^{39}$ erg s^{-1} (power-law model with photon index $\Gamma = 1.7$). These X-ray luminosity upper limits do not preclude the possibility of a weak interaction as in SN IIP 1999em. Indeed, SN 1999em was detected at a similar phase at fainter flux (∼10^{-14} erg cm^{-2} s^{-1} in both the 2–8 and 0.4–2 keV bands) thanks to the superior performance of *Chandra*. The corresponding X-ray luminosity is one order of magnitude smaller than our upper limit [L_{X}(99em) ∼2×10^{38} erg s^{-1}, in the 0.4–8 keV range, Pooley et al. 2002] because of the much shorter distance.

However, some observational evidence points in favour of weak CSM interaction in SN 2009bw. The spectral line contrast in the early photospheric period seems smaller than in other SNe IIP (cf. panels a and b of Fig. 8), as expected in the case of resonance scattering due to external illumination of the line-forming region by CSM interaction (the so-called top lighting; Branch et al. 2000). In addition, the spectra show the presence of secondary absorptions in the H Balmer lines that we interpret as HV features. The right-hand panel of Fig. 13 shows the presence of a blue Hα

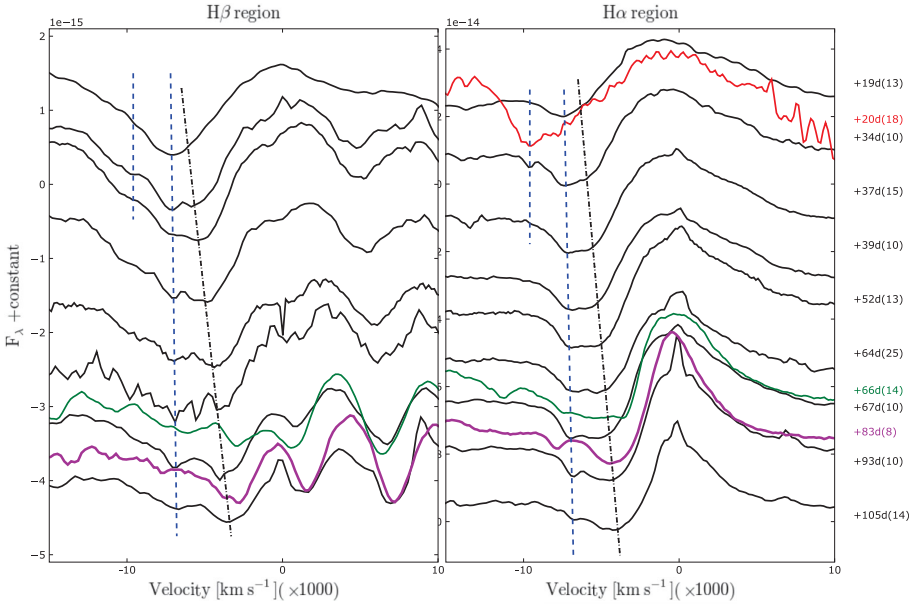

Figure 13. Zoom of the Hβ (left-hand panel) and Hα (right-hand panel) spectral regions during the plateau phase of SN 2009bw. The *x*-axes are in expansion velocity coordinates with respect to the rest-frame positions of the lines. In order to guide the eye, two black dot–dashed lines are drawn in the spectra corresponding expansion velocities. Similarly, two blue dashed lines follow the HV features of the Balmer lines. The red spectrum (+20 d) shows the NIR He I feature centred at 10830 Å. We have also reported the spectra of SN 2004dj (purple, +83 d) and SN 1999em (green, +66 d) for comparison.

component at about 7300 km s^{-1} that does not evolve with time, and a redder component decreasing progressively in velocity in analogy with other photospheric lines measured in Fig. 11. Careful analysis of Hβ (left-hand panel of Fig. 13) shows the same bluer non-evolving component as well as the photospheric one, despite the optical depth of the line being smaller than that of Hα. Blue secondary features, constant with time, were also identified in SN 1999em and SN 2004dj by Chugai, Chevalier & Utrobin (2007). According to these authors, the lines are HV components of the Balmer lines. Their analysis shows that the interaction of the ejecta of an SN IIP with an average RSG wind can be detected during the photospheric stage through the emergence of absorptions (shoulders) on the blue wings of the undisturbed H lines due to enhanced excitation of the outer unshocked ejecta. In SN 2009bw, the unshocked layers producing the HV absorptions are at about 7300 km s^{-1}, while the photospheric absorption moves from 6700 to 4400 km s^{-1} between the early and the very late photospheric phase (day 37–105). Chugai et al. (2007) also predicted that during the late photospheric phase the physical conditions in the cool dense shell behind the reverse shock allow the formation of a notch, a smaller and narrower absorption, at the fastest edge of the line, and recovered it in the spectra of SN 2004dj. We clearly see this notch with similar intensity and position in SN 2009bw starting from two months past explosion, both for Hα and Hβ. The line position is compatible with the expected position of Fe II lines at the earliest epoch, but the fact that it does not evolve disfavours such an identification.

Only one NIR spectrum is available, at an epoch (21 d) when the two components of the Balmer lines are blended. The NIR spectrum shows a strong feature at about 10500 Å. If we identify it as He I λ10830, the expansion velocity turns out to be larger ($v_{\rm He} \sim 10\,000$ km s^{-1}) than that of He I λ5876 (which has no sign of a photospheric component) and the HV Balmer components. A NIR spectrum of SN 1999em at a similar epoch is available (Elmhamdi et al. 2003), showing an absorption identified by Chugai et al. (2007) as HV He I at a velocity which was marginally higher than that of H and without a photospheric component. The alternative identification with Mg II λ10926 or Fe II λ10862 would imply even larger velocities. In conclusion, the close similarity with the features observed in SN 1999em and SN 2004dj and well modelled by Chugai et al. (2007) leads us to favour the HV Balmer component scenario. Line profile models suggest a typical RSG wind with a density of $w = \dot{M}_{-6}/u_{10} \sim 1$, i.e. $\dot{M} \sim 10^{-6}$ M$_\odot$ yr^{-1}, similar to those of SN 1999em and SN 2004dj (Chugai et al. 2007), or even higher. Assuming a typical duration of 10^6 yr, the mass lost by the progenitor star is about 1 M$_\odot$.

Late photospheric spectra of SN 2009bw show absorption features of CNO elements (see Section 3.2), indicating a potentially enhanced mixing with deep layers, which may be an indicator of a high-metallicity envelope, prone to enhance mass loss. Similar features in the red part of the optical spectra, related to the CNO elements, have been seen also in SN 1999em (Pastorello 2003) and SN 1995V (Fassia et al. 1998), both presenting signatures of weak CSM interaction (Pooley et al. 2002; Chugai et al. 2007). The presence of C in the photospheric spectra rises the possibility of CO molecules' formation, which with their rotation–vibration states are a powerful coolant and are a necessary condition for dust condensation in the ejecta. Indeed, SN 1999em showed both C in the photospheric spectra and dust formation in the inner ejecta after $t \sim 500$ d (Elmhamdi et al. 2003). In SN 2009bw there is no direct evidence of dust formation (neither photometric nor spectroscopic) though the last two points of the light curves, affected by large uncertainties, may indicate a steepening of the decline with respect to the slope of ^{56}Co.

Moriya et al. (2011) studied the interaction between SN ejecta and the CSM around RSGs. They showed that, if the temperature and the CSM density are high enough, the CSM around SNe IIP becomes optically thick and the effective photosphere forms at large radii inside the CSM. The interaction-powered phase is characterized by light curves with broad peaks, flat plateau brighter for large $\dot{M}$ and longer for an extended CSM. The observed expansion velocity at early times is expected to be that of the CSM, then turning to typical SN values when the photosphere recedes into the ejecta. In particular, the early light curves of very bright SNe IIP can be interpreted in terms of interaction with a dense CSM produced by a mass loss at a rate larger than $\sim 10^{-4}$ M$_\odot$ yr^{-1}. The ejecta–CSM interaction applied to the luminous SN 2009kf (Botticella et al. 2010) satisfactorily explained the early multicolour light curves, but failed in explaining the late behaviour and the kinematics, possibly because it was an energetic explosion with large ^{56}Ni production. We have seen above that the line profiles of SN 2009bw would point towards a normal RSG wind with a low value of $\dot{M}$, which is of the order of $\sim 10^{-6}$ M$_\odot$ yr^{-1} (or marginally higher). This is much smaller than the values expected to significantly increase the luminosity. In addition, we have not detected any unusual behaviour in the velocity evolution. Nevertheless, we cannot exclude that a fraction of the observed luminosity during the plateau of SN 2009bw might be due to the transformation of ejecta kinetic energy into radiation via interaction with the CSM. As already highlighted in Section 4, this may explain why, differently from our previous experience (Pumo & Zampieri 2011; Inserra et al. 2011; Pastorello et al. 2012) where the main observables are simultaneously reproduced by our modelling, here we fail to reproduce the kinetic evolution, whilst both the bolometric light curve (cf. Fig. 5) and the spectra in the nebular phase (cf. panel d of Fig. 8) are standard and very similar to those of SN 1999em.

As reported in Section 4, the ejecta mass is $\sim$8–12 M$_\odot$. Accounting for a compact remnant (NS) of $\sim$1.6 and about 1 M$_\odot$ of mass loss, the initial mass of the progenitor is of the order of 11–15 M$_\odot$, comparable with that of massive SAGB stars or a low-mass Fe CC-SN progenitor. Despite that, we want to note that the weak intensity of [O I] $\lambda\lambda$6300–6363 may be inconsistent with the progenitor mass (too high for the intensity observed), but the similarity between the late spectra of SN 2009bw and SN 1999em and the previous modelling case of the weak interacting SN 2007od (Inserra et al. 2011) are in favour of this mass range.

6 CONCLUSIONS

In this paper we show, for the first time, photospheric and spectroscopic data of SN 2009bw. The peak ($M_R = -17.82$) and the plateau ($M_R = -17.37$) magnitudes allow us to accommodate this SN in the small sample of the brightest SNe IIP. The fast jump from the plateau phase to the nebular tail ($\sim$2.2 mag in 13 d, unusual among bright SNe II), the proof of the presence of CNO elements in the photospheric spectra and the detection of HV features in the Balmer lines during the recombination phase, suggesting an early interaction, make this object atypical in the context of SNe IIP events.

The well-sampled light curve of SN 2009bw reaches a luminous plateau at $M_R = -17.37$ between $\sim$50 and 100 d. This is a standard duration for the plateau phase in SNe IIP. The high photospheric

luminosity contrasts with the moderate luminosity of the tail (similar to that of SN 1999em). The post-plateau decline is relatively rapid, resembles that of SN 1986L (although this object has not been well studied; Hamuy 2001) and has been well monitored, making this constraint rather solid. The remarkable magnitude drop is analogous to that observed in faint SNe IIP (Pastorello et al. 2004). The bolometric light curve tail follows the slope expected if the main energy source is the decay of ^{56}Co into ^{56}Fe. The ^{56}Ni mass derived from the quasi-bolometric (U to I) light curve is $M(^{56}\mathrm{Ni})\sim0.022$ $\mathrm{M}_{\odot}$, similar to that of the prototypical SN IIP 1999em. If instead, the ^{56}Ni mass is estimated from the post-plateau drop with a steepness $S = 0.57$, then $M(^{56}\mathrm{Ni})\sim0.002\,\mathrm{M}_{\odot}$ is obtained. This value suggests that for SN 2009bw the anti-correlation between the steepness function and ^{56}Ni mass does not work in this case, possibly masked by the presence of other effects, such as CSM interaction or dust formation.

Thanks to detailed synthetical spectral computed using the LTE code SYNOW, we noted the presence of the Si II λ6355 feature in the early spectra and of CNO element lines in the plateau spectra. Highly ionized C and N features have been tentatively identified in our first spectrum as being responsible for the prominent blend at 4600 Å. HV line components of the Balmer series (Hα and Hβ at $v \sim 7300\,\mathrm{km\,s^{-1}}$) have been clearly identified in the plateau spectra from $\sim$37 d onwards, though they become more prominent from day 52 to 105. These lines, similar to those observed in SN 2004dj and SN 1999em (Chugai et al. 2007), suggest an early interaction with a barely dense CSM. Based on the similitude between SN 2009bw and SN 1999em, the absence of remarkable changes in the light curve (see Moriya et al. 2011) and the early line velocity evolution, we roughly estimate the progenitor's mass loss to be in the range $10^{-6} < \dot{M} < 10^{-4}\,\mathrm{M}_{\odot}\,\mathrm{yr}^{-1}$, even though it is probably closer to the lower limit. Assuming a typical duration of 10^6 yr, the mass lost by the progenitor star is $1\,\mathrm{M}_{\odot}$. Our latest spectra have been useful to estimate the N2 and O3N2 indices (Pettini & Pagel 2004), revealing an average oxygen abundance of 12+log(O/H) $\sim$ 8.66, which corresponds to about solar metallicity.

The presence of CNO elements, the similarities with SN 1999em at late phase and the increased slope of the radioactive tail as suggested by the last two photometric points (although with a large uncertainty) might indicate late dust formation in the inner ejecta.

Modelling gives to us an ejecta mass of 8–12 $\mathrm{M}_{\odot}$, corresponding to an initial mass of the progenitor of the order of 11–15 $\mathrm{M}_{\odot}$. This is consistent with an RSG, which could be both with a massive SAGB star or a star exploded as small Fe CC-SN, explaining the most part of the peculiarities (early interaction, ^{56}Ni mass and CNO elements) of this object. The unsatisfactory fit of the velocity during the entire photospheric phase strengthens the idea of ejecta–CSM interaction. In fact, the interaction could have caused the formation of a pseudo-photosphere at a radius larger than expected by the model.

SN 2009bw shows some properties in common with both luminous and standard SNe IIP. Our study has revealed the following: (i) HV features as in SN 1999em, SN 2004dj and SN 2007od; (ii) ejecta–CSM interaction ongoing during the entire photospheric phase, reinforcing the idea that interaction can be significant also for SNe IIP; and (iii) the presence of CNO elements seen in few SNe IIP. Luminous SNe IIP with weak CSM interaction may bridge the gap between normal SNe IIP and interaction-dominated SNe IIn, and may thus be helpful to create a united scheme of all CC explosions.

ACKNOWLEDGMENTS

CI, SB, FB, EC and MT are partially supported by the PRIN-INAF 2009 with the project 'Supernovae Variety and Nucleosynthesis Yields' and by the grant ASI-INAF I/009/10/0. EB was supported in part by SFB 676, GRK 1354 from the DFG, NSF grant AST-0707704 and US DOE Grant DE-FG02-07ER41517. MLP acknowledges the financial support by the Bonino-Pulejo Foundation. The TriGrid VL project, the *'consorzio COMETA'* and the INAF - Padua Astronomical Observatory are also acknowledged for computer facilities. ST acknowledges support by the Transregional Collaborative Research Center TRR33 'The Dark Universe' of the German Research Fondation (DFG). DYT and NNP were partly supported by the Grant 10-02-00249 from RFBR. We thank the support astronomers at the Telescopio Nazionale Galileo, the Copernico Telescope, the 2.2-m Telescope at Calar Alto, the Liverpool Telescope, the Nordic Optical Telescope, the SAO-RAS Observatory and the Taurus Hill Observatory for performing the follow-up observations of SN 2009bw. CI thanks the Oklahoma University for the hospitality. This research has made use of the NASA/IPAC Extragalactic Database (NED) which is operated by the Jet Propulsion Laboratory, California Institute of Technology, under contract with the National Aeronautics and Space Administration. We acknowledge the usage of the HyperLeda data base (http://leda.univ-lyon1.fr). We also thank the High Energy Astrophysics Science Archive Research Center (HEASARC), provided by NASA's Goddard Space Flight Center, for the *Swift* data. The Supernova Spectrum Archive (SUSPECT, http://suspect.nhn.ou.edu/ suspect/) was used to access data, and the availability of this service is gratefully acknowledge.

REFERENCES

Agnoletto I., et al., 2009, ApJ, 691, 1348
Arnett W. D., 1996, Supernovae and Nucleosynthesis. Princeton Univ. Press, Princeton, NJ
Arnett W. D., Bahcall J. N., Kirshner R. P., Woosley S. E., 1989, ARA&A, 27, 629
Asplund M., Grevesse N., Sauval A. J., Scott P., 2009, ARA&A, 47, 481
Barbon R., Ciatti F., Rosino L., 1979, A&A, 72, 287
Baron E., et al., 2000, ApJ, 545, 444
Botticella M. T., et al., 2010, ApJ, 717, L52
Branch D., Jeffery D. J., Blaylock M., Hatano K., 2000, PASP, 112, 217
Cappellaro E., Mazzali P. A., Benetti S., Danziger I. J., Turatto M., della Valle M., Patat F., 1997, A&A, 328, 203
Chugai N. N., Chevalier R. A., Utrobin V. P., 2007, ApJ, 662, 1136
Clocchiatti A., et al., 1996, AJ, 111, 1286
Dessart L., Hillier D. J., 2005, A&A, 437, 667
Dickey J. M., Lockman F. J., 1990, ARA&A, 28, 215
Elmhamdi A., et al., 2003, MNRAS, 338, 939
Elmhamdi A., Chugai N. N., Danziger I. J., 2003, A&A, 404, 1077
Fassia A., Meikle W. P. S., Geballe T. R., Walton N. A., Pollacco D. L., Rutten R. G. M., Tinney C., 1998, MNRAS, 299, 150
Fassia A., et al., 2001, MNRAS, 325, 907
Fisher A., 2000, PhD thesis, Univ. Oklahoma
Garcia-Berro E., Iben I., 1994, ApJ, 434, 306
Hamuy M. A., 2001, PhD thesis, Univ. Arizona
Hamuy M., 2003, ApJ, 582, 905
Harutyunyan A. H., et al., 2008, A&A, 488, 383
Heger A., Fryer C. L., Woosley S. E., Langer N., Hartmann D. H., 2003, ApJ, 591, 288
Inserra C., et al., 2011, MNRAS, 417, 261
Landolt A. U., 1992, AJ, 104, 340

Maeder A., Meynet G., 2008, in de Koter A., Smith L. J., Waters L. B. F. M., eds, ASP Conf. Ser. Vol. 388, Mass Loss from Stars and the Evolution of Stellar Clusters. Astron. Soc. Pac., San Francisco, p. 3
Maguire K., et al., 2010, MNRAS, 404, 981
Moriya T., Tominaga N., Blinnikov S. I., Baklanov P. V., Sorokina E. I., 2011, MNRAS, 415, 199
Mould J. R., et al., 2000, ApJ, 529, 786
Nissinen M., Heikkinen E.P, Hentunen V.-P., 2009, Cent. Bureau Electron. Telegram, 1743, 1
Pastorello A., 2003, PhD thesis, Univ. Padova
Pastorello A., et al., 2004, MNRAS, 347, 74
Pastorello A., et al., 2006, MNRAS, 370, 1752
Pastorello A., et al., 2009, MNRAS, 394, 2266
Pastorello A., et al., 2010, ApJ, 724, L16
Pastorello A. et al., 2012, A&A, 537, A141
Patat F., Barbon R., Cappellaro E., Turatto M., 1994, A&A, 282, 731
Pettini M., Pagel B. E. J., 2004, MNRAS, 348, L59
Pilyugin L. S., Vílchez J. M., Contini T., 2004, A&A, 425, 849
Poole T. S., et al., 2008, MNRAS, 383, 627
Pooley D., et al., 2002, ApJ, 572, 932
Poznanski D., Ganeshalingam M., Silverman J. M., Filippenko A. V., 2011, MNRAS, 415, L81
Predehl P., Schmitt J. H. M. M., 1995, A&A, 293, 889
Pumo M. L., Zampieri L., 2011, ApJ, 741, 41
Pumo M. L., et al., 2009, ApJ, 705, L138
Pumo M. L., Zampieri L., Turatto M., 2010, Mem. Soc. Astron. Ital. Suppl., 14, 123
Quimby R. M., Wheeler J. C., Höflich P., Akerlof C. W., Brown P. J., Rykoff E. S., 2007, ApJ, 666, 1093
Quimby R. M., et al., 2011, Nat, 474, 487
Richardson D., Branch D., Casebeer D., Millard J., Thomas R. C., Baron E., 2002, AJ, 123, 745
Ritossa C., García-Berro E., Iben I., Jr, 1999, ApJ, 515, 381
Rutten R. J., 2003, Utrecht University Lecture Notes, 8th edn, Radiative Transfer in Stellar Atmospheres
Schlegel E. M., 1990, MNRAS, 244, 269
Schlegel D. J., Finkbeiner D. P., Davis M., 1998, ApJ, 500, 525
Schmidt B. P. et al., 1993, AJ, 105, 2236
Smartt S. J., 2009, ARA&A, 47, 63
Smartt S. J., Eldridge J. J., Crockett R. M., Maund J. R., 2009, MNRAS, 395, 1409
Sollerman J., Cumming R. J., Lundqvist P., 1998, ApJ, 493, 933
Stanishev V., Adamo A., Micheva G., 2009, Cent. Bureau Electron. Telegram, 1746, 1
Suntzeff N. B., Bouchet P., 1990, AJ, 99, 650
Tsamis Y. G., Barlow M. J., Liu X.-W., Danziger I. J., Storey P. J., 2003, MNRAS, 338, 687
Tully R. B., Rizzi L., Shaya E. J., Courtois H. M., Makarov D. I., Jacobs B. A., 2009, AJ, 138, 323
Turatto M., Cappellaro E., Barbon R., della Valle M., Ortolani S., Rosino L., 1990, AJ, 100, 771
Turatto M., Benetti S., Cappellaro E., 2003, in Hillebrandt W., Leibundgut B., eds, ESO Astrophys. Symp. Vol. XVII, From Twilight to Highlight: the Physics of Supernovae. Springer-Verlag, Berlin, p. 200
Wanajo S., Nomoto K., Janka H.-T., Kitaura F. S., Müller B., 2009, ApJ, 695, 208
Woosley S. E., Hartmann D., Pinto P. A., 1989, ApJ, 346, 395
Woosley S. E., Heger A., Weaver T. A., 2002, Rev. Modern Phys., 74, 1015
Zampieri L., Pastorello A., Turatto M., Cappellaro E., Benetti S., Altavilla G., Mazzali P., Hamuy M., 2003, MNRAS, 338, 711

This paper has been typeset from a TEX/LATEX file prepared by the author.

Monthly Notices
of the
ROYAL ASTRONOMICAL SOCIETY

Mon. Not. R. Astron. Soc. **422,** 1178–1185 (2012) doi:10.1111/j.1365-2966.2012.20691.x

Quantitative photospheric spectral analysis of the Type IIP supernova 2007od

C. Inserra,[1,2,3⋆] E. Baron[3,4,5] and M. Turatto[6]

[1]*Dipartimento di Fisica ed Astronomia, Universita' di Catania, Sezione Astrofisica, Via S.Sofia 78, 95123 Catania, Italy*
[2]*INAF – Osservatorio Astrofisico di Catania, Via S.Sofia 78, 95123 Catania, Italy*
[3]*Homer L. Dodge Department of Physics and Astronomy, University of Oklahoma, Norman, OK 73019, USA*
[4]*Hamburger Sternwarte, Gojenbergsweg 112, 21029 Hamburg, Germany*
[5]*Computational Research Division, Lawrence Berkeley National Laboratory, MS 50F-1650, 1 Cyclotron Road, Berkeley, CA 94720, USA*
[6]*INAF – Osservatorio Astronomico di Trieste, Via Tiepolo 11, 34143 Trieste, Italy*

Accepted 2012 February 3. Received 2012 February 3; in original form 2011 May 23

ABSTRACT

We compare and analyse a time series of spectral observations obtained during the first 30 d of evolution of SN 2007od with the non-local thermodynamic equilibrium code PHOENIX. Despite some spectroscopic particularities in the Balmer features, this supernova appears to be a normal Type II, and the fits proposed are generally in good agreement with the observations. As a starting point, we have carried out an analysis with the parametrized synthetic spectrum code SYNOW to confirm line identifications and to highlight differences between the results of the two codes. The analysis computed using PHOENIX suggests the presence of a high-velocity feature in Hβ and an Hα profile reproduced with a density profile steeper than that of the other elements. We also show a detailed analysis of the ions velocities of the six synthetic spectra. The distance is estimated for each epoch with the spectral-fitting expanding atmosphere method. Consistent results are found using all the spectra which give the explosion date of JD 245 4403 (2007 October 29) and a distance modulus $\mu = 32.2 \pm 0.3$.

Key words: line: identification – supernovae: general – supernovae: individual: SN 2007od – galaxies: distances and redshifts.

1 INTRODUCTION

SN 2007od, was discovered on 2007 November 2.85 UT in the nearby galaxy UGC 12846 (Mikuz & Maticic 2007). Blondin & Calkins (2007) classified it as a normal Type IIP supernova (SN IIP) about two weeks after explosion, and reported some similarity with the spectrum of the SN II 1999em, 10 d after explosion. SN 2007od, exploded in the Magellanic Spiral (Sm:) galaxy UGC 12846, which has a heliocentric recession velocity of 1734 ± 3 km s^{-1}, a distance modulus of 32.05 ± 0.15 and an adopted reddening of $E_{\rm tot}(B-V) = 0.038$ (Inserra et al. 2011). Extensive studies of the photospheric and nebular periods have been presented in Andrews et al. (2010) and Inserra et al. (2011).

SN 2007od, showed a peak and plateau magnitude, $M_V = -18.0$ and -17.7, respectively (Inserra et al. 2011), brighter than common SNe IIP (Patat et al. 1994; Richardson et al. 2002), but the luminosity on the tail is comparable with that of the faint SN 2005cs (Pastorello et al. 2009). The luminosity on the tail was affected by the early formation of dust ($\lesssim$220 d after explosion; Andrews et al. 2010). Based on mid-infrared observations in the nebular phase, the amount of dust has been determined to be up to 4.2×10^{-4} M$_\odot$ (Andrews et al. 2010) and the ejected mass ^{56}Ni $\sim 2 \times 10^{-2}$ M$_\odot$ (Inserra et al. 2011).

This object also shows interaction with a circumstellar medium (CSM). There is some evidence, in the form of high-velocity (HV) features, for weak interaction soon after the outburst and solid observational evidence for interaction in the nebular phase (Inserra et al. 2011). However, due to the good temporal coverage, the position inside the host galaxy and the low observed reddening, this SN is a good candidate for analysis by the generalized stellar atmosphere code PHOENIX in order to learn more about its physical structure. In Section 2, we present the codes and the strategy applied for modelling. In Section 3, we show the synthetic spectra and the comparison with observed spectra, while in Section 4 we provide an analysis of the principal characteristics of the synthetic spectra. A conclusion follows in Section 5.

2 METHOD

The preliminary line identification in the spectra of SN 2007od, confirming those obtained by Inserra et al. (2011), has been performed using the fast, parametrized SN synthetic spectra code SYNOW. The

⋆E-mail: cosimo.inserra@oact.inaf.it

code is discussed in detail by Fisher (2000) and recent applications include Branch et al. (2002), Moskvitin et al. (2010) and Roy et al. (2011). SYNOW assumes the Schuster–Schwarzschild approximation and the source function is assumed to be given by resonant scattering, treated in the Sobolev approximation. It correctly accounts for the effects of multiple scattering.

For a subsequent, more detailed analysis, we have used the generalized stellar atmospheres code PHOENIX (Hauschildt & Baron 2004, 1999). The code includes a large number of non-local thermodynamic equilibrium (NLTE) and LTE background spectral lines and solves the radiative transfer equation with a full characteristics piecewise parabolic method (Hauschildt 1992) without simple approximations such as the Sobolev approximation (Mihalas 1970). The process that solves the radiative transfer and the rate equations with the condition of radiative equilibrium is repeated until the radiation field and the matter converge to radiative equilibrium in the Lagrangian frame. These calculations assume a compositionally homogeneous atmosphere with a power-law density and steady-state conditions in the atmosphere.

3 SPECTRA MODELS

We have modelled the first six observed photospheric spectra, covering a period from 5 to 27 d since the adopted explosion date JD = 245 4404 ± 5 (∼2007 October 30; Inserra et al. 2011). The most interesting spectra are the first one of the series (5 d), with a flat-top Hα profile and two uncommon features at about 4400 and 6250 Å, and the last one (27 d), which has the best signal-to-noise ratio (S/N) among the plateau spectra. The detailed, comparative study of these epochs provides important information about the presence of ions and possible CSM interaction at early times.

Fig. 1 shows the line identifications determined by the SYNOW analysis for the first spectrum, obtained using $T_{\rm bb} \sim 12\,000$ K, $v_{\rm phot} \sim 7800\,{\rm km\,s^{-1}}$, optical depth $\tau(v)$ parametrized as a power law of index $n = 9$ and $T_{\rm exc} = 10\,000$ K assumed to be the same for all ions. The features visible in Fig. 1 are produced by only six chemical species. The P Cygni profiles of the Balmer lines are clearly visible, as well as He I λ5876, and significant contributions due to Ca II, Fe II, Ba II and Si II. The Balmer lines have been detached from the photosphere to better match the observed velocity. The uncommon lines mentioned above are identified as Ba II (λ4524) and Si II (λ6355). In our attempts, we have considered also the possible presence of N II λ4623, but the poor fit and the lack of N II λ5029 and N II λ5679 lines (stronger than the first one) lead us to the conclusion that there is no enhanced N in the spectra of SN 2007od, (cf. Inserra et al. 2011).

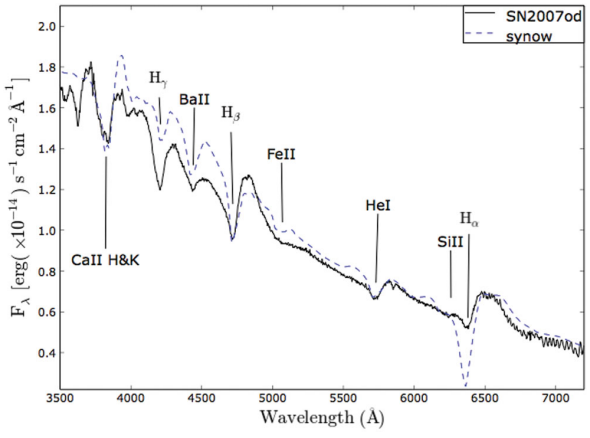

Figure 1. Comparison between the optical spectrum of SN 2007od, at 5 d post-explosion (JD 245 4404) and the SYNOW synthetic spectrum (for composition of synthetic spectra, see text).

Table 1. Parameters of PHOENIX models of SN 2007od,.

JD +240 0000	Phase[a] (d)	$T^b_{\rm model}$ (K)	v_0 (km s^{-1})	n^c	r (10^{14} cm)	L (10^{41} erg s^{-1})
54409.5	5.5	8000	7600	13	3.6	3.8
54412.5	8.5	7400	7200	9	5.3	6.0
54413.2	9.2	7300	7050	9	5.6	6.3
54417.4	13.4	6800	6000	9	6.9	7.2
54421.4	17.4	6200	5400	9	8.1	6.9
54431.5	27.5	6000	5000	9	11.9	13.1

[a]With respect to the explosion epoch (JD 245 4404) from Inserra et al. (2011).
[b]With a total $E(B-V) = 0.038$ (Inserra et al. 2011).
[c]Index of power-law density function.

With the adopted reddening [$E(B-V) = 0.038$] and the ions suggested by the SYNOW analysis, we have computed a grid of detailed fully line-blanketed PHOENIX models. We have explored variations in multiple parameters for each epoch adjusting the total bolometric luminosity in the observer's frame (parametrized by a model temperature, $T_{\rm model}$), the photospheric velocity (v_0), the metallicity (the solar abundances were those of Grevesse & Sauval 1998) and the density profile (described by a power law $\rho \propto r^{-n}$). Gamma-ray deposition was assumed to follow the density profile. We noted an increase of the emission profiles, especially those of Balmer lines, with the increase of gamma-ray deposition. However, in our final models the gamma-ray deposition was not included. We have estimated the best set of model parameters by performing a simultaneous χ^2 fit of the main observables. The relevant parameters for SN 2007od, for the entire early evolution are reported in Table 1, while the fits are shown in Figs 2 and 3.

In the first PHOENIX spectra, we have treated in NLTE the following ions: H I, He I, He II, Si I, Si II, Ca II, Fe I, Fe II, Ba I, Ba II. He I, Si I, Fe I and Ba I have been considered to reproduce the ionization levels of the corresponding atoms. The opacity for all other ions is treated

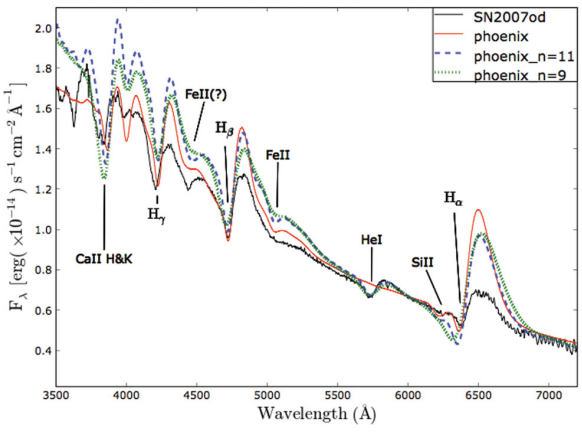

Figure 2. Comparison between the optical spectrum of SN 2007od, at 5 d post-explosion (JD 245 4404) and PHOENIX full NLTE spectra. The model parameters are those of the first row of Table 1 but for the n index reported in the legend.

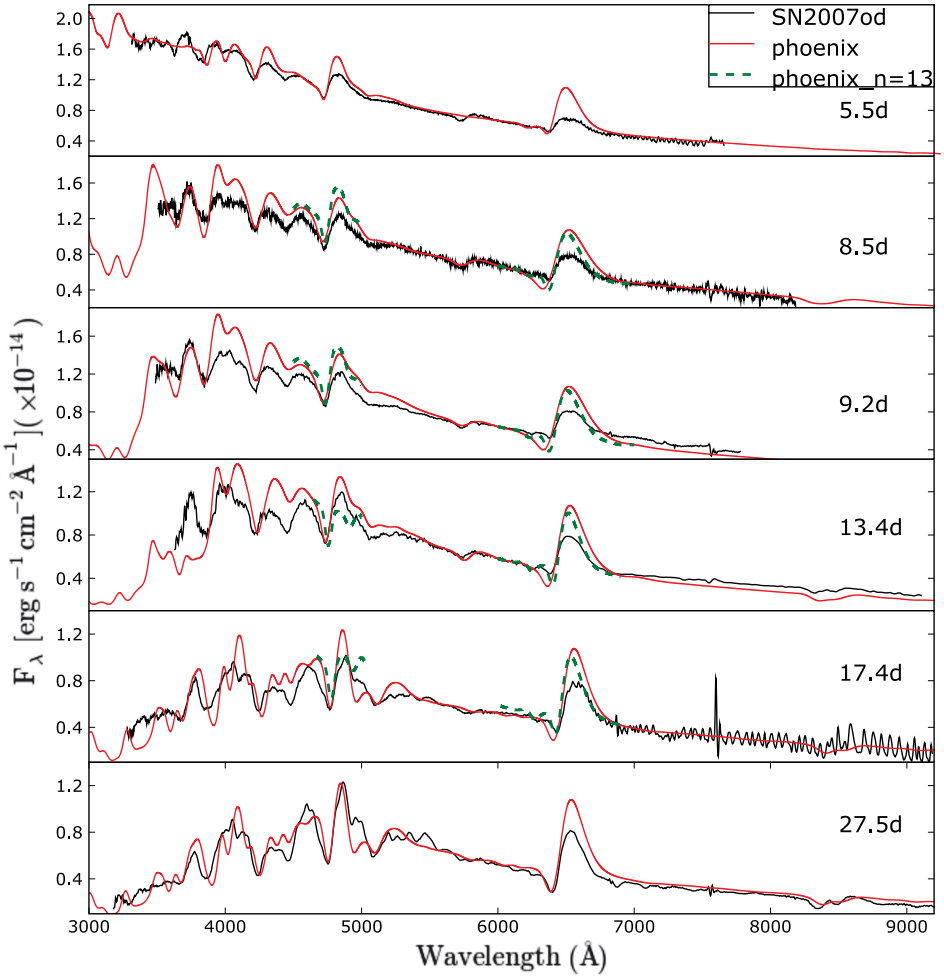

Figure 3. PHOENIX spectral evolution compared with observed spectrum. Model parameters for best-fitting spectra (red) are listed in Table 1. The dashed green lines in the spectra between day 8.5 and 17.4 in the Hβ and Hα regions are the line profiles computed with a density index $n = 13$.

in LTE with a constant thermalization parameter $\epsilon = 0.05$ (see Baron et al. 1996b, for further details). As shown in Fig. 2, there is no line that corresponds to Ba II, even though the identification for the absorption at 4400 Å seemed plausible in the SYNOW analysis. The temperature is too high to produce a Ba II line, all the more so with the observed strength. The presence of Ba II was checked by calculating a set of single ion spectra, i.e. calculating the spectrum with all continuum opacities, and only lines from Ba II as well as via the inverse procedure of turning off the line opacity from Ba II. The same procedure was performed for the He I ion, in order to study the feature that could arise around 4471 Å but no significant contribution can be seen in the synthetic spectra. The closest line to the 4440 Å feature is due to Fe II, though it is not as strong as in the observed spectrum. The evolution of the 4440 Å region (shown in Fig. 4) displays the inconsistency. The Fe II line explains the feature starting from day 9, though the velocity does not match the observed line position. It is likely that the observed profile of the 4440 Å feature is due to the combination of this line with HV feature of Hβ, formed by an increased line opacity that our simplified model ($\rho \propto r^{-n}$) is not able to reproduce (the HV features are discussed in Inserra et al. 2011). Though Ba II identification provided by SYNOW is not completely ruled out by the NLTE analysis, however, we consider it unlikely.

The presence of Si II at 6530 Å is confirmed by the PHOENIX analysis, despite the weakness of the synthetic feature. In Fig. 2, it is barely visible, but the same analysis performed for Ba II confirms its identification. The presence of Si II in SNe IIP is not uncommon. The other absorption features are successfully reproduced, except for Hα (see Section 4) and the absorption lines in the region of 3600 Å that are possibly related to Ti II, not included in the first NLTE spectra in order to minimize CPU time. As shown in Fig. 2, we tried different density indices to better match the entire profile. The best match for the overall spectrum is given by the model with $n = 13$ (in all figures, the best PHOENIX model is always plotted in red), even if the strengths, with respect to the normalized continuum, of Hγ and He I are better reproduced by the models with a density exponent lower than $n = 13$. The steeper density profile leads to greater emission than models with flatter density profiles.

Both the second (8.5 d) and third (9.2 d) spectra have been constructed using the same set-up that was used to calculate the first spectrum, except that the density index was decreased from 13 to 9. A profile steeper than $n = 9$ better reproduces the absorption profile

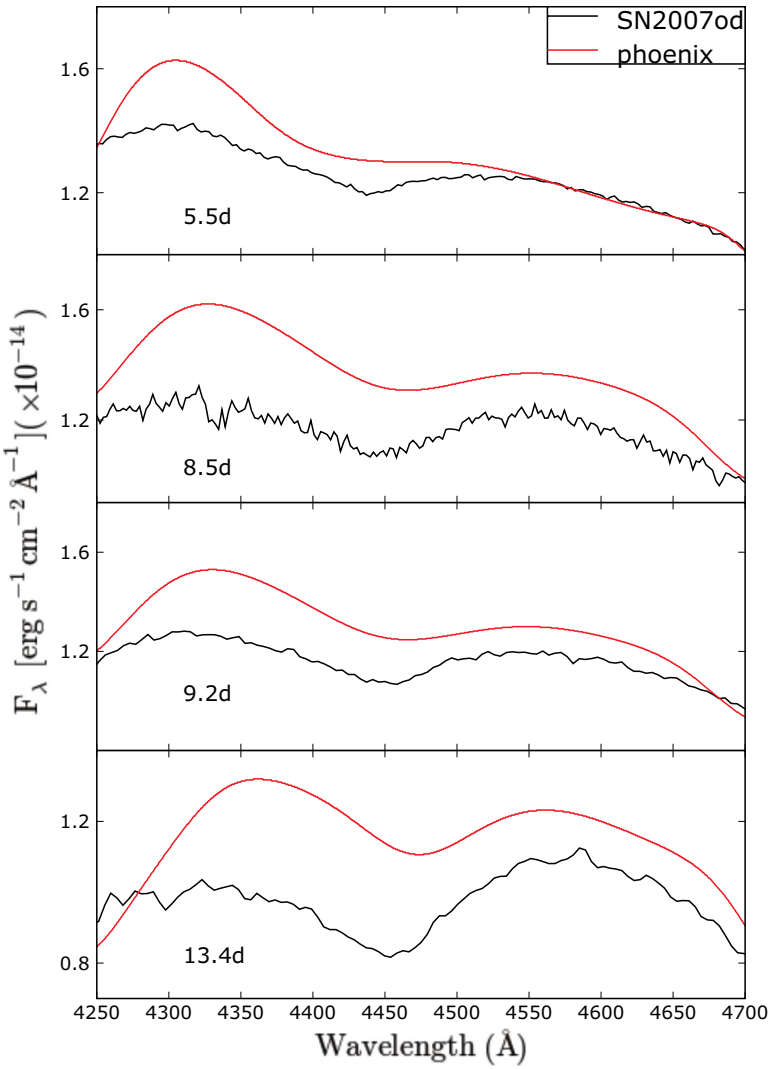

Figure 4. A blow-up of the 4440 Å region where the PHOENIX synthetic spectra are compared to observed ones.

of the Balmer lines, as seen in first epoch, but all the models show flux slightly higher bluewards of 5500 Å and especially at about 4000 Å. Also the strength of Hγ is greater than observed in the model with $n > 9$. The flux on the blue side of Ca II H&K is lower than observed. We found that a steeper density profile enhances the discrepancy between the observed and synthetic H&K line profile.

In general, the line profiles suggest a density distribution more complex that a single power law. Our calculations suggest that perhaps a broken power law would better reproduce the observed spectra, with a shallower density profile at lower velocities and a steeper profile at higher velocities. The Ca II or He I ions are clearly better reproduced by a density index close to 9, while the metal elements (e.g. Fe and Si) which form close to the photosphere (and are relatively weak) are less sensitive to the assumed density profile. The Fe I, Fe II and Si II are well reproduced with all density profiles, even if the steeper profile better reproduces the Si II profile than the flatter profile (see Fig. 2). While the more complex density profile could be intrinsic in the initial structure, it is also possible that early interaction of the SN ejecta with a close-in circumstellar region affects the line profiles. Indeed, the flat-topped nature of the Balmer lines may indicate circumstellar interaction. A broken power-law density distribution of the ejecta has been claimed also by Utrobin & Chugai (2011) in the case of SN 2000cb. To illustrate the case, we have overplotted in Fig. 3 the Hβ and Hα regions obtained by $n = 13$ models (green dashed line) for the spectra from 8.5 to 17.4 d.

The spectra at 13.4 and 17.4 d show the increasing effects of a few metal lines such as Fe II λ5169 and Sc II λ6300 that indicate the lower temperature at the beginning of the plateau phase. Moreover, the presence of metal ions changes the flux at ∼3800 Å in the spectra at 13 d. From this epoch onwards, the 4440 Å feature seems more clearly related to Fe II, strengthening our conclusion for the absence of Ba II.

The final spectrum we analyse was obtained on 2007 November 27 (27 d) when the SN is solidly on the plateau. At this epoch, the metal lines are fully developed, as is the Na I D feature that has replaced the He I λ5876 line. Thanks to the broad wavelength coverage, the good resolution (11 Å) and the high S/N (60), this is the best available spectrum of SN 2007od.

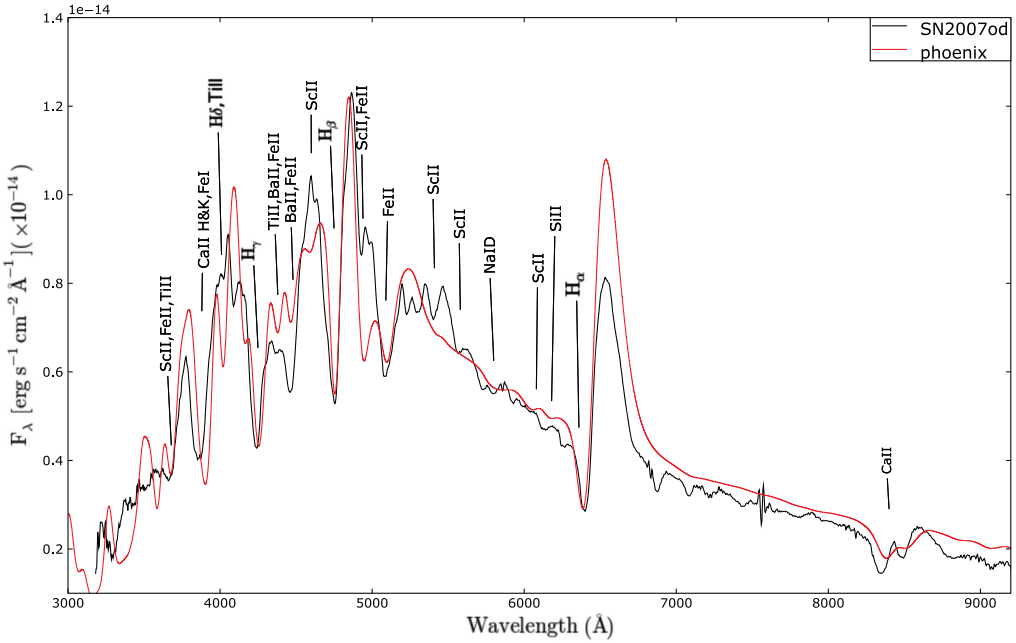

Figure 5. Comparison between the optical spectrum of SN 2007od, at 27 d post-explosion (JD 245 4404) and the PHOENIX full NLTE spectrum (for model parameters, see Table 1).

Fig. 5 displays our best NLTE model. The species treated in NLTE are H I, Na I, Si I, Si II, Ca II, Sc I, Sc II, Ti I, Ti II, Fe I, Fe II, Ba I and Ba II. Here, more than at earlier epochs, the presence of the neutral species changes the strength of some lines, especially in the blue (<4000 Å) and around 5000 Å. The H lines, Na I D, Fe II λ5169, Sc II λ5658 and Sc II λ6245 are well fitted. The Ca II lines also are well fitted. Other lines fit fairly well in terms of velocity width, but not necessarily in total flux. This is due to the fact that many lines are blended with others.

All models have solar abundances and metallicity. We studied the effects of reducing the model metallicity to that deduced for the SN 2007od, environment ($Z < 0.004$; see Inserra et al. 2011), but the changes in the spectra were negligible at the 3σ level.

The comparative evolution of SN 2007od has been discussed in section 3.3 of Inserra et al. (2011). The most interesting features noted in the earliest phases were the 4400 Å absorption and the boxy profile of the Balmer lines. In Fig. 6, we compare the spectra of SN 2007od at two phases (day 5.5 and day 27) with those of SN 1999em, the most similar SN IIP as determined by GELATO analysis (Harutyunyan et al. 2008), and with the two corresponding best synthetic spectra. Indeed, the overall similarity is remarkable. However, there are also interesting differences, in addition to the two major ones mentioned above. At the first epoch, the expansion velocity is larger in SN 1999em [full width at half-maximum, $\mathrm{FWHM(H}\alpha)_{99\mathrm{em}} \sim 11000 > \mathrm{FWHM(H}\alpha)_{07\mathrm{od}} \sim 9000\,\mathrm{km\,s^{-1}}$], while at the second epoch SN 2007od is faster than SN 1999em [$\mathrm{FWHM(H}\alpha)_{07\mathrm{od}} \sim 7000 > \mathrm{FWHM(H}\alpha)_{99\mathrm{em}} \sim 5500\,\mathrm{km\,s^{-1}}$]. However, the epochs are offset, so evolution could play a role. The slower velocity evolution of SN 2007od was already noted by Inserra et al. (2011). The model is able to reproduce consistently the spectra of SN 2007od at both epochs. The other major difference is in the line contrast. Considering the ongoing early interaction, we can interpret the effect as due to toplighting (Branch et al. 2000), which smooths the line contrast. At the second epoch, the difference between the line profiles of the two objects and the model is reduced.

4 ANALYSIS

The expansion velocities of Hα, Hβ, He I λ5876 and Fe II λ5169 as derived from fitting the absorption minima of the PHOENIX spectra are shown in Fig. 7, together with the measured values in the observed spectra. The filled symbols indicate the spectra shown in Fig. 3 (reported in Table 1), while the open symbols refer to spectra calculated with different density indexes ($n = 9$ for the first epoch, $n = 13$ for the following epochs).

In Figs 7 (top left-hand panel) and 3, the absorption minima in the NLTE ($n = 9$) spectra for Hα are too blue when compared with the observed spectra, particularly for the first three epochs. Instead, the models with $n = 13$ better reproduce the observed velocity. This could be due to several effects. The simple uniform power-law density profile, assumed here, may not be accurate enough to describe the ejecta. Also, ionization effects, perhaps due to circumstellar interaction, may reduce the Balmer occupations over those that are predicted in the $n = 9$ models. Combined with the evidence of the flat-top emission, it is somewhat possible that circumstellar interaction effects are responsible for the observed shape of the Balmer lines and for the different density profiles. The effect disappears with time. Also for Hβ, the PHOENIX and the observed velocity from 13.4 d are comparable within the errors for both models. From day 8.5 and onwards, the $n = 9$ models better reproduce the Hβ profile in velocity and strength. Neither He I nor Fe II shows this behaviour in the early epochs, indicating that the effect is most likely confined to the outermost layers of the ejecta. Except for the epochs reported above, all the line velocities are slightly smaller than observed. Though we have not included time-dependent rates in this calculation, this effect seems not so likely to explain the discrepancy

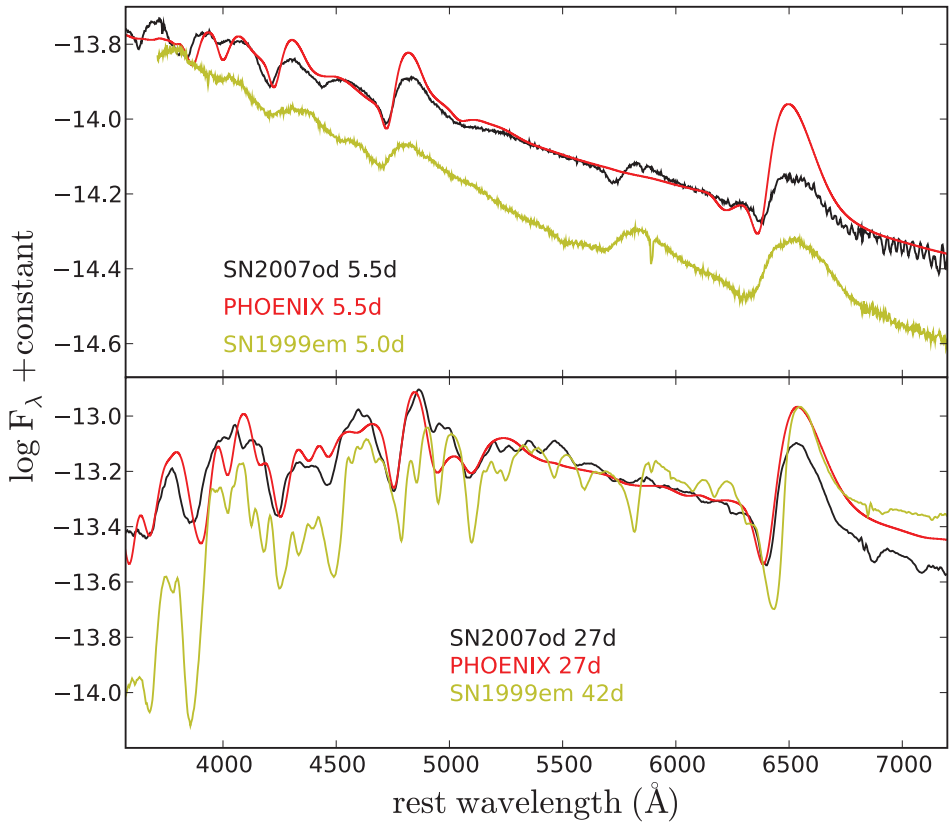

Figure 6. Comparison between observed spectra of SN 2007od, PHOENIX full NLTE spectra (for model parameters, see Table 1) and SN 1999em spectra at the first (top) and last epoch (bottom) of our series.

between the velocity of the synthetic and observed Hα (Utrobin & Chugai 2005; Dessart & Hillier 2007; De, Baron & Hauschildt 2009, 2010).

Clearly, our simplistic models do not reproduce the HV feature of Hβ and overestimate the emission strength of Hα, especially in the first spectrum. While interaction of the SN ejecta with circumstellar matter may be important, it is also possible that the density distribution we have adopted is too simplistic. The latter highlights the need for using the correct physical structure when modelling the SNe.

The sample of photospheric NLTE spectra collected for the SN 2007od, allow us to apply the spectral-fitting expanding atmosphere method (SEAM; Baron et al. 1993, 1995, 1996a; Baron, Hauschildt & Branch 1994) since, in addition to a good overall shape of the spectra, the models predict consistent fluxes. We can derive a distance modulus by subtracting our calculated absolute magnitudes from the published photometry (Inserra et al. 2011), assuming a reddening of $E(B-V)_{\rm tot} = 0.038$. Considering all the epochs, we obtain the distance modulus of the SN, $\mu = 32.5 \pm 0.3$, where the errors include the standard deviation of our fits and the error due to the uncertainty in the interstellar reddening. Since SEAM is strongly dependent on the uncertainties of the explosion date, it seems reasonable to give lower weight to early spectra, since a longer time baseline minimizes the error due to the uncertainties in the explosion day. If we consider only the later observed spectra, from 13.4 to 27.5 d, we find $\mu = 32.2 \pm 0.2$, in good agreement with the value reported in Inserra et al. (2011). Furthermore, model spectra for the last three epochs better fit the observations over the entire spectral range, and the derived distance modulus is comparable with the Mould et al. (2000) measurement within the uncertainties.

Indeed, a good agreement with the Inserra et al. (2011) distance ($\mu = 32.2 \pm 0.3$) is obtained by using all spectra and by taking the explosion date to be JD 245 4403 (2007 October 29). Hence, we conclude that the explosion date is October 29 $\pm$ 1.5 d. The explosion date should always be determined by a χ^2 minimization in a SEAM analysis.

5 CONCLUSIONS

We have shown that both direct synthetic spectral fits and detailed NLTE models do a good job in reproducing the observed optical spectra of SN 2007od,. We have also pointed out that detailed NLTE spectral modelling of early spectra does not support the line identification (Ba II, Fe II or He I) of the 4440 Å as suggested by the SYNOW model or as identified in previous SNe IIP. Rather, we interpret the line as a combination of Fe II and with an additional contribution from a possible HV feature of Hβ. The origin of the line could be due to increased opacity at high velocities due to variation in the level populations not accounted in the simple density profile of PHOENIX or due to possible interaction in the outermost layers. This result suggests extreme caution with line identifications in hot, differentially expanding flows. At the same time, it shows that PHOENIX calculations give reliable results and lend support to the reliability of the modelling. Our spectral analysis shows that during the plateau Sc II lines can arise even with standard solar abundances.

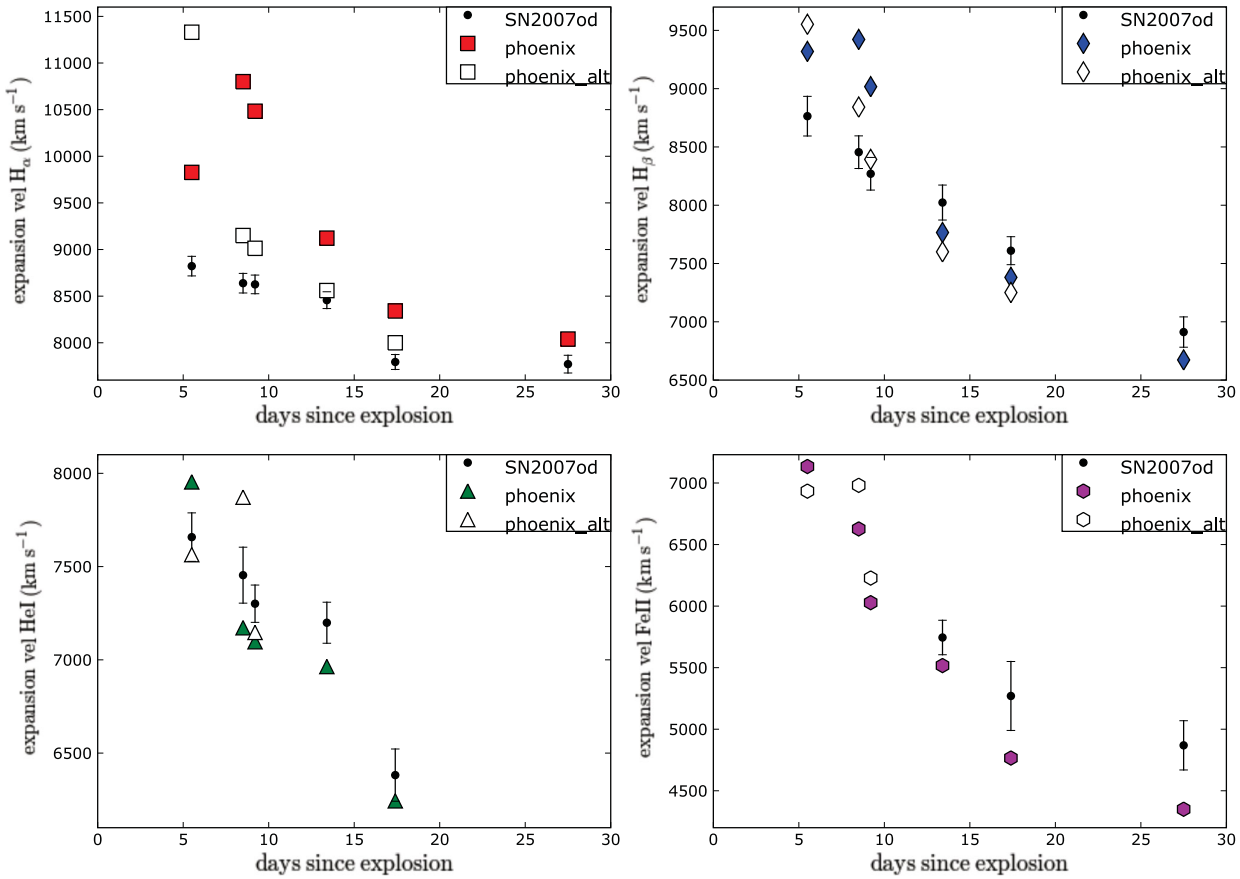

Figure 7. Expansion velocities of Hα, Hβ, He I and Fe II measured from synthetic PHOENIX NLTE spectra compared with those measured from the observed spectra (black dots with error bars) by Inserra et al. (2011). Filled symbols refer to the spectra shown in Fig. 3, while open symbols to spectra calculated with different density indexes ($n = 9$ for the first epoch, $n = 13$ for the following).

Also Si II lines are reliably identified in the spectra of our relatively normal SN IIP at early times. Another important issue is related to the difference between the density profile ($\rho \propto r^{-13}$) needed to reproduce Hα from 8.5 to 17.4 d and the density law required to reproduce the other elements ($\rho \propto r^{-9}$). The evidence for a broken power-law density profile shown by SN 2007od could be a general property of SNe II or may be a consequence of a perturbed ejecta, especially in the outermost layers. We have also discussed the velocity and strength evolution of the principal lines. We have also applied the SEAM to SN 2007od, obtaining good agreement with the distance modulus provided in Inserra et al. (2011) which allows us to better constrain the explosion date (2007 October 29).

ACKNOWLEDGMENTS

This work was supported in part by NSF grant AST-0707704, and US DOE Grant DE-FG02-07ER41517 and NASA programme number HST-GO-12298.05-A. Support for programme number HST-GO-12298.05-A was provided by NASA through a grant from the Space Telescope Science Institute, which is operated by the Association of Universities for Research in Astronomy, Incorporated, under NASA contract NAS5-26555. CI thanks David Branch for the useful discussions. MT is partially supported by the PRIN-INAF 2009 Supernovae Variety and Nucleosynthesis Yields'. We thank the anonymous referee for the useful suggestions that improved our paper.

REFERENCES

Andrews J. E. et al., 2010, ApJ, 715, 541
Baron E., Hauschildt P. H., Branch D., Wagner R. M., Austin S. J., Filippenko A. V., Matheson T., 1993, ApJ, 416, L21
Baron E., Hauschildt P. H., Branch D., 1994, ApJ, 426, 334
Baron E. et al., 1995, ApJ, 441, 170
Baron E., Hauschildt P. H., Branch D., Kirshner R. P., Filippenko A. V., 1996a, MNRAS, 279, 799
Baron E., Hauschildt P. H., Nugent P., Branch D., 1996b, MNRAS, 283, 297
Blondin S., Calkins M., 2007, Cent. Bureau Electron. Telegrams, 1119, 1
Branch D., Jeffery D. J., Blaylock M., Hatano K., 2000, PASP, 112, 217
Branch D. et al., 2002, ApJ, 566, 1005
De S., Baron E., Hauschildt P. H., 2009, MNRAS, 401, 2081
De S., Baron E., Hauschildt P. H., 2010, MNRAS, 407, 658
Dessart L., Hillier D. J., 2007, MNRAS, 383, 57
Fisher A., 2000, PhD thesis, Univ. Oklahoma
Grevesse N., Sauval A. J., 1998, Space Sci. Rev., 85, 161
Harutyunyan A. H. et al., 2008, A&A, 488, 383
Hauschildt P. H., 1992, J. Quant. Spectrosc. Radiative Transfer, 47, 433
Hauschildt P. H., Baron E., 1999, J. Comput. Applied Math., 109, 41
Hauschildt P. H., Baron E., 2004, Mitt. Math. Ges., 24, 1
Inserra C. et al., 2011, MNRAS, 417, 261

Mihalas D., 1970, Stellar Atmospheres. Series of Books in Astronomy and Astrophysics. Freeman, San Francisco
Mikuz H., Maticic S., 2007, Cent. Bureau Electron. Telegrams, 1116, 1
Moskvitin A. S., Sonbas E., Sokolov V. V., Fatkhullin T. A., Castro-Tirado A. J., 2010, Astrophys. Bull., 65, 132
Mould J. R. et al., 2000, ApJ, 529, 786
Pastorello A. et al., 2009, MNRAS, 394, 2266
Patat F., Barbon R., Cappellaro E., Turatto M., 1994, A&A, 282, 731
Richardson D., Branch D., Casebeer D., Millard J., Thomas R. C., Baron E., 2002, AJ, 123, 745
Roy R. et al., 2011, MNRAS, 414, 167
Utrobin V., Chugai N., 2005, A&A, 441, 271
Utrobin V. P., Chugai N. N., 2011, A&A, 532, A100

This paper has been typeset from a TEX/LATEX file prepared by the author.